THE
PHYSICAL REVIEW

A journal of experimental and theoretical physics established by E. L. Nichols in 1893

SECOND SERIES, VOL. 97, NO. 1 JANUARY 1, 1955

Pressure-Volume Isotherms of He^4 below 4.2°K*

WILLIAM E. KELLER
University of California, Los Alamos Scientific Laboratory, Los Alamos, New Mexico
(Received September 23, 1954)

A description is presented of a new apparatus for obtaining PV isotherms at very low temperatures, along with results of measurements on five isotherms at 3.961, 3.348, 2.862, 2.324, and 2.154°K for He^4 gas; the second virial coefficients, B, at these respective temperatures were found to be -83.70, -103.4, -123.6, -157.7, and -176.4 cc/mole. The reliability of previous data as well as of the several analytical treatments of the data is discussed, the conslusion being with respect to the latter that the He^4 isotherms below 4°K can be best represented by the equation $PV/N=RT(1+BN/V)$. When both the previous and the present data are analyzed in this way, a consistent set of values for B is obtained. From the values of RT measured here, corrections to the 1948 temperature scale are obtained in good agreement with modifications suggested by other authors.

I. INTRODUCTION

THE pressure-volume isotherms of He^4 were first determined at low temperatures by Kamerlingh Onnes and co-workers[1] in order to establish corrections to the helium gas thermometer. More recently the isotherms have been of interest primarily for the determination of the second virial coefficient, B, as a quantity useful in connection with the thermodynamic properties of the gas and one intimately associated with the intermolecular potential between two He particles. The demand for precise values of B below the normal boiling point has heretofore been satisfied by Keesom and collaborators[2-4] at Leyden.

It was the present author's original intention to construct an apparatus for the determination of B's for He^3 and to test the equipment by measuring one or two B values for He^4 using the generally accepted values as a guide. During the course of this work significant differences appeared between the present and previous data, an explanation for which was found to be an apparent error that was carried through all the Leyden work. It was therefore considered important to carry out a full-scale redetermination of the second virial coefficients at very low temperatures. We report in this communication a description of the apparatus in that it differs from that used at Leyden and the results of measurements with it on five isotherms of He^4 below 4.2°K.

II. APPARATUS AND EXPERIMENTAL PROCEDURE

In the introduction to their paper[4] Kistemaker and Keesom summarize the important difficulties encountered when one measures isotherms at very low temperature; briefly, these are: (1) uncertainty in determining pressures; (2) inability to maintain the bath at constant temperature for a time sufficiently long that equilibrium be established; and (3) uncertainty in determining the amount of gas in the noxious volumes or "dead" space. The apparatus employed for the present investigation was designed to avoid these difficulties in ways quite different from those used by Kistemaker and Keesom. Since, for the most part, we derived the gas-handling and cryogenic techniques from standard practices, in the following description we shall center our attention on the novel features of the apparatus.

A. Low-Temperature Cell

In order to avoid the difficulties and uncertainties often attendant to the measurement of the amounts of gas in the noxious volumes, the low-temperature cell

* Work done under the auspices of the U. S. Atomic Energy Commission.

[1] Complete references to the early low-temperature isotherm measurements are given in the monograph, *Helium*, W. H. Keesom (Elsevier Press, Amsterdam, Holland, 1942), pp. 31, 32, 143.

[2] W. H. Keesom and H. H. Kraak, Comm. Leiden, No. 234e (1935); Physica 2, 37 (1935).

[3] W. H. Keesom and W. K. Walstra, Comm. Leiden No. 260c (1940); Physica 7, 985 (1940).

[4] J. Kistemaker and W. H. Keesom, Comm. Leiden No. 269b (1946); Physica 12, 227 (1946).

was so designed as to eliminate the necessity for determining these amounts of gas while the gas remains in the connecting lines. The gas in the cell can be isolated from the gas in the connecting lines by a valve, as shown in Fig. 1. Hence measurements of pressure and temperature are made on a given number of moles of gas in the inner can with the valve open; the valve is then shut and the gas in the lines pumped away—to be discarded or sent to the volume-manometer (see below).

If one works above the λ point (2.19°K) of a liquid helium bath, great care must be exercised in order to determine the exact temperature of a gas held in a container immersed in the bath. In addition to the thermal gradient produced by the hydrostatic head of the liquid, transient gradients can arise from the combination of poor thermal conductivity of the liquid, heat leak from the warm portion of the apparatus, and inadequate stirring of the bath. To reduce the effects of these gradients the cell holding the gas [inner can (*A*), Fig. 1] is surrounded by an outer container (*B*) which can be evacuated. Furthermore, the temperature of the gas is measured with a helium vapor pressure thermometer (*C*), the lower end of which is surrounded by the experimental gas and the upper end vacuum jacketed. At the higher temperatures, where dP/dT is large, the thermometer serves as a very sensitive indicator for the attainment of equilibrium conditions in the cell. On the other hand, in order to reach equilibrium it is necessary to maintain the bath temperature essentially constant for periods of about one hour; to effect this control a Sommers-type[5] bath regulator is successfully employed with the heating element placed directly below the cell.

The inner and outer cans are coaxial cylinders of 0.794-mm-wall copper tubing, with respective inside dimensions of 2.311-cm diameter by 2.311-cm length and 3.175-cm diameter by 4.048-cm length. End plates are of 1.588-mm copper sheet except for the top of the inner can, which is copper 2.381 mm thick. All tubing connected to the cell is of thin-wall K-monel or inconel; the inside diameter of the vapor pressure thermometer tube is 1.422 mm. Solder connections to the inner can were made with helium gas flowing through it to avoid oxidation of the inner surfaces.

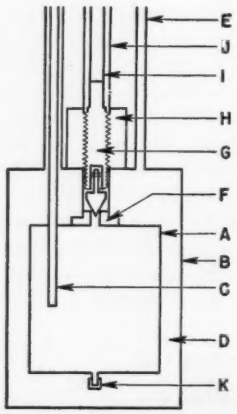

FIG. 1. Schematic diagram of low-temperature cell. *A*, inner can; *B*, outer can; *C*, vapor pressure thermometer; *D*, exchange gas or vacuum space; *E*, pumping tube; *F*, valve seat; *G*, valve stem; *H*, valve stem guide; *I*, valve stem extension; *J*, sample tube; *K*, seal of tube used during calibration.

Some of the details of the valve assembly are shown in Fig. 1. The valve seat (*F*) is copper and has an orifice 1.588 mm in diameter. A threaded cylinder of monel (*H*) (32 threads per inch) guides the stainless steel valve stem (*G*), while the tip of the stem possesses one degree of freedom so that it may find its own seat. Four slots 0.794 mm wide by 0.794 mm deep have been milled the length of the threaded portion of the stem to allow the passage of gas from the inner can to the anulus (inside diameter 3.175 mm; outside diameter 4.597 mm) formed by the extension of the valve stem (*I*) and the sample tube (*J*). The valve stem extension continues to the top of the cryostat and becomes accessible for operation by emerging from the sample space to the atmosphere through a double O-ring seal.

Calibration of the volume of the inner can was carried out only after the valve was opened and tightly closed many times in order to establish the final (or very nearly so) deformation of the seat. From the weight of air free distilled water the cell contained at 31.20°C, the cell volume at that temperature was determined to be 9.5907 cc with an average deviation of 0.0009 cc; from this value and with use of the formula for the thermal expansion of copper given by Keesom, van Agt, and Jansen[6] the volume of the cell at 20°K was calculated to be 9.4927 cc. It is assumed that no further volume changes take place on lowering the temperature to the liquid helium region.

B. Manometry

In the course of the experiment there are three sets of pressure measurements which must be made with high accuracy: that of the gas in the cell, in the vapor pressure thermometer, and in the volume-manometer. All of the manometers used for these determinations (with the exception of one arm of the volume-manometer—see below) are encased in a Lucite box, the air in which is vigorously circulated and accurately thermostated. Several Hg-in-glass thermometers resting in pools of mercury are placed at critical positions in the box. The manometers are viewed through a distortion-free section of plate glass with a 800-mm range Wild cathetometer, on which the scale reading may be safely estimated to 0.01 mm. An Invar standard meter-bar mounted adjacent to the manometers is used to calibrate the cathetometer scale, though invariably when the two are compared no correction need be applied to the latter within the precision of the measurements (±0.02 mm for full scale length).

[5] H. S. Sommers, Jr., Rev. Sci. Instr. **25**, 793 (1954).

[6] Keesom, van Agt, and Jansen, Comm. Leiden, No. 182a (1926).

The manometers for measuring the cell pressure (for $P>40$ mm Hg) and the helium vapor pressure each have a bore of 20 mm in diameter and are filled with mercury. Capillary depression corrections are applied according to tables given by Blaisdell,[7] although for the wide tubes used, the correction is never greater than 0.01 mm and seldom that large. Thermometer pressures are corrected to read in mm Hg at 20°C to coincide with those on the 1948 temperature scale; others are corrected to 0°C. A correction for the acceleration of gravity at Los Alamos is applied to all pressure readings.

For cell pressures less than 40 mm Hg a 20-mm bore manometer filled with dibutyl sebacate is employed. Before the manometer was filled, the oil was boiled to rid it of volatile components and occluded air, and a sample was then taken for density determinations. The density of the oil was measured with a 20 cc pycnometer at close temperature intervals extending over the range in which pressure readings were to be made. Five measurements between 27 and 32°C showed the density-temperature relationship to be linear within 1 part in 100 000. It is interesting to note that a similar determination on the unboiled oil resulted in a curve exactly parallel to that for the boiled oil but with density values lower by 1 part in 1500 at the same temperature. With this oil manometer it is possible to read pressures to 0.002 mm Hg.

Figure 2 shows schematically the volume-manometer with which amounts of gas in the cell are determined. Gas is admitted to the glass bulbs through the tube on the left (inside diameter 1.0 mm) whereupon mercury is brought up to fiducial mark 4. A choice of which of the three volumes is to be used is made according to the arbitrary rule that the pressure to be measured be greater than about 150 mm Hg. Mercury from the reservoir is brought up approximately to the appropriate fiducial mark—1, 2, or 3; reproducible (±0.01 mm) final positioning of the meniscus is accomplished by remote manipulation of the motor-driven plunger with the experimenter monitoring the operation through the cathetometer telescope.

The three bulbs have nominal volumes of 200, 100, and 50 cc. Volumes 1–2 and 1–3 were calibrated by determining the weight of mercury contained between the fiducial marks; volumes 2–4 and 3–4 were obtained from P-V-T measurements with He gas, using 1–2 as a standard. From these measurements consistent values were obtained for the volumes to be used, i.e., 1–4, 2–4, and 3–4, as 363.23±0.02 cc, 150.31±0.02 cc, and 47.753±0.016 cc, respectively (probable errors are given). All straight lengths of glass tubing, with the exception of the 1 mm capillary, are 10 mm inside diameter. The fiducial markers are centered in the tube and are attached to the tubing about 2 cm above the tip so that there is no distortion of the tubing where the menisci are to be read.

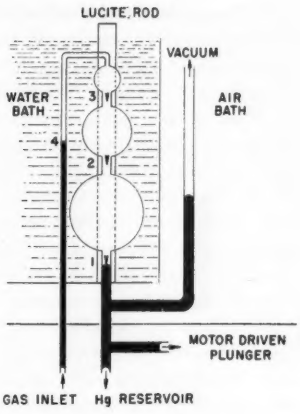

FIG. 2. Schematic arrangement of the volume-manometer.

A water bath surrounding the glass bulbs is thermostated to ±0.01°C and is maintained at a temperature no more than 1°C different from that of the air bath surrounding the other arm of the manometer. A Beckmann thermometer, direct reading to 0.01°C and calibrated against the $Na_2SO_4 \cdot 10H_2O$ transition temperature, is used to measure the water bath temperature. Optically, the water bath presents some problems, the most serious of which is a possible prism effect. To avoid this difficulty the plate glass window forming the side of the bath and through which the menisci are viewed is maintained perpendicular to the line of sight of the telescope. Frequent zero-pressure readings confirmed the absence of prism effects. Proper illumination of the menisci at the fiducial marks is accomplished by directing a beam of light down a 2-cm diameter rod of Lucite standing vertically in the water directly behind the marks (Fig. 2); horizontal cuts 1 cm wide at proper places on the rod scatter the vertical light beam and serve as excellent backgrounds for viewing the profiles of the menisci.

C. General Experimental Procedure

A typical experimental run begins, once the apparatus is cooled down to the approximate temperature of the run, with the filling of the cell and vapor pressure thermometer, helium exchange gas being in the space between the two cans. The helium gas used in the experiment is obtained from commercial tanks and is purified by passing through a charcoal trap at liquid air temperatures; any air picked up during gas-handling is removed from the experimental gas as it passes through a U-tube, partially immersed in the helium bath, before it enters the cell-filling line. After the cell is filled the U-tube is isolated from the experimental gas by closing a stopcock, the exchange gas is pumped away, and equilibrium is awaited.

Once equilibrium is obtained, the bath pressure, the vapor pressure thermometer, and the cell pressure are

[7] B. E. Blaisdell, J. Math. Phys. **19**, 217 (1940).

read. Immediately the cell valve is closed (in order to avoid a significant change in the volume of the system on closing the valve, during the wait for equilibrium the valve is kept open by 1/4 to 1/2 a turn). The gas in the lines is then pumped away and the valve opened for the next pressure measurements. Pressures are again read and the valve again closed. After the valve is closed this time—and succeeding times—the gas in the lines is pumped to the volume-manometer where we measure the decrement of the amount of gas corresponding to the drop of pressure in the cell. To test that all the gas has been removed from above the valve and to detect a possible leak through the valve, the pressure in the cell line is observed with the oil manometer. Excessive leak-up—greater than 1/5000 of the last cell pressure measured—is cause for discarding the run.

The cycle of measuring the cell pressure and the decrement of gas is continued until the lowest pressure and corresponding decrement is determined; then all of the gas remaining in the cell is pumped to the volume-manometer. By adding up all the decrements one may arrive at the amount of gas appropriate to the highest pressure, and so on. As few as one point and as many as four points on an isotherm were determined in a single run, this variation being an effort to determine the reproducibility of the experiment when we slightly change factors which should not affect the results.

III. RESULTS AND DISCUSSION

A. Data and Errors

Table I represents a collection of the data obtained for the five isotherms determined in the present investigation. In this table under the "Exp. No." column, A-9-1, for example, is to be interpreted as: isotherm A,

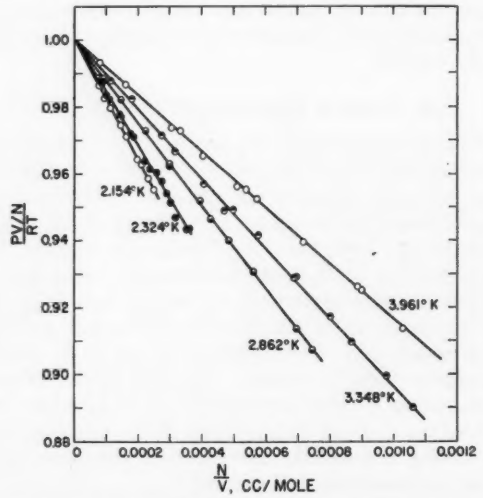

FIG. 3. Plot of $(PV/N)/RT$ *vs* N/V for He^4 gas below 4°K. Values of RT are taken from two-constant analysis.

TABLE I. Experimental data for the isotherms of He^4.

Exp. No.	P mm Hg	$(N/V)\times10^4$ cc/mole	$T_{vap(48)}$ °K	$(PV/N)_{corr}$ cc-mm/mole	δ_2
		$T_{48}=3.61$°K			
A-8-1	202.40	8.8713	3.956	228 713	− 90
A-8-2	127.30	5.4105	3.955	235 907	−135
A-8-3	80.65	3.3679	3.953	240 214	−227
A-9-1	205.45	9.0060	3.960	228 436	− 91
A-9-2	135.16	5.7515	3.961	235 250	−185
A-9-3	74.08	3.0817	3.963	240 452	126
A-11-1	231.49	10.2718	3.961	225 614	118
A-11-2	116.58	7.1878	3.961	232 002	98
A-11-3	120.67	5.1171	3.960	236 128	247
A-12-1	96.98	4.0649	3.968	238 393	155
A-12-2	40.095	1.6462	3.965	243 565	− 23
A-12-3	20.231	0.8252	3.963	245 232	− 6
		$T_{48}=3.348$°K			
B-1-1	163.01	8.6759	3.325	189 524	153
B-1-2	113.00	5.7961	3.332	196 152	−280
B-1-3	36.676	1.8002	3.336	204 674	−206
B-2-1	182.97	9.7495	3.355	187 415	− 48
B-2-2	133.89	6.9067	3.356	193 539	− 56
B-2-3	93.79	4.7326	3.359	197 677	483
B-3-1	64.23	3.1835	3.357	201 384	109
B-4-1	134.40	6.9601	3.343	193 592	−224
B-4-2	98.98	5.0149	3.345	197 745	−196
B-4-3	56.00	2.7703	3.347	202 391	− 10
B-4-4	24.422	1.1877	3.349	205 756	30
B-5-1	196.13	10.5701	3.352	185 486	116
B-5-2	153.56	8.0253	3.354	191 154	− 78
B-5-3	81.63	4.0860	3.358	199 339	212
		$T_{48}=2.862$°K			
C-3-1	66.95	3.9594	2.854	169 717	−147
C-3-2	25.923	1.4791	2.866	175 132	−103
C-4-1	120.85	7.4690	2.864	161 801	− 44
C-4-2	81.55	4.8679	2.863	167 590	− 20
C-4-3	51.85	3.0197	2.864	171 706	− 68
C-4-4	16.844	0.9553	2.866	176 193	− 11
C-5-1	113.71	6.9623	2.871	162 881	79
C-5-2	72.72	4.2949	2.873	168 753	78
C-5-3	52.10	3.0250	2.874	171 608	19
C-5-4	14.030	0.7926	2.876	176 261	279
C-6-1	93.61	5.6311	2.869	165 921	− 31
C-6-2	39.109	2.2490	2.871	173 454	−119
		$T_{48}=2.324$°K			
D-2-1	40.346	2.9234	2.325	138 072	− 17
D-2-2	25.103	1.7845	2.326	140 671	− 19
D-2-3	12.905	0.9021	2.330	142 807	−144
D-3-1	48.52	3.5557	2.325	136 519	94
D-3-2	26.510	1.8849	2.328	140 522	− 99
D-4-1	31.010	2.2310	2.318	139 498	136
D-5-1	44.14	3.2104	2.317	137 025	376
D-5-2	15.684	1.1042	2.324	142 169	34
D-6-1	37.530	2.7069	2.321	138 959	−410
D-6-2	20.574	1.4527	2.328	141 502	− 94
D-9-1	38.318	2.7686	2.323	138 589	−181
D-9-2	16.887	1.1901	2.329	141 707	300
D-10-1	49.62	3.6394	2.323	136 530	−107
D-10-2	33.560	2.4085	2.328	139 217	12
D-10-3	14.278	1.0006	2.332	142 325	114
D-11-1	41.65	3.0443	2.312	137 684	95
D-11-2	20.772	1.4751	2.316	141 444	− 87
		$T_{48}=2.154$°K			
E-1-1	19.138	1.4664	2.155	130 509	− 38
E-2-1	30.106	2.3463	2.154	128 375	18
E-2-2	14.989	1.1429	2.154	131 216	19
E-3-1	25.852	2.0024	2.154	129 169	37
E-3-2	12.406	0.9431	2.154	131 606	101
E-4-1	27.738	2.1448	2.161	128 952	− 83
E-4-2	10.718	0.8084	2.163	132 082	− 57
E-5-1	32.275	2.5216	2.156	127 931	48
E-5-2	21.604	1.6595	2.157	130 062	− 47

run number 9, point number 1. Entries missing in the "run number" column indicate discarded or discontinued runs; for example, four early runs on isotherm A were discarded because the temperature was measured from the bath pressure with correction for the bath height above the cell and not from the more reliable vapor pressure thermometer—these four runs yielded a curve parallel to the accepted one, but displaced about 0.005° in temperature.

It will be observed that for the isotherms at the two highest temperatures, A and B, the largest pressures measured are, respectively, only 39 percent and 67 percent of the saturation pressures. Since the main object of the experiment is the determination of second virial coefficients, i.e.,

$$\left[\frac{d(PV/N)}{d(N/V)}\right]_{P=0} \quad \text{or} \quad \left[\frac{d(PV/N)}{dP}\right]_{P=0},$$

ranges limited in the above way are considered adequate; consequently we concentrate on the low pressure region. The lower limit of pressure is determined by the fact that thermomolecular pressure corrections are not accurately known for a tube with annular cross section; from the geometry of the tube and by analogy with the circular cross section corrections, a conservative estimate was made that no corrections within experimental error need be applied to pressures larger than 10 mm Hg. For isotherms C, D, and E, the measurements were carried up to a large fraction of the saturation pressure because of the limited pressure range before the onset of liquefaction. Even in the case of isotherm D where P/P_{sat} is the largest—93.6 percent—calculations based on the results of Bowers[8] indicate that the amount of gas adsorbed on the cell walls is far from significant.

Although one may represent the PV/N product for a gas in terms of a power series in either the pressure or the density, there is *a priori* no way to determine which of these offers the better description. Analytically, the coefficient of the linear term—the second virial coefficient, B—is the same for both representations; but, in practice, the same data usually produce different values of B from the two methods. We have therefore adopted the procedure of using that representation which exhibits the least curvature, for in this way the extrapolation of the slope from finite values of P or N/V to zero is less indefinite. We are able to demonstrate that for He^4 at low temperatures the expansion in N/V is to be preferred, and that in order to achieve the same accuracy in B's using the pressure expansion, one should obtain data at pressures an order of magnitude lower than our lowest pressures.

It follows then that, since all the points of an isotherm are not taken at exactly the same temperature (Table I, column 4; temperatures determined from the vapor pressure thermometer and the 1948 scale[9] are given) a correction to the raw PV/N product must be made in the following form:

$$\Delta\left(\frac{PV}{N}\right)=R\Delta T\left[1+\frac{N}{V}\left(B+T\frac{dB}{dT}\right)\right]. \qquad (1)$$

Since B is negative and dB/dT positive for the isotherms measured here, the term in inner parentheses is small so that in most cases $R\Delta T$ is the only significant term. Where the term $(B+TdB/dT)$ could not be neglected, values of B and dB/dT were taken from Table I of the paper[10] by Kilpatrick, Keller, Hammel, and Metropolis. Corrected PV/N products are given in column 5 of Table I.

Figure 3 shows the data graphically: the isotherms are reduced to the same ordinate by plotting $(PV/N)/RT$ *vs* N/V, for which RT was obtained from the linear fit to the data.

Perhaps the best picture of the precision of the measurements can be obtained from the probable error in the individual points and in the constants calculated from these points; these probable errors for fitting the data with a linear equation by the method of least squares are shown in lines 2, 5, and 6 of Table II. Column 6 of Table I shows the individual residuals (δ_2) for the linear equation. The rather wide scatter in the points for isotherm D is attributed to poor temperature control. For this isotherm most of the points were obtained with the bath regulator working inefficiently—it is believed that tape wrapped around the heater prevented free bubble formation; and in the region just above the λ point vigorous stirring of the bath is important. When the tape was removed, much better control resulted, though none of the points measured previous to this could be considered bad enough to

TABLE II. Calculations from the data.

Isotherm T_{48} °K	A 3.961	B 3.348	C 2.862	D 2.324	E 2.154
Results using two-constant equation					
1. $A=RT$, cc-mm/mole	246 942	208 341	178 285	144 720	133 934
2. p.e.[a] in A, °K	0.0010	0.0014	0.0008	0.0010	0.0007
3. $T_{48}-T_{\text{isotherm}}$	0.0012	0.0073	0.0032	0.0034	0.0063
4. B, cc/mole	−83.70	−103.4	−123.6	−157.7	−176.4
5. p.e.[a] in B, cc/mole	0.43	0.65	0.61	1.79	1.82
6. p.e.[b] of a measured point, %	0.04	0.07	0.05	0.09	0.03
7. N/V of saturated vapor, g/cc	0.01315	0.00671	0.00369	0.00155	0.00109
8. $\Sigma\delta_2^2/(n-2)=E_2$	24 536	45 608	14 495	36 129	4050
Results using three-constant equation					
9. A, cc-mm/mole	246 921	208 297	178 134	144 488	133 768
10. B, cc/mole	−83.31	−102.4	−117.8	−140.8	−159.3
11. C, cc^2/mole^2	−358	−823	−7282	−3855	−5231
12. $\Sigma\delta_3^2/(n-3)=E_3$	27 125	49 504	12 031	37 144	4167
13. $Q=E_3/E_2$	0.905	0.921	1.205	0.973	0.972

[a] The probable error (p.e.) is calculated according to equations given by R. T. Birge, Phys. Rev. 40, 207 (1932).
[b] Calculated from the equation: p.e. $=0.6745[\Sigma\delta_2^2/(n-1)]^{\frac{1}{2}}$.

[8] R. Bowers, Phil. Mag. 44, 485 (1953).

[9] H. Van Dijk and D. Shoenberg, Nature 164, 151 (1949).

[10] Kilpatrick, Keller, Hammel, and Metropolis, Phys. Rev. 94, 1103 (1954).

discard. Indeed, it is felt that the large scatter of some other points such as B-2-3 and D-6-1, can also be attributed to nonequilibrium resulting from poor bath control. Evidence for this conclusion is found in the high precision in the measurements of the isotherm at 2.153°K. One would expect that because of the lower pressures and smaller amounts of gas involved, errors in P and N/V would be larger here than in the other isotherms; however, the temperature control was excellent, and below the λ point equilibrium was more rapidly established than above it.

B. Virial Coefficients

In the last section we mentioned only results derived from fitting the data with a two-constant equation, whereas previous authors[2–4] have analyzed their data in terms of three-constant equations, and, in one case, a four-constant equation. It is indeed obvious that if one has n sets of data the n sets will be better fitted the more constants are employed, this process reaching a limit in an n-constant polynomial exactly satisfied by all n-sets. However, the questions arise: What is the significance of these constants, and where does one stop this process? To answer these questions for our data, we proceed to justify the linear treatments.

For each isotherm, the data were fitted with two polynomials of the form

$$PV/N=a+b(N/V)+c(N/V)^2+\cdots,$$
$$a=A=RT;\quad b=aB;\quad c=\breve{a}C;\quad \text{etc.},\qquad (2)$$

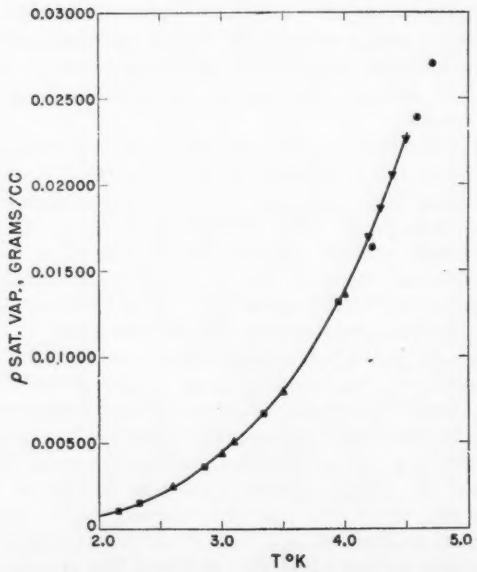

FIG. 4. Plot of the density of the saturated vapor of He^4 *vs* temperature. ● Mathias *et al.*; ▲ calculated from Keesom's accepted values of B and C; ▼ Berman *et al.*; ■ calculated from B's of the present work (two-constant equation).

in the first instance retaining only the first two terms and in the second only the first three terms. The constants obtained from these analyses are given on lines 1, 4, 9, 10, and 11 of Table II, from which it is seen that there is a significant difference in the B's obtained, especially for isotherms C, D, and E. One semiquantitative test which may be applied to effect a choice between the two analyses is to examine the quantity Q:

$$Q=E_k/E_{k'}=\left(\frac{\sum\delta_k^2}{n-k}\right)\Big/\left(\frac{\sum\delta_{k'}}{n-k'}\right),\quad k<k',\qquad (3)$$

where $\sum\delta_k^2$ is the sum of the squares of the deviations of the n experimental points from the k-constant equation. Setting $k=2$ and $k'=3$, we obtain the values of E_2, E_3 and Q as given on lines 8, 12, and 13 of Table II. For isotherms A, B, D, and E we see that Q is less than unity, indicating that the addition of a third constant is not only superfluous, but may even cause the data to be misrepresented. The value of Q for isotherm C does not depart sufficiently from unity to warrant inclusion of the square term in the equation. An alternate statement of the above conclusion is that the addition of a square term does not significantly lower the probable error of a measured point since the curvature introduced is of the same order of magnitude as the scatter of the points. This can be seen to be so, qualitatively, by examining Fig. 3. Especially for the two end isotherms, A and E, it is difficult to imagine how any curve but a straight line could be drawn to represent the data.

That the results of the two-constant fit are consistent with thermodynamic data, we cite the values of the density of the saturated vapor of He^4 above 4.2°K recently calculated by Berman and Swenson[11] from latent heat measurements of Berman and Poulter.[12] Four of the values given in reference 11 are plotted in Fig. 4 along with those measured by Mathias, Crommelin, Onnes, and Swallow,[13] those calculated from Keesom's "adopted values" of the virial coefficients,[14] and those calculated from our B's determined with the linear equations (Table II, line 7). A curve passing through the points of Berman and Swenson joins nicely onto the section determined by points of the present investigation. Below about 2.5°K, the values of the vapor density are relatively insensitive to the exact value of B.

A more qualitative argument is one which requires the plot of B *vs* T to be smooth. Figure 5 shows such a plot for a variety of data: Keesom's B's re-evaluated (see below) using a linear and a quadratic fit, Kistemaker's B's re-evaluated, and the present values of B determined by two- and three-constant equations. It is

[11] R. Berman and C. A. Swenson, Phys. Rev. **95**, 311 (1954).
[12] R. Berman and J. Poulter, Phil. Mag. **43**, 1047 (1952).
[13] Mathias, Crommelin, Onnes, and Swallow, Comm. Leiden, No. 172b (1926).
[14] See reference 1, p. 49.

TABLE III. Re-evaluation of data of Keesom and Walstra.

Isotherm °K[a]	4.245	3.721	3.105	2.610
Results using two-constant equation				
1. $A=RT$, cc-mm/mole	264 463	232 283	194 129	163 434
2. B, cc/mole	−74.45	−89.7	−114.6	−138.1
3. p.e. of a measured point, %	0.08	0.09	0.025	0.10
Results using three-constant equation				
4. A, cc-mm/mole	265 206	231 705	193 750	163 017
5. B, cc/mole	−78.25	−85.2	−108.3	−123.8
6. C, cc³/mole²	1013	−1747	−4361	−18 300
7. p.e. of a measured point, %	0.04	0.08	0.016	0.10
8. $Q=E_2/E_3$	4.454	0.991	1.808	0.981
Reported results of Keesom and Walstra				
9. A, cc-mm/mole	264 753[b]	232 095	193 660	162 809
10. B, cc/mole	−75.49	−87.9	−107	−118
11. C, cc³/mole²	−131	−779	−5280	−24 100

[a] These isotherms are labeled by the temperature given by Keesom and Walstra (reference 3).
[b] Keesom and Walstra give a value of D for this isotherm.

seen that when all the data are fitted to linear equations, B *vs* T is smoother than when fitted to quadratic equations, indicating that the former representation is to be preferred. The solid line in the figure represents a theoretical curve[15] calculated from potential constants which give the best fit to the low-temperature and high-temperature experimental second virial coefficients and high-temperature transport properties. Since the shape of the curve is not affected by a change in potential constants, it follows that its position could be adjusted by a fit of these constants to one experimental point. The nature of the agreement of this curve with all the "two-constant" B's is therefore extremely gratifying. On the other hand, whereas the present data and those of Keesom *et al.* yield a consistent set of B's calculated from two-constant equations, the values of C obtained from all the data by no means form a smooth pattern.

All of the above evidence taken together presents a compelling argument for terminating the virial expansion after the second term for the existing data on He⁴ gas below 4°K. This does not preclude the possibility that in the future more accurate measurements will determine precise nonzero C's; but we strongly suspect that B's from these data will be closer to the values we select here than those given by the present quadratic expressions. It may appear anomalous that the third virial coefficient of the gas be unimportant over a considerable temperature range, but then there is no theory which at present can predict the behavior of C. Incidentally, C being zero or small for the density virial expansion implies that the third and possibly higher coefficients for the pressure expansion are of importance.

C. Data of Keesom *et al.*

We must now seek an explanation for the disagreement between the published virials of Keesom *et al.* and the ones determined in the present investigation. In their paper, Keesom and Walstra[3] state that the analysis of the data was carried out independent of the temperature and that the calculated values of A confirmed that they measured the temperature of the isotherms correctly. However, when we analyzed the isotherm data of Keesom and Walstra using the method of least squares, quite different results were obtained as shown in Table III. If, on the other hand, one treats the data with a quadratic least-squares analysis keeping A *fixed* by the temperature (i.e., treating RT as an experimental point), one arrives at the published values of B and C. From the arguments presented in the second paragraph of Sec. II-A of this paper and from the fact that the temperature scale used by Keesom is at present considered to be in error, the fixing of A in the above manner is highly susceptible to criticism. A dramatic effect in the change of B resulting from a change in temperature scale may be observed by comparing the

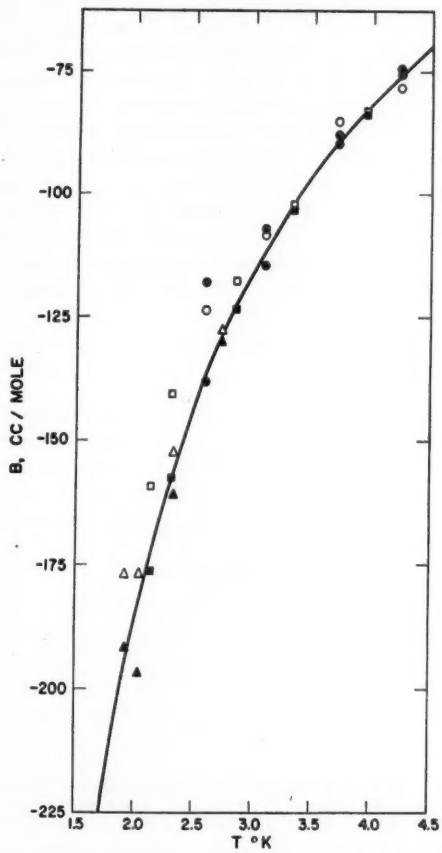

FIG. 5. Plot of B *vs* T. ⊕ Original values of Keesom and Walstra; ○ same data re-evaluated by three-constant equation; ● same data re-evaluated by two-constant equation. △ Original values of Kistemaker and Keesom; ▲ same data re-evaluated by two-constant equation. □ present data, three-constant equation; ■ same data, two-constant equation. Solid line represents theoretical curve.

[15] Kilpatrick, Keller, and Hammel, following paper [Phys. Rev. 97, 9 (1955)].

isotherms of Keesom and Kraak[2] with those of Keesom and Walstra.[3]

A glance at line 8 of Table III discloses that perhaps the choice between a two-constant and a three-constant fit to the Dutch data is not quite so clear-cut as in the case discussed above. Indeed, the fact that for the isotherm at 4.245°K there are 18 experimental points and the probable error of a point is reduced by a factor of two when the data are fitted to an equation with three constants rather than two, suggests that the C for this isotherm possesses significance. On the other hand, for the 3.105°K isotherm one is inclined to discount the increased precision on adding a third constant since there are only five experimental points for this temperature. Also it is highly unreal to consider C important for this isotherm when the value of Q for isotherms on either side indicate negligible C's for these.

We have already observed that when our experimental data along with those of Keesom and Walstra are represented by two constant equations a remarkably consistent set of B's is obtained. This indicates that the resultant of the systematic errors in both investigations either is in the same direction and of nearly same magnitude, or, what is more probable, is quite small. Here too is seen an advantage of the density expansion over the pressure expansion, for the agreement in B's is achieved in spite of the fact that Keesom and Walstra's lowest pressures are correspondingly much higher than ours, *viz.*: on the 4.245°K isotherm the lowest pressure is 105 mm Hg; at 3.721°K, 96.8 mm; at 3.105°K, 61.8 mm; and at 2.610°K, 28.7 mm. For the pressure range of our measurements we again refer the reader to Table I.

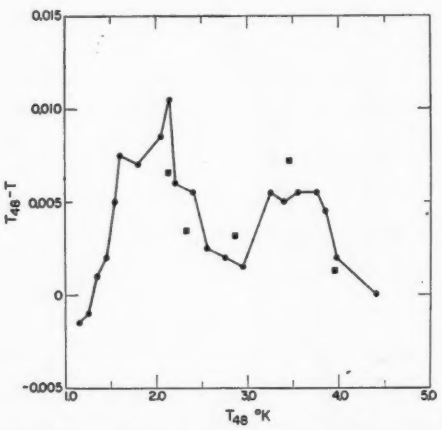

FIG. 6. Plot of deviations of the thermodynamic temperature from the 1948 scale *vs* T. ● Average values of Erickson and Roberts (Fig. 4, reference 17); ■ from isotherms of present work.

Accepting the conclusion that C is insignificant at least for the lowest three isotherms of Keesom and Walstra, the data of Kistemaker and Keesom[4] must be re-evaluated. Since the data for the isotherms below 2.7°K are not sufficiently precise to determine C's directly, the latter authors corrected their measured PV/N products using C's extrapolated from Keesom and Walstra's smoothed values of C above 2.7°K (these of course are erroneous even if the three-constant analysis were correct); the adjusted PV/N products were then used to determine B's. These and the B's that result if the corrections for C are not made are shown in Fig. 5.

D. The Temperature Scale

The type of measurements described here may serve to establish a thermodynamic temperature scale and at the same time to calibrate a convenient thermometric substance. Values of A divided by the gas constant R yield the absolute temperatures of the isotherms, which may be correlated with the vapor pressure of the liquid He in the thermometer. It has been suggested by Kistemaker[4,16] and more recently by Erickson and Roberts[17] from magnetic data that the 1948 temperature scale[9] is in error below 4.2°K. More weight is added to this conclusion by the present measurements, as shown on line 3 of Table II and in Fig. 6, where the deviations of the isotherm temperatures from the 1948 temperatures are compared with the average of all the magnetic data (reference 17, Fig. 4). The magnetic measurements are given relative to the chosen value for the temperature of the normal boiling point of He^4, whereas the isotherm data are independent of this value. However, Berman and Swenson[11] conclude that the accepted value of the boiling point is accurate to ±0.002°. It is seen from Fig. 6 that the agreement is within about 0.002° for the four highest isotherms and about 0.004° for the lowest; this is considered quite satisfactory, and is further confirmation of the above conclusion.

ACKNOWLEDGMENT

The author with great pleasure expresses his appreciation to Professor J. E. Kilpatrick and Drs. E. F. Hammel and H. S. Sommers, Jr., for many helpful suggestions and fruitful discussions during the course of the work; also to Mr. M. Goldstein and his group, who performed most of the least-squares calculations.

[16] J. Kistemaker, Physica **12**, 272, 281 (1946).
[17] R. A. Erickson and L. D. Roberts, Phys. Rev. **93**, 957 (1954).

Second Virial Coefficients of Helium from the Exp-Six Potential*

JOHN E. KILPATRICK,† WILLIAM E. KELLER, AND EDWARD F. HAMMEL
Los Alamos Scientific Laboratory, University of California, Los Alamos, New Mexico
(Received September 23, 1954)

A set of potential constants for the He-He exp-six intermolecular potential has been found which leads to calculated results in good agreement with the experimental second virial coefficients of He^4 both at high and at low temperatures and with the high-temperature viscosity and thermal conductivity data. A table of the second virial coefficients of He^3 and He^4 over the temperature range 0.3°K to 60°K is given. The position of a negative discrete energy as a function of some of the parameters of the exp-six potential has been investigated.

I. INTRODUCTION

RECENTLY we have published[1] the results of our calaulation of the second virial coefficients of He^3 and He^4 with a Lennard-Jones 12–6 intermolecular potential. For two reasons it has seemed desirable to repeat these calculations with a different type potential: (1) Mason,[2] Rice and Hirschfelder,[3] and Mason and Rice[4] have shown that the Lennard-Jones 12–6 potential is not capable of giving as good a representation of the high temperature equation of state and transport data for He^4 as is the exp-six potential (variously known as the Slater-Kirkwood, the modified Buckingham, the Mason-Rice, and the exp-six potential); (2) in the light of the work done recently by Keller[5] on the second virial coefficients of He^4 at low temperatures, it now appears that the true experimental values are distinctly more negative than is indicated by the results of earlier authors. In addition, these new data and re-analyzed older data lead to values of B that are considerably more consistent and are probably more accurate than the second virial coefficients previously published. We first calculated the second virial coefficients of He^4, using the exp-six potential with the constants given by Mason and Rice.[4] Since the calculated B's from this potential were not in good agreement with the low-temperature experimental data, the potential constants were modified in such a way as to preserve the agreement with the high-temperature data and also to give a good fit to the low-temperature second virial coefficients.

II. METHOD

The numerical method used in this work closely parallels that used in reference 1. The following modifications were made:

(1) The radial scaling factor was arbitrarily set at $\rho=2.77$A in order that the exp-six potential should have a zero at about the same location as that of the 12–6 potential used in reference 1.

(2) The integration pattern was $R=0.625$ (1/128) 1.5 (1/64) 16, rather than 0.625 (1/128) 1.5 (1/64) 4 (1/32) 8 as used in reference 1. This change resulted in somewhat higher accuracy in the phase shifts for the higher energies.

(3) The pattern of the reduced energy or wave-number parameter q was $q=0$ $(\frac{1}{8})$ 10.5 $(\frac{1}{2})$ 18. The wider spacing was shown to result in no appreciable loss in accuracy in the calculated virials, and the increased range eliminated the necessity for a tail-end correction on the integral for the virials at 50°–60°K.

(4) The junctions of the numerically integrated phase shifts to the Born approximation phase shifts were made uniformly according to the formula $l^*=[aq]$, where $a=3$ for He^4 and $a=4$ for He^3, the square brackets indicate the largest even integer contained in aq, and l^* is the last even l (and l^*+1 the last odd l) for which phase shifts were calculated numerically.

The natural constants used in this work are as follows:

Boltzmann's constant:	$k=1.380257\times10^{-16}$,
Planck's constant:	$h=6.62377\times10^{-27}$,
Avogadro's number:	$N_0=6.02380\times10^{23}$,
Atomic weight He^4:	4.00390,
Atomic weight He^3:	3.01700.

III. POTENTIALS

The several exp-six potentials used in this work will be designated by $MR1$, $MR2$, etc., and the Lennard-Jones 12–6 potentials used in reference 1 similarly by $LJ1$, $LJ2$, and $LJ2'$. The exp-six potential was taken in the standard form

$$V(r)=\frac{\epsilon}{1-6/\alpha}\left[\frac{6}{\alpha}e^{\alpha(1-r/r_m)}-\left(\frac{r_m}{r}\right)^6\right]. \quad (1)$$

The constant ϵ (given in this work as ϵ/k °K) is the depth of the potential minimum, r_m is the value of r at the minimum, and α determines the hardness of the repulsive core.

It is immaterial that this potential has a maximum at $r\ll r_m$ and then approaches minus infinity as r goes

* Work performed under the auspices of the U. S. Atomic Energy Commission.
† Department of Chemistry, The Rice Institute, Houston, Texas.
[1] Kilpatrick, Keller, Hammel, and Metropolis, Phys. Rev. **94**, 1103 (1954).
[2] E. A. Mason, J. Chem. Phys. **22**, 169 (1954).
[3] W. E. Rice and J. O. Hirschfelder, J. Chem. Phys. **22**, 187 (1954).
[4] E. A. Mason and W. E. Rice, J. Chem. Phys. **22**, 522 (1954).
[5] W. E. Keller, preceding paper [Phys. Rev. **97**, 1 (1955)].

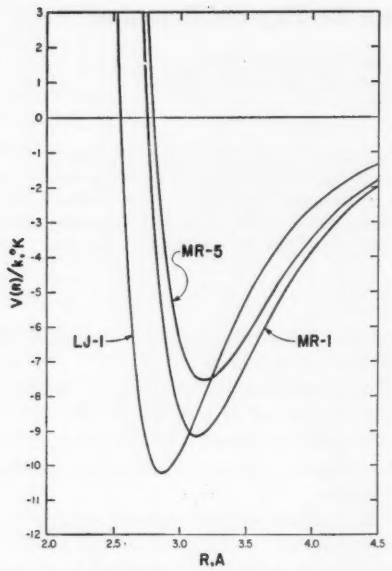

FIG. 1. Potential of interaction of two He atoms.

to zero. The phase shifts are not appreciably affected by the portion of the potential near the origin in the range of potential constants used.

In Table I the potential constants for the various exp-six potentials used in this work are listed, together with the constants of some Lennard-Jones 12–6 potentials and the original theoretical Slater-Kirkwood[6] potential. Figure 1 shows graphically the relation of potentials *LJ*1, *MR*1, and *MR*5.

According to Mason and Rice[4,7] it is necessary that $\alpha=12.4$ in order to preserve the fit to the high-temperature data. In all of the exp-six potentials used in this work this value of α has been used. On the other hand, the values of r_m and ϵ/k are not determined uniquely by the high-temperature data. Mason[7] has very kindly calculated for us several ϵ/k, r_m pairs which result in just as satisfactory a fit to the high-temperature data as does the original set of Mason-Rice[4] constants. These alternative constants satisfy the linear log-log relation,

$$-10.86957 \log r_m + 6.35368 = \log(\epsilon/k). \quad (2)$$

Since the very low-temperature second virial coefficients depend in a different way upon the relative values of r_m and ϵ/k than do the high-temperature virials, it was possible to adjust the low-temperature fit independently of the high-temperature fit.

The original Mason-Rice constants (*MR*1) lead to second virial coefficients for He^4 distinctly too negative in the 2°–4°K temperature range. Mason thereupon suggested the constants of *MR*2, which lead to results still too negative. *MR*3 was estimated by extrapolation from *MR*1 and *MR*2 and is about right but is not quite consistent with Eq. (2) (which was unknown to us at the time). *MR*4 gives nearly the same second virial coefficients as *MR*3 but is consistent with Eq. (2). *MR*5 is our final best potential. All of the figures given for the constants of *MR*5 in Table I are not significant in the sense of being required to fit the experimental data but are given as they were actually used in the calculation of the phase shifts.

In reference 1 an extensive table of the second virial coefficients of helium using *LJ*1, the original de Boer-Michels potential, is given, along with a brief table showing the effect of small variations in these constants (*LJ*2 and *LJ*2′). These data could readily be extrapolated to find a set of Lennard-Jones constants (*LJ*3) yielding results in agreement with the experimental virial data quoted in this paper. The parameter p^2 would be about 22.55. It is quite possible that the true He-He interaction potential is quite different from *MR*5. The evidence for this conclusion is that *LJ*3 and *MR*5, giving essentially the same virial coefficients, differ considerably in form.

TABLE I. Potential constants of various exp-six and 12–6 potentials.

	α	ϵ/k, °K	r_m, A
*MR*1	12.4	9.16	3.135
*MR*2	12.4	8.76	3.138
*MR*3	12.4	7.85	3.150
*MR*4	12.4	7.682	3.185
*MR*5	12.4	7.5628	3.1894
*LJ*1		10.22	2.86911
*LJ*2		10.3364	2.86911
*LJ*2′		10.22	2.88541
Slater-Kirkwood	13.54	9.25	2.943

[6] J. C. Slater and J. G. Kirkwood, Phys. Rev. **37**, 682 (1931).
[7] E. A. Mason and W. E. Rice (private communication).

IV. RESULTS

A. Second Virial Coefficients

Figure 2 shows some of the phase shifts for He^4 obtained from *MR*1 and *MR*5. The phase shifts for *MR*1 are always more positive than those for *MR*5; however, only when $l=0$ and q is small is this difference large. A system composed of two He^4 atoms interacting according to the *MR*5 potential has no discrete negative energy level; consequently the phase shift is zero at $q=0$. Since this potential very nearly has a discrete level, the phase shifts for $l=0$ increase rapidly to a maximum. The *MR*1 potential, on the other hand, has a discrete level, and phase shifts for $l=0$ start at π and decrease rapidly. The phase shifts for *LJ*1 [shown in reference (1)] are very slightly more negative than those for *MR*5.

The second virial coefficients of He^4 and He^3 (B_{44} and B_{33}) as calculated from potential *MR*5 are given in

TABLE II. Second virial coefficients of He^4 and He^3.

T°K	B_{44} cc/mole	B_{33} cc/mole	T°K	B_{44} cc/mole	B_{33} cc/mole	T°K	B_{44} cc/mole	B_{33} cc/mole
0.3	−2709.0	−490.2	3.5	−96.46	−73.22	10.5	−18.36	−12.78
0.4	−1711.4	−439.7	3.6	−93.18	−70.81	11.0	−16.60	−11.34
0.5	−1206.9	−395.0	3.7	−90.09	−68.52	11.5	−15.00	−10.03
0.6	− 914.1	−356.8	3.8	−87.15	−66.34	12.0	−13.53	− 8.83
0.7	− 727.7	−342.2	3.9	−84.37	−64.26	12.5	−12.18	− 7.72
0.8	− 600.9	−296.3	4.0	−81.73	−62.29	13.0	−10.94	− 6.70
0.9	− 510.1	−272.1	4.1	−79.22	−60.40	13.5	− 9.79	− 5.75
1.0	− 442.4	−251.14	4.2	−76.83	−58.60	14.0	− 8.73	− 4.87
1.1	− 390.2	−232.76	4.3	−74.56	−56.88	14.5	− 7.74	− 4.06
1.2	− 348.9	−216.57	4.4	−72.38	−55.23	15.0	− 6.82	− 3.29
1.3	− 315.3	−202.21	4.6	−68.33	−52.14	15.5	− 5.96	− 2.58
1.4	− 287.62	−189.41	4.8	−64.61	−49.30	16.0	− 5.16	− 1.91
1.5	− 264.33	−177.93	5.0	−61.19	−46.67	17.0	− 3.70	− 0.69
1.6	− 244.48	−167.60	5.2	−58.03	−44.24	18.0	− 2.41	0.39
1.7	− 227.34	−158.25	5.4	−55.11	−41.98	19.0	− 1.26	1.35
1.8	− 212.39	−149.75	5.6	−52.40	−39.87	20.0	0.25	2.21
1.9	− 199.23	−142.01	5.8	−49.88	−37.91	21.0	0.70	2.99
2.0	− 187.54	−134.92	6.0	−47.53	−36.06	22.0	1.53	3.69
2.1	− 177.08	−128.42	6.2	−45.33	−34.34	23.0	2.29	4.33
2.2	− 167.66	−122.42	6.4	−43.26	−32.72	24.0	2.98	4.92
2.3	− 159.14	−116.89	6.6	−41.33	−31.19	25.0	3.62	5.45
2.4	− 151.38	−111.76	6.8	−39.50	−29.75	26.0	4.20	5.94
2.5	− 144.28	−107.00	7.0	−37.78	−28.39	27.0	4.73	6.39
2.6	− 137.76	−102.56	7.2	−36.16	−27.10	28.0	5.22	6.80
2.7	− 131.75	− 98.42	7.4	−34.63	−25.88	29.0	5.67	7.19
2.8	− 126.20	− 94.56	7.6	−33.17	−24.72	30.0	6.09	7.54
2.9	− 121.04	− 90.93	7.8	−31.79	−23.62	35.0	7.80	8.98
3.0	− 116.24	− 87.53	8.0	−30.49	−22.57	40.0	9.02	10.02
3.1	− 111.76	− 84.33	8.5	−27.48	−20.16	45.0	9.92	10.79
3.2	− 107.57	− 81.31	9.0	−24.82	−18.02	50.0	10.61	11.37
3.3	− 103.64	− 78.46	9.5	−22.44	−16.09	55.0	11.13	11.81
3.4	− 99.94	− 75.77	10.0	−20.29	−14.35	60.0	11.53	12.16

Table II. The cross second virial coefficient, B_{34}, is probably very nearly as given in reference (1) and was not recalculated. In Fig. 3, these calculated results are shown together with the experimental data (from reference 5). For comparison, a portion of the calculated results from *MR*1 and from *LJ*1 are also shown. Although *MR*5 gives better agreement with the experimental data in the very low and the high temperature region, *LJ*1 (reference 1) is somewhat superior in the middle temperature region.

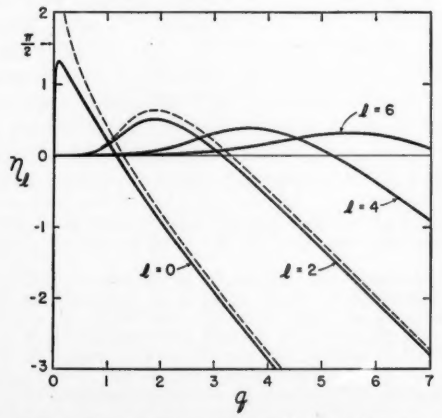

FIG. 2. Phase shifts for He^4; *MR*1 dashed curves, *MR*5 solid curves.

B. Discrete Levels

It was immediately apparent from the behavior of the low energy phase shifts for *MR*1 (He^4) that this system has a low-lying negative discrete energy level. We first determined the exact position of this level and then proceeded to a general investigation of such levels for the exp-six potential. A similar investigation has

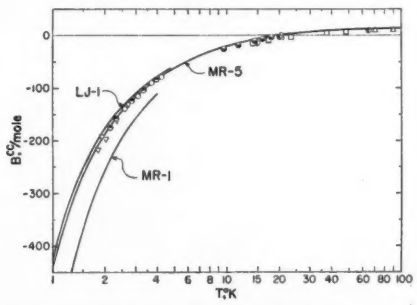

FIG. 3. Second virial coefficient of He^4 *vs* temperature. Experimental points: ◒ W. H. Keesom and W. K. Walstra, Physica **13**, 225 (1947); △ G. P. Nijoff and W. H. Keesom, Leiden Comm. 188b (1927); □ Nijoff, Keesom, and Iliin, Leiden Comm. 188c (1927); ◐ L. Holborn and J. Otto, Z. Physik. **38**, 359 (1926); ▽ J. Kistemaker and W. H. Keesom, Physica **12**, 227 (1946); revised by W. E. Keller, preceding paper [Phys. Rev. **97**, 1 (1955)]; ○ W. H. Keesom and W. K. Walstra, Physica **7**, 985 (1940); revised by W. E. Keller, preceding paper; ◓ W. E. Keller, preceding paper.

already been carried out for the Lennard-Jones 12–6 potential.[8]

A very simple technique was used. With the aid of the numerical integration system already on hand, very little time was required to integrate directly the wave equation out to a large value of R and to adjust the initial estimate of the negative eigenvalue on the basis of the behavior of the wave function. This process was continued until the eigenvalue was determined with sufficient accuracy.

TABLE III. Discrete levels for He^4, exp-six potential, $\alpha=12.4$.

ϵ/k, °K	$r_m(\epsilon/k)^{\frac{1}{2}}$	q^-	E^-/k, °K
	$r_m=3.0$A		
8.639887	8.818105	0.000000	0.000000
8.8	8.899437	0.0166	−0.00044
9.0	9.000000	0.04102	−0.00266
9.2	9.099450	0.06354	−0.00637
9.4	9.197826	0.086029	−0.011684
9.6	9.295161	0.108398	−0.018551
10.0	9.486834	0.152777	−0.036850
	$r_m=3.2$A		
7.593743	8.818159	0.000000	0.000000
7.7	8.879638	0.0132	−0.00027
7.8	8.937114	0.02539	−0.00102
7.9	8.994221	0.03662	−0.00212
8.0	9.050966	0.04932	−0.00384
8.4	9.274480	0.097142	−0.014898
8.8	9.492733	0.144500	−0.032965
	$r_m=3.4$A		
6.726675	8.818184	0.000000	0.000000
7.0	8.995553	0.03467	−0.00190
7.2	9.123159	0.06079	−0.00583
7.6	9.373154	0.111517	−0.019634

[8] J. E. Kilpatrick and M. F. Kilpatrick, J. Chem. Phys. **19**, 930 (1951).

It is convenient to give our results in terms of the reduced parameter q^-,

$$q^-=[-(2\mu/\hbar^2)\rho^2E^-]^{\frac{1}{2}}, \tag{3}$$

where μ is the reduced He^4 mass, $\rho=2.77$A, and E^- is the negative energy level. All of the following results are for a pair of He^4 atoms, since the physically realistic range of potential constants cannot result in a discrete level for He^3.

The potential $MR1$ has a discrete level at $q^-=0.146498$ or $E^-/k=-0.033883°$; $MR2$ at $q^-=0.101961$ or $E^-/k=-0.016413°$; and $MR4$ at $q^-=0.0020$ or $E^-/k=-0.000006°$. $MR3$ and $MR5$ have no discrete level.

It is of some interest to note that, since $LJ3$ (very nearly the equivalent of $MR5$ in terms of the very low-temperature second virial coefficient) definitely has a low-lying discrete level, the question of whether He^4 really has a discrete level is still open.

Table III shows the location of the discrete level for a number of r_m, ϵ/k pairs, always with $\alpha=12.4$. In the study of discrete levels for the Lennard-Jones potential,[8] it was found that q^- was very nearly linear in $r_m(\epsilon/k)^{\frac{1}{2}}$. This same relationship is valid for the exp-six potential. The value of $r_m(\epsilon/k)^{\frac{1}{2}}$ for $q^-=0$ is very nearly constant; the three curves ($r_m=3.0$, 3.2, and 3.4A) of q^- *vs* $r_m(\epsilon/k)^{\frac{1}{2}}$ are essentially straight and have almost the same slopes.

Experiments on the Behavior of an Ionized Gas in a Magnetic Field*

WINSTON H. BOSTICK AND MORTON A. LEVINE
Tufts College, Medford, Massachusetts

(Received March 15, 1954; revised manuscript received June 24, 1954)

Measurements with probes in a plasma of helium ions and electrons in the afterglow of an induction-excited discharge in a toroidal tube with a toroidal magnetic field reveal an oscillatory probe current which is presumably indicative of fluctuations in the ion density. The space distribution of these fluctuations and the dependency of their amplitude and frequency on the pressure and magnetic field are consistent with the assumption that plasma waves, similar to the magnetohydrodynamic type described by Alfvèn, exist in this toroid. Measurements of electron density by a microwave method in another toroidal tube, which is in the form of a microwave resonant cavity, show that in this tube the degree of diffusion control in helium at low pressures is apparently orders of magnitude less than one would calculate from the classical theory of ambipolar diffusion of ions and electrons in a magnetic field. The measurements show a marked minimum in the diffusion coefficient as a function of magnetic field at about 600 gauss. An attempt is made to explain this minimum and the lack of diffusion control in terms of plasma waves. Experimental evidence that plasma waves exist in this toroid in a magnetic field has been seen in oscillations which appear on the rf envelope of the exciting pulse from the magnetron.

THE rate of diffusion of ions and electrons across a magnetic field has attracted some interest.[1–5] Probe measurements reported by Bohm[1] have indicated that the degree of control of diffusion of ions and electrons by a magnetic field is not nearly so great as predicted by the orthodox collision theory. He attributed this lack of control of ion diffusion by the magnetic field to a turbulence which is, in some manner, associated with plasma oscillations.

In the pursuance of a research project specified in a contract with the Geophysics Research Division of the Air Force Cambridge Research Center, measurements have been performed at Tufts College on the properties of an ionized plasma in the presence of a magnetic field.

PROBE MEASUREMENTS OF PLASMA PROPERTIES IN A MAGNETIC FIELD IN THE AFTERGLOW OF A PULSED DISCHARGE

The first experiment involved the measurement by probes of the properties of a plasma in a toroidal tube in a magnetic field during the "afterglow" period which follows the pulsed induction-excited discharge. The toroidal tube was constructed of two Corning glass U bends, 1½ in. i.d., with two brass straight sections joining them in the race track tube diagrammed in Fig. 1. This tube was wound with No. 13 wire for the excitation of a toroidal dc magnetic field and was linked with two pulse transformer cores, the 10-turn primaries of which were excited by the circuit diagrammed in Fig. 1. Either electron current or positive-ion current to the probe could be measured during the period which followed the excitation pulse. The probe was connected to its resistor and amplifier only during an examining interval of about 1000 μsec which could be delayed at will to include any portion of the afterglow period under scrutiny. This arrangement prevented paralysis of the sensitive ampli-

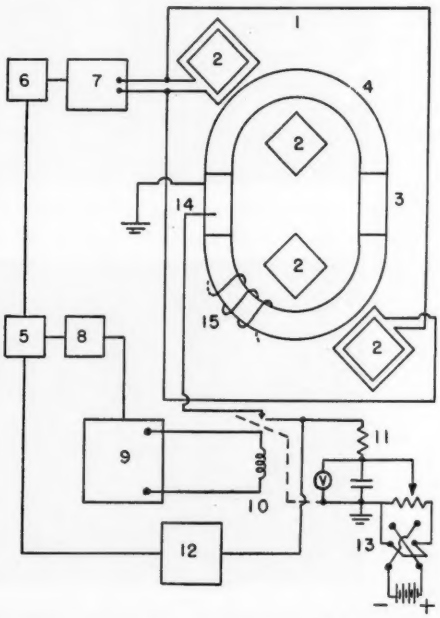

FIG. 1. Circuit used for induction-excitation of the toroidal discharge tube and measurement of ion density in the afterglow by means of a probe: (1) induction-excited toroid, (2) pulse transformer cores, (3) straight brass sections, (4) glass U bends, (5) master trigger source, (6) trigger amplifier, (7) pulse generator, 0.02 μf charged to 20 kv, (8) variable trigger delay, (9) pulse generator for relay coil, (10) Stevens-Arnold relay, (11) signal resistor for measuring positive-ion or electron current, (12) synchroscope, (13) dc voltage source for probe, (14) probe, and (15) coils for annular magnetic field.

* The work reported here was sponsored by the Geophysics Research Division of the Air Force Cambridge Research Laboratories.

[1] A. Guthrie and R. K. Wakerling, *The Characteristics of Electrical Discharges in Magnetic Fields* (McGraw-Hill Book Company, Inc., New York, 1949), first edition, pp. 11 and 68.

[2] M. H. Johnson and E. O. Hulburt, Phys. Rev. **79**, 802 (1950).

[3] M. H. Johnson in *Proceedings of the Conference on Ionospheric Physics*, Vol. II, Part B, 1950 (unpublished).

[4] O. T. Fundingsland and G. E. Austin, Phys. Rev. **79**, 232 (1950).

[5] H. Alfvèn, *Cosmical Electrodynamics* (Oxford University Press, London, 1950), first edition, p. 56.

fier by the excitation pulse and minimized the "robbing" of the plasma by the probe. The dc toroidal magnetic field current was supplied by means of storage batteries for intervals of a few seconds during which measurements were made. Magnetic fields were obtainable up to about 800 gauss.

The striking feature[6] of these probe measurements in both helium and nitrogen in a magnetic field is the fact that both electron current and positive-ion current are oscillatory in character. The measurements show (a) that these oscillations are absent in the absence of a magnetic field, (b) that their amplitude increases toward the periphery of the tube, (c) that their amplitude increases as the magnetic field and the pressure are reduced, and (d) that their frequency increases as the magnetic field and the pressure are increased. The authors have attempted to interpret[6] these oscillations in terms of plasma waves of a magneto-hydrodynamic type, i.e., a transverse wave with direction of propagation in the direction of the magnetic field.

Since this tube could not be baked, and hence the gas in this tube could not be purified to a high degree, no accurate measurements could be made upon the rate of diffusion loss of ions and electrons in the afterglow in a magnetic field. Attachment losses of electrons could easily obscure the diffusion loss under these conditions.

DETECTION OF OSCILLATIONS IN A DC CURRENT DISCHARGE IN A TOROID IN A MAGNETIC FIELD

A second experiment performed on the properties of a plasma in a magnetic field employed a large copper toroid with an inside diameter of about 2 in. and a large diameter of 3 ft. This toroid has a much more uniform magnetic field than that shown in Fig. 1. A dc discharge was excited in argon at pressures from 0.2 to 1 mm Hg by placing a constant potential difference of about 600 volts with a 3000-ohm resistor in series, across two probes which were located diametrically opposite each other around the toroid. A third probe, inserted into the

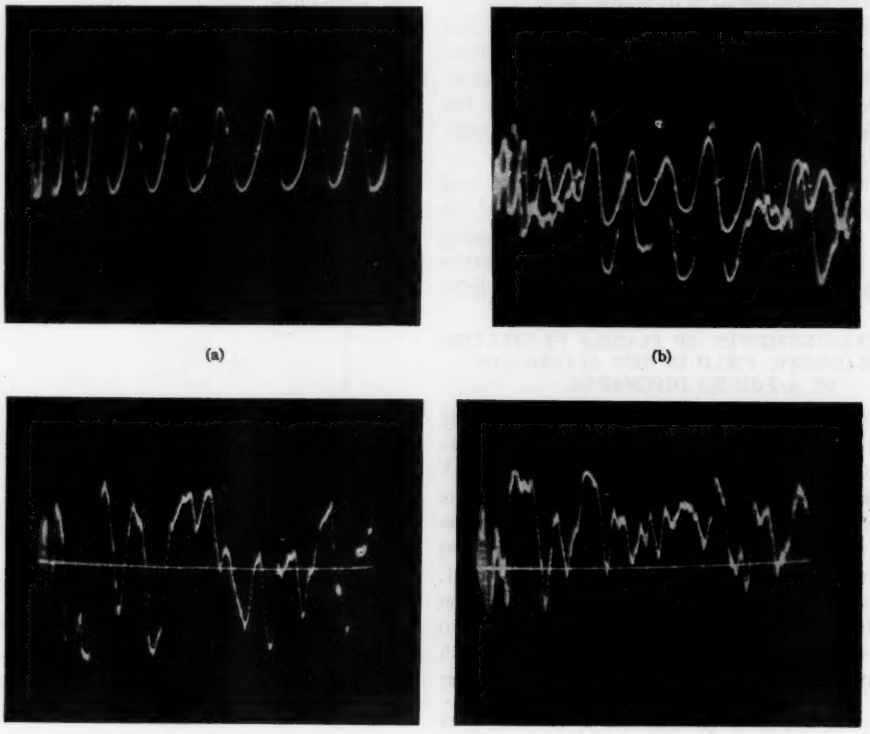

FIG. 2. (a) Argon at 0.5 mm Hg, $H=350$ gauss; frequency of oscillations is 6500 cps. (b) Argon at 0.5 mm Hg, $H=460$ gauss, $H=530$ gauss. (c) Argon at 0.2 mm Hg, $H=530$ gauss. (d) Argon at 0.2 mm Hg, $H=690$ gauss.

Current wave forms picked up by a probe in a plasma produced in the toroid shown in Fig. 1 at the indicated values of pressure and magnetic field in argon gas. The gas is excited by a dc potential of 600 volts between two probes which are diametrically opposite across the toroid. These wave forms are attributed to plasma waves of the magneto-hydrodynamic type. Note increase in higher-frequency components with increase in the magnetic field. Time is the abscissa and time marker dots are 100 μsec apart.

[6] W. H. Bostick and M. A. Levine, Phys. Rev. **87**, 671 (1950).

plasma in the toroid, was used to pick up the oscillations shown in Fig. 2, which reveal that the frequency of the oscillatory signals increases with the magnetic field value. This dependency of frequency on magnetic field is in the same direction as that found in the oscillations in probe current in the afterglow in the toroid shown in Fig. 1.

Later this tube, with nitrogen at a pressure of 10^{-4} to 10^{-2} mm Hg, was excited by means of a short microwave cavity placed at one station in the toroid. Under certain conditions it was possible to observe at the station diametrically opposite to the exciting station the light from the discharge excited by the microwave cavity. It was also possible under these conditions to pick up oscillations on the probes placed at three different stations around the toroid. Unfortunately, due to insufficient magnetron power the microwave cavity could be broken down at these relatively low pressures only over a small variation of magnetic-field values near gyroresonance at the microwave frequency for the electrons. The variation with magnetic field could therefore not be explored as it was with the dc discharge in this tube.

The gas in this large copper toroid could not be purified to a high degree and therefore it was impossible to devise, with this large tube, an experiment which would enable one to measure accurately the rate of diffusion of ions and electrons in a magnetic field.

MEASUREMENT OF DIFFUSION OF IONS AND ELECTRONS IN A MAGNETIC FIELD IN A MICROWAVE CAVITY RESONATOR IN THE FORM OF A TOROID

In order to measure accurately the rate of ambipolar diffusion of thermalized ions and electrons in a gas of high purity in a magnetic field the construction of a microwave coaxial cylindrical cavity with an annular magnetic field and associated equipment, (see Fig. 3), was planned by O. T. Fundingsland and G. E. Austin of the Geophysics Research Division. The construction of this cavity and equipment, and the subsequent measurements have been carried out in the laboratory at Tufts College. This tube was constructed of OFHC copper, baked on the pumps at 450°C, sealed off, wound with magnetic field coils, and resealed to the system without the admission of air. The system could be pumped to a pressure of 10^{-7} mm Hg, and the pressure rise rate of the tube shut off from the pumps was 1.4×10^{-6} mm/minute.

The measurements performed with this apparatus concern the ambipolar diffusion of the thermalized He^+ ions and electrons in helium gas across a magnetic field in a toroidal tube. No provision was made for the insertion of probes in this apparatus.

Measurements of electron density in the microwave cavity shown in Fig. 3, by means of the frequency-shift

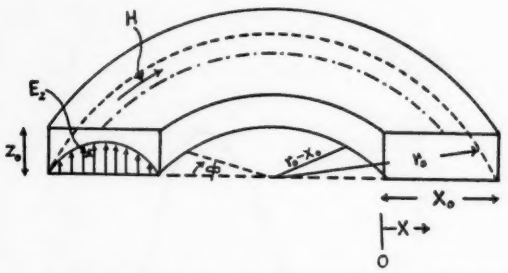

FIG. 3. Microwave cavity with an annular magnetic field used for measurement of diffusion of ions and electrons across a magnetic field. The electric field of the exciting signal is E_z while H is the annular magnetic field. Also, $r_0=6.00$ in. $=15.24$ cm; $x_0=2.00$ in. $=5.08$ cm; and $z_0=3.154$ cm.

method,[7] were performed first at one value of the annular magnetic field and over a range of pressures from 0.050 to 1.0 mm Hg. In this first set of experiments the frequency ($\omega/2\pi\cong2930$ Mc/sec) of the fundamental mode of the cavity (no ϕ variation and one half-cycle variation in r) was used for measurement of electron density in the afterglow following breakdown of the gas in the cavity at gyroresonance for the electrons at the centerline of the cavity on the sixth mode at 3970 Mc/sec.

The second set of measurements utilized the fundamental mode of the cavity for breakdown of the gas, and the frequency-shift measurement of the cavity was performed with either the fifth or sixth mode. With this arrangement it was found that breakdown could be achieved with values of the magnetic field of about 160 gauss and greater. It was thus possible to measure diffusion as a function of magnetic field for various pressures.

The arrangement for the first set of measurements with the fundamental mode used as the probing mode will now be discussed to illustrate the method of determining electron density.

The electron density n at the centerline of the cavity can be obtained from the following calculations: the angular frequency shift $\Delta\omega$ is given by

$$\Delta\omega=-\tfrac{1}{2}\epsilon_0\int\sigma_i E^2dv\Big/\int E^2dv, \qquad (1)$$

where σ_i is the imaginary part of the complex conductivity perpendicular to the magnetic field, E is the electric field of the unperturbed cavity, ϵ_0 is 8.85×10^{-12} farads/meter, and $\int(\ )dv$ represents an integral over the volume of the cavity.

Now[8]

$$\sigma_i=-e^2n\omega/[m(\omega^2-\omega_g^2)], \qquad (2)$$

[7] M. A. Biondi and S. C. Brown, Research Laboratory of Electronics, Massachusetts Institute of Technology, Technical Report No. 34, Feb. 26, 1947 (unpublished).

[8] B. Lax at the Conference on Gaseous Electronics, October, 1951, *c7* (unpublished).

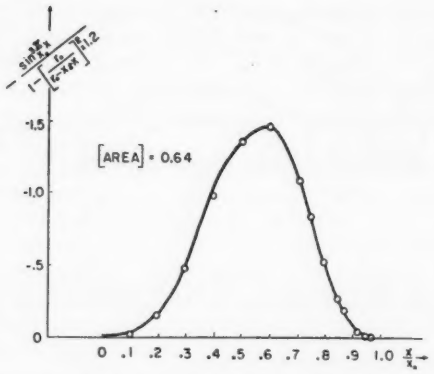

FIG. 4. A plot of the integrand of Eq. (6) so that $\Delta\omega$ in Eq. (7) can be evaluated from the area under the curve.

where ω_g is the gyroresonance frequency for electrons, m is the mass of the electron in kg, n is the number of electrons/meter,[3] and e is 1.6×10^{-19} coulomb.

If the cavity, see Fig. 3, is approximated by a straight rectangular box of width x_0, height z_0, and length L (equal to the mean circumference of the toroid), the variation of E with x may be approximated by

$$E=E_0\sin(\pi x/x_0), \tag{3}$$

and the variation of n with x may be approximated by

$$n=n_0\sin(\pi x/x_0). \tag{4}$$

With the use of Eqs. (1), (2), (3), and (4) there results

$$\Delta\omega=\frac{e^2n_0\omega}{2\epsilon_0 m}\int_0^{x_0}\frac{\sin^3(\pi x/x_0)}{\omega^2-\omega_g^2}dx\Big/\int_0^{x_0}\sin^2(\pi x/x_0)dx. \tag{5}$$

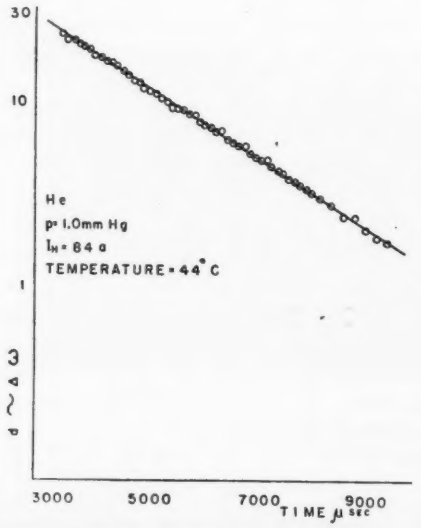

FIG. 5. Experimental plot of the values of d, the divisions on a Sperry wave meter ($\sim\Delta\omega$), which are proportional to the electron densities in the afterglow in a toroid with an annular magnetic field.

The integral in the denominator of Eq. (5) is equal to $x_0/2$ and $\omega_g^2=\omega_{g0}^2r_0^2/(r_0-x_0+x)^2$, where ω_{g0} is the gyroresonant frequency at the magnetic field corresponding to the position r_0 in Fig. 3. Thus Eq. (5) can be written

$$\Delta\omega=\frac{e^2n_0}{\epsilon_0 m\omega x_0}\int_0^{x_0}\frac{\sin^3(\pi x/x_0)}{1-[\omega_{g0}^2r_0^2/\omega^2(r_0-x_0+x)^2]}dx. \tag{6}$$

Now the total number of turns of the magnetic field coil is 1037, the mean circumference of the toroid is 79.8 cm, and the number of turns per cm at the mean radius r_m is 13.0.

The magnetic field at the mean radius (the center line) is then (16.32) I gauss, where I is the magnetic

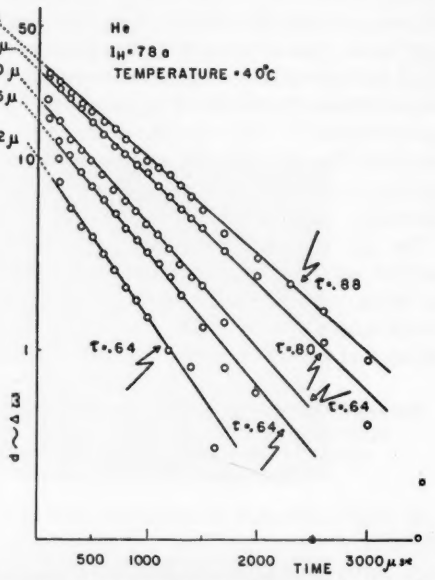

FIG. 6. Typical experimental plots of values of $d(\sim\Delta\omega)$, which are proportional to electron density, in a toroid with an annular magnetic field, at various pressures.

field current measured in amperes. Most of the first set of data have been taken at $I=84.0$ amperes which corresponds to a magnetic field at the mean radius of $H(r_m)=1370$ gauss. The value of H at r_0 is then $H(r_0)=1141$ gauss. The measured value of the wavelength λ used for gyroresonance breakdown is $\lambda=7.564$ cm which corresponds to $f=3970$ Mc/sec. The calculated value of gyroresonance, $H(r_m)=1370$ gauss, is

$$f(r_m)=\omega(r_m)/2\pi=3825\text{ Mc/sec},$$

which means that the position where gyroresonance breakdown was produced in the cavity was at a radius of $3825r_m/3970=0.965r_m$, which is approximately equal to r_m.

The calculated gyrofrequency at $r=r_0$ is 3190 Mc/sec. The frequency $\omega/2\pi$ of the probing signal is approximately constant and is 2934 Mc/sec. Figure 4 gives a

plot of the integrand of Eq. (6) with the assumption that $(\omega_{p0}/\omega)^2$ may be approximated by the constant value of 1.2. The abscissa in Fig. 4 is x/x_0 instead of x so that the integral of Eq. (6) is actually x_0 times the area under the curve.

The area is approximately equal to 0.64 and is negative, so that $\Delta\omega$ should theoretically come out to be negative, which it actually does experimentally.

Then

$$n_0=(8.75\times10^6)\Delta\omega \text{ electrons/m}^3$$
$$=8.75\Delta\omega \text{ electrons/cm}^3. \quad (7)$$

The minimum measurable $\Delta\omega/2\pi$ is 2×10^5 cps. Hence, the minimum measurable n_0 is 1.1×10^7 electrons/cm³. On the Sperry wave meter employed one small division equals 0.04 Mc/sec. Therefore

$$n_0=(2.2\times10^6)d \text{ electrons/cm}^3, \quad (8)$$

where d is the number of small divisions difference on the wave meter corresponding to $\Delta\omega$.

The experiments performed involve the measurement of the frequency shift as indicated by d on the wave meter. The values of log$d$ are then plotted against time, and the slope of the resulting straight line is proportional to the ambipolar diffusion coefficient D_{aH} at the particular values of pressure and magnetic field employed. The time taken for the value of d to decrease by the factor $1/e$ is the ambipolar diffusion time constant τ_{aH}.

Typical sets of experimental data yielding a plot of log$d$ *vs* t are shown in Figs. 5 and 6. Each set of data yields a value of τ_{aH}.

The quantity τ_{aH} measured in the magnetic field can be related to the effective ambipolar diffusion coefficient D_{aH} for the cavity whose characteristic diffusion length is Λ, by

$$\tau_{aH}=\Lambda^2/D_{aH}, \quad (9)$$

where $1/\Lambda^2=\pi^2/z_0^2+\pi^2/x_0^2$, or $\Lambda^2=0.675$ cm².

As already explained, the first set of experimental conditions involved the values of magnetic field of $H=1370$ gauss ($I=84$ amperes) and $H=1275$ gauss ($I=78$ amperes) at the mean radius of the toroid. Breakdown was produced at gyroresonance with the sixth mode of the cavity and the fundamental mode was used for the probing signal. A summary plot of the values of τ_{aH}, thus obtained at various pressures, is given in Fig. 7.

The second set of experimental conditions, as already explained, involved breakdown of the gas by the fundamental mode of the cavity and probing with the fifth and sixth modes. A variety of magnetic fields could be employed under these conditions. A summary plot of the experimental values of τ_{aH}, thus obtained, *vs* $I(\sim H)$ for various pressures is shown in Fig. 8. The oscilloscope display of the rf envelope of the 2000-μsec excitation pulse from the magnetron reflected from the cavity showed strikingly the presence of oscillations whose frequency increased and whose amplitude decreased as the magnetic field increased. The authors believe that these oscillations may have been produced by plasma waves of the magneto-hydrodynamic type already postulated in the interpretation of the probe measurements.

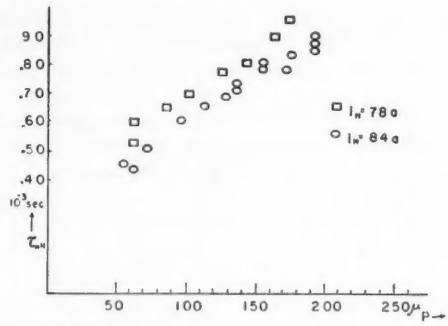

FIG. 7. Experimental values of the electron-density decay time τ_{aH} as a function of pressure in microns for two different magnetic fields.

ATTEMPT AT AN INTERPRETATION OF THE EXPERIMENTAL DATA

Figure 9 shows cross sections of both the microwave toroid and a circular cross section tube such as the induction-excited toroid. Let it be assumed that the ion

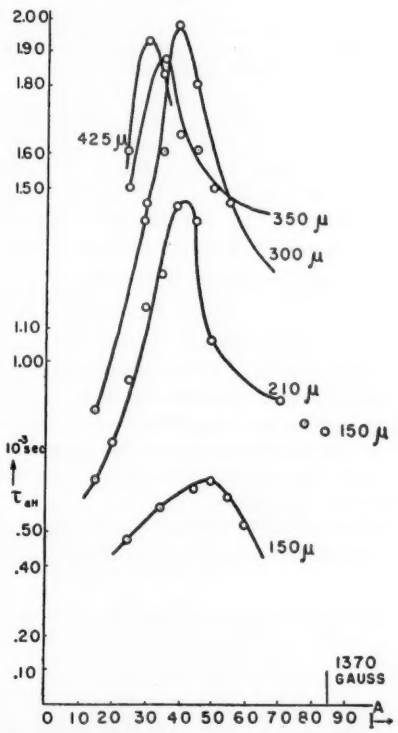

FIG. 8. Results of measurements of diffusion of He ions in helium gas in a toroid with an annular magnetic field. Ordinates are the decay times τ_{aH} which are proportional to $1/D_{aH}$, where D_{aH} is the ambipolar diffusion coefficient in a magnetic field. Abscissa is the magnetic field currents.

DETROIT PUBLIC LIBRARY

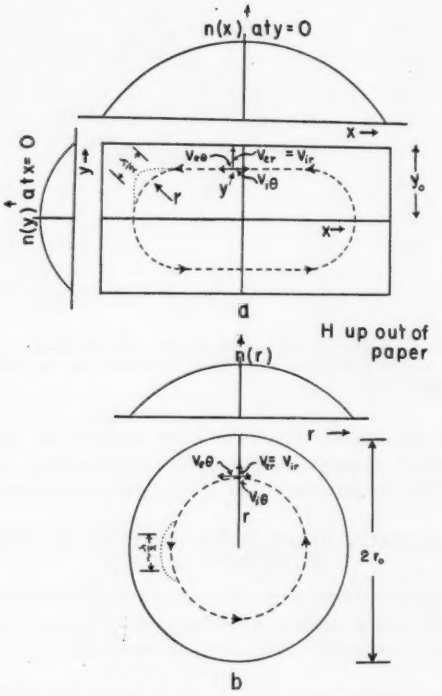

FIG. 9. Cross sections of rectangular and circular toroids showing the calculated direction of circulation of ions and electrons and the estimated ion density distributions.

density distributions are, to a first approximation, as diagramed in Fig. 9. We now apply the orthodox collision and ambipolar diffusion theory to compute the values of D_{aH} and τ_{aH} for Table I. The radial or outward velocities v_{er} and v_{ir} of the electrons and ions, respectively, are equal in sign and magnitude,[9] i.e.,

$$v_r=v_{er}=v_{ir}=2kT(\text{grad}n)/\{[\nu_i m_i(1+\omega_i^2/\nu_i^2)+\nu_e m_e(1+\omega_e^2/\nu_e^2)]n\}. \quad (10)$$

The subscript i refers to the positive ions, e to the electrons. The quantity ω is the angular gyrofrequency, ν the collision frequency, n the ion density, and m the mass, k is Boltzmann's constant, and T, the absolute temperature of the ions and electrons, is assumed to be constant and thermalized by the neutral gas atoms in our microwave experiment.

In the absence of a magnetic field the ambipolar diffusion coefficient D_a is related to the radial velocity of ions, v_r, by

$$v_r=D_a(\text{grad}n)/n=2kT(\text{grad}n)/(\nu_i m_i n),$$

or

$$D_a=2kT/(\nu_i m_i).$$

In the approximation that $\omega_e^2/\nu_e^2 \gg 1$, and also that $\omega_e^2\nu_e m_e/\nu_e^2 \gg \omega_i^2\nu_i m_i/\nu_i^2$, we can then write that the ambipolar diffusion coefficient D_{aH} in a magnetic field is given by

$$D_{aH}=D_a/[1+(m_e/m_i)^{\frac{1}{2}}\omega_e^2/\nu_e^2]. \quad (11)$$

[9] Reference 5, p. 61.

If we use the value of the magnetic field ($H=1370$ gauss) at the center line of the microwave cavity, ω_e is equal to $2\pi(3.82\times10^9)$. If $\nu_e=\bar{v}/l=P_c\bar{v}p$, where $\bar{v}$ is the average thermal electron speed in cm/sec, l the electron mean free path in cm, and $P_c=20$ cm^{-1} is the collision probability, p the pressure in mm Hg, and if from Biondi and Brown,[10] and Phelps,[11] $D_a p=540$ for He^+,

$$D_{aH}(He^+)=540/[p(1+169/p^2)]. \quad (12)$$

This expression for $D_a p$ is valid down to the pressure at which the mean free path of a positive ion becomes comparable with tube dimensions. This limiting pressure is about 0.01 mm Hg for the microwave toroidal cavity employed.

Equation (11) gives a pressure dependency for D_{aH} which is opposite from that observed experimentally (Fig. 7). Equation (11) also predicts $D_{aH}\sim 1/H^2$, and says nothing at all about the observed maximum in τ_{aH} as a function of H (Fig. 8). Furthermore, the magnitudes of $\tau_{aH}(\sim 1/D_{aH})$ computed for $H=1370$ gauss from Eq. (12) at various pressures, (Table I), are considerably larger than those observed (Fig. 7). Thus the values of D_{aH} calculated by orthodox collision theory do not agree with those measured by this experiment. The following arguments will be used in an attempt to explain these discrepancies.

Now, the velocities[9] of electrons and ions in the θ direction are

$$v_{e\theta}=\omega_e v_r/\nu_e,$$

and

$$v_{i\theta}=-\omega_i v_r/\nu_i.$$

It is these velocities in the θ direction which produce a resultant diamagnetic current which decreases the magnetic field in the interior of the toroid to an extent given by the equation

$$\text{grad}[nkT+H^2/(8\pi)]=0. \quad (13)$$

(The grad$H$ due to the toroidal geometry is neglected here, for the moment.)

Now, in the approximation that at the values of H and p used,

$$\omega_e^2/\nu_e^2 \gg 1 \quad \text{and} \quad \omega_e^2\nu_e m_e/\nu_e^2 \gg \omega_i^2\nu_i m_i/\nu_i^2,$$

$$v_r=2kT(\text{grad}n)/(n\nu_e m_e\omega_e^2/\nu_e^2), \quad (14)$$

and

$$v_{e\theta}=2kT(\text{grad}n)/(nm_e\omega_e), \quad (15)$$

and

$$v_{i\theta}=-2kT\nu_e\omega_i(\text{grad}n)/(nm_e\nu_i\omega_e^2). \quad (16)$$

The net momentum of an ion pair in the θ direction is given by

$$\begin{aligned} &m_e v_{e\theta}+m_i v_{i\theta} \\ &=(m_e\omega_e/\nu_e-m_i\omega_i/\nu_i)2kT\nu_e(\text{grad}n)/(nm_e\omega_e^2) \\ &=m_e\omega_e[1-m_i\omega_i\nu_e/(m_e\omega_e\nu_i)]2kT(\text{grad}n)/(nm_e\omega_e) \\ &\cong[1-(m_i/m_e)^{\frac{1}{2}}]2kT(\text{grad}n)/(n\omega_e) \\ &\cong-(m_i/m_e)^{\frac{1}{2}}2kT(\text{grad}n)/(n\omega_e). \end{aligned}$$

[10] M. A. Biondi and S. C. Brown, Phys. Rev. 75, 1700 (1949).
[11] A. V. Phelps and S. C. Brown, Phys. Rev. 86, 102 (1952).

There is then essentially a net mass hydrodynamic motion in the $-\theta$ direction with a velocity

$$v_{\theta\,\text{hydro}}=(m_e v_{e\theta}+m_i v_{i\theta})/(m_e+m_i)$$
$$\cong -2kT(\text{grad}n)/[n\omega_e(m_e m_i)^{\frac{1}{2}}].$$

In a tube of finite cross-sectional dimensions the velocities $v_{e\theta}$, $v_{i\theta}$, and $v_{\theta\,\text{hydro}}$ may be expected to be of a rotational nature because of the radial electric field set up by the initial free diffusion (non-ambipolar) of the positive ions and electrons, and because of the radial grad$n$. (The free diffusion of the positive ions in the magnetic field is considerably larger than that of the electrons.)

If the $v_{e\theta}$ and $v_{i\theta}$ represent rotational velocities occurring at a radius r from the center, the quantities $v_{e\theta}^2/r$ and $v_{i\theta}^2/r$ represent the centripetal accelerations of the electrons and positive ions, respectively. The centripetal acceleration of an element of volume of plasma is $v_{\theta\,\text{hydro}}^2/r$. In these accelerated frames of reference there is effectively an outward gravitational force acting antiparallel to grad$n$. Such a condition may be expected to be unstable[12] and any small perturbation will grow with an e-folding time constant (time to grow to a value e-fold as great) given by

$$\tau=[\lambda/(2\pi a)]^{\frac{1}{2}}\text{ sec}, \tag{17}$$

where λ is the wavelength associated with a small disturbance or bump, see Figs. 9(a) and 9(b), and a is centripetal acceleration in cm/sec^2. The value of λ may be expected to be of the order of r and is equal to a few centimeters.

Let us take $\lambda=2$ cm. For the electrons

$$a=v_{e\theta}^2/r;$$

and

$$\tau=(r/\pi v_{e\theta}^2)^{\frac{1}{2}}=(r/\pi)^{\frac{1}{2}}/v_{e\theta}$$
$$=(r/\pi)^{\frac{1}{2}}/[2kT(\text{grad}r)/(nm_e\omega_e)]. \tag{18}$$

If $(r/\pi)^{\frac{1}{2}}\cong 1$, Eq. (18) may be written (19)

$$\tau=[2kT(\text{grad}n)/(nm_e\omega_e)]^{-1}. \tag{20}$$

For $H=1000$ gauss, and for $T=300°$K, the quantity

$$2kT/m_e\omega_e=3.7\times 10^4. \tag{21}$$

Also, since $n\sim\cos(\pi r/2r_0)$ and $(\text{grad}n)=dn/dr\sim(\pi/2r_0)\times\sin(\pi r/2r_0)$,

$$(\text{grad}n)/n\cong(\pi/2r_0)\tan(\pi r/2r_0). \tag{22}$$

Hence, Eq. (18) becomes, in seconds,

$$\tau\cong 2.7\times 10^{-5}[(\pi/2r_0)\tan(\pi r/2r_0)]^{-1}$$
$$=1.7\times 10^{-5}r_0\cot(\pi r/2r_0). \tag{23}$$

If the approximation of Eq. (19) is not employed, the expression for τ given by Eq. (23) would involve an $r^{\frac{1}{2}}$.

In Eq. (23), r_0 for the circular cross section case is indicated in Fig. 9(b), and for Fig. 9(a), r_0 may be approximated by y_0. It can be seen from Eqs. (18) and (23) that the e-folding time τ for the values $r/r_0=\frac{1}{2}$ and $r_0=2$ cm is approximately 30 μsec, and that for points nearer the periphery, the value of $\tau<30$ μsec is certainly short enough to permit the plasma waves in the microwave toroid to become well established before and during the measured ion-decay time constants of approximately 10^{-3} sec. If in computing the acceleration a used in Eq. (17), $v_{\theta\,\text{hydro}}$ instead of $v_{e\theta}$ is used, the values for τ will be increased in the ratio $(m_i/m_e)^{\frac{1}{2}}$, which is approximately a factor of 80 for He^+ ions. Even this longer τ is short enough to permit the buildup of waves during the period of excitation and observation in the microwave experiment.

The concept[12] of an e-folding disturbance leading to Eq. (17) was developed under the assumption that the disturbance is so small that the magnetic lines of force are not appreciably bent but are merely spread. However, as the original disturbance, which is very likely somewhat localized in the magnetic field direction, grows in magnitude, it must necessarily cause appreciable bending of the magnetic lines, and the disturbance may then be expected to be propagated as a wave in the direction of the magnetic field. For lack of a better theory at present, we shall assume that the e-folding of the disturbance continues as an e-folding of the amplitude of a magneto-hydrodynamic or plasma wave. The amplitude build-up time constant τ will, of course, be shorter toward the periphery of the tube.

The build-up rate for energy in the wave may then be expected to be $2/\tau$, and if we use the value of τ corresponding to $v_{\theta\,\text{hydro}}$, we may write that the rate of energy build-up in the wave is equal to

$$2/\tau=4kT(\text{grad}n)/[n\omega_e(m_i m_e)^{\frac{1}{2}}]. \tag{24}$$

We have now postulated and given a rudimentary discussion of a mechanism whereby disturbances can be set up in the plasma. These disturbances, even though they may be propagated as waves, nevertheless constitute a kind of turbulence in the plasma. Although it is rash to attempt to describe a phenomenon as complicated as turbulence, we shall nevertheless attempt to

TABLE I. Theoretical values of D_{aH} for He^+ computed on the basis of standard diffusion theory according to Eqs. (11) and (12) for $H=1370$ gauss.

p mm Hg	$D_a=540/p$	$\tau_a=0.67/D_a$ 10^{-3} sec	$D_{aH}=540/[p(1+169/p^2)]$	$\tau_{aH}=0.67/D_{aH}$ 10^{-3} sec	Expected degree of control $=\tau_{aH}/\tau_a$
2	270	2.5	6.4	105	43
1	540	1.25	3.2	210	168
0.8	676	1.0	2.6	260	260
0.6	900	0.75	1.92	350	466
0.4	1340	0.5	1.28	520	1040
0.2	2700	0.25	0.64	1050	4200
0.1	5400	0.125	0.32	2100	16 000
0.05	10 800	0.06	0.16	4200	70 000

[12] M. Kruskal at the Gaseous Electronics Conference, Princeton, New Jersey, September, 1952 (unpublished).

compare the implications of the foregoing theory with the experimentally observed oscillations in probe and microwave signals.

Presumably the e-folding wave increases in amplitude until twice its reciprocal damping time constant, $2/\tau'$, which represents the proportional rate at which energy is taken out of the wave, is equal to twice its reciprocal e-folding time constant, $2/\tau$, which represents the proportional rate at which energy is fed into the wave.

The damping of the wave can conceivably come about (a) by collisions of the ion pairs participating in the wave with neutral gas atoms, and (b) through loss of the participating ion pairs to the walls of the tube by the diffusion processes resulting from the wave motion. Let us first consider damping mechanism (a).

If $s=s_0 \sin\omega_{MH}t$ represents the lateral displacement of a particle in a magneto-hydrodynamic wave of angular frequency ω_{MH}, the wave energy of an ion pair in the wave is

$$[(m_i+m_e)/2](ds/dt)_{\max}{}^2=[(m_i+m_e)/2](\omega_{MH}s_0)^2. \quad (25)$$

The rms damping force on an ion pair in the wave may be given by

$$[(m_i+m_e)/2]\omega_{MH}s_0\nu_i/\sqrt{2}, \quad (26)$$

where ν_i is the effective collision frequency of positive ions with neutral atoms, and where it has been assumed that an He^+ ion in colliding with a neutral He atom loses, on the average, one half of its directed wave momentum. The rms damping power is obtained by multiplying Eq. (26) by the rms wave velocity, $\omega_{MH}s_0/\sqrt{2}$. Thus, the rms damping power is given by

$$[(m_i+m_e)/2](\omega_{MH}s_0)^2\nu_i/2. \quad (27)$$

The proportional rate of energy damping $2/\tau'$, (twice the proportional rate of amplitude damping $1/\tau'$) is then given by Eq. (27) divided by Eq. (25), or

$$2/\tau'=\nu_i/2. \quad (28)$$

The Q of the wave, defined as stored wave energy divided by energy lost per radian, may be written as $\tau'\omega_{MH}/2$. The Q of a critically damped wave is $\frac{1}{2}$. If the Q of a wave is somewhat greater than 1, it may be expected that the wave can exist and grow if energy is fed into it with sufficient rapidity. The value of $Q=\tau'\omega_{MH}/2=2\omega_{MH}/\nu_i>1$ therefore sets a lower limit to the frequency of the waves permitted for a given ν_i.

The initial perturbation whose rate of energy growth is $2/\tau$ [see Eq. (20)] will grow if $2/\tau$ is greater than its rate of energy decay $2/\tau'$, given by Eq. (28). On the other hand if $2/\tau<2/\tau'$, the initial perturbation will be damped out.

We must now inquire into the value of ν_i used in Eq. (26). The value of ν_i may be given by

$$\nu_i=v_iP_cp=v_i\sigma n_a, \quad (29)$$

where v_i is the appropriate velocity in cm/sec for the positive ions, P_c, the collision probability in cm^{-1} for positive ions on gas atoms, p, the pressure in mm Hg, σ, the collision cross section in cm^2 for positive ions on gas atoms, and n_a, the atom density in cm^{-3}. The appropriate velocity v_i is presumably given by

$$v_i=(v_{i\text{thermal}}{}^2+v_{i\text{wave}}{}^2)^{\frac{1}{2}}, \quad (30)$$

where $v_{i\text{thermal}}$ is the thermal velocity of the positive ions, and $v_{i\text{wave}}$ is the wave velocity of the positive ions.

When the wave is in its initial stages (small amplitude), $v_{i\text{thermal}}\gg v_{i\text{wave}}$, and

$$v_i\cong v_{i\text{thermal}}=(3kT/m_i)^{\frac{1}{2}}$$

in Eq. (29). Then, if the following inequality initially exists [see Eq. (18)],

$$2/\tau=4kT(\text{grad}n)/[n\omega_e(m_im_e)^{\frac{1}{2}}]>\nu_i/2,$$
$$=(P_cp/2)(v_{i\text{thermal}}{}^2+v_{i\text{wave}}{}^2)^{\frac{1}{2}}, \quad (31)$$

the wave will grow in amplitude until $v_{i\text{wave}}$ becomes large enough to increase v_i until $2/\tau$ is no longer greater than $2/\tau'$.

Thus, the equilibrium between the damping of the wave and the growing of the wave yields the equality

$$4kT(\text{grad}n)/[n\omega_e(m_im_e)^{\frac{1}{2}}]$$
$$=(P_cp/2)(v_{i\text{thermal}}{}^2+v_{i\text{wave}}{}^2)^{\frac{1}{2}}, \quad (32)$$

where $v_{i\text{wave}}$ in Eq. (32) is now the equilibrium value for the ions in the wave at a given r.

From Eq. (32) we can conclude that $v_{i\text{wave}}$ (a) will decrease as p increases, (b) will increase with $(\text{grad}n)/n$, and (c) will decrease as $H(\sim\omega_e)$ increases. In a magneto-hydrodynamic wave of a given frequency,[13] wave perturbations in the magnetic field, wave displacements, and wave electric fields may all be expected to be proportional to $v_{i\text{wave}}$; wave perturbation in the ion density may be expected to be proportional to $v_{i\text{wave}}{}^2$. The probe measurements (which can detect variations in ion density) described in this paper showed oscillations in probe current whose amplitudes are therefore presumably proportional to $v_{i\text{wave}}{}^2$.

We are now prepared to draw the following qualitative comparisons between the conclusions drawn from Eq. (32) and the probe measurements performed in the induction excited toroid in an annular magnetic field. As has already been described, these measurements show (1) that the magnitude of fluctuations in probe current, (presumably proportional to the square of the wave amplitude) decreases with pressure, thereby confirming conclusion (a); (2) that the wave amplitude increases markedly toward the periphery of the tube, thereby confirming (b)—this same experimental result is reported by Bohm;[1] and (3) that the wave amplitude decreases with increasing H, thereby confirming (c).

[13] Reference 5, p. 80.

Probe measurements on the induction-excited toroid also show that the lower limit of the frequency of the waves increases with pressure. This result confirms the prediction that, if the Q of the wave must be greater than 1,

$$Q=\tau'\omega_{MH}/2=2/\nu_i=2\omega_{MH}/(v_iP_cp)>1.$$

Hence the lower limit of the allowed values of ω_{MH} must increase with pressure. As has already been stated in this paper, probe measurements and oscillations on the microwave rf envelope also show that the frequency of the oscillations increases with magnetic field. This result may be explained by recognizing that the wave propagation velocity in cm/sec is

$$V=H/[4\pi(m_i+m_e)n]^{\frac{1}{2}},$$

and that whether eigenfunctions of standing waves can be set up around the toroid or whether the disturbances are strictly running waves, the observed frequency of probe signal should increase with H.

In view of the foregoing qualitative agreement between theoretical description of these waves and their experimentally observed properties, it seems reasonable to accept at least some of the elements of this rudimentary theory. At any rate, one should seriously consider the possible mechanism here described for the spontaneous generation of these waves.

Although in the microwave experiment the oscillations on the signal were not observed directly during the measuring period of the afterglow, it is possible that plasma waves were nevertheless present. They may not have been observed because of the small net integrated effect their reduced amplitude would produce on the cavity resonance frequency.

Indeed, it would be very rash to attempt to describe how turbulence in the form of plasma waves might influence D_{aH}, the effective ambipolar diffusion coefficient of ions and electrons across a magnetic field. In a quiescent plasma, the theoretical value of D_{aH} varies as does $1/H^2$ [see Eqs. (10) and (11)]. Bohm[14] explains the large discrepancy between his measured and calculated values of D_{aH} by saying that plasma oscillations bring about electric fields which are perpendicular to the magnetic field, and that the resultant outward drift velocities are therefore proportional to $1/H$. We have some arguments[15] which indicate that if the damping of the plasma waves comes about by collisions with neutral gas atoms, the diffusion coefficient should vary somewhere between $1/H$ and $1/H^2$, but, should be considerably larger than that given by Eq. (11) which assumes a quiescent plasma. These arguments further indicate that if the damping of the waves is produced by collisions of the waves with the wall, the diffusion coefficient should vary as $1/H$. Either or both of these arguments might explain the large discrepancy in general magnitude of our measured values of diffusion rate compared with the values calculated for a quiescent plasma. The peculiar pressure dependency, [Fig. 7], of the measured rates of diffusion might be explained by Eq. (32) which shows that the velocity (and amplitude) of ions in the waves, and hence the rate of diffusion perpendicular to H, increase when the pressure decreases.

There is another consideration concerning the influence of the magnetic field in our toroids which we have not as yet discussed in detail, namely, the effect of grad$H$ which results from the toroidal geometry. This variation in H across the toroid, which is 40 percent in the microwave toroid, represents a far greater variation in $H^2/(8\pi)$ than can possibly be compensated for by nkT, i.e., the pressure balance equation cannot be satisfied. In an attempt to satisfy Eq. (14) the plasma should move to the region of lower magnetic field and build up nkT in this region. The manner in which the plasma crosses the magnetic field to the region of lower field is probably influenced by the turbulence in the form of waves. The rate ($\sim D_{aH}$) at which the plasma crosses the field in an attempt to set up an equilibrium condition one would expect to increase with H. It may, therefore, be this outward motion produced by grad$H$ which produces the high-field portion of the experimental curves of Fig. 8. The low-field portion of the curves of Fig. 8 presumably indicates $D_{aH}\sim 1/H$ or $1/H^2$, and the minimum in D_{aH} (maximum in τ_{aH}) comes where the $\sim 1/H$ process and the $\sim H$ process are equal. We therefore have a possible explanation of the maxima in the experimental curves of Fig. 8.

It is planned to repeat the microwave experiment in a straight tube which has no grad$H$ and in which probes will be inserted for the possible detection of plasma waves.

ACKNOWLEDGMENTS

The authors wish to thank O. T. Fundingsland and G. E. Austin of the Geophysics Research Division of the Air Force Cambridge Research Center who planned and supported the experiment. The authors also wish to acknowledge the skillful and painstaking work of George W. Woodsum and Professor I. Koncius in the construction of the apparatus and the taking of data.

[14] Reference 1, p. 12.

[15] It is not felt that these arguments are in a sufficiently satisfactory state to take up space in the Physical Review. The reader is referred to Scientific Report No. 8, Contract AF 19(122)-89 which will be sent by the authors on request.

Thickness of the Helium Film as a Function of Height

LOTHAR MEYER
Institute for the Study of Metals, The University of Chicago, Chicago, Illinois
(Received August 16, 1954)

The thickness of a film adsorbed on a vertical wall is derived from adsorption thermodynamics as a function of height. The thickness of the helium film calculated from adsorption data is, within the error of the experiments, consistent with those obtained by direct observation.

BOWERS[1,2] has shown that the adsorption of A, N_2, O_2, and of He even in the He II region obeys near saturation, i.e., for P/P_0 between 0.7 and 0.99 (P being the vapor pressure of the adsorbed layer, P_0 that of the bulk liquid), the adsorption isotherm proposed by Frenkel,[3] Halsey,[4] and Hill:[5]

$$-\ln(P/P_0)=k/\nu^3, \tag{1}$$

where ν is the number of adsorbed layers and k a constant. This relation, specifically the third power of ν therein, is a consequence of the fact that the van der Waal's potential of the wall decreases with the third power of the distance.

From the same premise Schiff[6] and Frenkel[7] found that the thickness t of the saturated helium film should vary inversely with the 1/3 power of the height:

$$t_h=t_1/h^{1/3}, \tag{2}$$

where t_1 is the thickness at the height 1. Experimental evidence has never confirmed relation (2); the exponent of h found to describe the experimental results varies from 1/7 to 1. Atkins,[8] Jackson,[9] Bowers,[10] and Picus[11] have recently found values between 0.4 and 0.5 rather than 1/3. Bijl, de Boer, and Michels[12] predict an exponent 1/2 for h in Eq. (2), by considering the zero-point energy of the more or less two-dimensional layer of film and by neglecting the van der Waals' forces. However, their argument would require in Eq. (1) an exponent 2 instead of 3.

It seems important, therefore, to find the reason for the apparent inconsistency and the great variety of the experimental evidence.

As both Schiff[6] and Frenkel[7] derive only the general form of the dependency of t on h by Eq. (2), an alternative derivation of $t=t(h)$ shall be given here by using the thermodynamics of adsorption as given by Guggenheim[13] and by Hill[14] in order to evaluate the different constants numerically.

The differential of the Gibbs free energy F_f of an adsorbed layer is

$$dF_f=-S_f dT+V_f dP-Ad\gamma+\mu_f dn=\mu_f dn+nd\mu_f, \tag{3}$$

or, written in analogy to the Gibbs-Duhem equations:[15]

$$-S_f dT+V_f dP-Ad\gamma-nd\mu_f=0, \tag{4}$$

or, per mole,

$$-s_f dT+v_f dP-(A/n)d\gamma-d\mu_f=0. \tag{4a}$$

S_f is the differential entropy of the film, V_f its volume, μ_f the chemical potential, A the surface area, and n the number of moles. T denotes the temperature, P the pressure, and γ the surface tension. The adsorbed layer is in equilibrium with the vapor:

$$d\mu_f=d\mu_g=-s_g dT+v_g dP, \tag{5}$$

s_g being the molal entropy and v_g the molal volume of the gas. Combining (4a) with (5) at constant T, using the ideal gas law and neglecting v_f compared with v_g, yields:

$$RT\partial \ln P/\partial\gamma=-(A/n), \tag{6}$$

often called the Gibbs adsorption isotherm. Equation (6) is derived without taking the gravitational field into account; it is, therefore, strictly valid only for an adsorbed phase and a vapor at the same height.

TABLE I. Surface tension γ in dynes/cm as a function of the thickness of the film in number of adsorbed layers.

ν	γ_ν
∞	0.3
100	0.33
10	2.8
5	10.3
3	31.2

[1] R. Bowers, Phil. Mag. **44**, 467 (1953).
[2] R. Bowers, Phil. Mag. **44**, 485 (1953).
[3] J. Frenkel, *Kinetic Theory of Liquids* (Oxford University Press, London, 1946), p. 332.
[4] G. D. Halsey, J. Chem. Phys. **16**, 931 (1948).
[5] T. L. Hill, review in *Advances in Catalysis* (Academic Press, Inc., New York, 1952), Vol. 4, p. 225.
[6] L. I. Schiff, Phys. Rev. **59**, 839 (1941).
[7] J. Frenkel, J. Phys. (U.S.S.R.) **2**, 365 (1940).
[8] K. R. Atkins, "Advances in Physics," Phil. Mag. Supplement **1**, 169 (1952); Proc. Roy. Soc. (London) **A203**, 119 (1950).
[9] D. G. Henshaw and L. C. Jackson, *Proceedings of the National Bureau of Standards Symposium on Low Temperature Physics, 1951*, National Bureau of Standards Circular 519 (U. S. Government Printing Office, Washington, D. C., 1952), p. 183.
[10] R. Bowers, Phil. Mag. **44**, 1309 (1953).
[11] G. S. Picus, Phys. Rev. **94**, 1459 (1954).
[12] Bijl, de Boer, and Michels, Physica **8**, 655 (1941).
[13] E. A. Guggenheim, *Thermodynamics* (Interscience Publications, New York, 1949), p. 36.
[14] T. L. Hill, J. Chem. Phys. **17**, 520 (1949).
[15] Compare reference 13, p. 59, or, reference 14, Eq. (10).

Let us now assume an infinitely long and high wall dipping into a liquid as shown schematically in Fig. 1(a). The height above the liquid level is h. We want to calculate $t=t(h)$. In Eq. (4) two terms have to be added: the weight per mole: $(A/n)\rho_f g dh$ (ρ_f being the density of the film) hangs essentially on the surface tension, and furthermore the pressure exerted on the film is not P, but

$$P'=P+(1/r_h+1/r_0)\gamma, \tag{7}$$

where r_h is the radius of curvature of the free surface of the film in vertical direction, and r_0 an eventual radius of curvature of the wall itself in horizontal direction. From the fact that $(\partial\mu_f/\partial h)_T=0$, and noting that $(A/n)t=v_f$ and $M=\rho_f v_f$, we get:

$$Mgdh+v_f d[\gamma(1/r_h+1/r_0)]-(v_f/t)d\gamma=0. \tag{8}$$

In order to get a relationship between t and h only, we have to eliminate γ. Making the plausible assumption that γ is a unique function of the thickness t (at constant temperature), we can eliminate γ in the range of validity of Eq. (1) by combining it with Eq. (6) and $t=a\nu$, where a is the spacing of the layers

TABLE II. Thickness of the helium film in number of layers as a function of height in cm and the corresponding change in equilibrium pressure.

h(cm)	ν	$\Delta P/P_0$
0	∞	0
1	126	$2.5\cdot10^{-6}$
5	74	$1.3\cdot10^{-4}$
10	59	$2.5\cdot10^{-4}$
20	47	$5.0\cdot10^{-4}$
50	34	$1.3\cdot10^{-3}$
100	27	$2.5\cdot10^{-3}$

assumed to be 3.6A for the numerical evaluation:

$$d\gamma=-(3RTka/\nu^3 v_f)d\nu \tag{9}$$

and

$$\gamma=\tfrac{3}{2}(RTka/v_f\nu^2)+\gamma_\infty, \tag{10}$$

where γ_∞ is the surface tension of the bulk liquid for $\nu=\infty$. Using the value $k=50$ as found by Bowers[2] for helium in the neighborhood of the λ temperature, and $\gamma_\infty=0.3$ dyne/cm (compare Keesom[16]), we get for P/P_0 between 1 and 0.6, i.e., for ν between ∞ and 3 layers, the values for γ_ν listed in Table I. This table shows the rapid increase of γ with decreasing ν for thin films. Inserting Eq. (9) into Eq. (8) leads to

$$Mgdh+V_f d[\gamma(1/r_h+1/r_0)]+(3RTk/\nu^4)d\nu=0, \tag{11}$$

with

$$1/r_h=(d^2h/dl^2)\frac{1}{(1+dh/dl)^{\frac{1}{2}}}. \tag{12}$$

[16] W. H. Keesom, *Helium* (Elsevier, Amsterdam-New York, 1942), p. 263.

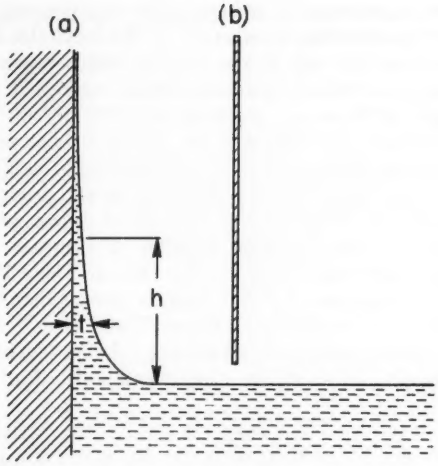

FIG. 1. (a) Schematic profile of the surface of a liquid on an infinitely long plane wall dipping into the liquid. (b) Thin wall not touching the liquid.

Equation (11) can be integrated in principle, at least numerically. However, in the case of helium and an infinitely long straight wall dipping into the liquid, the middle term of Eq. (11) can be neglected as $r_0=\infty$ and the minimum of r_h is greater than 10 cm in a region where $\nu>10$ and $\gamma<2$. We then get:[17]

$$\nu=[RTk/Mg]^{\frac{1}{3}}\cdot(1/h^{\frac{1}{3}}) \quad \text{or} \quad t=t_1/h^{\frac{1}{3}}, \tag{13}$$

and the numerical values of Table II.

The absolute values of the film thickness derived in this way from adsorption data of the *unsaturated* film are in surprisingly good agreement with the experimental results for the saturated film (compare the review given by Bowers[10]). This result is a confirmation of a view expressed in a previous paper[18] that the relation between film thickness, pressure, and temperature is essentially "classical" even in the He II region.

Column 3 in Table II gives the relative changes in gas pressure due to the gravitational field which are also the changes in equilibrium pressure of the film as a function of height h. As pointed out in the earlier paper,[18] experimental determinations of the film thickness are extremely sensitive to minute changes in P due to the asymptotic infinity of Eq. (1) near $P/P_0\sim1$. This is again reflected by the third column of Table II. The whole change in film thickness from infinity at $h=0$ to 34 layers at a height of 50 cm corresponds to a relative change of equilibrium pressure of 10^{-3}. A temperature difference of only 10^{-4} degree can produce the same change in pressure due to the steepness of the vapor pressure curve. Even in extremely carefully con-

[17] Combining Eq. (1) with $\ln(P/P_0)=-Mgh/RT$ for the change of gas pressure with height or considering the balance of forces: The surface tension has to increase by decreasing the thickness of the film in order to carry the weight of the film: $d\gamma=g\rho_f dh$, and using Eq. (9) leads again to Eq. (13).

[18] L. Meyer, Phys. Rev. 93, 655 (1954).

ducted experiments it is beyond the experimental accuracy to determine whether or not the inevitable heat influx from the top of the cryostat did not produce temperature differences of this order of magnitude over a length of 50 cm, i.e., gradients of 2.10^{-6} °K/cm. This consideration is confirmed by Bowers'[10] observation that the film thickness is extremely sensitive to radiation.

Any heat influx from the top of the cryostat producing temperature differences of only 10^{-5} degree would, therefore, cause the film thickness to decrease with height faster than given by Eq. (12) or Table II, so that the exponent of h must become greater than 0.33. Jackson's[9] value of 0.4 and Bowers'[10] and Picus'[11] value of 0.5 must therefore be considered as being consistent, within the errors of the experiments, with Eq. (13) or (2).

A small heat influx from the top has the additional effect that in the He II range the film starts flowing to the source of heat. Picus[11] found that the thickness of the film as a function of height is appreciably different for a flowing film than for a stationary film. This result is plausible because the kinetic energy of the motion should be included in a free energy consideration as used above to derive the film thickness.

Such a minute and practically undetectable heat influx can also cause great differences in film thickness when passing the λ point. The same heat influx produces in the He I region much greater temperature differences due to the poor heat conductivity of the film compared with the He II range and therefore reduces the film thickness in a much greater degree above than below the λ point.

Equation (13) gives not only the approximately right value for the thickness of the film, but also its temperature dependence. Bowers[10] and Jackson[9] report that the film thickness and its dependence on height is essentially independent of the temperature in the He II region.

Inserting Eq. (1) into the Clausius Clapeyron equation yields

$$d\ln(P/P_0)/d(1/T)=(\Delta H_f-\Delta H_0)/R=dk/d(1/T), \quad (14)$$

where ΔH_f is the differential heat of vaporization of the film (heat of adsorption) and ΔH_0 the heat of vaporization of the bulk liquid. The middle term of Eq. (14) represents the increase in heat of vaporization due to the van der Waals' forces of the wall and is essentially independent of temperature. As a consequence k has to be inversely proportional to T as borne out by the Teller-McMillan[19] approximation.[20] The factor $(RTk/Mg)^{\frac{1}{3}}$ in Eq. (13) and the equivalent factor in Eq. (10) are therefore independent of the temperature just as the experimental results require. The physical reason is that the balance between the attractive forces of the wall and the gravitational field which produces the film profile is more or less unaffected by the temperature.

There are many cases where the middle term in Eq. (12) arising from the curvature of the film surface does become important. Two of them shall be discussed:

1. Film transfer rates and film oscillations usually have been measured by using beakers of a diameter of ~0.1 cm. Such a small r_0 in Eq. (8) or (11) must influence the film thickness, and the asymmetry often found in filling or emptying the beaker might be caused by this fact as r_0 has the opposite sign at the outer wall compared with the inner wall.

2. It has been claimed that the so-called thick helium film is only formed on surfaces in contact with bulk liquid, and is absent on a specimen not touching the surface of the liquid as shown in Fig. 1(b).

If the specimen touches the liquid, we have the case discussed above and the thickness of the film should correspond to the values of Table II. If the specimen—which is usually a thin foil—does not touch the liquid, a rather sharp convex curvature of the order of 10^{-2} cm is created at the bottom which produces a relative increase in vapor pressure of the film—just as for small drops—of 10^{-4}. Column 3 of Table II shows that such a change in pressure reduces the film thickness at $h=0$ to about 75 layers where it would approach infinity if the specimens touched the liquid. Furthermore, a minute heat influx would also cause a radical change in film thickness when the specimen was pulled out of the liquid, as the heat reaching the specimen cannot be delivered to the bulk liquid as a sink and consequently one gets appreciably greater overheating.

Thanks are again due to Morrel H. Cohen for valuable discussions.

[19] W. G. McMillan and E. Teller, J. Chem. Phys. **19**, 25 (1951).

[20] The curve as drawn by Bowers (see reference 2) for $k=k(T)$ is near the λ point inconsistent with Eq. (14); however, a line obeying (14) can be drawn through his experimental points within the error of experiments.

Flow of Helium II Through Narrow Slits*

R. T. SWIM† AND H. E. RORSCHACH, JR.
The Rice Institute, Houston, Texas

(Received August 23, 1954)

The hydrodynamic properties of helium II have been studied by observation of the flow rate in a narrow slit between two flat glass plates. The isothermal, pressure-induced flow rates have been measured with hydrostatic pressures up to 2300 dynes/cm², at temperatures between 1.39 and 2.10°K, and with average slit widths of 2.4 and 4.3 microns. For a fixed pressure head, the observed flow rates have the same temperature dependence as the superfluid concentration in helium II. At pressure heads below 1600 dynes/cm² the flow rate is proportional to a power of the pressure. This power is nearly independent of temperature, but may be a function of slit width.

INTRODUCTION

ONE of the most characteristic properties of helium II is the superfluid nature of the flow of the liquid through narrow channels. The flow of helium II can be initiated either by a mechanical potential or by a thermal potential. In the experiments described here only pressure-induced, isothermal flow has been investigated.

A number of investigations[1–5] have shown that in channels wider than 10^{-2} cm the flow properties of helium II are extremely complex, but in some respects are similar to those predicted for a viscous fluid by classical hydrodynamics. As the channel width is decreased below 10^{-2} cm the flow behavior departs from that of a classical viscous fluid. In channels whose width is of the order of one micron or less the flow velocity tends to become independent of the pressure head and the length of the flow channel. Bowers and Mendelssohn[4] have shown that in radial flow through a slit between two annular plates the pressure gradient is practically zero everywhere in the slit except at its narrowest perimeter. The pressure heads employed in their experiments did not exceed six cm of helium. The investigation reported here is an extension of the flow measurements to pressure heads of approximately 15 cm of helium by means of the geometrical arrangement of Bowers and Mendelssohn.

EXPERIMENTAL TECHNIQUE

The apparatus used to study the flow properties of helium II under the influence of a hydrostatic pressure gradient is shown in Fig. 1. It consists of a glass tube (the liquid reservoir) which ends in a polished flange. A flat glass plate is pressed against the flange by means of a clamp and spring. In this way a flow channel whose width is fairly uniform over the area of the slit is formed. The width of the slit is not constant, since after assembly of the apparatus a few broad and slightly curved interference fringes can be seen. From the shape of the fringes and from the shape of the clamping device it is probable that the slit is slightly wider at the inner perimeter than at the outer. In order to measure the hydrostatic pressure at an intermediate point in the flow channel, a one-mm diameter glass tube opens into a small circular groove cut in the flange. The pressure at this point is determined by the height of the liquid column in the tube. The size of the groove is chosen so that the Bernoulli force on the liquid column in the side tube is negligible.

Both the central reservoir and the side tube are provided with approximately 1-mm holes at the top. These holes insure that the temperature of the liquid in the reservoir and in the side tube is the same as the bath temperature. Temperature equalization occurs by evaporation of the liquid or condensation of the vapor, whichever is necessary.[3] If such isothermal conditions were not maintained, the thermomechanical effect would contribute to the flow, and the results would be difficult to interpret. The holes also allow the mobile surface film of helium II to flow into or out of the reservoir. The direction of the film flow is such as to give an apparent increase in flow rate through the slit. To determine the correction to the measured flow rates, an experiment has been made with the slit blocked with glycerine. The rate of film flow was found to be 1×10^{-4} cm³/sec at a temperature of 1.4°K and to be nearly

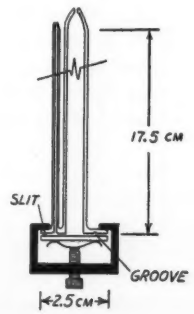

FIG. 1. The experimental apparatus.

* Supported in part by the Office of Naval Research and the National Science Foundation.

† Now at the Bell Telephone Laboratories, Murray Hill, New Jersey.

[1] J. F. Allen and A. D. Misener, Proc. Roy. Soc. (London) **A172**, 467 (1939).

[2] Johns, Wilhelm, and Grayson Smith, Can. J. Research **A17**, 149 (1939).

[3] K. R. Atkins, Proc. Phys. Soc. (London) **A64**, 833 (1951).

[4] R. Bowers and K. Mendelssohn, Proc. Phys. Soc. (London) **A63**, 178 (1950); Proc. Roy. Soc. (London) **A213**, 158 (1952).

[5] G. K. White, Proc. Phys. Soc. (London) **A64**, 554 (1951).

independent of pressure. At all the temperatures to be considered the correction for the film flow amounts to a few percent at very low pressures and is completely negligible at the higher pressures. Since the correction is within the experimental uncertainty in the measured flow rates, it has been ignored in the analysis of the results.

In order to detect the presence of small temperature differences between the reservoir and the bath, a carbon resistance thermometer was placed in the reservoir, and a similar thermometer in the bath. These thermometers are quite sensitive at low temperatures,[6] and temperature changes of a few tenths of a millidegree can be measured. In the case of the resistor in the reservoir the electrical leads were brought out through the hole in the top of the reservoir. They were then dipped into the helium bath before being taken outside the cryostat in order to minimize heat leaks through the wires. As a further precaution these leads were made from No. 40 tantalum wire, which is superconducting at the temperatures under consideration and hence has a greater thermal resistance than normal metals. Any runs in which there was a measurable temperature difference between the bath and the reservoir were discarded. However, the smallest temperature difference which could be measured was about 0.001°K, so that small thermomechanical pressures may have existed, particularly when the reservoir was above the bath level. Several runs were also made with the resistors removed. They yielded the same results as the runs in which the resistors were present.

The apparatus was suspended from a brass holder, which could be raised out of the helium bath or lowered into it. The technique of measurement was as follows. The position of the reservoir relative to the bath level was quickly changed. Then readings were taken of the heights of the levels in the reservoir and in the side tube, relative to the bath level, as a function of time, as the liquid flowed either into or out of the reservoir. The level heights were determined by observation of a scale, graduated in millimeters and 17.5 cm in length, etched onto the side of the glass reservoir. Time measurements were made in two ways. The first measurements were made by concurrent visual observation of the reservoir level and a stop watch. These measurements were later checked with an Esterline-Angus recording milliammeter as a time indicator. A graphic record of the time intervals was made by energizing the meter with a hand switch while visually observing the reservoir. The roll speed was approximately 3 in./min, so that time measurements could be made to better than $\frac{1}{4}$-sec accuracy. The illumination necessary for these measurements was provided by six two-watt neon bulbs, mounted in a vertical column and located one meter from the cryostat. During a measurement the temperature of the bath was kept constant to within four thousandths of a degree by means of a differential oil manometer and a needle valve in the pumping line.

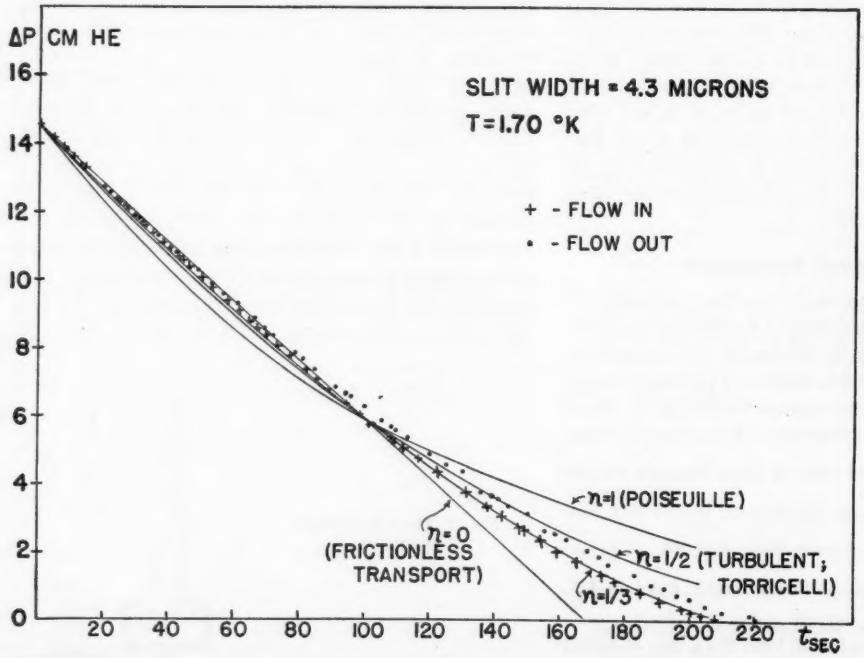

FIG. 2. Experimental observations of liquid height *vs* time. The points are the experimental points of several different measurements normalized at high pressures. The solid lines are obtained from $\dot{V} \propto (\Delta p)^n$.

[6] Boorse, Zemansky, and Brown, Phys. Rev. 84, 1050 (1951).

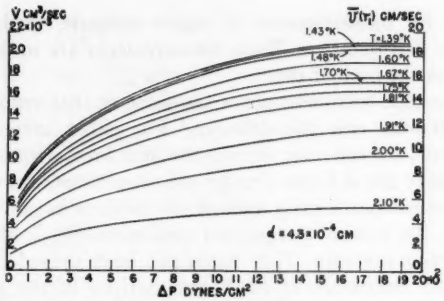

FIG. 3. Volume and linear flow rates *vs* pressure at constant temperature. Slit width = 4.3μ.

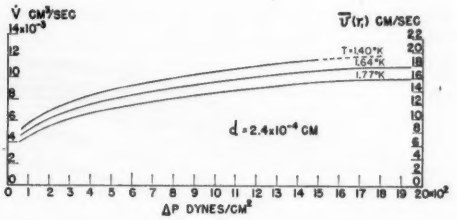

FIG. 4. Volume and linear flow rates *vs* pressure at constant temperature. Slit width = 2.4μ.

The vapor pressures were converted to temperatures on the 1949 temperature scale.[7]

In order to determine the flow velocities, the slope of the curves of height h *versus* time t must be obtained. (See Fig. 2.) This analysis has been done in two ways. The flow rates were first obtained by differentiation of the expression $h=h_0+a_1t+a_2t^2+a_3t^3$, where the constants h_0, a_1, a_2, and a_3 were obtained from the experimental data by the method of least squares. From five to twenty measurements were made at one temperature, and the resulting values of h *versus* t plotted on a single graph. The least-squares fit was made to a smooth curve drawn through these points.

The second method of obtaining the slopes of the h *versus* t curves utilizes the information obtained by the first method. The first method revealed that at least for low pressure heads, the discharge rate was proportional to a power of the pressure head $\dot{h}\propto(\Delta p)^n$ with $n\simeq\frac{1}{2}$. Since the bath level is practically constant during a measurement, the flow rate is proportional to $\dot{h}$ and the pressure head proportional to h, where h is the difference between the bath level and the reservoir level. Integration of the relation $\dot{h}=-\alpha h^{\frac{1}{2}}$ yields an expression of the form $h=h_0(1-t/t_0)^{\frac{1}{2}}$, which contains two adjustable parameters and can be fitted to the experimental points. One of the solid curves in Fig. 2 is a plot of this function. Both of the above methods of analysis yield analytic curves that fit the data within the experimental error and give the same results at low pressure heads. They yield somewhat different results at the highest pressure heads.

The volume rate of flow of liquid through the slit, $\dot{V}$, at a given pressure head Δp is the derivative dh/dt, at a given value of h, multiplied by the cross-sectional area of the reservoir, which is 0.196 cm². The pressure is given by ρgh, where ρ is the density of liquid helium at the temperature under consideration, g the acceleration of gravity, and h the height. To determine the linear velocities of flow, the width of the slit must be measured. This was done by observation of the rate of flow of helium I through the slit.[4] The average linear velocity of flow in the slit is given by $\bar{v}(r)=\dot{V}/(2\pi rd)$, where r is the distance from the axis of the reservoir to the point in the slit at which $\bar{v}$ is desired, and d is the average or effective width of the slit. In the curves to follow, the average linear velocity is calculated for r equal to the inner radius of the slit, which is 0.41 cm. This is the maximum velocity, since the velocity decreases as r^{-1} as one proceeds to the outer perimeter of the slit.

[7] H. van Dijk and D. Shoenberg, Nature **164**, 151 (1949).

EXPERIMENTAL RESULTS

By the methods described in the preceding section the volume rate of flow of liquid helium through the slit may be calculated as a function of the hydrostatic pressure head, at a constant temperature. Experiments have been made using two different slit widths, and the results will be classified into two groups, corresponding to the two widths. The first group, with a slit width of 4.3×10^{-4} cm, covers the temperature range between 1.39°K and 2.10°K in steps of at most 0.11°K. The pressures involved extend to 2300 dynes/cm², i.e., that given by about 16 cm of helium. This range of temperatures and pressures represents the greatest variation which can be obtained in a simple way. At temperatures close to the λ point the flow rate is so small that the normal fluid flow and the film flow become an appreciable fraction of the total flow. On the other hand, although temperatures below 1.39°K can be obtained, the quantity of liquid which remains is too small to allow the use of large pressure heads. The other group involves measurements at three temperatures made with a slit width of 2.4×10^{-4} cm. From the results of the two groups it is possible to estimate the influence of the slit width on the flow rate.

The pressure dependence of the flow rate for the two groups is shown in Figs. 3 and 4. The quantity $\dot{V}$ is the volume rate of flow of liquid in cm³/sec. The quantity $\bar{v}(r_1)$ is the average linear velocity of flow in cm/sec through the slit at its inner perimeter (r_1). The curves give the results obtained by the first method of analysis. The second method gives values for the flow rates which are the same as those of the first method at low pressure heads but which are about 15 percent larger at the highest pressure heads. In order to determine if a relation of the form $\dot{V}=(\text{constant})(\Delta p)^n$ is valid for these results, logarithmic plots of flow rate *versus* pressure head are given in Figs. 5 and 6. The solid lines indicate the results of the first method of

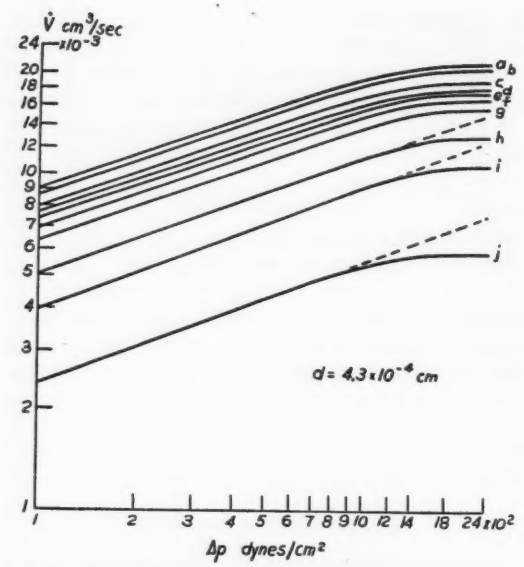

FIG. 5. Logarithmic plot of volume flow rate *vs* pressure at constant temperature for the 4.3-μ slit. Curves *a–j* represent temperatures of 1.39, 1.48, 1.60, 1.67, 1.70, 1.75, 1.81, 1.91, 2.00, and 2.10°K respectively. The solid curves are obtained from the 1st method of analysis and the dashed curves from the 2nd method.

analysis. The second method of analysis yields straight lines that are extrapolations of the lower pressure curves obtained from the first method. Some of these lines are indicated with dashed lines. From Figs. 5 and 6 it is evident that for the lower values of the pressure head the flow rate is proportional to a power of the pressure. In agreement with other workers,[1,4,5] the value of the index n is nearly independent of temperature, although there may be a slight increase in n at temperatures near the λ point. The following table gives n as a function of temperature for the two slit widths:

(a) $d=4.3\mu$, $\Delta p=800$ dynes/cm²:

T=1.39 1.48 1.60 1.67 1.70 1.75 1.81 1.91 2.00 2.10

n=0.33 0.34 0.33 0.33 0.33 0.33 0.33 0.35 0.37 0.36;

(b) $d=2.4\mu$, $\Delta p=1400$ dynes/cm²:

T=1.40 1.64 1.77

n=0.27 0.27 0.28.

Figures 5 and 6 show that the first method of analysis yields flow rates that approach saturation values at the highest pressures. Since these saturation values do not appear in the second method of analysis, we conclude that they may well be due to a systematic error inherent in the first method of analysis. Since the difference between a pressure independent flow rate and a flow rate depending on the $\frac{1}{3}$ power of the pressure cannot be distinguished at these pressures, we must wait for measurements at higher pressure heads to settle this question. These measurements are in progress at the present time.

The side tube behavior is the same as that reported by Bowers and Mendelssohn.[4] For either inflow or outflow, the side tube follows the bath level within the capillary rise of 1 mm. During one set of three runs with substantially the same average slit width as in previous runs, the side tube registered approximately $\frac{1}{10}$ of the reservoir pressure. This may have been caused by a chance confluence of small irregularities in the glass which did not affect the flow of helium I, from which the slit width was determined, but which did affect the flow of helium II. However, the reservoir level behaved in the usual way in these runs, and we have not been able to reproduce the unusual side tube behavior.

The linear velocities of flow through the slit have also been determined in these studies. Since the determination of these velocities requires a knowledge of the slit width, they are subject to a greater uncertainty than are the volume flow rates. The uncertainty in the measured width of the slit amounts to about 15 percent. In view of this it is not possible to make a precise comparison between the results for the two slit widths. However, it is evident from the curves of Figs. 3 and 4 that the average linear velocity of flow does not decrease when the slit is made narrower. It is likely that the average linear velocity actually increases as the slit width is decreased, as has been found to be the case by Allen and Misener[1] and by Bowers and Mendelssohn.[4]

Figure 7 shows the temperature variation of the volume flow rate at various values of the pressure head, for the 4.3-micron slit. In Fig. 8 the temperature dependence of the flow rate is compared with that of the superfluid concentration ρ_s/ρ. The values of ρ_s/ρ are taken from Andronikashvili.[8] The comparison is made at pressures of 200, 700, and 1800 dynes/cm². The values of $\dot{V}$ are normalized to agree with the ρ_s/ρ curve at 1.81°K. It is evident that the temperature dependence of the flow is essentially the same as that of the superfluid concentration.

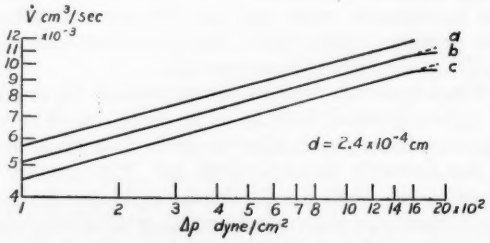

FIG. 6. Logarithmic plot of volume flow rate *vs* pressure at constant temperature for the 2.4-μ slit. Curves *a*, *b*, and *c* represent temperatures of 1.40, 1.64, and 1.77°K respectively. The solid curves are obtained from the first method of analysis and the dashed curves from the second method.

[8] E. L. Andronikashvili, J. Exptl. Theoret. Phys. (U.S.S.R.) 18, 424 (1948).

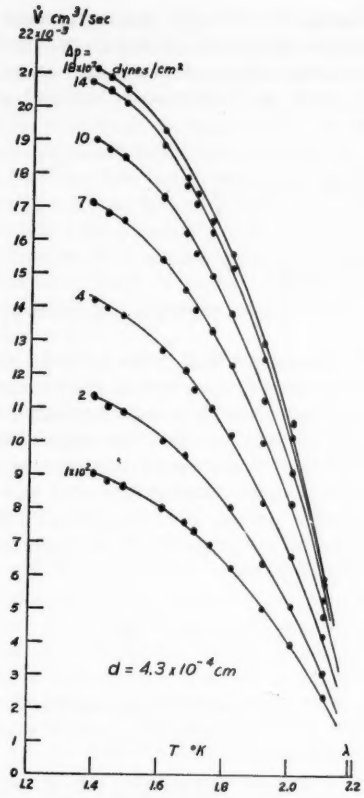

FIG. 7. Volume flow rate *vs* temperature at constant pressure. Slit width=4.3 μ (first method of analysis).

DISCUSSION OF THE RESULTS

(A) Accuracy of the Flow Rates

The maximum uncertainty in the experimental observations amounts to 0.05 cm in the height of the liquid column and 0.25 second in the time. This leads to a maximum uncertainty in flow rate of 15 percent at high rates and 10 percent at very low flow rates, or at high pressures and low pressures respectively. The associated uncertainty in the pressure varies from a negligible quantity at high pressures to about 10 percent at low pressures. These uncertainties are greater than the errors of measurement of the geometrical constants of the apparatus by a factor of 2 or more, so that the latter errors were neglected. The power n in the relation $\dot{V} \propto (\Delta p)^n$ which best fits the experimental points over the whole range of pressure heads can be determined within approximately 10 percent. It cannot be accurately determined at high pressure heads, as evidenced by the different results of the two methods of analysis.

Several mechanisms exist which can give rise to errors in the observed flow rates. These errors will vary with the pressure head and can influence the measured pressure dependence of the flow rates. If isothermal conditions are not maintained in the flow process, the resulting thermomechanical pressure gradient will be opposite in sign to the hydrostatic pressure gradient. Thus the net pressure on the liquid in the reservoir will be smaller than the measured pressure. Another possible source of error, which will have the same effect on the flow rates as the above situation, is the absorption of radiant energy by the liquid in the reservoir when the latter is raised above the bath level. The contribution of this effect to the flow velocities should be greatest at low pressures, i.e., when the volume of liquid in the reservoir is small. Excessive evaporation losses can also cause high apparent flow rates if the reservoir is too far above the bath level.

Experimental verification of these errors has been obtained. Upon plotting the experimental results of height *versus* time, nearly all the points corresponding to measurements made with the reservoir below the bath level lie on a smooth curve. On the other hand, the points corresponding to the reservoir above the bath level show much more scatter and deviate slightly from the points obtained with the reservoir below the bath (see Fig. 2). In view of these observations, and also in view of the divergence of the streamlines during outflow, the flow rates have been calculated from only those measurements made with the reservoir below the bath level. It is felt that in this way the errors introduced by the thermomechanical effect and excess evaporation are minimized, because temperature equalization will take place more rapidly when the reservoir is below the bath level than when it is above the bath.

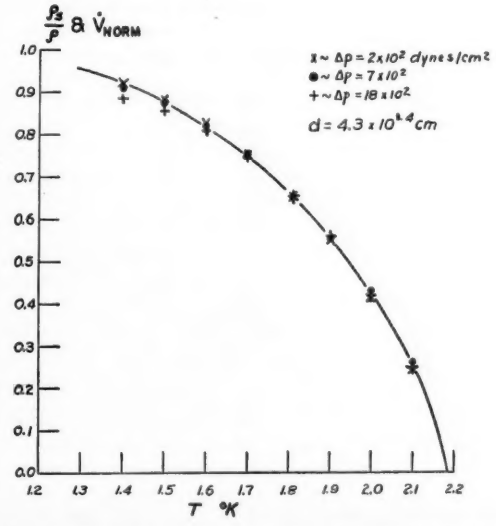

FIG. 8. Comparison of the temperature dependence of the volume flow rate with that of the superfluid concentration. The solid curve represents ρ_s/ρ. The flow rate is normalized to ρ_s/ρ at 1.81°K. Slit width=4.3 μ.

A further possibility of error arises from the presence of the side tube. When the position of the reservoir and side tube is changed relative to the bath level, the liquid level in the side tube adjusts itself rapidly to approximate coincidence with the bath level. During the time of equalization of levels, the flow in the side tube will decrease the flow in the reservoir. Such an error is avoided by delaying the start of a measurement until the level in the side tube is static. The time required for this is from 6 to 10 seconds, depending on the temperature.

Contamination by solidified gases is a frequent source of difficulty in flow measurements. This is especially true in the case of the helium film. Little is known of the effect of contamination on flow in narrow channels. We have taken no special care to outgas the flow equipment, other than to carefully evacuate the apparatus and flush it with helium. Elaborate vacuum techniques[9] are required to obtain a surface free from any adsorbed gases. Extremely high temperatures and low pressures (10^{-10} to 10^{-11} mm Hg) are necessary to remove the last layer. It is likely that no flow measurements have been made on surfaces not contaminated by at least one layer of adsorbed gas. A test was made to determine the effect of allowing air to come in contact with the flow apparatus. At the end of two of the runs, a small amount of air was let into the system. No observable difference could be detected in the flow rates or side tube behavior. It seems likely that contamination does not easily occur unless the flow surfaces are directly exposed to the gas, as is the case in film experiments.

These mechanisms are believed to be the only important ones which could falsify the observed pressure dependence of the flow velocity. The measurements are made in such a way as to minimize these errors.

(B) Theoretical Considerations

To summarize the experimental results, the dependence of volume flow rate on pressure head indicates the following facts. For pressure heads below approximately 10 cm of helium, the flow rate is proportional to a power n of the pressure head. The constant of proportionality depends on the temperature as the superfluid concentration, ρ_s/ρ. The index n is nearly independent of temperature, but may decrease with decreasing slit width. Its value is approximately $\frac{1}{3}$. For the highest pressure heads, there is some indication that the flow rates become less dependent on the pressure, although this behavior can only be established by measurements at higher pressures. The flow rates can be expressed as:

$$\dot{V}=B(\rho_s/\rho)(\Delta p)^{\frac{1}{3}}\ \text{cm}^3/\text{sec},$$

with Δp the pressure head in dynes/cm^2 and $B=2.1\times10^{-3}$ cgs units for the 4.3-μ slit.

An attempt has been made to correlate the experimental observations with the existing theories of the hydrodynamical properties of helium II. In the absence of a temperature gradient, the equations of motion as given by Gorter and Mellink[10] may be written as:

$$\rho_s\frac{d\mathbf{v}_s}{dt}=-\frac{\rho_s}{\rho}\nabla p-\mathbf{F}_{sn}-\mathbf{F}_s,$$

$$\rho_n\frac{d\mathbf{v}_n}{dt}=-\frac{\rho_n}{\rho}\nabla p+\mathbf{F}_{sn}+\eta_n[-\nabla\times\nabla\times\mathbf{v}_n+4/3\nabla(\nabla\cdot\mathbf{v}_n)]-\mathbf{F}_n.$$

The flow of the normal fluid in the 4.3-μ slit is a small fraction of the total flow, except at temperatures very close to the λ point. Measurements in helium I indicate that the normal fluid flow is of the order of 1/100 of the superfluid flow. Under these circumstances, we may disregard the second equation and put $v_n=0$. The pressure distribution and flow characteristics will then be determined by the properties of the superfluid. The first equation becomes:

$$\rho\frac{d\mathbf{v}_s}{dt}=-\nabla p-\frac{\rho}{\rho_s}\mathbf{F}_{sn},$$

where $\mathbf{F}_{sn}$ is the force between the superfluid, and the normal fluid and the walls. We consider several different possibilities.

(a) *Perfect Fluid:* $\mathbf{F}_{sn}=0$

For this case the equation of motion integrates to give Bernoulli's equation. If we assume streamline flow filling the slit, the following behavior would be expected:

1. The index n in the relation for the pressure dependence of the flow rate should be $=\frac{1}{2}$ (Torricelli's theorem). This value is not observed. In addition, the pressure drop necessary to produce the average velocities of approximately 20 cm/sec is much smaller than the measured drop:[11]

$$h=(v^2/2g)\simeq 2\ \text{mm of He}.$$

2. Because of the increase of the cross section of the flow channel with increase in r, the flow rates for flow out should be greater than those for flow in. However, the streamlines are diverging for flow out, and the flow pattern is extremely unstable.[12] It is probable that streamline flow would break down near the narrowest section of the slit and the liquid would break away from one wall. In this case the two rates would be nearly equal. This consideration suggests that the flow ge-

[9] Homer D. Hagstrum, Rev. Sci. Instr. **24**, 1122 (1953).

[10] C. J. Gorter and J. H. Mellink, Physica **15**, 285 (1949).

[11] This drop would be increased by the assumption of an effective mass for the acceleration of the superfluid in the slit greater than the gravitational mass.

[12] L. Prandtl and O. G. Tietjens, *Applied Hydro- and Aeromechanics* (McGraw-Hill Book Company, Inc., New York, 1934), p. 52.

ometry is probably not a good one to use to determine in what ways He II behaves as a perfect fluid.

3. The side tube behavior depends on the conditions that exist in the groove. If there is no dissipation (streamline flow from the inner radius to the outer), the side tube should follow the reservoir for flow out and the bath for flow in. If the kinetic energy of the fluid flowing into the groove is completely dissipated, then the side tube pressure should be $\frac{1}{3}$ of the total pressure head for flow out and $\frac{1}{4}$ the total head for flow in. On the other hand, if the flow breaks down as described under 2, the side tube would follow the bath for either flow in or flow out.

The model of a perfect fluid is thus not very satisfactory, since it gives the wrong magnitude for the flow rate and also a wrong power dependence. Qualitatively, the behavior of the side tube and the equality of inflow and outflow rates can be explained if we assume that the flow does not fill the channel except in the narrowest constriction.

(b) *Mutual Friction:* $\mathbf{F}_{sn}=A\rho_n\rho_s\mathbf{v}_s^3$

This expression for $\mathbf{F}_{sn}$, due to Gorter and Mellink,[10] can be used in the equation for the superfluid motion and a solution obtained for the slit geometry of these experiments. We assume a constant velocity profile and take from the equation of continuity:

$$\mathbf{v}_s(r)=v_s(r_i)[r_i/r]\mathbf{i}_r,$$

where $v_s(r_i)$ is the (maximum) velocity at the inner radius of the slit and $\mathbf{i}_r$ is the unit vector in the r direction. We must solve:

$$\rho\frac{d\mathbf{v}_s}{dt}=\rho\left[\frac{\partial\mathbf{v}_s}{\partial t}+(\mathbf{v}_s\cdot\nabla)\mathbf{v}_s\right]=-\nabla p-A\rho\rho_n\mathbf{v}_s^3.$$

Now,

$$(\mathbf{v}_s\cdot\nabla)\mathbf{v}_s=\tfrac{1}{2}\nabla\mathbf{v}_s^2-\mathbf{v}_s\times\nabla\times\mathbf{v}_s.$$

The first term on the right (the Bernoulli term) is negligible, as shown in (a), and we take $\nabla\times\mathbf{v}_s=0$ (irrotational flow). Also, for steady flow $\partial\mathbf{v}_s/\partial t=0$. Then we obtain

$$\nabla p=-A\rho\rho_n\mathbf{v}_s^3,$$

or, since $\nabla p=(\partial p/\partial r)\mathbf{i}_r$,

$$p_r-p_{r0}=\tfrac{1}{2}A\rho\rho_n\mathbf{v}_s^3(r_i)r_i^3\left[\frac{1}{r^2}-\frac{1}{r_0^2}\right],$$

with r_0=outer radius of flow channel. The following results are obtained:

1. For the total pressure drop, we obtain

$$\Delta p=0.026A\rho_n v_s^3(r_i),\text{ or }v_s(r_i)=38(A\rho_n)^{-\frac{1}{3}}(\Delta p)^{\frac{1}{3}}.$$

The dependence of the average velocity on pressure head is correctly given. However, the temperature dependence of the velocity at constant pressure is wrong, if we take A as a constant. Also, the pressure heads required to produce the observed average velocities of approximately 20 cm/sec are too low. If we take $A\rho_n=2$ cgs units, in accordance with the work of Hung, Hunt, and Winkel,[13] then $\Delta p=3$ cm of He is the required pressure head. This is too small by almost an order of magnitude.

2. Side tube behavior. The observed behavior is a strong argument against the presence of any dissipative force, such as mutual friction, in the slit. The side tube pressure should be $\frac{1}{3}$ of the total pressure head, or at least $\frac{1}{6}$ of 3 cm of helium, according to the mutual friction theory. It has been suggested by Heaps[14] that the dissipation could occur in a wider part of the flow channel as the fluid enters the slit, since the mutual friction seems operative in wide channels. However, it is likely that this success of the mutual friction theory is associated with the presence of normal fluid flow, and in any event there should be a similar dissipation as the fluid leaves the slit.

The mutual friction theory does not seem adequate to explain the observed behavior. Although the correct pressure dependence of the flow rates is given, the temperature dependence and the side tube behavior are in disagreement with the theory. This conclusion does not mean that the mutual friction theory is not of importance for higher velocities and wider slits. In fact, much of the most recent work[13] indicates that it is not applicable to the low velocities and narrow slits encountered in our experiments.

(c) *Critical Velocity Theory*

Mendelssohn and his co-workers[4] have advanced a theory for the flow of helium II involving the existence of a critical velocity. The theory has not been formalized to the extent of the Gorter-Mellink theory. The liquid flow is described as a frictionless transport under zero pressure gradient if the flow velocity is less than a critical velocity of the order of 20–50 cm/sec. The entire pressure drop is supposed to occur across the part of the flow channel having the greatest resistance to flow, and in particular across the narrowest constriction. For velocities greater than critical, frictional forces come into consideration which in some cases can be described by the Gorter-Mellink equations.

Since many of the elements of the critical velocity theory were inferred from experiments similar to those presented here, the results obtained are in qualitative agreement with the theory. However, the theory is not quantitative, and there are many unclarified points. The pressure dependence of the flow for velocities less than critical is not given, and in fact no reason is given for any pressure drop at all. There is no positive evidence of a critical velocity in our experiments, although sufficiently high pressure heads may not have been used.

Thus, the critical velocity theory is capable of explaining some of the qualitative features of the results.

[13] Hung, Hunt, and Winkel, Physica **18**, 629 (1952).
[14] W. V. Houston and C. W. Heaps (private communication).

It fails in providing any quantitative relations for the flow behavior. In the next section we suggest a way of providing some of these relations by combining some of the characteristics of the critical velocity theory with the properties of a perfect fluid.

(d) *Modification of the Velocity Profile*

It has been suggested by Houston[14] that the anomalous pressure dependence of the flow could be brought into a theoretical frame-work by modifying the velocity profile. Prandtl[15] has shown how a velocity profile can be chosen to yield any given pressure dependence for the average velocity. However, his arguments apply only to turbulent flow, and imply a dissipative interaction with the walls. The behavior of the side tube rules out such dissipation, and Prandtl's theory is not directly applicable.

Most interpretations of the flow velocities suffer from two defects: the velocity of flow is taken as a constant across the flow channel, and the average flow velocity is equated to the superfluid velocity. There is considerable evidence[16] to indicate that the velocity profile is not a straight line, but that the transfer in narrow channels is a surface effect. Mott[17] has presented arguments to show that a surface flow of the superfluid around a stationary core of liquid can be stable under certain conditions. Kapitza[18] suggested the same picture on the basis of the results of his experiments on heat conduction in capillaries. We tentatively adopt such a picture and choose a velocity profile as in Fig. 9. The experimental results can be summarized as:

$$\Delta p=\left[\frac{\rho}{\rho_s}\frac{\dot{V}}{B}\right]^3, \quad \dot{V}=2\pi r_i d\langle(\rho_s/\rho)v_s(r_i)\rangle_{Av}.$$

(The average flow velocity $\bar{v}$ is set equal to $\langle(\rho_s/\rho)v_s\rangle_{Av}$.) If we adopt a modified Bernoulli theorem, then $\Delta p=\frac{1}{2}\langle\rho v_s^2\rangle_{Av}$ gives the pressure drop at the entrance to the slit. For the velocity profile of Fig. 9,

$$\langle v_s\rangle_{Av}=\frac{2}{d}\int_0^{d/2} v_s(z)dz=2v_0t/d,$$

$$\langle v_s^2\rangle_{Av}=2v_0^2t/d,$$

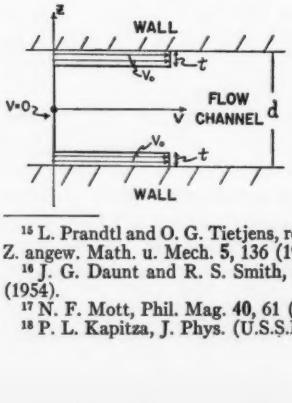

FIG. 9. Velocity profile for flow of the superfluid through a narrow slit: $v=0$ for $|z|<(d/2-t)$; $v=v_0$ for $(d/2-t)<|z|<(d/2)$.

where v_0 is the average velocity of the superfluid in a layer of thickness t. To satisfy the Bernoulli equation, we must have

$$\tfrac{1}{2}\langle\rho v_s^2\rangle_{Av}=\left(\frac{\rho/\rho_s}{B}\right)^3\dot{V}^3$$

or

$$\tfrac{1}{2}\rho\langle v_s^2\rangle_{Av}=\left(\frac{\rho}{\rho_s}\right)^3\left(\frac{2\pi r_i d}{B}\right)^3\left(\frac{\rho_s}{\rho}\right)^3\langle v_s(r_i)\rangle_{Av}^3.$$

Putting in the values of $\langle v_s\rangle_{Av}$ and $\langle v_s^2\rangle_{Av}$, we obtain

$$v_0t^2=C, \quad C=\frac{\rho}{d}\left(\frac{B}{4\pi r_i}\right)^3.$$

The quantity C is a constant and can be evaluated from the experimental results: $C=23\times10^{-9}$ cm^3/sec. The product v_0t is proportional to the flow rate: $(\rho_s/\rho)v_0t=\dot{V}/4\pi r_i$. Therefore, as the discharge rate increases, v_0 must increase and t decrease. Values of v_0 and t can be obtained from the experimental results: $v_0=7.2(\Delta p)^{\frac{1}{3}}$ cm/sec, $t=5.7\times10^{-5}(\Delta p)^{-\frac{1}{3}}$ cm. For $\Delta p=2100$ dynes/cm^2 the values are $v_0=12$ m/sec and $t=4.5\times10^{-6}$ cm. These figures are in some respects reasonable. v_0 is of the order of the critical velocities calculated on the basis of Landau's theory,[19] and t is of the order of the film thickness.

The temperature dependence of the flow is explained on the basis of the two-fluid theory. If we assume thermal equilibrium in the slit, only a fraction ρ_s/ρ of the slit cross section will be available for flow of the superfluid. At a given pressure head, the velocity of the superfluid is determined. Therefore, the flow rate will have the same temperature dependence as the "effective" slit cross section, or as ρ_s/ρ. Also, the average velocity of the superfluid is, on this picture, not equal to $\bar{v}$. Instead, $\bar{v}_s=\bar{v}\rho/\rho_s$ gives the average superfluid velocity.[20] $\bar{v}_s$ is, of course, the average velocity measured at sufficiently low temperatures.

ACKNOWLEDGMENTS

The writers wish to express their deep appreciation to Dr. K. Mendelssohn, who initiated this research while he was a visiting professor at the Rice Institute. His continued interest and advice have been of great value in this work. The helpful advice and assistance of Professors C. F. Squire, W. V. Houston, and C. W. Heaps are gratefully acknowledged. We also thank Clarence Belcher for technical assistance. During the course of this work, one of us (R.T.S.) was in receipt of a fellowship from the Magnolia Petroleum Company.

[15] L. Prandtl and O. G. Tietjens, reference 12, p. 70; L. Prandtl, Z. angew. Math. u. Mech. **5**, 136 (1925).
[16] J. G. Daunt and R. S. Smith, Revs. Modern Phys. **26**, 177 (1954).
[17] N. F. Mott, Phil. Mag. **40**, 61 (1949).
[18] P. L. Kapitza, J. Phys. (U.S.S.R.) **4**, 181 (1941).
[19] R. B. Dingle, Advance in Physics **1**, 111 (1952).
[20] J. G. Daunt and R. S. Smith, Revs. Modern Phys. **26**, 217 (1954).

Double Scattering of Electrons with Magnetic Interaction*

H. MENDLOWITZ† AND K. M. CASE
Harrison M. Randall Laboratory of Physics, University of Michigan, Ann Arbor, Michigan
(Received September 20, 1954)

The Mott theory of double scattering of electrons by nuclei is extended to the case where a constant homogeneous magnetic field intervenes between the two scattering centers. The problem is treated in the Foldy-Wouthuysen representation. It is found that the presence of the magnetic field causes the asymmetry in the double-scattering cross section to be altered, and that this change in the asymmetry can be utilized to determine the gyromagnetic ratio of the free electron.

I. INTRODUCTION

THE Mott theory[1] of double scattering of electrons by nuclei is extended to the case where a constant homogeneous magnetic field intervenes between the two targets. If there is no anomalous moment interaction, it is found that the double-scattering cross section into a given direction is the same cross section, as in the field-free case, into another direction. The new direction (magnetic field present) can be obtained from the first direction (field-free) by rotating about the direction of the field by an amount equal to the space rotation of the particles between the scatterers. However, with an anomalous-moment interaction, there is an additional change in the cross section which depends upon the relative orientation of the constant homogeneous magnetic field with the directions of motion of the initial beam and first scattered beam. The way in which the asymmetry is altered is discussed, and it is demonstrated how it can be employed to determine the gyromagnetic ratio of the free electron.

II. MOTT THEORY

We will briefly outline the Mott theory of double scattering in a vacuum, and then show how the intervention of a magnetic field between the two scatterers alters the cross section.

An unpolarized beam along the direction IA (Fig. 1) is incident upon the first target at A. The part of the beam which is scattered into the direction of AB is allowed to fall upon the target at B. The beam is then scattered into direction BC. It is found that for a given angle θ_2 (Fig. 1), the double scattering cross section exhibits an asymmetry about the azimuthal direction in the $x'y'z'$ coordinate system.

Although the Mott theory starts with the Dirac equation, it restricts itself to transitions between positive energy states and neglects all contributions to the cross section arising from transitions from negative energy states. This approximation is quite good because it is found that the asymmetry in the double scattering cross section washes out for energies such that $\beta=v/c$ is greater than about 0.7.[2] This can be explained by noting that transitions between the positive and negative energy states can cause a depolarization of the first scattered beam. Thus, only where the contribution to the cross section from the negative-energy states is negligible can we expect that the asymmetry will not be negligible.

Because we limit the discussion to positive-energy states only, we can describe the spin polarization of the beam in terms of a two-by-two spin density matrix.[3] The original beam which is incident on the first target is unpolarized. The spin density matrix is given by

$$\rho_{mm'}{}^{(s)}=\tfrac{1}{2}\delta_{mm'} \tag{1}$$

where m and m' refer to two states of spin polarization. The beam of particles are considered to have the same momentum, and so the momentum density matrix describes a pure momentum state. In order that our notation be close to that of Mott,[1] we take the z component Pauli spin matrix diagonal. The scattering is described by a scalar transition operator (scalar under simultaneous rotations of spin and space) which transforms an initial momentum and spin state to a final state. It is given by

$$V=f(\theta)+ig(\theta)(\sigma_x\sin\varphi+\sigma_y\cos\varphi). \tag{2}$$

The $f(\theta)$ and $g(\theta)$ are the Mott f and g functions which depend on the polar angle θ between the beam incident on the target and the scattered beam (Fig. 1), and φ is the azimuthal angle. The angles θ and φ describe the difference in direction between the initial momentum and momentum after the scattering. The σ's are the usual Pauli spin matrices.

After the initial scattering, the density matrix is

$$\bar{\rho}=V(\theta_1,\varphi_1)\rho V^\dagger(\theta_1,\varphi_1). \tag{3}$$

* Supported in part by the U. S. Atomic Energy Commission.
† Now at National Bureau of Standards, Washington, D. C.
[1] N. F. Mott, Proc. Roy. Soc. (London) **A124**, 425 (1929); **A135**, 429 (1932).
[2] N. F. Mott, Proc. Roy. Soc. (London) **A135**, 429 (1932); H. A. Tolhoek and S. R. deGroot, Physica **17**, 1 (1951). This does not mean that the single scattering Mott formula is not exact, because there it is legitimate to consider only the positive energy states.
[3] Density matrices are discussed by: J. von Neuman, Göttingen Nachr. 245 (1927); R. C. Tolman, *Principles of Statistical Mechanics* (Oxford University Press, London, 1938), p. 327; H. A. Tolhoek and S. R. deGroot, Physica **17**, 1 (1951); U. Fano, National Bureau of Standard Report 1214 (unpublished) and others.

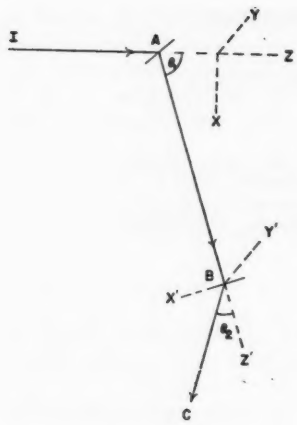

FIG. 1. Schematic diagram of double-scattering experiment.

Since V is a function of the angle between the initial and scattered directions, the density matrix after the first scattering $\bar{\rho}$ is a function of θ_1, φ_1 (Fig. 1). The direction of the incident beam being taken as the polar axis. The cross section can be obtained by taking the trace over the spin states, and is

$$d\sigma(\theta_1,\varphi_1)\sim[|f(\theta_1)|^2+|g(\theta_1)|^2], \tag{4}$$

which is independent of the azimuthal angle φ_1. If instead of measuring the cross section after the first scattering, the beam is then scattered by the target at B (Fig. 1), the cross section after the second scattering will exhibit an asymmetry in the azimuthal direction.

Following Mott, we consider the first scattered beam to be in the direction $\theta=\theta_1$ and $\varphi_1=0$. It is incident on the second target. The spin density matrix of this beam is, from Eq. (3),

$$\bar{\rho}^{(s)}=\tfrac{1}{2}N\{|f(\theta_1)|^2+|g(\theta_1)|^2 -i\sigma_y[f(\theta_1)g^*(\theta_1)-f^*(\theta_1)g(\theta_1)]\}, \tag{5}$$

where N is a normalization constant. It will be dropped in future calculations but its presence is implied. Note that the form of $\bar{\rho}^{(s)}$ differs from the spin density matrix of the incident beam. This means that the portion of the scattered beam in a specified direction in space is polarized. The degree of polarization of the beam incident on the second target is given by[4]

$$P=\frac{2|f(\theta_1)|^2|g(\theta_1)|^2-[f(\theta_1)g^*(\theta_1)+f^*(\theta_1)g(\theta_1)]}{[|f(\theta_1)|^2+|g(\theta_1)|^2]}. \tag{6}$$

If the f and g functions are real, the polarization vanishes as has been pointed out by Mott.

[4] The degree of polarization is defined as $P=|a|^2$, where the spin density matrix is defined in terms of the Pauli spin vector as

$$\rho^{(s)}=\tfrac{1}{2}[1+a\cdot\sigma].$$

This is the same as Fano's definition in reference 3. Fano's definition differs from that of Tolhoek and deGroot, but both are related to the same invariant properties of the density matrix.

The beam incident on the second target is a partially polarized beam and the momentum density matrix describes a pure momentum state along the z' direction (Fig. 1). The second scattering is described by the scalar operator $V(\theta_2,\varphi_2)$ which is given by Eq. (2) in that representation where $\sigma_{z'}$ is diagonal. The spin density matrix $\bar{\rho}^{(s)}$ is transformed to this representation by rotating about the y axis through an angle θ_1 (Fig. 1).

Since the y direction remains invariant, the spin density matrix $\rho'^{(s)}$ in the representation where $\sigma_{z'}$ is diagonal is given by Eq. (5) with σ_y replaced by $\sigma_{y'}$. The density matrix after the second scattering is

$$\bar{\rho}'=V(\theta_2,\varphi_2)\rho' V^\dagger(\theta_2,\varphi_2), \tag{7}$$

and the double-scattering cross section is obtained by taking the trace of $\bar{\rho}'$ over the spin states. Thus,

$$d\sigma\sim\{[|f_1|^2+|g_1|^2][|f_2|^2+|g_2|^2] -[f_1g_1^*-f_1^*g_1][f_2g_2^*-f_2^*g_2]\cos\varphi_2\}, \tag{8}$$

where f_1 means $f(\theta_1)$ and f_2 means $f(\theta_2)$, etc. This can be written as

$$d\sigma\sim 1-\delta\cos\varphi_2, \tag{9}$$

where

$$\delta=\frac{[f_1g_1^*-f_1^*g_1][f_2g_2^*-f_2^*g_2]}{[|f_1|^2+|g_1|^2][|f_2|^2+|g_2|^2]}. \tag{10}$$

Equation (9) gives the Mott double-scattering formula in free space.

If the transition operator V were independent of the spin, the first scattered beam would have remained unpolarized. The cross section of the double scattering would have been given by the first term of (8), and would not have exhibited any asymmetry in the azimuthal direction. Thus, the asymmetry is seen to arise from the spin dependence of the scattering potential. Therefore, in principle, one could determine the spin magnetic moment by measuring the asymmetry. However, it is difficult to measure an absolute cross section in the double-scattering experiment, and so it would not be feasible to employ this method to measure the gyromagnetic ratio of the free electron. The fact that there is an asymmetry in the cross section demonstrates the existence of the spin magnetic moment of the free electron. In order to make a quantitative measurement of the gyromagnetic ratio of an electron not bound to an atom, one can allow the spin magnetic moment to interact with a magnetic field between the two scattering events. The magnetic interaction causes the asymmetry to be altered and this can be utilized to determine the gyromagnetic ratio.

III. EXTENSION OF THE MOTT THEORY

The Mott theory is adequate to describe the double scattering experiment in free space. However, it has to

be modified where there is a magnetic field present between the two scattering centers.

It is assumed that within a region of about 10^5 wavelengths from the scatterer, about 10^{-5} cm for an electron with energy as low as one hundred kilovolts, the effect of the magnetic field upon the particle is negligible compared to the scattering potential. This is justified, because for magnetic field of about one hundred gauss, the spin precession frequency is given by

$$\omega_s=(e\mathfrak{H}/m_0c)(1-\beta^2)^{\frac{1}{2}}g/2, \tag{11}$$

where g=gyromagnetic ratio (about 2), e=electronic charge, $\mathfrak{H}$=magnetic field strength, m_0=rest mass of electron, c=velocity of light, $\beta=v/c$ (the ratio of electron's velocity to the velocity of light), and the spin precession will be about the order of 10^{-6} radian. The change in orbit direction will be of the same order of magnitude. For electrons of higher energy this approximation will be even better. Within this region the particle can be considered as traveling in free space. The scattering is then completely determined by the scattering potential. The same assumption is made for the second scattering. Thus the only effect of the magnetic field will be to change the wave function between the two scattering events.

The equations of motion of the wave function is discussed in the Foldy-Wouthuysen representation.[5] Although the Mott theory is based on the Dirac representation,[1] Mott actually employs a Pauli type approximation[6] as has been noted previously. It has been demonstrated that in the low-energy limit the positive energy eigenfunctions of this new representation readily go over to the Pauli limit.

If we consider only positive-energy states, the Hamiltonian is shown in the appendix to be, up to terms of first order in $\mu_0\mathfrak{H}$ (μ_0 is the Bohr magneton),

$$H=\left\{\mathcal{E}_\pi-\mu_0\boldsymbol{\sigma}\cdot\mathfrak{H}[(1-\beta^2)^{\frac{1}{2}}+a]+a\mu_0\frac{(\boldsymbol{\sigma}\cdot\mathbf{v})(\mathbf{v}\cdot\mathfrak{H})}{v^2}[1-(1-\beta^2)^{\frac{1}{2}}]\right\}. \tag{12}$$

Furthermore $\mathcal{E}_\pi$ is the energy operator in the absence of spin and is

$$\mathcal{E}_\pi=[m_0^2c^4+c^2\pi^2]^{\frac{1}{2}}, \tag{13}$$

where $\boldsymbol{\pi}=\mathbf{p}-e\mathbf{A}/c=m\mathbf{v}$, $\mathbf{p}$=momentum, $\mathbf{A}$=vector potential, and $a=\alpha/2\pi$ is the second order radiative correction to the spin magnetic moment.[7] This can be shown to be independent of the momentum[8] for a particle in a constant magnetic field.

The equations of motion of the coordinate operator $\mathbf{r}$ is given by

$$\dot{\mathbf{r}}=\frac{1}{i\hbar}[\mathbf{r},H]=c^2(\mathbf{p}-e\mathbf{A}/c)/\mathcal{E}_\pi, \tag{14}$$

which is just the equation of motion of a particle in a magnetic field rotating with the relativistic cyclotron frequency $\omega_L=e\mathfrak{H}(1-\beta^2)^{\frac{1}{2}}/m_0c$. If we consider the terms in the Hamiltonian containing the spin operator (defined as $\boldsymbol{\sigma}$ acting in this representation), we find the equations of motion for the spin operator for the following interesting cases are given as:

(1) $\mathfrak{H}\|\mathbf{v}$: $\quad d\boldsymbol{\sigma}/dt=[1+a]\omega_L\boldsymbol{\sigma}\times\mathbf{h}$, (15a)

(2) $\mathfrak{H}\perp\mathbf{v}$: $\quad d\boldsymbol{\sigma}/dt=[1+a/(1-\beta^2)^{\frac{1}{2}}]\omega_L\boldsymbol{\sigma}\times\mathbf{h}$; (15b)

$\mathbf{h}$ is a unit vector in the direction of the field. Thus, we find that the spin can be considered as precessing about the direction of the field with a frequency different from the cyclotron frequency by an amount that depends upon the relative orientation of the field and the particle's velocity.

The effect of the Hamiltonian can be considered as changing the space state and the spin state separately. The Hamiltonian acting on the initial space part of the wave function gives a wave function which describes a particle which has been displaced along the direction of the field and rotated about the direction of the field by an amount $\omega_L t$, t being the time spent between the two scattering events. Similarly one can see that the action of the field on the spin state is to rotate the spin state about the direction of the field by an amount $\omega_s t$, where ω_s is given by Eq. (15).[9]

Thus, if the wave function after the first scattering is Ψ, then just prior to the second scattering it is

$$\Psi_{inc_2}=e^{i\gamma t}P(t)Q(t)\Psi. \tag{16}$$

[5] L. L. Foldy and S. A. Wouthuysen, Phys. Rev. **78**, 29 (1950); K. M. Case, Phys. Rev. **95**, 1323 (1954); H. Mendlowitz, thesis, University of Michigan, 1954 (unpublished), gives a detailed treatment in the Foldy-Wouthuysen representation of an electron with an anomalous moment in a constant magnetic field.

[6] This is because he allows only positive energy eigenfunctions of the Dirac equation to be incident upon the second target.

[7] J. Schwinger, Phys. Rev. **76**, 790 (1949); **82**, 664 (1951).

[8] Schwinger has shown in Phys. Rev. **76**, 790 (1949), Eq. (1.114) that the extra term appears as

$$(\alpha/2\pi)\mu_0c\frac{\partial}{\partial x_\nu}\int F_0(x-x')m_{\mu\nu}(x')d\omega' A_\mu(x).$$

Also

$$F_0(x)=\delta(x)+(1/6\kappa^2)\Box^2\delta(x)+\cdots O(\Box^4),$$

where

$$\kappa=\hbar/m_0c.$$

Following K. M. Case, Phys. Rev. **76**, 1 (1949), and S. Borowitz and W. Kohn, Phys. Rev. **76**, 818 (1949), we integrate by parts and apply the d'Alembertian operator on the vector potential. For a constant magnetic field, the terms in $\Box^2$ and all higher order terms in this operator fall out.

[9] Note that ω_s depends on the relative directions of the motion of the particle and the magnetic field.

The operators $P(t)$ and $Q(t)$ are operators which rotate the space and spin states respectively, and are given by

$$P(t)=\exp\left[\frac{i}{\hbar}\omega_L \mathbf{L}\cdot\mathbf{h}t\right], \tag{17a}$$

$$Q(t)=\exp\left[\frac{i}{\hbar}\frac{\omega_s}{2}\boldsymbol{\sigma}\cdot\mathbf{h}t\right], \tag{17b}$$

where $\mathbf{L}$ is the angular momentum operator. The term $e^{i\gamma t}$ in (16) can be considered as a constant phase factor arising from the displacement of the particle along the direction of the field, and it will be dropped in future calculations.

After the first scattering, the spin density matrix in the representation where $\sigma_{z'}$ is diagonal is given by [from Eq. (15)]

$$\rho'^{(s)}=\tfrac{1}{2}\{[|f_1|^2+|g_1|^2]-i\sigma_{y'}[f_1g_1^*-f_1^*g_1]\}. \tag{18}$$

The momentum density matrix describes a beam of particles traveling along the z' direction, a pure momentum state. If there were no magnetic field, the density matrix ρ' would describe the beam incident on the second target. However, in the presence of the magnetic field, both the spin and space states of the beam are altered. The density matrix (in the primed coordinate system) describing the beam incident on the second target, after spending a time t in the field, is

$$\rho''=P(t)Q(t)\rho'Q^{-1}(t)P^{-1}(t). \tag{19}$$

The density matrix after the second scattering is then

$$\tilde{\rho}''=VP(t)Q(t)\rho'Q^{-1}(t)P^{-1}(t)V^\dagger, \tag{20}$$

where V is defined by Eq. (2) in the representation where $\sigma_{z'}$ is diagonal.

Let

$$Q(t)=Q_P(t)Q_\epsilon(t), \tag{21}$$

where $Q_P(t)$ corresponds to the same angle of rotation as $P(t)$, and $Q_\epsilon(t)$ rotates the spin state through the angle corresponding to the difference between $Q(t)$ and $Q_P(t)$. Then

$$\tilde{\rho}''=VP(t)Q_P(t)Q_\epsilon(t)\rho'Q_\epsilon^{-1}(t)Q_P^{-1}(t)P^{-1}(t)V^\dagger. \tag{22}$$

Since V is a scalar under simultaneous spin and space rotations, $\tilde{\rho}''$ can be expressed as

$$\tilde{\rho}''=P(t)Q_P(t)VQ_\epsilon(t)\rho'Q_\epsilon^{-1}(t)V^\dagger Q_P^{-1}(t)P^{-1}(t). \tag{23}$$

The scattering cross section for the double scattering is obtained by taking the trace of Eq. (23) over the spin states. This gives

$$d\sigma\sim P(t)\left\{\operatorname*{trace}_{\text{spin}}[VQ_\epsilon(t)\rho'Q_\epsilon^{-1}(t)V^\dagger]\right\}P^{-1}(t). \tag{24}$$

Consider $Q_\epsilon(t)$ to be given in the primed coordinate system by

$$Q_\epsilon(t)=\exp(i\boldsymbol{\sigma}\cdot\mathbf{n}\xi/2), \tag{25}$$

where $\mathbf{n}$ is a unit vector in the direction specified by

$$n_x=\sin\theta\cos\beta,\quad n_y=\sin\theta\sin\beta,\quad n_z=\cos\theta,$$

where θ is the polar angle β is the azimuthal angle in the primed coordinate system. The cases of interest are when $\mathbf{n}$ is along the direction of the field. Now

$$\begin{aligned}&\operatorname*{trace}_{\text{spin}}\{VQ_\epsilon(t)\rho'Q_\epsilon^{-1}(t)V^\dagger\}\\&=\{[|f_1|^2+|g_1|^2][|f_2|^2+|g_2|^2]\}\\&\quad-\{[f_1g_1^*-f_1^*g_1][f_2g_2^*-f_2^*g_2]\}\\&\quad\times\{\cos\varphi_2[\cos^2(\xi/2)\cos\theta\sin^2(\xi/2)]\\&\quad-\sin^2\theta\sin^2(\xi/2)\cos(2\beta-\varphi_2)\\&\quad-\sin\varphi_2\cos\theta\sin\xi\}.\end{aligned} \tag{26}$$

Therefore, the cross section given by (24) can be obtained from Eq. (26) by rotating the primed coordinate system about the direction of the field in the direction of rotation of the particle and through the same angle.

Consider the case $Q_\epsilon(t)=1$. This is true when $\xi=0$, which means the anomalous moment vanishes. Then (26) reduces to

$$\begin{aligned}&\{[|f_1|^2+|g_1|^2][|f_2|^2+|g_2|^2]\\&\quad-[f_1g_1^*-f_1^*g_1][f_2g_2^*-f_2^*g_2]\cos\varphi_2\}.\end{aligned} \tag{27}$$

The double-scattering cross section of (24) into a given direction is the same as the field-free cross section into another direction. The new direction is obtained by rotating the direction specified by Eq. (27) in the primed coordinate system about the field by an angle corresponding to $P(t)$. If the space state was rotated through angle $2n\pi$ (n being an integer), the cross section would correspond to the field free cross section.

If the magnetic field is oriented along the y' direction, the direction perpendicular to the initial and first scattered beams, then

$$Q_\epsilon(t)=\exp(i\sigma_{y'}\epsilon/2),$$

and

$$\theta=\pi/2,\quad \beta=\pi/2,\quad \xi=\epsilon.$$

This is substituted into Eq. (26) and gives Eq. (27). Thus, this case does not differ from the case where there is no anomalous moment, and the effects of the anomalous moment cannot be detected.

If the magnetic field is along the z' direction, the direction of the first scattered beam,

$$Q_\epsilon(t)=\exp(i\sigma_{z'}\epsilon/2),$$

and

$$\theta=0.$$

Then Eq. (26) gives

$$\{[|f_1|^2+|g_1|^2][|f_2|^2+|g_2|^2] -[f_1g_1^*-f_1^*g_1][f_2g_2^*-f_2^*g_2]\cos(\varphi_2+\epsilon)\}. \quad (28)$$

The scattering cross section for the double-scattering experiment is obtained from (28) by rotating the direction about the z' axis. If, before the rotation, a direction is specified by θ and φ in the primed system, after it has been rotated through an angle $\omega_L t$, the direction is specified by θ and $\varphi+\omega_L t$ in the primed system. Therefore, the cross section (24) is, in the primed system,

$$d\sigma\sim\{[|f_1|^2+|g_1|^2][|f_2|^2+|g_2|^2] -[f_1g_1^*-f_1^*g_1][f_2g_2^*-f_2^*g_2] \times\cos(\varphi_2+\omega_L t+\epsilon)\}, \quad (29)$$

or

$$d\sigma\sim 1-\delta\cos(\varphi_2+\omega_L t+\epsilon). \quad (30)$$

For these experimental conditions, if ϵ is not too small, one can determine both the magnitude and sign of the anomalous moment. If $\omega_L t=2n\pi$ (n being an integer), the effect of the anomalous moment on the asymmetry could be detected. In the experiment of Louisell, Crane, and Pidd,[10] the time of flight between the two scatterers was too small for ϵ to be significantly different from zero, and so they effectively measured the rotation of the asymmetry about the direction of the field which was caused by the normal moment. This corresponds to the case where $Q_\epsilon=1$ discussed above.

If the magnetic field is along the x' direction, then

$$Q_\epsilon(t)=\exp(i\sigma_{x'}\epsilon/2),$$

and

$$\theta=\pi/2, \quad \beta=0, \quad \xi=\epsilon.$$

Equation (26) gives

$$[|f_1|^2+|g_1|^2][|f_2|^2+|g_2|^2] -[f_1g_1^*-f_1^*g_1][f_2g_2^*-f_2^*g_2]\cos\varphi_2\cos\epsilon. \quad (31)$$

If $P(t)$ corresponds to a rotation of $2n\pi$ radians (n being an integer), then the double scattering cross section, for the case where the magnetic field is in the same plane as the initial and first scattered beams but perpendicular to the scattered beam, is given by

$$d\sigma\sim 1-\delta\cos\varphi_2\cos\epsilon. \quad (32)$$

It is seen that the effects of the anomalous moment on the cross section are detectable because of the alteration of the asymmetry. However, in this case the sign of the anomalous moment cannot be determined because the change is independent of the sign of ϵ. Also, the direction of the field along the x' axis is not important. In the limit of small ϵ,

$$d\sigma\sim 1-\delta\cos\varphi_2. \quad (32a)$$

It is therefore necessary that the time between the two scatterings be long enough that ϵ be at least a significant fraction of π.

[10] Louisell, Pidd, and Crane, Phys. Rev. 94, 7 (1954).

In the experiment to measure the magnitude of the gyromagnetic ratio to such accuracy that the second order radiative corrections are significant, it will be necessary for the number of spatial revolutions about the field to be of the order of 10^3 to 10^4.

IV. CONCLUSION

It is shown, that up to first order of $\mu_0\mathcal{H}$ in the energy, the precession frequency of the spin about the direction of the magnetic field is given by:

(1) Field parallel to velocity of the particle,

$$\omega_s=\omega_L[1+a]. \quad (33)$$

(2) Field perpendicular to the direction of the velocity of the particle,

$$\omega_s=\omega_L[1+a/(1-\beta^2)^{\frac{1}{2}}]. \quad (34)$$

The ratio of the spin precession frequency ω_s to the cyclotron frequency ω_L is for the two cases:

$$(1) \quad \omega_s/\omega_L=g/2=[1+a], \quad (35)$$

$$(2) \quad \omega_s/\omega_L=g/2=[1+a/(1-\beta^2)^{\frac{1}{2}}], \quad (36)$$

where g is the gyromagnetic ratio for the spin moment. Although the magnitude of the second order correction to the moment is constant in a time-independent homogeneous magnetic field, the gyromagnetic ratio depends upon the relative orientation of the field to the velocity of the particle and also on the magnitude of the velocity.

The Mott double-scattering cross section is modified by the intervention of a magnetic field between the two scattering centers. For the case where the magnetic field is along the direction of the first scattered beam (z' direction), the cross section is given by

$$d\sigma_1\sim 1-\delta\cos[\varphi_2+\omega_L t(1+a)]. \quad (37)$$

When the magnetic field is perpendicular to the direction of the first scattered beam but parallel to the plane of the initial and first scattered beams, the expression for the cross section is more complicated. If the particle executes an integral number of revolutions about the direction of the field, the cross section is given by

$$d\sigma_2\sim 1-\delta\cos\varphi_2\cos[a\omega_L t/(1-\beta^2)^{\frac{1}{2}}]. \quad (38)$$

If the particles do not make an integral number of revolutions, the double scattering cross section can be obtained from Eq. (38) by rotating the primed coordinate system about the field through the same angle that the electrons have been rotated. The cross section is given by Eq. (38) in the new coordinate system.

The effects of depolarization of the electron beam on the double-scattering cross section will be discussed in a later paper.

APPENDIX

Consider the Dirac equation for a particle in a constant homogeneous magnetic field,

$$H_D=c\rho_1\boldsymbol{\sigma}\cdot\boldsymbol{\pi}+\rho_3 m_0c^2 =\rho_1O_1+\rho_3O_3, \quad (A\text{-}1)$$

where O_1 and O_3 are the operators which are the coefficients of the ρ_1 and ρ_3, respectively. This Hamiltonian is then transformed to another representation by the following transformation

$$H=e^{-i\rho_2\varphi/2}H_De^{i\rho_2\varphi/2}, \tag{A-2}$$

where φ is independent of the ρ operators and assumed to be independent of time. Then

$$H=\rho_3[O_3\cos\varphi-O_1\sin\varphi] +\rho_1[O_1\cos\varphi+O_3\sin\varphi]. \tag{A-3}$$

If φ is chosen such that

$$\tan\varphi=-O_1/O_3, \tag{A-4}$$

then

$$H=\rho_3[O_1^2+O_3^2]^{\frac{1}{2}}. \tag{A-5}$$

This new Hamiltonian is the Hamiltonian of the particle in the Foldy-Wouthuysen representation, and for the above case it is

$$H=\rho_3[m_0^2c^4+c^2\pi^2-e\hbar c\boldsymbol{\sigma}\cdot\mathfrak{IC}]^{\frac{1}{2}}=\rho_3\mathbf{E}_\pi. \tag{A-6}$$

If ρ_3 is taken diagonal with the eigenvalues of ±1, the energy eigenvalues are just $\pm$ the square bracket above.

In this representation the positive eigenvalue of ρ_3 refers to the positive-energy states and the negative eigenvalues to the negative-energy states.

In the usual Dirac representation, a particle with an anomalous moment of magnitude $a\mu_0$ is described by a Hamiltonian given by

$$H_D'=c\rho_1\boldsymbol{\sigma}\cdot\boldsymbol{\pi}+\rho_3(m_0c^2-a\mu_0\boldsymbol{\sigma}\cdot\mathfrak{IC}). \tag{A-7}$$

This is transformed to the Foldy-Wouthuysen representation and gives

$$H'=e^{-i\rho_2\varphi/2}H_D'e^{i\rho_2\varphi/2}=A-a\mu_0B, \tag{A-8}$$

where A is given by Eq. (A-6) and B is

$$B=e^{-i\rho_2\varphi/2}\boldsymbol{\sigma}\cdot\mathfrak{IC}e^{i\rho_2\varphi/2}. \tag{A-9}$$

Therefore

$$B=\rho_3\{\cos(\varphi/2)\boldsymbol{\sigma}\cdot\mathfrak{IC}\cos(\varphi/2)-\sin(\varphi/2)\boldsymbol{\sigma}\cdot\mathfrak{IC}\} +\rho_1\{\sin(\varphi/2)\boldsymbol{\sigma}\cdot\mathfrak{IC}\cos(\varphi/2) +\cos(\varphi/2)\boldsymbol{\sigma}\cdot\mathfrak{IC}\sin(\varphi/2)\}. \tag{A-10}$$

Now φ is given by Eq. (A-4), so that $\cos(\varphi/2)$ is a function of

$$[(\boldsymbol{\sigma}\cdot\boldsymbol{\pi})(\boldsymbol{\sigma}\cdot\boldsymbol{\pi})]^n\sim[\pi^2-(e\hbar/c)\boldsymbol{\sigma}\cdot\mathfrak{IC}]^n.$$

Since $\mathfrak{IC}$ is a constant homogeneous field, $\cos(\varphi/2)$ commutes with $\boldsymbol{\sigma}\cdot\mathfrak{IC}$. However, $\sin(\varphi/2)$ is a function of

$$(\boldsymbol{\sigma}\cdot\boldsymbol{\pi})[(\boldsymbol{\sigma}\cdot\boldsymbol{\pi})(\boldsymbol{\sigma}\cdot\boldsymbol{\pi})]^n\sim(\boldsymbol{\sigma}\cdot\boldsymbol{\pi})[\pi^2-(e\hbar/c)\boldsymbol{\sigma}\cdot\mathfrak{IC}]^n$$

so that

$$\sin(\varphi/2)(\boldsymbol{\sigma}\cdot\mathfrak{IC})=[(1-\cos\varphi)/2]^{\frac{1}{2}}(\boldsymbol{\sigma}\cdot\boldsymbol{\pi})(\boldsymbol{\sigma}\cdot\mathfrak{IC})/|\boldsymbol{\pi}|. \tag{A-11}$$

Therefore

$$B=\rho_3\left[\boldsymbol{\sigma}\cdot\mathfrak{IC}\cos(\varphi/2)-\frac{(\boldsymbol{\sigma}\cdot\boldsymbol{\pi})(\boldsymbol{\sigma}\cdot\mathfrak{IC})(\boldsymbol{\sigma}\cdot\boldsymbol{\pi})}{\pi^2}\sin^2(\varphi/2)\right] +\rho_1\left[\frac{(\boldsymbol{\sigma}\cdot\boldsymbol{\pi})(\boldsymbol{\sigma}\cdot\mathfrak{IC})+(\boldsymbol{\sigma}\cdot\mathfrak{IC})(\boldsymbol{\sigma}\cdot\boldsymbol{\pi})}{|\boldsymbol{\pi}|}\sin(\varphi/2)\cos(\varphi/2)\right],$$

where the trigonometric functions in Eq. (A-11) are now independent of $\boldsymbol{\sigma}\cdot\boldsymbol{\pi}$. Now

$$(\boldsymbol{\sigma}\cdot\boldsymbol{\pi})(\boldsymbol{\sigma}\cdot\mathfrak{IC})(\boldsymbol{\sigma}\cdot\boldsymbol{\pi})=2(\boldsymbol{\sigma}\cdot\boldsymbol{\pi})(\boldsymbol{\pi}\cdot\mathfrak{IC}) -(e\hbar/c)\mathfrak{IC}^2-\pi^2(\boldsymbol{\sigma}\cdot\mathfrak{IC}),$$

and

$$(\boldsymbol{\sigma}\cdot\boldsymbol{\pi})(\boldsymbol{\sigma}\cdot\mathfrak{IC})+(\boldsymbol{\sigma}\cdot\mathfrak{IC})(\boldsymbol{\sigma}\cdot\boldsymbol{\pi})=2\boldsymbol{\pi}\cdot\mathfrak{IC}.$$

Therefore,

$$B=\rho_3\{\boldsymbol{\sigma}\cdot\mathfrak{IC}-(1-m_0c^2/\mathbf{E}_\pi) \times[(\boldsymbol{\sigma}\cdot\boldsymbol{\pi})(\boldsymbol{\pi}\cdot\mathfrak{IC})/\pi^2-(e\hbar c/2)\mathfrak{IC}^2/c^2\pi^2\} -\rho_1(\boldsymbol{\pi}\cdot\mathfrak{IC}/|\boldsymbol{\pi}|)(1-m_0^2c^4/E_\pi^2). \tag{A-12}$$

Since we are restricting ourselves only to positive-energy solutions of the wave equation, the terms in ρ_1 are dropped, and for ρ_3 we substitute its positive eigenvalue. The Hamiltonian is then given by

$$H=\mathcal{E}_\pi[1-e\hbar c\boldsymbol{\sigma}\cdot\mathfrak{IC}/\mathcal{E}_\pi^2]^{\frac{1}{2}}-a\mu_0\{\boldsymbol{\sigma}\cdot\mathfrak{IC}-(1-m_0c^2/\mathbf{E}_\pi) \times[\boldsymbol{\sigma}\cdot\boldsymbol{\pi}(\boldsymbol{\pi}\cdot\mathfrak{IC})/\pi^2-(e\hbar c/2)(\mathfrak{IC}^2/c^2\pi^2)]\}. \tag{A-13}$$

The first term in (A-13) is expanded to give

$$\mathbf{E}_\pi=\mathcal{E}_\pi-\frac{e\hbar}{2\mathcal{E}_\pi/c}\boldsymbol{\sigma}\cdot\mathfrak{IC}-\frac{1}{2\mathcal{E}_\pi}\left(\frac{e\hbar\mathfrak{IC}}{2\mathcal{E}_\pi/c}\right)^2-\cdots.$$

Since the minimum eigenvalue of $\mathcal{E}_\pi$ is m_0c^2, then up to terms which are linear in $\mu_0|\mathfrak{IC}|$, we can write

$$\mathbf{E}_\pi=\mathcal{E}_\pi-\left(\frac{e\hbar}{2\mathcal{E}_\pi/c}\right)\boldsymbol{\sigma}\cdot\mathfrak{IC}.$$

The correction terms are smaller by a factor of 10^{-11} for a field of about one hundred gauss. Therefore up to terms which are linear in $\mu_0|\mathfrak{IC}|$, the Hamiltonian in Eq. (A-13) becomes

$$H=\mathcal{E}_\pi-\frac{e\hbar}{2\mathcal{E}_\pi/c}\boldsymbol{\sigma}\cdot\mathfrak{IC}-a\mu_0\boldsymbol{\sigma}\cdot\mathfrak{IC} +a\mu_0(1-m_0c^2/\mathcal{E}_\pi)(\boldsymbol{\sigma}\cdot\boldsymbol{\pi})(\boldsymbol{\pi}\cdot\mathfrak{IC})/\pi^2. \tag{A-14}$$

If we consider wave functions which are product functions of eigenfunctions of $\mathcal{E}_\pi$ and a function of σ, then we can replace $\mathcal{E}_\pi$ in the denominator by its eigenvalue $m_0c^2/(1-\beta^2)^{\frac{1}{2}}$, which gives

$$H=\mathcal{E}_\pi-u_0\boldsymbol{\sigma}\cdot\mathfrak{IC}[(1-\beta^2)^{\frac{1}{2}}+a] +a\mu_0\frac{(\boldsymbol{\sigma}\cdot\mathbf{v})(\mathbf{v}\cdot\mathfrak{IC})}{v^2}[1-(1-\beta^2)^{\frac{1}{2}}], \tag{A-15}$$

because

$$m\mathbf{v}=\boldsymbol{\pi}.$$

Thus this now corresponds to Eq. (12) in the text.

Infrared Lattice Absorption in Ionic and Homopolar Crystals*

MELVIN LAX, *Physics Department, Syracuse University, Syracuse, New York and Naval Research Laboratory, Washington, D. C.*

AND

ELIAS BURSTEIN, *Crystal Branch, Naval Research Laboratory, Washington, D. C.*

(Received July 12, 1954)

The evidence, from the photoelastic properties of alkali halides and MgO, and from the deviations from the Cauchy relation among the elastic constants in these crystals, for the existence of an appreciable deformation of the charge distribution about the atoms during lattice vibration, is discussed. The deformation of the charge distribution is suggested as a possible alternative explanation to that of anharmonic forces for the auxiliary bands in the infrared absorption and reflection spectra of the alkali halides and MgO. It is suggested, on the other hand, that the infrared absorption spectra of pure homopolar crystals, such as diamond, silicon, and germanium in which a linear moment is absent, must involve the deformation of the charge distribution during vibration, since anharmonic forces alone cannot account for any infrared absorption in the absence of a linear moment.

The deformation of the charge distribution in a crystal during vibration is shown to lead to a second order electric moment (quadratic in the displacements) as well as to a modification of the first order moment. A qualitative understanding of the contribution of the second order moment to infrared absorption is obtained with the help of a one-dimensional calculation.

An analysis is made of the infrared absorption in diamond, silicon, and germanium. Part of the absorption is judged to be intrinsic and to be reasonably explained by a second order electric moment arising from charge deformation. The remainder seems to vary with the specimen and is explained as an impurity-induced first order moment. The second order electric moment can also be used to explain the side bands in the absorption and reflection spectra of the alkali halides. However, it fails to explain the observed broadening of the main absorption line, indicating that anharmonic forces are probably the principal mechanism in the latter phenomenon.

1. INTRODUCTION

THE absorption of infrared light by an ionic cubic diatomic crystal would be expected, according to elementary theory, to yield a single band associated with the optical mode of essentially zero propagation constant. Observations of Czerny,[1] Barnes,[1] and others[1] on alkali halide crystals indicated, however, the presence of side bands on the short wavelength side of the main absorption or reflection band. Attempts at explaining these side bands by Born and Blackman,[2] Blackman,[3] and Barnes, Brattain, and Seitz,[4] were based on the presence of anharmonic terms (e.g., cubic) in the potential energy associated with lattice vibrations. Since these terms are difficult to calculate from fundamental considerations they were introduced phenomenologically. The location of the bands could reasonably be explained by regarding them as combination bands.

Recently, Born[5] in his work on pyroelectricity, and Burstein *et al.*[6] in explaining the infrared properties of MgO, have suggested that the side bands may be due to second order terms in the electric moment rather than to third order terms in the potential energy. Furthermore, in hompolar materials like diamond, silicon, and germanium where the linear terms in the electric moment are absent, Burstein and Oberly[7] have suggested that the intrinsic lattice absorption must be explained on the basis of a second order electric moment, since an harmonicity alone provides no mechanism for absorption.

The purpose of the present paper is: (1) to review the experimental evidence for second order electric moment terms; (2) to define the concepts more precisely by formulating the transition probabilities on a quantum mechanical basis; and (3) to illustrate the qualitative nature of the results to be expected by performing a one-dimensional calculation.

2. EXPERIMENTAL BACKGROUND

Polar Crystals

The reflection spectra for a series of alkali halides and for MgO are given in Fig. 1. These spectra exhibit a main peak and a secondary side peak at a shorter wavelength. As can be seen from Table I, the relative width of the main peak decreases in the order LiF, MgO, NaF, NaCl, KCl. The relative heights of the secondary to the major peak also decrease in exactly the same order. A similar trend is found in these crystals for the deviation from the Cauchy relations $(C_{44}/C_{12})-1$ and for the strain polarizability constant λ_0 (see Table I).

The deviation from the Cauchy relations in a classical treatment implies a deviation from central forces. Löwdin,[8] in a quantum-mechanical treatment using free

* This work has also been supported in part by the U. S. Air Force under a contract monitored by the Office of Scientific Research, Air Research and Development Command, and in part by the Office of Naval Research.

[1] M. Czerny, Z. Physik **65**, 600 (1930); R. B. Barnes and M. Czerny, Z. Physik **72**, 447 (1931); R. B. Barnes, Z. Physik **75**, 723 (1932); K. Korth, Nachr. Akad. Wiss. Göttingen, Math.-phys. Kl., 576 (1932); C. H. Cartwright and M. Czerny, Z. Physik **85**, 269 (1933); **90**, 457 (1934); H. W. Hohls, Ann. Physik **29**, 433 (1937).

[2] M. Born and M. Blackman, Z. Physik **82**, 551 (1933).

[3] M. Blackman, Z. Physik **86**, 421 (1933); Trans. Roy. Soc. (London) **A236**, 102 (1936).

[4] Barnes, Brattain, and Seitz, Phys. Rev. **48**, 582 (1935).

[5] M. Born, Revs. Modern Phys. **17**, 245 (1945).

[6] Burstein, Oberly, and Plyler, Proc. Indian Acad. Sci. **28**, 388 (1948).

[7] E. Burstein and J. J. Oberly, Phys. Rev. **78**, 642 (1950).

[8] Per Olav Löwdin, J. Chem. Phys. **18**, 365 (1950).

spherical-ion wave functions, was able to show that some Cauchy relation deviations could be obtained from the non-orthogonality terms arising in his Heitler-London treatment. However the deviations he obtained did not follow the trend exhibited in Table I. It therefore seems necessary to take account of the deformation of the ionic wave functions to explain the experimental results. (Such a deformation and its changes during vibration will lead to terms in the electric moment of second order in the displacement, as well as to a modification of the "effective charge" in the first order terms.)

The strain polarizability λ_0 represents the fractional change in molar polarizability with fractional change in density. The existence of a strain polarizability also suggests the existence of charge deformation, and its magnitude is also a measure of the extent of charge deformation with strain. As a consequence, both the Cauchy deviations and the strain polarizability represent a measure of the charge deformation that will occur during lattice vibrations.

The experimental evidence therefore indicates a correlation between the peak widths and side-band intensities with a measure of the size of the second order terms in the electric moment. As we shall show later in this paper, second order moments can give rise to combination bands and the latter may constitute the mechanism for the side-band absorption.

We can visualize the mechanism for absorption involving second order terms in the electric moment by considering the effect of compressional modes on a rocksalt lattice. A compressional mode produces a shift in the effective charges on the ions, but no moment. If in addition an optical vibration is present, a second order contribution to the electric moment will be made

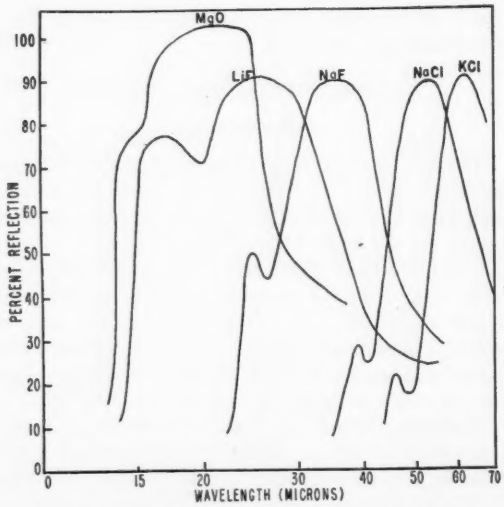

FIG. 1. Infrared reflection spectra of alkali halides and magnesium oxide.

TABLE I. Infrared reflection peaks.

Crystal	Major peak (μ)	Fractional band width	Minor peak (μ)	Height ratio	λ_0	$\frac{C_{44}}{C_{12}}-1$
MgO	22[a]	0.43	16	0.7	1.4[e]	0.4[d]
LiF	26[b]	0.46	17	0.85	0.7[e]	0.3[e]
NaF	36[b]	0.34	25	0.56	...	0.2[f]
NaCl	53[b]	0.28	39	0.32	0.6[e]	0.1[e,d]
KCl	63[b]	0.18	46	0.25	0.6[e]	0.0[e,d]

[a] See reference 6.
[b] H. W. Hohls, Ann. Physik **29**, 433 (1937).
[c] E. Burstein and P. L. Smith, Proc. Indian Acad. Sci. **28**, 377 (1948).
[d] M. A. Durand, Phys. Rev. **50**, 449 (1936).
[e] H. Huntington, Phys. Rev. **72**, 321 (1947).
[f] Burstein, Smith, and Arenberg, Phys. Rev. **82**, 314 (1951).

by the vibration of the charge increments. This contribution is proportional to the product of the amplitudes of both the acoustical and optical modes, and results in absorption at the sum and difference frequencies. Because of the high density of short-wavelength modes, a combination of short-wavelength acoustical and optical modes will lead to side bands.

Homopolar Crystals

In this section we shall be concerned primarily with homopolar crystals of diamond structure (e.g., diamond, silicon, germanium, and gray tin). The diamond structure consists of two identical interpenetrating face-centered cubic lattices with one of these lattices displaced relative to the other one-quarter of the distance up the main body diagonal. Because of the crystal symmetry (O_h), the displacement of one sublattice relative to another will not result in an electric moment. The fundamental optical vibration is therefore infrared-inactive, although it is Raman-active. Weak absorption bands have been observed, however, in diamond,[9] and more recently in silicon[7,10] and germanium.[7,10,11]

The lattice vibration absorption bands in diamond are shown in Fig. 2. Diamond crystals are found to fall into two types which exhibit different absorption spectra. Type I diamonds exhibit absorption in two regions: from 2 to 6μ and from 8 to 13μ. Type II diamonds, on the other hand, exhibit absorption only in the 2 to 6μ region. The absorption in the 8 to 13μ region for Type I diamonds varies from specimen to specimen and appears therefore to be an impurity or structure sensitive property. The 2 to 6μ absorption does not vary from specimen to specimen nor from Type I to Type II diamonds[12–14] and therefore may be regarded as an intrinsic property of diamond.

The classification of diamond into two types is based

[9] Robertson, Fox, and Martin, Trans. Roy. Soc. (London) **A232**, 463 (1934).
[10] R. C. Lord, Phys. Rev. **85**, 140 (1952).
[11] H. B. Briggs, J. Opt. Soc. Am. **A42**, 686 (1952); R. J. Collins and H. Y. Fan, Phys. Rev. **86**, 648 (1952).
[12] G. B. B. M. Sutherland and H. H. Willis, Trans. Faraday Soc. **41**, 289 (1945).
[13] K. G. Ramanathan, Proc. Indian. Acad. Sci. **A24**, 130 (1946).
[14] D. E. Blackwell and G. B. B. M. Sutherland, J. chim. phys. **46**, 9 (1949).

TABLE II. Some properties in which Type I and Type II diamonds differ.

	Type I	Type II
Infrared absorption[a]	2 to 6μ and 8 to 13μ	Only 2 to 6μ
Ultraviolet absorption[a]	Below 3000A	Below 2250A
Photoconductivity[a]	Poor	Good
Radiation counting[b]	Poor	Good
Anomalous x-ray spots[c]	Present	Absent
Crystal texture[d]	Perfect	Mosaic

[a] Robertson, Fox, and Martin, Trans. Roy. Soc. (London) **A232**, 463 (1934).
[b] R. Hofstadter, Phys. Rev. **73**, 631 (1948); F. C. Champion, Proc. Phys. Soc. (London) **B65**, 465 (1952).
[c] K. Lonsdale, Proc. Roy. Soc. (London) **A179**, 315 (1942).
[d] K. Lonsdale, Phys. Rev. **73**, 1467 (1948).

on differences in physical properties[9] (see Table II). The properties that distinguish the two types of diamond are those which are commonly sensitive to impurities and structure defects in other materials. Properties such as lattice constant, refractive index, dielectric constant, Raman spectra, and specific heat which are not structure-sensitive exhibit essentially no differences between the two diamond types.

We believe that Type I diamonds have the same fundamental octahedral structure as Type II diamonds, but differ from the latter by the presence of impurities[7,15] or structure defects which are introduced during growth, and whose concentration determines the extent to which the properties of a given crystal differ from the perfect octahedral structure.

Recent data,[16] obtained at the Naval Research Laboratory, on the influence of impurities on the growth and properties of a wide variety of crystals indicate that certain types and concentrations of impurities reduce the mosaic structure of crystals and make possible the growth of large, clear crystals which could not otherwise be obtained. It is therefore probable that it is precisely the presence of appropriate impurities that enable near-perfect Type I diamonds to grow in nature.

The infrared absorption bands from 8 to 13μ in Type I diamond occur in the region of the fundamental optical vibration frequencies of the diamond lattice in spite of the fact that absorption associated with the "optical modes" of vibration are explicitly forbidden by the selection rules associated with the octahedral symmetry of the diamond lattice. The presence of these bands can be readily accounted for by impurities since they destroy locally the center of symmetry of the diamond structure and thereby permit an electromagnetic coupling to the fundamental optical vibration frequencies.

The 2 to 6-μ bands do not vary from specimen to specimen and hence constitute intrinsic absorption. They cannot be explained on the basis of a first order (fundamental) lattice absorption, since the latter is forbidden for the perfect diamond lattice. Furthermore these bands occur at a higher frequency than the fundamental optical vibration at 1332 cm^{-1}. We suggest that this 2 to 6-μ intrinsic absorption is lattice absorption associated with two-phonon processes arising from second-order terms in the electric moment produced by charge deformation.

The customary mechanism for explaining summation bands (in the alkali halides), namely anharmonic forces, is inadequate in diamond structures since anharmonic forces without charge deformation can produce no electric moment of any order and hence no absorption.

Second order electric moments are adequate to explain the existence of summation bands without benefit of anharmonic terms, although the latter may indeed be present and produce additional broadening and/or side bands.

It may be of interest to note that a charge deformation mechanism has also been invoked to explain the pressure dependent fundamental infrared absorption of homonuclear molecules.[17] Although anharmonic forces are present in such molecules, no vibrational absorption is to be expected unless an electric moment is induced, *viz.*, by collisions.

We can visualize the second-order terms in the electric moment in a manner similar to that described in the alkali halides: one vibrational mode induces charges on the atoms (which would otherwise not be present). A second mode simultaneously causes a vibration of the induced charges thus producing an electric moment and coupling to the radiation field. Since a long-wavelength acoustical or optical mode does not alter the effective charges of the atoms on the two equivalent Bravais lattices, we expect that such long-wavelength modes will be ineffective in producing second order moments. On the other hand, short-wavelength modes introduce asymmetric displacements within the two sublattices and therefore produce charge deformations. Thus we

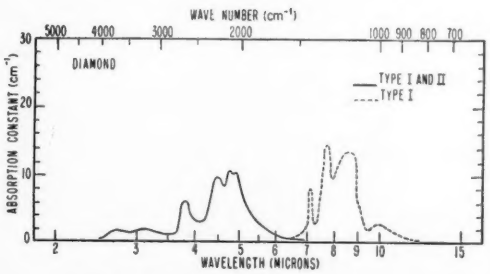

FIG. 2. Infrared absorption spectra of Type I and Type II diamond.

[15] Blackwell and Sutherland (reference 14) have also suggested that impurities may play a role.
[16] Paul H. Egli and S. Zerfoss, Discussions Faraday Soc. No. 5, 61 (1949).
[17] Crawford, Walsh, and Locke, Phys. Rev. **75**, 1607 (1949); **76**, 580 (1949); J. Van Kranendonk and R. Byron Bird, Physica **17**, 953 (1951); **17**, 968 (1951).

may expect that the absorption will be produced primarily by a pair of short-wavelength phonons.

3. THE TRANSITION PROBABILITY

Let the initial and final states of the crystal be denoted by $\psi_i(\mathbf{r},\mathbf{x})$ and $\psi_f(\mathbf{r},\mathbf{x})$, where $\mathbf{r}$ is an abbreviation for the electronic coordinates $\mathbf{r}_1\mathbf{r}_2\cdots\mathbf{r}_j\cdots$ and $\mathbf{x}$ is an abbreviation for the nuclear positions $\mathbf{x}_1\mathbf{x}_2\cdots\mathbf{x}_l\cdots$. In the presence of an incident electromagnetic field described by the vector potential $\mathbf{A}(\mathbf{r})$, the perturbing potential,

$$V=-\sum(e_j/m_jc)\mathbf{A}(\mathbf{r}_j)\cdot\mathbf{p}_j-\sum(Z_l/M_lc)\mathbf{A}(\mathbf{x}_l)\cdot\mathbf{P}_l, \quad (3.1)$$

determines the rate at which transitions occur. Here $e_j=-e$ is the charge on the jth electron and Z_l is the charge on the lth nucleus. Also M_l is the mass of the lth nucleus, $\mathbf{p}_j=-i\hbar\nabla_{\mathbf{r}_j}$, $\mathbf{P}_l=-i\hbar\nabla_{\mathbf{x}_l}$.

For a system such as a crystal, whose size is large compared to the wavelength, the customary electric dipole approximation cannot be applied. Since we are dealing, however, with valence or core electrons, we are always concerned with *filled* bands. And such a determinant of band functions can always be rewritten as a determinant of localized orbitals. Finally, since we are concerned with the matrix elements of one-body operators, the determinant may be replaced by the corresponding Hartree product of localized orbitals. Thus we may regard each electron $\mathbf{r}_j$ as attached to a given atom, of equilibrium position $\mathbf{r}_j^0$ in the lattice. It is then permissible to make the "dipole" approximation:

$$\exp(i\nu\cdot\mathbf{r}_j)\rightarrow\exp(i\nu\cdot\mathbf{r}_j^0), \quad (3.2)$$

$$\sum\exp(i\nu\cdot\mathbf{r}_j^0)[e_j\mathbf{p}_j/m_j+Z_j\mathbf{P}_j/M_j]\rightarrow 2\pi i\nu[\sum\exp(i\nu\cdot\mathbf{r}_j^0)(e_j\mathbf{r}_j+Z_j\mathbf{x}_j)]. \quad (3.3)$$

The effect of phase retardation is therefore taken into account by adding the dipole moments of each atom with an appropriate phase factor. With this modification all of the formulas associated with electric dipole radiation and absorption may be applied. The transition from the initial Born-Oppenheimer state,

$$\psi_i(\mathbf{r},\mathbf{x})=\varphi_a(\mathbf{r},\mathbf{x})X_{am}(\mathbf{x}), \quad (3.4)$$

to the final state,

$$\psi_f(\mathbf{r},\mathbf{x})=\varphi_b(\mathbf{r},\mathbf{x})X_{bn}(\mathbf{x}), \quad (3.5)$$

is accordingly described by an absorption cross section:[18]

$$\sigma(\nu)=\left[\frac{n}{\epsilon}\left(\frac{E_e}{E}\right)^2\right]\frac{8\pi^3\nu}{c}I_{ba}(\nu), \quad (3.6)$$

$$I_{ba}(\nu)=A v_m\sum_n\left|\int X_{bn}^*(\mathbf{x})\mathbf{M}_{ba}(\mathbf{x},\nu)X_{am}(\mathbf{x})d\mathbf{x}\right|^2\times\delta(E_{bn}-E_{am}-h\nu). \quad (3.7)$$

[18] See M. Lax, J. Chem. Phys. **20**, 1752 (1952), Eqs. (2.1), (2.3), ff for further discussion.

The "phased" transition electric moment $\mathbf{M}_{ba}(\mathbf{x},\nu)$ is defined by:

$$\mathbf{M}_{ba}(\mathbf{x},\nu)=\sum_j\exp(i\nu\cdot\mathbf{r}_j^0)\times\int\varphi_b^*(\mathbf{r},\mathbf{x})(e_j\mathbf{r}_j+Z_j\mathbf{x}_j)\varphi_a(\mathbf{r},\mathbf{x})d\mathbf{r}. \quad (3.8)$$

For electronic transitions ($b\neq a$), the term in $\mathbf{x}_j$ vanishes because of orthogonality. We shall be concerned primarily with pure vibrational transitions: $b=a$. In this case, the nuclear charge Z_j is of importance. It will, however, be largely cancelled by the moments associated with the core electrons that move "rigidly" with the nucleus, namely those electrons j for which the wave function, $\varphi_a(\mathbf{r},\mathbf{x})=\varphi(\mathbf{r}_1,\mathbf{r}_2,\cdots;\mathbf{x}_1,\mathbf{x}_2,\cdots)$, is a function only of $\boldsymbol{\varrho}_j=\mathbf{r}_j-\mathbf{x}_j$. By introducing the change of variable,

$$\varphi_a(\mathbf{r},\mathbf{x})=\varphi_a(\boldsymbol{\varrho}+\mathbf{x},\mathbf{x})=\chi(\boldsymbol{\varrho},\mathbf{x}), \quad (3.9)$$

the electric moment can be written

$$\mathbf{M}_{aa}(\mathbf{x},\nu)=\sum_j\exp(i\nu\cdot\mathbf{r}_j^0)\times\left[Z_j^{\text{ion}}\mathbf{x}_j+\int\chi^*(\boldsymbol{\varrho},\mathbf{x})(e_j\boldsymbol{\varrho}_j)\chi(\boldsymbol{\varrho},\mathbf{x})d\boldsymbol{\varrho}\right], \quad (3.10)$$

where Z_j^{ion} is the net charge of the nucleus plus all electrons at the site j, i.e. it is the ionic charge in an ionic crystal, or zero in a nonionic crystal. The moment $\mathbf{M}_{aa}(0,\nu)$ is usually zero, and if not, is a static moment of no consequence for optical transitions. We are concerned, therefore, only with the part of $\mathbf{M}(\mathbf{x},\nu)$ that depends on the nuclear positions $\mathbf{x}$. For all of the core electrons, however, χ depends only on $\boldsymbol{\varrho}_j$, so these yield no contribution to the $\mathbf{x}$ dependence. We shall call deformable those electrons whose wave function depend on $\mathbf{x}$ as well as $\boldsymbol{\varrho}$. It is then permissible to regard $\chi(\boldsymbol{\varrho},\mathbf{x})$ as the many-body wave function of all the *deformable* electrons.

If we expand $\chi(\boldsymbol{\varrho},\mathbf{x})$ in powers of $\mathbf{x}=(\mathbf{x}_1,\mathbf{x}_2,\cdots)$ and set

$$\int\chi^*(\boldsymbol{\varrho},\mathbf{x})e_j\boldsymbol{\varrho}_j\chi(\boldsymbol{\varrho},\mathbf{x})d\boldsymbol{\varrho}=\sum_l\mathbf{B}_l{}^j\cdot\mathbf{x}_l+\sum_{l,m}\mathbf{x}_l\cdot\mathbf{C}_{lm}{}^j\cdot\mathbf{x}_m+\cdots, \quad (3.11)$$

the electric moment (3.10) can be written

$$\mathbf{M}(\mathbf{x},\nu)=\sum\exp(i\nu\cdot\mathbf{r}_l^0)[\mathbf{B}_l\cdot\mathbf{x}_l+\mathbf{x}_l\cdot\mathbf{C}_{lm}\cdot\mathbf{x}_m], \quad (3.12)$$

where

$$\mathbf{B}_l=\sum_j\exp[i\nu\cdot(\mathbf{r}_j^0-\mathbf{r}_l^0)]\mathbf{B}_l{}^j+Z_l^{\text{ion}},\qquad \mathbf{C}_{lm}=\sum_j\exp[i\nu\cdot(\mathbf{r}_j^0-\mathbf{r}_l^0)]\mathbf{C}_{lm}{}^j. \quad (3.13)$$

We may interpret $\mathbf{B}_l$ as the effective charge on atom l, with the lattice in its equilibrium position, and $\mathbf{C}_{lm}\cdot\mathbf{x}_m$

as the charge induced at l due to displacement $\mathbf{x}_m$ of atom m from its equilibrium position.

Note that in three dimensions, $\mathbf{x}_l$ and $\mathbf{M}$ are vectors, so that $\mathbf{B}_l$ is a dyad, and $\mathbf{C}_{lm}$ is a triad.

4. GENERAL INVARIANCE REQUIREMENTS

In this section, we shall be concerned with deriving those relations obeyed by the expansion coefficients $\mathbf{B}_l$ and $\mathbf{C}_{lm}$ of the electric moment that follow from general invariance requirements. For this purpose it will usually be convenient to work with the static moment $\mathbf{M}(\mathbf{x}) = \mathbf{M}(\mathbf{x},0)$ whose transformation properties are known to be those of an ordinary vector.

The requirement that a crystal be invariant against lattice displacements may be expressed in the statements that $\mathbf{B}_l{}^i$ is a function only of $(j-l)$ and $\mathbf{C}_{lm}{}^i$ is a function only of the relative indices $(j-l)$ and $(l-m)$. It follows from (3.13) then, that $\mathbf{B}_l$ is independent of l and $\mathbf{C}_{lm}$ is a function only of $l-m$. Of course, if there are several atoms per unit cell, the type of atom denoted by α or β, our statement would take the more complicated form

$$\mathbf{B}_l{}^\alpha = \mathbf{B}^\alpha, \tag{4.1}$$

$$\mathbf{C}_{lm}{}^{\alpha\beta} = \mathbf{C}^{\alpha\beta}(m-l). \tag{4.2}$$

The expansions (3.13) for $\mathbf{B}_l$ and $\mathbf{C}_{lm}$ converge extremely rapidly since we may expect the displacement of a nucleus introduces moments only on nearby atoms. Furthermore, since the infrared wavelengths are large compared to the lattice spacing, it is permissible to set $\nu \simeq 0$ in (3.13) so that $\mathbf{B}_l{}^\alpha$ and $\mathbf{C}_{lm}{}^{\alpha\beta}$ are closely approximated by their static ($\nu=0$) values.

The static moment can now be written in the form

$$\mathbf{M}(\mathbf{x}) = \sum_{l,\alpha} \mathbf{B}^\alpha \cdot \mathbf{x}_l{}^\alpha + \sum_{\substack{l,\alpha \\ m,\beta}} \mathbf{x}_l{}^\alpha \cdot \mathbf{C}_{lm}{}^{\alpha\beta} \cdot \mathbf{x}_m{}^\beta, \tag{4.3}$$

where $\mathbf{x}_l{}^\alpha$ is the displacement of the atom of type α in cell l and

$$\mathbf{C}_{lm}{}^{\alpha\beta} = \mathbf{C}_{ml}{}^{\beta\alpha}, \tag{4.4}$$

since any coefficient of a quadratic form can be symmetrized.

If the complete crystal is electrically neutral, the electric moment is independent of the origin used to calculate it, i.e., it is invariant against an arbitrary displacement:

$$\mathbf{M}(\mathbf{x}+\mathbf{d}) = \mathbf{M}(\mathbf{x}). \tag{4.5}$$

This leads to the requirements

$$\sum_\alpha \mathbf{B}^\alpha = 0, \quad \sum_{m,\beta} \mathbf{C}_{lm}{}^{\alpha\beta} = 0, \quad \sum_{l,\alpha} \mathbf{C}_{lm}{}^{\alpha\beta} = 0, \tag{4.6}$$

the first of which states that any adjustment of the equilibrium effective charges must be such as to preserve the neutrality of the unit cell. The second requirement is equivalent to the third because of (4.4).

5. THE ABSORPTION CONSTANT

The linear absorption constant, $k(\nu)$, may be obtained from the cross section for absorption of the crystal (3.6) by dividing by the volume of the crystal:

$$k(\nu) = (N\Omega)^{-1}\sigma(\nu) = \left[\frac{n}{\epsilon}\left(\frac{E_e}{E}\right)^2\right]\frac{8\pi^3\nu}{c}\frac{I(\nu)}{N\Omega}, \tag{5.1}$$

where N is the total number of cells and Ω is the volume of each. Using (3.7) and omitting unnecessary indices (since $b=a$), one gets

$$I(\nu) = A\nu_i \sum_f \left| \int X_f{}^*(\mathbf{x}) \mathbf{M}(\mathbf{x},\nu) X_i(\mathbf{x}) d\mathbf{x} \right|^2 \times \delta(E_f - E_i - h\nu), \tag{5.2}$$

where the electric moment from (3.12) and (4.1) takes the form

$$\mathbf{M}(\mathbf{x},\nu) = \sum_{l,\alpha} \exp(i\nu \cdot \mathbf{r}_l{}^0)\mathbf{B}^\alpha \cdot \mathbf{x}_l{}^\alpha + \sum_{l,\alpha,m,\beta} \exp(i\nu \cdot \mathbf{r}_l{}^0)\mathbf{x}_l{}^\alpha \cdot \mathbf{C}_{lm}{}^{\alpha\beta} \cdot \mathbf{x}_m{}^\beta. \tag{5.3}$$

The vibrational wave functions $X_m(x)$ are products of harmonic oscillator wave functions, one for each normal coordinate. The normal coordinates may be obtained by solving the equations of motion associated with the Hamiltonian:

$$H = \tfrac{1}{2}\sum (p_l{}^\alpha)^2/M_\alpha + \tfrac{1}{2}\sum \mathbf{x}_l{}^\alpha \cdot \mathbf{K}_{lm}{}^{\alpha\beta} \cdot \mathbf{x}_m{}^\beta, \tag{5.4}$$

where $\mathbf{K}_{lm}{}^{\alpha\beta}$ obeys the same general invariance requirements (4.2, 4.4, and 4.6) as $\mathbf{C}_{lm}{}^{\alpha\beta}$. A typical solution of these equations may be written in the form

$$\mathbf{x}_l{}^\alpha = \mathbf{b}^\alpha \exp(i\mathbf{k} \cdot \mathbf{r}_l{}^0) \exp(-i\omega t), \tag{5.5}$$

where $b^\alpha(\mathbf{k})$ and $\omega(\mathbf{k})$ are obtained by solving the set of simultaneous equations:

$$\sum_\beta \mathbf{R}^{\alpha\beta}(\mathbf{k}) b^\beta = M_\alpha \omega^2 \mathbf{b}^\alpha, \tag{5.6}$$

where

$$\mathbf{R}^{\alpha\beta}(\mathbf{k}) = \sum_m \mathbf{K}_{lm}{}^{\alpha\beta} \exp[i\mathbf{k} \cdot (\mathbf{r}_m{}^0 - \mathbf{r}_l{}^0)]. \tag{5.7}$$

The number of solutions of (5.6) is equal to three times the number of atoms per cell, in three dimensions. These solutions are labelled by the index t (e.g., longitudinal acoustic) and can be made to obey the orthonormality requirement:

$$\sum_\alpha \mathbf{b}_{t'}{}^\alpha(\mathbf{k})^* \cdot M_\alpha \mathbf{b}_t{}^\alpha(\mathbf{k}) = \delta_{t't}. \tag{5.8}$$

Because $\mathbf{R}^{\alpha\beta}(-\mathbf{k}) = \mathbf{R}^{\alpha\beta}(\mathbf{k})^*$, we can require that

$$\mathbf{b}_t{}^\alpha(-\mathbf{k}) = \mathbf{b}_t{}^\alpha(\mathbf{k})^*. \tag{5.9}$$

The electric moment (5.3) can be expressed in terms of normal coordinates $q_{\mathbf{k},t}$ by the transformation:

$$\mathbf{x}_l{}^\alpha = N^{-\frac{1}{2}} \sum_{k,t} q_{\mathbf{k},t} \mathbf{b}_t{}^\alpha(\mathbf{k}) \exp(i\mathbf{k} \cdot \mathbf{r}_l{}^0). \tag{5.10}$$

The linear part of the moment becomes

$$\mathbf{M}_1=N^{\frac{1}{2}}\sum_{\alpha,t}\mathbf{B}^{\alpha}\cdot\mathbf{b}_t^{\alpha}(-\nu)q_{-\nu,t}, \tag{5.11}$$

and the second order moment becomes

$$\mathbf{M}_2=\sum_{t',t,k}q_{\mathbf{k}+\nu,t'}^{*}q_{\mathbf{k},t}\mathbf{H}_{t't}^{\mathbf{k}}, \tag{5.12}$$

where

$$\mathbf{H}_{t't}^{\mathbf{k}}=\sum_{\alpha,\beta}\mathbf{b}_{t'}^{\alpha}(\mathbf{k}+\nu)^{*}\cdot\mathbf{S}^{\alpha\beta}(\mathbf{k})\cdot\mathbf{b}_t^{\beta}(\mathbf{k}), \tag{5.13}$$

and

$$\mathbf{S}^{\alpha\beta}(\mathbf{k})=\sum_m\mathbf{C}_{lm}^{\alpha\beta}\exp[i\mathbf{k}\cdot(\mathbf{r}_m^{0}-\mathbf{r}_l^{\beta})]. \tag{5.14}$$

Reality requirements on $\mathbf{x}_l^{\alpha}$ imply that

$$q_{-\mathbf{k},t}=q_{\mathbf{k},t}^{*}. \tag{5.15}$$

The operator $q_{\mathbf{k},t}$ can be expressed in terms of conventional "creation" and "destruction" operators, $a_{\mathbf{k},t}^{\dagger}$ and $a_{\mathbf{k},t}$, by the (canonical) transformation:

$$q_{\mathbf{k},t}=[\hbar/2\omega_t(\mathbf{k})]^{\frac{1}{2}}(a_{\mathbf{k},t}+a_{-\mathbf{k},t}^{\dagger}), \tag{5.16}$$

where the operators $a_{\mathbf{k},t}$ obey the commutation rules,

$$(a_{\mathbf{k},t},a_{\mathbf{k}',t'}^{\dagger})=\delta_{\mathbf{k}\mathbf{k}'}\delta_{tt'}, \tag{5.17}$$

with all other commutators vanishing.

The linear part of $\mathbf{M}$ leads to a vibrational transition in which one phonon is created or destroyed. On absorption, we need only consider the creation part of $q_{-\nu,t}$ or $[\hbar/2\omega_t(\nu)]^{\frac{1}{2}}a_{\nu,t}^{\dagger}$ so that (5.2) yields

$$I(\nu)=N\sum_t|\textstyle\sum_{\alpha}\mathbf{B}^{\alpha}\cdot\mathbf{b}_t^{\alpha}(-\nu)|^2[\hbar/2\omega_t(\nu)]\times[\bar{n}(\omega_t(\nu))+1]\delta(h\nu-\hbar\omega_t(\nu)). \tag{5.18}$$

Thus the absorption is a line spectrum. Since the optical wavelength is large compared to the lattice constant, ν is small on the vibrational scale and the absorption peak occurs essentially at $h\nu\simeq\hbar\omega_t(0)$. It is sufficiently accurate, therefore, to set the photon propagation constant $\nu\simeq0$ everywhere in (5.18).

We note that for any of the (three) acoustic modes, $\mathbf{b}_t^{\alpha}(0)$ is independent of α. The absorption is then proportional to $\sum\mathbf{B}^{\alpha}$ which vanishes according to (4.6). Thus the requirement of displacement invariance shows that the acoustical modes make no contribution to the first order electric moment absorption—a well-known result.

In general, $\sum_{\alpha}\mathbf{B}^{\alpha}\cdot\mathbf{b}_t^{\alpha}(0)$ represents the electric moment induced in one cell by the displacements $\mathbf{b}_t^{\alpha}(0)$ associated with a normal mode of type t. The long-wavelength optical modes are thus completely intra-cell vibrations. The symmetry of these intra-cell vibrations can then be examined as one would the vibrations of a molecule to determine which normal modes are "optically active."

The quadratic part of the electric moment $\mathbf{M}_2$ of (5.12) leads to two-phonon transitions. Because of (5.16) and (5.17), matrix elements are available to create two phonons, to create one and destroy one, or to destroy two phonons. The last process is inconsistent with conservation of energy. The first process will lead to a "summation band" and the second process to a "difference band."

Upon inserting (5.13) and (5.16) into (5.2), the summation band yields the result

$$I(\nu)=\mathrm{Av}\sum_{k,t',t}|\mathbf{H}_{t't}^{\mathbf{k}}|^2\frac{\hbar}{2\omega_{t'}(\mathbf{k}+\nu)}\frac{\hbar}{2\omega_t(-\mathbf{k})}\times[n(\omega_{t'}(\mathbf{k}+\nu))+1][n(\omega_t(-\mathbf{k}))+1]\times\delta(h\nu-\hbar\omega_t(-\mathbf{k})-\hbar\omega_{t'}(\mathbf{k}+\nu)). \tag{5.19}$$

The process "Av" over the initial states replaces the initial occupation number n by its thermal equilibrium value:

$$\bar{n}(\omega)=[\exp(\hbar\omega/kT)-1]^{-1}. \tag{5.20}$$

Since $\nu\ll\mathbf{k}$, we can set $\nu\simeq0$ in (5.19). Roughly speaking, the photon has zero momentum, so that the two phonons are created with equal and opposite propagation constants, $\mathbf{k}$ and $-\mathbf{k}$. A further simplification in (5.19) can be made for nonpiezoelectric crystals by noting that

$$\omega_t(-\mathbf{k})=\omega_t(\mathbf{k}). \tag{5.21}$$

At temperatures well below the Debye temperature, $kT\ll\hbar\omega$ and $\bar{n}\ll1$, so that only the spontaneous part (in the Einstein sense) contributes to the emission of phonons, the induced part being small since no phonons are present before the absorption of light. In this limiting case, the absorption is practically independent of temperature. If $kT\sim\hbar\omega$, the absorption increases with increasing temperature.

The difference band has two contributions of the form

$$I(\nu)=\sum_{k,t',t}|\mathbf{H}_{t't}^{\mathbf{k}}|^2\frac{\hbar}{2\omega_{t'}(\mathbf{k}+\nu)}\frac{\hbar}{2\omega_t(\mathbf{k})}\times[\bar{n}(\omega_{t'}(\mathbf{k}+\nu))+1]\bar{n}(\omega_t(\mathbf{k}))\times\delta(h\nu-\hbar\omega_{t'}(\mathbf{k}+\nu)+\hbar\omega_t(\mathbf{k})), \tag{5.22}$$

$$I(\nu)=\sum_{k,t',t}|\mathbf{H}_{t't}^{\mathbf{k}}|^2\frac{\hbar}{2\omega_{t'}(-\mathbf{k}-\nu)}\frac{\hbar}{2\omega_t(-\mathbf{k})}\times\bar{n}(\omega_{t'}(-\mathbf{k}-\nu))[\bar{n}(\omega_t(-\mathbf{k}))+1]\times\delta(h\nu+\hbar\omega_{t'}(-\mathbf{k}-\nu)-\hbar\omega_t(\mathbf{k})). \tag{5.23}$$

If one sets $\nu\simeq0$ and uses (5.21), these two contributions are equal. At temperatures well below the Debye temperature, $\bar{n}\ll1$ for the optical modes. Thus the contribution in which an optical phonon is absorbed will be small. It is possible, however, to get an appreciable contribution from the creation of an optical (or acoustic) phonon, and the destruction of a low energy acoustic phonon. In this case $\bar{n}$ can be given its classical value

$kT/\hbar\omega$, and the absorption associated with the difference band will be approximately proportional to the temperature.

The extent to which a given pair of modes l' and l will interact to give absorption is determined by the coefficient $\mathbf{H}_{l'l}^{\mathbf{k}}$. This coefficient may be readily interpreted using (5.13) and (5.14). If the electric moment for an arbitrary displacement $\mathbf{x}$ is written in the suppressed index form

$$\mathbf{M}=\mathbf{xCx}, \tag{5.24}$$

the coefficient $\mathbf{H}_{l'l}^{\mathbf{k}}$ is given by

$$\mathbf{H}_{l'l}^{\mathbf{k}}=\mathbf{x}_{l'}(\mathbf{k})\cdot\mathbf{C}\cdot\mathbf{x}_{l}(\mathbf{k}), \tag{5.25}$$

where $\mathbf{x}_l(\mathbf{k})$ represents the displacements associated with the normal mode $\mathbf{b}_l^{\alpha}(\mathbf{k})\exp(i\mathbf{k}\cdot\mathbf{r})$. We can interpret $\mathbf{Q}=\mathbf{C}\cdot\mathbf{x}_l$ as the charge induced by the normal mode x_l, and $\mathbf{H}=\mathbf{x}_{l'}\cdot\mathbf{Q}$ as the moment produced by allowing the induced charge Q to vibrate in the mode $x_{l'}(\mathbf{k})$. A comparison between the symmetry properties of $\mathbf{C}_{lm}^{\alpha\beta}$ compared to the vibrational matrix $\mathbf{K}_{lm}^{\alpha\beta}$ will lead to selection rules for $\mathbf{H}_{l'l}^{\mathbf{k}}$.

6. ONE-DIMENSIONAL MODEL FOR DIAMOND-TYPE LATTICES

The coefficients $\mathbf{C}_{lm}^{\alpha\beta}$ in the electric moment expansion are not all independent when any crystal symmetry is present. The symmetry requirements available to all crystals have already been considered in Sec. 4. A given crystal will in addition be characterized by a group of symmetry operators S that transform the crystal into itself. Under such a symmetry operation, the displacement $\mathbf{x}$ gets replaced by $S\mathbf{x}$ and the electric moment, as a function of the displacements $\mathbf{x}$, becomes

$$S\mathbf{M}(\mathbf{x})=\mathbf{M}(S\mathbf{x}). \tag{6.1}$$

On the other hand, the electric moment must transform as an ordinary vector under rotations, reflections, etc., so that we also have

$$S\mathbf{M}(\mathbf{x})=\mathbf{M}'(\mathbf{x}), \tag{6.2}$$

where $\mathbf{M}'$ is related to $\mathbf{M}$ by a rotation or reflection. The requirement that (6.1) and (6.2) be consistent with one another leads to a set of conditions on the coefficients $\mathbf{C}_{lm}^{\alpha\beta}$. This consistency requirement can be applied for each element of the group, but some of the conditions obtained will be redundant. It is sufficient to use the generating elements of the group.

One point should be kept in mind: not only does $S\mathbf{x}_l^{\alpha}$ perform some rotation or reflection of the components of the vector $\mathbf{x}_l^{\alpha}$, it also produces the same rotation or reflection of the equilibrium position (α,l) from which $\mathbf{x}_l^{\alpha}$ is the displacement, i.e., it converts $\mathbf{x}_l^{\alpha}$ to $\mathbf{x}_m^{\beta}$ where (β,m) is the new position of equilibrium point (α,l).

To illustrate the concepts involved, and to obtain some qualitative conclusions, we shall apply the above procedure to a one-dimensional model of the diamond structure.

The diamond structure can be represented by a one-dimensional chain with two identical atoms per unit cell equidistant from the center of each cell (see Fig. 3).

The center of each cell is a center of symmetry. The cell is labelled by the index l, and the left and right hand atoms of any cell are labelled $\alpha=-1$ and $\alpha=+1$ respectively.

This model exhibits the inversion symmetry of the three-dimensional diamond lattice but not the latter's tetrahedral symmetry. The symmetry requirements on the electric moment matrix $C_{lm}^{\alpha\beta}$ derived from this one-dimensional model remain valid in three dimensions. The presence of tetrahedral symmetry simply leads to additional requirements.

We shall consider displacements only along the chain, and we shall regard the electric moment M as a vector that changes sign under inversion, i.e.,

$$M'=IM=-M, \tag{6.3}$$

under the transformation

$$Ix_l^{\alpha}=-x_{-l}^{-\alpha}. \tag{6.4}$$

Application of (6.3) and (4.6a) demonstrates that the linear part of M vanishes. For the quadratic part,

$$M=\sum x_l^{\alpha}C_{lm}^{\alpha\beta}x_m^{\beta}, \tag{6.5}$$

and

$$\begin{aligned} IM&=\sum(-x_{-l}^{-\alpha})C_{lm}^{\alpha\beta}(-x_{-m}^{-\beta})\\ &=\sum x_l^{\alpha}C_{-l,-m}^{-\alpha,-\beta}x_m^{\beta}. \end{aligned} \tag{6.6}$$

From (4.2),

$$C_{-l,-m}^{-\alpha,-\beta}=C_{m,l}^{-\alpha,-\beta}. \tag{6.7}$$

The requirement (6.3) then leads to the condition,

$$C_{m,l}^{-\alpha,-\beta}=-C_{lm}^{\alpha\beta}. \tag{6.8}$$

If we set $\alpha=-1$, $\beta=1$ in (6.8) and use (4.4), we learn that

$$C_{m,l}^{1,-1}=-C_{m,l}^{1,-1}=0, \tag{6.9}$$

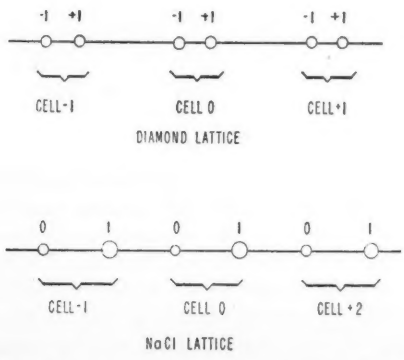

FIG. 3. One-dimensional diamond and sodium chlorice lattices.

for all m, l. If we set $\alpha=1$, $\beta=1$ in (6.8) and use symmetry (4.2), we find that

$$C_{m,\,l}{}^{-1,-1}=-C_{l,\,m}{}^{11}=-C_{ml}{}^{11}. \tag{6.10}$$

If one uses the notation $C_{lm}{}^{11}=C^{11}(m-l)$, the only independent coefficients that remain are $C^{11}(m)$ for $m=0, 1, 2, 3\cdots$. [Note that $C^{11}(m)$ is even in m.]

Displacement invariance (4.6b) then leads to one additional constraint:

$$\sum_{-\infty}^{+\infty} C^{11}(m)=C^{11}(0)+2C^{11}(1)+2C^{11}(2)+\cdots=0. \tag{6.11}$$

The number of coefficients $C_{lm}{}^{\alpha\beta}$ has therefore been drastically reduced by symmetry requirements. A further reduction can be made by requiring that interactions extend no further than second nearest neighbors. In this case $C^{11}(m)=0$ for $m>1$ and

$$C^{11}(0)=-2C^{11}(1), \tag{6.12}$$

so that only *one independent coefficient remains!*

These results (6.9) to (6.12) may be summarized by writing the general matrix in the form

$$C_{lm}{}^{\alpha\beta}=\alpha\delta_{\alpha\beta}[\delta_{l+1,\,m}+\delta_{l-1,\,m}-2\delta_{l,\,m}]C^{11}(1). \tag{6.13}$$

Thus $C_{lm}{}^{\alpha\beta}$ is completely known except for a normalizing constant.

To calculate the infrared absorption we need the quantities

$$S^{\alpha\beta}(k)=-2(1-\cos kd)C^{11}(1)\alpha\delta_{\alpha\beta}=S(k)\alpha\delta_{\alpha\beta}, \tag{6.14}$$

$$H_{l'l}{}^{k}=S(k)[b_{l'}{}^{1}(k)^{*}b_{l}{}^{1}(k)-b_{l'}{}^{-1}(k)^{*}b_{l}{}^{-1}(k)], \tag{6.15}$$

calculated from (5.14) and (5.13) with d as the lattice constant.

To obtain selection rules on $H_{l'l}{}^{k}$, we need information concerning the normal modes $b_{l}{}^{\alpha}(k)$. The requirement that the potential energy remain invariant under inversion leads to the conditions:

$$|b_{l}{}^{-\beta}(k)|=|b_{l}{}^{\beta}(k)|=(2M)^{-\frac{1}{2}}, \tag{6.16}$$

where the mass dependence of the result follows from the orthonormality condition (5.8). Combining (6.16) with (6.15) we obtain the selection rule that

$$H_{ll}{}^{k}=0. \tag{6.17}$$

In other words, there are no two-phonon contributions to infrared absorption with both phonons coming from the same branch. In the one-dimensional case this implies that one phonon is optical and the other phonon acoustical. In three dimensions there will in addition be the possibility of infrared absorption by optical phonons from two distinct optical branches, or acoustical phonons from two distinct acoustic branches.

If use is made of the orthogonality of the optical (o) and acoustical (a) modes, it follows from (6.15) that

$$|H_{oa}{}^{k}|=|H_{ao}{}^{k}|=M^{-1}|S(k)| =2(1-\cos kd)C^{11}(1)/M. \tag{6.18}$$

The absorption spectrum (5.19) may be simplified by converting the sum over k to an integral:

$$\Sigma\rightarrow(N/\pi)\int_{0}^{\pi} d\phi, \tag{6.19}$$

where $\phi=kd$, and introducing the change of variable $x=(1-\cos\phi)$:

$$I(\nu)=\frac{Nh}{4\pi\omega_{o}{}^{3}(0)}\sum_{l'l}\int_{0}^{2}\frac{dx}{[x(2-x)]^{\frac{1}{2}}}|H_{l'l}{}^{k}|^{2} \times\frac{(\bar{n}_{l}+1)(\bar{n}_{l'}+1)}{f_{l}(x)f_{l'}(x)}\delta(\epsilon-f(x)), \tag{6.20}$$

$$=\frac{Nh}{4\pi\omega_{o}{}^{3}(0)}\sum_{l'l}\frac{|H_{l'l}{}^{k}|^{2}}{[x(2-x)]^{\frac{1}{2}}}\frac{(\bar{n}_{l}+1)(\bar{n}_{l'}+1)}{f_{l}(x)f_{l'}(x)}\frac{dx}{df}\Big|_{\epsilon=f(x)}, \tag{6.21}$$

where

$$\epsilon=h\nu/\hbar\omega_{0}(0) \tag{6.22}$$

is a measure of the photon energy in units of the long-wave optical energy $\hbar\omega_{o}(0)$,

$$f_{l}(x)=\omega_{l}(k)/\omega_{o}(0), \tag{6.23}$$

$$f(x)=f_{l}(x)+f_{l'}(x). \tag{6.24}$$

To illustrate this result more specifically, we shall assume that the stiffness constant between two atoms in the same cell is K, and that between a pair of adjacent atoms in neighboring cells is $K'=\alpha K$. Then the two vibrational branches are given by

$$\left.\begin{matrix}M\omega_{o}{}^{2}(k)\\ M\omega_{a}{}^{2}(k)\end{matrix}\right\}=(K+K') \pm[(K+K')^{2}-2KK'(1-\cos kd)]^{\frac{1}{2}}. \tag{6.25}$$

Then

$$\omega_{o}(0)=[2K(1+\alpha)/M]^{\frac{1}{2}}, \tag{6.26}$$

$$f_{o}(x)=2^{-\frac{1}{2}}\{1+[1-(2\alpha x/1+\alpha)^{2}]^{\frac{1}{2}}\}^{\frac{1}{2}}, \tag{6.27}$$

$$f_{a}(x)=2^{-\frac{1}{2}}\{1-[1-(2\alpha x)/(1+\alpha)^{2}]^{\frac{1}{2}}\}^{\frac{1}{2}}, \tag{6.28}$$

$$x=(1+\alpha)^{2}(\epsilon^{2}-1)^{2}/(2\alpha). \tag{6.29}$$

In terms of the dimensionless photon energy ϵ, the spectrum $I(\nu)$ can now be rewritten in the form:

$$I(\nu)=\frac{2N\hbar}{\pi\omega_{o}{}^{3}(0)}|H_{oa}|^{2}\frac{\epsilon[\bar{n}(\omega_{o})+1][\bar{n}(\omega_{a})+1]}{(\epsilon^{2}-1)[(\epsilon^{2}-\epsilon_{l}{}^{2})(\epsilon_{m}{}^{2}-\epsilon^{2})]^{\frac{1}{2}}}, \tag{6.30}$$

where

$$|H_{o\alpha}|^2=|C^{11}(1)|^2(1+\alpha)^4(\epsilon^2-1)^4/(M\alpha)^2, \quad (6.31)$$

$$\epsilon_l=(1-\sqrt{\alpha})/(1+\alpha)^{\frac{1}{2}}, \quad (6\,32)$$

$$\epsilon_m=(1+\sqrt{\alpha})/(1+\alpha)^{\frac{1}{2}}, \quad (6.33)$$

$$\bar{n}(\omega)=[\exp(\hbar\omega/kT)-1]^{-1}, \quad (6.34)$$

$$\left.\begin{matrix}\omega_o\\ \omega_a\end{matrix}\right\}=\omega_o(0)[1\pm\epsilon(2-\epsilon^2)^{\frac{1}{2}}]^{\frac{1}{2}}2^{-\frac{1}{2}}. \quad (6.35)$$

An examination of the spectrum (6.30) indicates that it covers the range $1\leqslant\epsilon\leqslant\epsilon_m$. The point ϵ_l is outside this range. The factor $(\epsilon^2-1)^3$ emphasizes the high end of the spectrum over the low end. In addition, the factor $(\epsilon_m-\epsilon)^{-\frac{1}{2}}$ exhibits an integrable singularity at the top of the spectrum. This singularity arises because $\partial\omega/\partial k$ vanishes for the highest propagation constant. The nature of this singularity is similar to the one which usually arises in the calculation of the density of states (per unit frequency interval). In two dimensions a $\log|\epsilon_m-\epsilon|$ singularity would be expected, and in three dimensions a $(\epsilon_m-\epsilon)^{\frac{1}{2}}$ singularity would be expected.[19] The singularity need not always occur at the maximum of the spectrum. In general, its location depends on the vanishing of $\nabla_k h\nu(\mathbf{k})$. In most cases, however, the maximum energy ϵ_m will also be a relative maximum, so that a singularity will frequently occur at the top of the spectrum.

The ratio of the maximum energy to the minimum energy, or to the long wave optical energy is simply ϵ_m. An examination of (6.27) shows that $\epsilon_m\leqslant\sqrt{2}$ and the latter value is assumed when $\alpha=(K'/K)=1$. The particular value $\sqrt{2}$ depends on our assumption of nearest neighbor forces and cannot be expected to hold too accurately in three dimensions. Furthermore, in a three-dimensional polyatomic lattice, many pairs of vibrational branches will interact. Each pair will give a spectrum of finite width, with one or more peaks. The complete spectrum will be a superposition of these many contributions.

7. ONE-DIMENSIONAL MODEL FOR NaCl TYPE LATTICES

The NaCl type lattice can be represented by a one-dimensional chain of equidistant atoms alternating Na, Cl, Na, Cl, etc. (see Fig. 3). Let us choose one Na atom as origin. That Na atom and its Cl neighbor to the right will be the members of a cell 0. The displacement of an arbitrary atom can be denoted by x_l^α, where $\alpha=0$ for Na and $\alpha=1$ for Cl, and the integer 1 indicates the cell index.

For NaCl, the linear term in the electric moment makes the dominant contribution. With the help of (4.6), however, the effective charge on the sodium ion and that on the chlorine ion are related by $B^0=-B^1$ so that the ions have equal and opposite charges even in the presence of deformation. Thus the usual theory of absorption due to the linear terms results, with the ionic charge replaced by an "effective charge." Such an "effective charge" has already been introduced heuristically to explain the experimental results.[20] The formula for the absorption has, indeed, already been given: (5.18). It is simply necessary to insert the fact that for the long-wavelength optical mode, the amplitudes of the Na and Cl are out of phase and inversely proportional to the respective masses:[21]

$$b_o^0/b_o^1\simeq-(M_1/M_0). \quad (7.1)$$

Together with the normalization condition (5.8), (7.1) and (5.18) determine the first order absorption.

The second order electric moment may be investigated by introducing an inversion through the Na atom at the origin:

$$Ix_j^\alpha=-x_{-j-\alpha}^\alpha. \quad (7.2)$$

The condition $IM=-M$ leads to the general requirement:

$$C^{\alpha,\beta}(l-m+\alpha-\beta)=-C^{\alpha\beta}(m-l), \quad (7.3)$$

or

$$C^{\alpha\alpha}(m)=0, \quad (7.4)$$

and

$$C^{01}(-m)=-C^{01}(m-1). \quad (7.5)$$

Thus the only independent coefficients are $C^{01}(0)$, $C^{01}(1)$, $C^{01}(2)$, etc. Displacement invariance (4.6b) leads to

$$\sum_{m=-\infty}^{+\infty}C^{01}(m)=0. \quad (7.6)$$

However, (7.6) is automatically obeyed because of (7.5).

The final limitation on the number of independent constants can be made by limiting the interactions to second nearest neighbors. But $C^{01}(1)$ is a third neighbo-interaction. Thus $C^{01}(0)$ is the sole remaining inder pendent coefficient:

$$C^{10}(0)=C^{01}(0), \quad C^{01}(-1)=-C^{01}(0). \quad (7.7)$$

Using (5.13) and (5.14) we obtain

$$S^{01}(k)=C^{01}(0)[1-\exp(-i\phi)]; \quad S^{10}(k)=S^{01}(k),^* \quad (7.8)$$

$$H_{oo}{}^k=2C^{01}(0)[(1-\cos\phi)\,\mathrm{Re}\,b_o^0(k)^*b_o^1(k) +i\sin\phi\,\mathrm{Im}\,b_o^0(k)^*b_o^1(k)], \quad (7.9)$$

$$H_{aa}{}^k=2C^{01}(0)[(1-\cos\phi)\,\mathrm{Re}\,b_a^0(k)^*b_a^1(k) +i\sin\phi\,\mathrm{Im}\,b_a^0(k)^*b_a^1(k)], \quad (7.10)$$

$$H_{oa}{}^k=C^{01}(0)(1-\cos\phi)[b_o^0(k)^*b_a^1(k)+b_o^1(k)^*b_a^0(k)] +iC^{01}(0)\sin\phi[b_o^0(k)^*b_a^1(k)-b_o^1(k)^*b_a^0(k)]. \quad (7.11)$$

[19] L. van Hove, Phys. Rev. 89, 1189 (1953).

[20] B. Szigeti, Trans. Faraday Soc. 45, 155 (1949); also, Rept. Brit. Elect. Allied Industr. Research Assoc. (Ref. L/T 203).

[21] L. Brillouin, *Wave Propagation in Periodic Structures* (McGraw-Hill Book Company, Inc., New York, 1946).

To illustrate these results more specifically we shall assume nearest neighbor interactions only with stiffness K. The frequencies and relative amplitudes are then given by[21]

$$M_0M_1\omega^2=(M_0+M_1)\pm(M_0^2+M_1^2+2M_0M_1\cos\phi)^{\frac{1}{2}}, \tag{7.12}$$

$$b^0/b^1=2\cos(\tfrac{1}{2}\varphi)/[1-\alpha\mp(1+\alpha^2+2\alpha\cos\phi)^{\frac{1}{2}}], \tag{7.13}$$

$$\alpha=M_0/M_1, \tag{7.14}$$

where the upper and lower signs refer to the optical and acoustical cases respectively.

It follows from (7.13) that the amplitudes b^0 and b^1 are always in phase and hence can be chosen real. Thus the second terms in (7.9) and (7.10) may be dropped.

We see from (7.9)–(7.11) that all of the coefficients H vanish for $\phi=0$. Thus long-wavelength modes of any type are ineffective in producing an electric moment or dipole absorption.

The only other value of ϕ that can lead to a singularity or peak in the absorption is $\phi=\pi$ (the shortest wavelength). However, an examination of (7.13) near $\phi=\pi$ shows that for the acoustic mode the light particle obeys $b_a^0=0$ whereas for the optical mode the heavy particle obeys $b_o^1=0$. Thus $b_a^0b_a^1=b_o^0b_o^1=0$ and $H_{aa}^{\pi}=H_{oo}^{\pi}=0$. Thus the double optical transition and the double acoustical transition will show no strong peak.

The mixed transition H_{oa} however takes the value

$$H_{oa}^{\phi}=\frac{C^{01}(0)}{M_1\sqrt{\alpha}}\left[\frac{(1-\cos\phi)(1-\alpha)}{(1+\alpha^2+2\alpha\cos\phi)^{\frac{1}{2}}}-2i\sin\phi\right], \tag{7.15}$$

which does not vanish at $\phi=\pi$. In addition,

$$d[\omega_o(\phi)+\omega_a(\phi)]/d\phi=0$$

at $\phi=\pi$, so that as in the diamond case a singularity of the form $(\epsilon_m-\epsilon)^{-\frac{1}{2}}$ will be observed in the spectrum. With the vibration spectrum (7.12), the absorption is still given by the diamond result (6.30) providing we replace $|H_{oa}|^2$ by the value appropriate to NaCl:

$$|H_{oa}|^2=\frac{|C^{01}(0)|^2}{4M_1^2\alpha^3}\left[\frac{(1-\alpha^2)^2(\epsilon^2-1)^4}{(2-\epsilon^2)\epsilon^2}+4(1+\alpha)^2(\epsilon^2-1)^2(\epsilon_t^2-\epsilon^2)(\epsilon_m^2-\epsilon^2)\right]. \tag{7.16}$$

To summarize then, the only important transition for the NaCl case is the mixed optical acoustical transition, and its spectrum is qualitatively similar to the corresponding spectrum for the diamond case. We note that Eqs. (6.27)–(6.29) for diamond are directly applicable to the NaCl model with the new definition of α. So too are Eqs. (6.32)–(6.35).

If we interpret the observed side band in NaCl as due to the acoustical optical transition at $\phi=\pi$, the peak should be located at

$$\epsilon=\epsilon_m=[1+\sqrt{\alpha}]/(1+\alpha)^{\frac{1}{2}}, \tag{7.17}$$

measured in units of the main absorption frequency. The function $\epsilon_m(\alpha)$ has an absolute and a relative maximum of $\sqrt{2}$ at $\alpha=1$ and is not sensitive to α over a wide range. Since the observed ratio of side band/main band frequency is close to $\sqrt{2}$ for all of the alkali halides the above suggested interpretation is plausible.

8. IMPURITY INDUCED LATTICE ABSORPTION

We have already considered in some detail the linear and quadratic terms in the electric moment for perfect lattices. If impurities are present, certain of the invariance requirements used to simplify or eliminate terms in the electric moment expansion are no longer valid. In this section we shall indicate qualitatively the major changes brought about by abandoning these invariance requirements.

If an impurity is introduced into the lattice that modifies the electronic structure in its neighborhood, the predominate effect will be the introduction of a polar character, i.e., linear terms in the electric moment, in the immediate vicinity of the impurity. To see this point we note that the crystal is no longer perfectly periodic, or invariant against lattice displacements so that (4.1) is no longer valid. The effective charge B_l^{α} does depend on l. In addition it depends on the position (β,m) at which the impurity is introduced. Thus an additional term in the electric moment will be introduced of the form

$$\mathbf{M}=\sum\mathbf{B}_l^{\alpha}\binom{\beta}{m}\cdot\mathbf{x}_l^{\alpha}\exp(i\mathbf{v}\cdot\mathbf{r}_l^0). \tag{8.1}$$

The effective charges $\mathbf{B}_l^{\alpha}\binom{\beta}{m}$ will depend on $l-m$ and will decrease rapidly as $l-m$ increases, since the presence of an impurity will disturb the electronic structure only locally. If (8.1) is re-expressed by using (5.10) in terms of the normal coordinates, q_k:

$$\mathbf{M}=N^{-\frac{1}{2}}\sum_l\sum_{\alpha}b_l^{\alpha}(\mathbf{k})\cdot\mathbf{D}^{\alpha\beta}(\mathbf{k}+\mathbf{v})q_l(\mathbf{k})\times\exp[i(\mathbf{k}+\mathbf{v})\cdot\mathbf{r}_m^0], \tag{8.2}$$

where

$$\mathbf{D}^{\alpha\beta}(\mathbf{k}+\mathbf{v})=\sum_l\mathbf{B}_l^{\alpha}\binom{\beta}{m}\exp[i(\mathbf{k}+\mathbf{v})\cdot(\mathbf{r}_l^0-\mathbf{r}_m^0)]. \tag{8.3}$$

The coefficient $\mathbf{D}^{\alpha\beta}(\mathbf{k})$, that measures the extent to which mode $\mathbf{k}$ will contribute to the electric moment, is the Fourier transform of $\mathbf{B}_l^{\alpha}\binom{\beta}{m}$. If $\mathbf{B}_l^{\alpha}\binom{\beta}{m}$ is appreciable to a certain range of values of $l-m$, $\mathbf{D}^{\alpha\beta}(k)$ will be appreciable for all k whose wavelengths are comparable to, or longer than, the range associated with $l-m$. Since these wavelengths for an optical branch usually have only a small range of frequencies, we may expect in the absence of damping effects a

fairly sharp absorption maximum close to the fundamental optical vibration frequency.

If the presence of the impurity does not modify the vibration properties of the lattice in the immediate neighborhood of the impurity, an absorption peak should occur at each of the maxima in the density of optical modes (per unit energy). In such a case the absorption bands would provide a rough mapping of this density of modes.

If on the other hand, the impurity distorts the lattice in its vicinity, the vibrational spectrum will be modified near the impurity and a quasi-molecular viewpoint toward the absorption can be adopted. In such cases the observed frequencies will be shifted from those determined by the density of modes of the normal lattice.

If $\mathbf{B}_l^{\alpha}\binom{\beta}{m}$ had an extremely long range, i.e., if it were essentially independent of l, then we would rediscover in $D^{\alpha\beta}(\mathbf{k}+\nu)$ the usual selection rule $\delta(\mathbf{k}+\nu, 0)$ appropriate to a perfect crystal.

In addition to the impurity induced linear term (8.1), corresponding additional terms will appear in the second order electric moment. Since the concentration of impurities is not large, these second order terms may be difficult to observe in presence of the absorption associated with the intrinsic second order terms.

9. COMPARISON BETWEEN THEORY AND EXPERIMENT

The body of this paper has been concerned primarily with charge deformation effects, the resulting second order electric moments and the infrared absorption associated with the latter. The infrared absorption is also influenced by the presence of cubic terms in the potential energy. In this section, we shall review the experimental evidence briefly in the light of the present theory and of Born and Blackman's[2,3] so as to assess the relative importance of charge deformation and anharmonic effects in various situations.

A. The Side Bands in the Alkali Halides

According to the treatment of Born and Blackman,[2] Blackman,[3] and Seitz,[4] the radiation couples to the linear part of the electric moment, which would produce a single band, but the anharmonicity introduces combination frequencies in the vibration and hence also in the absorption. Blackman, who studied the alkali halides in detail, predicted the location of the side bands by treating them as summation bands. In the deformation theory the second order terms in the electric moment also give rise to summation bands. Thus both theories predict the same location of the major side band.

In Sec. 2 we discussed the ratio of the height of the reflection side band to that of the corresponding main reflection peak. This height decreased in the order LiF, MgO, NaF, NaCl, and KCl. This order correlated with changes in Cauchy relation deviations and with the strain polarizability both of which may be related to the charge deformation. Thus the side-band intensities support a charge deformation hypothesis. We do not mean to imply by these remarks that cubic terms in the potential have no important influence on the absorption or reflection spectrum, but that second order electric moments must, on the experimental evidence, be considered.

B. Fundamental Absorption in the Alkali Halides

The integrated strength of the fundamental absorption line depends on the effective charge B^{α} on the ions. This effective charge may differ from e because of the presence of some "homopolar bonding" in the formation of the crystal. In addition, we have shown that there will be a dynamic contribution to B^{α} associated with charge deformation, i.e., the displacement of the center of charge of the electrons on an ion may differ from the displacement of the corresponding nucleus. The presence of cubic terms as such will not yield any dynamic modification of the effective charge on the ions. No attempt has as yet been made to estimate the effective charge from the infrared absorption intensity. Szigeti[20] has, however, been able to estimate the effective charge on the ions using the static dielectric constant, the refractive index and the fundamental lattice absorption frequency. He obtains an effective charge of the order of $0.9e$ for the alkali halides indicating that homopolar and dynamic contributions together are of the order of 10 percent.

C. Broadening of Bands in the Alkali Halides

Second order electric moments can produce absorption near the main band by combining an optical phonon with a low-energy acoustical phonon. (This process is not too probable in the one-dimensional calculation.) Such a two-phonon process occurs independently of the main absorption, however, and will not change the latter from an infinitely sharp line. It merely superimposes a continuous background to the main line.

Anharmonicity has been shown by Blackman to provide a logical explanation of the broadening of the main absorption line into a band. Since the experimental results exhibit a broad band, we can conclude that an harmonic terms are appreciable in the alkali halides.

The second order electric moment yields side bands that are already a continuum. The breadths so obtained are relatively insensitive to temperature (well below the Debye temperature). Similar conclusions apply to the side bands produced by anharmonic terms.

Since we have concluded that anharmonic broadening is important for the main band, we can use the relative width of the main band as a measure of the importance of the cubic terms. There is a systematic correlation, through the alkali halides, between the main band

width and the side-band intensity (see Table I). A mechanism based on anharmonicity as an explanation of the side bands is therefore also consistent with the trends in the data.

D. Diamond: Intrinsic Absorption

Anharmonic forces are undoubtedly present in the diamond structure, but without the help of second order electric moment terms they can yield no absorption. The second order moment due to charge deformation is therefore necessary to account for the absorption. Since absorption resulting from a second order moment is already a continuum consisting of sum and difference bands, anharmonicity is not necessary to explain broadening. The effect of anharmonicity is to produce additional broadening and to produce higher order side bands.

The prominent peaks in the intrinsic absorption of diamond (see Fig. 2) at 3.98, 4.20, 4.59, 4.85, and 4.98μ (2510, 2380, 2180, 2060, 2010 cm^{-1}) are within a factor of 2 of the fundamental vibration at 1332 cm^{-1} and may reasonably be designated as summation bands associated with two-phonon processes of the sort discussed in this paper. An accurate prediction of the locations of these peaks requires a detailed analysis of the vibration spectrum of the sort carried out by Smith.[22] In addition, a determination of the electric moment coefficients $\mathbf{C}_{lm}^{\alpha\beta}$ and the intensity factors $|H_{l'l}^{k}|^2$ must be made to determine which lines will appear in strength and which will be forbidden. Simeral[23] has made a detailed analysis of the locations of the summation bands based on the peaks in the vibration spectrum as determined by Helen Smith. F. Herman and J. Calloway (private communication) have made a corresponding analysis for germanium, extending Helen Smith's vibrational calculations by adding interactions to third neighbors. Such analyses lead in general to a great number of possible lines because there are six vibrational branches which may combine in pairs at many different propagation constants. Simeral eliminates lines by assuming that the selection rules for infrared absorption are complementary to the second order Raman selection rules which were obtained by Helen Smith. The major contribution of the present paper, in this connection, is to indicate the basis on which correct selection rules may be obtained. An extension of the present analysis to the three-dimensional diamond structure is now being made by Hirshberg.[24] The selection rules that she has obtained thus far indicate that Simeral's complementarity assumption is not valid.

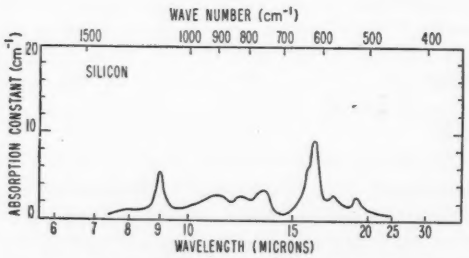

FIG. 4. Infrared absorption spectrum if high-purity silicon due to lattice vibration.

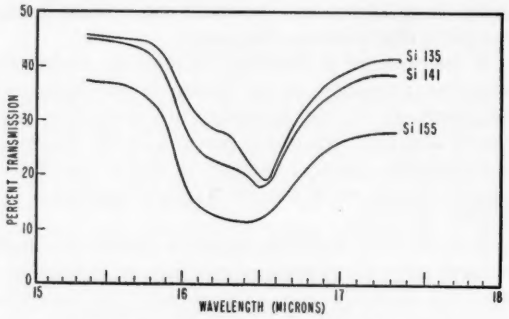

FIG. 5. Variations in the 16-micron lattice vibration band in silicon.

The weak intrinsic absorption lines at 3660 and 3120 cm^{-1} are in a region to be explained by three-phonon processes. Such three-phonon processes could occur through third order terms in the electric moment, or the absorption could be produced by second order electric moment terms in conjunction with anharmonicity effects.

E. Diamond: Impurity Absorption

According to our discussion in Sec. 8, linear terms in the electric moment can contribute to lattice absorption in the diamond structure if "impurities" are present. The strongest band in the absorption spectrum of Type I diamond at 1280 cm^{-1} can indeed be interpreted as an impurity-induced coupling of the radiation to the fundamental optical vibrations of the diamond lattice. The fact that this band has about 4 percent lower frequency than the Raman frequency (1332 cm^{-1}) is in agreement with Smith's result[22] (see her Fig. 6) that maximum density of the optical modes occurs at 5 or 6 percent below the Raman frequency. From the observed sharpness of this fundamental line we can conclude that anharmonic forces are considerably less important in diamond than in the alkali halides.

The bands in the region from 1000 to 1330 cm^{-1} may perhaps be regarded as a rough mapping of the density of the optical vibrational modes in the diamond spectrum for low impurity densities. Distortion occurs because of the presence of the weighting coefficient $D^{\alpha\beta}(\mathbf{k})$ of (8.3) that favors long-wavelength modes.

[22] Helen M. J. Smith, Trans. Roy. Soc. (London) **A241**, 105 (1948).

[23] W. G. Simeral, thesis, University of Michigan (unpublished); also presented as a technical report of the Engineering Research Institute of Michigan.

[24] J. F. Hirshberg, thesis in progress, Syracuse University (unpublished).

But the correspondence between the absorption and the density of modes in Fig. 6 of Helen Smith's paper is not too unreasonable considering the distortions involved.

Since the relative intensities of the 1010, 1190, and 1280 cm^{-1} peaks change somewhat from specimen to specimen, it is also possible that these peaks are associated with different impurities.[25]

The peak at 1390 cm^{-1} is so much sharper than the other impurity bands and so much lower in integrated strength that it may be due to an impurity whose mechanical coupling to the lattice is weak. Other very sharp impurity peaks have been observed by Blackwell and Sutherland,[14] even in the intrinsic region. These impurities are apparently not simple substitutional impurities.

F. Silicon and Germanium

The conclusions given above apply to all diamond structures, *viz.*, to silicon, germanium, and gray tin. Infrared absorption measurements on a wide variety of single crystal and polycrystalline specimens of silicon and germanium have been reported.[7, 10–12] There have been no data as yet reported for gray tin.

The lattice absorption spectrum in silicon is given in Figs. 4 and 5. Variations[26] have been observed from specimen to specimen in the structure of the 625-cm^{-1} and 1110-cm^{-1} bands in silicon, thus indicating that these bands may be due to impurities or imperfections.

In the absence of data for the fundamental Raman frequency the classification of the observed bands into fundamental and combination bands is somewhat ambiguous. An estimate of the fundamental optical frequency from the elastic constants by using Smith's[22] procedure yields 850 cm^{-1}. For comparison, the Debye temperature in the same units is 460 cm^{-1}. The impurity induced band at 625 cm^{-1} probably provides the most reliable estimate of the Raman frequency. This would indicate that the bands at 770, 830, and 910 cm^{-1} are intrinsic summation bands. The band at 1110 cm^{-1} which varies from specimen to specimen is possibly due to the presence of oxygen impurities.

TABLE III. Elastic constants.

Crystal	Debye temperature θ°K	Elastic constants[a] C_{11}	C_{12}	C_{44}	Calculated Raman line[b] $\lambda^{-1}(c)$ cm^{-1}	$\lambda^{-1}(\theta)$ cm^{-1}
Diamond	1950[c]	9.5[d]	4.3[d]	3.9[d]	1370[e]	1360
Silicon	658[f]	1.657[f]	0.639[f]	0.796[f]	850	460
Germanium	362[g]	1.288[g]	0.483[g]	0.671[g]	390	250

[a] All stiffnesses measured in units of 10^{12} dynes/cm^2.
[b] First column $\lambda^{-1}(c)$ is Raman line calculated from elastic constants by Helen Smith's method. Second column $\lambda^{-1}(\theta)$ is Debye temperature converted to units of reciprocal centimeters.
[c] K. S. Pitzer, J. Chem. Phys. **6**, 68 (1938).
[d] S. Bhagavantam and J. Bhimasenachar, Proc. Roy. Soc. (London) **A187**, 381 (1946). The value of C_{44} is questionable according to Helen Smith.
[e] Experimental Raman line is at 1332 cm^{-1}.
[f] N. Pearlman and P. H. Keesom, Phys. Rev. **88**, 398 (1952); H. J. McSkimin, J. Appl. Phys. **24**, 988 (1953).
[g] P. H. Keesom and N. Pearlman, Phys. Rev. **91**, 1347 (1953).

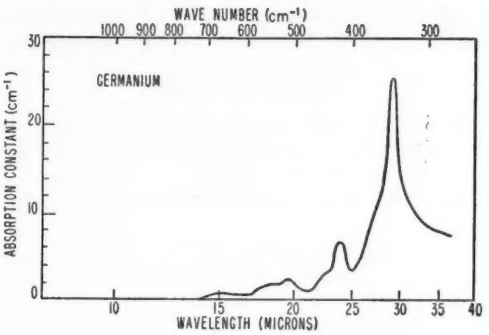

FIG. 6. Infrared absorption spectrum of relatively high-purity germanium due to lattice vibration.

The lattice absorption spectrum in germanium is shown in Fig. 6. Except for the occasional presence of a band at 830 cm^{-1} (not shown in the figure) due to presence of impurities (analogous to the 1110 cm^{-1} in silicon), the bands from 345 cm^{-1} to 640 cm^{-1} do not appear to vary significantly from specimen to specimen even with the addition of appreciable amounts of silicon as an impurity.

The Raman frequency for germanium has not yet been measured directly. An estimate from the elastic constants (see Table III) using Smith's[22] procedure is 390 cm^{-1}. The Debye frequency for comparison is 250 cm^{-1}. It would appear then, that the strong absorption at 345 cm^{-1} is close to the Raman frequency, and may actually correspond to the fundamental optical vibration frequency of the germanium lattice. Since the 345-cm^{-1} band has been observed in the purest specimens of germanium, and does not vary significantly with addition of 1 percent silicon, the present evidence is against interpreting this band as an impurity band.

There is always the possibility that the Raman frequency, when measured, will occur at a lower frequency than the above estimate, and the 345-cm^{-1} band might then be an ordinary summation band.

Another possible explanation[23] for this band is the high isotope content for germanium: Simeral[23] has suggested that this high isotope concentration breaks down the selection rule against a linear moment. However, in the Born-Oppenheimer approximation the electronic structure for a given configuration is unchanged by an isotopic substitution, so that the electric moment and its selection rules will be unaltered. The magnitude and character of the vibrations in the neighborhood of the isotope will, however, be altered by the change in mass. Thus a pair of modes which at large distances from the isotope impurity would not absorb, may have an appreciable absorption near the impurity. This can lead,

[25] Chesley has carried out a spectrographic analysis of a wide variety of diamonds and found the presence of an appreciable number of impurities. F. G. Chesley, Am. Minerologist **27**, 20 (1942).

[26] We are indebted to Mrs. Bertha W. Henvis for the data given in Fig. 5.

for example, to a combination band absorption with frequency near the fundamental optical absorption.

ACKNOWLEDGMENT

The authors wish to acknowledge the helpful suggestions and active interest and encouragement given to our work by Mr. Paul H. Egli.

Note added after completion of manuscript.—R. J. Collins and H. Y. Fan[27] have recently reported measurements on the infrared lattice absorption of germanium, silicon, and diamond as a function of temperature. They conclude that the observed absorption in silicon and germanium and of Type II diamond is made possible by the thermal vibrations of the atoms. However, they do not suggest any mechanism for the absorption.

[27] R. J. Collins and H. Y. Fan, Phys. Rev. **93**, 674 (1954).

PHYSICAL REVIEW VOLUME 97, NUMBER 1 JANUARY 1, 1955

Soft X-Ray Absorption of Evaporated Thin Films of Tellurium*

ROBERT W. WOODRUFF† AND M. PARKER GIVENS
Institute of Optics, University of Rochester, Rochester, New York

(Received July 28, 1954)

The linear absorption coefficient of tellurium has been measured in the wavelength region 100A to 400A. A double peak was observed at about 300A; it is due to transitions from the N_{IV} and N_V levels to the conduction band. A large peak at shorter wavelengths was also observed.

I. INTRODUCTION

THE energy levels of materials in the solid state are broadened into bands by the interaction of the overlapping atomic wave functions. The bands may be considered to be composed of a very large number of levels so close together that they may be described by a continuous function $N(E)$, where $N(E)dE$ is the number of energy levels between E and $E+dE$.

The absorption of light associated with an electronic transition from some lower energy level to the levels in the range E to $E+dE$ is proportional to the function $N(E)$, and also to the transition probability, $f(E)$. Since $f(E)$ depends on the exact wave functions, its value is not known and, hence, measurement of the absorption can give only a qualitative picture of $N(E)$. Also to be considered is the fact that raising an electron out of an inner level alters the charge of one ion so that the observed energy level structure is that of a slightly perturbed lattice.

The lower or x-ray levels are broadened due to radiation damping and Auger transitions. These two effects have been studied by Prins.[1] He showed that on a linear energy scale the soft x-ray levels, which are about 100 volts below the valence band, are narrower than the deeper-lying levels such as the K and L levels. In studying the structure of the conduction band it is advantageous, therefore, to use the soft x-ray levels rather than the deeper-lying levels.

The experimental resolving power required to reveal a conduction band structure 0.1 volt wide is only about 1000 when using soft x-rays, but will be more than a hundred times that much when using transitions from the K levels. The soft x-ray region therefore offers experimental as well as theoretical advantage over the conventional x-ray region.

II. EXPERIMENT

The vacuum spectrograph used in this research was modeled after one used by Skinner and Johnston[2] and has been described by Siegmund[3] with certain modifications discussed by Carter.[4] In brief, the instrument is a grazing incidence mount of a two meter aluminum grating with 30 000 lines/inch. The source, the grating and the photographic plate holder are on the Rowland circle. The angle of incidence is 85°.

A vacuum of 5×10^{-5} mm Hg is maintained by means of two oil diffusion pumps, one on the main chamber and the other on the source chamber. The source is a spark between copper or silver electrodes from a 0.15-μf condenser charged to about 30 000 volts. This was effectively controlled by an air gap in series with the internal spark. The plate holder, situated behind an occulting diaphragm, was designed to be movable from outside through an "O" ring seal. Five exposures could be made on Eastman Kodak Spectroscopic Plates, type SWR Extra-thin, size 2 in.$\times$10 in.

The wavelengths were determined from tables of the copper spark spectrum prepared by Kruger and

* This research was supported by the U. S. Office of Naval Research.

† Now with the Research Division, Photo Products Department, E. I. du Pont de Nemours and Company, Inc., Parlin, New Jersey.

[1] J. A. Prins, Physica **2**, 231 (1935).

[2] H. W. B. Skinner and J. E. Johnston, Proc. Roy. Soc. (London) **A161**, 420 (1937).

[3] W. P. Siegmund, thesis, The University of Rochester Library, 1951 (unpublished); for a brief account of this work see Phys. Rev. **85**, 313–314 (1952).

[4] D. E. Carter, thesis, The University of Rochester Library, 1954 (unpublished).

Cooper.[5] They list the prominent lines found in a similar vacuum spark. Using this data and the calculated position, a fit can be made between existing lines and listed lines on a smooth curve of wavelength *versus* distance along the plate. Once this curve is firmly established, the wavelength may be read off for any plate so long as any one line is recognized.

Two films of tellurium, one thick and one thin to eliminate the effects of the interface, were deposited by vacuum evaporation onto two identical celluloid substrates. These were mounted close to the slit on the grating side in a device that allowed change from one absorber to the other from outside the spectrograph. Celluloid was chosen for a substrate because tellurium deposits on it in a continuous layer; because thin films of it are easily made by dropping cellulose nitrate dissolved in amyl acetate on water; and because the absorption in this region is known to be small from a measurement by O'Bryan.[6] The thicknesses of several tellurium films were measured with a Fizeau-type interferometer and a curve of thickness *versus* optical density established. It was then only necessary to measure optical density of later tellurium films to ascertain the physical thickness. The accuracy of these measurements was approximately 5 percent.

Recently it has been shown[7] that evaporated films of tellurium are not completely crystalline when deposited on substrates below 200°C. The resistivity of these films is, however, of the same order of magnitude as bulk tellurium. This indicates that there is probably a tendency for microcrystals to anneal into near-crystalline form. That the films are continuous layers is borne out by microscopic study of the evaporated films on celluloid. There is no evidence of grainy appearance. It has been concluded from the work of Keck[8] and Hendus[9] on selenium that the valence structure is the same in amorphous and crystalline forms. Since selenium and tellurium are isomorphous, the same argument is applicable here.

Five exposures were made with each set of absorbers, two through the thick film differing by a factor of two in number of sparks, two through the thin film with the same factor but different numbers of sparks, and a repeat exposure through the thin film to check the reproducibility. The plates were developed in *D*-19 in a tray with continuous agitation supplied by rocking while the temperature was maintained at 65°F. Care was taken to avoid contamination of the plates in any way.

A microdensitometer trace was made of each spectrum using a radiometer type device in which the deflection of the vane is proportional to the intensity transmitted by the plate. The instrument was run slowly enough to give accurate values for the narrow lines.

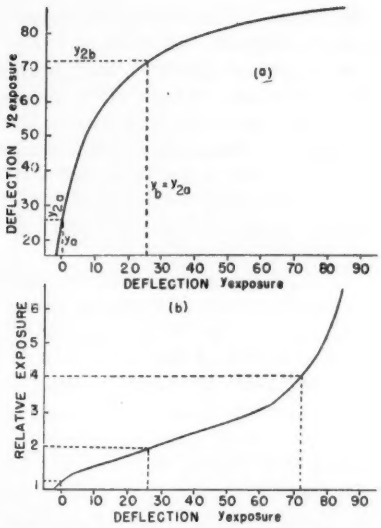

FIG. 1. Calibration of the photographic emulsion. (a) Deflection for twice exposure *vs* deflection for single exposure. (b) Plate sensitivity, relative exposure *vs* densitometer deflection.

Mounting appropriate traces on a comparator, the deflections for one exposure and twice that exposure can be read and plotted as in Fig. 1(a). This was done for both thick and thin absorbers and the average taken. Data from this curve were then used to construct a plot of relative exposure *versus* deflection, Fig. 1(b). First there was arbitrarily taken some point, y_a, on the curve Fig. 1(a) in the region of small deflection. This was established as relative exposure 1 and plotted in Fig. 1(b). Now it can be seen that for twice that exposure the deflection was y_{2a}. This was relative exposure of 2. Now for deflection $y_b = y_{2a}$ there was found a corresponding y_{2b} for which exposure was 2×2 or 4. This process, continued to the largest values of y available, established a curve. More points were determined by taking as a starting value some other point on the relative exposure curve and repeating the process.

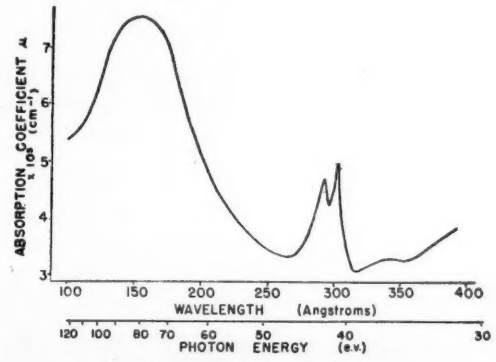

FIG. 2. The absorption of tellurium.

[5] F. S. Kruger and P. G. Cooper, Phys. Rev. **44**, 826 (1933).
[6] H. M. O'Bryan, J. Opt. Soc. Am. **22**, 739 (1932).
[7] T. Sakurai and S. Munesue, Phys. Rev. **85**, 921 (1952).
[8] P. H. Keck, J. Opt. Soc. Am. **41**, 53 (1951).
[9] H. Hendus, Z. Physik **119**, 265 (1942).

From this curve can be read an exposure to correspond to each measured deflection of every spectral line. The ratio of these exposures, thick to thin, multiplied by the inverse ratio of the actual number of sparks through each film gives the transmission at that line of the spectrum of a thickness of tellurium equal to the difference in thickness of the thick and thin samples. Using $T=e^{-\mu x}$, where x is the thickness, the value of μ, the absorption coefficient, can be computed for the wavelength of each spectral line.

If one compares curves from different samples, and allows for possible errors in thickness measurements, some discrepancies in the curves were still observed. For example, the slope of the curve (Fig. 2) at 200A was uncertain by about 10 percent. A short calculation showed that this could be accounted for by very large variations in the film thickness (i.e., pinholes) covering approximately 0.05 percent of the useful area of the sample. Microscopic examination of the samples indicated that this was quite possible. As a result of these calculations and observations the curves showing maximum slope were selected as being most typical of tellurium without pinholes.

III. RESULTS

Figure 2 shows the plot of absorption coefficient from 100A to 400A. The salient features are the double peak at about 300A and the large peak at about 155A. The double peak indicates that the transitions from the N_{IV} and N_V levels to the valence band are separated in this experiment. The peaks occur at 292A and 302A with width at half-maximum of 20A for the double peak. The edges as defined by Skinner[10] are estimated to be at 309A and 299A (40.0 ev and 41.3 ev). Bohr and Coster[11] predicted these edges from limiting frequencies of emission bands to be at 303A and 314A. More recently Chamberlain and Lindsay[12] proposed 289A and 291A.

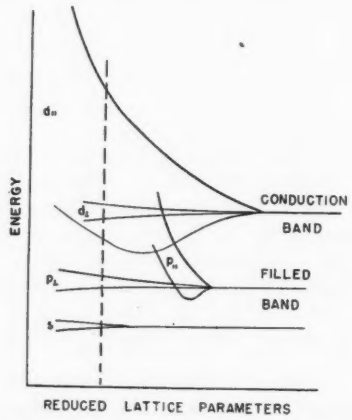

FIG. 3. Schematic diagram of the energy levels of tellurium (after Nussbaum and Callen) showing the broadening of the bands as the atoms are brought together. The subscripts indicate that the symmetry of the wave functions is perpendicular or parallel to the chain axis of the crystal.

The shape of the band can be interpreted to mean that there is a relatively narrow band with a high density of states superimposed on a broader band of low density. Figure 3 shows a diagram by Callen[13] and Nussbaum[14] indicating the band structure of tellurium as a function of the lattice parameter. The $\perp$ and $\parallel$ subscripts indicate that the symmetry of the wave functions is prependicular or parallel to the chain axis of the crystal, the parallel functions overlapping first. The l-selection rule requires that $\Delta l=\pm 1$ so the final state must be p or f since the N_{IV-V} levels are d states. It is possible that the peak arises from transitions from an N level to the middle part of d-perpendicular, which can be nearly pure p (of f) from mixing of d and p (or f) type states. The broadening at the base of the absorption curve can be attributed to the p (or f) states within the d-parallel band. Of course, the argument applies to both the N_{IV} and N_V levels separately.

The broad absorption band centered around 155A has an estimated width at half maximum of nearly 100A. The "edge" falls at 207A (59.6 ev). The expected transition is from N_{II-III} to the conduction band and should occur at about 105A (117.5 ev) according to Bohr and Coster[15] or 108A (114.5 ev) according to Nishina.[16] The discrepancy between these values and the experimental one is so large that there is serious doubt of the identification. The width of the band is very large, too large to be explained by the width of the N levels or valence band with any reasonable numbers. It may possibly be due to Kronig structure.

[10] H. W. B. Skinner, Trans. Roy. Soc. **A239**, 95–134 (1940).
[11] N. Bohr and D. Coster, Z. Physik **12**, 342 (1923).
[12] K. Chamberlain and G. A. Lindsay, Phys. Rev. **30**, 369 (1927). There is no mention in their paper of their recognition of the doublet nature of one of the initial levels. Disregard of this fact could produce error in the 291A value of the N_V level.
[13] H. B. Callen, J. Chem. Phys. **22**, 518–522 (1954).
[14] A. Nussbaum, Phys. Rev. **94**, 337–342 (1954).
[15] N. Bohr and D. Coster, Z. Physik **12**, 342–374 (1923).
[16] V. Nishina, Phil. Mag. **49**, 521 (1925).

Domain Rotation in Nickel Ferrite

FIELDING BROWN AND CHARLES L. GRAVEL
Sprague Electric Company, North Adams, Massachusetts
(Received June 16, 1954)

An experiment has been performed which leads to the conclusion that the initial permeability and radio-frequency dispersion in sintered nickel ferrite are due principally to rotation of crystallite magnetic moments in an equivalent anisotropy field. Samples have been prepared by the partial sintering of nickel ferrite particles of size 0.5 to 1.0 micron. For a series of samples sintered to various maximum temperatures, complete permeability spectra have been obtained, and it has been found that the susceptibility at low frequencies is related to the resonant frequency of the dispersion, defined as the point where susceptibility reduces to one-half its low-frequency value, in a manner which is predictable from the theory of domain rotation. Significant contribution from domain wall motion is probably inhibited by the small grain size in the samples studied. Our results do not preclude the existence of domain wall motion as a significant phenomenon in the behavior of certain ferrites, but indicate the importance of polycrystalline structure in determining the mechanism of initial polarization.

INTRODUCTION

THE process by which ferrites polarize in an external magnetic field has been studied in the past by a number of workers. Using single crystals of magnetite, Galt[1] has shown that the initial permeability is due to motion of a domain boundary and that the dispersion region at 3000 cps is due to this mechanism. In the case of polycrystalline ferrites formed by a sintering process the evidence has not been as clear.

Snoek's original work[2] on the permeability spectra of various Ni—Zn and Mn—Zn ferrites has shown that the resonant absorption of energy in the radio-frequency region could be explained as a gyromagnetic resonance of the magnetic moments of the crystallites in internal anisotropy fields. This conclusion was based on a comparison of the susceptibility at very low frequencies, as attributed to rotation of the magnetic moments, with the frequency at which these moments resonate. The assumption was made that the governing equations are those of Landau and Lifshitz[3] and that the equivalent internal fields tending to orient the moments of grains along certain equilibrium positions were the same for the static as for the dynamic case. The existence of heavy damping, distributions of resonant frequencies among crystallites, internal demagnetization, and the effective g factor for the two-sublattice ferrites[4] were not considered by Snoek. It was further assumed that, in the sintered ferrites studied, the motion of domain walls did not contribute to the susceptibility. Nevertheless, Snoek obtained rough agreement between theory and experiment. The view that the initial permeability of these materials is due mainly to domain rotations and that the dispersion of the permeability at high frequencies is a process of gyromagnetic resonance has also been expressed by Wijn.[5]

More recently the measurements of Rado *et al.*[6] on Ferramic A, a commercial sintered magnesium ferrite, have been interpreted to demonstrate the existence of domain wall motions and to show that this process is the principal one evident in the initial susceptibility. In observing the permeability spectrum of Ferramic A, Rado found two dispersion regions, one at approximately 40 Mc/sec and another at 1400 Mc/sec. The former resonance disappeared when the material was divided into particles of approximately single domain size, whereas the higher-frequency resonance remained in altered form. From this fact it was concluded that the lower-frequency resonance was due to a domain wall resonance which was removed when the domain walls were eliminated by subdivision. Quantitative tests of this hypothesis gave approximate agreement between the experimental data and the theory of domain wall motion.

Before describing the present results on the initial permeability spectra of sintered nickel ferrites, it seems worthwhile to emphasize the importance of differences in composition and preparation in determining the behavior of ferrites. Thus, although a number of investigators have found domain rotation to be predominant, the possibility of wall motions in other samples is by no means excluded. For instance, in Ferramic A the wall resonance observed by Rado can be ascribed to the existence of relatively large grains in the solid material (5–50 microns) although the samples of ferrite composed of much smaller grains, as for the cases we will describe, may show a resonance understandable only on the basis of domain rotation. It is the purpose of the present work to describe experiments done on certain specially prepared materials which serve as examples of the case in which the initial polarization of the material proceeds mainly by rotation of magnetization within a domain

[1] J. K. Galt, Phys. Rev. **85**, 664 (1952); Revs. Modern Phys. **25**, 93 (1953).
[2] J. L. Snoek, Nature **160**, 90 (1947).
[3] L. Landau and E. Lifshitz, Physik Z. Sowjetunion **8**, 153 (1935).
[4] R. K. Wangsness, Phys. Rev. **93**, 68 (1954); F. Brown and D. Park, Phys. Rev. **93**, 381 (1954).
[5] H. P. J. Wijn, Leiden University, thesis, 1953 (unpublished).
[6] G. T. Rado, Revs. Modern Phys. **25**, 81 (1953).

under the joint influence of the applied signal and an equivalent anisotropy field.

EXPERIMENTAL

In initiating the present work it was our purpose to attempt a stepwise reversal of the experimental procedure used by Rado[6] in which the permeability spectrum of solid Ferramic A was compared with the subsequently obtained spectrum of the material in finely powdered form. Our procedure was, therefore, to start with a fine ferrite powder whose spectrum had been determined and to sinter pressed samples of this powder at various maximum temperatures in order to trace the appearance of the lower-frequency absorption peak described by Rado.

A. Sample Preparation

The toroidal samples used for measurements of the permeability spectrum were prepared in a manner similar to that used in standard ferrite manufacture except that extra precaution was taken to assure a powder of known properties as the starting material. To do this, stoichiometric proportions of NiO and Fe_2O_3 were thoroughly mixed with KCl in powdered form in the ratio of approximately twenty parts by weight of KCl to NiO and Fe_2O_3. This mixture was then heated to 960°C in an "Alundum" crucible, a temperature sufficient to melt the salt. Upon cooling the contents and dissolving away the KCl, a fine brown ferromagnetic powder was obtained which was shown by x-ray analysis to consist of more than 95 percent nickel ferrite. Chemical tests showed that the ratio of nickel to iron was stoichiometric nor could we detect by chemical analysis the presence of unreacted NiO or Fe_2O_3. The particle sizes of this powder were determined by electron microscope observation and were found to be principally within the range of 0.5 to 1.0 micron.

After washing and drying the powder, the toroidal samples were pressed using a pressure of about 30 000 lb/in.^{2} The nominal dimensions of the samples were $\frac{1}{2}$ in. o.d.$\times\frac{1}{4}$ in. i.d.$\times\frac{1}{16}$ in., but the subsequent firing caused shrinkage so that permeability measurements were based on final dimensions. Individual samples were fired to maximum sintering temperatures in the range 960°C–1327°C in such a way that a distribution of permeability values was obtained. Results and conclusions have been based on comparison of the spectra obtained for the various samples, no quantitative reference being made to the firing conditions with the exception that the packing factor (relative density) of each sample was determined and used in applying the theory of domain rotation.

We have noted a distinct color change in the material as sintering was carried to higher temperatures. Before sintering, the powder was reddish brown changing gradually to black at the highest firing temperatures. We attribute this change to an increase in particle size as sintering progresses, and have found by microscopic observation that the most thoroughly sintered samples were made up of grains as large as 2 to 3 microns in diameter. Color changes were not attended by detectable changes in chemical composition.

B. Measurements

In determining the magnetic spectra of the various partially sintered toroids, Rado's method[6] was used in the frequency region above 140 megacycles. This is essentially a standing wave technique in which the standing wave pattern of a short-circuited coaxial line is measured with and without a specimen placed next to the short circuit. The shift in position of the voltage minimum gives the real part of the permeability, μ', whereas the standing wave ratios give the imaginary part, μ''. Rather than grind the numerous samples to an exact fit with the coaxial line, we have adjusted the measured values of μ' and μ'' according to relations given previously.[7] When corrected for misprints, these relations are

$$\mu'/\mu_0=[(\mu_m'/\mu_0)\log(D_4/D_1)-\log(D_2/D_1)-\log(D_4/D_3)][\log(D_3/D_2)]^{-1}, \quad (1a)$$

$$\mu''/\mu'=(\mu_m''/\mu_m')[\log(D_2/D_1)+\log(D_4/D_3)+(\mu'/\mu_0)\log(D_3/D_2)][(\mu'/\mu_0)\log(D_3/D_2)]^{-1}, \quad (1b)$$

where μ' and μ'' are the corrected values, μ_m' and μ_m'' are the corresponding measured values, D_4 is the inside diameter of the outer conductor of the coaxial line, D_3 is the outside diameter of the sample toroid, D_2 the inside diameter of the sample, and D_1 is the diameter of the inner conductor of the coaxial line. μ_0 is the permeability of free space.

In the frequency range between 30 Mc/sec and 140 Mc/sec we have used a measuring technique adapted from a method of van der Burgt *et al.*[8] This consists of determining the capacity required to resonate a small section of short-circuited coaxial line ($L\ll\frac{1}{4}\lambda$) with and without a sample toroid at the shorted end. If the Q of this resonant circuit is also found in both cases, μ' and μ'' can be calculated. The relations are

$$\mu'=(\omega^2L_B)^{-1}(C_F^{-1}-C_A^{-1}), \quad (2a)$$

$$\mu''=(\omega^2L_B)^{-1}[(C_FQ_F)^{-1}-(C_AQ_A)^{-1}], \quad (2b)$$

where L_B, the inductance of the space occupied by the toroid, is given by $L_B=0.4606\,h\log(b/a)\times10^{-6}$ henry, in which b/a is the ratio of outer to inner diameter of the toroidal specimen and h is its height in meters. Further, C_A and Q_A are the resonant capacity and Q of the circuit with the specimen absent, and C_F and Q_F

[7] Massachusetts Institute of Technology Technical Report XXXVI, Laboratory for Insulation Research, July, 1950 (unpublished).

[8] Van der Burgt, Gevers, and Wijn, Philips Tech. Rev. 14, 245 (1953).

are the corresponding values with the toroid in place. In practice, the Q's and capacities were measured using a Q meter with a 3-inch coaxial line suitably mounted at its terminals to receive specimens. For each spectrum an additional measurement was made at 2 Mc/sec using a separate permeameter[9] designed for use at this frequency in conjunction with a Q meter. Since it is important in all magnetic measurements on ferrities at radio-frequencies to eliminate the possibility of dimensional resonance, we have checked our permeability spectra with samples of thickness from 3 millimeters to 0.5 millimeter with no significant changes in our results.

RESULTS

In Fig. 1 are shown the spectra of five of the sample toroids sintered at progressively higher temperatures and consequently exhibiting progressively higher packing factors (density of samples relative to that of a single crystal of nickel ferrite). All of the curves show a marked disperion region occurring around 2000 Mc/sec for the lightly sintered sample and moving to lower frequencies as the sintering temperature is increased. The toroids with packing factor 0.746 and 0.770 have spectra in qualitative agreement with that measured by Rado.[6] However, we have been unable to identify, within the significance of our measurements, the slight absorption peak which occurs in Rado's measurement at around 3000 Mc/sec. The fact that others have observed this peak whereas we do not strongly suggests that the high-frequency peak in this this material is dependent upon the nature of the specific sample used and is not an inherent property of nickel ferrite. On the other hand, the broad resonance occurring at some hundreds of Mc/sec is certainly a general characteristic of the material. We have therefore concentrated our attention on the nature of the processes underlying this lower frequency peak.

As proposed by Snoek,[2] the dispersion may be due to the precession of the magnetic moments of domains in an equivalent anisotropy field. This anisotropy field may have contributions from magnetocrystalline anisotropy such as has been found to affect the resonance conditions in single crystals at microwave frequencies, from internal strains in the sintered material, from the internal magnetic fields created by a distribution in direction of crystallites, and from the shape anisotropy of grains. Polder has pointed out[10] further that the relative orientation and interaction of adjacent grains in the material may cause the dynamic demagnetizing factor to differ from the static one, thus shifting the position of the resonance frequency away from a value predicted taking only the other above mentioned anisotropy sources into account. It is very difficult to estimate the magnitudes of these effects in a sintered ferrite, so that it is sufficient to note that the resonances we observed between 200 and 2000 Mc/sec occur at roughly

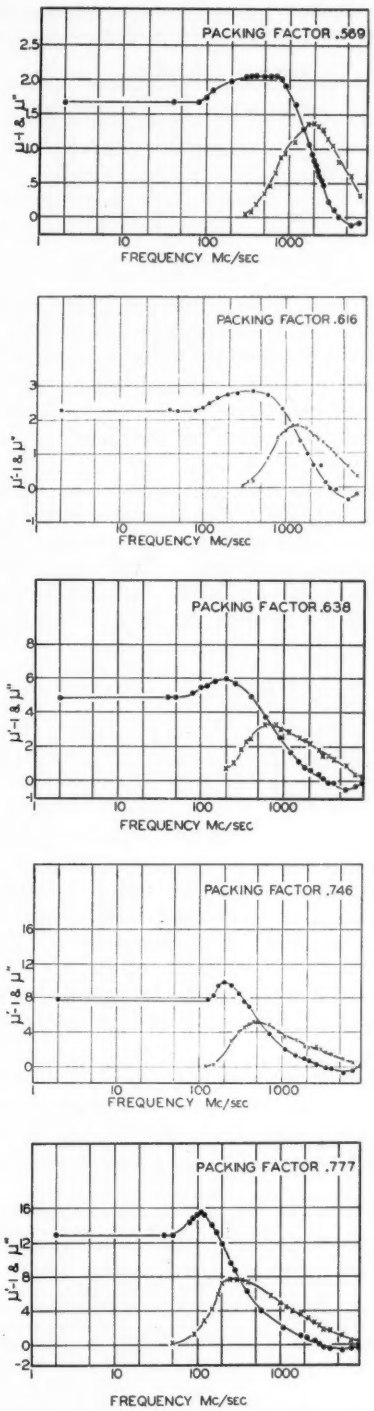

FIG. 1. Permeability spectra of partially sintered nickel ferrite. From top to bottom the five samples represented were sintered at progressively higher maximum temperatures in the range 960–1327°C. The circles represent $\mu'-1$ and the crosses represent μ''.

[9] Made by National Electronics Laboratories, Inc.
[10] D. Polder and J. Smit, Revs. Modern Phys. 25, 89 (1953).

TABLE I. Comparison of observed susceptibilities with those calculated from the theory of domain rotation.

p	$\omega_r \times 10^9$	$\omega_2 \times 10^9$	$\omega_1 \times 10^9$	χ_0/p (expt)	χ_0/p [Eq. (3a)]	χ_0/p [Eq. (3b)]	Bracket [Eq. (3a)]	Bracket [Eq. (3b)]
0.569	12.6	3.8	0.31	0.23	0.28	0.28	1.0	1.0
0.616	10.7	3.8	0.25	0.29	0.32	0.32	0.99	1.0
0.638	6.0	3.8	0.13	0.60	0.50	0.47	0.87	0.82
0.565	4.4	···	1.0	0.76	···	0.74	···	0.95
0.746	4.4	3.8	0.13	0.83	0.74	0.80	0.95	1.0
0.662	3.5	···	0.75	0.96	···	0.91	···	0.93
0.777	2.5	3.8	1.1	1.39	1.2	1.4	0.85	1.0
0.805	1.9	···	0.75	1.45	···	1.8	···	1.0

the same frequencies as that predicted by an extrapolation of microwave resonance conditions to the case of zero field. On the above basis one would expect a zero-field intercept at around 900 Mc/sec for the case of single crystals of nickel ferrite, or 1400 Mc/sec extrapolating the data of Okamura[11] on sintered samples.

In our analysis we have therefore assumed that the resonance field is determined in some unknown manner by the above factors, but that in every case the position of the resonance frequency is related to the initial susceptibility by a relation, similar to that of Snoek,[2] which has recently been derived by Park.[12] Park's theoretical expression is

$$\omega_r(\chi_0/p)=\tfrac{2}{3}\gamma_E M_S[(2\omega_1/\omega_2)^{\frac{1}{2}}\ln(\omega_2/\omega_1)], \qquad (3a)$$

where ω_r=angular frequency at which χ reduces to one-half its low-frequency value, χ_0; $\chi_0=(\mu'-1)/4\pi$ at low frequencies; p=packing factor of the sintered ferrite, i.e., the density of the material relative to that of a single crystal; γ_E=effective value[4] of $ge/2mc=19.4\times10^6$ (oersted)$^{-1}$; M_s=saturation moment of nickel ferrite=265 emu; ω_2=angular frequency at which $\mu'-1$ is a minimum, and ω_1=angular frequency at which $\mu'-1$ is a maximum. It can be seen that Eq. (3a) is similar to that given by Snoek, except that porosity of the material is accounted for through p, and that an additional factor appears on the right-hand side of the equation.

However, in applying Eq. (3a) it is necessary to determine the spectrum up to the frequency at which $\mu'-1$ is a minimum (about 6000 Mc/sec) so that it is often more convenient to use a slightly modified form of the expression. In most cases encountered experimentally, it can be shown that $\omega_r \approx (\omega_1\omega_2)^{\frac{1}{2}}$, in which case Eq. (3a) becomes

$$\omega_r(\chi_0/p)=\tfrac{2}{3}\gamma_E M_S\left[\frac{2\sqrt{2}\omega_1}{\omega_r}\ln(\omega_r/\omega_1)\right]. \qquad (3b)$$

Under these conditions it is only necessary to extend the measurement up to ω_r, which in the present case would never exceed 2000 Mc/sec.

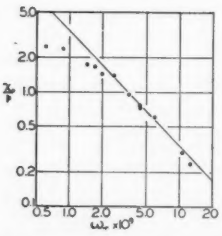

FIG. 2. Comparison of magnetic spectral data on partially sintered nickel ferrites with theory of domain rotation. $\chi_0=(\mu'-1)/4\pi$ is the low-frequency susceptibility, p is the packing factor, and ω_r is the angular frequency where $\chi=\frac{1}{2}\chi_0$. The circles give the experimental points, and the solid line is a plot of Eq. (3a) in which the term in brackets has been taken as unity.

In Table I are shown experimental values of the various quantities which enter Eqs. (3a) and (3b), as determined from the curves of Fig. 1, along with data from other spectra not shown. In column 5 of the table, the experimental values of χ_0/p are to be compared with the calculated values in columns 6 and 7 which have been determined from the two forms of the theory mentioned. It can be seen that the agreement is quite good in both cases, being well within experimental uncertainties. In columns 8 and 9, it is also seen that the approximation used to get Eq. (3b) is quite valid in those cases where our data have permitted use of the more exact expression. It is further interesting to note that the inclusion of a distribution of resonant frequencies among crystallites in the derivation of Eqs. (3), giving rise to the term in brackets, does not strongly modify Snoek's original equation in which such a distribution was not considered, since the bracket never departs from values close to unity.

The inverse proportionality indicated by Eqs. (3), and exhibited by the data, is shown in Fig. 2, where the solid line represents the theoretical expression plotted under the assumption that the term in brackets is in fact unity. For values of χ_0/p less than 1.5 the agreement is adequate but is not as satisfactory for larger ordinates, a possible explanation being that the bracketed term of Eqs. (3) could depart strongly from unity in these cases. However, since the spectra associated with the points of highest χ_0/p contained no resonant rise of $\mu'-1$, the bracketed term could not be determined.

Inherent in the derivation of Eqs. (3) has been the assumption that the equivalent anisotropy field for resonance is the same as that experienced at very low frequencies. The absence of any appreciable effect of the type proposed by Polder[10] has thus been assumed.

[11] Okamura, Torizuka, and Kojima, Phys. Rev. **88**, 1425 (1952).
[12] D. Park, Phys. Rev. **95**, 652(A) (1954). See also the succeeding article [Phys. Rev. **97**, 60 (1954)].

In view of the present agreement between theory and experiment, an agreement obtained without recourse to the Polder effect, it can be concluded that the initial susceptibility in the nickel ferrites we have studied is due principally to domain rotation in an equivalent anisotropy field with little contribution from the dynamic interaction of crystallite magnetic moments.

For comparison we may estimate the resonance conditions to be expected if the initial suceptibility in our material were principally due to the motion of domain walls. Rado *et al.*[13] give an approximate expression for the relation between the susceptibility at low frequencies due to wall motion, which we will call χ_{01}, and the resonance frequency of walls, designated here as ω_{01} Their expression can be written as

$$\omega_{01}(\chi_{01}/p)^{\frac{1}{2}}=\gamma_E M_s(8\pi\delta/d)^{\frac{1}{2}}, \tag{4}$$

where $\delta\sim(kT_c/Ka)^{\frac{1}{2}}$ and d is an average domain size. Clearly, if we assume that δ and d do not change sufficiently during sintering to alter the right-hand side of (4), the predicted relationship between ω_{01} and χ_{01} is quite different from the one we have observed experimentally in which ω_0 and χ_0 are inversely proportional. We have further observed that d does not increase in our material to values larger than 2 to 3 microns (assuming that each grain contains one or more domains) in those samples sintered to highest packing factor. For the lightly sintered samples d was 0.5 to 1.0 micron so that the right side of (4) could not decrease by a factor of more than 2.5 in the sintering process. The anisotropy constant, K, is the only other quantity in (4) which could change in sintering in such a way as to cause ambiguity in applying (4). In order that wall resonance give an inverse proportion between these two quantities, we find that K would have to increase by a factor of 10^4 which seems quite unlikely.

It is also worthwhile to inquire to what extent our dispersion phenomena may be explained by domain wall relaxation, since the approximate governing equation[13] predicts an inverse proportion between χ_{01}, and the relaxation frequency, ω_{02}. We write Rado's expression as

$$\omega_{02}(\chi_{01}/p)=M_s^2R/\eta, \tag{5}$$

where $R=\delta/d$, $\eta=\beta\gamma\delta$, and β is the wall velocity parameter. Inserting $\beta=0.026$,[14] we obtain $M_s^2R/\eta\sim2\times10^{10}$. Inasmuch as our experimental results indicate a $\omega_0\chi_0$ product of around 2×10^9, it seems unlikely that domain wall relaxation can contribute strongly. Further qualitative evidence in agreement with this conclusion is obtained by noting the distinct rise in $\mu'-1$ which occurs in most of our samples just below the region of maximum absorption; this aspect of our curves suggests a resonance process rather than a pure relaxation.

CONCLUSIONS

The experiment described above has lead to the conclusion that the initial permeability in our samples is due principally to domain rotation. This result is probably due to the fact that the crystallite size in the materials studied was restricted to values small enough to inhibit the formation and motion of domain boundaries in the usual sense. In this respect our samples exhibit pronounced single domain behavior.

It seems hardly necessary to emphasize that the results of our experiment do not preclude the existence of domain wall motion as an important model in understanding the initial permeability in certain ferrites. Nor can contributions from wall motion be completely excluded in the present case. Our experiment presents, however, an example of a situation in which, because of the relatively small size of crystallites in the sintered material, the principal contribution to initial permeability comes from domain rotation.

We wish to acknowledge our debt to David Park and J. Kenneth Moore for continued discussions and suggestions on all phases of the work and to V. R. Abate for help in making the measurements.

[13] Rado, Wright, and Emerson, Phys. Rev. **80**, 273 (1950).

[14] J. K. Galt and H. G. Hopper, Revs. Modern Phys. **25**, 93 (1953).

Magnetic Rotation Phenomena in a Polycrystalline Ferrite*

DAVID PARK
Williams College, Williamstown, Massachusetts
(Received August 13, 1954)

In order to calculate the initial susceptibility at high frequencies of a polycrystalline sample of ferrite, one must take account of the interaction between neighboring crystallites, and of the fact that the crystallites differ from each other in their orientation (assumed random) and in their characteristic resonant frequencies. Each crystallite is acted upon by an oblique alternating field, and its magnetization precesses in an elliptical cone. A simple solution of this problem is given by the use of complex variables involving two different imaginaries. It is found that the interaction between crystallites has little effect on the magnetic spectrum other than to raise the effective value of the resonant frequencies, and that the spectrum obtained is not very sensitive to the exact form chosen for the distribution of resonant frequencies among the crystallites.

The resulting expressions for the real and imaginary parts of the susceptibility are compared with the results of some measurements by F. Brown and C. L. Gravel on a lightly-sintered sample of nickel ferrite, assuming that the major part of the susceptibility is due to rotation processes. The agreement is satisfactory and shows among other things that the damping constant need be no larger in these materials than it is found to be in a single crystal.

1. INTRODUCTION

THE magnetic spectrum of unmagnetized polycrystalline samples of ferrite has usually been considered in two ranges, the boundary between them lying roughly at 500 Mc/sec. Above this value, the effects of domain rotation are identified, while below it the permeability is attributed largely to the effects of domain wall motion.[1] Recently, however, an extensive series of experiments[2] has been done on samples of nickel ferrite in which the crystallite sizes are rather small—of the order of a few microns—and there appears to be considerable evidence that rotation phenomena are largely responsible for the permeability over the entire range of frequencies studied (2 to 10 000 Mc/sec).[3] Since these conclusions have been discussed elsewhere,[2] we shall only summarize them briefly here. First, the spectra of grains of single-domain size embedded in wax (where wall motions would not be expected to play any part) are qualitatively similar to, and form part of a continuous progression with, the spectra of samples sintered at progressively higher temperatures. Second, the evidence provided by Snoek's relation between initial susceptibility and resonant frequency[4] (see Sec. 4) is against the hypothesis of wall motion, and third, there is the intuitive objection that the numerous holes, traps and impurities present in any sintered mass would so immobilize any domain walls which might be formed there that they would hardly be expected to react at all to an applied field. This objection ceases to apply, of course, when the crystallites are large enough to contain several domains.

2. THE THEORETICAL MODEL

The theory of domain rotations in a sintered mass of ferrimagnetic material differs from that previously developed for a crystalline sample[5] in three respects. First, the sintered crystallites must be taken to be randomly oriented; second, they will interact magnetically with each other somewhat in the manner of coupled oscillators; and third, the magnetic properties of the material will vary from one crystallite to another, according to their chemical purity, shape, size, state of stress, etc. In what follows we shall suppose that the resonant frequencies characterizing the individual crystallites are distributed in some arbitrary manner. The problem of determining the magnetic response of such a substance is, as it stands, of course quite insoluble, so we shall approximate it by means of the following model, which is capable of exact calculation.

We shall suppose that any given crystallite X is surrounded by several neighbors N, oriented at random, but numerous enough so that their, average magnetization is the same as that characterizing the sample as a whole. Let us suppose that under the influence of an external alternating magnetic field $\mathbf{h}$, whose frequency is ω, this average magnetization is $\mathbf{M}(\omega,t)$. It is clear from symmetry that the average magnetization of a randomly oriented mass cannot have its direction other than parallel to the external magnetizing field $\mathbf{h}$. Clearly also, the averaged field produced by the neighboring crystallites must lie along this line; though it will be directed oppositely to $\mathbf{M}$, since the lines of force external to a magnetized body go round continuously outside it. If a crystallite (or lump of crystallites) N is of size l, it will have a magnetic moment of the order of

* This work was supported by the Sprague Electric Company, North Adams, Massachusetts.

[1] G. T. Rado, Revs. Modern Phys. **25**, 81 (1953). This article reviews the extensive evidence in support of this view, and contains references to most of the earlier work. See also H. P. J. Wijn, dissertation, Leyden, 1953 (unpublished).

[2] F. Brown and C. L. Gravel, Phys. Rev. **95**, 652(A) (1954); see also preceding article [Phys. Rev. **97**, 55 (1954)].

[3] The possibility that the dispersion is all due to rotation was first put forward by members of the Philips group [J. Went and H. Wijn, Phys. Rev. **82**, 269 (1951)].

[4] J. L. Snoek, Physica **14**, 207 (1948).

[5] F. Brown and D. Park, Phys. Rev. **93**, 381 (1954).

$M\beta$, and will produce at X a field of the order of $M\beta/\beta$, so that the total field acting upon X is given by

$$\mathbf{H}=\mathbf{h}-\rho\mathbf{M}, \tag{1}$$

with ρ, depending on permeability and on crystalline properties, at least of the order of unity.[6] In such a field (we assume a toroidal sample so that $\mathbf{h}$ is not demagnetized) the crystallite X will exhibit a certain rotating magnetization $\mathbf{M}_X$, characteristic of the individual magnetic properties of X. To find the magnetization of a large number of crystallites X, we average this response to the applied field over their resonant frequencies (and, later, over their orientations). But this average $\mathbf{M}$, characterizing the whole mass, must be the same as that which was assumed to characterize the neighbors of any X. This identification will be written in the form of an equation which can then be solved for $\mathbf{M}$. Finally, comparison of this average magnetization with the exciting field $\mathbf{h}$ permits us to find the real and imaginary parts of the susceptibility, which can be compared with experiment.

3. THE SUSCEPTIBILITY

We shall write the equation of motion for the magnetization of the crystallite X in the form given by Landau and Lifschitz:[7]

$$\dot{\mathbf{M}}_X=\gamma\mathbf{M}_X\times\mathbf{H}_T-\frac{\lambda}{M_X^2}\mathbf{M}_X\times\mathbf{M}_X\times\mathbf{H}_T, \tag{2}$$

where $\mathbf{H}_T$, composed of the alternating field $\mathbf{H}$ and the fixed anisotropy field $\mathbf{H}_{A0}$ (we assume that there is no fixed external field), is the total magnetic field acting on $\mathbf{M}$, and γ is the effective value of the gyromagnetic ratio for the two-lattice system.[5] Let us adopt a coordinate system $\mathfrak{X}$, with the z-axis chosen to coincide with the direction of $\mathbf{H}_{A0}$. Then if the applied field is not too large, we can neglect its z-component entirely. With respect to these axes, the direction of $\mathbf{h}$ will have some arbitrary orientation, given by the polar angles θ and φ:

$$h_{Xx}=h_0\sin\theta\cos\varphi e^{-j\omega t},\quad h_{Xy}=h_0\sin\theta\sin\varphi e^{-j\omega t}, \tag{3}$$

where the time variation has been put into complex form in order to facilitate the consideration of phase relationships later. It is convenient to consider the x-y plane in the coordinate system $\mathfrak{X}$ as a complex plane in which the y-direction is denoted by the imaginary quantity i. This is, of course, an actual physical plane, as contrasted with that whose imaginary unit is j, and which is merely a computational device. Letting $M_{Xx}+iM_{Xy}=M_{X+}$, and similarly with other quantities, we find that (2) can be expressed in the simple form

$$\dot{M}_{X+}=-i\gamma'(H_{A0}M_{X+}-H_{X+}M_s), \tag{4}$$

where

$$\gamma'=(1-i\alpha)\gamma,\quad \alpha=\lambda/\gamma M_s, \tag{5}$$

and M_s, the saturation magnetization of the crystallite, is the approximately constant value of M_z. Thus the only effect of the damping, as introduced in this way, is to give to the effective value of the gyromagnetic ratio a negative imaginary part in i.

To put in the field $\mathbf{h}$, let us introduce an average alternating susceptibility of the entire sample,

$$\chi_+=M_+/h_+. \tag{6}$$

With this, we can put (1) into (4) to get, for the magnetization of the crystallite X,

$$\dot{M}_{X+}=-i\gamma'[H_{A0}M_{X+}-(1-\rho\chi_+)M_sh_{X+}], \tag{7}$$

where, by (3),

$$h_{X+}=h_{X0+}e^{-j\omega t},\quad h_{X0+}=h_0\sin\theta e^{i\varphi}. \tag{8}$$

Then, if we assume that M_{X+} in the steady state is of the form $M_{X0+}e^{-j\omega t}$, we can readily solve this [with (5)] to get

$$M_{X0+}=\frac{\gamma M_s(1-\rho\chi_+)h_{X0+}}{[ij\omega/(1-i\alpha)]+\omega_X}, \tag{9}$$

where ω_X, the characteristic frequency of X, is given by γH_{A0}.

The susceptibility of X is determined by the storage and dissipation of energy in X as $\mathbf{h}$ goes through its cycle. Thus we need only consider that part of $\mathbf{h}$ which does work on $\mathbf{M}_X$, and the susceptibility can be written as

$$\chi_{X+}=(M_{X0+}h_{X0-})/h_+h_-. \tag{10}$$

When (9) is put into this, we encounter the product

$$h_{X0+}h_{X0-}=h_0^2\sin^2\theta.$$

We can now immediately average this over all possible orientations of X. The $\sin^2\theta$ becomes $\frac{2}{3}$, and we find[8]

$$\bar{\chi}_{X+}=\tfrac{2}{3}\gamma M_s(1-\rho\chi_+)\frac{1}{[ij\omega/(1-i\alpha)]+\omega_X}. \tag{11}$$

Now we are to average this over the different resonant frequencies ω_X that X may have. It is certain, of course, that, besides ω_X, other parameters such as γ and M_s will vary from one crystallite to another. However, the most marked effect on the resulting permeability is produced by the statistical distribution in ω_X, and we shall consider only this. Suppose that the distribu-

[6] This problem of averaging is somewhat similar to that encountered by Lorentz in calculating the internal field of an electrically polarized body [H. A. Lorentz, *The Theory of Electrons* (Dover Publications, Inc., New York, 1952), p. 138 and Note 55]. The approach in this paper consists essentially in assuming that there is no appreciable short-range order in the precession of the spins.

[7] L. Landau and E. Lifschitz, Physik. Z. Sowjetunion **8**, 153 (1935).

[8] The occurrence of i in formulas (9) and (11) shows that the magnetization, both of X and of the directionally averaged X, precesses in an elliptical cone under the action of the applied field.

tion is according to some law $q(\omega_X)$, where

$$\int_0^\infty q(\omega_X)d\omega_X=1.$$

Then, if we define

$$p(\omega)=\int_0^\infty \frac{q(\omega_X)d\omega_X}{[ij\omega/(1-i\alpha)]+\omega_X}, \tag{12}$$

the average susceptibility of the entire mass will be

$$\chi_+=\tfrac{2}{3}\gamma M_s(1-\rho\chi_+)p(\omega).$$

The hypothesis mentioned earlier—that the average susceptibility of the neighbors of any X is the average susceptibility of all X—equates the two χ_+'s in the expression above, and we find that

$$\chi_+=\tfrac{2}{3}\gamma M_s p(\omega)/[1+\tfrac{2}{3}\rho\gamma M_s p(\omega)].$$

χ_+ is, however, closely related to the measured permeability of the sample, for the latter is defined (again, in terms of energy storage and dissipation) as

$$\chi=\frac{M_x h_x+M_y h_y}{h_x^2+h_y^2}=\frac{1}{h_+h_-}\,\mathrm{Re}_i M_+h_-=\mathrm{Re}_i\chi_+,$$

where Re_i denotes that the real part with respect to i is to be taken, and we have chosen coordinates such that $\mathbf{h}$ has no z-component. Thus, we have finally

$$\chi=\tfrac{2}{3}\gamma M_s\,\mathrm{Re}_i\{p(\omega)/[1+\tfrac{2}{3}\rho\gamma M_s p(\omega)]\}. \tag{13}$$

As a first orientation, let us consider the case in which the distribution $q(\omega_X)$ is infinitely narrow and centered around some frequency ω_0. In this case, (13) is[9]

$$\chi=\tfrac{2}{3}\gamma M_s \times\frac{(1+\alpha^2)(\omega_0+\tfrac{2}{3}\rho\gamma M_s)-j\alpha\omega}{(1+\alpha^2)(\omega_0+\tfrac{2}{3}\rho\gamma M_s)^2-\omega^2-2j\alpha\omega(\omega_0+\tfrac{2}{3}\rho\gamma M_s)}. \tag{14}$$

It is clear from this, and can be verified to hold for the more general cases to be discussed later, that the principal effect of the intercrystallite interaction is merely to make the frequency at which resonance occurs somewhat greater than ω_0. Since, however, ω_0 (or, in the case of a distribution q, the central value of the distribution) is itself only determinable empirically, we shall henceforth omit the term in ρ and consider ω_0 to represent the increased value. The resultant error in the shapes of the permeability spectra can be expected to be less than that which will result from other assumptions.

Although (14) must be considered an idealization, still it exhibits a number of features which characterize most of the experimental data. Not only is the general shape of the curves (for large enough values of α) the same as those observed, but it is also significant that the asymptotic behavior for large ω is right: writing $\chi=\chi'+j\chi''$, we see that $\chi'\sim\omega^{-2}$ and $\chi''\sim\omega^{-1}$, as observed. The correctness of the asymptotic behavior in this respect is a rather stringent test of any theory. Introducing damping through the use of a relaxation time in the equations of motion,[10] for example, fails to predict this behavior, no matter how the relaxation time is assumed to depend on ω. Equation (14), however, cannot be considered a satisfactory result. First, the data require values of α of the order of 0.8, whereas the measurements of Yager[11] and Healy[12] on single crystals give a value of 0.0045. One would expect it be increased by sintering, but not by so much. Second, the data on χ' are not well fitted for any choice of α; and third, as we have pointed out above, it is not reasonable to expect that the crystallites will all resonate at the same frequency.

In order to continue, we need to assume a distribution function $q(\omega_X)$ which leads to analytically tractable results. A first attempt was made[13] with a rectangular distribution, and the resulting formulas showed a surprising agreement with experiment. Typical curves, together with the assumed distribution function, are shown in Fig. 1. Some qualitative predictions which agree well with the available data[2] are that if A and B are the upper and lower limiting frequencies of the rectangular distribution, then they are the frequencies at which[14] μ' takes its extreme values and they are at the same time the "half-power" points of the curve of μ''. Two other features characteristic of the observed spectra are the great asymmetry of the two extremes of μ' (the asymmetry about $\mu'=1$ is frequently as great as 20 to 1) and the fact that the frequency at which μ' equals unity is usually much greater than that at which μ'' has its maximum (a factor of 10 is not uncommon

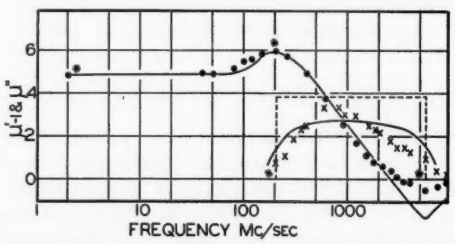

FIG. 1. Data on a sample of nickel ferrite sintered at 1216°C. The circles represent $\mu'-1$ and the crosses represent μ''. The theoretical curves (solid lines) are obtained by assuming a rectangular distribution of crystallite frequencies (dashed line), and are fitted to the data at the points marked with asterisks. This includes an arbitrary scaling of μ so as to fit the data at low frequencies.

[9] If ρ is neglected, this formula becomes identical (except for the sign of j) with one given by Kittel (see reference 1). The formula appears in C. Kittel, J. phys. radium **12**, 332 (1951).

[10] N. Bloembergen, Phys. Rev. **78**, 572 (1950).
[11] Yager, Galt, Merritt, and Wood, Phys. Rev. **80**, 744 (1950).
[12] D. W. Healy, Jr., Phys. Rev. **86**, 1009 (1952).
[13] D. Park, Phys. Rev. **95**, 962(A) (1954).
[14] We write $\mu=1+4\pi\chi=\mu'+j\mu''$.

here). These features are very difficult to understand from the standpoint of wall motions, but both are immediate consequences of our formulas. [For example, the frequency ratio just mentioned is given as approximately $(A/2B)^{\frac{1}{2}}$, which is equal to 3 for the calculation of Fig. 1, as compared with the experimental value of 4.] More exactly, the peak value of μ'' occurs at a frequency of $(AB)^{\frac{1}{2}}$, and the zero of $\mu'-1$ occurs at $[\frac{1}{2}(A^2+B^2)]^{\frac{1}{2}}$. These characteristics also do not follow from the equations of motion in which damping is introduced through a relaxation time. It is interesting to note, however, that Young and Uehling[15] find that experiments on ferromagnetic metals decide in favor of the latter equations.

4. A FOUR-PARAMETER DISTRIBUTION

If we are to avoid nonphysical hypotheses such as that of the rectangular distribution, and at the same time not become involved in analytical work disproportionate to the accuracy of our theory, there is not a very wide range of forms available for q. We shall discuss here the consequences of a distribution of the form

$$q(\omega_X)=\frac{1}{\pi(A-B)}\left(\tan^{-1}\frac{A-\omega_X}{\sigma_1}-\tan^{-1}\frac{B-\omega_X}{\sigma_2}\right), \quad (15)$$

with $\sigma_1 \ll A$ and $\sigma_2 \ll B$. This is a natural generalization of the rectangular distribution; an example is shown in Fig. 2. The conditions are imposed on the σ's so that the contribution to q from values of ω_X equal to zero and below can be neglected. If σ_1 and σ_2 are taken to be equal, we can conveniently represent this as

$$q(\omega_X)=\frac{\sigma}{\pi(A-B)}\int_B^A \frac{d\omega_0}{(\omega_X-\omega_0)^2+\sigma^2} \quad (\sigma \ll B), \quad (16)$$

a superposition of bell-shaped distributions centering about various values of ω_0. If σ_1 is not equal to σ_2 (and

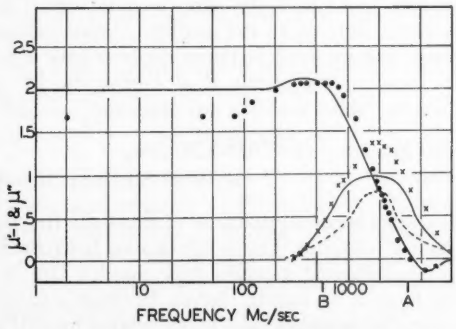

FIG. 2. Data on a sample of nickel ferrite lightly sintered at 960°C. The circles represent $\mu'-1$ and the crosses represent μ''. The theoretical curves (solid line) have been obtained by adjusting the assumed distribution of crystallite frequencies (dashed line) so as to obtain a fit. (There has been no arbitrary scaling.)

[15] J. A. Young, Jr., and E. A. Uehling, Phys. Rev. 94, 544 (1954).

it seems usually to be necessary to assume this), we can still write (15) as

$$q(\omega_X)=\frac{1}{\pi(A-B)}\left\{\sigma_2\int_B^\infty \frac{d\omega_0}{(\omega_X-\omega_0)^2+\sigma_2^2} -\sigma_1\int_A^\infty \frac{d\omega_0}{(\omega_X-\omega_0)^2+\sigma_1^2}\right\}. \quad (17)$$

Changing the order of integration, we have first to evaluate (12) using a q of the form $\sigma/\pi[(\omega_X-\omega_0)^2+\sigma^2]$. The result of doing this is rather complicated;[16] we shall give it here in unrationalized form, omitting terms in α^2:

$$\chi_\sigma=\tfrac{2}{3}\gamma M_s\left[\frac{\omega_0-j\alpha\omega}{(\omega_0-j\alpha\omega)^2+(\sigma+j\omega)^2} +\sigma\frac{2\alpha\omega(\omega-\omega_0)+j((\omega-\omega_0)^2+\sigma^2)}{[(\omega-\omega_0)^2+\sigma^2]^2}\right], \quad (18)$$

from which one can verify the asymptotic properties at high frequencies mentioned above, and in the form which it assumes when all terms in α are neglected:

$$\chi_\sigma'=\tfrac{2}{3}\gamma M_s\omega_0\frac{\omega_0^2+\sigma^2-\omega^2}{(\omega^2-\omega_0^2+\sigma^2)^2+4\omega_0^2\sigma^2}, \quad (19)$$

and

$$\chi_\sigma''=\tfrac{2}{3}\gamma M_s\sigma\frac{\omega_0^2+\sigma^2+\omega^2}{(\omega^2-\omega_0^2+\sigma^2)^2+4\omega_0^2\sigma^2}. \quad (20)$$

These can be compared with the expressions[9] which follow from (14), if one neglects ρ and assumes that all the width comes from the damping α:

$$\chi_\alpha'=\tfrac{2}{3}\gamma M_s\omega_0\frac{(1+\alpha^2)^2\omega_0^2-(1-\alpha^2)\omega^2}{[\omega^2-(1-\alpha^2)\omega_0^2]^2+4\alpha^2\omega_0^4}, \quad (21)$$

and

$$\chi_\alpha''=\tfrac{2}{3}\gamma M_s\alpha\omega\frac{(1+\alpha^2)\omega_0^2+\omega^2}{[\omega^2-(1-\alpha^2)\omega_0^2]^2+4\alpha^2\omega_0^4}. \quad (22)$$

It will be noted that these two pairs of equations are very similar, with σ replaced by $\alpha\omega_0$ (in fact, it is in general impossible to distinguish experimentally between effects of α and effects of σ), except that χ_α'' in (22) vanishes with ω, as it should, whereas in (20) one can see the spurious effect of a $q(\omega_X)$ which does not vanish with ω_X.

The integrations in (17) can now easily be carried out to give

$$\chi'=\frac{1}{6}\frac{\gamma M_s}{A-B}\ln\frac{(\omega^2-A^2+\sigma_1^2)^2+4A^2\sigma_1^2}{(\omega^2-B^2+\sigma_2^2)^2+4B^2\sigma_2^2}, \quad (23a)$$

[16] The integral can be evaluated by means of a contour, but since there are here two imaginaries, it is necessary to use some discretion in determining where the singularities lie.

and

$$\chi''=-\frac{1}{3}\frac{\gamma M_s}{A-B}\left(\tan^{-1}\frac{A+\omega}{\sigma_1}+\tan^{-1}\frac{A-\omega}{\sigma_1}-\tan^{-1}\frac{B+\omega}{\sigma_2}-\tan^{-1}\frac{B-\omega}{\sigma_2}\right) \quad (23b)$$

$$=-\frac{1}{3}\frac{\gamma M_s}{A-B}\left(\tan^{-1}\frac{2A\sigma_1}{\omega^2-A^2+\sigma_1^2}-\tan^{-1}\frac{2B\sigma_2}{\omega^2-B^2+\sigma_2^2}\right). \quad (23c)$$

From these we can find the values at zero frequency,

$$\chi'(0)=-\frac{1}{3}\frac{\gamma M_s}{A-B}\ln\frac{A^2+\sigma_1^2}{B^2+\sigma_2^2}, \quad (24a)$$

and

$$\chi''(0)=-\frac{2}{3}\frac{\gamma M_s}{A-B}\left(\tan^{-1}\frac{\sigma_2}{B}-\tan^{-1}\frac{\sigma_1}{A}\right). \quad (24b)$$

The imaginary part should, of course, vanish. That it is small is a consequence of the conditions laid on (15). It is often convenient (and accurate enough) to choose $\sigma_1/A=\sigma_2/B$ in order to simplify the analysis generally, and this, in (24b) has the desired effect, although for the wrong reason. We have in this case

$$\chi'(0)=-\frac{2}{3}\frac{\gamma M_s}{A-B}\ln\frac{A}{B}, \quad \chi''(0)=0 \quad \left(\frac{\sigma_1}{A}=\frac{\sigma_2}{B}\right). \quad (24c)$$

If (as will generally be the case) $A\gg B$, we find that the minimum of χ' occurs at a frequency

$$\omega_1\approx\frac{A^2+\sigma_1^2}{(A^2-\sigma_1^2)^{\frac{1}{2}}}, \quad \chi'(\omega_1)\approx-\frac{1}{3}\frac{\gamma M_s}{A-B}\ln\frac{A^2+\sigma_1^2}{2A\sigma_1}, \quad (25)$$

while the maximum is at

$$\omega_2\approx(B^2-\sigma_2^2)^{\frac{1}{2}}, \quad \chi'(\omega_2)\approx-\frac{1}{3}\frac{\gamma M_s}{A-B}\ln\frac{A^2+\sigma_1^2}{2B\sigma_2}, \quad (26)$$

and, between these, χ' vanishes at a frequency close to $\omega_1/\sqrt{2}$. A measure of the peaking of χ' is given by

$$P=\frac{\chi'(\omega_1)-\chi'(0)}{\chi'(0)}\approx\ln\left(\frac{B^2+\sigma_2^2}{2B\sigma_2}\right)\Big/\ln\left(\frac{A^2+\sigma_1^2}{B^2+\sigma_2^2}\right). \quad (27)$$

There is an important difference between the results of this work and those of the earlier calculation[13] based on the rectangular distribution of frequencies. It is that, when q rises or falls off in a distance σ, it is σ and not α (if α is small enough) that determines the extreme values of χ'. Thus α may be as small as desired, and the data can still roughly be fitted.

It will be convenient to consider specially two frequencies characteristic of the resonance; those at which χ' drops to half its peak and DC values will be called respectively $\omega_{\frac{1}{2}}$ and ω_r. The latter is the "resonant frequency" by which Wijn[1] characterizes a material. If $A\gg B$, these approach the values

$$\omega_{\frac{1}{2}}\approx[2B\sigma_2(A^2+\sigma_1^2)]^{\frac{1}{2}} \text{ and } \omega_r\approx[(A^2+\sigma_1^2)(B^2+\sigma_2^2)]^{\frac{1}{4}}; \quad (28)$$

and in the case which we have discussed above, in which $\sigma_1/A=\sigma_2/B=\lambda$, say, these become

$$\omega_{\frac{1}{2}}\approx\left(\frac{2\lambda}{1+\lambda^2}\omega_1^2\omega_2^2\right)^{\frac{1}{4}} \text{ and } \omega_r\approx(\omega_1\omega_2)^{\frac{1}{2}}. \quad (29)$$

The first of these can be solved to give an estimate of λ:

$$\frac{\lambda}{1+\lambda^2}\approx\frac{1}{2}\left(\frac{\omega_{\frac{1}{2}}^2}{\omega_1\omega_2}\right)^2 \quad (30)$$

in which it is usually permissible to neglect the λ^2, while the extent to which the second is satisfied provides a very simple check on the applicability of this simplified form of the theory to any given set of data.

The quantity ω_r also enters into Wijn's formulation of Snoek's relation[4] between resonant frequency and static permeability. Again in the simplified case, (24c) and (29) give

$$\omega_r(\mu'-1)_0=\frac{8\pi}{3}\gamma M_s\frac{(\omega_1\omega_2)^{\frac{1}{2}}}{A-B}\ln\left(\frac{A}{B}\right).$$

If (as seems to be quite common) λ is in the neighborhood of $\frac{1}{2}$, then it is easily verified that A is close to $\omega_1/\sqrt{2}$, the frequency at which χ' vanishes. Neglecting B in the denominator and making an unimportant approximation in the logarithm now gives

$$\omega_r(\mu_0-1)_0=(8\pi/3)\gamma M_s(2\omega_2/\omega_1)^{\frac{1}{2}}\ln(\omega_1/\omega_2). \quad (31)$$

Without the terms in ω on the right, this is Snoek's relation. The terms in ω provide a factor which is normally very close to unity. Brown and Gravel[2] have applied this formula to the analysis of data obtained by them, and we shall therefore apply it here only to Wijn's data on his sample E of Ferroxcube IV (the only one for which the data are adequate): we find[17]

$$\omega_r=350 \text{ Mc/sec}, \quad \omega_1=2700\sqrt{2} \text{ Mc/sec}, \quad \omega_2=250 \text{ Mc/sec}, \quad M_s=197,$$

where ω_1 has been estimated as $\sqrt{2}$ times the frequency at which χ' vanishes. The factor in ω on the right is in this case 0.98, and explains why Snoek's law in its simple form is so closely obeyed by Wijn's data. In this case, the values of $(\mu'-1)_0$ calculated by (31) and observed are 14 and 12, respectively.

In comparing these formulas with experiment it is necessary to take account of the porosity of the poly-

[17] The constants are given in terms of ordinary frequency, not angular frequency.

crystalline samples—their packing factor (density of sample divided by density of pure crystalline substance) is seldom over 75 percent. It is clear that the saturation magnetization M_s will be reduced in the same ratio, and that the susceptibility will also be correspondingly less, though the effect of the magnetic poles induced on the crystallite boundaries is difficult to evaluate.[18] In the present work we assume that the effect of porosity can be accounted for by using instead of M_s the saturation magnetization of the polycrystalline sample, but we hope to return later to a quantitative discussion of this point.

In comparing theory with experiment there are two considerations which limit us in the choice of data. The first is the fact that we have neglected the effect of the interaction between crystallites on the shape of the resonance curves, so that it will be advantageous to examine data taken on a sample which has been relatively lightly sintered. The second is more serious: the slowness with which χ'' decreases at high frequencies (this is particularly evident in Wijn's data[1]) entails a value of σ_1 which is comparable with A or even greater, contradicting an assumption which was made in order to obtain results in tractable form. It is fortunate that this effect is less pronounced precisely in the ferrite samples which have been sintered at relatively low temperatures;[2] accordingly, we shall pick for comparison Brown's measurements on a sample sintered at 960°C, with a packing factor $p=0.54$. Figure 2 shows the comparison of theory with experiment in this case. The constants used here are,[17] in kMc/sec (10^9 cps):

$$A=4.2,\quad \sigma_1=2.1,\quad B=0.58,\quad \sigma_2=0.29;$$

but the choice could probably be improved upon. In particular, the error in $\chi'(0)$ should not be regarded as significant. Also, the choice of a $q(\omega_X)$ which was more sharply peaked would certainly have brought the theoretical curve of μ'' higher. It is characteristic of the *Ansatz* (15) that the peaks possible with it are not as high as generally required. For pure crystals of nickel ferrite, M_s is[1] 265, and the effective value[5,17] of γ is 1.1×2.80 Mc/sec oersted. The results indicate quite strongly that the mechanism which we have discussed above is in this case the correct one.

5. REMARKS

A detailed discussion, from the above standpoint, of the various experiments which have been performed on resonance phenomena in ferrites is beyond the scope of this paper, though we hope to return to the subject elsewhere. For the present, let us merely note that the mechanism which we have assumed here leads directly to a slightly modified form of Snoek's relation and, conversely, that whenever it is found by experiment that the susceptibility exhibits a resonance which satisfies this relation, there is some likelihood that domain rotation, rather than wall motion, plays the leading part in the resonant process. But there are certain instances[1,19] in which a substance (notably Ferramic A) shows two resonances, of which one, in the rf region, approximately obeys Snoek's law and the other, a much lower peak in the microwave region, does not. If we consider the possibility that the rf resonance is due to domain rotation, we must then look for an alternative explanation for the other peak.

It is possible that the microwave resonance is due to the free gyration of electron spins. The fact that in some materials the magnitude, and even the existence, of the high-frequency peak vary from sample to sample[20] suggests that this resonance is not a property of the crystallites themselves (it has not been reported in single-crystal samples) but of their state of aggregation. Let us suppose, accordingly, that these electrons are trapped in various lattice imperfections.[21] If the trap is effectively a spherical cavity, the electron will experience a field[22] of magnitude $4\pi M_e/3$, where M_e is some effective value of the local magnetization. For want of a better value, we shall use for it M_s, the saturation magnetization of the sintered mass. The electron's spin will resonate at the frequency

$$\omega_e=\gamma(4\pi/3)M_e=11.7M_e \text{ Mc/sec},$$

and the width of the resonance is due more to the lack of sphericity of the trapping region than to any process of dissipation. In support of this hypothesis, there are data[1] at room temperature on Ferramic A ($M_s=99$ oersteds, $\omega_e=1100$ Mc/sec, observed value 1100 Mc/sec), $Li_{\frac{1}{2}}Fe_{\frac{1}{2}}Fe_2O_4$ ($M_s=258$, $\omega_e=3000$, observed value about 2000 Mc/sec) and $NiOFe_2O_3$ ($M_s=163$, $\omega_e=1900$, observed value 3000 Mc/sec). All the observed resonance peaks are at least 1000 Mc/sec wide. Also, in Rado's results on nickel ferrite, the fact that the resonance is barely observable at room temperature but pronounced at 77°K is explainable on the ground that more electrons are trapped at lower temperatures. The same effect is observable in Rado's data on Ferramic A. His measurements on nickel-zinc ferrite, however, do not at all support this view.

If the foregoing explanation of the high-frequency peak is wrong, it is probably for one of two reasons: the effect might be inappreciable,[23] or the spread in the field strengths experienced by the electrons might be so great as not to produce a resonance at all,[24] but only a general distortion of the microwave end of the sus-

[18] D. Polder and J. Smit, Revs. Modern Phys. **25**, 89 (1953).

[19] Rado, Wright, and Emerson, Phys. Rev. **80**, 273 (1950).

[20] F. Brown (private communication).

[21] I am indebted to F. J. Dyson for this suggestion.

[22] Reference 6, Note 54.

[23] The situation here differs from that in a metal, where the skin effect prevents the magnetic field from penetrating more than a short distance below the surface. In metals, however, the corresponding effect has been observed. [G. T. Rado and J. R. Weertman, Phys. Rev. **94**, 1411(A) (1954).]

[24] It should be noted that in all cases, the microwave resonance peak is far broader than the rf one; the logarithmic presentation of frequencies is deceptive in this respect.

ceptibility curve, and in particular, a lifting of the curve of χ''. Such an effect is apparent in the experiments of Wijn[1] and Brown,[2] and the latter measurements were carried out to a frequency high enough so that one can be sure there is no microwave peak present. In the absence of any theoretical or experimental justification, however, these speculations must remain very tentative.

I am grateful to Fielding Brown and J. Kenneth Moore for communicating to me the results of their measurements and calculations, and for making many contributions to the work presented here.

PHYSICAL REVIEW VOLUME 97, NUMBER 1 JANUARY 1, 1955

Effect of Strong Electrostatic Fields on the Resistance of Tungsten Wires in High Vacua

W. J. Deshotels* and A. H. Weber
Saint Louis University, St. Louis, Missouri

(Received March 11, 1954; revised manuscript received July 26, 1954)

The effect of a radial electrostatic field upon the resistance of tungsten in high vacua was reinvestigated employing lower pressures and better vacuum technique than in the original experiments of Worthing *et al.* Wires of 0.004-in. and 0.00045-in. diameter were subjected to negative and positive fields (retarding or assisting respectively electron motion from filament to plate) up to 9.0×10^6 and 1.4×10^6 volts/cm, respectively. The resistance abruptly decreased upon application of the electric field, increased slightly with time while the field was constant, and increased abruptly upon removal of the field regardless of the direction of the field. The abrupt increase was usually somewhat less than the abrupt decrease. The abrupt resistance changes satisfied the equation $\Delta R=\alpha E^{\frac{1}{2}}$, where ΔR is resistance change, E is applied field in volts/cm$\times10^{-6}$, and $\alpha=0.46$. A large part of the small resistance change with constant field was due to an observed filament temperature increase resulting from bombardment by the electronic portion of the observed ion-, photo-, and field-emission current. It was found that the photo and ion currents were much larger than the field-emission currents. No observable electrostatic effect was found which could account for the abrupt resistance changes. It has not been possible to offer a theory for the observed effects.

INTRODUCTION

THE effect of a radial electrostatic field upon the resistance of tungsten wires in high vacua was reinvestigated, with lower pressures and better vacuum techniques than in the original experiments.[1–3]

Worthing[1] observed that in the absence of the electric field, the resistance of a hot (2500°K) tungsten filament increased as expected because of the evaporation of the filament. Upon application of electric field strengths greater than about 0.5×10^6 volts/cm, he observed that the resistance abruptly decreased and simultaneously the time-rate of increase of resistance became less than for the no-field case. Estabrook,[2] employing molybdenum filaments at temperatures of 1462 and 1644°K, observed an abrupt increase in resistance upon application of the field along with a lessening of the time-rate of increase of resistance due to evaporation. Vissat,[3] employing tungsten in the temperature range 293°K to 853°K, observed an abrupt increase in resistance upon application of the field, agreeing with Estabrook but not with Worthing. He did not investigate the time rate of change of resistance. In each of these experiments the electric field was applied in cylindrical geometry with the filament positive with respect to the surrounding plate so as to inhibit electron emission from the filament. The pressures ranged from 10^{-5} to 10^{-6} mm Hg obtained with dynamic vacuum systems containing waxed joints. The systems probably were not very well outgassed. The filaments were dc heated, resulting in dc etch[4] of the surfaces and consequently the calculated electric field strengths were inaccurate. (Worthing and Estabrook employed Wimshurst machines as high-voltage sources for their fields.)

There appear to be only two theoretical papers concerning this effect.[5,6] Greibach[5] examined the problem from the thermodynamical point of view and was able to obtain qualitative agreement with Worthing but his calculated values for the resistance changes were but 1 percent of Worthing's experimental values. He attributed this to his assumption of an ideal filament surface, perfectly smooth and clean. Reid,[6] from kinetic theory, supported Estabrook[2] and by proper choice of parameters was able to obtain good agreement with Estabrook's measured resistance changes. However, Vissat's results[3] disagreed with Reid's predictions for tungsten.

In the present investigation, with improved experimental apparatus and technique, more complete information has been obtained concerning the effect of strong

* Now at Jackson and Church, Saginaw, Michigan.
[1] A. G. Worthing, Phys. Rev. **17**, 418 (1921).
[2] G. B. Estabrook, Phys. Rev. **63**, 352 (1943).
[3] P. L. Vissat, Phys. Rev. **64**, 119 (1944).
[4] C. Herring and M. H. Nichols, Revs. Modern Phys. **21**, 185 (1949), p. 99 ff. See also D. B. Langmuir, Phys. Rev. **89**, 911 (1953).
[5] E. H. Greibach, Phys. Rev. **33**, 844 (1929).
[6] W. P. Reid, Phys. Rev. **63**, 359 (1943).

electrostatic fields on the resistance of tungsten. Additional insight into the complex nature of the effect is thereby obtained but a complete explanation of all observations is still lacking.

EXPERIMENTAL

The improvements over previous investigations were primarily in the vacuum techniques and high-voltage source for the field resulting in lower pressures, cleaner filaments, and steadier electric fields. The apparatus here used consisted of an electronic power-supply for the electric field, the experimental wires sealed into evacuated glass tubes, and the circuit for measurement of the changes in the resistance of the wires.

The high-voltage source was a half-wave rectifier power-supply (Fig. 1). Because the load current in the experiments is negligible, it was decided that electronic regulation with its accompanying transients would be a liability rather than an asset. With the circuit of Fig. 1, and a maximum current of 1.0 ma through the resistor R', the ripple factor was less than 0.035.

Three experimental tubes were used in this investigation. In the first tube a 0.004-in. tungsten filament wire and a tantalum cylindrical plate (8-cm length, 2-cm diameter) were used for the preliminary experiments which, though not described in the present report, yielded essentially the same results as the final experiments.

The second and third tubes were identical but different from the first tube. The "plate" (A, Fig. 2) was a three-turn spiral of tungsten wire (diameter, 0.03-in.) which was spotwelded to the 0.08-in. diameter nickel press leads (D, Fig. 2). An alternating current of 25 amperes through the spiral heated it to 2400°K. (The spiral "plate" structure was chosen to simplify the outgassing procedure and to eliminate local heating

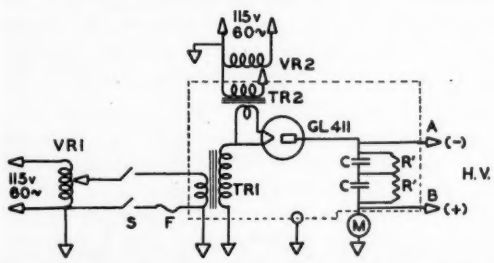

FIG. 1. Electronic power supply producing high voltage for electric field. VR_1, Powerstat operating from constant voltage transformer; S, double-pole single-throw switch; F, 6-amp fuse; TR_1, high-voltage transformer, 100-kv maximum; TR_2, filament transformer, insulated for 150 kv; VR_2, Variac input to filament transformer; $GL411$, high vacuum rectifier, capable of rectifying 150 kv; C, 0.025-μf, 40-kv dc capacitor; R', five 10-megohm resistors in series; M, 0–1 dc milliammeter in series with R' to measure high-voltage output; A, B, high-voltage terminals. A is connected to plate of experimental tube, B is connected to grounded end of tungsten filament. Components contained in dashed rectangle were immersed in oil in steel drums, providing electrostatic shielding and diminishing corona discharge. The output of the power supply was continuously variable from 0 to 72 kv.

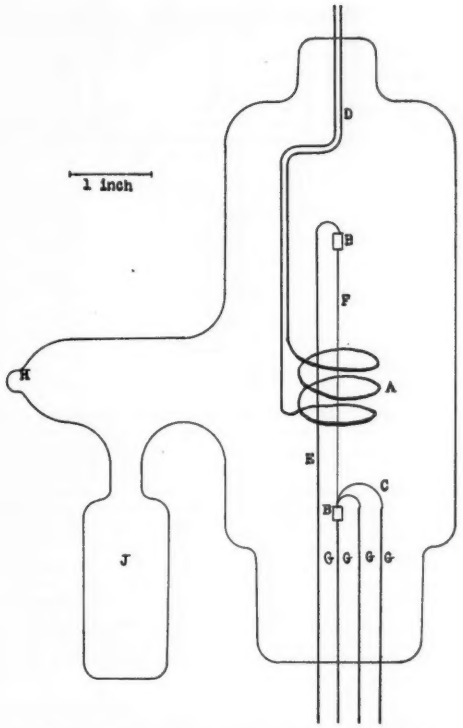

FIG. 2. Experimental tubes No. 2 and No. 3. A, spiral "plate," 3 turns of 0.030-in. tungsten rod, 2.54-cm diameter, 1.90-cm length; B, nickel chucks supporting filament and thermocouple hot junction; C, iron-constantan thermocouple—the iron and constantan wires were spotwelded to 0.050-in. nickel wires G (diameter of thermocouple wires was 0.001-in., hot junction was spotwelded to 0.004-in. diameter nickel wire which was inserted into chuck B and held in contact with filament by a set-screw); D, plate support leads, 0.080-in. diameter nickel rods spotwelded to the tungsten spiral and press leads; E, 0.030-in. diameter tungsten rod, sealed in 4-wire press and sealed in glass over its entire length except for hook at top; F, tungsten filament, 0.00045-in. diameter, 3-in. long, mounted along axis of spiral and 0.25 in. from support rod E; G, 0.050-in. diameter nickel-to-tungsten leads sealed in 4-wire press and supporting the tube elements; H, Seal-off; J, $VG1A$ ion gauge. Glass envelope and presses were Pyrex. Lower press was skirted (not shown). One end of filament F was connected to ground and terminal B' of Fig. 3 and B of Fig. 1, the other end was connected to terminal A' of Fig. 3 through support rod E.

of the glass walls of the tube experienced with the first tube.) The filament (F, Fig. 2) was a 0.00045-in. diameter tungsten wire. One end of the wire was supported by a tungsten rod, 3 in. long and sealed into a glass tube (E, Fig. 2). This glass covering minimized the escape of adsorbed gases from the support rod into the experimental tube after seal-off. (Since the thick rod was connected to the fine-wire filament, it could not be outgassed without burning out the filament.) Both tubes were evacuated to a pressure of 10^{-8} mm Hg. While outgassing tube No. 2, the thermocouple burned out, and after six days a gassy lead had raised the pressure to a value too high to permit high-voltage runs.

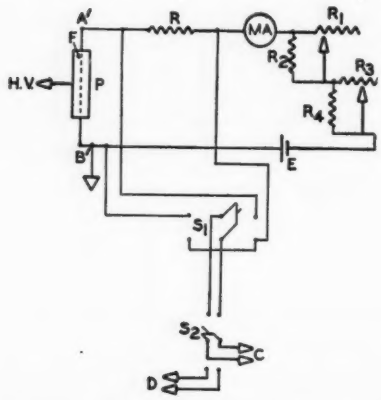

FIG. 3. Filament resistance and temperature measuring circuit. A', B', connected to ends of filament of experimental tubes (F, Fig. 2); R, standardized resistor, 9.9951±0.0003 ohms; MA, 0–10 dc milliammeter for approximate setting of current; R_1, 20K-ohm micropot variable resistor for fine adjustment of current; R_2, 200-ohm resistor; R_3, 250-ohm resistor, variable for coarse adjustment of current; R_4, 750-ohm resistor; E, new 2-volt lead-plate cell supplying current for measuring circuit; C, to Leeds and Northrup student-type potentiometer; D, to thermocouple of experimental tube; S_1, double-pole double-throw switch for connecting potentiometer across R, and R and F (filament) in series; S_2, double-pole double-throw switch for connecting potentiometer to either thermocouple or measuring circuit; P, plate of experimental tube; F, filament of experimental tube; H.V., to terminal A, Fig. 1.

The third tube survived the outgassing procedure and was used for most of the experiments.

The ion gauges used for pressure measurement also served to clean-up the tubes after seal-off by electrical pumping action.[7] The ultimate vacuum attained in each tube was 10^{-8} mm Hg or lower. The outgassing procedure for all tubes included the following steps:

(1) The presses, chucks, springs, and plates were placed in an auxiliary vacuum system and outgassed by induction-heating at temperatures of 1800°K to 2000°K for one hour.

(2) After assembling the experimental tubes, they were evacuated to a pressure of 10^{-6} mm Hg. The spiral "plate" (A, Fig. 2) of tubes No. 2 and No. 3 was heated to 2400°K by an alternating current of 25 amp for 1 hour. The filaments (F, Fig. 2) were outgassed by flashing several times to 2700°K by using alternating current to eliminate "dc etch" and insure a smoother surface. Throughout the outgassing of the tube elements, a refrigerated trap (acetone and solid carbon dioxide) was used.

(3) The entire experimental tube was baked at 500°C for 5 hours while the pressure was maintained at 10^{-6} mm Hg or lower.

(4) Steps (2) and (3) were repeated.

(5) The refrigerant was changed to liquid air. The plates and filaments were again outgassed [step (2)] until the ion gauge registered no change in pressure when the elements were flashed.

[7] D. Alpert, J. Appl. Phys. 24, 860 (1953).

(6) The tubes were sealed off while the elements were hot. The ion gauge was operated continuously, and used for "electrical pumping"[7] after seal-off.

This procedure consistently resulted in an ultimate pressure of 10^{-8} mm Hg or lower. As a result of the outgassing, a visible layer of metal was deposited on the walls of the tubes except where the skirted presses by shadowing prevented the deposition of a continuous conducting layer between filament and plate.

The measuring circuit (Fig. 3) consisted of a standardized resistor, a Leeds and Northrup student-type potentiometer, and a constant current source. The standardized resistor (R, Fig. 3) and the experimental filament F were connected in series with the constant current source and the potentiometer was used to measure the potential drop across R and that across R and F in series. The filament resistance R_F was calculated by

$$R_F = R(V_{R+F} - V_R)/V_R, \qquad (1)$$

where V_{R+F} is the potential drop across the resistor R and the filament F in series and V_R is the potential drop across R alone. The standardized resistor R was calibrated with a precision-type Wheatstone bridge as 9.9951±0.0003 ohms. The resistor was mounted in a copper cup filled with transformer oil in turn immersed in a constant temperature bath at 0°C. The constant current source (R_1, R_2, R_3, R_4 and the lead plate cell E, Fig. 3) was adjusted for currents of the order of 3 ma, the exact value being set such as to simplify the calculations. The magnitudes of the currents were small enough so that no measurable heating of the filament took place. The potential drops were measured with the potentiometer to 1 part in 100 000; hence the resistance of the filament was known with the same accuracy as the resistance of the standardized resistor R, about 3 parts in 100 000 or 0.003 percent. The potentiometer also was used to measure the thermocouple emf. The temperature of the filament was determined from standard conversion tables[8] to 0.01°C. The

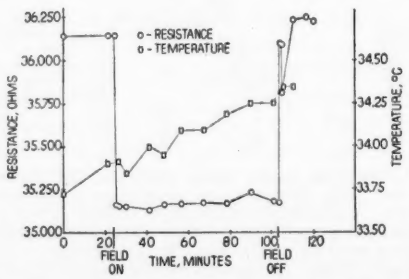

FIG. 4. Variation of tungsten filament resistance and temperature *vs* time at a *negative* (filament positive) electrostatic field of 4.54×10^6 volts/cm; tube No. 3; filament diameter, 0.00045 in.; initial no-field resistance, 36.140±0.003 ohms; initial no-field temperature, 33.90±0.01°C; pressure, 10^{-8} mm Hg.

[8] *Standard Conversion Tables* (Std. 21031) (Leeds and Northrup Company, Philadelphia).

TABLE I. Variation of filament resistance and temperature with time for a given applied negative field. Tube No. 3, filament diameter, 0.00045 inch; summary of Fig. 4-type runs.

Run No.	Applied field megavolts/cm	Abrupt change in filament resistance upon application and removal of field, ohms		Filament temperature change during time field was on,[a] °C	Calculated filament resistance change corresponding to observed temperature change,[a,b] ohms	Observed filament resistance change during time field was on,[a] ohms
		Decrease	Increase			
1	0.114	0.220	0.250	−0.02	−0.032	−0.095
2	0.227	0.100	0.150	+0.30	+0.050	+0.520[e]
3	0.454	0.420	0.174	−0.17[d]	−0.280	+0.420[e]
4	1.36[e]	0.500	0.500	+0.56	+0.088	+0.100
5	1.36[e]	0.480	0.650	+0.42	+0.070	+0.160
6	2.27	0.440	0.572	−0.55	−0.081	−0.230
7	2.72	0.900	0.773	−0.48	−0.078	−0.025
8	4.54[e]	0.995	0.937	+0.35	+0.057	+0.050
9	4.54[e]	1.110	1.050	+0.25	+0.039	+0.020
10	5.68	1.230	1.165	+0.17	+0.028	+0.010
11	7.26	1.160	1.300	+0.46	+0.075	+0.040

[a] A plus (+) sign denotes an increase; a minus (−) sign denotes a decrease.
[b] These resistance changes were calculated from the temperature coefficient of resistance of tungsten.
[c] The final resistances are considerably greater than the initial resistances, something not ordinarily observed.
[d] This is the only case of a resistance increase accompanied by a temperature decrease.
[e] These measurements were made to investigate the possibility of an electrostatic capacitance effect as the cause of the resistance decrease upon application of the field. For the first pair of values, the ground connection was reversed before the second measurement; i.e., the filament was inverted relative to the connections A and B and A' and B' (Figs. 1 and 3). The same was done between the second pair of measurements at a field of 4.54×10^6 volts/cm. In both cases, the resistance decreased upon application of the field and increased upon its removal. It was concluded therefore, that the resistance change is not due to an electrostatic effect involving the polarity of the filament.

following procedure was used in making each run involving measurement of the resistance of the filament:

(1) Ice and water were placed in the constant temperature bath of the standardized resistor. About one hour was allowed for attainment of thermal equilibrium. The constant current source was turned on and adjusted to a chosen value.

(2) The pressure in the experimental tube was measured and the ion gauge turned off and all elements grounded. A few minutes were allowed for the tube to cool to room temperature following the heating caused by the ion gauge.

(3) The potentiometer was calibrated against a new calibrated standard cell.

(4) The potential drops appearing across the resistor R and across R and the filament F in series were measured.

In some cases, the filaments were flashed (as described in the outgassing procedure) just before the filament resistance was measured. This was done to clean the filament of adsorbed gases. The filament resistance was measured as soon as the filament cooled to room temperature (requiring about 3 to 5 minutes). No difference in resistance was observed when the filaments were flashed or not prior to measurement. At the operating pressures employed, the gases evaporated during the flashing were very likely re-adsorbed while the filaments were cooling. Hence for most of the experiments, the filaments were not flashed.

RESULTS

The several experiments performed may be classified as follows:

1. The resistances of the filaments were measured as functions of time for given negative and positive electrostatic fields. A *positive* field is one with the plate electrically positive relative to the filament; a *negative* field is one with the plate negative relative to the filament.

2. The resistances of the filaments were measured *vs* increasing and decreasing negative and positive electrostatic fields.

3. The temperatures of the filaments were measured *vs* time for given negative and positive fields; and *vs* increasing and decreasing electrostatic fields.

4. The filament-to-ground electric current was measured as a function of the fields before and after the filament were vaporized. This was done in order to determine the relative magnitudes of the ion current, photocurrent, and the leakage current along the glass envelope of the experimental tubes.

Most curves for the experimental data are drawn with straight lines connecting plotted points. Smooth curves are drawn where a continuous variation is suggested or suspected.

A typical curve from the first and third groups of experiments (resistance and temperature *vs* time for given negative field) is shown in Fig. 4. The principal results obtained in this series of experiments are tabulated in Table I. Figure 5 is a typical curve of the same kind of experiment for a positive field. Table II lists the principal results of this set of experiments. The positive fields were necessarily weaker than the negative fields because of the possibility of field emission of electrons by the filament. Field strengths were calculated from assumed ideal cylindrical geometry.

It is observed for the experiments summarized in Tables I and II that in *every case* the resistance of the filament decreased abruptly upon application of the electric field and increased abruptly upon its removal,

TABLE II. Variation of filament resistance and temperature with time for a given applied positive field. Tube No. 3, filament diameter, 0.00045 inch; summary of Fig. 5-type runs. (The values for the weak fields show a smaller abrupt resistance change than for corresponding negative fields; whereas for the strong fields, the abrupt resistance change is larger than for corresponding negative fields.)

Run No.	Applied field megavolts/cm	Abrupt change in filament resistance upon application and removal of field, ohms		Filament temperature change during time field was on,[a] °C	Calculated filament resistance change corresponding to observed temperature change,[a,b] ohms	Observed filament resistance change during time field was on,[a] ohms
		Decrease	Increase			
1	0.454	0.088	0.062	+0.19	+0.032	+0.076
2	0.908	0.073	0.034	+0.16	+0.032	+0.035
3	1.14	0.605	0.265	+0.09	+0.016	+0.305
4	1.36	0.815	0.350	+0.30	+0.048	+0.420

[a] A plus (+) sign denotes an increase; a minus (−) sign denotes a decrease.
[b] These resistance changes were calculated from the temperature coefficient of resistance of tungsten.

regardless of the direction of the field. The abrupt decrease in resistance of the tungsten filament upon application of the field is contrary to Vissat's[3] results, but agrees with Worthing's.[1] In all, some fifty cases of this decrease were observed with tube No. 3 and some six cases with tube No. 2 before the filament was destroyed by arcing over in the latter case. All curves followed the same general pattern; upon application of the field the resistance of the filament abruptly decreased, while the field was held constant the resistance increased slightly; upon removal of the field the resistance of the filament increased abruptly to nearly its initial no-field value. The magnitudes of the abrupt resistance changes depend upon the field strength and vary from a few tenths to slightly more than one ohm; the slight change during the time the field was constant seemed to be independent of the field strength and was of the order of a few hundredths ohm.

In nearly every case, the temperature change of the filament is enough to account for a considerable part of (and sometimes nearly all) the resistance change during the time the field was on, but cannot account for the abrupt decrease or increase upon application or removal of the field.

Figures 5 and 6 were obtained at the same positive and negative field strengths of 1.36×10^6 volts/cm.

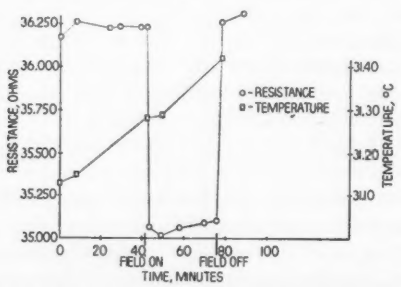

FIG. 5. Variation of tungsten filament resistance and temperature *vs* time at a *positive* (filament negative) electrostatic field of 1.36×10^6 volts/cm; tube No. 3; filament diameter, 0.00045 in.; initial no-field resistance, 36.240±0.003 ohms; initial no-field temperature, 31.28±0.01°C; pressure, 10^{-8} mm Hg. Calculated resistance change from observed temperature change, 0.022 ohm; observed resistance change, 0.085 ohm.

They were taken in immediate succession. In both cases the resistance change upon application of the field was about 1.25 ohms. Except for the difference in time, the two curves may be almost superimposed. Again, the temperature change was sufficient to account for a considerable part of the resistance change while the field was on.

The initial abrupt resistance decrease upon application of the negative field *vs* the applied electric field is shown plotted in Fig. 7, the data being taken from Table I. The smooth curve shown, which fits the experimental curve quite well, is a parabola and its equation is

$$\Delta R=\alpha E^{\frac{1}{2}}, \tag{2}$$

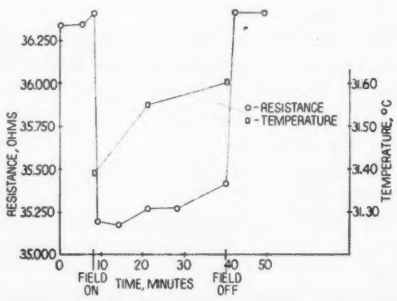

FIG. 6. Variation of tungsten filament resistance and temperature *vs* time at a *negative* field of 1.36×10^6 volts/cm (same magnitude as Fig. 5); tube No. 3; filament diameter, 0.00045 in.; initial no-field resistance, 36.352±0.003 ohms; initial no-field temperature, 31.39±0.01°C; pressure, 10^{-8} mm Hg. Figures 5 and 6, for the same magnitude of field strength, show that the temperature and resistance changes of the filament do not depend upon the direction of the applied field. Calculated resistance change from observed temperature change, 0.032 ohm; observed resistance change, 0.208 ohm.

where ΔR is the abrupt decrease in filament resistance upon application of the field, α is a constant of value 0.46 ohm cm$^{\frac{1}{2}}$ volts$^{-\frac{1}{2}}$ and E is the magnitude of the applied field in megavolts/cm.

Figure 8 shows the variation with applied electric field of the abrupt increase in filament resistance upon removal of the field. The smooth curve is a parabola satisfying Eq. (2) with $\alpha=0.46$ as in Fig. 7. It is clear that both the decrease and increase in filament resist-

ance upon application and removal of the electric field vary with the field in the same way. Curves similar to Figs. 7 and 8 obtained from the data for the positive field curves are not very informative because all the points are clustered in the low-field region; however there appears to be no contradiction with Eq. (2).

The smaller long-time resistance changes cannot be correlated with field strength.

Figure 9 is a typical curve showing the variation of filament resistance *vs* negative applied electric field (class 2 experiments). This, and the other curves like it for both positive and negative fields also satisfy Eq. (2) with $\alpha=0.46$ as before, as is seen by Fig. 10. However, the agreement at larger strengths is not as good as for Figs. 7 and 8. No large temperature variation

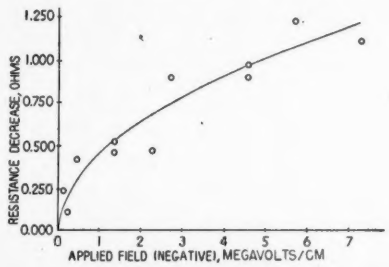

FIG. 7. Variation of the initial abrupt resistance decrease of the tungsten filament upon application of the negative field *vs* the magnitude of the applied electric field; tube No. 3; filament diameter, 0.00045 in. The smooth curve is a parabola satisfying the equation $\Delta R=\alpha E^2$, where $\alpha=0.46$ and E are the abscissa values. Data for this curve was taken from column 2, Table I.

was observed for these resistance *vs* field experiments; any observed temperature changes were not nearly large enough to account for the resistance change.

The maximum no-electric field variation of filament temperature (measured over a period of about one hour) was 0.06°C. The variation of filament temperature during any given run (class 3 experiment) was of the order of 0.3°C to 0.8°C, approximately five or more times greater than the no-field variation. Thus the temperature change appears to be largely due to the electric field, and hence electron and/or ion bombardment of the filament resulting in a temperature rise is indicated. To explore the temperature effect more thoroughly, experiments were performed to determine the magnitude of the total direct electric currents passed by the experimental tubes. This was done by inserting a calibrated galvanometer in the ground connection to the filaments. The total direct current through the tube was assumed to consist of ion currents, photocurrents, leakage currents, and perhaps field-emission currents. Some subsequent incomplete experiments indicate that a significant percentage of the observed currents was photocurrent.

Figure 11 shows the variation of total current through a tube with negative applied electric field. The maximum current was 7.1×10^{-9} amp, at a field of 9×10^{6}

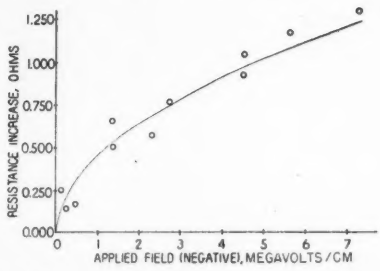

FIG. 8. Variation of the abrupt increase in resistance of the tungsten filament upon removal of the negative field *vs* the magnitude of the applied negative field; tube No. 3, filament diameter 0.00045 in. The smooth curve is a parabola satisfying the same equation as Fig. 7. Data for this curve was taken from column 3, Table I.

volts/cm. A similar experiment with the same filament and a maximum positive field of 1.36×10^{6} volts/cm yielded a maximum current of 11.55×10^{-9} amp. Thus, if the positive fields could have been large enough, the total current would have been many hundreds of times greater than for the corresponding negative fields.

The final experiment performed on each tube was the measurement of the leakage current as a function of the applied field. The negative field only was used; for leakage current the same results should be observed for both positive and negative fields. The filaments were completely vaporized by connecting them across the output of a Variac and turning it on full after first heating the filaments to white heat at a low voltage. This worked effectively; no pieces of the filaments were observed remaining in the chucks. (It is noted that the tube pressure was not appreciably increased by vaporizing the filaments.) With the filament removed, it was assumed that the electric current through the tube upon application of the electric field was due primarily to leakage current with a small amount of ion current flowing between plate and filament chucks. A small amount of photocurrent also might be possible. The leakage current *vs* applied increasing and decreasing electric fields is shown by Fig. 12, and the fact that the curve shown is not a straight line indicates the presence of ion current along with the leakage current. A straight line determined by

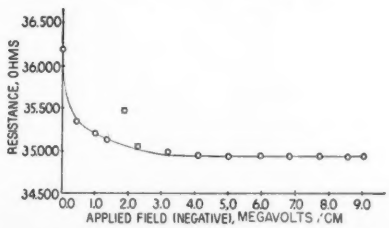

FIG. 9. Variation of tungsten filament resistance *vs* increasing applied negative electric field; tube No. 3. Curve is best smooth fit ignoring the point-well off the curve. Initial no-field resistance, 36.190 ± 0.003 ohms; filament diameter, 0.00045 in.; pressure, 10^{-8} mm Hg.

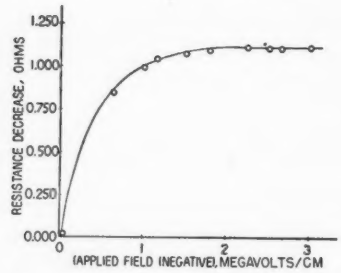

FIG. 10. Figure 9 data plotted as resistance change *vs* applied electric field, following Figs. 7 and 8. The smooth curve is the plot of Eq. (2) as before.

the small field points was drawn on the leakage current curve (dashed line, Fig. 12) to show the true leakage (Ohm's law variation) current.

The curve of Fig. 13, obtained by plotting the difference between the ordinates of Figs. 11 and 12 *vs* field, was considered to be the ion current (filament-to-plate alone) *vs* applied negative electric field.

The maximum ion current, 5.8×10^{-9} amp, in Fig. 13, yields 2.0×10^{12} (ions/sec) per cm^2 striking the filament. By kinetic theory, the number of molecules impinging per cm^2 of filament per second is 14.2×10^{12} at the measured pressure. Since the two values are about the same order of magnitude it may be concluded that there was enough gas present in the tube to produce the ion currents observed. Another simple calculation indicates that if any field emission current was present, it was so small as to be completely masked by the ion and photocurrents in the tube.

SUMMARY AND DISCUSSION

The experiments show in general that the resistance of a tungsten filament decreases abruptly upon application of a radial electrostatic field, increases slightly with time while the field remains constant, and increases abruptly when the field is removed. The magnitudes of the abrupt resistance changes are related to the magnitude of the field by Eq. (2). The resistance *vs* continuously varying electric field strength also follows Eq. (2).

Several experiments were performed in an attempt to detect some electrostatic capacitance effect which could account for the abrupt resistance changes, but none was found. Since no complete investigation of this type of effect was made, it is still possible that some obscure capacitance effect is present.

The small resistance change with time during the application of a constant applied electric field was always accompanied by a temperature change. The observed temperature change accounted for a significant part of this resistance change, and since the temperature distribution of the filament was not known, it seems quite reasonable to assume that the entire small resistance change is associated with temperature. This temperature change would be due to the heating of the filament by current-carrier bombardment.

No specific attempt was made to determine the effect of pressure on the change in resistance.

It was generally observed that the final resistance (after the field was removed) was approximately equal to the initial no-field resistance, although not exactly so as reported by Worthing and Estabrook.

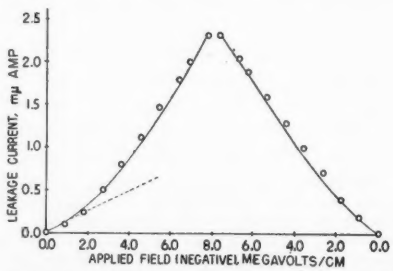

FIG. 12. Variation of leakage current *vs* increasing and decreasing negative field; tube No. 3. Dotted line indicates an Ohm's-law variation. Maximum current, $(2.3\pm0.1)\times10^{-9}$ amp; filament diameter, 0.00045 in.; pressure, 10^{-8} mm Hg; current was measured with a calibrated galvanometer in series with filament and ground.

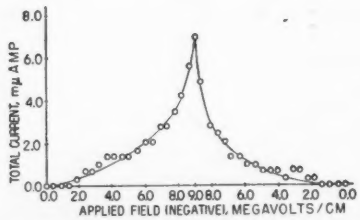

FIG. 11. Variation of total direct electric current (ion plus leakage) through tube *vs* increasing and decreasing negative applied electric field; tube No. 3; filament diameter, 0.00045 in.; pressure, 10^{-8} mm Hg; current was measured with a calibrated galvanometer in series with filament and ground.

It is interesting to compare the present results with those of Worthing,[1] Estabrook[2] and Vissat.[3] Worthing observed an abrupt *decrease* in the resistance of a heated tungsten filament upon application of a negative field and an increase upon removal of the field. This is in agreement with the results of the present investigation. Estabrook observed an abrupt *increase* in the resistance of a heated molybdenum filament upon application of the field and an abrupt decrease upon its removal. He assumed that this result was due to the use of molybdenum instead of tungsten. Vissat, with tungsten at temperatures up to 580°C, observed an abrupt *increase* in resistance upon application of the field and an abrupt decrease upon its removal. This agrees with Estabrook (assuming tungsten and molybdenum behave similarly) but not with Worthing or the present results.[9]

[9] During some of the preliminary experiments of the present investigation increases in tungsten resistance with applied electric field were observed—in apparent agreement with Vissat. However,

Again, it should be emphasized that in the present investigation much better vacuum techniques were available, making possible higher vacua (10^{-8} mm Hg or lower as compared with 10^{-5} to 10^{-7} mm Hg for Worthing, Estabrook, and Vissat). More vigorous outgassing of the experimental tubes was employed in the present work and the tubes were sealed off, whereas Estabrook and Vissat employed waxed glass-metal seals and continuously pumped their tubes. Reid[6] states that no resistance change should occur at lower pressures than those of Estabrook and Vissat—in contradiction to the present experimental findings.

None of the earlier investigators[1–6] considered positive fields; nor did they observe resistance changes below 0.5×10^6 volts/cm. The previous investigators did not include direct measurement of the filament temperature although Vissat[3] attributed the resistance change to heating of the filament. As noted above, the temperature effect is significant, accounting roughly for the time change of resistance with field on but not for the more unusual abrupt change upon application or removal of the field.

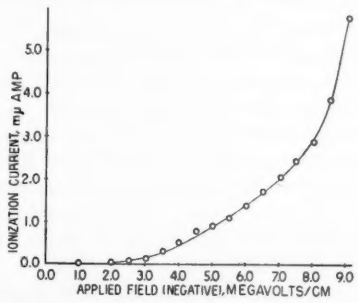

FIG. 13. Variation of ion current *vs* negative electric field; tube No. 3. Points obtained by subtracting ordinates of Fig. 11 from those of Fig. 10 and plotting *vs* field. Maximum current, $5.8\pm0.1\times10^{-9}$ amp; filament diameter, 0.00045 in.; pressure, 10^{-8} mm Hg.

Several theories have been developed for the resistance *vs* applied field effect but none has been found very successful. Greibach[5] attempted a theoretical explanation of Worthing's results based on classical thermodynamics of dipoles. He expressed the thermodynamic probability of evaporation of an atom from the surface of the filament in terms of the filament temperature and the applied electrostatic field. The uncharged evaporated atom becomes a dipole through the effect of the radial field which is more uniform and stronger at the end of the dipole nearest the filament resulting in attraction of the dipole for the filament. Thus the electrostatic field inhibits evaporation of the metal and the rate of evaporation (and consequently the rate of change of filament resistance) decreases. Analytically, integrating throughout the volume of the system, Greibach obtained an expression for the ratio of evaporation rate with field on to field off. His theoretical result for this ratio is but 1 percent approximately of Worthing's experimental value. Greibach attributes this discrepancy to his assumption of ideally clean, smooth surfaces whereas experimental filaments possess surface irregularities. (Since Worthing used dc heating of his filaments, they were subject also to dc etch production of patches.[4])

A different approach was employed by Reid[6] who designed an adsorption theory specifically for Estabrook's data.[2] He calculates, from a Maxwellian distribution of the velocities of the evaporated Mo atoms (including also some oxygen atoms which are carried off with the molybdenum), the ratio of evaporation rates of Mo with the electric field on to that with field off. The analytic theory requires the insertion of certain somewhat arbitrary parameters dependent on surface conditions of the Mo wires. Different wires require different values for these parameters, and there is no experimental procedure to enable an unique determination of these parameters. Hence, though plausible, the theory contains undesirable arbitrary procedures. Also, it should be noted that a suitable theory should explain the sudden resistance decrease upon application of the field and the increase upon removal of the field. Reid's theory attempted an explanation of the increase upon application of the field and decrease upon its removal.

It has not been possible so far to work out a theory explaining the present results. Reid's theory[6] does suggest that the abrupt resistance changes observed may depend on the gas content of the tungsten filament surface. A confident use of his theory will require a good deal more information on the exact nature of the tungsten filament surfaces, obtained perhaps by employing the Müller field-emission microscope technique.

there were indications that large temperature changes (large compared to what was observed in the later more reliable experiments), caused perhaps by considerable ion bombardment in the higher-pressure vacua of the preliminary experiments, were present. Hence a true resistance increase *vs* applied field effect was not considered to be present.

Empirical Relation between Superconductivity and the Number of Valence Electrons per Atom

B. T. MATTHIAS
Bell Telephone Laboratories, Inc., Murray Hill, New Jersey
(Received September 28, 1954)

The relation between the transition temperature of a superconductor and its number of valence electrons/atom has been investigated. Optimum conditions for the occurrence of superconductivity seem to exist for 5 and 7 valence electrons/atom.

IN a previous paper[1] an attempt was made to find for superconductors the empirical relation between their transition temperatures and the electronic configurations of their atoms. It was found that for an average valence electron/atom ratio (R) slightly below 5 the transition temperatures tend toward a maximum. Anomalous results, however, were obtained for the transition elements and their compounds, which had much larger R values.

The purpose of this paper is to resolve this anomaly and to include in the discussion all the recently discovered compounds and alloys, as well as technetium.[2]

When Daunt and Cobble discovered the superconducting transition temperature of technetium near 11°K, it became obvious that the maximum of transition temperatures for compounds and elements with an R near 5 could not be the only one because Tc has seven valence electrons/atom.[3] As a matter of fact, superconducting transition temperatures in the horizontal rows of the periodic system seemed to be more or less symmetrical with respect to the sixth column (see Table I).

The study of alloys of Mo with elements of the eighth column further strengthened the validity of this assumption,[4] so that today it seems very probable that a second maximum for superconducting transition temperatures occurs for elements and compounds with an R near 7.

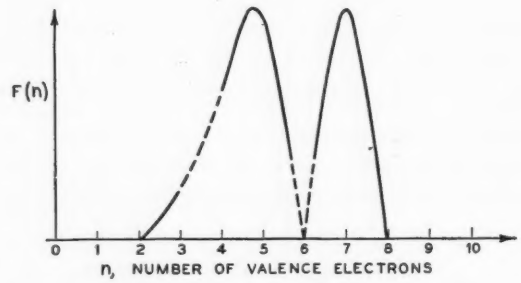

FIG. 1. Variation of superconducting transition temperature with number of valence electrons per atom.

Our data now suggest tentatively that the qualitative dependence of the transition temperature on R is as indicated in Fig. 1.

In this plot the effects of mass and volume, which are now well recognized, are neglected.[1,5,6]

In the next four paragraphs, we would like to give four examples of how this curve was traced experimentally.

(a) SOLUTIONS OF RHODIUM IN ZIRCONIUM

We have found that up to approximately 15 percent Rh can be dissolved in Zr without appreciably[7] changing the size of the lattice constant. Above 15 percent Rh, additional lines in the x-ray powder photograph indicate that either a superlattice or a new crystal structure closely related to that of Zr exists. (Further investigation of the crystallography of this system will be carried out by S. Geller.) Whereas results obtained for Zr-Rh alloys with more than 15 percent Rh have therefore to be considered with caution, it becomes obvious for smaller Rh amounts how strongly the superconducting transition temperature is affected by the electron concentration, i.e., the R value (see Fig. 2).

These data on the Zr-Rh system should be considered only of preliminary nature outside the range of 1 percent to 30 percent Rh. For Rh percentages below 1 percent the purity of our Zr (99 percent) was not good enough, and above 33 percent Rh we seem to have

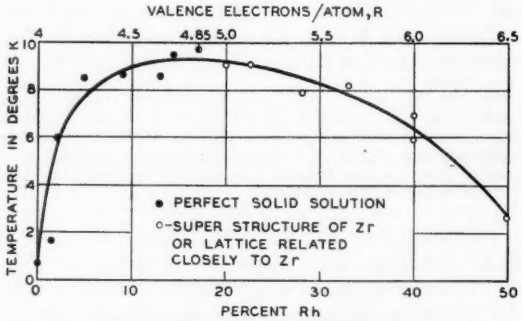

FIG. 2. Superconductivity of Zr-Rh alloys.

[1] B. T. Matthias, Phys. Rev. **92**, 874 (1953).
[2] L. G. Daunt and L. W. Cobble, Phys. Rev. **92**, 507 (1953).
[3] Valence electrons are here considered to be all electrons outside of closed shells.
[4] B. T. Matthias and E. Corenzwit, Phys. Rev. **94**, 1069 (1954).
[5] P. Marcus, Phys. Rev. **94**, 837 (1954).
[6] D. Shoenberg, Nuovo cimento **10**, Suppl. No. 4 (1953).
[7] By "appreciably" we mean to an extent which would affect the transition temperature if we assume $T_c \sim (\text{Volume})^{10}$.

TABLE I. Superconducting transition temperatures for elements of the fourth to the eighth column.

IV	V	VI	VII	VIII
Zr 0.7°	Nb 8.6°	Mo[a]	Tc 11°	Ru 0.47°
Hf 0.35°	Ta 4.4°	W[a]	Re 1.7°	Os 0.71°

[a] Not superconducting above 0.05°K.

a two-phase system.[8] All we wish to show now is how the maximum transition temperature occurs here for an R value slightly below 5 as observed so often before.[1]

(b) SUPERCONDUCTING COMPOUNDS WITH THE BETA-W STRUCTURE

Because in this type structure it was not possible to vary the R value continuously, we were limited to a number of discrete points corresponding to the available compounds. In order not to confuse the issue too much by variation of mass and volume, we restricted ourselves to compounds of two elements, niobium and molybdenum, which are next to one another in the periodic system. Figure 3 shows the variation of the superconducting transition temperature with R. It shows the existence of maxima near 5 and 7 and a minimum near 6. Mo_3Si and Mo_3Ge and their superconducting transition temperatures have been described recently by Hardy and Hulm.[9] The niobium compounds were discovered in the course of this work and will be described in detail.[10]

(c) THE RHODIUM-SELENIUM AND RHODIUM-TELLURIUM SYSTEMS

Rhodium-selenide crystallizes in the pyrite structure over a wide homogeneity range from about $RhSe_{1.5}$ to $RhSe_{2.5}$.[10] As reported before[11] superconductivity occurs only inside this range. The cell size decreases with increasing Se content, but considering that the transition temperature appears proportional to not more than the tenth power of the volume this change is

TABLE II. Transition temperatures of Mo and W alloys.

Alloy	Crystal structure	Average number of valence electrons/atom	Transition temperature °K
Mo_3Os	β-W	6.5	7.2
Mo_3Ir	β-W	6.75	8.8
1 Mo:1 Ru	hcp[a]	7	9.5 −10.5
1 Mo:1 Rh	hcp[a]	7.5	1.97
1 Mo:1 Ir	hcp[a]	7.5	below 1
1 Mo:4 Ru	hcp[a]	7.6	1.66
W_3Os	?	6.5	3.02−2.21
W_3Ir	?	6.75	3.82−2.1
1 W:1 Ru	hcp[a]	7	7.5
1 W:1 Rh	hcp[a]	7.5	3.37−2.64; 1.9

[a] Hexagonal close packed.

[8] We were not able to find any literature on the Zr-Rh system.
[9] G. F. Hardy and J. K. Hulm, Phys. Rev. **93**, 1004 (1954).
[10] S. Geller (to be published).
[11] Matthias, Corenzwit, and Miller, Phys. Rev. **93**, 1415 (1954).

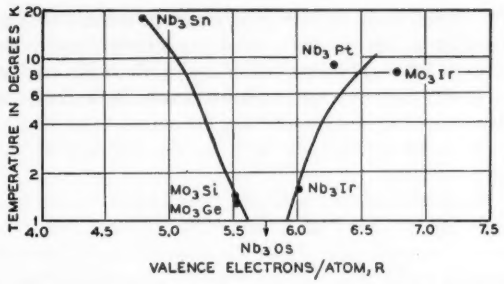

FIG. 3. Superconductivity of compounds with the β-W structure.

negligible. The maximum transition temperature at 6°K was observed for $RhSe_{1.75}$ corresponding to an R value of 7.1. The structure of $RhTe_2$, at which composition the transition temperature reaches the maximum at 1.51°K is unknown[10] but may be related to that of $RhSe_2$. Its R value is 7.

(d) THE MOLYBDENUM AND TUNGSTEN ALLOYS

These again serve to illustrate the maximum transition temperature near R values of 7.[4] However, as W is nearly twice as heavy as Mo the comparison is not quite so clear cut. Table II and Fig. 4 compare the observed values of transition temperature with the corresponding R values.

Raub had discovered[12] that these alloys of the body-centered cubic Mo and W with the face-centered cubic Rh, Ir, and Pt form a hexagonal close-packed phase.

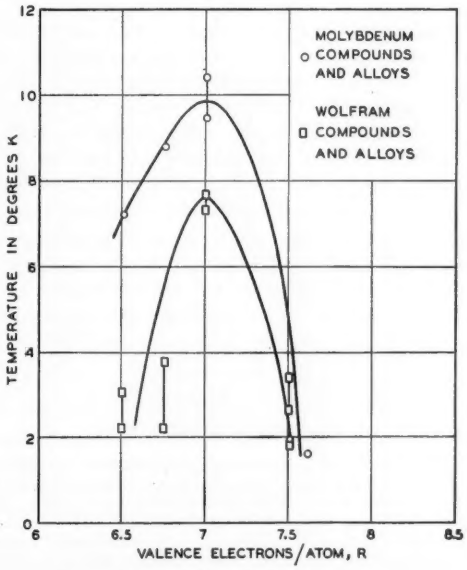

FIG. 4. Superconductivity of Zr-Rh alloys.

[12] E. Raub and P. Walter, Festschrift Heraeus 100 Jahre; Seite 124 E. Raub, Z. Metallkunde **45**, 23 (1954).

This seems to be an averaging which produces behavior like that in the elements which are intermediate in the periodic table. The large solubility of Mo in Ru enables us to simulate technetium quite closely both in crystal structure and superconducting transition temperature, thus strengthening our faith in the validity of this point of view.

An additional remark may be justified concerning these alloys: previously superconductivity had only been observed, apart from the elements, in either well defined compounds with very small homogeneity ranges or in solid solutions. We believe this is the first time that disordered alloys of nonsuperconducting elements have become superconducting and it may indicate that superconductivity is a long-range order effect rather than a short-range one.

CONCLUSION

There seems to be a rule linking the superconducting transition temperatures to the number of electrons outside filled shells, the valence electrons. At present we do not understand the theoretical implications of this. It seems, however, reasonable to suggest that a large number of valence electrons is quite favorable for the occurrence of superconductivity. Then why is there a dip for a value near six valence electrons? The answer to this may be roughly that this dip corresponds to the dip in paramagnetic susceptibility and in electronic specific heat for the same elements, which is commonly supposed to be due to a low effective number of free electrons.

My thanks to P. W. Anderson and J. K. Galt for their enlightening discussions.

PHYSICAL REVIEW VOLUME 97, NUMBER 1 JANUARY 1, 1955

Paramagnetic Resonance Absorption in Praseodymium Trichloride*

JOHN H. ANDERSON† AND CLYDE A. HUTCHISON, JR.
Institute for Nuclear Studies and Department of Chemistry, University of Chicago, Chicago, Illinois

(Received August 5, 1954)

Paramagnetic resonance absorption in crystalline solutions of $PrCl_3$ in $LaCl_3$ has been investigated at a frequency of 2.32×10^{10} sec^{-1} and at the boiling point of He. The apparent g's, when H is parallel and perpendicular to the c axis have been found to be 1.79 and 3.98 respectively. The results have been discussed in terms of the known crystalline structure and Stark splittings.

INTRODUCTION

THE static magnetic and optical spectroscopic properties of crystalline praseodymium compounds have been successfully interpreted, at least in general outline, by Van Vleck,[1] Penney and Schlapp,[2] Kynch,[3] Spedding,[4] Hellwege and Hellwege,[5] and others. The ground state of the trivalent magnetic ion is the Hund state, $^3H_4$, for two $4f$ electrons[1] and Russell-Saunders coupling is obeyed approximately. The perturbations by the crystalline electric field play an important role in determining the temperature variation of the magnetic susceptibility and the details of the optical absorptions. The magnitudes of these perturbations are found generally to be considerably smaller than the spin-orbit coupling energies as is to be anticipated on the basis of the theoretical expectation that $4f$ orbitals lie deep inside the magnetic ion.

Recently Davis, Kip, and Malvano,[6] Altshuler, Kurenev, and Salikhov,[7] and Bleaney and Scovil[8] have observed magnetic resonances in compounds of praseodymium. The general theory of the paramagnetic resonance absorption in rare-earth salts has been given in great detail by Elliott and Stevens[9–12] although they have given only brief consideration to the specific case of Pr^{+3}.

In this paper experimental results of an investigation of paramagnetic resonance in a solution of $PrCl_3$ in $LaCl_3$ are presented and their interpretation discussed.

EXPERIMENTAL

Preparation of Crystals

The crystals employed for the measurements were right circular cylinders with their crystallographic c axes perpendicular to their cylinder axes. These were cut

* This work received financial support from the U. S. Office of Naval Research and from the U. S. Atomic Energy Commission.
† U. S. Atomic Energy Commission Predoctoral Fellow, 1951–1953.
[1] J. H. Van Vleck, *The Theory of Electric and Magnetic Susceptibilities* (The Oxford University Press, London, 1932).
[2] W. G. Penney and R. Schlapp, Phys. Rev. **41**, 194 (1932).
[3] G. J. Kynch, Trans. Faraday Soc. **33**, 1402 (1937).
[4] F. H. Spedding, Phys. Rev. **58**, 255 (1940).
[5] A. M. Hellwege and K. H. Hellwege, Z. Physik **127**, 334 (1950).
[6] Davis, Kip, and Malvano, Alti. accad. mayl, Lincei **11**, 77
[7] Altshuler, Kurenev, and Salikhov, Doklady Akad. Nauk S.S.S.R. **70**, 201 (1950).
[8] B. Bleaney and H. E. D. Scovil, Phil. Mag. **43**, 999 (1952).
[9] K. W. H. Stevens, Proc. Phys. Soc. (London) **A65**, 209 (1952).
[10] R. J. Elliott and K. W. H. Stevens, Proc. Roy. Soc. (London) **A215**, 437 (1952).
[11] R. J. Elliott and K. W. H. Stevens, Proc. Roy. Soc. (London) **A218**, 553 (1953).
[12] R. J. Elliott and K. W. H. Stevens, Proc. Roy. Soc. (London) **A219**, 387 (1953).

from irregularly shaped single crystals prepared by cooling fused $PrCl_3$ and $LaCl_3$ in a Pt crucible in an HCl atmosphere from a temperature approximately 50°C above the melting point of the mixture (about 820–830°C) to room temperature. The melts were cooled at rates of from 40° to 80°C per hour. Single crystals were selected from the irregular pieces so produced and these were oriented by means of polarized light and ground to shape on a lathe. All cutting, grinding, and orienting operations were performed in an atmosphere of carefully dried N_2. The $PrCl_3$ in $LaCl_3$ was prepared by heating the hydrated salts in a Pt boat from room temperature to the melting point over a period of about 48 hr. The heating was done in an HCl atmosphere. The very slow heating and the HCl atmosphere were necessitated by the very strong tendency toward hydrolysis to the oxychloride. Crystals of $LaCl_3$ prepared by this method contained 0.1 percent of material insoluble in H_2O and identified by Professor W. H. Zachariasen by x-ray diffraction as LaOCl. The hydrated $LaCl_3$ was prepared by evaporation of an aqueous solution of La_2O_3 and HCl, and the hydrated $PrCl_3$ by evaporation of a solution of Pr_6O_{11} and HCl. The La_2O_3 was prepared by the Lindsay Light and Chemical Company and found by them to contain 99.99 percent La_2O_3. The Pr_6O_{11} was Baker and Adamson brand and was stated to contain 99.8 percent Pr_6O_{11}. Spectrophotometric analyses showed that the crystals which were used contained 11 ± 0.5 mole percent $PrCl_3$. The amount of $NdCl_3$ was found to be about 0.07 mole percent and there was about 0.1 weight percent oxychloride.

MICROWAVE EXPERIMENTS

The paramagnetic resonance absorption was investigated at 2.32×10^{10} sec^{-1} and at the boiling point of He. The crystals were mounted on a polyethylene post with their cylinder axes parallel to the rf magnetic field and perpendicular to the static magnetic field. They were rotated about their cylinder axes and thus any desired angle between the crystallographic c axis and the static field could be obtained. A polyethylene cap was placed over the crystal and thermally sealed to the post in a helium atmosphere. The resonant reflection cavity was evacuated but because of possible very small leaks probably contained a low pressure of He. A single resonance absorption peak was observed. The spectroscopic splitting factor for one crystal as a function of angle θ between the c axis and the static field is presented in Fig. 1. The measurements on a second crystal were in agreement with these. The largest errors were in the determination of the angles of orientation of the crystal and were not greater than $\pm0.015\pi$. The apparent g's, when H is parallel and perpendicular to the c axis are 1.791 and 3.975 respectively.

No nuclear hyperfine structure was observed at the concentration of $PrCl_3$ used in these experiments. The absorptions were narrowest, about 25 gauss, when the c axis made an angle $\pi/2$ with the static magnetic field and widest, about 180 gauss, when the angle was 0.

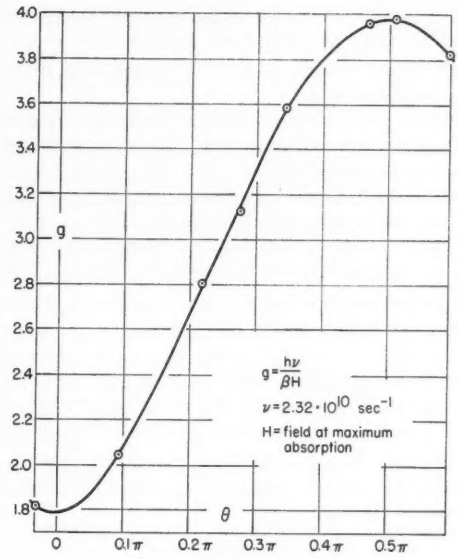

FIG. 1. g *vs* θ for $PrCl_3$.

A very weak resonance with an intensity not greater than ~0.01 of the intensity of the main absorption was observed at $g\sim2$ independent of θ and was attributed to traces of impurities on the walls of the cavity or to unoriented oxychloride in the sample.

DISCUSSION

The crystal structures of $LaCl_3$ and $PrCl_3$ are known to be of the UCl_3 type[13] belonging to the space group $C6_3/m$. The nearest neighbors of the Pr^{+3} ion are nine Cl^- ions, each at a distance of about 2.9A. These nearest neighbors lie in a configuration with C_{3h} symmetry. The point group of the symmetry at a Pr^{+3} considering the whole crystal is also C_{3h}. When such a potential is expanded in spherical harmonics one need consider no l values greater than 6 (because one is dealing with f electrons) and no odd l if one is dealing with a single configuration. The only m values involved are consequently 0 and 6, and therefore the only nonzero matrix elements of the electrostatic potential in the J,J_z representation are those for which $\Delta M=0, 6$. The secular problem therefore consists of three quadratics involving the pairs of states $-4, 2$; $-2, 4$; $-3, 3$; the three states $-1, 0, 1$ are not connected by any elements of the potential. The diagonalization of the electrostatic energy gives rise to two twofold-degenerate states from the quadratics $-4, 2$ and $-2, 4$ (denoted by Hellwege by the quantum numbers $\mu=\pm2$) and one twofold-de-

[13] W. H. Zachariasen, J. Chem. Phys. **16**, 254 (1948). See also Acta Cryst. **1**, 265 (1948).

generate state consisting of the pair $-1, 1$ (denoted by $\mu=\pm 1$). The two states from the quadratic $-3, 3$ (denoted by $\mu=3$) and the 0 state (denoted by $\mu=0$) are all nondegenerate.

When a static magnetic field is applied the degeneracy of the doublets will in general be removed. There are however no matrix elements of the magnetic moment between the components of such a doublet and therefore no magnetic transitions are allowed and $g_\perp$ is 0. This situation has been discussed by Elliott and Stevens[12] and by Bleaney and Scovil.[8] They have assumed that the Jahn-Teller[14] effect will be operative to lower the symmetry and remove the degeneracy of a ground state such as $\mu=\pm 2$. In this way other states which will permit transition will be mixed in, and if the separation so produced is small the value of $g_{||}$ will still be near that for C_{3h} symmetry and $g_\perp$ will be small. In such a case the $g_{||}$ would for example be $8/5=1.60$ for the doublet $\mu=\pm 1$; or for $\mu=\pm 2$ would be 1.69 if the states are assumed to be

$$\cos\varphi|J_z=\pm 2\rangle-\sin\varphi|J_z=\mp 4\rangle,$$

with $\varphi=0.15\pi$ as supposed by Elliott and Stevens.[12] $g_\perp$ would be close to 0. The behavior of g for $PrCl_3$ is obviously not in accord with such a model.

Another possibility that might be considered is that one of the crystal field levels to which transitions are possible from the ground state lies very close to the ground state. If the separation were of order 1 cm^{-1} then transitions would be observable at the frequencies employed in the present experiments. If, for example, the state $\mu=\pm 2$ were separated from the state $\mu=\pm 1$ by about 0.4 cm^{-1} and all the other states were much higher, then quite satisfactory agreement with experiment is obtained. The best fit in this case is for $\varphi=\pi/2$. There are undoubtedly several other satisfactory cases of this sort. Sayre and Freed[15] have, however, located the three doublet states (a $\mu=\pm 2$ state is the ground state) and one of the $\mu=3$ states by means of polarization spectrum studies. Their results would indicate that neither the $\mu=\pm 1$ state nor a $\mu=3$ state can lie near the ground state. An explanation of this type would therefore seem to be eliminated from consideration.

The crystal field splittings are found by Sayre and Freed[15] to be as large as 130 cm^{-1} and are hence not negligible compared with the spin-orbit splittings ($J=5$ is ~ 2000 cm^{-1} higher than $J=4$).[11] However, as long as C_{3h} symmetry is maintained, the mixing of states of higher J with the state $J=4$ will not result in transitions between the components of the doublets. The case in which there is both lowered symmetry and mixing of higher J's has not been considered.

Other possibilities of interpretation lie in the consideration of configuration interaction or of large effects of departure from C_{3h} symmetry. It is probably doubtful that other configurations interact sufficiently to play an important part. On the other hand it may be true that at low temperatures there could be appreciable effects of lowering of the symmetry which might conceivably account for the magnetic observations (the optical data of Sayre and Freed at low temperatures are apparently in agreement with the assumption of C_{3h} symmetry).

The analyses mentioned above would indicate that quite pure crystals were used in the experiments. Any PrOCl would most probably have been randomly oriented since LaOCl is insoluble in $LaCl_3$[16] and presumably the same is true for PrOCl in $PrCl_3$. Moreover if all the oxychloride were present as PrOCl only 1 percent of the Pr^{+3} would be in that form.

ACKNOWLEDGMENTS

The kindnesses of Edward V. Sayre and Simon Freed in communicating the results of their work in advance of publication, of the Institute for the Study of Metals in supplying the liquid He, of Professor W. H. Zachariasen in identifying the oxychloride, of Professor J. W. Stout and Professor L. Meyer in offering their help in the construction of the low temperature apparatus, of Jack Boardman in assisting with the chemical preparations and of Edward Bartal in constructing part of the apparatus are gratefully acknowledged.

[14] H. A. Jahn and E. Teller, Proc. Roy. Soc. (London) **A161**, 220 (1937).

[15] E. V. Sayre and S. Freed (private communication).

[16] Koch, Broich, and Cunningham, J. Chem. Soc. **74**, 2349 (1952).

Macroscopic Aspects of Neutron Interaction in Magnetics

LOUIS GOLD
Massachusetts Institute of Technology, Cambridge, Massachusetts
(Received August 27, 1954; revised manuscript received September 27, 1954)

The interaction of neutrons with magnetic materials, as described by the Halpern-Holstein relations that properly include the role of the domain structure, is characterized macroscopically. Certain interesting properties of these relations are delineated, such as the inequality $K^2+Kp-w^2\geq 0$ which restricts the physically meaningful combinations of the absorption coefficient K and the polarization and depolarization parameters w and p, respectively. This particular finding establishes a criterion for the validity of theoretically evaluated constants derived from microscopic treatment of neutron scattering and depolarization phenomena.

FOLLOWING the fundamental suggestion of Bloch[1] —the magnetic moment of the neutron should give rise to polarization when a beam traverses a magnetic substance since the two spin states must interact differently—Schwinger[2] developed an atomic theory which later was improved by Halpern *et al.*[3] who properly included the effects of crystal and domain structure.[4]

The basic Halpern-Holstein (H–H) relations for the attenuation and associated polarization of a neutron beam can be derived by elementary considerations involving three macroscopic interaction parameters: K the cumulative absorption coefficient for magnetic, nuclear, and incoherent scattering plus the true absorption due to capture; w a quantity expressing the separate contributions to the absorption associated with the two spin states interacting differently with the magnetic field; p a depolarization factor which (H−H) related to the domain structure via

$$p=(8\pi/3)^2M_0\Delta M(\tau/v^2), \quad 2\pi\gamma M_0(\tau/v)<1, \quad \text{(1a)}$$

$$p=(4/3)(\Delta M/M_0)\tau^{-1}, \quad 2\pi\gamma M_0(\tau/v)>1, \quad \text{(1b)}$$

where τ is the average domain size, v is the neutron velocity, γ is the neutron gyromagnetic ratio, and ΔM is the deviation of the magnetization M_0 from the saturation value M_s, i.e., $\Delta M=M_s-M_0$.

The (H−H) relations may be conveniently expressed in the following manner:

$$I=I_0e^{-ax}(A\sinh\alpha x+\cosh\alpha x)+\zeta_0Be^{-ax}\sinh\alpha x, \quad \text{(2a)}$$

$$\zeta=\zeta_0e^{-ax}(\cosh\alpha x-A\sinh\alpha x)+I_0Be^{-ax}\sinh\alpha x, \quad \text{(2b)}$$

with the abbreviations

$$a=p/2+K, \quad \alpha=[(p/2)^2+w^2]^{\frac{1}{2}}, \quad A=[(2w/p)^2+1]^{-\frac{1}{2}}, \quad B=[(p/2w)^2+1]^{-\frac{1}{2}}. \quad \text{(2c)}$$

The intensity I is made up of the separate contribution from the two spin states $\pm\frac{1}{2}$, *viz.*, $I=I_{\frac{1}{2}}+I_{-\frac{1}{2}}$, while the quantity $\zeta=I_{\frac{1}{2}}-I_{-\frac{1}{2}}$ so that the degree of polarization is expressed by $P=\zeta/I$. Note too that A and B are simply related since $A^2+B^2=1$.

PROPERTIES OF THE HALPERN-HOLSTEIN RELATIONS

The availability of intense neutron beams has stimulated a broader investigation of neutron behavior in magnetic materials.[5] (H−H) limited their evaluation of the interaction equations to the then practical circumstances in the early single and double transmission experiments[6] where

$$wx\ll 1, \quad px\sim 1, \quad p\gg w,$$
$$wx\ll 1, \quad p\sim w, \quad px\ll 1.$$

Our purpose here is to indicate some general properties of the (H−H) formulas which are precluded by the above restrictions which reduce these to very elementary expressions.

A. Transmission Matrix Viewpoint

An interesting way of looking at the neutron passage phenomenon is contained in the matrix equation:

$$\begin{vmatrix} I \\ \zeta \end{vmatrix}=(T)\begin{vmatrix} I_0 \\ \zeta_0 \end{vmatrix}, \quad \text{(3a)}$$

where $\left|\begin{smallmatrix} I \\ \zeta \end{smallmatrix}\right|$ and $\left|\begin{smallmatrix} I_0 \\ \zeta_0 \end{smallmatrix}\right|$ are column matrices and (T) is a symmetrical transmission matrix:

$$(T)=e^{-ax}\begin{pmatrix} P_+ & Q \\ Q & P_- \end{pmatrix} \quad \text{(3b)}$$

in which

$$P_\pm=\cosh\alpha x\pm A\sinh\alpha x, \quad Q=B\sinh\alpha x. \quad \text{(3c)}$$

Thus propagation through N slabs is described by

$$\begin{vmatrix} I_N \\ \zeta_N \end{vmatrix}=(T_1)(T_2)\cdots(T_N)\begin{vmatrix} I_0 \\ \zeta_0 \end{vmatrix},$$

[1] F. Bloch, Phys. Rev. **50**, 259 (1936).
[2] J. Schwinger, Phys. Rev. **51**, 544 (1937).
[3] O. Halpern and T. Holstein, Phys. Rev. **59**, 960 (1941).
[4] E. Fermi, *Nuclear Physics* (University of Chicago Press, Chicago, 1948), p. 204.
[5] Hughes, Wallace, and Holtzman, Phys. Rev. **73**, 1277 (1948).
[6] P. N. Powers, Phys. Rev. **54**, 827 (1938).

which for identical slabs reduces to

$$\begin{vmatrix} I_N \\ \zeta_N \end{vmatrix} = (T)^N \begin{vmatrix} I_0 \\ \zeta_0 \end{vmatrix}. \tag{4a}$$

It can be shown that

$$(T)^N = e^{-N\alpha x} \begin{pmatrix} \cosh N\alpha x + A \sinh N\alpha x & B \sinh N\alpha x \\ B \sinh N\alpha x & \cosh N\alpha x - A \sinh N\alpha x \end{pmatrix}, \tag{4b}$$

so whether one deals with multiple slabs or a single slab, the effect is the same so long as the material is uniform and the net thicknesses identical.

B. Extrema Conditions

In line with the usual experimental situation, we set $\zeta_0=0$ so that the relations to be examined for extrema are:

$$I = I_0 e^{-\alpha x}(A \sinh\alpha x + \cosh\alpha x), \tag{5a}$$

$$\zeta = I_0 e^{-\alpha x} B \sinh\alpha x, \tag{5b}$$

$$\zeta/I = P = B(A+\coth\alpha x)^{-1}. \tag{5c}$$

Clearly maximum polarization is allied with

$$B \to 1, \quad A \to 0, \quad \coth\alpha x \to 1, \quad \alpha x \to \infty,$$

which in turn relate to x and $w \to \infty$ for all values of p, but with x and/or w prescribed an optimum value of p exists as may be inferred from

$$p \to \infty \text{ causes } B \to 0,\ A \to 1,\ \coth\alpha x \to 1, \quad P \to 0;$$

$$p \to 0 \quad \text{causes } B \to 1,\ A \to 0,\ \coth\alpha x \to \infty,\ P \to 0.$$

Naturally, in practice, it is desirable to operate in the latter domain ($p \to 0$) since this corresponds to higher beam intensities and lower magnetic fields for prescribed levels of polarization.

1. Thickness as the Independent Variable

First, for $(\partial I/\partial x)_{w,p}$, the extremum condition is contained in

$$(Bw/K-A)^{-1} = \tanh\alpha x \leq 1.$$

Since no physical meaning associates with such extrema (intensity cannot increase with x), this defines a restriction:

$$w^2 - Kp - K^2 \leq 0. \tag{6}$$

In the limit where $p \to 0$, $K \geq w$. Halpern *et al.*,[7] have indeed found that for iron $K \sim 1$ while $w \sim 0.1$ to 0.45 for neutron wavelengths from 1.5 to 4.5A. The inequality (19) provides a check of theoretically calculated coefficients.

Next, $(\partial\zeta/\partial x)_{w,p}$ has an extremum condition:

$$[B(K+p)/w - A]^{-1} = \tanh\alpha x \leq 1,$$

so that the extrema are defined precisely by (6), which means they always occur. The remaining functional dependence $(\partial P/\partial x)_{w,p}$ can never exhibit an extremum since

$$(\partial P^{-1}/\partial x)_{w,p} = -(\alpha/\beta)\cosh^2\alpha x.$$

2. Polarization Coefficient w as the Independent Variable

Here the quantity $(\partial I/\partial w)_{x,p}$ manifests extrema when

$$[4p^2 - x(4w^2+p^2)][4p + x(1-4w^2p^2)] \geq 0, \tag{7}$$

which in the domain $p \to 0$ reduces to

$$(2wx)^2(1-4w^2) \geq 0, \quad w \leq \tfrac{1}{2}$$

as admitting them.

The other two functionals can never have extrema. Thus for $(\partial\zeta/\partial w)_{x,p}$ we find the required condition:

$$-Bx\,d\alpha/dB = \tanh\alpha x,$$

which can never be obeyed since the left-hand side is always negative and the right-hand side positive. Likewise the admission of extrema for $(\partial P/\partial w)_{x,p}$ would require another impossible situation, *viz*:

$$B^{-1}(dB/dw)(A+\coth\alpha x) = dA/dw - x(d\alpha/dw)\,\operatorname{csch}^2\alpha x.$$

Here, dA/dw being always negative with dB/dw always positive means that the two sides of the equation never can have the same sign so that the equality is violated.

3. Depolarization Coefficient p as the Independent Variable

Examination of $(\partial I/\partial p)_{x,w}$ reveals the extremum condition:

$$|\tfrac{1}{2}x(p^2+4w^2)^{\frac{1}{2}}| \leq 1. \tag{8}$$

The quantity $(\partial\zeta/\partial p)_{x,w}$ requires the fulfillment of the inequality,

$$x(p^2+4w^2)[x(p^2-4w^2)-4p] - 4p^2 \leq 0, \tag{9}$$

for extrema; in the limit $w \to 0$, (22) reduces to

$$px(px-4) \leq 4,$$

so that relatively large values of x and/or p combine to effect their occurrence. The combinations of p, x, and w which give extrema for $(\partial P/\partial p)_{x,w}$ are defined by the roots of the equation:

$$(p^2+4w^2)^{\frac{1}{2}}(1-\tfrac{1}{2}px\,\operatorname{csch}^2\alpha x) + p\coth\alpha x = 0, \tag{10}$$

which reflects an involved behavior of the polarization with changes in the domain structure.

[7] Halpern, Hammermesh, and Johnson, Phys. Rev. **59**, 981 (1941).

Energy Distributions of Field Dependent Secondary Electrons

FRANK A. BRAND AND HAROLD JACOBS
Signal Corps Engineering Laboratories, Fort Monmouth, New Jersey
(Received August 3, 1954)

Retarding-potential experiments were conducted to determine the energy spectrum of electrons emitted from thin films of magnesium oxide under conditions of field-dependent secondary emission.

The present method is correlated to the techniques utilized for probe studies in a gas plasma, and a means of determining the apparent surface potentials on the magnesium oxide films is indicated. Determinations of electron temperatures and velocities as a function of the applied field are made, based upon this correlation.

The spectrum, having a spread from zero up to ninety electron volts, is shown to be Maxwellian with average energies ranging between ten and twenty electron volts, depending on the applied field.

I. INTRODUCTION

RECENTLY we reported the results of a study on field dependent secondary emission from thin, porous films of magnesium oxide.[1] At that time, a mechanism, based on the principles of the gas discharge laws, was proposed to describe the effects noted when thin films of magnesium oxide were bombarded with electrons. It was found that an equation of the form

$$i=i_0e^{\alpha x}, \tag{1}$$

where i is the secondary current, i_0 is the primary or bombarding current, α is the number of new electrons formed per centimeter per electron, and x is the depth within the film at which an ionizing event occurs, would accurately describe the experimental results.

Briefly, the theory may be stated as follows: primary electrons bombard the magnesium oxide film creating a positive surface charge due to ordinary secondary emission in combination with the relatively high resistivity of the semiconducting layer. Previous measurement had shown the film thickness to be 10^{-4} cm.[1] Thus a high field is formed across the film as a result of the surface charge. Subsequent bombarding electrons penetrate into the porous film and create secondaries. Then, under the influence of the high field, the liberated secondary electrons can gain sufficient energy to cause further ionization. The process continues until an equilibrium avalanche is established.

In an attempt to gain further information regarding the fundamental processes involved, a study was made of the energy distribution of the emitted electrons.

II. EXPERIMENTAL PROCEDURES

A. Tube Design

The fact that the gas discharge theory and equations could be used to explain the previous experimental results suggested the possibility that a method for analyzing the energy spectrum might be found in that field. Accordingly, a technique utilizing retarding potentials and based on the theory of probes in a gas plasma,[2] was found to provide a simple, direct and reasonably accurate means of measuring the electron energy distributions.

The tube employed in these experiments is illustrated in Fig. 1, and the test circuit is shown in Fig. 2. Essentially, the tube structure consists of a magnesium evaporator (not shown in either sketch) for depositing the magnesium through low pressures of oxygen onto a cylindrical anode. After evaporation, the dynode

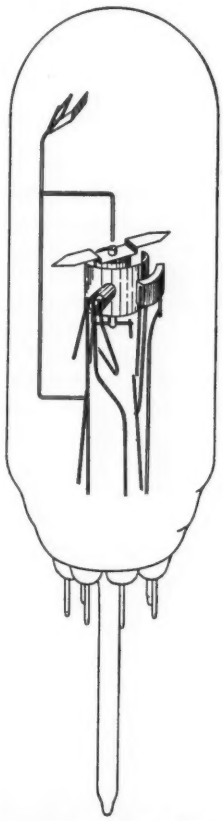

FIG. 1. Structure of vacuum tube utilized in determining electron energies and surface potentials.

[1] Jacobs, Freely, and Brand, Phys. Rev. **88**, 492–499 (1952).

[2] See, for example, L. B. Loeb, *Fundamental Processes of Electrical Discharge in Gases* (John Wiley and Sons, Inc., New York, 1939), pp. 232–257; J. D. Cobine, *Gaseous Conductors* (McGraw-Hill Book Company, Inc., New York, 1941), pp. 134–142.

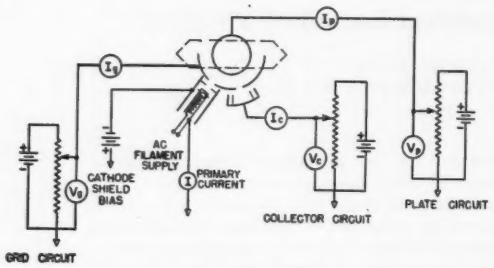

FIG. 2. Test circuit.

could be rotated, by means of a magnet external to the tube envelope, to place the newly formed magnesium oxide film in front of the grid structure. The grid, consisting of a solid, semicylindrical sheet, has two small holes to allow the passage of electron beams. One aperture, directly facing the cathode gun, allowed the primary beam to enter and bombard the film. The other hole, just opposite the collector electrode, permitted a portion of the emitted secondaries to pass through the grid and be recorded at the collector. The collector electrode, fabricated in the form of a box, had its inner surface coated with carbon black in order to reduce the possibility of reflected electrons.

Tube processing, exhaust, and magnesium oxide deposition were carried out in accordance with procedures previously reported.[3]

In previous experiments it was noted that the MgO surfaces exhibited a faint blue fluorescence while emitting electrons. The present tube design was based upon the assumption that the area of fluorescence was very nearly the same as the area of emission. If this were the case, it would be a simple matter to place a relatively large portion of the emitting area directly in front of the collector hole and still have part of it in line with the primary beam. If, on the other hand, the area were small it would not be possible to orient the emitting area so that both grid aperatures faced the active area at the same time.

In order to justify the assumption that the area of emission coincides with the area of fluorescence, parts of a tube were dusted with willemite prior to processing. The completed tube was then operated under standard conditions (see following section), while observations were made on the degree of fluorescence as various circuit parameters were changed.

It was observed that the inner surface of the grid exhibited a typical willemite fluorescence over an area almost exactly corresponding to the area of MgO fluorescence. In addition, the location and intensity of both grid and MgO fluorescence were not affected by potentials applied to the collector.[4]

[3] H. Jacobs, Phys. Rev. 84, 877 (1951).

[4] Experiments similar to the foregoing were carried out by L. R. Koller and R. P. Johnson in relation to the Malter effect [Phys. Rev. 52, 519–523 (1937)].

These results verified the original assumption and indicated the general feasibility of the present approach.

In operation then, a large fraction of the emitting area is placed before the collector aperture and one may assume that the electrons leave the MgO normal to the surface.

B. Testing Procedures

After exhaust and processing, the circuit of Fig. 2 was used to make direct measurements of the energy spectra and surface potentials in the following way: a small negative (with respect to ground) voltage was applied to the cathode shield in order to achieve a close definition of the primary beam. Positive potentials of approximately 100 and 200 volts were applied to the dynode and grid respectively. Under these conditions, the surface of the magnesium oxide film acquired a positive charge, and a controlled equilibrium avalanche current was established. Positive potentials were then applied to the collector in small steps and the collector current was measured while holding all other parameters constant. Similar sets of data were taken for various values of the electric field in the magnesium oxide film. The field was varied by changing either the grid or dynode potentials.

It should be noted that until the collector reaches the same voltage as that of the magnesium oxide surface, its potential is negative or retarding with respect to that of the surface. Hence, any electrons which reach the collector under these conditions must do so by virtue of their initial velocities.

III. EVALUATION AND INTERPRETATION OF EXPERIMENTAL DATA

According to the theory of probes,[5] a semilog plot of probe current as a function of probe potential will provide direct information regarding the plasma potential and electron energy distribution. Figure 3 shows a series of curves representative of data obtained in the present experiment. Figure 4 illustrates similar data but with retarding potential as the abscissa.

The curve of Fig. 4 may be readily interpreted in terms of electron energies. At point A, only electrons possessing very high initial velocities are recorded. At point B, electrons of medium as well as high energies are measured, and finally at C, electrons of all energies, including zero, are noted. At C then, the collector potential must equal the surface potential if zero energy electrons are being recorded. Hence, the knee of the

[5] Actually, one does not have to follow the probe analogy for the present case. We can simply imagine the tube to be a diode, with the collector as the anode and the magnesium oxide film as the cathode. The grid then is necessary only to maintain the discharge and need not receive direct consideration. The general development employed here, however, would still be applicable since electrons emitted from a thermionic cathode also follow a maxwellian energy distribution.

curve provides a measure of the surface voltage,[6] just as an analogous interpretation is made in the measurement of plasma potentials. Beyond C, the collector current exhibits a saturation tendency which is to be expected if the tube is free of any electron space charge. A second method of determining surface potentials has been developed and the results were found to check very well.[7] Surface voltages determined by both methods were observed to be from 20 to 30 volts lower than the grid potential, which would make the voltage across the MgO film about 80 volts, depending on electric field and current.

Following the gas discharge analogy further, one determines from the linear logarithmic variation of current with voltage (see Figs. 3 and 4), the energy distribution of emitted electrons to be Maxwellian. If this is the case, it is possible to calculate certain physical quantities which are of interest, such as the average electron energy and electron temperature.[8]

For a Maxwellian distribution, the average electron energy ($\bar{E}$) is determined by

$$\bar{E}=\tfrac{3}{2}(0.434)/m, \tag{2}$$

where m is the slope of region A-C in Fig. 4, and (0.434) is the ratio of common to natural logarithms. The electron temperature (T_e) is given by

$$T_e=0.434(1/m)(e/k), \tag{3}$$

where e is the electronic charge and k is Boltzmann's constant.

Now, from the electron temperature, we may

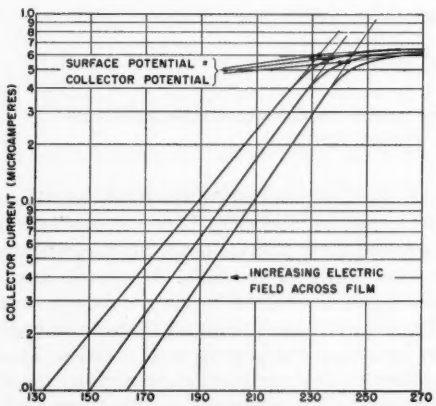
SURFACE POTENTIAL = COLLECTOR POTENTIAL
INCREASING ELECTRIC FIELD ACROSS FILM
COLLECTOR CURRENT (MICROAMPERES)
COLLECTOR POTENTIAL (VOLTS)
130 150 170 190 210 230 250 270

FIG. 3. Collector current as a function of collector potential. The variation of electron energies and surface potentials as a function of the electric field are also illustrated.

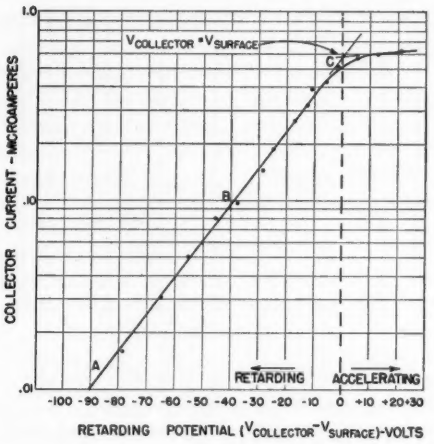

FIG. 4. Collector current as a function of retarding potential (dynode potential 100 volts and surface potential 226 volts), assuming the knee of the curve to represent zero surface potential.

calculate the average velocity ($\bar{v}$) of the emitted electrons according to the following expression:

$$\bar{v}=1.128[(2/m)kT_e]^{\frac{1}{2}}, \tag{4}$$

where m is the electron mass. This equation provides a means of experimentally determining the average velocity based on the slope of the curves in Figs. 3 and 4.

It has previously been pointed out that the knee of these curves is a direct measure of the surface potential, and since the film thickness is known to be approximately 10^{-4} cm, the electric field developed across the dielectric is also experimentally determined. Figure 3 illustrates the manner in which the surface potentials and average velocities change with increasing electric field.

We now seek an expression relating the average velocity to the field in the film. The gas discharge equations again provide a suitable answer in the following expression:[9]

$$\bar{v}=(2^{1/4}/\pi^{1/8})[(e/m)EL_e]^{1/2}, \tag{5}$$

where E is the electric field in the magnesium oxide and L_e is the mean free path of electrons in the film. The assumption is made here that all collisions are inelastic. Based on previous considerations,[10] L_e is estimated to have a value of 10^{-5} cm. From Eq. (5) a linear curve may be plotted for the average velocity as a function of the square root of the field. Equation (4), together with the experimentally determined values for electron temperatures and electric fields, may be used to obtain a similar, but purely experimental, plot. Figure 5 is a comparison of these two plots, in which the lower curve is based on Eq. (5) and the upper curve on the experi-

[6] A similar approach was utilized by Nelson in measuring the potentials of luminescent screens [J. Appl. Phys. 9, 592–599 (1938)].

[7] Dobischek, Jacobs, and Freely, Phys. Rev. 91, 804–812 (1953).

[8] J. Millman and S. Seely, *Electronics* (McGraw-Hill Book Company, Inc., New York. 1951), pp. 286–289. See also reference 3.

[9] See L. B. Loeb, reference 2, p. 368.

[10] See reference 1.

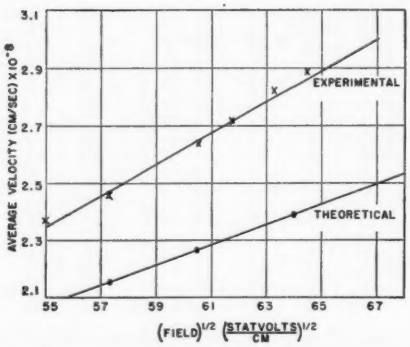

FIG. 5. Comparison of experimental and theoretical curves showing the relationship between average electron velocity and applied electric field. The experimental values are derived from a series of curves similar to those shown in Fig. 3, and the theoretical curve is determined from Eq. (5).

mental data and Eq. (4). A series of curves, similar to those shown in Fig. 3 provides the necessary experimental values. The average velocity as calculated from the electron temperature is plotted against the square root of the corresponding electric field for each case.

In comparing the two curves of Fig. 5, it is evident that the experimental data is in fairly good agreement with what one might expect on a theoretical basis. Not only does the experimental curve follow a straight line, again indicating that the gas discharge laws may be suitably applied in describing the phenomenon of field dependent secondary emission, but the slope and magnitude of the experimental curve agree well with those of the theoretical plot. This may be regarded as a check on the form of the equations used and on the value utilized for the mean free path.

IV. CONCLUSIONS

Through the use of retarding potentials it has been experimentally determined that the emitted electrons closely follow a Maxwellian energy distribution with a rather wide energy range. Then, on the basis of such a distribution, equations normally associated with gaseous discharges have been used to explain the experimental results. Furthermore, values have been obtained for the average electron energy and for the mean free path of electrons in the oxide film.

In addition, the present method provides a means of measuring the surface potentials of magnesium oxide films.

We should like to acknowledge the many helpful suggestions offered by J. B. Freely and W. G. Matthei.

PHYSICAL REVIEW VOLUME 97, NUMBER 1 JANUARY 1, 1955

Microwave Spectra of Tritium Iodide and Tritium Bromide*

B. ROSENBLUM AND A. H. NETHERCOT, JR.
Columbia University, New York, New York

(Received September 30, 1954)

The $J=1\leftarrow0$ rotational transitions in TI and TBr have been observed. A tritium-deuterium mass ratio has been determined, and electronic effects which cause errors in this ratio considered.

THE microwave spectra of tritium iodide and tritium bromide have been observed by the use of a klystron-driven harmonic generator and techniques previously described.[1] The observed transitions and frequencies as well as ν_0 and eqQ are given in Table I.

Nuclear mass ratios can be determined by microwave spectroscopy from the ratio of the rotational constants, B_e, for two isotopic molecules. However, small electronic effects whose size is difficult to predict theoretically can cause small errors. In principle, these errors appear in all mass ratios determined by microwave spectroscopy, but they are particularly large for the isotopic hydrogen halides because of the large speed of rotation. This case is therefore an ideal one in which to measure the size of these errors and compare them with theoretical predictions.

TABLE I. Observed frequencies for the $J=1\leftarrow0$ transition and molecular constants of TI and TBr (Mc/sec).

	TI^{127}	TBr^{79}	TBr^{81}
$\Delta F=+1$	131 592.95±0.25	172 472.72±0.40	172 320.96±0.40
$\Delta F=0$	131 210.20±0.40	172 604.60±0.40	172 431.49±0.40
ν_0	131 501.75±0.40	172 499.10±0.40	172 343.07±0.40
eqQ	−1 822.6 ±3.0	527.6 ±2.0	442.1 ±2.0

All these small electronic effects can be represented as a single term in a perturbation calculation, but in order to estimate the size of this term it may be broken up into its components. For the hydrogen halides, the largest of these components is L-uncoupling (the excitation of higher electronic states by the rotation of the molecule).[2] Unless corrections are made for L-uncou-

* This work was supported jointly by the Department of the Army (Signal Corps), the Department of the Navy (Office of Naval Research), and the Department of the Air Force (Air Research and Development Command).

[1] Nethercot, Klein, and Townes, Phys. Rev. 86, 798 (1952).

[2] C. H. Townes and A. L. Schawlow, *Microwave Spectroscopy* (to be published), Chap. 8.

pling the apparent tritium-deuterium mass ratio will be smaller than the actual value. From the pure precession hypothesis (which is probably not an accurate representation in this case) an approximate expression for the fractional error in the mass ratio (δ) can be derived:

$$\delta=\frac{L(L+1)h(\nu_0'-\nu_0'')}{2J(W_\Pi-W_\Sigma)},$$

where L and J are both one in this case, $(\nu_0'-\nu_0'')$ is the frequency difference between the two isotopic molecules, and $(W_\Pi-W_\Sigma)$ is the energy separation of the Π and Σ states. δ can also be approximately determined from a measurement of the $\mathbf{I}\cdot\mathbf{J}$ interaction. A smaller error in the opposite direction is caused by the ionic character of the bond since part of an electron is removed from the hydrogen isotope. Other electronic effects should be considerably smaller. The difference between the Dunham coefficient Y_{01} and B_e leads to an error somewhat smaller than those considered here.

Equilibrium rotational constants B_e were calculated from the ν_0's given for TI and TBr in Table I, the B_0's for DI[3,4] and DBr,[5] and the published infrared values of α and D.[6,7] The apparent mass ratios were then computed to be $1.497467\pm12\times10^{-6}$ for the iodide and $1.497469\pm10\times10^{-6}$ for the bromide. The mass ratio from nuclear reaction data[8] is $1.497466\pm7\times10^{-6}$. This good agreement is probably spurious in view of the appreciable electronic effects expected in this case.

For the iodide the L-uncoupling calculated from the above equation should decrease the apparent mass ratio by 60×10^{-6}. The ionic character of the bond of about 5 percent should increase the apparent mass ratio by 7×10^{-6} for a net decrease of 53×10^{-6}. A calculation based on the measured value[4] of the $\mathbf{I}\cdot\mathbf{J}$ interaction in DI gives a value for the L-uncoupling about thirty percent lower than the pure precession hypothesis. In the bromide the calculated L-uncoupling should give a decrease of 80×10^{-6} and the ionic character of about 11 percent should give an increase of 14×10^{-6}. This leaves an expected net decrease in the apparent mass ratio of 66×10^{-6}.

New infrared measurements[9] on the 2—0 and 3—0 bands of HI with somewhat higher accuracy indicate the existence of a quadratic term (γ) in the expansion for B_v, which slightly modifies the value of B_e calculated from infrared data. From these measurements an apparent mass ratio of $1.497448\pm20\times10^{-6}$ is derived, which is 18×10^{-6} lower than the nuclear reaction value. Within the large error this is almost the shift expected. The apparent absence of electronic effects in the bromide will probably be explained by a more accurate measurement of α and γ.

The present uncertainty in the magnitude of the electronic effects in HI is due largely to an uncertainty of ±0.0013 cm^{-1} in α. Further infrared measurements to determine α and γ more accurately in both molecules seem feasible and would be of considerable interest in fixing the magnitude of the electronic effects. In spite of the uncertainty in the value of α, it can be said that the error in the mass ratio is not greater than that predicted from the pure precession hypothesis. This indicates that mass ratios previously determined by microwave spectroscopy are not affected by the excitation of higher electronic states within their stated error.

The authors wish to thank Professor C. H. Townes for his aid and encouragement, Dr. G. A. Silvey for his help in preparing the samples, and D. R. J. Boyd for his helpful discussion of the infrared measurements, and for his kindness in making available new infrared results before publication.

[3] J. A. Klein and A. H. Nethercot, Phys. Rev. **91**, 1018 (1953).
[4] C. A. Burrus and W. Gordy, Phys. Rev. **92**, 1437 (1953).
[5] W. Gordy and C. A. Burrus, Phys. Rev. **93**, 419 (1954).
[6] D. R. J. Boyd and H. W. Thompson, Spectrochim. Acta **5**, 308 (1952).
[7] Thompson, Williams, and Callomon, Spectrochim. Acta **5**, 311 (1952).
[8] Li, Whaling, Fowler, and Lauritsen, Phys. Rev. **83**, 512 (1951).
[9] D. R. J. Boyd (private communication).

Age of Meteorites by the $A^{40}-K^{40}$ Method*

G. J. WASSERBURG, *Institute for Nuclear Studies, University of Chicago, Chicago, Illinois*

AND

R. J. HAYDEN, *Argonne National Laboratory, Lemont, Illinois*

(Received August 11, 1954; revised manuscript received September 29, 1954)

The ages of two stony meteorites were determined by measuring the A^{40}/K^{40} ratio using an isotopic dilution technique. With a branching ratio $\lambda_e/\lambda_\beta=0.085$ and a decay constant $\lambda=0.55\times10^{-9}$ yr^{-1}, the ages obtained were $(4.82\pm0.20)\times10^9$ and $(4.58\pm0.20)\times10^9$ years.

THE radiogenic argon content of two stony meteorites was determined using an isotopic dilution technique. These meteorites were Beardsley, a grey chondrite, and Forest City, a brecciated spherical bronzite chondrite.[1] The extraction procedure used has been described previously.[2] The only modification of the procedure was that a CuO furnace at 500°C was attached directly to the reaction vessel. This was necessary in order to convert the large quantity of hydrogen, which was produced in the reaction of the metallic iron in the meteorite with the NaOH flux, into water. Additional experiments with mixtures of feldspar and metallic iron indicate that the continuous reaction of the hydrogen does not effect the mixing of tracer and evolved argon. Two sets of A^{38} tracers were used, each of which contained better than 80 percent A^{38}. The amount of radiogenic argon was computed from data given in Tables I and II. The correction for normal argon contamination was made assuming that the mass 36 peak was due to atmospheric argon. The discrimination of the mass spectrometer was determined by running normal argon of spectroscopic purity before and after each sample. Nier's values for the isotopic composition of normal argon were assumed.[3] No hydrocarbons were observed in the mass 36 to 40 region. In the first Beardsley experiment the HCl correction to the A^{36} peak resulted in a 1 percent change in the amount of radiogenic A^{40}. In the second Beardsley and Forest City experiments, the HCl correction resulted in 0.4 percent and 0.0 percent corrections, respectively, to the amount of radiogenic A^{40}.

In the second Beardsley experiment, a considerable portion of the material splattered to the cooler part of the reaction vessel and was unreacted. The amount of hydrogen and water produced during the reaction was much less than in the other two experiments.

The potassium determination was made using an isotopic dilution technique. K^{41} obtained from Oak Ridge was used as a tracer. The K^{39}/K^{41} ratio in the tracer was 0.00922.

Two aliquots of Beardsley meteorite and two aliquots of Forest City meteorite were analyzed for potassium. Two synthetic standards, one composed of a mixture of feldspar containing 10.43 percent potassium and olivine (containing less than 0.001 percent potassium) and the other a feldspar containing 8.06 percent potassium were analyzed along with the meteorites. The samples were dissolved in HF and H_2SO_4, and aliquots of the K^{41} tracer solution added. SiF_4 was removed by evaporation, and HCl was added. A potassium-rich filtrate was obtained by precipitating Al, Fe, Mg, and Ca with NH_4OH and $(NH_4)_2CO_3$ solutions.

The isotopic composition was determined with a surface ionization technique using an oxidized tungsten filament. The samples were run on a mass spectrometer with a 12-inch radius of curvature and 60° deflection. The discrimination of the instrument was determined by running a mixture of tracer K^{41} and normal K and also by running a sample of normal potassium. By assuming Nier's value for the isotopic ratio in normal potassium[3] a value for the discrimination was obtained which agrees within 1.5 percent with the value obtained from the tracer—normal mixture. It was assumed that the isotopic composition of the meteoritic potassium was normal.

By assuming a decay constant $\lambda=0.55\times10^{-9}$/yr and a branching ratio $\lambda_e/\lambda_\beta=0.085$,[4] the following ages are calculated: Beardsley I, $(4.82\pm0.20)\times10^9$ yr; Beardsley II, $(4.50\pm0.20)\times10^9$ yr; Forest City, $(4.67\pm0.20)\times10^9$ yr. The lower age obtained for Beardsley II is believed to be due to the incomplete reaction discussed earlier.

The branching ratio which was used in the calculation was determined by the authors by determining the A^{40}/K^{40} ratio and the Pb^{206}/U^{238}, Pb^{207}/U^{235} ages of several coexisting potassium and uranium minerals from over a considerable span of geologic time.[4] The value for λ given above was assumed in the branching ratio calculations. The values given for the error in the ages were obtained by assuming a 3 percent error in λ and 6 percent error in $\lambda/\lambda_e(A^{40}/K^{40})$.

Previous measurements of the age of meteorites by

* This work was supported in part by a U. S. Atomic Energy Commission contract and in part by a National Science Foundation grant.

[1] Meteorites were obtained from H. H. Nininger, Sedona, Arizona.

[2] G. J. Wasserburg and R. J. Hayden, Phys. Rev. 93, 645 (1954).

[3] A. O. Nier, Phys. Rev. 77, 789 (1950).

[4] G. J. Wasserburg and R. J. Hayden, Presented at the May, 1954, meeting of the American Geophysical Union.

Gerling *et al.*[5] using the $A^{40}-K^{40}$ method gave values ranging from 0.5×10^9 yr to 3.03×10^9 yr. These values were computed by using a decay constant $\lambda=0.55\times10^{-9}$ yr^{-1} and a branching ratio $\lambda_e/\lambda_\beta=0.124$. Recomputing their data using a branching ratio of 0.085, we obtain an age for their oldest sample of 3.55×10^9 yr. The A^{40}/K^{40} ratios which we obtain differ from Gerling's largest value by a factor of 2.2.

Paneth *et al.*[6] have found that a considerable portion of the helium contained in iron meteorites was produced by cosmic radiation. The amount of helium found by Paneth *et al.* in iron meteorites is less than 4×10^{-5} cc STP per gram. If it is assumed that the iron meteorites have retained most of the helium produced in them by cosmic radiation, and that they are of the same age as the stony meteorites, one can calculate the effect of the cosmic-ray products on the A^{40} age. As the stony meteorites contain approximately 25 percent iron, the amount of helium produced from this iron is about 10^{-5} cc STP per gram. If the same amount of A^{40} were produced this would have a 2 percent effect on the $A^{40}-K^{40}$ age. This estimate of the amount of argon produced by cosmic radiation on iron is certainly much too high.

TABLE I. Argon analysis.

Sample	Sample wt (g)	A^{38} tracer (cc STP)	A^{36}/A^{38}	A^{38}/A^{40}	Radiogenic A^{40} (cc STP) per g
Beardsley I	79.485	3.74×10^{-6}	0.0383	0.00623 ± 0.00004	7.13×10^{-5}
Beardsley II	29.862	8.31×10^{-6}	0.0236	$0.0358\ \pm0.0002$	5.87×10^{-5}
Forest City	71.762	8.72×10^{-6}	0.0227	0.01987 ± 0.00004	5.34×10^{-5}

[5] E. K. Gerling and T. G. Pavlova, Doklady Akad. Nauk S.S.S.R. **77**, No. 1, 85 (1951); E. L. Krinov, Priroda Izd. Akad. Nauk S.S.S.R., Moskva **40**, No. 10, 83, (1951).

[6] F. A. Paneth and K. I. Mayne, Nature **172**, 200 (1953), F. A. Paneth *et al.*, Geochim. et Cosmochim. Acta **3**, 257 (1953).

TABLE II. Potassium analysis.

Sample	Sample wt (g)	K tracer added (mg)	K^{41}/K^{39}	% K (by wt)
Beardsley *A*	3.600	0.792	0.294 ± 0.003	0.101
Beardsley *B*	1.980	0.792	0.474 ± 0.007	0.101
Standard (0.104% K)	10.455	1.584	0.214 ± 0.004	0.110
Forest City *A*	2.317	0.792	0.492 ± 0.006	0.0827
Forest City *B*	1.015	0.792	1.016 ± 0.010	0.0835
Standard (8.06% K)	0.1243	1.584	0.231 ± 0.002	8.25

If A^{36}, A^{38}, and A^{40} are produced equally to within two orders of magnitude, then the effect of cosmic-ray produced argon is to make the computed age less than the true age. If it is also true that the He/A ratio in spallation products from iron is 1000 or greater the effect on the age is negligible.

The authors have found no evidence for the loss of argon by diffusion in terrestrial feldspars,[7] but it is possible that the meteorites have lost some argon by this means. Hence the values reported are interpreted as lower limits to the age of the samples. If it is assumed that the meteorites are cogenetic with the solar system, the above value may also be applied as a lower limit to the age of the solar system.

The value of 4.8×10^9 years obtained for Beardsley is a lower limit to the age of the universe. This value is in accord with the lower limit of 4.5×10^9 yr calculated by Patterson[8] from the isotopic composition of modern terrestrial lead and meteoritic lead.

ACKNOWLEDGMENT

The authors are greatly indebted to Professor M. G. Inghram and to Professor H. C. Urey for their valuable suggestions during the progress of this work.

[7] G. J. Wasserburg and R. J. Hayden, Geochim. et Cosmochim. Acta (to be published).

[8] C. Patterson, *Nuclear Processes in Geologic Settings* (National Research Council, Washington, D. C., 1953), p. 36.

Long-Lived Isomer of Np^{236}

M. H. STUDIER, J. E. GINDLER, AND C. M. STEVENS
Argonne National Laboratory, Lemont, Illinois

(Received September 9, 1954)

A long-lived isomer of Np^{236}, identified by chemical and mass spectrometric means, has been prepared by the $U^{238}(d,4n)$ reaction. The alpha half-life of this isomer has not been established, but a lower limit of 5000 years has been placed on the beta half-life. The cross section for the $U^{238}(d,4n)Np^{236,236*}$ reaction for 21.6-Mev deuterons has been calculated to be approximately 35 millibarns. A slow-neutron fission cross section of 2800 barns has been determined for the long-lived isomer.

EVIDENCE for the existence of a long-lived isomer of Np^{236} was first obtained from a deuteron bombardment of uranium metal in which the isotopic ratio U^{235}/U^{238} was reduced to 1/2800.[1] A solid metal disk was bombarded for 1200 microampere-hours with 22-Mev deuterons in the Berkeley 60-inch cyclotron. Two successive layers (three and five mils, respectively) were milled from the face of the target and dissolved in acid. Neptunium was isolated chemically from each solution. Slow neutron fission measurements made upon the individual neptunium fractions showed the fissionability to decrease with a two-day half-life characteristic of Np^{238} beta decay. In addition to this fissionability, a long-lived fissionable material was found in the three-mil layer of the target but not in the five-mil layer. This long-lived fissionable material persisted in the neptunium fraction even after further chemistry had been performed which should have removed any other element. Since the slow-neutron fission cross section of Np^{237} was too small to account for the observed number of fissions and since the long-lived fissionability was found only in the upper three-mil layer of the target, it was assumed that this fissionability was due to a Np^{236} isomer formed by a $(d,4n)$ reaction. No fissionability characteristic of 22-hour Np^{236} was found because of its relatively short half-life and low yield.

In the present experiment, a 100-milligram target of U_3O_8 having an isotopic ratio U^{235}/U^{238} of 1/3190 was evenly deposited over an area of seven square centimeters and bombarded for 2700 microampere-hours with 21.6-Mev deuterons in the Argonne 60-inch cyclotron. After bombardment, the uranium was dissolved in acid and allowed to remain undisturbed for fifteen months. At the end of this period, neptunium was chemically separated, purified, and isotopically analyzed in a 12-in., 60° mass spectrometer using a multiple-filament surface ionization source.[2] Masses 236 and 237 were observed; the mole ratio 236/237 was found to be 0.062 ± 0.001 and to remain constant during analysis. This constant ratio, together with the chemical separation in which the quantities of Pu^{236} and U^{236} were reduced below the detection limit ($\sim10^{-13}$ grams) of the mass spectrometer, showed the 236 mass to be an isotope of neptunium.

A total of approximately 50 alpha counts per minute was isolated in the neptunium fraction. In a preliminary pulse analysis of this fraction no alpha energy other than that attributed to Np^{237} was apparent. This indicated either that the alpha activity of long-lived Np^{236} is low because of a very long alpha half-life or that the alpha-decay energy is very similar to that of Np^{237}. A beta half-life of ≥5000 years has been calculated for the Np^{236} isomer on the basis of a beta-to-alpha ratio of ~25 found in the neptunium fraction and by assuming the beta activity to be due to Np^{236} and the alpha activity due to Np^{237}.

With an electron capture-to-beta ratio of two[3] for the decay of 22-hour Np^{236} it was calculated, on the basis of the observed Pu^{236} yield, that $\frac{1}{6}$ of the product formed in the $U^{238}(d,4n)Np^{236,236*}$ reaction was the long-lived isomer. This may have been formed directly and/or by isomeric transition of the 22-hour Np^{236}. The cross section for the $U^{238}(d,4n)Np^{236,236*}$ reaction for 21.6-Mev deuterons is approximately 35 millibarns.

Three Np^{236} samples subjected to different degrees of chemical purification were tested for thermal neutron fissionability in the Argonne CP-3′ heavy water pile.[4] The fission-to-alpha ratio for each of the neptunium samples was the same, indicating chemical purity. Again by assuming that all the alpha activity was due to Np^{237}, the fission cross section of Np^{236} (long-lived) was found to be approximately 2800 barns.

We wish to thank J. Fitzpatrick, W. Ramler, and members of the Argonne cyclotron group who made the deuteron bombardment possible. The technical assistance of J. Mech and D. Henderson in making the pulse analyses and W. C. Bentley in making the fission measurements is gratefully acknowledged. We also wish to thank W. M. Manning for his helpful suggestions.

[1] Studier, Hopkins, Ghiorso, and Bentley, Atomic Energy Commission Report CF-3762, 1947; reviewed by G. T. Seaborg, *The Actinide Elements* (McGraw-Hill Book Company, Inc., New York, 1954), National Nuclear Energy Series, Plutonium Project Record, Vol. 14A, Div. IV, Chap. 11.

[2] M. G. Inghram and W. A. Chupka, Rev. Sci. Instr. 24, 518 (1953).

[3] D. A. Orth and G. D. O'Kelley, Phys. Rev. 82, 758 (1951).

[4] The method of fission counting is described by A. Ghiorso and W. C. Bentley, *The Transuranium Elements* (McGraw-Hill Book Company, Inc., New York, 1949), Paper No. 22.29, National Nuclear Energy Series, Plutonium Project Record, Vol. 14B, Div. IV.

Coulomb Excitation of Neodymium*

B. E. Simmons, D. M. Van Patter,† K. F. Famularo, and R. V. Stuart
University of Minnesota, Minneapolis, Minnesota

(Received August 4, 1954, revised manuscript received September 24, 1954)

Three gamma rays produced by bombardment of neodymium metal with protons of energies up to 3.34 Mev have been observed. Measurements indicate gamma-ray energies and isotopic identifications of 71±4 kev from Nd^{145}, 300±3 kev from Nd^{148}, and 131±2 kev from Nd^{150}, with total cross sections for production of the last two radiations of 0.7±0.2 and 2.4±0.3 mb, respectively, for 2.25-Mev protons. Excitation functions found for the even-even isotopes agree with those predicted for $E2$ Coulomb interactions, leading to $0\rightarrow 2+\rightarrow 0$ level assignments; $E1$ excitation seems ruled out only for Nd^{150}. The theory of Alder and Winther for $E2$ excitation gives only qualitative agreement with the measured 131-kev gamma-ray angular distribution. Low-energy proton bremsstrahlung were also observed.

INTRODUCTION

THE use of Coulomb excitation and detection of the resulting gamma rays to investigate the positions, lifetimes, and spin and parity assignments of low-lying energy levels in medium-to-heavy nuclides is attractive in its complementary role with respect to beta-decay work. By this method it should be possible, in particular, to fill in some of the gaps in existing data upon the apparently quite regular variations of properties of even-even isotope level structures.[1] The results reported herein, of proton bombardment of neodymium isotopes just above the 82-neutron shell, confirm the expected trends of some of these regularities.

EXPERIMENTAL ARRANGEMENT

The experimental apparatus, set up in conjunction with the Minnesota electrostatic generator, consisted essentially of a thin-walled, 4-inch diameter, cylindrical aluminum reaction chamber (see Fig. 1) and a NaI(Tl) scintillation spectrometer. The 1-inch diameter by 1-inch long NaI(Tl) crystal was placed outside the chamber so that it subtended an angle ~9° at the target, and could be rotated about the chamber axis from laboratory angles of 23° to 147°. Extensive lead shielding reduced background from machine x-rays to a negligible amount.

The electronic equipment was of the non-overloading type, consisting of a Chase-Higinbotham pulse amplifier[2] and a 10-channel discriminator[3] preceded by a slightly modified Johnstone window amplifier.[4] One-volt channels were used throughout the experiment with good stability.

Targets were of 99.85 percent minimum purity neodymium metal[5] in the form of a $\frac{3}{16}$ inch thick metal sample and also foils made by evaporating neodymium onto thin nickel backings. The foils were thick to protons, yet thin to the gamma rays. A thick target of Nd_2O_3 enriched in Nd^{150} was also bombarded.[6]

EXPERIMENTAL RESULTS AND ANALYSIS

Gamma-ray spectra covering 30 to 800 kev exhibited three peaks due to gamma radiations from neodymium superposed upon a continuum of up to five times empty-chamber background. A typical spectrum is given in Fig. 2, which also depicts three other gamma-ray peaks. These latter peaks (A, B, and C), appearing only from the metal target and later removed by surface cleaning, were probably due to fluorine and sodium impurities. Table I lists the energy measurements of the neodymium peaks, as calibrated against a Hf^{181} gamma-ray source having peaks at 135, 345, and 481 kev;[7] these are compatible with the 136.5-kev assignment[8] to the lowest excited state in Ta^{181} and with the 37-kev peak from neodymium K x-rays. (This laboratory's earlier quoted value[9] for the 131-kev Nd gamma

TABLE I. A summary of data on gamma radiation excited by proton bombardment of neodymium.

E_γ kev	Source[a]	Percent natural abundance	σ_{total}[b] mb	τ[c] seconds	Q_0[d] barns
71±4	$_{60}Nd^{145}$	8.3	weak	...	...
300±3	$_{60}Nd^{148}$	5.7	0.7±0.2	2.6×10^{-10}	2.6
131±2	$_{60}Nd^{150}$	5.6	2.4±0.3	0.7×10^{-8}	4.0

[a] Identification by Temmer and Heydenburg (see reference 10) and by this laboratory.
[b] Cross section, corrected for natural abundance, for gamma-ray production at E_p=2.25 Mev.
[c] Estimated excited-state lifetime, assuming $E2$ Coulomb excitation.
[d] Estimated intrinsic quadrupole moment, assuming $E2$ Coulomb excitation.

* Assisted in part by the joint program of the U. S. Office of Naval Research and the U. S. Atomic Energy Commission.

† Now at the Bartol Research Foundation, Swarthmore, Pennsylvania.

[1] G. Scharff-Goldhaber, Phys. Rev. **90**, 587 (1953); F. Asaro and I. Perlman, Phys. Rev. **91**, 763 (1953); P. Stähelin and P. Preiswerk, Nuovo cimento **10**, 1219 (1953).

[2] R. L. Chase and W. A. Higinbotham, Rev. Sci. Instr. **23**, 34 (1952).

[3] W. C. Elmore and M. Sands, *Electronics* (McGraw-Hill Book Company, Inc., New York, 1949), p. 241 ff.

[4] C. W. Johnstone, Nucleonics **11**, No. 1, 36 (1953).

[5] We are indebted to Professor F. H. Spedding of Iowa State College for making available the spectroscopically-analyzed neodymium metal.

[6] The neodymium oxide enriched in Nd^{150} was obtained from the Oak Ridge National Laboratory, Oak Ridge, Tennessee.

[7] Hollander, Perlman, and Seaborg, Revs. Modern Phys. **25**, 469 (1953).

[8] Cork, Nester, LeBlanc, and Brice, Phys. Rev. **92**, 119 (1953).

[9] Simmons, Van Patter, Famularo, and Stuart, Bull. Am. Phys. Soc. **29**, No. 5, 15 (1954).

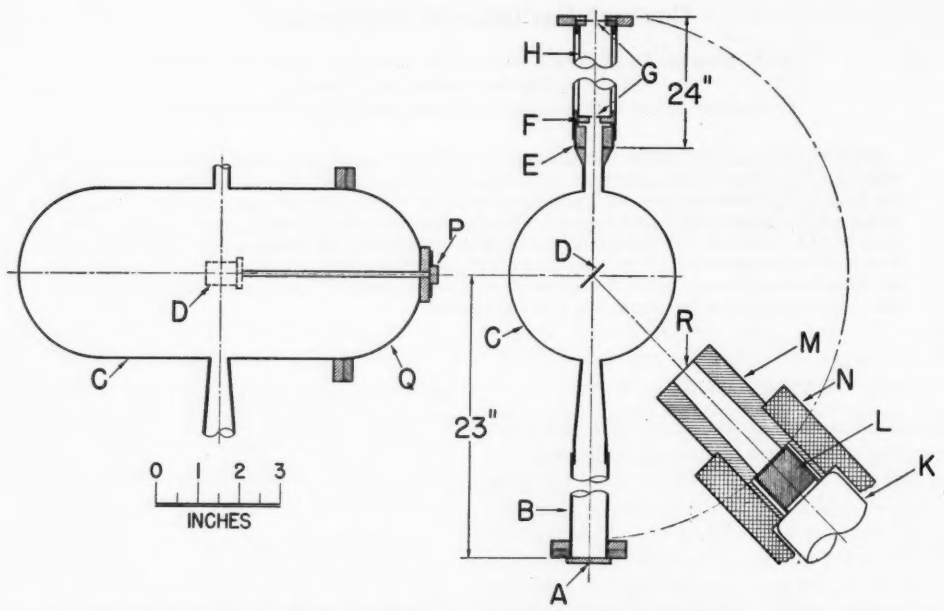

FIG. 1. Experimental apparatus, not showing extensive lead shielding used overall. *A*, quartz end window; *B*, beam exit tube, lined with nickel and tantalum; *C*, 32-mil aluminum chamber wall; *D*, target; *E*, Lucite insulator; *F*, Lucite spacer-insulator for slit system; *G*, two of four collimating slits (others not shown); *H*, steel tube containing tantalum lining and slits; *K*, DuMont 6292 photomultiplier tube; *L*, NaI(Tl) crystal; *M*, brass collimator-shield; *N*, lead shield; *P*, target angle adjustment; *Q*, removable end cap with target and holder. Chamber and exit tube are insulated for current collection, while the slit system is insulated separately to permit voltage biasing against secondary electrons. The counter rotates between the angles 23° and 147°.

ray is in error, having been assigned with reference to an impure Ce^{141} gamma-ray source.) The latest values[10] of Heydenburg and Temmer, who have previously reported these radiations,[11,12] are 70, 300, and 128 kev, in the order of listing of Table I.

Heydenburg and Temmer have bombarded neodymium oxides enriched in the isotopes Nd^{143}, Nd^{145}, and Nd^{148} with alpha particles and obtained the identifications listed in Table I.[10] Work here with protons and neodymium oxide enriched in Nd^{150} also indicated Nd^{150} to be the source of the 131-kev gamma rays.

The intensity of the 71-kev radiation was quite low and this gamma ray has not been further investigated. The 131- and 300-kev yields at 90° as functions of proton energy are shown in Fig. 3. The solid curves are least-squares fits for the theoretical total cross section *E*2 excitation functions as given by Alder and Winther.[13] The assumption here of isotropic angular distributions produces no significant error in the shape of these curves. A theoretical *E*1 excitation function,[14] shown in Fig. 3 as the broken curve, does not fit the data very well for the 131-kev radiation. This was fitted only to the low-energy data. However, the data for the 300-kev gamma rays can be fitted by either *E*1 or *E*2 excitation functions, the former not being shown in Fig. 2. In these and following computations, the stopping cross

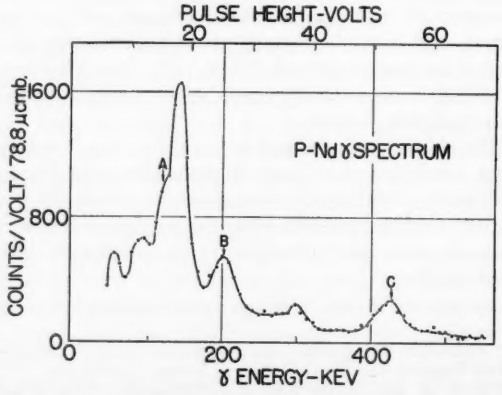

FIG. 2. A spectrum of the radiation emitted from a thick neodymium metal target when bombarded by 2.25-Mev protons; a 67-mil copper absorber was employed. The peaks *A*, *B*, and *C*, appearing only from this target and later removed by surface cleaning, are probably due to fluorine and sodium impurities. Gamma rays from neodymium give rise to the peaks at 71, 131, and 300 kev, while neodymium *K* x-rays form the low-energy peak. The underlying continuum is due principally to proton bremsstrahlung.

[10] N. P. Heydenburg (private communication).
[11] N. P. Heydenburg and G. M. Temmer, Phys. Rev. **93**, 906 (1954).
[12] G. M. Temmer and N. P. Heydenburg, Phys. Rev. **94**, 1399 (1954).
[13] K. Alder and A. Winther, Phys. Rev. **91**, 1578 (1953).
[14] K. Alder and A. Winther (private communication).

section of neodymium for protons enters. Interpolated values for this were obtained by means of an approximate form of the Bethe-Bloch formula least-squares fitted to existing data[15,16] for copper, silver, and gold. Uncertainty in these values should have little effect upon the validity of the curves in Fig. 2, but do contribute ±7 percent probable error in estimates of absolute cross sections for neodymium.

The points in Fig. 4 give angular-distribution data obtained for the 131-kev gamma ray for 2.25-Mev protons incident upon a thick target, the large probable errors being due principally to uncertainty in background subtraction. The solid curve in Fig. 4 represents a three-parameter least-squares fit to the data, having a normalized form $1+0.00\cos^2\theta+0.27\cos^4\theta$. A theoretical angular-distribution estimate[14] of Alder and Winther, $1+0.55\cos^2\theta-0.22\cos^4\theta$ (not shown), fits the data only qualitatively. This assumes a $0\rightarrow 2+\rightarrow 0$ transition scheme for Nd^{150} and takes no account of the slight variation of coefficients with decreasing proton energy in the target. As a check to the neodymium data, the angular distribution of the Ta^{181} gamma ray was measured to be isotropic to within 2 percent, in agreement with the results of others.[17,18]

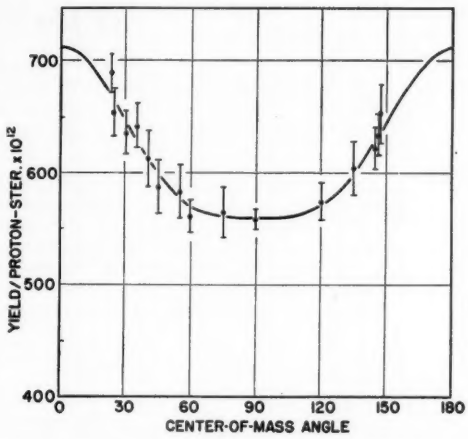

FIG. 4. The angular distribution for the 131-kev gamma radiation excited by proton bombardment of neodymium. The curve represents the function $560+000\cos^2\theta+150\cos^4\theta$, a least-squares three-parameter fit to the data; this has the normalized form $1+0.00\cos^2\theta+0.27\cos^4\theta$. The indicated probable errors are principally due to background subtraction.

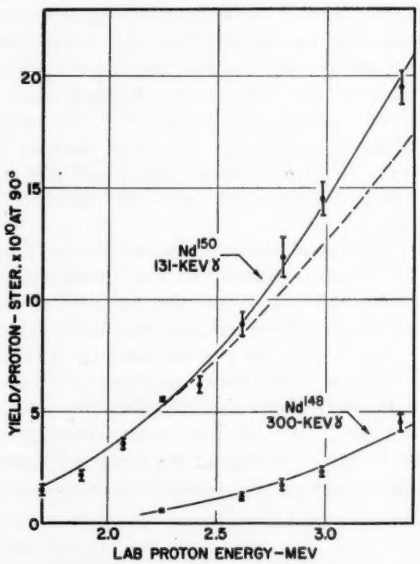

FIG. 3. Excitation functions for 300- and 131-kev gamma radiation excited by proton bombardment of neodymium. The data are uncorrected for NaI(Tl) crystal efficiency. The solid curves are least-squares fits to the data of the theoretical excitation functions, assuming $E2$ Coulomb interaction. The broken curve represents the theoretical $E1$ prediction for the 131-kev radiation, fitted to the data at the lower proton energies where its shape is almost that of the $E2$ curve. The theoretical $E1$ curve for the 300-kev data, not shown, would almost coincide with the corresponding $E2$ curve.

Production cross sections for two of the observed gamma rays are given in Table I. These are based upon an assumed efficiency[19] for the NaI(Tl) crystal of 100 percent for the 131-kev gamma ray, and 77 percent for the 300-kev gamma ray. For the former all the counts were assumed[19] to fall under the photopeak; for the latter, 72±6 percent fell under the photopeak, the remainder making up the here-unobservable Compton distribution. The cross-section computation for the 131-kev radiation incorporates the three parameters from the best-fit angular-distribution curve, which are assumed to be constant with proton energy below 2.25 Mev. The 300-kev radiation is taken as isotropically distributed, an assumption which at worst, according to theory, should make the listed cross section 10 percent low. Lifetime estimates for the excited states are based upon $E2$ internal-conversion coefficients[20] of 33 percent and 7 percent for the Nd^{150} and the Nd^{148} levels, respectively. Intrinsic quadrupole moments computed on this basis by means of the Bohr-Mottelson theory[21] are also listed.

No indication of gamma rays from known levels[1,22] in Nd^{144} and Nd^{146} was found. The lower limits of observability indicate that the maximum cross section

[15] S. K. Allison and S. D. Warshaw, Revs. Modern Phys. **25**, 779 (1953).
[16] R. Fuchs and W. Whaling, "Stopping Cross Sections," Kellog Radiation Laboratory, California Institute of Technology (unpublished).
[17] W. I. Goldburg and R. M. Williamson, Phys. Rev. **95**, 767 (1954).
[18] Eisinger, Cook, and Class, Phys. Rev. **94**, 735 (1954).
[19] For these estimates and a thorough discussion of problems involved, see Maeder, Mueller, and Wintersteiger, Helv. Phys. Acta **27**, 3 (1954).
[20] Rose, Goertzel, Spinrad, Harr, and Strong, Phys. Rev. **83**, 79 (1951).
[21] A. Bohr and B. Mottelson, Kgl. Danske Videnskab. Selskab, Mat-fys. Medd. **14**, No. 16 (1954).
[22] Bernstein, Markowitz, and Katcoff, Phys. Rev. **93**, 1073 (1954).

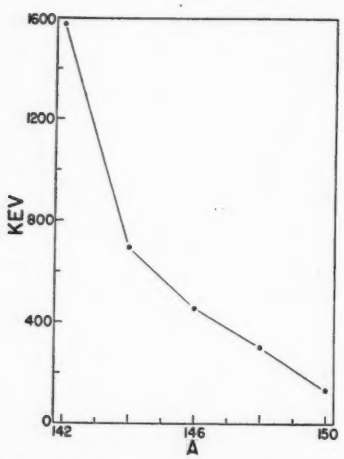

FIG. 5. The lowest-excited-state energies of the even-even isotopes of neodymium plotted against mass number A. Nd^{142} is magic in having 82 neutrons.

for production of a 455-kev gamma ray from Nd^{146} is about 1 mb at 2.79-Mev proton energy, and for production of a 695-kev gamma ray from Nd^{144} about 0.6 mb at 3.34 Mev. No search was made for a 1695-kev gamma ray[1] from Nd^{142}.

It is believed, in agreement with Zupančič and Huus,[23] that the continuum referred to at the beginning of this section is due to proton bremsstrahlung. Similar radiation was recorded from lead and from praseodymium targets, which had no observable gamma-ray peaks in their spectra, and no change was observed after coating the inside of the chamber with Aquadag. The theory of Sommerfeld[24] give rough agreement with these data.

DISCUSSION

It appears probable that the levels excited in Nd^{148} and Nd^{150} should both have a 2+ assignment. Since the estimated cross section for compound-nucleus formation by 3.8-Mev protons is only 3×10^{-5} mb, the interaction force in this experiment should be essentially of Coulomb type. This leads to an excitation function dependent, in shape, only upon the nuclear properties charge, mass, and energy-level position, plus the relative spins of the levels involved in the excitation. The excitation function is, then, a measure of the number of units of angular momentum transferred during the interaction. This is the significance of the fit of the $E2$ excitation functions shown in Fig. 2. It will be noted that the relative parity of the levels is also established if these fits are unique.

The possibility of a magnetic interaction with these even-even nuclei seems unlikely, as does electric interaction of octupole or higher order. It is possible that $E1$ interaction could occur by means of an induced dipole moment in the target nucleus, but this seems improbable at least for Nd^{150} because of the poor fit to the data of the corresponding excitation function. For the Nd^{148} one cannot make a spin assignment on the basis of excitation-function fits, but even then the nuclear systematics indicate that in this region of A and Z the lowest excited state should be 2+.

The large probable errors associated with the angular distribution do not explain the seemingly real disagreement with the theory there, but it may be that some smearing from atomic motions occurs during the lifetime of the excited state. A recalculation now underway by Alder and Winther[14] of the numerical integrations in the theory may also lead to better agreement. Unfortunately no theoretical $E1$ angular distribution calculations are yet available for comparison.

The positions of the first excited states of all the stable even-even isotopes of neodymium are now believed known[1,22] and fall into the regular pattern depicted in Fig. 5. It seems likely that all of these levels are 2+, based upon the present data, upon the shape of beta spectra, upon decay schemes, and upon the known trend toward this property for even-even nuclei of medium and high mass. The computed intrinsic electric quadrupole moments are consistent with known moments for nearby odd-even nuclei.

[23] Č. Zupančič and T. Huus, Phys. Rev. 94, 205 (1954).
[24] A. Sommerfeld, Ann. Physik (5) 11, 257 (1931); for a complete listing of associated material see reference 23.

Radioactivity of In^{117} and Sb^{117}

CARL L. MCGINNIS
National Bureau of Standards, Washington, D. C. and Nuclear Data Group, National Research Council, Washington, D. C.

(Received September 24, 1954)

The $p_{1/2}$ isomeric level of In^{117} decays with a 1.9-hr half-life 49 percent by a 1.777-Mev β^- to the $s_{1/2}$ ground state of Sn^{117}, 23 percent by a 1.616-Mev β^- to the 0.161-Mev $d_{3/2}$ level of Sn^{117}, and 28 percent by an $M4$ 0.311-Mev γ to the $g_{9/2}$ ground state of In^{117}. The latter decays with a 1.1-hr half-life by a 0.740-Mev β^- to the $g_{7/2}$ level of Sn^{117} which is de-excited by a 0.565-Mev γ and a 0.161-Mev γ in cascade. There is no cross-over γ (<1 percent). Less than 10 percent of the 3.0-hr Cd^{117} decays to the 1.9-hr level. Less than 1 percent of the 1.1-hr ground state populates the 14-day Sn^{117m}. The 2.8-hr Sb^{117} decays to the 0.161-Mev level of Sn^{117} by a 0.61-Mev $\beta^+(\beta^+/\epsilon=0.026)$ but does not decay to the 0.323- or 0.726-Mev levels (<0.5 percent).

I. INTRODUCTION

THE systematics of nuclear energy levels predict that the decay scheme of In^{117} will be similar to that of In^{113} and In^{115}, i.e., will be characterized by an $M4$ isomeric γ ray from the $p_{\frac{1}{2}}$ level to the $g_{9/2}$ ground state. In addition, both levels are expected to decay by β^- emission with accompanying γ rays. The radioactivity of In^{117} has been studied for the purpose of verifying such a decay scheme.

Previous investigations[1] of In^{117} have shown that it decays with a 1.95-hr half-life,[2] a 1.73-Mev β^-,[3,4] and 0.161- and 0.558-Mev γ's.[4] In indium obtained from uranium fission, Coryell and co-workers[5] found half-lives of 70 min and ~2.5 hr, both of which they assigned to In^{117}. It has also been reported[6] that ~0.036 percent of the 3.0-hr Cd^{117} decays to the 14-day Sn. During the course of this work LeBlanc *et al.*[7] published the results of their work on In^{117} giving a 2.3-hr half-life and 0.160-, 0.312-, 0.562-, and 0.725-Mev γ's. The 0.312-Mev γ was assigned to the isomeric transition on account of its high conversion coefficient and because of the absence of coincidences between β's and this γ.

II. EXPERIMENTAL PROCEDURE

Cadmium metal was bombarded with 15-Mev deuterons from the Department of Terrestrial Magnetism, Carnegie Institution of Washington cyclotron. The indium that was formed during the bombardment was first removed by co-precipitation with $Fe(OH)_3$. After allowing 70 minutes for the indium activities, In^{117} plus In^{115}, to grow in from their cadmium parents, indium was again precipitated with $Fe(OH)_3$. The iron was removed with 1.5M HCl from a Dowex-2 ion exchange column and then the indium was washed off with 0.1M HCl. This procedure removed all silver and cadmium but carried along any tin that might have grown from the indium. The particle spectrum was measured with a magnetic lens spectrograph. The electromagnetic spectrum and coincidences were measured with a NaI scintillation spectrometer. All In^{117} measurements, with the exception of that of the half-life of the ground state, were made with the mixed 1.1-hr and 1.9-hr activities.

III. RESULTS

In^{117}

A value of 1.90±0.05 hours was obtained for the half-life of the isomeric level of In^{117} by observing the decay of 0.804-Mev betas with the lens spectrometer (Fig. 1).

A value of 1.1±0.1 hours was obtained for the half-life of the ground state by observing the decay of the 0.161- and 0.565-Mev γ's with a scintillation spectrometer (Fig. 1) from a source prepared in the following

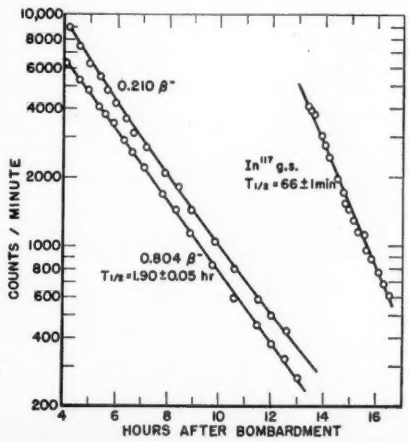

FIG. 1. Decay curves of 0.210- and 0.804-Mev betas of In^{117m} as measured with the lens spectrometer and the decay curve of the 0.161-Mev γ of the In^{117} ground state.

[1] For complete references see K. Way *et al.*; *Nuclear Data*, National Bureau of Standards Circular No. 499 (U. S. Government Printing Office, Washington, D. C., 1950) and Nuclear Science Abstracts **6**, 24B(1952); **7**, 24B(1953).
[2] J. L. Lawson and J. M. Cork, Phys. Rev. **57**, 982 (1940).
[3] J. M. Cork and J. L. Lawson, Phys. Rev. **56**, 291 (1939).
[4] J. D. Knight and G. A. Cowan, quoted by Hollander, Perlman, and Seaborg, Revs. Modern Phys. **25**, 469 (1953).
[5] Coryell, Lévêque, and Richter, Phys. Rev. **89**, 903(A) (1953).
[6] G. A. Cowan, quoted by M. Goldhaber and R. D. Hill, Revs. Modern Phys. **24**, 179 (1952).
[7] LeBlanc, Cork, and Burson, Phys. Rev. **93**, 916(A) (1954).

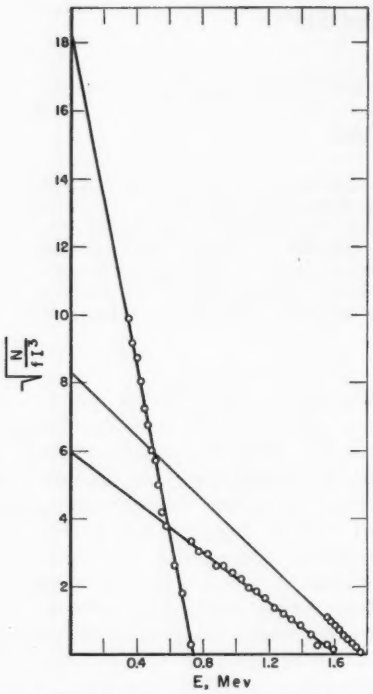

FIG. 2. Fermi-Kurie plot of the In^{117} beta spectra showing the end points of 1.772, 1.616 and 0.740 Mev.

manner. Twelve hours after the bombardment indium was chemically removed from the cadmium, the Cd^{117} was allowed to decay for 70 minutes and indium was again separated. The γ-ray spectrum of this sample was measured with a scintillation spectrometer. The 0.161- and 0.565-Mev γ's decayed with a 1.1 ± 0.1 hour half-life and an 0.333-Mev γ with the expected 4.5-hr half-life of In^{115m}. It was not possible to resolve the 0.311-Mev γ of the 1.9-hr In^{117m} from the 0.333-Mev γ.

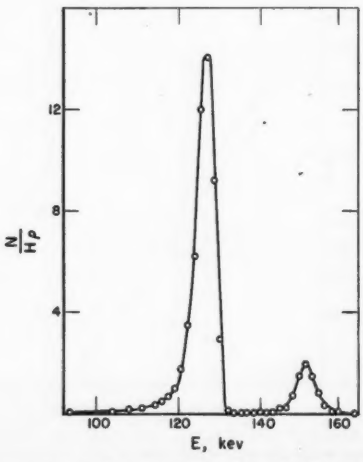

FIG. 3. Conversion electron spectrum of the 0.161-Mev γ of Sb^{117}.

From the linearity of the decay of this peak it is concluded that less than 10 percent of the 3.0-hr Cd^{117} decays to the isomeric level of In^{117}. The 1.1-hr half-life is in good agreement with the 70-min value found by Coryell *et al.*[5] The previously reported[8] value of 40 min is retracted. When the decay of the In^{117} γ rays was observed several hours after the chemical separation of indium from cadmium, a "half-life" of about 2.3 hours was observed as was expected for the parent-daughter growth and decay.

Figure 2 shows the Fermi-Kurie plot of the beta spectrum. The end-point energies, relative intensities (as determined from the intercepts[9] of the straight lines with the ordinate axis), and logft values[10] are given in Table I. The decay of 0.21-Mev betas, i.e.,

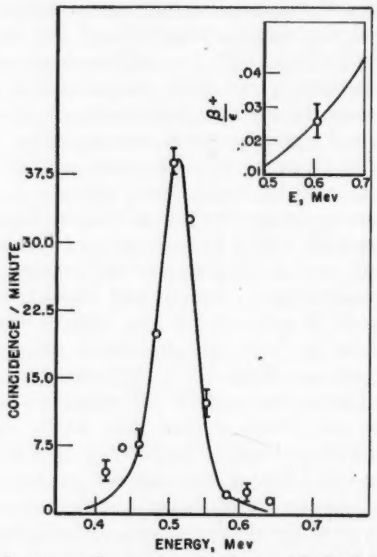

FIG. 4. Spectrum of γ rays in coincidence with the 0.161-Mev γ in the decay of Sb^{117}. The solid curve is the Na^{22} annihilation radiation energy calibration. The insert is a graph of the theoretical β^+/ϵ ratio for Sb with the experimentally measured ratio shown as a point.

about the most probable β's of the 0.74-Mev component, as measured with the β-ray spectrometer, showed little complexity, decaying mainly with a 1.9-hr half-life. If this component had originated solely as a result of the decay of the 1.9-hr isomeric level to the 1.1-hr ground state, the half-life curve would have shown a typical parent-daughter growth and decay. However, the 1.1-hr ground state is also produced directly from the decay of the 3-hr Cd^{117}. The 1.9-hr isomeric level grows from the 50-min Cd.

With these data it was then possible to analyze the decay curve of the 0.21-Mev β's into that portion

[8] C. L. McGinnis, Phys. Rev. **94**, 780(A) (1954).
[9] H. Brown and V. Perez-Mendez, Phys. Rev. **78**, 812 (1950).
[10] Rose, Perry, and Dismuke, Oak Ridge National Laboratory ORNL-1459, 1953 (unpublished); J. R. Reitz, Phys. Rev. **77**, 10 (1950).

which originated directly from the 3-hr Cd and into that portion which grew from the isomeric level of In^{117}. Under the conditions of this experiment 59 percent of the measured 0.740-Mev β^- spectrum was produced directly from the decay of the 3-hr Cd. The percentages of the three modes of decay of the 1.9-hr isomeric level given in Table I have been computed on the assumption that 41 percent of the measured 0.740-Mev beta spectrum originated from the decay of the isomeric level. This correction has not been made in Fig. 2.

The internal conversion coefficients for the three γ rays given in Table II are based on the relative intensities of the beta spectra given in Table I. The conversion electrons of the 0.565-Mev γ were scarcely observable above the β background and therefore the agreement with an $E2$ assignment is quite fortuitous.

The energies of the three gamma rays were measured by the following methods: 0.565±0.007 Mev by scintillation spectrometer studies, 0.311±0.002 Mev by observing the K-conversion electrons with the lens spectrometer (the L electrons were obscured by the more intense K electrons of the 4.5-hr In^{115m} 0.333-Mev γ ray); and 0.161±0.001 Mev by observing the K- and L-conversion electrons from the 2.8-hr Sb^{117}. The scintillation spectrometer showed a peak at 0.726 Mev. However, by varying the geometry of the measurement it was shown that this peak was due to the pile-up of the 0.161- and 0.565-Mev pulses. If a true crossover gamma ray is present, its intensity is less than 1 percent of the 0.565-Mev γ ray.

With a scintillation spectrometer and single channel differential discriminators the following coincidences were measured: $(\beta)(0.161\gamma)$, $(\beta)(0.565\gamma)$, and $(0.161\gamma)(0.565\gamma)$. No coincidences were observed between the 0.311γ and either β's or γ's.

2.8-hr Sb^{117}

Tin was bombarded with 15-Mev deuterons and the electron spectrum of the chemically separated Sb was measured with the lens spectrometer. The energy of the γ ray is 0.161±0.001 Mev. $K/(L+M)=8.3\pm0.1$ (Fig. 3). This result is in agreement with the previous data[11] on the decay of Sb^{117}.

Indium metal was bombarded with 22- to 32-Mev alphas from the Brookhaven 60-inch cyclotron and the following coincidence intensity results were found with a scintillation spectrometer and two single-channel differential discriminators: $(0.161\gamma)(0.511\gamma)/(0.161\gamma)=0.051\pm0.01$, $(\text{x-ray})(0.161\gamma)/(\text{x-ray})=0.68\pm0.02$, $(\text{x-ray})(0.565\gamma)/(\text{x-ray})<0.005$.

Figure 4 shows the γ-ray spectrum in coincidence with the 0.161γ. The solid curve is the Na^{22} annihilation radiation energy. The geometry for the measurement of the intensity ratio $(0.161\gamma)(0.511\gamma)/(0.161\gamma)$ was calibrated with Na^{22}. Allowance was made for its 10 percent electron capture.[12] On the basis of this calibration the intensity ratio β^+/ϵ is 0.026±0.005. For an allowed decay this ratio is a unique function of the decay energy. The insert in Fig. 4 is a plot of β^+/ϵ *vs* E the positron energy from 0.5- to 0.7-Mev. f_+ was computed from the tables of Rose *et al.*,[10] f_K from the formula given by Moszkowski[13] and the ratio of L_1 capture to K capture from the graph of Rose and Jackson.[14] From the observed ratio of 0.026 the maximum positron energy was then found equal to 0.61±0.03 and the logft for the transition equal to 4.80. The ground-state decay energy of 1.79 Mev is in excellent agreement with the predicted 1.8 Mev of the β-decay systematics.[15]

Te^{123} was used to calibrate the geometry for the $(\text{x-ray})(0.161\gamma)/(\text{x-ray})$ measurement. If all the electron capture transitions go to the 0.161-Mev level the expected ratio is 0.687 when account has been taken of the previously measured conversion data and the L_1- to K-capture ratio[14] of 0.12. Hence all ($\geq$95 percent) of the decays go to this level.

An attempt was made to observe a possible weak transition to the 0.726-Mev level by measuring coincidences between the 0.565γ and either the 0.161γ or x-rays. The greater intensity of the $(0.161\gamma)(0.511\gamma)$ coincidences obscured the possible $(0.161\gamma)(0.565\gamma)$ coincidences. With x-rays the only coincidences observed in the 0.5-Mev energy region were those with the 0.511γ which are expected to occur in 1 percent of the disintegrations. From this negative result if was concluded that <0.5 percent of the decay takes place to the 0.726-Mev level.

TABLE I. 1.1-hr In^{117} and 1.9-hr In^{117m} beta spectra.

Energy (Mev)	Rel. intensity	f	t(sec)	logft
0.740±0.010	22	8.75	3 960	4.54
1.616±0.005	23	166	28 600	6.68
1.772±0.005	55	241	12 450	6.48

IV. DISCUSSION

In^{117}

The measured[1] spin of $\frac{1}{2}$ and magnetic moment of −0.9951 support the shell model designation of $s_{\frac{1}{2}}$ for

TABLE II. Data for the gamma rays of In^{117}.

Energy (Mev)	$K/(L+M)$	α_K(expt)	α_K(theory)[a]
0.161±0.001	8.3±0.1	0.13±0.001	$M1$ 0.14
0.311±0.002	(3.6)[b]	1.3±0.2	$M4$ 1.26
0.565±0.007	(7.8)[b]	~0.005	$E2$ 0.0047

[a] Rose, Goertzel, and Perry, Oak Ridge National Laboratory Report ORNL-1023, 1951 (unpublished).
[b] Interpolated from empirical curves (reference 17).

[11] G. M. Temmer, Phys. Rev. **76**, 424 (1949).

[12] R. Sherr and R. H. Miller, Phys. Rev. **93**, 1076 (1954).
[13] S. A. Moszkowski, Phys. Rev. **82**, 35 (1951).
[14] M. E. Rose and J. L. Jackson, Phys. Rev. **76**, 1540 (1949).
[15] K. Way and M. Wood, Phys. Rev. **94**, 119 (1954).

the ground state of Sn^{117}. The angular correlation[16] between the K-conversion electrons of the 14-day isomeric γ ray and the 0.161-Mev gamma which is in cascade with it show that the latter is ~99.9 percent $M1$. This result identifies the 0.161-Mev level as $d_{3/2}$. The conversion coefficient and $K/(L+M)$ ratio reported here agree with this assignment. The empirical[17] lifetime-energy relationship for $M4$ transitions assign $h_{11/2}$ to the 14-day isomeric level of Sn^{117}. In this region of the periodic table it appears that the simple shell model is particularly applicable. Hence single-particle designations are used for levels.

From the energy difference between the 1.772-Mev β and the 1.616-Mev β it is concluded that the former goes to the ground state and the latter to the 0.161-Mev level of Sn^{117}. The ft values for these two β transitions indicate that both are first forbidden and thus that the isomeric level of In^{117} is the expected $p_{1/2}$ state. The internal conversion coefficient and lifetime of the 0.311-Mev γ show that this is an $M4$ transition and thus that the ground state is $g_{9/2}$. In^{111}, In^{113}, and In^{115} also have $g_{9/2}$ ground states. It is interesting to note the similarity between the indium $M4$ transitions by comparing the ratio of the experimental to the predicted γ-ray lifetimes. For In^{113}, In^{115}, and In^{117} these ratios are 0.41, 0.33, and 0.50 based on the theoretical formula[18] and 1.9, 1.6, and 2.5 based on the empirical relationship.[17]

The 1.1-hr level decays by a 0.740-Mev β followed by 0.565- and 0.161-Mev γ's in cascade. The logft of 4.54 for this beta clearly shows that transition is allowed and permits the 0.726-Mev level to have a spin of 11/2, 9/2, or 7/2 with even parity. With either of these first two assignments the predominant mode of decay would be by an $E1$ γ to the 14-day $h_{11/2}$ level rather than by an $E4$ or $M3$ γ to the 0.161-Mev level. Since the observed yield of the 14-day Sn^{117m} from In^{117} is ~0.036 percent,[6] the only assignment for the 0.725-Mev level is $g_{7/2}$. An estimate for the intensity of the possible 1.14-Mev beta from the $g_{9/2}$ ground state of In^{117} to the 14-day $h_{11/2}$ level of Sn^{117} can be obtained by making use of the logft of 8.80 for the 1.61-Mev β^1 from the 43-day isomeric $h_{11/2}$ level of Cd^{115} to the $g_{9/2}$ ground state of In^{115} on the assumption that the matrix elements for both transitions are the same. Such an estimate gives a branching of 0.02 percent which agrees with the observed yield of the 14-day Sn^{117m}.

The decay energy of the ground state of In^{117} of 1.466 Mev is in good agreement with the prediction of the beta decay systematics.[15]

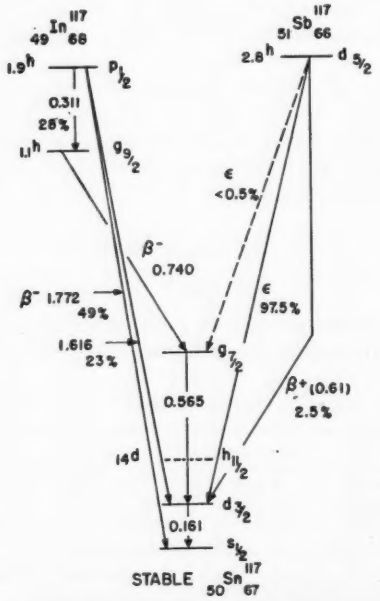

FIG. 5. Decay scheme for In^{117} and Sb^{117}.

Sb^{117}

The logft of 4.80 for the decay of the Sb^{117} ground state to the $d_{3/2}$ level of Sn^{117} characterizes this transition as allowed. Hence the ground state of Sb^{117} has even parity and a spin of either 1/2, 3/2 or 5/2. A spin of 1/2 or 3/2 would forbid decay to the 0.726-Mev $g_{7/2}$ level but permit decay to the $s_{1/2}$ ground state, while a spin of 5/2 would do just the reverse. *Neither* decay to the 0.726-Mev level *nor* the ground state was observed. The upper limit for the first is 0.5 percent and for the second 5 percent of the main decay. If either of these transitions were allowed, the branching would be 40 percent or 120 percent respectively of that to the 0.161-Mev level. Thus the first is forbidden by a factor of >80 and the second by one of >20.

Since the experimental data are not sufficient to permit a choice between $1/2^+$, $3/2^+$, and $5/2^+$, other evidence must be considered. It seems possible that l-forbiddenness may play a role here. If it were the controlling factor, no choice would be possible between $3/2^+$ and $5/2^+$ for the Sb^{117} ground state. At present arguments about configuration rearrangements seem to hold more force than do considerations of l-forbiddenness.

The most plausible neutron configuration for Sb^{117} is $(g_{7/2})^8(d_{5/2})^6(h_{11/2})^2$.[19] No rearrangement of this configuration is necessary for the decay of a $d_{3/2}$ or $s_{1/2}$ proton to the $s_{1/2}$ ground state of Sn^{117}, therefore no reduction in the expected branching is to be expected on this account. However, one would expect the decay of a $d_{5/2}$ proton to a $g_{7/2}$ neutron to be very strongly impeded since the $g_{7/2}$ neutron shell is already full. A rearrangement of the neutron configuration to something like $(g_{7/2})^6(d_{5/2})^6(h_{11/2})^4$ is necessary before the decay can take place. A logft of 9.2 for an apparently

[16] R. K. Golden and S. Frankel, Phys. Rev. **95**, 613(A) (1954).
[17] M. Goldhaber and A. W. Sunyar, Phys. Rev. **83**, 906 (1951).
[18] V. F. Weisskopf, Phys. Rev. **83**, 1073 (1951).
[19] P. F. A. Klinkenberg, Revs. Modern Phys. **24**, 63 (1952).

allowed transition in Kr^{85} has been ascribed[20] to a similar rearrangement. Thus the assignment of $d_{5/2}$ to the ground state of Sb^{117} makes plausible the lack of observed transitions both to the ground state of Sn^{117} and also to the 0.726-Mev level. This is actually the assignment most strongly suggested by the shell model and is consistent with the assignments, from measured spins and moments, of $d_{5/2}$ and $g_{7/2}$ to the ground states of stable Sb^{121} and Sb^{123} respectively.

The proposed decay scheme for In^{117} and Sb^{117} is given in Fig. 5.

[20] Sunyar, Mihelich, Scharff-Goldhaber, Goldhaber, Wall, and Deutsch, Phys. Rev. 86, 1023 (1952).

V. ACKNOWLEDGMENT

I wish to express my appreciation to R. W. Hayward for his generosity in placing the facilities of his laboratory at my disposal, to D. Hoppes for his cooperation in the experiments, to D. Cowie, N. Heydenburg, and S. Buynitzky of the Department of Terrestrial Magnetism for the cyclotron bombardments, to G. Scharff-Goldhaber, and A. W. Sunyar for their cooperation in making it possible for me to do part of the experimental work at Brookhaven, and to K. Way and R. W. King for their helpful discussions throughout the course of this work.

PHYSICAL REVIEW VOLUME 97, NUMBER 1 JANUARY 1, 1955

Decay Scheme of the Mirror Nucleus P^{29} and Related Results*†

H. RODERICK, O. LÖNSJÖ,‡ AND W. E. MEYERHOF
Stanford University, Stanford, California

(Received September 27, 1954)

The decay of P^{29} has been investigated with scintillation spectrometers, single and in coincidence. Positron emission (3.945±0.005 Mev end-point energy for the most energetic spectrum) occurs with a half-life of 4.45±0.05 sec to the ground state and to excited levels of Si^{29} at 1.28, 2.43, and possibly 2.03 Mev. Branching ratios (in percent) of 98.8±0.4 (ground state), 0.8±0.2 (1.28-Mev level), <0.15 (2.03-Mev level), and $0.24_{-0.08}^{+0.26}$ (2.43-Mev level) were measured. A study of γ rays from the decay of Al^{29} to Si^{29} led to branching ratios (in percent) of 15±9 (1.28-Mev level), <4 (2.03-Mev level), and 85±9 (2.43-Mev level). The intensity of a 1.15-Mev γ ray (cascading from the 2.43-Mev level) has been set at <11 percent of the total Al^{29} decays. Spin and parity assignments of the Si^{29} levels are discussed and compared with the results of other experiments. The *ft* values of the P^{29} decay are shown to agree with values calculated from the coupling constants of β decay if the theories of Feenberg and Bohr are used.

I. INTRODUCTION

PHOSPHORUS-29 had previously been found to decay to Si^{29} with a half-life of 4.6±0.2 sec by emitting positrons of 3.67±0.07 Mev.[1] The positron transition was presumed to be an image transition. The present work shows that the disintegration of P^{29} proceeds by two, or possibly three, alternative positron transitions to the low excited states of Si^{29} in competition with the image transition.[2]

II. METHOD

The method used to study the weak modes of β^+ decay in competition with the intense β^+ transition to the ground state was to search in the radioactivity for γ rays from the excited states to which the lower energy positrons decayed. Such a method is suitable even if the branching ratio to the excited state is quite small, because any low-intensity γ rays produced are of discrete energy. Hence the gamma rays can be detected relatively free of background, and can be identified.[3] The success of this method depends entirely on the use of NaI scintillation counters with their high sensitivity to and selectivity of γ rays. The apparatus used in this work for selecting, analyzing and presenting the pulse energy distribution produced in the NaI scintillation counter has been described in the literature.[4]

III. PRODUCTION AND HALF-LIFE OF P^{29}

P^{29} was produced by the $Si^{28}(d,n)$ reaction by bombarding Si crystals with 2.8-Mev deuterons from the Stanford cyclotron. The half-life of P^{29} was determined by measuring the activity of annihilation radiation (detected by the photoelectric peak in a NaI scintillation spectrometer) as a function of time. A scaler

* Condensation of a dissertation submitted by H. Roderick to the Department of Physics and the Committee on Graduate Study at Stanford University in partial fulfillment of the requirements for the degree of Doctor of Philosophy.

† Supported in part by the joint program of the U. S. Office of Naval Research and the U. S. Atomic Energy Commission.

‡ Fulbright Travel Fellow. Present address: Physics Department, University of Oslo, Blindern, Norway.

[1] White, Creutz, Delsasso, and Wilson, Phys. Rev. 59, 63 (1941).

[2] A preliminary report of this work has been given earlier: Roderick, Lönsjö, and Meyerhof, Phys. Rev. 90, 371(A) (1953).

[3] The intense β^+ ray transition to the ground state, of course, produced no discrete γ ray, except annihilation quanta, although, as shown below, bremsstrahlung and annihilation in flight gave disturbing background effects.

[4] H. I. West, Jr., and L. G. Mann, Rev. Sci. Instr. 25, 129 (1954).

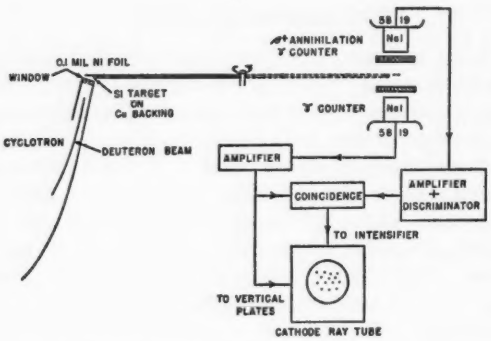

FIG. 1. Coincidence arrangement used for measurement of branching ratios of P^{29}.

and a clock together were photographed with a movie camera. Only a very small background activity (0.6 percent of the initial total activity) was obtained. The half-life of P^{29} was found to be 4.45 ± 0.05 sec.

IV. γ RAYS

Excited states of Si^{29} which could be reached by decay from P^{29} occur at 1.28, 2.03, 2.43, 3.07, 3.62, and 4.08 Mev.[5] In order to assure that γ rays from these states could be properly observed and in order to search for possible γ-ray transitions between excited states, the *prompt* γ-ray spectrum produced in the $Si^{29}(d,p)$ reaction was measured. A NaI scintillation spectrometer was used and the pulse height distribution was photographed. The results are shown in Table I. It is clear that only direct transitions from each excited state of Si^{29} to the ground state were observed.§

Next, using the same apparatus, the *radioactivity* of P^{29} was observed, and γ rays of 2.43, 1.28, and possibly 2.03 Mev were identified by their photopeak pulses. These γ-ray energies correspond to transitions between the three lowest excited states[5] and the ground state of Si^{29}. No higher-energy gamma rays were detected. The half-life of each of these γ rays was measured by observing each photopeak pulse activity as a function of time and found to be the same as that of P^{29}.

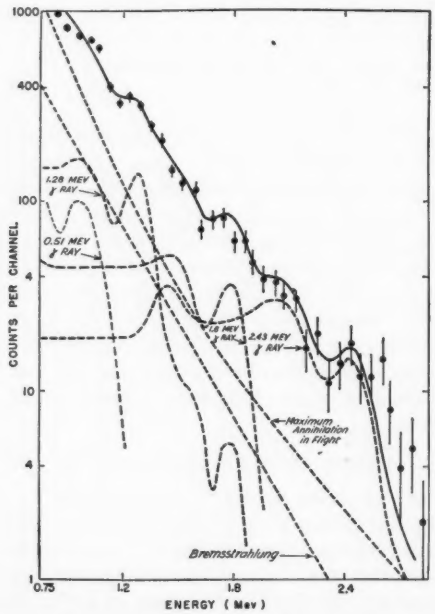

FIG. 2. Pulse energy distribution of P^{29} radiation coincident with pulses >0.4 Mev. Composite graph showing fit of the sum of 1.28-, 1.8-, and 2.43-Mev γ rays plus maximum continuous background.

[5] P. M. Endt and J. C. Kluyver, Revs. Modern Phys. **26**, 95 (1954).

V. BRANCHING RATIOS

Assuming electron capture to be negligible,[6] the branching ratios of the various β^+ spectra to the excited states of Si^{29} are given directly by the intensities of the γ rays per positron decay. Hence coincidence measurements were made with two NaI scintillation spectrometers between the γ rays and the annihilation quanta of the positrons from P^{29}. The coincidence arrangement is shown in Fig. 1. Absorbers were used to prevent the positrons from entering the counters. The counter labelled β^+ *annihilation* γ *ray* was set to observe mainly annihilation quanta (i.e., pulses >0.4 Mev) while the counter labelled γ *ray* was set to observe only γ rays (pulses >0.74 Mev). Coincident pulses from the two counters caused the γ-*ray* counter pulse to be recorded. Figure 2 shows this coincident pulse energy distribution. It was fitted by discrete γ rays of 2.43, 1.8, and 1.28-Mev energy after subtraction of the continuous background.

TABLE I. *Prompt* γ rays from the $Si^{28}(d,p)Si^{29*}$ reaction.

γ-ray energy[a] (Mev)	Estimated relative intensity
6.38	4
4.93	10
3.07	2
2.43	1
2.03	4
1.28	6

[a] Known excited states of Si^{29} which can be reached by the (d,p) reaction with 2.8-Mev deuterons are at 6.38, 6.10, 5.95, 4.93, 4.90, 4.84 Mev, in addition to those mentioned in the text.

An appreciable continuous background was found to be present which was caused by bremsstrahlung[7]

§ *Note added in proof.*—Some of the γ rays observed here have also been observed by L. C. Thompson, Phys. Rev. **96**, 369 (1954).

[6] Theoretically electron capture can be shown to contribute at most one percent to the branching ratios in the present case. See E. Feenberg and G. Trigg, Revs. Modern Phys. **22**, 402 (1950).

[7] Bremsstrahlung from radioactive sources has been observed and compared with theory by Goodrich, Levinger, and Payne, Phys. Rev. **91**, 1225 (1953).

and annihilation in flight[8] of the positrons. The absolute pulse height distribution of the background was calculated from the work of Heitler.[9] The number of coincident annihilation-in-flight pulses depends sensitively on the place of annihilation because of the angular correlation between the two quanta.[10] Because the exact region in which all the positrons were annihilated was not known, only upper and lower limits could be set to the annihilation-in-flight background. The maximum annihilation-in-flight background is shown in Fig. 2, the minimum in Fig. 3.

Because of the strong γ-ray transition from the 2.03-Mev level to the ground state found in the prompt γ-ray spectra from the $Si^{28}(d,p)$ reaction, the possible presence of a 2.03-Mev γ ray in the coincident distribution could not be ignored. Only when the minimum annihilation in flight background was subtracted, could a 2.03-Mev γ ray be fitted into the observed distribution as shown in Fig. 3. The intensities of the 2.43, 1.8, and 1.28-Mev γ rays are not appreciably changed by this fit.

The coincident 1.8-Mev γ ray was assigned to (138 sec)Al^{28}, produced in the $Si^{30}(d,\alpha)$ reaction.[11] The intensity of the 1.8-Mev γ ray was in approximate agreement with expectations based on calculation of chance coincidences and bremsstrahlung—1.8-Mev γ-ray coincidences.[12]

The peak labelled *0.51-Mev γ ray* in Figs. 2 and 3 was produced by the chance pile-up of annihilation quanta in the *γ-ray* counter while one of the quanta was in true coincidence with its twin in the *β^+ annihilation γ-ray* counter. Measurements made with a pure positron source (N^{13}) verified this hypothesis and calculations based on this measurement yielded an intensity for the chance peak in reasonable agreement with observation.

The half-life of the coincident pulse distribution was also measured and found to be the same as that of P^{29}, when the 1.8-Mev γ-ray pulses were assigned to Al^{28}.

In order to be able to determine branching ratios from the data of Figs. 2 and 3, the coincidence system was calibrated for γ-ray intensity per positron with the known[13] positron radioactivity Na^{22} in the identical geometry. The branching ratios of the decay of P^{29} to Si^{29} are listed in Table II.

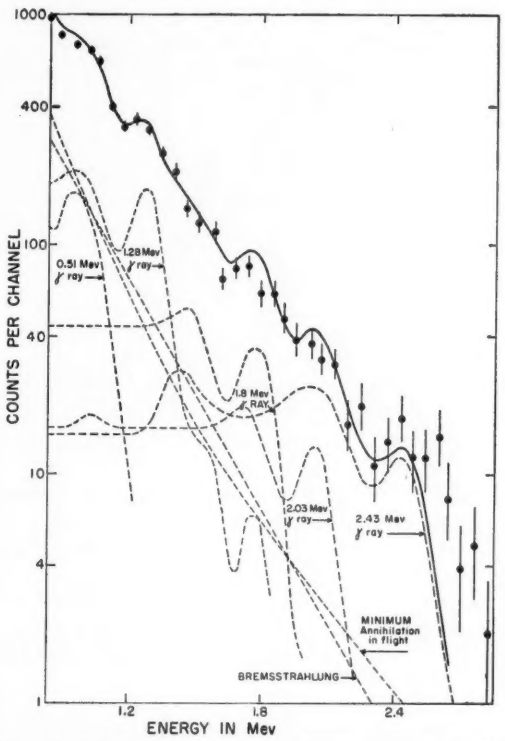

FIG. 3. Pulse energy distribution of P^{29} radiation coincident with pulses >0.4 Mev. Composite graph showing fit of the sum of 1.28-, 1.8-, 2.03-, and 2.43-Mev γ rays plus minimum continuous background.

VI. CASCADE TRANSISITONS AND Al^{29} DECAY

393-sec Al^{29} decays by β^- emission to the excited states of Si^{29}.[11] Previous investigation[14] had left some doubt as to which excited states of Si^{29} were involved in the Al^{29} decay. Therefore the γ rays from the decay of Al^{29} were investigated to clarify this matter and also to obtain further information about possible cascade transitions between the low excited states of Si^{29}.

Al^{29} was produced by an (n,p) reaction on Si. Gamma rays, from the radioactivity thus produced, yielded the pulse energy distribution shown in Fig. 4. The 1.28-Mev and 2.43-Mev γ rays are assigned to Al^{29} while the 1.78-Mev γ ray is assigned to Al^{28}.[15] Cascade γ-ray

TABLE II. Branching ratios of the P^{29} decay to Si^{29}.

Level of Si^{29}[a] (Mev)	Branching ratio (percent)
2.43	$0.24^{+0.26}_{-0.08}$
2.03	≤ 0.15
1.28	0.80 ± 0.20
0	98.8 ± 0.4

[a] An upper limit to the branching ratios to higher excited states of Si^{29} was calculated to be 0.05 percent.

[8] Annihilation in flight has been observed and compared with theory by Gerhart, Carlson, and Sherr, Phys. Rev. **94**, 917 (1954). We are very much indebted to Dr. Sherr for sending us a manuscript of this paper prior to publication and for enlightening discussions.

[9] W. Heitler, *The Quantum Theory of Radiation* (Oxford University Press, London, 1944), second edition, pp. 151–177, 204–209, 230–231.

[10] H. Roderick, Ph.D. thesis, Stanford University, 1954 (unpublished), Appendix I.

[11] Hollander, Perlman, and Seaborg, Revs. Modern Phys. **25**, 469 (1953).

[12] The relative yield of Al^{28} to P^{29} was determined from half-life measurements of pulses >1.4 Mev.

[13] R. Sherr and R. H. Miller, Phys. Rev. **93**, 1076 (1954).

[14] Seidlitz, Bleuler, and Tendam, Phys. Rev. **76**, 861 (1949).

[15] Al^{28} was produced in the $Si^{28}(n,p)$ reaction.

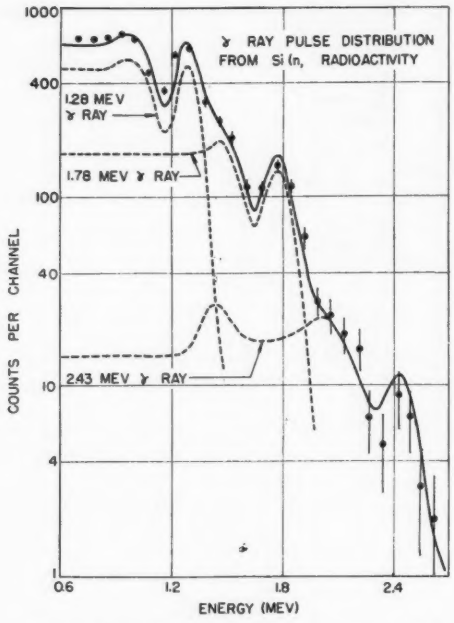

FIG. 4. γ-ray pulse energy distribution from Al^{28} and Al^{29} radioactivity produced by $Si(n,p)$ reaction.

transitions were sought, using two NaI counters in a coincidence arrangement similar to that shown in Fig. 1. All coincidences found were accounted for by other processes, that is, cosmic ray and room background, chance coincidences and γ-ray—bremsstrahlung coincidences. An upper limit to the amount of 1.15-Mev γ ray in coincidence with the 1.28-Mev γ ray was calculated to be 11 percent of the total decays. Tables III and IV lists the intensities of the γ rays found in the decay of Al^{29} and the calculated branching ratios and *ft* values to the excited levels of Si^{29}.[16]

VII. β RAYS OF P^{29}

The end-point energy of the P^{29} positron transition to the ground state of Si^{29} was accurately measured with a lens-type magnetic spectrometer and found to be equal to 3.945±0.005 Mev.[17] The *ft* values of the competing β^+ transitions from P^{29} are listed in Table V.

VIII. DECAY SCHEME OF P^{29}

The decay scheme of P^{29} is shown in Fig. 5. The 2.43-Mev and 1.28-Mev excited levels of Si^{29} are both assigned spin 3/2, even parity, since the ground state of Si^{29} and hence of P^{29} is known to have spin 1/2, even parity.[18,19] Al^{29} is assigned spin 5/2, even parity. Since only lower limits to the *ft* values to the 2.03-Mev level of Si^{29} could be set from both P^{29} and Al^{29} and these limits were such that allowed β transitions were possible, no spin or parity assignment of the 2.03-Mev level could be made from this work.[20]

IX. DISCUSSION

A. Shell Model

The above-designated parity and spin uniquely define the orbital angular momentum of the various states that could be assigned on the basis of the single-particle shell model. These assignments are in agreement with Mrs. Mayer's shell model.[21] $_{13}Al^{29}$ has 13 protons in its odd group which leaves one vacancy in the $d_{5/2}$ shell, while Si^{29} and P^{29} have 15 particles in the odd group which assigns the 15th particle to sole occupancy in the $2s_{1/2}$ shell. The assignment of $d_{3/2}$ to the 1.28-Mev level and/or the 2.43-Mev level is consistent with the statement that the low excited states should be those in which the odd nucleon is raised to another level in the same shell, which in this case is $d_{5/2}$ or $d_{3/2}$.[21]

B. Related Experiments

Agreement between the above assigned spins and parities and the results of the (d,p) stripping[19,22] and (n,γ)[23] reactions on Si^{28} is generally good. However, an

TABLE III. Intensity of γ rays from Al^{29}.

γ-ray energy (Mev)	Intensity per decay (percent)
2.43	9.4±2.1
2.03	⩽ 3.8
1.28	89 ±3.4
1.15	⩽10.8

TABLE IV. Branching ratios of Al^{29} decay to Si^{29}.[a]

Level of Si^{29} (Mev)	Branching ratio (percent)	Log(*ft*)[b]
2.43	15±9	5.0±0.4
2.03	⩽3.8	⩾6.0
1.28	85±9	5.3±0.2

[a] Assuming no decay to the ground state.
[b] Assuming a total decay energy of Al^{29} equal to 3.98±0.10 Mev (see reference 16).

[16] After completion of this work the published paper of M. Nahmias and A. Wapstra, J. phys. et radium **15**, 570 (1954) was received. They find, for the Al^{29} decay, branching ratios of 25 and 75 percent to the 2.43- and 1.28-Mev levels, respectively. They measure the end-point energy of the weaker β^- spectrum to be 1.55±0.10 Mev.

[17] This result has been previously reported: H. Roderick and C. Wong, Phys. Rev. **92**, 204 (1953). However, a numerical mistake led to an overestimation of the error reported.

[18] Williams, McCall, and Gutowsky, Phys. Rev. **93**, 1428 (1954).

[19] J. R. Holt and T. N. Marsham, Proc. Phys. Soc. (London) **A66**, 467 (1953).

[20] The results of the $Si^{28}(d,p)$ stripping experiment of reference 19 lead to an assignment of even parity and spin 3/2 or 5/2 to the 2.03-Mev level.

[21] M. G. Mayer, Phys. Rev. **78**, 16 (1950).

[22] C. F. Black, Phys. Rev. **90**, 381 (1953).

[23] Kinsey, Bartholomew, and Walker, Phys. Rev. **83**, 519 (1951). Results revised in B. B. Kinsey and G. A. Bartholomew, Phys. Rev. **93**, 1260 (1954). We are indebted to Professor Kinsey for sending us a preprint and for private communication of his results.

isotropic angular distribution has been found for the (d,p) reaction to the 2.43-Mev level, but there is reason to doubt this result.[19]

In the $Si^{28}(n,\gamma)$ work[23] the existence of an observable γ-ray transition between the neutron capture level and the ground state of Si^{29} is of considerable interest. This transition should be strictly forbidden if the states concerned could really be expressed by $s_{1/2}$ single particle orbitals. However, as discussed below, the ground state of Si^{29} can be considered to be a mixture of $S_{1/2}$ and $P_{1/2}$ states with even parity. In that case the transition could be considered $M1$ and the observed intensity is in reasonable agreement with that calculated from Weisskopf's formula.[24]

C. Image Transition

The ft value of the image transition P^{29} (see Table IV) is in good agreement with the results obtained using the coupling constants of β decay determined by Winther,[25] if the ground states of Si^{29} and P^{29} are assumed to be a roughly equal mixture of $S_{1/2}$ and $P_{1/2}$ states of even parity.[26] The amount of this mixture is determined by the magnetic moment of Si^{29} (0.55 nm[27]). Similarly, Bohr's theory of the nucleus[28] leads to reasonably good agreement between the observed ft value and that calculated from Winther's constants (and also to agreement with the magnetic moment of Si^{29}), if the ground state of Si^{29} is made up of the superposition of single-particle orbital states $s_{1/2}$, $d_{3/2}$, and $d_{5/2}$ with expectation values 1/3, 1/6, and 1/2, respectively.

TABLE V. ft values of P^{29} decay to Si^{29}.

Level of Si^{29} [a] (Mev)	End-point energy of β^+ spectrum (Mev)	Log (ft) [b]
2.426±0.007	1.519±0.009	$4.51\ ^{+0.17}_{-0.32}$
2.027±0.007	1.918±0.009	≥ 5.15
1.278±0.007	2.667±0.009	5.03 ±0.11
0	3.945±0.005	3.723±0.007

[a] See reference 5.
[b] The ft value includes both positron emission and electron capture.

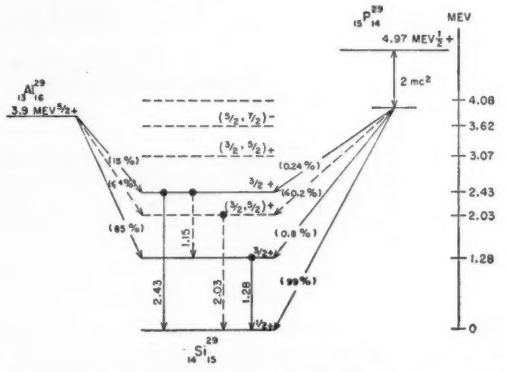

FIG. 5. Decay schemes of P^{29} and Al^{29}. Known levels of Si^{29} which presumably are not reached in either decay are shown with dotted lines. The upper limit for the intensity of the 1.15-Mev γ ray is roughly equal to the intensity of the 2.43-Mev γ ray.

D. Transitions to the Excited States

Since the ground state of Si^{29}, and hence of P^{29}, can be considered as a mixture of states with different l values, it is not surprising that an allowed-unfavored β^+ transition occurs to the 1.28-Mev level ($d_{3/2}$) in spite of the l-forbiddenness rule.[29]

In fact one can calculate from the ft values given in Table IV that the 1.28- and 2.43-Mev levels of Si^{29} can be thought of as states of even parity and $D_{3/2}$ character with minimum $P_{3/2}$ admixtures of 3.6 and 12 percent, respectively.[26] There is also other evidence that the 2.43-Mev level is a many-particle state.[19] The unfavored factors[28] F of 0.096±0.025 and $0.32^{+0.34}_{-0.10}$ calculated for the transitions to the 1.28- and 2.43-Mev levels, respectively, are of the same order of magnitude as those of other allowed-unfavored transitions listed in Bohr's work.[28]

We would like to thank Dr. L. G. Mann and Mr. H. I. West, Jr. for their help with the experiments, and Dr. E. Feenberg for many stimulating discussions.

[19] J. M. Blatt and V. F. Weisskopf, *Theoretical Nuclear Physics* (John Wiley and Sons, Inc., New York, 1952), p. 627.
[23] A. Winther and O. Kofoed-Hansen, Kgl. Danske Videnskab. Selskab, Mat.-fys. Medd. **27**, No. 14 (1953).
[26] E. Feenberg (private communication).
[27] S. S. Dharmatti and H. Weaver, Phys. Rev. **84**, 843 (1951).
[28] A. Bohr and B. R. Mottelson, Kgl. Danske Videnskab. Selskab, Mat.-fys. Medd. **27**, No. 16 (1953).
[29] Mayer, Moszkowski, and Nordheim, Revs. Modern Phys. **23**, 315 (1951).

Half-Life of Yttrium-90*

HERBERT L. VOLCHOK AND J. LAURENCE KULP
Lamont Geological Observatory, Columbia University, Palisades, New York
(Received September 10, 1954)

A series of determinations on the half-life of yttrium-90 have been made, resulting in an average value of 64.24±0.30 hours. Y^{90} was separated from its Sr^{90} mother by either a carbonate or phosphate precipitation, followed by conversion to oxalate as the final counting vehicle. The efficiency of the chemical separations, precision of the determinations, and good agreement with the latest published results suggest that the half-life of this nuclide is now known to an accuracy of 0.7 percent.

PAST measurements of the half-life of Y^{90} have resulted in values ranging from 60.5±2 hours[1] to 65 hours[2,3] with intermediate values of 61±1 hours,[4] 62 hours,[5] and most recently 64.60±0.43 hours.[6] As a by-product of the use of certain radioactive tracers to study the separation of alkaline earth and rare earth elements, a new determination of the half-life of Y^{90} has been made, giving 64.24±0.30 hours.

A Sr^{90}—Y^{90} calibrated standard supplied by the National Bureau of Standards was utilized in the study. The chemical technique consisted of a two step procedure, (*a*) a precipitation to separate the Sr^{90} from the Y^{90} and, (*b*) a re-precipitation of the Y^{90} in a form suitable for beta counting. The separation step was carried out either by the precipitation of the phosphate or the hydroxide of yttrium. In hot well-stirred HCl solution, in the presence of excess phosphate ions, the phosphate of yttrium is completely precipitated below *p*H of 1.5, but strontium phosphate does not crystallize until about *p*H of 2.2. Careful *p*H control produces a quantitative removal of Y with negligible quantities of strontium. (Less than 0.05 percent of the initial activity of the separated yttrium precipitate can be attributed to Sr^{90}.) The hydroxide separation consists merely of adding NH_4OH to the acid solution until the gelatinous $Y(OH)_3$ precipitate appears at about *p*H of 8. In both separation methods sufficient "dead" yttrium is added to carry the Y^{90}. The precipitate is washed with distilled water after which the filtrate and washings are stored for re-accumulation of Y^{90} and subsequent milking. The precipitate is then dissolved off the filter paper with warm, dilute HCl solution. The re-precipitation step is identical for both phosphate and hydroxide methods. Concentrated NH_4OH is added dropwise to the yttrium solution until the first signs of precipitation appear, then dilute HCl is added dropwise to barely dissolve the precipitate. Concentrated oxalic acid is then added in excess. This results in an abundant, heavy precipitate of the crystalline yttrium oxalate. The oxalate precipitate is digested for about ten minutes before suction filtering through a steel precipitation funnel with one and one-eighth inch diameter Whatman No. 42 paper. The sample is dried by pulling air through the sample for about fifteen minutes after the filtrate had been removed. The filter paper with the yttrium oxalate sample (about 20 mg/cm²) is mounted under a thin pliofilm cover on a brass disk and ring assembly for counting.

TABLE I. Half-life measurements of Y^{90}.

Sample No.	Initial counts/min	Half-life (hours)
HC-97	1087±15	64.4±1.1
HC-98	1358±20	64.0±1.0
HC-99	1171±20	63.5±1.0
HC-100	940±10	65.0±0.5
HC-101	1010±10	64.3±0.4
HP-100	1220±10	64.6±0.5
HP-101	860±9	64.0±0.3
HP-102	1000±10	63.5±0.5
HP-103	1260±11	64.5±0.5
	Average 64.24±0.30	

The counting apparatus consists of an Anton Electronic Laboratories Model 1007 mica window flat Geiger counter. The counter is mounted in a special Lucite housing to insure reproducible geometry in sample changing. The normal background of this unit, encased in a lead shield and an anticoincidence ring, is 2.51±0.03 counts per minute on a "dead" yttrium sample.

A total of 9 samples were prepared in this way and periodically counted over a period of about three weeks (about 8 half-lives). Semilogarithmic plots of the data gave well-defined decay curves. The pertinent data are presented in Table I.

The samples with letters HC were run as hydroxides in step (*a*) while those with HP were precipitated as phosphates. The average value for the half-life has been calculated by weighting the individual value with the reciprocal of the square root of the error of the particular run. The error on the average is 2σ for the nine runs (95 percent confidence level). The final result of 64.24 ±0.30 is in good agreement with the determination by Chetham-Strode and Kinderman.[6]

* This research was supported by a contract with the U. S. Atomic Energy Commission. Lamont Geological Observatory Contribution No. 126.

[1] Stewart, Lawson, and Corls, Phys. Rev. **52**, 901 (1937).

[2] A. Notlorf, *Radiochemical Studies: The Fission Products*, edited by C. D. Coryell and N. Sugarman (McGraw-Hill Book Company, Inc., New York, 1951), Paper No. 77, National Nuclear Energy Series, Plutonium Project Record, Vol. 9, Part V.

[3] G. L. Schott and W. W. Meinke, Phys. Rev. **89**, 1156 (1953).

[4] M. Bothe, Z. Naturforsch. **1**, 179 (1946).

[5] R. H. Goeckermann and I. Perlman, Phys. Rev. **76**, 628 (1949).

[6] A. Chetham-Strode, Jr., and E. M. Kinderman, Phys. Rev. **93**, 1029 (1954).

Energy Levels of Hf^{177}†

P. MARMIER AND F. BOEHM
California Institute of Technology, Pasadena, California
(Received September 3, 1954)

The nuclear spectrum of Lu^{177} has been investigated. Three excited levels of Hf^{177} have energies of 112.97 kev, 249.69 kev, and 321.33 kev. A decay scheme is proposed.

THE decay of 6.8-day Lu^{177} has been studied with the curved-crystal γ-ray spectrometer and the axial-focusing β-ray spectrometer. High specific activity Lu^{177} was produced by irradiation of 1.5 mg of lutecium chloride in the Arco reactor.[1] A source of about 200 mC was used in the γ-ray spectrometer and several weak β-ray sources were prepared by evaporation. The momentum resolution obtained with the β-ray spectrometer was 0.15 percent.

In addition to the well-known lines at 113 kev, 208 kev, and 321 kev, weak lines were found at 72 kev and 250 kev (Table I). The conversion coefficients of the 113-kev and 208-kev transitions show that they are, respectively, $E2$ and $E1$ transitions, in agreement with the results of McGowan *et al.*[2] From the L-conversion data (Fig. 1) it can be concluded that the 113-kev transition has pure $E2$ character, the upper limit of an $M1$ admixture being 2 percent. The conversion coefficient of the 321-kev crossover line indicates an $E3$ or $M1$ transition, rather than an $E1$. In order to agree with the requirement of parity change indicated by the multipolarity of the 113-kev and 208-kev lines, the $M1$ possibility must be eliminated. No conversion electrons of the 72-kev line could be detected. The small conversion probably indicates an $E1$ transition. The 250-kev line is strongly converted and is probably an $M1$ transition.

The ordering of the energy levels was established by coincidence measurements between γ rays and β-spectrum electrons, using a scintillation detector mounted at the source end of the β spectrometer for the detection of the photons. The end point of the spectrum going to the 321-kev level is 176-kev ($\log ft=6.3$) and that of the spectrum going to the 113 kev level is 384 kev ($\log ft=7.7$). The most intense spectrum leads to the ground state. Its upper limit has been found at 497 ± 2 kev, ($\log ft=6.8$) in agreement with the results of Douglas.[3] The 72-kev and 250-kev lines were too weak to permit coincidence work in the β spectrometer. Using

TABLE I. γ transitions in Hf^{177}.

Energy (kev)	Relative γ intensity	Absolute conversion coefficients α_K	α_{LI}	α_{LII}	α_{LIII}	Decay fraction percent	Multipolarity
71.644±0.020	2	...	...	...	...	0.1	($E1$)
112.965±0.020	100	0.75	0.12	0.70	0.58	10	$E2$
208.362±0.020	220	0.044	0.007	...	...	7	$E1$
250.0 ±0.5	3	0.3	0.1	...	...	0.1	($M1$)
321.36 ±0.10	3.2	0.2	...	...	...	0.1	($E3$)

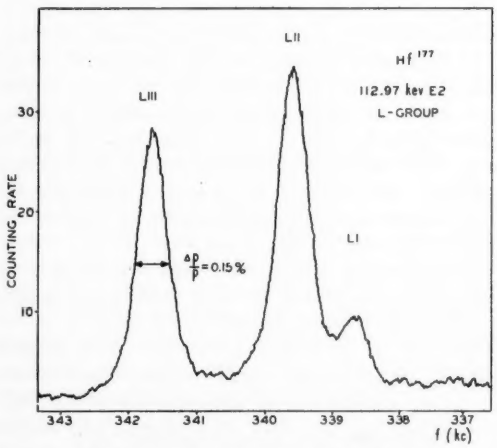

FIG. 1. L-conversion spectrum of the 113-kev line.

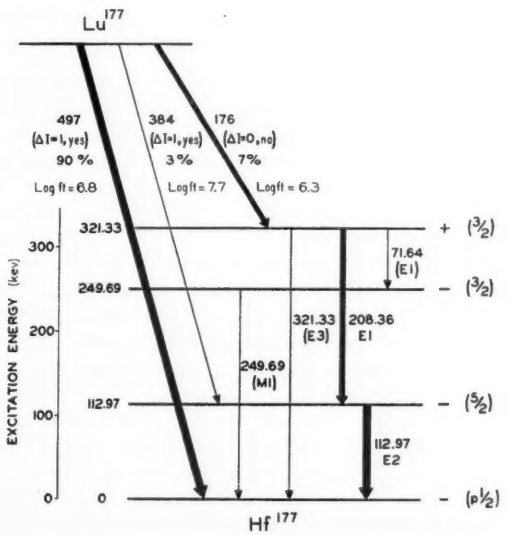

FIG. 2. Proposed energy level scheme for Hf^{177}. Data in parentheses ( ) are uncertain.

† Assisted by contracts with the U. S. Atomic Energy Commission and the Office of Ordnance Research (U. S. Army).

[1] We wish to thank Dr. R. B. Day, Los Alamos Scientific Laboratory, who suggested these measurements and made the arrangements for procurement of the source.

[2] McGowan, Klema, and Bell, Phys. Rev. 85, 152 (1952).

[3] D. G. Douglas, Phys. Rev. 75, 1960 (1949).

two scintillation spectrometers in coincidence it was however possible to show that the two lines are in cascade. The 250-kev line might be identical with the one reported by Temmer and Heydenburg,[4] found by Coulomb excitation of an odd Hf isotope.

The proposed decay scheme appears in Fig. 2. The intensity ratio of the 72-kev and 208-kev lines is in agreement with the value expected from the theoretical lifetime relation.[5] On the same basis, however, the relative intensity of the 321-kev line is much larger than that expected for an $E3$ transition. No transition was observed between the 250-kev and 113-kev levels.

According to their ft value, spin and parity change, the three β spectra can be classified as allowed, $\Delta I=0$, no (176 kev); first forbidden $\Delta I=1$, yes (384 kev); and first forbidden $\Delta I=1$, yes (497 kev). The spin of the ground state of Hf^{177} is either $\frac{1}{2}$ or $\frac{3}{2}$.[6] The shell model predicts a $p_{\frac{1}{2}}$ configuration,[7] which is used as a basis for the tentative spin assignment in Fig. 2. According to McGowan's angular correlation experiments[2] the 208-kev—113-kev dipole-quadrupole cascade involves a spin change of $+1$ and -2 units and a spin 7/2 for the intermediate level (113 kev). A spin 5/2 for this level, however, would not be in serious contradiction with McGowan's results. One finds then a spin $\frac{3}{2}$ and even parity for the ground state of Lu^{177}, which is not in contradiction with the predictions of the shell model. We would like to acknowledge the interest of Professor Jesse W. M. DuMond in this work. We are indebted to Mr. E. Hatch and Mr. P. Snelgrove for their help during the measurements.

[4] G. M. Temmer and N. P. Heydenburg, Phys. Rev. **94**, 1399 (1954).
[5] R. Montalbetti, Can. J. Phys. **30**, 660 (1952).
[6] E. Rasmussen, Naturwiss. **23**, 69 (1935).
[7] P. F. A. Klinkenberg, Revs. Modern Phys. **24**, 63 (1952).

PHYSICAL REVIEW VOLUME 97, NUMBER 1 JANUARY 1, 1955

Angular Distribution of Gamma Rays from Proton Capture in B^{11}

H. E. Gove and E. B. Paul
Physics Division, Atomic Energy of Canada Limited, Chalk River, Ontario, Canada
(Received September 2, 1954)

The γ-ray yield at 90° from the bombardment of B^{11} by protons shows resonances for proton energies of 0.67, 1.4, and 2.7 Mev. The angular distributions of the two γ rays of high energy, $\gamma_0\sim17$ Mev and $\gamma_1\sim12$ Mev, have been measured at these resonances to obtain evidence concerning the spins and parities of the excited nucleus. The evidence favors 2− for the 0.67-Mev resonance, 1− for that at 1.4 Mev, and 2+ at 2.7 Mev, but these assignments cannot be made with certainty.

I. INTRODUCTION

THE most recent and most complete investigation to date on the capture gamma radiation from proton bombardment of B^{11} is that of Huus and Day.[1] A brief summary of this work follows. Using a sodium iodide scintillation counter they have examined the gamma-ray spectrum and find the capture gamma rays which occur in a direct transition to the ground state of C^{12} and in a cascade through the 4.44-Mev level in C^{12}. Yield curves for the transition to the ground state ($h\nu\sim17$ Mev) and to the first excited state at 4.44 Mev ($h\nu\sim12$ Mev) were measured at 90° at proton energies from 0.15 Mev to 2.8 Mev. Cross sections for the various gamma rays were also measured. In addition to the well-known resonance at 0.163 Mev, resonances were observed at 0.675 with $\Gamma=0.33$ Mev and at 1.388 with $\Gamma=1.27$ Mev. Spins and parities of these states are deduced from these measurements and measurements of the $B^{11}(p,\alpha)Be^8$ reaction made by Beckman, Huus, and Zupančič[2] to be 2− or 3+ for the 0.675 resonance and 1− for the 1.388 resonance. The latter result is based primarily on single-particle limit[3] and radiation width[4] considerations. In addition, the yield curve for a 2.13-Mev gamma ray produced in an inelastic scattering reaction involving the first excited state of B^{11} was observed and showed a resonance at 2.664 Mev with a width of 48 kev. A comprehensive list of references to previous work in this field is contained in the paper of Huus and Day.

Recently some measurements on the angular distributions of the ground and first excited state gamma transitions have been reported[5] by Givin *et al.*

The work to be reported here comprises measurements of the yield curve at 90° to the proton beam of the capture gamma rays in the range of proton energies between 0.55 and 2.85 Mev. In addition, their angular distributions have been measured at several energies in this range.

[1] T. Huus and R. B. Day, Phys. Rev. **91**, 599 (1953).
[2] Beckman, Huus, and Zupančič, Phys. Rev. **91**, 606 (1953).
[3] T. Teichmann and E. P. Wigner, Phys. Rev. **87**, 123 (1952).
[4] J. M. Blatt and V. F. Weisskopf *Theoretical Nuclear Physics* (John Wiley and Sons, Inc., New York, 1952), first edition, p. 627 S. Moszkowski, Phys. Rev. **89**, 474 (1953).
[5] Givin, Farney, Hahn, and Kern, Phys. Rev. **95**, 641(A) (1954).

II. BEAM AND TARGET ARRANGEMENT

The Chalk River electrostatic generator provided the source of bombarding protons. The protons were analyzed in momentum by a 90° magnet whose field was held constant by a proton resonance fluxmeter. A pair of tantalum slits at the exit of this magnet provided a signal to control the corona load and this kept the proton energy constant to about 0.1 percent. The protons passed along a fifteen-foot section of evacuated tubing terminated with a hollow brass cylinder with $\frac{1}{16}$-in. walls containing the target. This arrangement ensured cylindrical symmetry in the gamma-ray absorption. A $\frac{1}{8}$-in. diameter aperture in a 0.02-in. thick tantalum disk located about four feet from the target defined the beam to a spot on the target $\frac{1}{4}$-in. in diameter. Beam currents were normally from five to twenty microamperes.

The target was prepared by mixing finely powdered boron with benzene and spreading evenly on a 0.04-inch tantalum backing and allowing to dry. In the process of drying the powder tended to concentrate

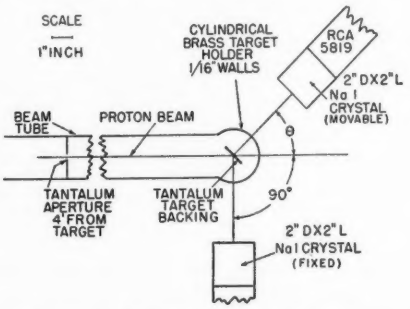

FIG. 1. Schematic diagram of experimental arrangement.

in small patches producing a somewhat nonuniform thickness varying from zero to 200 kev. Later evaporated targets were prepared but most of the work reported here was done with the powder.

The gamma rays were measured in a sodium iodide scintillation counter consisting of a NaI(Tl) crystal 2 in. in diameter and 2 in. long mounted in a polished aluminum case and coupled optically to an RCA 5819 photomultiplier by a short Lucite light pipe. Output pulses were amplified by a linear amplifier and displayed on a thirty-channel pulse-height analyzer. A similar scintillation counter was used as a monitor for angular distribution measurements. The counter subtended a solid angle of about 1 percent. The target and counter arrangements are illustrated in Fig. 1.

III. EXPERIMENTAL PROCEDURE

Both the 90° yield curve and the angular distributions were obtained by recording the complete gamma-ray spectrum on the thirty-channel pulse height analyzer as a function of proton energy or angle. Typical spectra are shown in Figs. 2 and 3. Figure 2 shows

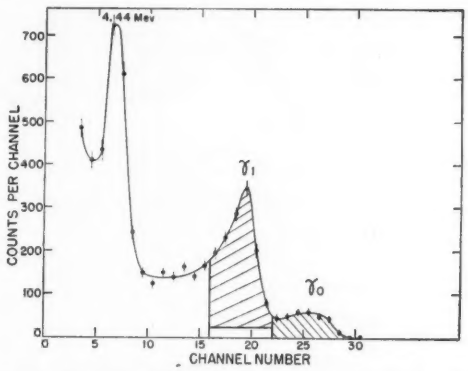

FIG. 2. Spectrum of high-energy gamma rays emitted at the 0.67-Mev resonance in $B^{11}(p,\gamma)$, showing the ground state transition γ_0, the transition γ_1 to the first excited state in C^{12} at 4.44 Mev, and the cascade gamma ray of energy 4.44 Mev. The two shaded areas were taken as proportional to the yields of γ_0 and γ_1 respectively.

the gamma-ray spectrum measured near the 0.68-Mev resonance while Fig. 3 shows the spectrum near the 1.4-Mev resonance. The yield or angular distribution of the capture gamma ray to the ground state of C^{12} ($h\nu \sim 17$ Mev) was obtained by counting only the pulses in channels beyond those corresponding to the transition to the first excited state. However, to measure the yield or angular distribution of this latter gamma ray the contributions from the Compton tail of the ground-state gamma ray must be subtracted. To determine the shape of the gamma-ray spectrum, measurements were made on a single energy gamma ray from the $F^{19}(p,\alpha\gamma)$ reaction, $E_\gamma = 6.13$ Mev, which showed that a long flat portion exists in the spectrum below the pair peaks—the ratio of height of the pair peak to this flat portion being about 3.5 for a crystal 2 in. in diameter and 2 in. long. The results on boron indicate that at gamma energies around 14 Mev this ratio had dropped to about 2.5. It is then only necessary to subtract from the region under the 12-Mev gamma-

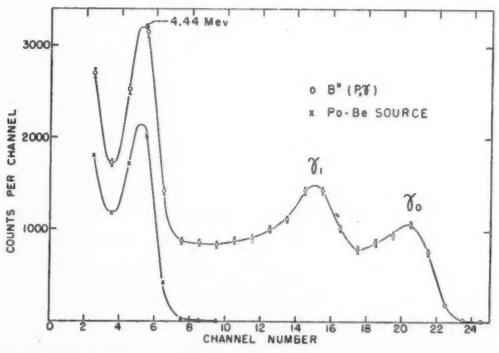

FIG. 3. Spectrum of high-energy gamma rays emitted near the 1.4-Mev resonance in $B^{11}(p,\gamma)$, showing the ground state transition γ_0, the transition γ_1 to the first excited state in C^{12} at 4.44-Mev, and the cascade gamma ray of energy 4.44 Mev. This is compared with the same gamma ray from a Po-Be source.

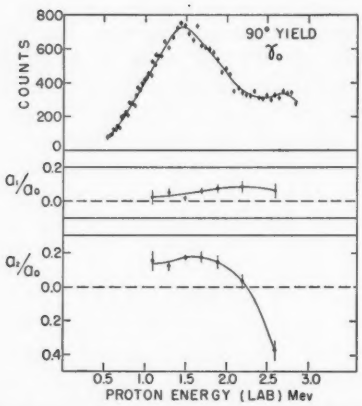

FIG. 4. The upper curve shows the 90° yield curve of gamma rays leading to the ground state of C^{12} from proton capture in B^{11}. The two lower curves show the variation of the coefficients of the Legendre polynomial expansion of the angular distribution of this gamma ray, $W(\theta)=P_0+(a_1/a_0)P_1+(a_2/a_0)P_2$, with proton bombarding energy.

ray spectrum an amount equal to 0.4 times the peak of the 17-Mev gamma-ray spectrum. Figure 2 is a spectrum taken during the 90° yield measurements and the shaded areas show the actual quantity that was taken to be proportional to the yield of the two high-energy gamma rays.

The angular distributions were measured by recording the spectrum at 10 to 20 angles between 0° and 150°. The distributions were measured at nine different energies between 0.8 and 2.6 Mev. A cobalt-60 source which could be placed in the target position was used to check that the angular symmetry was good to one or two percent.

In the yield measurements the beam current incident on the target was measured with a current integrator.[6] Because of the nonuniformity of the target mentioned above, these measurements were subject to more fluctuation than the angular distributions which were measured relative to the monitor counter.

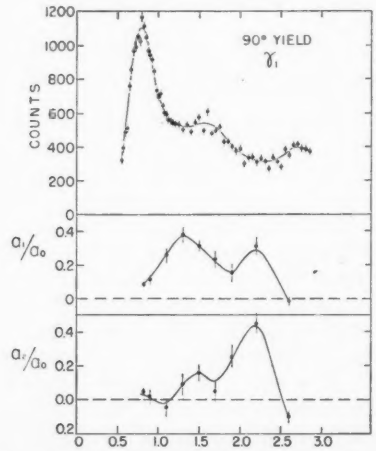

FIG. 5. The upper curve shows the 90° yield curve of gamma rays leading to the first excited state of C^{12} from proton capture in B^{11}. The two lower curves show the variation of the coefficients of the Legendre polynomial expansion of the angular distribution of this gamma ray, $W(\theta)=P_0+(a_1/a_0)P_1+(a_2/a_0)P_2$, with proton bombarding energy.

IV. EXPERIMENTAL RESULTS

The yield curves for the ground-state gamma transition (γ_0) and the transition to the first excited state (γ_1) are shown at the upper part of Figs. 4 and 5 respectively. No correction to the energy has been made for target thickness since it was not accurately known and hence the positions of the resonances on our energy scale are higher than those observed by Huus and Day.

Examples of the observed angular distributions taken at three different energies are shown in Figs. 6, 7, and 8. Figure 6 is the distribution of the capture gamma radiation leading to the first excited state of C^{12} measured at $E_p=0.85$ Mev, corresponding to the 0.68-Mev resonance. The ground state transition is not resonant here and is in fact quite weak, hence its angular distribution was not measured. Figure 7 shows the angular distribution of both the ground-state (γ_0) and the first excited state (γ_1) transition measured near the 1.4-Mev resonance. Figure 8 shows the distributions measured at 2.6 Mev. The angular distributions have been analyzed by the method of least squares in a Legendre polynomial expansion containing the terms P_0, P_1, and P_2. Figure 4 shows the P_1 coefficient a_1/a_0 and the P_2 coefficient a_2/a_0 plotted *versus* proton energy for γ_0 below the 90° yield curve of γ_0, while Fig. 5 shows corresponding data for γ_1. The probable error of each coefficient is given.

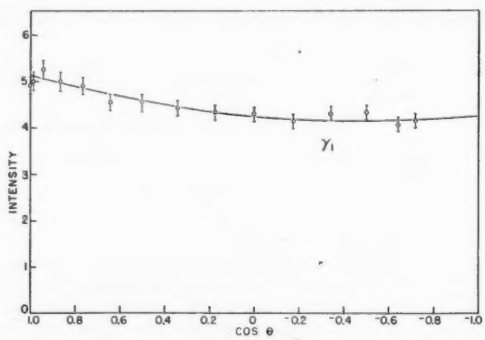

FIG. 6. The angular distribution of the gamma ray (γ_1) leading to the first excited state in C^{12}, taken at a proton energy corresponding to the 0.67-Mev resonance. The smooth curve is a least-squares fit to a series of Legendre polynomials up to P_2.

V. DISCUSSION

Theoretical expressions for (p,γ) angular distributions have been given recently by Biedenharn and Rose[7]

[6] H. T. Gittings, Rev. Sci. Instr. **20**, 325 (1949).

[7] L. C. Biedenharn and M. E. Rose, Revs. Modern Phys. **25**, 729 (1953).

and Sharp, Kennedy, Sears, and Hoyle.[8] In calculating the theoretical angular distributions, a spin[9] of $\frac{3}{2}$ and negative parity[10] for the B^{11} ground state has been used. The spin and parity of the ground and first excited state of C^{12} are 0+ and 2+ respectively.[9] We have assumed that contributions from orbital angular momentum greater than two for the incoming particles are negligible and that only radiations of electric or magnetic dipole or electric quadrupole character will be observed with any intensity. Under these circumstances no terms higher than P_2 will occur in the theoretical expressions and, in fact, none higher than P_2 are observed experimentally.

The yield curve for the ground-state gamma transition, Fig. 4, shows a broad resonance at 1.45 Mev on our energy scale and probably another one of low intensity at about 2.7 Mev. Both of these also appear in the yield curve for the first excited state gamma transition and in addition a resonance at 0.8 Mev is observed. This corresponds to the 0.67-Mev resonance of Huus and Day.

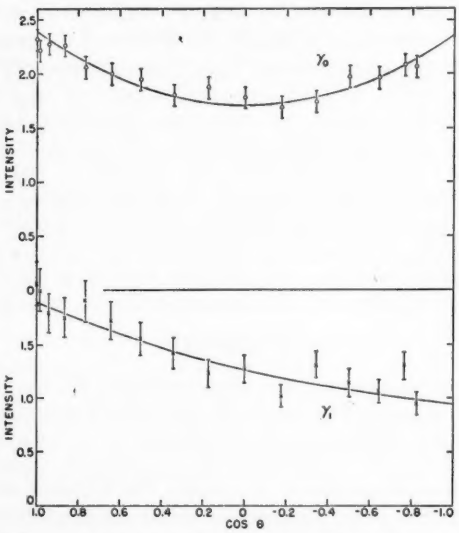

FIG. 7. The upper curve shows the angular distribution of the gamma ray (γ_0) leading to the ground state of C^{12}, and the lower curve that of the gamma ray (γ_1) leading to the first excited state of C^{12}, taken at a proton energy near the resonance at 1.4 Mev. The smooth curves are least-squares fits to a series of Legendre polynomials up to P_2.

Since the level at 0.67 Mev is not resonant for either γ_0 or α_0, its spin and parity are expected to be 2− or 3+. The angular distribution of γ_1 is consistent with either assignment. However, arguments based on single-particle limits and gamma-ray transition probabilities favor the 2− assignment. In this case the (p,α_1) cross-section measurements of Beckman *et al.*[2] give equal partial widths for proton formation and α_1 decay of 165 kev while those of French[11] give either 290 kev or 40 kev. The single-particle widths calculated according to Lane[12] are 350 kev for s-wave protons and 20 kev for p-wave which indicates an assignment of 2− for this state. This is consistent with the observed gamma-ray partial width.[4] *Note added in proof.*—The angular distribution of the 12-Mev radiation has been measured by Grant, Flack, Rutherglen, and Deuchars, Proc. Phys. Soc. (London) **67A**, 751 (1954), from 0.4 to 0.67 Mev. Assuming $J=1^-$ for the 1.4-Mev resonance, they conclude that the 0.67-Mev resonance has $J=2^+$.

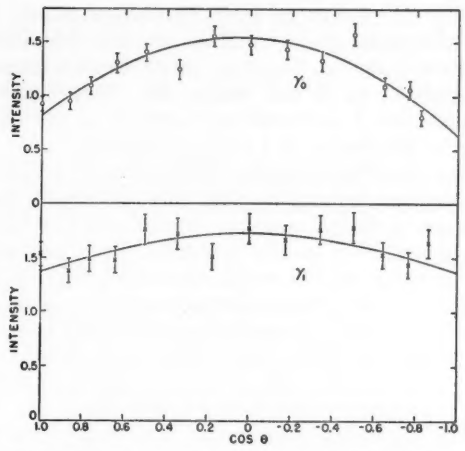

FIG. 8. The upper curve shows the angular distribution of the gamma ray (γ_0) leading to the ground state of C^{12}, and the lower curve that of the gamma ray (γ_1) leading to the first excited state of C^{12}, taken at a proton energy of 2.6 Mev. The smooth curves are least squares fits to a series of Legendre polynomials up to P_2.

The level at a proton bombarding energy of 1.4 Mev is resonant for γ_0 and γ_1 as well as for[2] α_0 and α_1 from the $B^{11}(p,\alpha)$ reaction. Hence its spin and parity are almost certainly either 2+ or 1−. When one takes account of all the present experimental evidence, it appears that there is still some ambiguity as to which of these two assignments is correct.

The experimental angular distributions for (p,γ_0) show a small P_1 term (Fig. 4) which rises slowly from a value of ~0.03 at 1.1 Mev to ~0.1 at 2.6 Mev. Hence it appears that interference effects between states of opposite parity which decay by emission of γ_0 are small and may be due to a broad level higher than 2.8 Mev. The P_2 coefficient remains substantially constant at +0.17 from 1.1 to 1.9 Mev (the region covered by the 1.4-Mev resonance) and then drops

[8] Sharp, Kennedy, Sears, and Hoyle, Tables of Coefficients for Angular Distributions, Atomic Energy of Canada Limited, Chalk River Project, AECL-97, December 1953 (unpublished).

[9] F. Ajzenberg and T. Lauritsen, Revs. Modern Phys. **24**, 321 (1952).

[10] J. R. Holt and T. N. Marsham, Proc. Phys. Soc. (London) **A66**, 1032 (1953).

[11] A. P. French and G. A. Dissanaike (as quoted by Beckman *et al.*, reference 2).

[12] A. M. Lane, Atomic Energy Research Establishment Report AERE T/R 1289, Harwell, England, January 1954 (unpublished).

rapidly to −0.4 at 2.6 Mev. The constancy over the 1.4-Mev resonance may indicate very little interference between states of the same parity which decay by emission of γ_0 in this region. We shall, therefore, assume that a noninterference analysis of the (p,γ_0) angular distribution at 1.4 Mev is justified.

The theoretical angular distribution for a spin of 2+ for this resonance agrees with experiment for a mixture of channel spin 2 to channel spin 1 of 0.5 for the ground-state gamma transition. There are many parameters in the theoretical expression for the angular distribution of γ_1 for $J=2+$ and no useful conclusions can be deduced. The coefficient of the odd Legendre polynomial P_1 which occurs in the (p,γ_1) distribution (Fig. 5) could also indicate that the state at 1.4 Mev has the opposite parity to that at 0.67 Mev.

The theoretical distribution for $J=1-$ for the ground-state transition also fits the observed distribution if only channel spin 2 participates. Since the channel spin mixture of formation should be independent of the mode of decay, the P_2 coefficient for the first excited state transition γ_1 can be calculated to be 0.02. The observed value is 0.12 which may reflect interference with the other negative-parity state at 0.67 Mev.

Some support for the assignment of 2+ comes from the relative intensities of the two alpha groups at this resonance which favor the transition to the first excited state of Be^8 (assumed 2+) to the ground state 0+ by a factor of 10–20 to one.[2,13] This can be explained in part if the compound level is 2+, since d-wave alphas are required for the ground state while s-wave alphas could decay to the first excited state. This gives a computed factor of 4 in favor of the latter. If the compound state were 1−, the groups would be expected to have equal intensity from barrier penetrabilities. One cannot regard this as a very conclusive argument.

The arguments favoring an assignment of $J=1-$ for the resonance at 1.4 Mev are the following. From the $B^{11}(p,\alpha_1)$ cross-section measurements of Beckman *et al.*[2] and French and Dissanaike,[11] the proton width of formation is about 1.1 Mev if one assumes it to be larger than the alpha width. This is greater than the single-particle limit for p-wave formation.[12] If, however, the alpha width is assumed to be the larger, p-wave formation and hence $J=2+$ is permitted. This has the effect of making the partial widths for emission of γ_0 and γ_1 of the order of a few hundred electron volts which is greater than one might expect.[4]

Recent work[14] on the angular distribution of γ_0 at the 0.163-Mev resonance shows an appreciable P_1 term. This may indicate interference between this resonance and the broad 1.4-Mev resonance. Since the 0.163-Mev resonance is very probably 2+,[9] this would imply that the 1.4-Mev resonance is 1−.

Measurements on the $B^{11}(p,\alpha_1)$ distribution up to 1.6 Mev by French and Dissanaike[15] indicate that the 0.67 and 1.4-Mev levels have the same parity. Again this favors 1− for the 1.4-Mev resonance.

The weight of the evidence argues for the assignment of $J=1-$. The variation of the P_1 coefficient in the (p,γ_1) distribution could be rendered compatible with this by invoking the presence of a broad positive parity state underlying both the 0.67- and the 1.4-Mev resonance. This would also explain the P_1 coefficient in the (p,γ_0) angular distribution.

The level at 2.7 Mev appears to be weakly resonant for both γ_0 and γ_1. The large P_2 coefficient of −0.39 which occurs in the angular distribution of the ground-state gamma transition (Fig. 4) is consistent with a spin of 2+ although the possible presence of higher resonances makes the assignment uncertain. Levels have previously been reported in this region by Paul and Clarke[13] at 2.65 Mev with a width of 300 kev, resonant for both α_0 and α_1 in the $B^{11}(p,\alpha)$ reaction, and by Huus and Day[1] at 2.664 Mev with a width of 48-kev resonant for gamma rays of 2.13-Mev energy from the $B^{11}(p,p'\gamma)$ reaction. It is not clear whether or not these three sets of observations correspond to the same level.

VI. SUMMARY

Resonances have been observed in the $B^{11}(p,\gamma)$ reaction at proton energies of 0.67, 1.4, and 2.7 Mev and the angular distributions of the gamma ray to the ground state and first excited state of C^{12} have been measured at several energies in this range. The evidence favors spin and parity assignments of 2− for the 0.67-Mev resonance, 1− for that at 1.4 Mev, and 2+ at 2.7 Mev, but these assignments cannot be made with certainty.

A determination of the parities of the levels at 0.67 and 1.4 Mev would be sufficient to render their spin assignments unambiguous and this might be accomplished by measuring the internal electron-positron pair angular correlation.[16] Another approach would be triple correlation measurements on the 4.44-Mev gamma ray and γ_1. In addition it would be useful to extend the present data beyond 2.7 Mev.

We wish to thank Dr. L. G. Elliott and Mr. W. T. Sharp for their interest in this work and for many instructive discussions of the results.

[12] E. B. Paul and R. L. Clarke, Phys. Rev. **91**, 463(A) (1953).
[14] Craig, Cross, and Jarvis, Phys. Rev. **96**, 825(A) (1954).
[15] A. P. French (private communication).
[16] Devons, Goldring, and Lindsey, Proc. Phys. Soc. (London) **A67**, 134 (1954).

Electron-Neutrino Angular Correlation in the Beta Decay of Neon^{19}†*

D. R. Maxson, J. S. Allen, and W. K. Jentschke
University of Illinois, Urbana, Illinois

(Received August 25, 1954)

The electron-neutrino angular correlation in the beta decay of Ne^{19} has been measured by observing the energy spectrum of F^{19} recoil ions. The constant λ in the angular correlation function $[1+\lambda(v_e/c)\cos\theta_{e\nu}]$ was found to be $\lambda=-0.21\pm0.08$, indicating that the beta-decay interaction is of the form *STP* and not *VTP*. The observed angular correlation leads to the result

$$C_S^2\left|\int 1\right|^2 / C_T^2\left|\int \sigma\right|^2 = 0.69\pm0.17,$$

which is consistent with $C_S^2 \simeq C_T^2$ if the nuclear configuration is $(d_{5/2})^3_{1/2}$, but not if the configuration is $(s_{1/2})^3_{1/2}$. Most of the F^{19} recoils carried one unit of negative charge, but singly charged positive ions were also detected. The coincidence rate due to positive ions was about 10 percent of that due to negative ions. No doubly charged recoils were observed.

I. INTRODUCTION

RECENT measurements[1,2] of the electron-neutrino angular correlation in the beta decay of He^6 have indicated that the beta-decay interaction includes a tensor component and that the axial vector component is small or zero. The interaction must also include a scalar or (polar) vector component, as has been recognized since the discovery[3,4] of allowed $J=0\rightarrow 0$ transitions in the decay of C^{10}, O^{14}, and Cl^{34}. The principal objective of this experiment was to identify the Fermi (*S* or *V*) part of the interaction by measuring the angular correlation in an allowed transition of the type $\Delta J=0$, with no change of parity.

The most general interaction (excluding derivatives of wave functions), consistent with the requirement of relativistic invariance of the interaction Hamiltonian, is the linear combination

$$H'(\beta)=G[C_S H_S'+C_V H_V' + C_T H_T'+C_A H_A'+C_P H_P'], \quad (1)$$

where

$$C_S^2+C_V^2+C_T^2+C_A^2+C_P^2=1, \quad (2)$$

and the subscripts refer to the five "pure" interactions Scalar, Vector, Tensor, Axial Vector, and Pseudoscalar. The transition probability for allowed beta decay with an interaction Hamiltonian of the form (1) has been calculated by de Groot and Tolhoek.[5] If there is no Fierz interference, the decay probability is proportional to $[1+\lambda(v_e/c)\cos\theta_{e\nu}]$, where v_e is the speed of the electron, $\theta_{e\nu}$ is the angle between the directions of emission of the electron and the neutrino, and λ is given by[6]

$$\lambda=-\frac{(C_S^2-C_V^2)\left|\int 1\right|^2-\frac{1}{3}(C_T^2-C_A^2)\left|\int \sigma\right|^2}{(C_S^2+C_V^2)\left|\int 1\right|^2+(C_T^2+C_A^2)\left|\int \sigma\right|^2}. \quad (3)$$

The assumption of no Fierz interference, as justified by the linear Kurie plots obtained for several allowed beta transitions,[7-9] leads to the conclusion that the interaction cannot include both *S* and *V*, nor can it include both *T* and *A*. The results of the He^6 recoil experiments then indicate that the interaction is either *STP* or else *VTP*, where the pseudoscalar component probably should be included to account for the shape of the RaE beta spectrum.[10] Substitution of $C_A=0$ and either $C_S=0$ or $C_V=0$ in (3) reveals that if the Fermi component is *S*, then $-1\leq\lambda<\frac{1}{3}$, whereas if this component is *V*, then $\frac{1}{3}<\lambda\leq 1$. The interaction type can therefore be determined uniquely by a measurement of the angular correlation in a transition obeying Fermi selection rules. In transitions with $\Delta J=0$, $J\neq 0$, the angular correlation is dependent on both the Fermi (F) and Gamow-Teller (G-T) interaction components, and consequently the experimental results may be used not only to distinguish between the possible interaction types, but also to determine the relative magnitudes of the F and G-T components.

The angular correlation constant λ can be determined by observing coincidences between the beta particles and the recoil ions, the most direct procedure

† Based on a thesis submitted in partial fulfillment of the requirements for the degree of Doctor of Philosophy at the University of Illinois.

* This work was supported jointly by the U. S. Atomic Energy Commission and the Office of Naval Research.

[1] J. S. Allen and W. K. Jentschke, Phys. Rev. **89**, 902(A) (1953).
[2] B. M. Rustad and S. L. Ruby, Phys. Rev. **89**, 880 (1953).
[3] Sherr, Muether, and White, Phys. Rev. **75**, 282 (1949); R. Sherr and J. B. Gerhart, Phys. Rev. **91**, 909 (1953).
[4] W. Arber and P. Stähelin, Helv. Phys. Acta. **26**, 433 (1953).
[5] S. R. de Groot and H. A. Tolhoek, Physica **16**, 456 (1950).
[6] In Eq. (3) the negligibly small terms corresponding to the pseudoscalar component have been omitted.
[7] H. M. Mahmoud and E. J. Konopinski, Phys. Rev. **88**, 1266 (1952).
[8] J. P. Davidson and D. C. Peaslee, Phys. Rev. **91**, 442 (1953); Phys. Rev. **91**, 1232 (1953); Phys. Rev. **92**, 1584 (1953).
[9] O. Kofoed-Hansen and A. Winther, Phys. Rev. **89**, 526 (1953). These authors have emphasized that the possibility of appreciable Fierz interference is not ruled out by the available experimental evidence.
[10] A. Petschek and R. Marshak, Phys. Rev. **85**, 698 (1952).

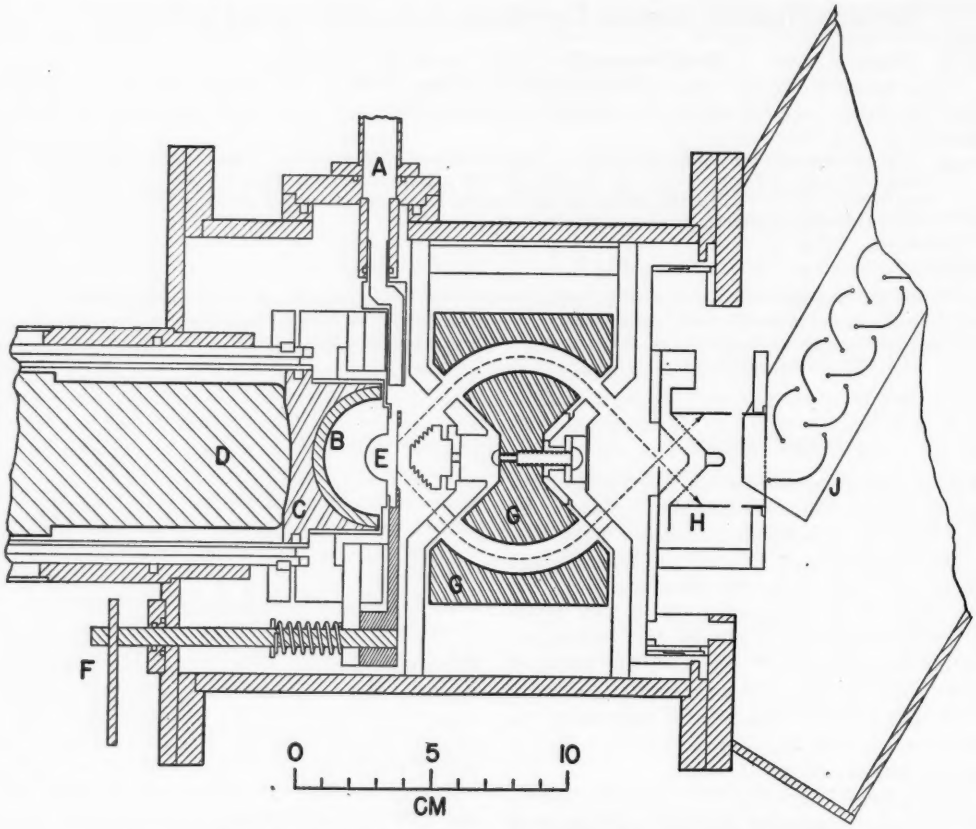

FIG. 1. Cross section of recoil chamber showing electrostatic spectrometer and detectors.

being to measure the coincidence rate as a function of the angle between the momentum vectors of these two particles. Alternatively, the coincidence rate can be observed as a function of the energy of one of the particles and the value of λ inferred from the shape of the resultant spectrum. The latter method has the advantage that the detectors can be made to subtend very large solid angles at the source, thus decreasing the running time required for a given statistical accuracy. In this experiment the energy spectrum of the recoil ions was observed, using an electrostatic spectrometer as an energy selector for the recoils.

The selection of a suitable isotope for investigation was limited by the requirement that the source be in the form of a (preferably monatomic) gas which could be produced by cyclotron bombardment and separated readily from the target material. The decision was made to use Ne^{19}, a positron emitter which undergoes a superallowed mirror transition with $J=\frac{1}{2}\rightarrow\frac{1}{2}$. The maximum kinetic energy of the positrons is 2.18 ± 0.03 Mev and the half-life is 18.5 ± 0.5 seconds,[11] corresponding to $ft\simeq2000$ sec. The beta spectrum is simple and has an allowed shape.[11–13] The maximum kinetic energy of the F^{19} recoil ions is about 200 electron volts.

II. APPARATUS AND PROCEDURE

A. Description of Apparatus

Ne^{19} was produced in the reaction $F^{19}(p,n)Ne^{19}$ by the bombardment of SF_6 gas with 6-Mev protons from the University of Illinois cyclotron. After separation from the SF_6, the neon was admitted to the recoil chamber, where the normal operating pressure was about 5×10^{-6} mm Hg. A vertical cross section of the chamber is shown in Fig. 1. The radioactive gas entered the chamber through tube *A* and diffused throughout the vacuum system, but useful data were provided only by those disintegrations which occurred within the "source volume" (*E*), a region approximately 2 cm^3 in volume located between the electron detector and the electrostatic analyzer. The source volume was defined on the side nearest the beta detector by a hemispherical bubble of plastic foil, which was about 0.8 mg/cm^2 thick and was aluminized on its concave surface to

[11] G. Schrank and J. R. Richardson, Phys. Rev. **86**, 248 (1952).

[12] Blaser, Boehm, Marmier, and Scherrer, Helv. Phys. Acta. **24**, 465 (1951).

[13] White, Delsasso, Fox, and Creutz, Phys. Rev. **56**, 512 (1939).

make it electrically conducting. The opposite side of the source was defined by the "gate," a flat sheet of aluminum leaf approximately 0.25 mg/cm² thick, which was sensibly transparent to the positrons, but of adequate thickness to stop completely the recoil ions. This gate was supported by an aluminum plate which could be rotated by an external handle (*F*). There were two holes in the movable plate, each 10.5 mm in radius, either of which could be centered in front of the source volume. One hole was covered by the gate and the other was left open. Coincidence counts were observed with the "gate open" and with the "gate closed," and the difference between these two sets of data represented the coincidence rate due to disintegrations within the source.

The geometry of the source region was the same with the gate either open or closed, and the radioactive gas could diffuse freely on both sides of the gate. Positrons from the source volume were recorded by means of a scintillation counter consisting of a hemispherical shell (*B*) of plastic phosphor cemented into a Lucite light pipe (*C*), which was in contact with an RCA Type 5819 photomultiplier tube (*D*). Since the scintillator was made much larger than the source volume, all positrons from the source entered the phosphor at roughly normal incidence, and the detection efficiency was nearly constant for different positions within the source. Recoil ions originating within the source volume were focused into the ion collector electrode (*H*) by an electrostatic field between the concentric spherical electrodes (*G*) of the spectrometer. Typical ion trajectories are indicated by the dotted lines in Fig. 1. The spectrometer electrodes were supported and centered by two end plates which also served to cut off the fringing field at the ends of the gap. Since most of the fluorine recoil ions carried one unit of negative charge, the inner electrode was normally positive and the outer one negative. Ions focused into the collector electrode *H* were accelerated through a potential difference of 2 kv in passing between two conical grids, and impinged on the inner surface of a cylindrical electrode where secondary electrons were released. The structure, consisting of the larger conical grid, two coaxial cylinders, and a flat grid, was so shaped that electrons ejected by ion impact at the inner wall of the first cylinder were focused through the flat grid onto the first dynode of a standard Allen-type[14] electron multiplier (*J*).

In order to prevent the detection of positrons which could not produce true coincidences, the region between the source volume and the scintillator was sealed off from the main vacuum chamber and evacuated with a separate mechanical pump. The background counting rate of the ion detector was minimized by allowing the radioactive gas to enter the ion detector vacuum can only through the small aperture of the ion collector. The vacuum can enclosing the electron multiplier was evacuated by a separate diffusion pump.

Figure 2 illustrates the main components of the auxiliary apparatus employed in producing Ne^{19} and recording data. Sulfur hexafluoride, previously purified and stored in a metal tank at about 5 lb/in.² above atmospheric pressure, was admitted continuously into the cyclotron target, from which the neon was carried along with the SF_6 through about 40 feet of copper tubing to the main experimental setup. Here the sulfur hexafluoride was frozen solid in a glass trap cooled with liquid nitrogen. Ne^{19} entering the recoil chamber was first purified by passage through a steel trap in which any possible contaminants were removed by chemical reactions with chips of calcium metal heated to 400°C.

Delayed positron-recoil coincidences were recorded by means of an oscilloscope and a camera in which 35-mm film moved continuously at about 1.5 cm per minute. Voltage pulses produced by the arrival of positrons at the electron detector were amplified and then triggered the 1 μsec/cm sweep of the oscilloscope. Recoil fluorine ions entering the ion detector produced pulses which, after amplification and shaping, were applied both to the vertical plates and to the intensity grid of the cathode ray tube. Data were read from the film by counting the number of pulses in each of 24 time channels. When the results were plotted as a histogram, the true coincidences produced by disintegrations in the source region appeared as a well defined peak superimposed on a uniform chance background. The differential energy spectrum of the recoil ions was determined by recording data for several

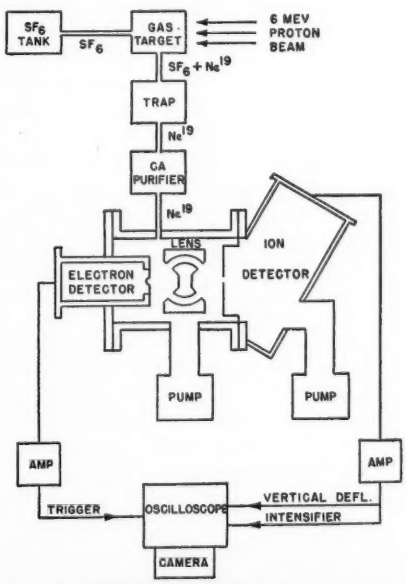

FIG. 2. Simplified schematic diagram of apparatus used in producing Ne^{19} and in recording delayed positron-recoil coincidences.

[14] J. S. Allen, Rev. Sci. Instr. 18, 739 (1947).

spectrometer voltages and counting the total number of true coincidences in each case.

B. Performance of the Spectrometer and Detectors

The electrostatic spectrometer was designed in accordance with the theory due to Purcell[15] and also to Browne *et al.*,[16] the choice of dimensions amounting to a compromise between the conflicting requirements of good detection efficiency *versus* good focusing and energy resolution. The solid angle for the detection of monoenergetic recoil ions from the source center was approximately $0.07\times(4\pi)$ steradians. The performance of the spectrometer was investigated using a source which provided a beam of singly charged argon ions of 210-ev energy. For twelve source positions, corresponding to points within the source volume in the recoil experiment, the observed relation between the ion energy and the total deflecting voltage was in agreement with the calculated value to within 4 percent, and for nine of these positions the agreement was within 2 percent. The measured half-width of the spectrometer resolution curve for a point source was 2.5 percent, as predicted by the first-order focusing theory. The detection efficiency of the spectrometer plus ion detector, as measured with a given flux of ions entering the spectrometer, was found to depend on the location of the source, with a variation of about a factor of three within the source volume. These results, which could not be calculated readily, were included in the computation of the expected recoil energy spectrum.

The ion collector electrode was designed to permit the detection of recoil ions with an efficiency independent of recoil energy. Conical grids were used in order to accelerate the ions along their initial direction of motion and also to cause them to strike the wall of the first cylinder at a location independent of their initial energy. The shapes of the electrodes needed to focus the secondary electrons into the main multiplier structure were determined by plotting trajectories with model electrodes in an electrolytic bath. The performance of the ion collector electrode was investigated with Po alpha particles, and it was found that the detection efficiency increased as the focusing voltage between the cylindrical electrodes was increased up to about 600 v, at which a plateau was reached. Consequently, the highest focusing voltage which gave no evidence of breakdowns, about 750 volts, was used in the recoil experiment. The 2-kv ion accelerating voltage between the conical grids corresponded to about ten times the maximum recoil energy in the Ne^{19} decay. The highest accelerating voltage which could be used was limited by the background counting rate, presumably due to field emission at the first grid, which increased with voltage above about 1 kv. Since most of the investigations[17–19] of secondary emission due to ion bombardment have been carried out using positive ions or neutral atoms, and since no measurements of the detection efficiency *versus* ion energy were made in connection with this experiment, it cannot be stated with certainty that the response of the detector to negative fluorine ions was energy independent. Experimental work has demonstrated,[17] however, that an electron multiplier of this type will count 2-kev Li ions with nearly 100 percent efficiency, and since all of the F ions which could produce true coincidences were (after acceleration) of the same energy to within ± 5 percent, the data were analyzed with the assumption that the ion detection efficiency was independent of the recoil energy.

The positron detection efficiency of the scintillation counter was measured using a 90-degree beta spectrometer with a Na^{22} source. The response was determined as a function of the energy of the positrons for each of several angles ranging from 0 to 75 degrees and measured between the positron beam and the axis of symmetry of the detector (measured at the center of curvature of the phosphor). Most of the measurements with positrons were made in one plane, and the response at other azimuthal angles about the axis of symmetry of the detector was determined by an auxiliary series of observations with a Po^{210} alpha source. The results demonstrated that the detection efficiency dropped off rapidly as the angle between the positron beam and the symmetry axis was increased beyond 40 degrees, and that there was also a pronounced dependence of the efficiency on the azimuthal angle. The first of these effects was to be expected in view of the relatively inefficient collection of light originating far from the center of the scintillator, and the second was found to result from a nonuniform sensitivity of the 5819 photocathode. The positron energy corresponding to a detection efficiency of 50 percent, averaged over six azimuthal positrons, varied from 130 kev at the center to about 920 kev at the extreme edge of the phosphor. These results were used in calculating the expected recoil energy distribution.

C. The Identification of Ne^{19}

A compilation of possible reactions resulting from the proton bombardment of SF_6 indicated that, other than Ne^{19}, no radioactive product with a maximum beta energy between 1.5 and 3 Mev could be formed. In addition, the presence of contaminants with half-lives between 5 seconds and 30 minutes would be unlikely. The Ne^{19} was identified in a preliminary experiment by an energy measurement with aluminum absorbers and a half-life determination using a Brush type BL 202 recorder. The half-life was measured again as a check at the conclusion of the data run. A single activity was

[15] E. M. Purcell, Phys. Rev. **54**, 818 (1938).
[16] Browne, Craig, and Williamson, Rev. Sci. Instr. **22**, 952 (1951).
[17] J. S. Allen, Proc. Inst. Radio Engrs. **38**, 346 (1950).
[18] H. D. Hagstrum, Phys. Rev. **89**, 244 (1953).
[19] J. H. Parker, Jr., Phys. Rev. **93**, 652, 1148 (1954).

observed, with energy and half-life in agreement with the values reported for Ne^{19}.

III. CALCULATION OF THE EXPECTED RECOIL SPECTRUM

In calculating the expected recoil energy distribution, the source volume was divided into five cylindrical and thirteen ring-shaped volume elements and the spectrum was computed for a representative point in each element. Complete calculations were carried out for ten of the eighteen points, and the results for the other points were determined by graphical interpolation. The computed spectra for the different elements were then combined with appropriate weighting factors to obtain the spectrum for the whole source. Since the efficiencies of the detectors and the focusing properties of the spectrometer were included in the computations, the calculated energy distribution could be compared directly with the data.

Schrank and Richardson[11] have investigated the beta spectrum of Ne^{19} and found the maximum kinetic energy of the positrons to be 2.18 ± 0.03 Mev. Willard and Bair[20] have observed the threshold of the $F^{19}(p,n)Ne^{19}$ reaction to be 4.253 ± 0.005 Mev. If one uses atomic masses listed in reference 21 and a neutron-proton rest energy difference[22] of 1.293 Mev, the beta energy calculated from this threshold value is 2.235 Mev. A maximum positron energy of 2.200 Mev was assumed in calculating the recoil spectrum. The neutrino was assumed to have zero rest mass, and the nonrelativistic approximation was used for the kinetic energy of the recoil ion. The Coulomb factor in the beta spectrum was obtained from the tables of Dismuke *et al.*[23] Negligible Fierz interference was assumed. Calculated recoil energy spectra for the case of He^6 decay which illustrate the effect of possible Fierz interference have been given by Rose.[24]

The final result of the computations was an expected recoil energy distribution of the form

$$N(E_R,\lambda)=A[N_0(E_R)+\lambda N_1(E_R)], \qquad (4)$$

where E_R is the recoil energy of ions originating at the center of the source volume and focused into the ion detector. A is a normalizing constant and λ is the constant characterizing the electron-neutrino angular correlation, as given by Eq. (3). $N(E_R,\lambda)$ represents the expected true coincidence rate for a deflecting voltage $V=[(r_2^2-r_1^2)/r_1r_2](E_R/q)=0.576(E_R/q)$ between the spectrometer electrodes, where E_R is the recoil energy in electron volts, q is the number of electronic charges carried by an ion, and r_1, r_2 are the radii of the electrodes. The functions $N_0(E_R)$ and $N_1(E_R)$ were obtained in graphical form. The value of λ (and incidentally the value of A) was found by fitting expression (4) to the data.

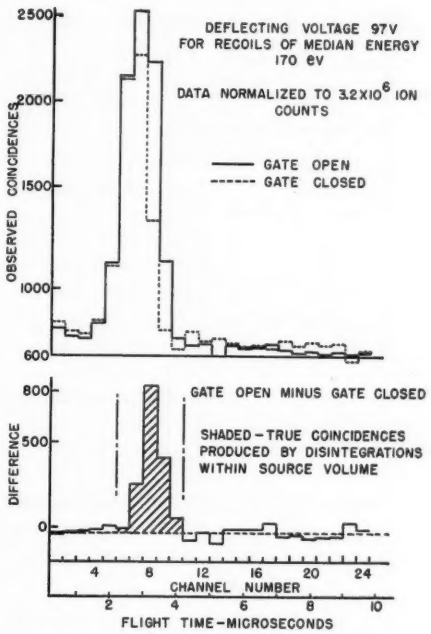

FIG. 3. Time-of-flight distributions of F^{19-} recoil ions with gate open and closed.

IV. RESULTS AND CONCLUSIONS

A. Experimental Results for Negative Recoils

The time of flight distributions corresponding to negative ions observed at a spectrometer voltage of 97v are shown in Fig. 3. At this voltage the detection efficiency should be greatest for ions (from the source center) of 170 ev energy, corresponding to about 85 percent of the maximum possible recoil energy in the decay of Ne^{19}. In the figure are shown the results obtained with the gate open and closed, as well as the difference (open minus closed) which represents the true coincidence count produced by disintegrations within the source volume. The data have been normalized to a total ion count of 3.2×10^6, which is within 5 percent of the numbers actually recorded. Most of the true coincidences with the gate in either position were produced by disintegrations which occurred between the gate and the spectrometer. Recoil ions from this region have shorter flight paths than those originating within the source volume, and consequently the peaks of both directly observed distributions are centered at flight times shorter than that of the difference count. The vertical dotted lines on either side of the peak in the latter distribution represent the limits of the region within which counts were totaled to determine one point of the recoil spectrum. The horizontal

[20] H. B. Willard and J. K. Bair, Phys. Rev. **86**, 629 (1952).
[21] Hornyak, Lauritsen, Morrison, and Fowler, Revs. Modern Phys. **22**, 291 (1950).
[22] Tollestrup, Fowler, and Lauritsen, Phys. Rev. **78**, 372 (1950).
[23] Dismuke, Rose, Perry, and Bell, Oak Ridge National Laboratory Report ORNL-1222, March 7, 1952 (unpublished).
[24] M. E. Rose, Oak Ridge National Laboratory Report ORNL 1593, October 19, 1953.

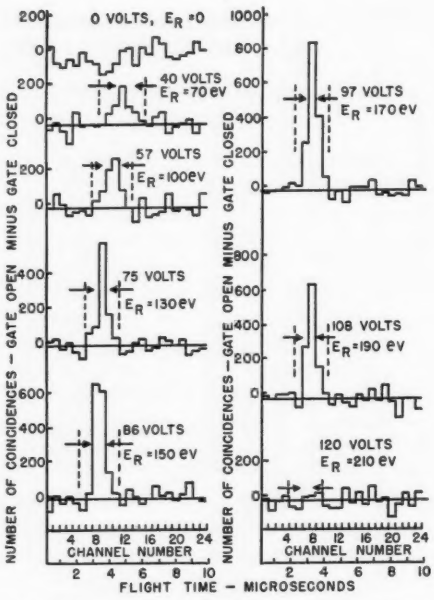
0 VOLTS, E_R =0
40 VOLTS E_R =70 eV
57 VOLTS E_R =100eV
75 VOLTS E_R =130eV
86 VOLTS E_R =150 eV
97 VOLTS E_R =170 eV
108 VOLTS E_R =190 eV
120 VOLTS E_R =210 eV
NUMBER OF COINCIDENCES – GATE OPEN MINUS GATE CLOSED
CHANNEL NUMBER
FLIGHT TIME – MICROSECONDS

FIG. 4. Time-of-flight distributions of F^{19} ions from source volume.

dotted line indicates the average net chance count per channel computed from the numbers in all channels outside of the vertical lines, and the shaded area under the peak represents the total number of disintegrations which occurred within the source volume.

Time of flight distributions for all of the recoil energies observed are shown in Fig. 4, in which only difference counts are plotted. The polarity of the spectrometer and ion collector voltages permitted the detection of negative ions only. All of the results have been normalized to 3.2×10^6 ion counts. The total ion counts actually recorded were within ±12 percent of this for all cases except at the spectrometer voltages of zero and 120 volts, for which the running time was shorter and the count was only about 1.6×10^6 in each case. Each histogram is labeled according to the spectrometer voltage and the corresponding value of E_R for singly charged ions coming from the source center. The observation of a large peak at 108 volts ($E_R=190$ ev), and the absence of one at 120 volts ($E_R=210$ ev), proved the calculated value of $E_R(\max)=200$ ev to be correct to within ±5 percent. The horizontal arrows in Fig. 4 show the expected location of each peak and the limits of the flight times calculated for ions originating at the source center. These computed time limits correspond to the different flight times of ions moving along trajectories near the inner and outer spherical electrodes. The observed peaks are wider than the limits indicated by the arrows because of the finite source dimensions and the spread in the recoil velocities of ions focused into the ion detector. A small additional broadening, amounting to about 0.2 microsecond, was introduced because the time delay between the incidence of a positron on the scintillator and the start of the oscilloscope sweep was not independent of the size of the triggering pulses. As is evident from Fig. 4, the observed flight times were in good agreement with the expected values. The vertical dotted lines have the same significance as those in Fig. 3, and the horizontal lines indicate the average net background count per channel. The net background, although small in comparison with the heights of the peaks, was consistently negative. This observation can be explained by the assumption that the average specific activity within the source volume was greater with the gate closed than with the gate open. No systematic error in the true coincidence count would result from a concentration of gas behind the closed gate, provided that the specific activity between the gate and the spectrometer were independent of the gate position. In view of the construction of the apparatus as shown in Fig. 1, it seems highly unlikely that the density of gas between the gate and the spectrometer could have been significantly influenced by the gate position, and it is therefore believed that any systematic error which might be inferred by the observation of a negative net background count is small in comparison with the statistical uncertainties. The peaks in the histograms of Fig. 4 were all produced by singly charged negative ions. Recoils of this charge would be expected in Ne^{19} decay, since after the disintegration the fluorine nucleus of charge 9 is left with the ten electrons originally present in the neon atom. Negative ions with two units of charge would not be expected, but it might be mentioned that any appreciable number of such ions would have produced a second peak in the distribution obtained at 40 volts. Such a peak, corresponding to doubly charged ions of 140-ev energy, would be centered at a flight time of about 3.5 microseconds, or 1.4 microseconds earlier than that for the singly charged ions of 70-ev energy detected at the same voltage. There is no indication of any such peak in Fig. 4.

The observed recoil energy spectrum and also the expected distributions calculated for various possible

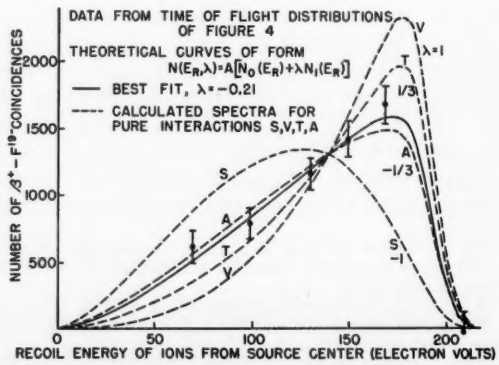

FIG. 5. Energy spectrum of recoil ions from Ne^{19} β^+ decay.

electron-neutrino angular correlations are shown in Fig. 5. Each experimental point in this figure was obtained from the total true coincidence count in the peak of the corresponding histogram in Fig. 4. The "theoretical" spectrum in best agreement with the experimental results was determined by fitting the calculated distribution (4) to the data by the method of least squares, with the result

$$\lambda=-0.21\pm0.08,$$

where the indicated uncertainties are standard deviations. There are believed to have been no systematic errors of magnitude comparable to the statistical uncertainties, and no allowance for such errors has been made in the limits stated above. In addition to the curve corresponding to $\lambda=-0.21$, the calculated spectra given by Eq. (4) for the "pure" interactions S, V, T, A are shown in Fig. 5. Each of these curves has been normalized to the same area as that beneath the plot for $\lambda=-0.21$.

B. Beta-Decay Interaction

According to Eq. (3), the experimental result $\lambda=-0.21$ indicates that the beta-decay interaction contains a scalar component and that the (polar) vector component is small or zero. The interaction is therefore of the form STP. This conclusion is based on (1) the results of the He^6 experiments of Allen and Jentschke[1] and of Rustad and Ruby,[2] (2) the results of this experiment, and (3) the assumption of negligible Fierz interference.[7-9] The result that the interaction is STP is in agreement with the conclusions of Mahmoud and Konopinski[7] and of Peaslee,[25] who have analyzed the shapes of beta spectra observed in allowed and forbidden transitions, and is also consistent with the observations of Alford and Hamilton[26] in their recoil experiment on Ne^{19}.

An expected value of the angular correlation constant λ can be estimated[27] from the observed ft values for Ne^{19} and O^{14}. With $ft=1970\pm100$ sec[28] for Ne^{19} and 3275 ± 75 sec[29] for O^{14}, the expected result is $\lambda=-0.07\pm0.02$ if one assumes the Fermi interaction component to be S, or $\lambda=+0.53\pm0.01$ if one assumes that component to be V. Although the expected value for the STP combination is not in good agreement with the result obtained in this experiment, the VTP interaction definitely appears to be ruled out.

The form of the interaction and the value of $\lambda=-0.21\pm0.08$ having been determined, Eq. (3) may be rewritten to yield the ratio

$$\frac{C_S^2\left|\int 1\right|^2}{C_T^2\left|\int \sigma\right|^2}=\frac{1}{3}\left(\frac{1-3\lambda}{1+\lambda}\right)=0.69\pm0.17. \qquad (5)$$

Unfortunately the value of $|\int\sigma|^2$ for the decay of Ne^{19} is not known with certainty. Peaslee[30] has assumed the nuclear configuration to be $(d_{5/2})^3{}_{1/2}$ and quoted the value $|\int\sigma|^2=1.6$. Winther and Kofoed-Hansen[28] have assumed $(s_{1/2})^3{}_{1/2}$, "probably in strong admixture with $d_{5/2}{}^2s_{1/2}$," and found $|\int\sigma|^2=2.59$, in agreement with the value of 2.65 given earlier by Trigg.[31] The theoretical value of $|\int\sigma|^2=1.6$, however, agrees with the value of 1.6 obtained by Kofoed-Hansen and Winther from a semiempirical relation between the ft values and matrix elements of other mirror transitions. Substitution of $|\int\sigma|^2=2.6$ and $|\int 1|^2=1$ in (5) yields $C_S^2/C_T^2=1.8\pm0.4$, whereas with $|\int\sigma|^2=1.6$ the result is $C_S^2/C_T^2=1.1\pm0.3$, where the limits of error include only the statistical uncertainty in the results of this experiment, and neglect the much larger error associated with the uncertainty in the value of $|\int\sigma|^2$. The value 1.1 ± 0.3 is consistent with the results of Blatt[32] ($0.54_{-0.25}{}^{+0.5}$), of Konopinski and Langer[33] (1.4 ± 0.7 from H^3 and He^6, $0.8_{-0.3}{}^{+0.5}$ from O^{14} and He^6), of Gerhart[29] ($0.73_{-0.21}{}^{+0.16}$), of Bouchez and Nataf[34] (0.99 ± 0.24), and of Kofoed-Hansen and Winther[28] (1.0 ± 0.2). From these results it may be concluded that the nuclear configuration is probably $(d_{5/2})^3{}_{1/2}$ and not $(s_{1/2})^3{}_{1/2}$.[35]

The conclusion STP might be checked by an experimental determination of the electron-neutrino angular correlation in a $J=0\rightarrow0$ transition. With a transition of the type $0\rightarrow0$ the expected result would be either $\lambda=1$ or $\lambda=-1$, and consequently a more certain conclusion might be reached with no greater accuracy than that achieved in the present experiment. Once the interaction type has been definitely established, additional information relative to the magnitudes of the coupling constants might be obtained through further recoil experiments, by measuring the angular correlation in other allowed transitions for which $\Delta J=0$, $J\neq0$.

[25] D. C. Peaslee, Phys. Rev. **91**, 1447 (1953).
[26] W. P. Alford and D. R. Hamilton, Phys. Rev. **94**, 779 (1954).
[27] The estimation of the expected angular correlation from the ft values of O^{14} and Ne^{19} was suggested to us by D. C. Peaslee.
[28] A. Winther and O. Kofoed-Hansen, Kgl. Danske Videnskab. Selskab, Mat.-fys. Medd. **27**, No. 14 (1953); Phys. Rev. **86**, 428 (1952).
[29] J. B. Gerhart, Phys. Rev. **95**, 288 (1954).
[30] D. C. Peaslee, Phys. Rev. **89**, 1148 (1953).
[31] G. L. Trigg, Phys. Rev. **97**, 506 (1952).
[32] J. M. Blatt, Phys. Rev. **89**, 83 (1953).
[33] E. J. Konopinski and L. M. Langer, Ann. Revs. Nuclear Sci. **2**, 261 (1953).
[34] R. Bouchez and R. Nataf, J. phys. et radium **14**, 217 (1953).
[35] In a private communication, Peaslee has pointed out that the calculation of $|\int\sigma|^2=2.6$ for the $(s_{1/2})^3$ configuration assumes a deformable nuclear core, whereas that leading to $|\int\sigma|^2=1.6$ for the $(d_{5/2})^3$ configuration does not. A value of $|\int\sigma|^2=3$ for the $(s_{1/2})^3$ configuration, obtained without the assumption of a deformable core, might therefore be more appropriate than 2.6 for a comparison of the two configurations. With $|\int\sigma|^2=3$, Eq. (5) would yield a ratio of $C_S^2/C_T^2=2.1\pm0.5$ in greater disparity with the other results quoted above, thus strengthening the conclusion that the configuration is not $(s_{1/2})^3$.

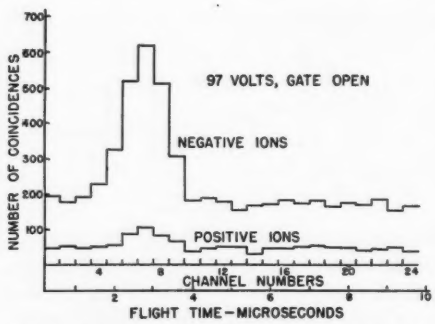

FIG. 6. Time-of-flight distributions of positive and negative F^{19} recoil ions of 170-ev energy.

A^{35} would furnish a good example, and since it is an inert gas it could be handled with apparatus similar to that described above.

C. Positively Charged Recoil Ions

The results of a search for positive recoil ions are shown in Fig. 6, in which time of flight distributions of both positive and negative recoils are plotted. The histogram having the larger peak represents a portion of the data obtained in the observation of the recoil energy spectrum of negative ions, and shows the number of coincidences per channel recorded in about four hours with the gate open. With 97 volts between the spectrometer electrodes, the energy of the ions detected was about 170 ev. The distribution with the smaller peak was observed in about six hours of running time, with experimental conditions which were the same as before, except that the deflecting and accelerating voltages were reversed to permit the detection of positive recoils. The histogram for positive ions has been normalized to the same total positron count as that recorded in the observation of negative ions, so that the two distributions correspond to the same number of disintegrations in the vacuum chamber. The average positron counting rates during the two runs differed by less than 5 percent. The histogram for positive ions shows a definite peak at the same flight time as that observed for negative ions. A comparison of the numbers of counts within the peaks of the two distributions reveals that the true coincidence rate due to positive recoils was about ten percent of that due to negative recoils.

The observed ratio of positive to negative recoils is not amenable to direct comparison with theoretical predictions of the ionization produced in beta decay. Since the absolute disintegration rate was not measured, the relative number of neutral fluorine atoms produced is not known. The relative detection efficiencies for positive and negative ions are also uncertain. According to the calculations of Levinger[36] and of Schwartz,[37] the change of nuclear charge in the decay process should cause the ejection of an electron from either the K or L shells of the daughter atom with a probability of about $2.7/Z^2$ per disintegration, or about 3 percent in this case. A larger ionization probability is predicted if the screening of the nucleus by the electrons is taken into account. The increase amounts to a factor of three for $Z=80$, but would be less for $Z=9$. For the production of positive ions, however, two electrons must have been ejected from the F^- recoils. Serber and Snyder[38] have estimated that the average excitation of the ion, due to the change of nuclear charge, is 54 electron volts for $Z=10$. The ejection of two electrons from an F^- ion requires[39,40] only about 21.5 ev, and is therefore energetically possible. The loss of more than one electron in the K capture of A^{37} has been observed by Perlman and Miskel,[41] who found the average charge of the daughter Cl^{37} ions to be $+3.41\pm0.14$ electron charges. The possibility that the positive ions observed in this experiment might have been produced by scattering seems unlikely, since the work function of the metal surfaces,[42] about 4 ev, is much smaller than the energy required for the removal of two electrons from an F^- ion. Neutralization of negative recoils at a surface was possible, as the electron affinity of fluorine[39] is only 4.1 ev, but neutral particles could not be detected. Although the possibility of scattering cannot be ruled out conclusively, the evidence seems to indicate that the positive ions observed were produced by the ejection of two electrons in the shakeup following the beta-decay process.

V. ACKNOWLEDGMENTS

The helpful cooperation and assistance of the cyclotron staff is gratefully acknowledged. We are also indebted to several other members of the Physics Department staff, in particular to Mr. Y. C. Tang for his assistance in testing the spectrometer, taking data, and performing calculations. We wish to thank Professor D. C. Peaslee for his helpful comments on certain theoretical aspects of the work and on the interpretation of the experimental results.

[36] J. S. Levinger, Phys. Rev. **90**, 11 (1953).
[37] H. M. Schwartz, J. Chem. Phys. **21**, 45 (1953).
[38] R. Serber and H. N. Snyder, Phys. Rev. **87**, 152 (1952).
[39] H. S. W. Massey, *Negative Ions* (Cambridge University Press, Cambridge, England, 1950).
[40] *Handbook of Chemistry and Physics* (Chemical Rubber Publishing Company, Cleveland, 1953).
[41] M. L. Perlman and J. A. Miskel, Phys. Rev. **91**, 899 (1953); Phys. Rev. **94**, 1683 (1954).
[42] F. Seitz, *The Modern Theory of Solids* (McGraw-Hill Book Company, Inc., New York, 1940).

Studies on the Isomeric Pair, Nb^{89m} and Nb^{89}*

HIRDAYA B. MATHUR,† EARL K. HYDE, CHARLES A. LEVINE,‡ AND PER K. KOFSTAD§
Radiation Laboratory and Department of Chemistry, University of California, Berkeley, California
(Received August 18, 1954)

By bombardment of zirconium, niobium, yttrium, and silver targets in the 184-inch cyclotron it has been possible to produce the isomer pair Nb^{89m} and Nb^{89}. The isomerism arises from the odd 41st proton below the 50-proton closed shell of the single-particle nuclear model. $Nb^{89}(g_{9/2})$ is a 1.9-hour activity emitting 2.85-Mev positrons to produce Zr^{89}. The yield of the $Nb^{89m}(p_{\frac{1}{2}})$ is about 30–100 fold less and its radiations were not directly observed. By scintillation spectrometer measurements on zirconium daughter activity it is shown that Nb^{89m} decays with about a 2-hour half-life to 4.4-minute $Zr^{89m}(p_{\frac{1}{2}})$. The $M4$ gamma transition between the two niobium levels is not observed, indicating that the level spacing is small and the upper level deactivates primarily by positron emission. The log ft values are larger than expected and are discussed in terms of the even-even core rearrangement considerations of A. De-Shalit and M. Goldhaber [Phys. Rev. **92**, 1211 (1953)]. Nb^{89} was also prepared by bombardment of NaBr with accelerated carbon ions in the 60-inch cyclotron.

I. INTRODUCTION

STUDY of the radioactivity present in the niobium fraction isolated from targets of several elements bombarded in the 184-inch cyclotron has resulted in the determination of the properties of the previously unreported isomeric pair Nb^{89} and Nb^{89m}. This information is summarized in Fig. 1. The reactions by which Nb^{89} was made and the evidence for the mass assignment are briefly given in Sec. II. Following this, a report is given of the detailed study of Nb^{89m} and Nb^{89} by means of scintillation spectroscopy. The suggested decay scheme of Fig. 5 is discussed at the end of the paper.

Independent work on these isomers has recently been prepared for publication by Diamond.[1] Our findings are similar, with one exception which is discussed later.

II. ORIENTATION EXPERIMENTS

Samples of zirconium metal were bombarded with 40-Mev protons for 30 minutes. G-M decay curves on the niobium fraction isolated from these targets within an hour of the end of the bombardment indicated that >80 percent of the activity originated with one unknown activity of 1.9-hour half-life, most of the rest being 14.6-hour Nb^{90} and a small amount of longer-lived activity, principally 79-hour Zr^{89} from the decay of Nb^{89}. Measurements in a beta-ray spectrograph of low resolution showed the 1.9-hour activity to consist of positrons of about 3-Mev energy. The isolation of 79-hour Zr^{89} activity from the purified niobium fraction proved the presence of Nb^{89} parent activity. Quantitative timed milkings of the zirconium daughter activity showed that the Nb^{89} half-life was about 2–4 hours and hence Nb^{89} was identified with the 1.9-hour, ~3-Mev positron acitivity. Chemical difficulties in obtaining quantitative separation of the zirconium without appreciable loss of niobium made the results less exact than was desired.

Very similar results were obtained by studying the niobium fraction isolated from niobium foils bombarded with 90-Mev protons, or from silver foils bombarded with 340-Mev protons,[2] or from yttrium oxide targets bombarded with 60–100-Mev helium ions. In every case the two chief activities were 14.6-hour Nb^{90} and 1.9-hour Nb^{89}. The ratio by activity of Nb^{89} to Nb^{90} was roughly the same (~2–6) in each case.[3]

III. GAMMA-RAY STUDIES ESTABLISHING THE ISOMERISM

Nb^{89} has 41 protons, and according to the single-particle shell model may well exist in the states $g_{9/2}$ and $p_{1/2}$, differing in spin by 4. Hence there is the strong possibility of isomerism in Nb^{89}. The systematics of the $g_{9/2}-p_{1/2}$ separation in this region as given by Fig. 75

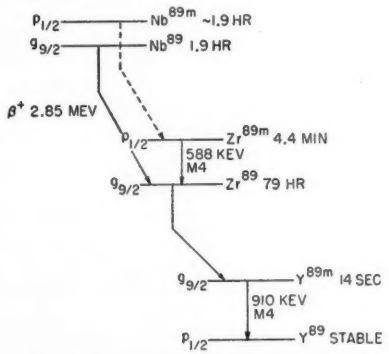

FIG. 1. Decay scheme of Nb^{89} and Nb^{89m}.

† On leave of absence, Department of Chemistry, University of Delhi, Delhi, India.

* This work was carried out with the support of the U. S. Atomic Energy Commission.

‡ Present address: Dow Chemical Company, Pittsburg, California.

§ Present address: Oslo, Norway.

[1] R. M. Diamond, Phys. Rev. **95**, 410 (1954).

[2] P. K. Kofstad, Ph.D. thesis, University of California Radiation Laboratory Unclassified Report UCRL-2265, June 30, 1953 (unpublished).

[3] In unpublished University of California Radiation Laboratory reports, we had indicated that we had evidence for Nb^{87} as well as Nb^{89}. On the basis of more complete study we conclude that we have no reliable evidence on the properties of Nb^{87}.

of an article on nuclear isomerism by Goldhaber and Hill[4] suggest that this separation in Nb^{89} is very slight and the decision as to which spin state is the ground state is quite uncertain. Consequently one would expect the upper state of Nb^{89} to deactivate predominantly by positron emission rather than by gamma emission. Zr^{89} is known[5] to exist in two isomeric forms by virtue of its 49 protons which give it an odd proton immediately below the 50-proton shell. The upper state is the $p_{1/2}$ state and has a half-life of 4.4 minutes for its predominant decay by emission of 588-kev gamma rays to the ground state (see Fig. 1). This ground state with spin $p_{1/2}$ decays with a half-life of 79 hours to 13-second Y^{89m}.[6] A pair of isomers occurs again in Y^{89} because of the odd proton below the 50-proton shell. $Y^{89m}(g_{9/2})$ decays by emission of a 910-kev gamma ray to stable $Y^{89}(p_{1/2})$.

From these facts it was possible to design experiments to check for the expected isomerism in Nb^{89}. These experiments consisted chiefly in the examination of the zirconium daughter activity milked from niobium for the 588-kev gamma radiation of Zr^{89m} and the 910-kev radiation of Y^{89}. This was done successfully with the aid of a sodium iodide-photomultiplier combination coupled to a 50-channel pulse-height analyzer.

A 5-mil niobium foil was bombarded for 1 hour with 100-Mev protons. After dissolving the foil in an HF-HNO_3 mixture, LaF_3 was precipitated several times to remove zirconium and yttrium activity. After the last scavenge precipitation an 8-minute growth period was allowed to pass, and LaF_3 was precipitated and quickly separated to remove zirconium which had grown in. The LaF_3 was placed in the scintillation spectrometer and data were taken on the gamma spectrum for 1 minute with the purpose of observing the 4.4-minute Zr^{89m} activity, if present. The registers were then reset and data taken again for 1 minute. Figure 2 shows the series of curves thus obtained. The 588-kev gamma radiation of Zr^{89m} and the 910-kev gamma radiation resulting from the decay of Zr^{89} to Y^{89m} are plainly evident. The activity in the 588-kev peak after correcting for coincidence losses in the mechanical registers decayed with a half-life of 4 ± 1 minutes.

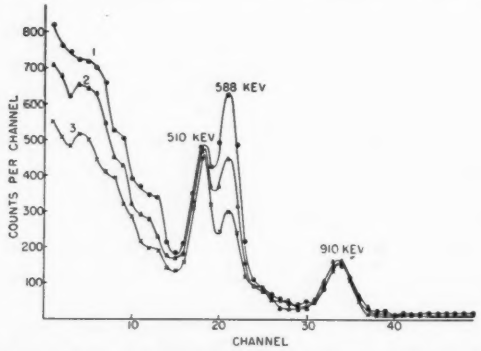

FIG. 2. Gamma spectrum of Zr^{89m} and Zr^{89} isolated from Nb^{89} after an 8-minute growth period. Curve one is a one-minute run started 8.2 minutes after an 8-minute growth period. The 588-kev gamma ray of Zr^{89m} is plainly visible. Succeeding one-minute runs show the rapid decay of this 4.4-minute activity.

After complete decay of Zr^{89m}, the gamma spectrum obtained corresponded to the annihilation radiation and the 910-kev gamma radiation expected of a sample of Zr^{89} (see Fig. 3). This activity decayed with the proper 79-hour half-life. Subsequent experiments in which the niobium was given more extensive purification and the zirconium was isolated by precipitation of barium fluozirconate gave the same results.

In a careful series of measurements taken of activity isolated after 2-minute growth periods, it was possible to determine the atom ratio of Zr^{89m} and Zr^{89} formed from the decay of niobium. This was done by integrating under the photopeaks and making suitable corrections for half-life and counting efficiency. The counting efficiency of the 588-kev gamma ray was taken as 12 percent and the total conversion coefficient as 0.076.[5] The counting efficiency of the 910-kev gamma ray was taken as 7.3 percent and K conversion was considered negligible. The atom ratio obtained was $1.2\pm0.5\times10^{-2}$, showing that the major decay was going to the $g_{9/2}$ ground state of Zr^{89}. This atom ratio was determined for zirconium daughter fractions isolated after 2-minute growth periods at various times from 1 hour after bombardment up to 8 hours after bombardment. There appeared to be no significant change in the ratio during this time which was taken as an indication that the half-life of $Nb^{89}(p_{1/2})$ is close to that of $Nb^{89}(g_{9/2})$.

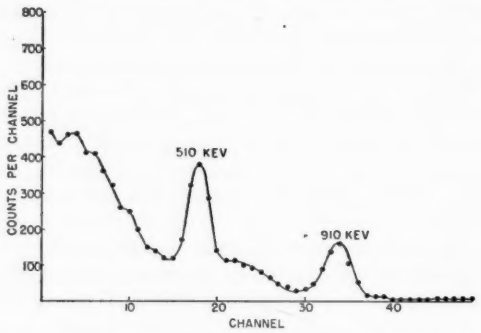

FIG. 3. Gamma spectrum of Zr^{89} daughter activity isolated from initially pure niobium fraction.

The whole series of measurements was repeated on a different bombardment of niobium. The same atom ratio within an experimental error of about 30 percent was obtained and this ratio underwent no significant change in a series of milkings covering a 6-hour period after the bombardment.

[4] M. Goldhaber and R. D. Hill, Revs. Modern Phys. 24, 179 (1952).
[5] Shore, Bendel, Brown, and Becker, Phys. Rev. 91, 1203 (1953).
[6] M. Goldhaber *et al.*, Phys. Rev. 83, 661 (1951).

It was considered desirable to know whether the $Nb^{89}(p_{1/2})$ to $Nb^{89}(g_{9/2})$ ratio was different in a sample prepared by a different method. For this purpose the niobium fraction of a silver target bombarded with 340-Mev protons was studied. After a 40-minute bombardment the target was dissolved in $10M$ HNO_3. Niobium was coprecipitated on MnO_2. This precipitate was dissolved in $12M$ HCl and contacted with diisopropyl ketone to extract the niobium.[7] After niobium was backextracted into water and evaporated to dryness it was taken up in a mixture of $10M$ HNO_3 and HF. Zirconium daughter activity was removed periodically by addition of zirconium and barium carrier to precipitate barium fluozirconate. Scintillation spectrometer curves on zirconium fractions so isolated after brief growth periods showed the 588-kev radiation of Zr^{89m}, and the annihilation radiation and 910-kev radiation of Zr^{89}. The atom ratio of Zr^{89m} to Zr^{89} was again observed to be constant for the activity milked at 1-hour intervals for a period of 5 hours. However, a significant difference in this ratio from that obtained from niobium bombardments was found. In the niobium isolated from silver spallation targets the observed atom ratio was 3×10^{-3}, or a factor of 4 lower. This difference is believed to be well outside the experimental error.

As a further check the same ratio was measured in a similar manner on a niobium sample prepared by bombardment of zirconium metal foil with the 32-Mev proton beam of the Berkeley linear accelerator. In this case an atom ratio of about $(2.6\pm0.5\times10^{-2}$ was obtained which is a factor of approximately 2 greater than in the samples isolated from niobium targets and a factor of about 9 greater than in the silver bombardment case.

The gamma spectrum of the purified niobium fraction was run at a time when more than $\frac{3}{4}$ of the activity was Nb^{89}, and on samples purified 24 hours later when Nb^{90} was the chief activity. A comparison of the two spectra showed that Nb^{89} did not emit any gamma rays in addition to the annihilation radiation and the only gamma rays in both spectra were those of Nb^{90} reported by Boyd.[8] The 588-kev gamma ray was not intense enough in comparison to the 510-kev annihilation radiation peak for it to be observed. If Nb^{89m} decayed chiefly by isomeric transition, a prominent gamma ray of less than 300 kev should have been observed.

During the course of these studies considerable data on the radiations of Nb^{90} were obtained. This will be reported in a separate paper.

The positron end-point energy was determined by using an anthracene crystal photomultiplier combination coupled to a 50-channel pulse analyzer. Figure 4 shows a typical end-point determination of 2.85 ± 0.10 Mev for the $Nb^{89}\rightarrow Zr^{89}$ transition. It was established that these positrons decayed with a 2-hour half-life.

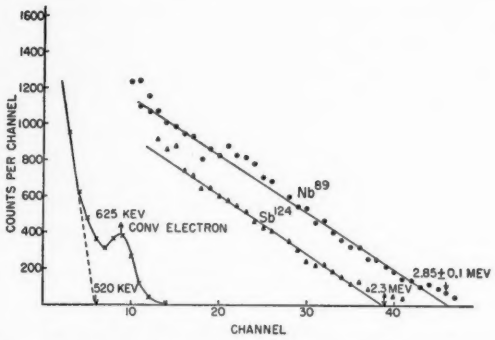

FIG. 4. Positron endpoint of Nb^{89} as determined on anthracene crystal spectrometer. Standards used were Cs^{137} and Sb^{124}.

IV. CARBON ION BOMBARDMENTS

In addition to the bombardments already mentioned, Nb^{89} was prepared in a novel way by the bombardment of bromine with accelerated carbon ions. This was done in the 60-inch cyclotron by using a beam of hextuply charged carbon ions (C^{6+}).[9] The carbon ions in the beam have a continuous spread of energy with a maximum energy of 120 Mev. Sodium bromide powder wrapped in thin tantalum foil was bombarded to carry out the reactions:

$$_6C^{12}+{}_{35}Br^{81}\rightarrow{}_{41}Nb^{90}+3\ {}_0n^1,$$
$$_6C^{12}+{}_{35}Br^{81}\rightarrow{}_{41}Nb^{89}+4\ {}_0n^1.$$

After bombardment the sodium bromide was dissolved in $10M$ HNO_3 and extracted with CCl_4 to remove bromine. MnO_2 was precipitated to remove niobium. The MnO_2 was dissolved in $12M$ HCl and from this solution niobium was extracted with diisopropyl ketone. Backextraction of the niobium into water completed the purification. Resolution of a G-M decay curve extrapolated back to the end of the bombardment showed $\frac{5}{6}$ of the activity to be 1.9-hour Nb^{89} and $\frac{1}{6}$ to be 14.6-hour Nb^{90}. The atom ratio, assuming equal counting efficiencies, is 0.7. Gamma analysis within 2 hours of the end of the bombardment showed the gamma rays of Nb^{90} and no others. Gamma analysis of zirconium daughter fractions showed the 910-kev gamma ray of Y^{89m}. No attempt was made to search quickly for Zr^{89m}.

V. DISCUSSION

The experimental data are best summarized by the decay scheme of Fig. 1. This scheme is incomplete because the energy separation of the Nb^{89} states and the identity of the higher state have not been deter-

[7] H. G. Hicks and R. S. Gilbert, California Research and Development Corporation Reports CRD-R-57 and MTA-33, April 1953 (unpublished).

[8] G. E. Boyd and B. H. Ketelle (unpublished data, 1951), as reported by Hollander, Seaborg, and Perlman in Revs. Modern Phys. 25, 469 (1953).

[9] Miller, Hamilton, Putman, Haymond, and Rossi, Phys. Rev. 80, 486 (1950).

mined. The small ratio of the Nb^{89m} to Nb^{89} in the samples we were able to prepare made it impractical to get the energy separation by the resolution of the positron spectrum into two components. From the systematics of the $p_{1/2}-g_{9/2}$ separation quoted previously,[4] it is expected that this separation in Nb^{89} is quite small and that hence the isomeric transition branching must be slight. By preparing very active samples and looking for the electrons of a highly converted $M4$ transition in the 0–200-kev range with a precision spectrometer, it might be possible to learn this energy separation.

Figure 1 differs from a very similar scheme presented by Diamond[1] only in that he assigns a half-life of 0.8 hour to the $p_{1/2}$ level of Nb^{89}. This was done on the basis of a series of quantitative timed milkings of zirconium daughter activity carried out in much the same manner as described in this report, except that the determination of the relative amounts of 4.4-minute Zr^{89m} and 78-hour Zr^{89} activity was done by the resolution of a decay curve taken on a scintillation counter without pulse-height analysis. Because our data are based only on the activity in the 588-kev and 910-kev gamma peaks we feel they are somewhat more trustworthy.

As already mentioned, the atom ratio of $Nb^{89}(p_{1/2})$ to $Nb^{89}(g_{9/2})$ was constant over a period of several hours for niobium samples prepared from niobium, silver, and zirconium targets. This is inconsistent with the half-life of 0.8 hour reported by Diamond for $Nb^{89}(p_{1/2})$. It is not clear why the two methods give different results.

From Moszkowski's[10] graphs the logft value for the 2.85-Mev positron transition $Nb^{89}(g_{9/2})\rightarrow Zr^{89}(g_{9/2})$ is 6.1, which is considerably higher than that expected

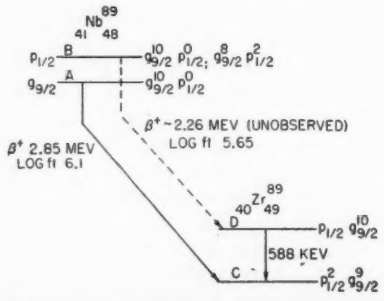

FIG. 5. Decay scheme for Nb^{89}, showing the main configurations of the protons (left) and the neutrons (right). The $g_{9/2}$ proton in A stabilizes the even-even core in a $(g_{9/2})^{10}$ configuration. The transition AC is delayed because of the necessity for rearrangement of the neutron core to produce two $p_{1/2}$ neutrons in C. B is indicated with a mixed neutron configuration, but the $(g_{9/2})^8(p_{1/2})^2$ configuration probably predominates. Hence the transition BD would be delayed.

[10] S. A. Moszkowski, Phys. Rev. 82, 35 (1951).

(5.0 ± 0.3) for an allowed transition. If the unknown $Nb^{89m}-Nb^{89}$ separation is neglected, the logft value of the $Nb^{89m}(p_{1/2})\rightarrow Zr^{89m}(p_{1/2})$ transition is 5.65 which is still somewhat higher than expected. These two transitions can be added to a growing list of apparent exceptions to the usual rules of beta decay discussed by De-Shalit and Goldhaber.[11] For example, the well-established $Zr^{89}(g_{9/2})\rightarrow Y^{89m}(g_{9/2})$ transition has a logft value of 6.1 and similarly, the transition $Zr^{89m}(p_{1/2})\rightarrow Y^{89}(p_{1/2})$ has a logft value of 6.85. These and other examples are discussed by De-Shalit and Goldhaber[11] who give an explanation in terms of a rearrangement of nucleons in the even-even core of an odd-A nucleus.

From their development the decay scheme of Fig. 1 can be redrawn in the form of Fig. 5.

VI. SPECTROMETER EQUIPMENT

Scintillation spectrometer.—The gamma scintillation spectrometer used during the course of this work was assembled by A. Ghiorso and A. E. Larsh of this laboratory. A sodium iodide crystal of 1.5-inch diameter and 1.0-inch thickness was used for the initial detection of the gamma ray. The photomultiplier coupled to the crystal was a Dumont-6292 tube, and mounting of the crystal was done by the methods of Borkowski.[12] The crystal-photomultiplier assembly was enclosed in a 2-inch thick lead shielding.

The output from the photomultiplier was amplified in a preamplifier and then in a linear amplifier. The final pulse was then analyzed by a 50-channel differential pulse-height analyzer designed by Ghiorso and Larsh. Calibration of the instrument was carried out with known radiations such as those from Na^{22}, Cd^{109}, Cs^{137}, U^{235}, and Am^{241} at identical gain and bias settings. A detailed description of the instrument will be given in a forthcoming publication of Ghiorso and Larsh.[13]

The positron energy measurements were made with a $\frac{1}{4}$-inch thick crystal of anthracene used in connection with the above equipment.

VII. ACKNOWLEDGMENTS

The cyclotron bombardments were carried out by James T. Vale, Lloyd B. Houser, and the 184-inch cyclotron crew except for the nitrogen beam bombardments for which we owe thanks to G. Bernard Rossi, A. Ghiorso, and the crew of the 60-inch cyclotron. The bombardments on the linear accelerator were carried out with the help of Robert D. Watt and Wendell W. Olson. We wish also to acknowledge helpful discussions with Dr. Richard M. Diamond.

[11] A. De-Shalit and M. Goldhaber, Phys. Rev. 92, 1211 (1953).
[12] C. J. Borkowski, Oak Ridge National Laboratory Report ORNL-1336, September 1952 (unpublished).
[13] A. Ghiorso and A. E. Larsh (to be published).

Decay of V^{49}

W. S. LYON
Analytical Chemistry Division, Oak Ridge National Laboratory, Oak Ridge, Tennessee
(Received September 29, 1954)

V^{49}, produced by proton bombardment of chromium, has been found to be a pure K-capture nuclide with less than 0.05 percent β^+ branching or gamma radiation; the half-life is 334±20 days.

VANADIUM-49 is listed in the literature[1] as a K-capture nuclide of 600-day half-life with converted gamma rays of energy 0.12 Mev and 0.08 Mev. The basis of this assignment is work done by Cork *et al.*,[2] who observed such an activity in vanadium irradiated in the ORNL graphite reactor. The presumption was that the activity observed was formed by an $(n,2n)$ reaction on the 0.25 percent abundant V^{50}. No chemical separation was performed. It was thus of interest to verify the decay of V^{49}.

A chromium target was irradiated with 22-Mev protons in the ORNL 86-in. cyclotron. Vanadium-49 could be produced by the reaction $Cr^{50}(p,2p)V^{49}$, $Cr^{52}(p,\alpha)V^{49}$ and $Cr^{50}(p,2n)Mn^{49}$ with decay to V^{49}. In addition, some vanadium-48 (16-day) might be expected from a $Cr^{52}(p,\alpha n)V^{48}$ reaction. The chromium target after irradiation also contained Cr^{51}(27.8-day), Mn^{52}-(6-day), and Mn^{54}(310-day). It was dissolved in hydrochloric acid and allowed to stand five months to permit the V^{48} to decay. In addition, this cooling period reduced the level of radioactivity in the sample, since the manganese-52 activity was lowered to a non-detectable level, and the Cr^{51}(27.8-day) was reduced to about one-fortieth of its original value.

A portion of the target solution (containing 1 mg of vanadium carrier and 10 mg of manganese holdback carrier) was evaporated to near dryness, made to 10 ml in volume with 4 percent sulfuric acid, cooled in ice, and a cupferron precipitation of the vanadium was made by addition of a few drops of 6 percent cupferron solution.[3]

The vanadium precipitate was centrifuged, washed, and redissolved in sulfuric acid. After addition of chromium and manganese holdback carrier, the precipitation was repeated.

After three cycles of the above procedure, the vanadium cupferron precipitate was filtered, washed, and ignited to V_2O_5.

By use of a calibrated argon-methane filled proportional counter spectrometer equipped with linear amplifier and differential and integral pulse-height selector, the x-ray peak resulting from the K capture in V^{49} was observed. The energy calibration was made using x-rays from Fe^{55}, Mn^{54}, and Cr^{51}. The x-rays from the vanadium source were of the energy calculated for titanium x-rays. The total number of K-capture processes occurring in the sample ($\sim 10^7$ dis/min) was estimated from a previous calibration of the counter. This V_2O_5 source was then examined using a 3 inch×3 inch NaI(Tl) gamma-ray spectrometer. No photopeaks corresponding to gamma rays of any energy above 30 kev were observed. It is thus concluded that the upper limit of β^+ branching is about 0.05 percent; the same limit is placed on any γ rays of energy <0.51-Mev. Absorption data in aluminum obtained with a helium-filled Geiger-Mueller counter (window thickness 2.3 mg/cm^2) failed to reveal any conversion electrons or beta particles.

Portions of V_2O_5 from two different separations were used to make decay measurements. The decay was followed on a windowless methane-flow beta proportional counter. The data for eight weeks, when analyzed by "least squares", indicate the half-life of V^{49} to be 334±20 days.

Another target which had cooled only one month was processed through the chemical procedure. Vanadium-48 was found in addition to the vanadium-49. The relative amounts were roughly in the ratio 300 to 1 in favor of the V^{49}. No other activity was found to carry through with the vanadium precipitate.

The author is indebted to Farno Green, who suggested the problem and supervised the irradiations, and to A. R. Brosi who assisted in the decay measurements.

[1] Hollander, Perlman, and Seaborg, Revs. Modern Phys. **25**, 469 (1953).
[2] Cork, Keller, and Stoddard, Phys. Rev. **76**, 575 (1949).
[3] G. E. F. Lundell and J. I. Hoffman, *Outlines of Methods of Chemical Analysis* (John Wiley and Sons, Inc., New York, 1938), p. 117.

Independent-Particle Model and the Nuclear Photoeffect. II*

J. S. LEVINGER
Louisiana State University, Baton Rouge, Louisiana
(Received August 26, 1954)

A simple harmonic oscillator independent-particle model is used for sum-rule calculation of electric dipole transitions in the nuclear photoeffect. First we find the level spacing $\hbar\omega=42A^{-\frac{1}{3}}$ Mev for nuclear radius parameter $r_0=1.2$. Combining this result with the integrated cross section, we find the bremsstrahlung-weighted cross section $\sigma_b=\int(\sigma/W)dW=0.36A^{4/3}$ millibarns. The calculated σ_b is not inconsistent with a preliminary analysis of experimental measurements for He, Be, C, Al, Cu, Mo, Ag, Ta, Pb, and U. We also use the simple harmonic oscillator independent-particle model to calculate the increase in the integrated cross section due to neutron-proton exchange forces. We find that the relative increase is not far from the Levinger-Bethe value of $0.8x$ (where x is the fraction of exchange force) for the closed-shell nuclei He^4, O^{16}, and Ca^{40}, for both Gaussian and Yukawa neutron-proton potentials, and for two values of the radius parameter r_0: 1.2 or 1.5.

I. INTRODUCTION

In a previous paper[1] (here designated by I), the author and D. C. Kent used sum-rules to calculate various moments of the $\sigma(W)$ curve for nuclear absorption cross section *vs* photon energy. We used nuclear wave functions for an independent-particle model (IPM) in a finite square well, for two nuclei of mass number 68 and 184, respectively. We found that the calculations were not inconsistent with present experimental data on Cu and Ta, provided: (i) that in the calculations we used a rather small nuclear radius, with radius parameter $r_0=1.2$; and (ii) that we also included the effects of exchange forces in increasing the harmonic mean energy for photon absorption.

In this paper we would like to study further the applicability of the IPM for the nuclear photoeffect. To simplify calculations we have changed from the finite square well IPM used in I to a simple harmonic oscillator IPM. The parameter ω, defined using the IPM potential $\frac{1}{2}M\omega^2r^2$, is evaluated in terms of the radius parameter r_0 in the following section. In Sec. III we use the simple harmonic oscillator IPM to evaluate the bremsstrahlung-weighted cross section,

$$\sigma_b=\int(\sigma/W)dW; \tag{1}$$

σ_b is the electric dipole cross section for the nuclear photoeffect weighted by the dW/W approximation to the bremsstrahlung spectrum. Thus σ_b is rather easily compared with measured bremsstrahlung yields for photonuclear processes. Also the calculated σ_b is not changed by the presence of neutron-proton exchange forces. The calculated σ_b is proportional to the square of the nuclear radius, and we can obtain reasonable agreement between calculations and experiment if we use $r_0=1.2$ for the radius parameter. (The radius is $R=r_0A^{\frac{1}{3}}\times10^{-13}$ cm.)

In Sec. IV we calculate the increase in the integrated cross section σ_{int} due to the neutron-proton exchange force. Levinger and Bethe[2] (here referred to as LB) calculated

$$\sigma_{\text{int}}=\int\sigma dW=0.015A(1+0.8x)\text{ Mev-barns}. \tag{2}$$

Here x is the fraction of the neutron-proton force that has an exchange character. The coefficient 0.8 depends on the nucleon wave functions that are assumed. LB used a model of a degenerate Fermi gas; while we shall use nucleon wave functions for a simple harmonic oscillator IPM. We find that the simple harmonic oscillator IPM calculation gives a coefficient with a value rather close to that found in the LB calculation. These phenomenological calculations of σ_{int} are being superseded by the more fundamental dispersion-theory calculations of Gell-Mann, Goldberger, and Thirring.[3] However it seems worthwhile to repeat the phenomenological calculation for a somewhat different nuclear model, to provide a firmer number to compare with the dispersion theory result.

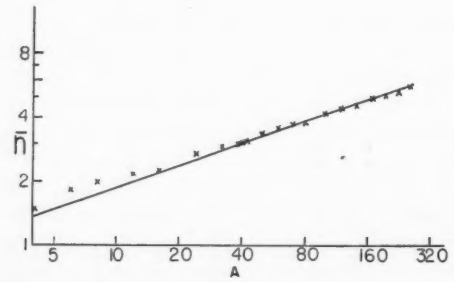

FIG. 1. The graph shows that the average quantum number $\bar{n}$ [defined by Eq. (5)] for a simple harmonic oscillator independent-particle model can be approximately represented by the relationship $\bar{n}=0.87A^{\frac{1}{3}}$. The line shows this equation; the points are shown for calculations for individual nuclei.

* This work was supported by the National Science Foundation.
[1] J. S. Levinger and D. C. Kent, Phys. Rev. **95**, 418 (1954), designated by I.
[2] J. S. Levinger and H. A. Bethe, Phys. Rev. **78**, 115 (1950), designated by LB.
[3] Gell-Mann, Goldberger, and Thirring, Phys. Rev. **95**, 1612 (1954).

II. SIMPLE HARMONIC OSCILLATOR POTENTIAL

In this section we shall evaluate the classical angular frequency ω for the simple harmonic oscillator potential in terms of the nuclear radius. This evaluation has been done by Wu[4] for several light nuclei. Wu uses an oscillatory wave function for the least bound nucleon for $r<R$, and a damped wave function for $r>R$. Matching at the nuclear radius R determines the parameter ω. In this paper we shall match the radius R in a different manner, which gives us a rather smaller value of ω.

Our method consists in calculating the expectation value $\langle r^2\rangle$ for each nucleon in a simple harmonic oscillator potential. This mean square radial distance is then averaged over all nucleons in the nucleus, giving $\langle r^2\rangle_A$ for the nucleon density distribution, in terms of ω and A. We equate $\langle r^2\rangle_A$ to the value $\frac{3}{5}R^2$ for a sphere of uniform density out to radius $R=r_0A^{\frac{1}{3}}\times10^{-13}$ cm. Thus we determine ω in terms of A and r_0.

Our present method of using r_0 implies that the values given (e.g., Hofstadter *et al.*[5] and Fitch and Rainwater[6]) are based on the mean square radius for the nucleon density distribution. Actually different measurements weight the density distribution with different factors,[7] and also measure the nuclear charge distribution rather than the possibly different nucleon density distribution.

For a nucleon with quantum number n, the mean square radial distance

$$\langle r^2\rangle=(\hbar/M\omega)(n+3/2). \tag{3}$$

The nuclear mean square radial distance $\langle r^2\rangle_A$ is found averaging over all A nucleons:

$$\langle r^2\rangle_A=(\hbar/M\omega)\textstyle\sum_n c_n(n+3/2)/A=(\hbar/M\omega)\bar{n}, \tag{4}$$

where c_n is the number of nucleons with quantum number n. (We are neglecting any differences among nucleons due to spin or charge.) Figure 1 shows that $\bar{n}$, the average value of n, is well represented by

$$\bar{n}=\textstyle\sum_n c_n(n+3/2)/A=0.87A^{\frac{1}{3}}. \tag{5}$$

(The "breaks" at the magic numbers are quite small.) Matching the nuclear mean radial distance with $\frac{3}{5}R^2$, we solve for $\hbar\omega$:

$$\hbar\omega=1.45(\hbar^2/Mr_0^2)A^{-\frac{1}{3}}=42A^{-\frac{1}{3}}\text{ Mev}. \tag{6}$$

Here the numerical result is based on $r_0=1.2$. The proportionality of the nuclear energy scale to $r_0^{-2}A^{-\frac{1}{3}}$ was found in I for a finite square well, and is characteristic of any IPM.[8]

TABLE I. Nuclear energies calculated from the IPM.

Nucleus	This paper[a] $r_0=1.37$	This paper[a] $r_0=1.2$	Wu[b] $r_0=1.37$	Paper I[c] $r_0=1.2$
He^4	20 Mev	—	36 Mev	—
Be^9	15	—	29	—
Ne^{20}	12	—	24	—
Ca^{40}	9.4	—	16	—
Cu	—	10	—	13
Ta	—	7.4	—	8.7

[a] The value of $\hbar\omega$ is given by Eq. (6).
[b] See reference 4.
[c] See reference 1, Tables VI and VII, for the harmonic mean energy (not including exchange effects).

We could obtain a better fit to the low-A points in Fig. 1 if we used an exponent slightly lower than $\frac{1}{3}$, giving an exponent of -0.35 in Eq. (6), and a somewhat larger coefficient. This refinement seems unwarranted at present, in view of the following approximations: (a) We have assumed that $\langle r^2\rangle_A$ is proportional to $A^{\frac{1}{3}}$ for all nuclei, even those as light as He^4; (b) we have neglected Coulomb effects on the proton; we use $A=2Z$ throughout this paper; (c) we have assumed that the simple harmonic oscillator potential continues to indefinitely large R; (d) we have neglected spin-orbit coupling, and configuration interactions.

For the alpha-particle and lighter nuclei, we can use the LB calculation[2] of the harmonic mean energy W_H, since for these nuclei there are no Pauli principle correlations to change the result. With $r_0=1.2$, the LB value is $W_H=72A^{-\frac{1}{3}}$ Mev$=29$ Mev, for He^4, in reasonable agreement with 26 Mev given by Eq. (6). For the alpha particle W_H and σ_b are determined entirely by the value of $\langle r^2\rangle_A$. (We plan in subsequent work to calculate $\langle r^2\rangle_A$ from alpha-particle wave functions. Here we use the dubious extrapolation of the nuclear radius to very small nuclei, to find approximate analytical expressions for W_H and σ_b in terms of A.)

Equation (6) gives lower values for light nuclei than those calculated by Wu. In Table I we compare the two results, for $r_0=1.37$. We also compare Eq. (6) for $\hbar\omega$ for Cu and Ta with the calculation in I for the harmonic mean energy for these two nuclei using a finite square well, with $r_0=1.2$. Our value of $\hbar\omega$ is different from Wu's, since we have interpreted the nuclear radius R in terms of a mean square radial distance, rather than as the limit of the classically allowed region. Our value of $\hbar\omega$ here is somewhat lower than the harmonic mean energy calculated in I for Cu and Ta, even though the same $\langle r^2\rangle_A$ is used.

Our present value of $\hbar\omega$ can be compared unfavorably both with photonuclear experiments and with measurements of low-lying nuclear energy levels. The former experiments show that the bulk of levels that can be reached by dipole transitions from the ground state have an excitation energy of about 17 Mev for medium nuclei such as Cu; while Eq. (6) gives only 10 Mev, even if we use a small nuclear radius. However, (see I)

[4] S. S. Wu, Ph.D. thesis, University of Illinois, 1951 (unpublished).
Note added in proof.—Also see B. C. Carlson and I. Talmi, Phys. Rev. **96**, 436 (1954).
[5] Hofstadter, Hahn, Knudsen, and McIntyre, Phys. Rev. **95**, 512 (1954).
[6] V. L. Fitch and J. Rainwater, Phys. Rev. **92**, 789 (1954).
[7] D. L. Hill and K. W. Ford, Phys. Rev. **94**, 1617 and 1630 (1954).
[8] J. S. Levinger, Ann. Revs. Nuclear Sci. 4 (1954).

exchange forces increase the harmonic mean energy for photon absorption by about forty percent, greatly improving the agreement between calculations and experiment. (The argument of I is somewhat inconsistent: it is claimed that the IPM holds to a reasonable approximation for all nucleons in their ground state; but that nucleons excited by electric dipole absorption experience quite a different potential, the difference being caused by neutron-proton exchange forces. Since the potential has not yet been derived from two body forces the effect of exchange forces cannot at present be included in the nuclear potential. We believe that our method of including the effect of exchange forces on the harmonic mean energy has a heuristic value, in spite of its inconsistency.)†

On the other hand, our value $\hbar\omega = 10$ Mev for medium nuclei is much larger than the values of several Mev found for the excitation energy of low-lying nuclear levels which might well be identified as the next nucleon level for a simple harmonic oscillator potential. A detailed analysis of low-lying levels to identify them with oscillator levels is desirable.

We shall not try to justify our value of $\hbar\omega$, but shall use it in this paper as an admittedly crude approximation to an IPM treatment of the nuclear photoeffect.

III. BREMSSTRAHLUNG-WEIGHTED CROSS SECTION

In this section we shall evaluate the bremsstrahlung-weighted cross section σ_b using a simple harmonic oscillator IPM, and we shall compare with experimental data.

LB[2] evaluate the bremsstrahlung-weighted cross section as

$$\sigma_b = \int_0^\infty (\sigma/W)dW$$

$$= (e^2/hc)(4\pi^2)\{[(N/A)\textstyle\sum_i z_i - (Z/A)\sum_j z_j)]^2\}_{00}. \quad (7)$$

Here $\sum_i z_i$ is the sum of the components of proton displacements along the direction of polarization of the photon; while $\sum_j z_j$ refers to neutrons. The expectation value is taken for the ground state of the nucleus. LB assumed that there were no correlations among the nucleons. In I we included Pauli principle correlations among pairs of protons, and among pairs of neutrons, for a square well IPM. In this paper we shall include the Pauli principle correlations for a simple harmonic oscillator IPM.

The Pauli principle correlations decrease σ_b, since due to the Pauli principle each proton is surrounded by an "exchange hole" in which there is a decreased likelihood of finding another proton.[9] There may also be significant dynamical correlations, causing a neutron and proton in a triplet S state, for example, to tend to remain close together, further decreasing the value of σ_b. These dynamical correlations, which are most marked in a sub-unit model[10] are neglected in the IPM treatment of this paper.

In I we calculated σ_b using Eq. (7). Our present calculation is done by the same method in the Appendix. However we shall find it shorter to calculate the same answer for σ_b by a round-about approach: i.e.,

$$\sigma_b = \sigma_{\text{int}}/W_H. \quad (8)$$

Here we have utilized the LB definition of the harmonic mean energy W_H. For the simple harmonic oscillator potential, with pure ordinary forces, W_H is just $\hbar\omega = 42A^{-\frac{1}{3}}$ Mev since electric dipole absorption causes transitions only between adjacent levels. (The special property that the harmonic mean energy equals the mean energy only for the case of an oscillator potential is discussed in the appendix, and related to the Heisenberg uncertainty principle.) Also, for pure ordinary forces, the numerator is (LB)

$$\sigma_{\text{int}} = \int \sigma dW = 15A \text{ Mev-millibarns.} \quad (9)$$

Substituting in Eq. (8) we have the bremsstrahlung-weighted cross section

$$\sigma_b = 15A/42A^{-\frac{1}{3}} = 0.36A^{4/3} \text{ mb.} \quad (10)$$

Our value for σ_b is proportional to r_0^2, since r_0 determines the scale for proton displacement z_i in Eq. (7), and the proton displacement enters squared. (Our numerical value is based on $r_0 = 1.2$.) σ_b is proportional to $A^{4/3}$, rather than $A^{5/3}$ as found by LB, since the Pauli principle correlations are increasingly effective for large A in decreasing the sum in Eq. (7). Our present value for σ_b is somewhat higher than that given in I for Cu and Ta, corresponding to the comparison in Table I that our $\hbar\omega$ is somewhat lower than W_H of I. (The numerator σ_{int} is independent of the model, for pure ordinary forces.) σ_b depends on the ground state nuclear wave functions, but is not changed by the existence of neutron-proton exchange forces. Thus we can calculate σ_b for pure ordinary forces, and compare our result with experimental data on actual nuclei, where there are significant exchange forces.

In comparing Eq. (10) with experiments we shall not attempt any exhaustive treatment of the experimental data. Our purpose here is to call attention to the significance of the bremsstrahlung-weighted cross section as a useful source of information concerning nuclear wave functions; and to make only a preliminary comparison between experiment and theory. In I we integrated to an upper limit of 70 Mev in using the experi-

† *Note added in proof.*—A more consistent interpretation is that two-body exchange forces contribute to a velocity-dependent nuclear potential for the IPM. This velocity-dependence increases W_H.

[9] J. Blatt and V. Weisskopf, *Theoretical Nuclear Physics* (John Wiley & Sons, Inc., New York, 1952), Sec. III. 3.

[10] A. Winslow, Ph.D. thesis, Cornell University, 1952 (unpublished).

TABLE II. Analysis of the experimental contributions to the bremsstrahlung-weighted cross section σ_b (in millibarns).

1. Nucleus	2. Neutrons 0–22 Mev	3. Protons 0–22 Mev	4. Neutrons 22–62 Mev[a]	5. Protons 22–62 Mev	6. 62–150 Mev[a]	σ_b[k]
He[b]	—	—	—	—	—	$1.5 \leq \sigma_b \leq 3$
Be	4.3[c]	0.5[d]	$1 \leq \sigma_b \leq 3$	~ 0.1	0.5	$5.8 \leq \sigma_b \leq 8.4$
C	0.9[d,e]	2.5[f]	$2 \leq \sigma_b \leq 2.5$	$\sim 6.$	0.4	$5.4 \leq \sigma_b \leq 12$
Al	5. [d,g]	5.1[f]	$4 \leq \sigma_b \leq 7$	$\sim 5.$	2.5	$14. \leq \sigma_b \leq 24$
Cu	40. [d,g]	15. [f,h]	$10 \leq \sigma_b \leq 26$	$\sim 7.$	6.	$65. \leq \sigma_b \leq 94$
Mo	80. [d,g]	6. [f]	$20 \leq \sigma_b \leq 46$	$\sim 3.$	9.	$110. \leq \sigma_b \leq 140$
Ag	100. [d,g]	small	$20 \leq \sigma_b \leq 50$	small	12.	$120. \leq \sigma_b \leq 160$
Ta	190. [e,g,i]	small	$30 \leq \sigma_b \leq 74$	small	20.	$220. \leq \sigma_b \leq 280$
Pb	240. [d,g,i]	small	$30 \leq \sigma_b \leq 80$	small	25.	$270. \leq \sigma_b \leq 340$
U	420. [e,g,j]	small	$30 \leq \sigma_b \leq 110$	small	35.	$450. \leq \sigma_b \leq 560$

[a] Jones and Terwilliger, reference 21; [b] Fuller, reference 26, Benedict and Woodward, reference 27; [c] Nathans and Halpern, reference 15; [d] Montalbetti, Katz, and Goldemberg, reference 13; [e] Nathans and Halpern, reference 12; [f] Halpern *et al.*, reference 18; [g] Price and Kerst, reference 11; [h] Byerly and Stephens, reference 19; [i] Wilkinson *et al.*, and Hanson *et al.*, reference 16; [j] Duffield and Huizenga, reference 17. [k] The last column is the sum of the contributions of the various processes to the bremsstrahlung cross section σ_b, which is defined in Eq. (1) of the text. The lower limit is found by using the lower limit of column 4 (neutron multiplicity from compound nucleus estimate) and omitting the contributions of columns 5 and 6. The upper limit is found by using the upper limit of column 4 (neutron multiplicity equals unity) and including all the other contributions. The value of σ_b is plotted in Fig. 2, and compared with theory.

mental data to determine σ_b [Eq. (1)] and σ_{int} [Eq. (9)]; but we have changed to an upper limit of 150 Mev for consistency with the value used by Gell-Mann, Goldberger, and Thirring.[3] (A real advantage of working with σ_b rather than σ_{int} is that the experimental value is rather insensitive to the cross section at high energies, where the experiments are less complete, and where we face the question of what upper limits to use in the integrals.)

The experimental data on the nuclei Be, C, Al, Cu, Mo, Ag, Ta, Pb, and U are treated in three energy ranges: medium (0 to 22 Mev); high (22 to 62 Mev) and very high (62 to 150 Mev). In the medium-energy region we can determine the contribution to σ_b directly from the yield curve[11–13] or we can determine the contribution to σ_b by numerical integration of the published excitation curves.[12,13] The yield Y is

$$Y = \int \gamma(W)\sigma(W)dW \cong \varphi(W_m)\int \sigma(W)dW/W, \quad (11)$$

where we have written the bremsstrahlung spectrum $\gamma(W) = \varphi(W)/W$; $\varphi(W)$ is a slowly varying function of W and may to a first approximation be taken out of the integral and evaluated at the energy W_m corresponding to the peak cross section. In our preliminary work we have taken $\varphi(W)$ as the Schiff thin-target spectrum, corrected for absorption, and appropriately normalized to the ionization in roentgens.[14]

Our values for σ_b using the 22-Mev bremsstrahlung yield given in column 2 of Table II are in good agreement with integrations from the $\sigma(W)$ curve. The 22-Mev yield method is inapplicable to a case such as C, where the peak cross section occurs at just about 22 Mev,[13] and also to the double-peaked cross section[15] for Be.

We shall use the data based on particle (neutron and proton) yields, even though such measurements tend to give too large an absolute cross section since multiple reactions are counted more than once. Corrections of 20 percent are made for multiple neutron emission for Ta,[16] Pb (assumed the same as Ta); and corrections of 35 percent for fission and emission of two neutrons by U.[17] Corrections for multiple particle emission are believed small in this energy region for the other nuclei.

Proton yields in the medium energy region are of importance for nuclei up to Mo as shown by column 3 of Table II. The contributions to the bremsstrahlung-weighted cross section are taken from the measurements of Montalbetti, Katz, and Goldemberg;[13] Halpern *et al*;[18] and Byerly and Stephens.[19] (Also see Chastel,[20] who finds a larger proton yield for Li gammas on Cu than would be expected from the work of Halpern or Stephens with 24-Mev bremsstrahlung.)

The neutron yields above 22 Mev have been measured by Jones and Terwilliger.[21] Their $\nu\sigma(W)$ curves have been treated in two different ways to obtain upper and lower limits for the neutron contribution to σ_b from 22 to 62 Mev given in column 4 of Table II. We find the upper limit by assuming that only one neutron is emitted (multiplicity ν equals one) and calculating $\int(\sigma/W)dW$. We obtain a lower limit for the contribution to σ_b by assuming that neutron multiplicity has the approximate upper limit of $W/\bar{E}$, where $\bar{E}$, the average energy per neutron emission, is about $\frac{3}{2}$ the neutron

[11] G. A. Price and D. W. Kerst, Phys. Rev. **77**, 806 (1950).
[12] R. Nathans and J. Halpern, Phys. Rev. **93**, 437 (1954).
[13] Montalbetti, Katz, and Goldemberg, Phys. Rev. **91**, 659 (1953).
[14] R. Nathans, Ph.D. thesis, University of Pennsylvania, 1954 (unpublished), Table IVa. Also see reference 12.
[15] R. Nathan and J. Halpern, Phys. Rev. **93**, 940 (1953).
[16] E. A. Whalin and A. O. Hanson, Phys. Rev. **89**, 324 (1953); Carver, Edge, and Wilkinson, Phys. Rev. **89**, 658 (1953).
[17] R. B. Duffield and J. R. Huizenga, Phys. Rev. **89**, 1042 (1953).
[18] E. V. Weinstock and J. Halpern, Phys. Rev. **94**, 1651 (1954), and earlier papers by Halpern *et al.*
[19] P. R. Byerly and W. E. Stephens, Phys. Rev. **83**, 54 (1951).
[20] R. Chastel, J. phys. et radium **15**, 459 (1954).
[21] L. W. Jones and K. M. Terwilliger, Phys. Rev. **91**, 699 (1953).

binding energy.[22] With this assumption the contribution to σ_b has a lower limit of $\bar{E}\int(\sigma/W^2)dW$.

Rather little is known about proton reactions in the high-energy region. We estimate this contribution to σ_b by using the neutron contribution to σ_b in this energy region and assuming the proton/neutron yield ratio is about the same in the high-energy region as in the medium-energy region. The resulting numbers, given in column 5 of Table II are most uncertain, even though, particularly for C and Al, high-energy proton yield contributes a large part of the total bremsstrahlung-weighted cross section. (Nathans and Halpern[12] have suggested a substantial contribution of the high-energy proton cross section to σ_{int} for light elements.)

The contribution of the very high-energy region from 62 to 150 Mev is estimated in column 6 of Table II. Here we find the absorption cross section at 140 Mev as done by Jones and Terwilliger.[21] Assuming that the cross section is about constant from 62 to 150 Mev, the integration for the bremsstrahlung-weighted cross section is then performed. This rather uncertain contribution to σ_b is rather small (10 percent or less). We have not included in this table the contributions from inelastic[23] or elastic[24] gamma scattering. They are probably less than 10 percent of the total.

The values for σ_b given in the last column of Table II are given as lower and upper limits. The lower limit is found by adding the values of columns 2 and 3 to the lower limit in column 4, and omitting the contributions of columns 5 and 6. For the upper limit to σ_b, we use the upper limit for the high-energy neutron yield given in column 4, and add all the other contributions to σ_b. An additional allowance of at least 20 percent (Nathans and Halpern)[12] should be made for systematic errors in the various absolute measurements.

The rather poorly known bremsstrahlung-weighted cross section for He^4 is based on work by Halpern *et al.*[25] up to 26 Mev; on Fuller's work[26] up to 36 Mev; and on Benedict and Woodward's measurements[27] at the higher energies. Halpern's data give 0.2 mb for the neutron contribution to σ_b up to 26 Mev; while Fuller's data give a contribution of 0.6 mb for the proton yield up to 36 Mev. (Fuller's proton cross sections are about 25 percent higher than Halpern's neutron cross sections, for the same photon energies.) If we take 0.2 mb as an average cross section for proton emission in the high-energy region,[27] we have a proton contribution to σ_b of 0.3 mb from 36 to 150 Mev. The total proton contribution of 0.9 mb is doubled to account for single neutron emission; and might be increased somewhat further to take account of multiple disintegration of the alpha particle. However, Halpern's neutron measurements suggest a reduction of 20 percent. We take 1.5 mb $\leq\sigma_b\leq$3 mb.

Figure 2 compares the experimental bremsstrahlung-weighted cross sections estimated in Table II with the calculated value of σ_b given in Eq. (10). We also show a dashed line from Cu to Ta giving the finite square well IPM calculations of I. The agreement between experiment and theory is rather better than expected, considering the preliminary character of both estimates. More accurate experimental data for σ_b would be of great help in deciding both the size of the nucleus, and the extent of dynamical sub-unit correlations. The present agreement between experiment and theory (if we use a rather small radius, with radius parameter $r_0=1.2$) indicates that sub-unit correlations are not of great significance for moderate energy photonuclear reactions. (Note that σ_b weights the $\sigma(W)$ curve favoring low W.) That is, the IPM is not unsuccessful in the moderate-momentum region, for the nuclear ground state. (If we used $r_0=1.5$, the disagreement between experiment and theory would suggest sub-unit correlations significantly modifying the IPM.)

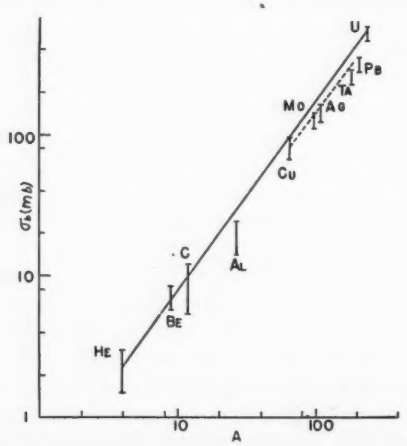

FIG. 2. Comparison of experimental and theoretical values for the bremsstrahlung-weighted cross section $\sigma_b=\int(\sigma/W)dW$. The experimental values shown by vertical bars are given in Table II. The bars show the lower and upper limits for σ_b, based on different analyses of the experiments. They do not include errors in measurement of absolute values. The solid line shows $\sigma_b=0.36A^{4/3}$ millibarns, derived from a simple harmonic oscillator independent-particle model [Eq. (10)]. The dotted line is based on calculations for Cu and Ta (reference 1) for a finite square well independent-particle model.

IV. EXCHANGE FORCE CONTRIBUTION TO INTEGRATED CROSS SECTION

The increase by a factor $(1+Cx)$ in σ_{int} due to exchange forces was calculated by Levinger and Bethe (LB)[2] using nuclear wave functions for a degenerate perfect Fermi gas, normalized to give the correct

[22] J. S. Levinger and H. A. Bethe, Phys. Rev. **85**, 577 (1952).
[23] C. S. Del Rio and V. L. Telegdi, Phys. Rev. **90**, 439 (1953).
[24] E. G. Fuller and E. Hayward, Phys. Rev. **95**, 1106 (1954).
[25] Ferguson, Halpern, Nathans, and Yergin, Phys. Rev. **95**, 776 (1954).
[26] E. G. Fuller, Phys. Rev. **96**, 1306 (1954).
[27] T. S. Benedict and W. M. Woodward, Phys. Rev. **83**, 1269 (1951).

nucleon density. (Also see Feenberg[28] and Siegert.[29]) In this paper we shall present the results of calculations using the simple harmonic oscillator IPM discussed above. We start with LB, Eq. (11), for the summed oscillator strength for electric dipole transitions:

$$\sum_n f_{0n} = NZ/A - (2M/\hbar^2)x(1/6)\int \Psi_0^* \sum_i \sum_j r_{ij}^2 \times V(r_{ij}) P_{ij} \Psi_0 d\tau. \quad (12)$$

Here x is the fraction of the neutron proton force that has an exchange character; Ψ_0 is the complete nuclear wave function; i denotes protons and j neutrons, the double sum being over all pairs of neutrons and protons; r_{ij} is the distance between proton i and neutron j, while $V(r_{ij})$ is the neutron-proton potential; and P_{ij} is the Majorana exchange operator. Three approximations were made: (i) The LB approximation of a degenerate Fermi gas model allowed replacing the double sum in Eq. (12) by integrals over the momenta of protons and neutrons. (ii) In evaluating the integral over r_{ij} the Fermi gas approximation also neglects surface effects that might be appreciable for a real nucleus. (iii) LB found that the exchange operator P_{ij} gave a significant decrease in the integral. On the other hand, for a very light nucleus such as the alpha particle, all particles have the same spatial wave function, to the extent that we neglect the spin and charge dependence of nuclear forces, as we shall do in this paper. Then for the alpha particle the exchange operator cannot decrease the integral, as it does for the Fermi gas model. These three differences suggest that a calculation with discrete IPM wave functions for a finite nucleus might give a rather different result than found using the LB approximations. However we find that the LB approximation gives results quite close to those for a harmonic oscillator IPM for closed shell nuclei. Apparently the main contribution to the integral of Eq. (12) comes from rather small neutron-proton distances, so that the details of the neutron and proton wave functions are not significant.

Evaluating Eq. (12) with a neutron-proton Gaussian potential $[-V_0 \exp(-r^2/\beta^2)]$ and simple harmonic oscillator wave functions is straightforward, though tedious, so we shall not present the details of the calculation. We perform the integrations in Cartesian coordinates, and for this reason find it convenient to use a Gaussian neutron-proton potential, which can be simply expressed in terms of the Cartesian coordinates of the two particles. The integral of Eq. (12) is evaluated for each sextet of quantum numbers for the neutron-proton pair: (n_x,n_y,n_z) for proton, and (n_x',n_y',n_z') for neutron. The double sum over neutron-proton pairs is then done algebraically. Since here we neglect the spin and charge dependence of nuclear forces, the double sum does not involve a prohibitive amount of work: thus for Ca^{40} the 400 different neutron-proton pairs amount to only 15 different sextets of neutron and proton quantum numbers, combined with appropriate weights.

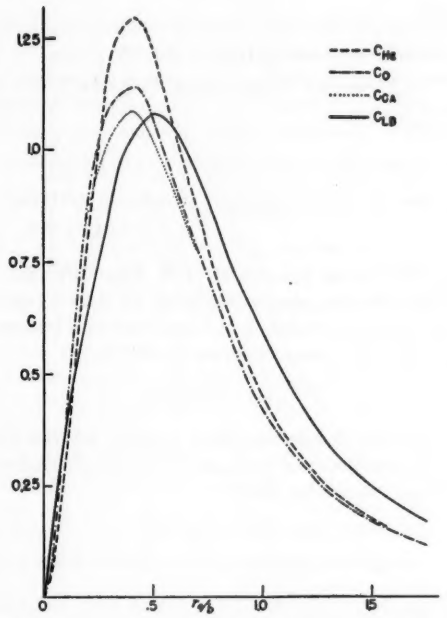

FIG. 3. The coefficient C for the increase of the integrated cross section is plotted against the parameter r_0/b for several different nuclei. The integrated cross section $=0.015A(1+Cx)$, where x is the fraction of neutron-proton exchange force; r_0 is the nuclear radius parameter, and b is the intrinsic range of the Gaussian neutron-proton potential. The four curves are C_{LB} (reference 2) for the Fermi gas model; C_{He} for He^4; C_O for O^{16}; and C_{Ca} for Ca^{40}. The last three are calculated using a simple harmonic oscillator independent-particle model. See Eqs. (20), (16), (17), and (18) for the four curves.

The neutron-proton potential is taken as a weighted average of the singlet and triplet potentials for the Gaussian case. We use an intrinsic range b of 2.2×10^{-13} cm, and a well-depth parameter $s=1.3$. We express our results for the coefficient C of x in terms of the two related parameters v and u.

$$v = 1/\beta^2\alpha, \quad (13)$$

$$\alpha = M\omega/\hbar = 1.46A^{-\frac{1}{3}}r_0^{-2}\times10^{26}\ \text{cm}^{-2}, \quad (14)$$

$$u = r_0/b = (0.71A^{-\frac{1}{3}}v)^{\frac{1}{2}}. \quad (15)$$

Here $b=1.44\beta$ from the effective range theory; and we use $\hbar\omega$ from Sec. II. (The actual calculation is done in terms of v, giving polynomials with integral coefficients. The parameter u is useful for comparing calculations for the various nuclei.) Our equations for the coefficient C for the closed-shell nuclei He^4, O^{16}, and Ca^{40} are given below; plotted against u in Fig. 3; and evaluated in Table IV for the values $r_0=1.2$ and $r_0=1.5$. For He^4,

$$C = 14.0v(1+2v)^{-5/2} = 31.5u^2(1+4.48u^2)^{-5/2}. \quad (16)$$

[28] E. Feenberg, Phys. Rev. 49, 328 (1936).
[29] A. J. F. Siegert, Phys. Rev. 52, 787 (1937).

For O^{16},

$$C=3.50v(4+6v+31v^2)(1+2v)^{-9/2}$$
$$=12.4u^2(4+21.3u^2+391u^4)(1+7.1u^2)^{-9/2}. \quad (17)$$

For Ca^{40},

$$C=1.75v(8+24v+176v^2+168v^3+389v^4)(1+2v)^{-13/2}$$
$$=8.43u^2(8+116u^2+4080u^4+18\,800u^6+209\,000u^8)\times(1+9.64u^2)^{-13/2}. \quad (18)$$

Using the Fermi gas model [LB, Eq. (19)] for this Gaussian neutron-proton potential, we find it convenient to express the coefficient C in terms of a parameter t, as well as the parameter u used above.

$$t=(\beta k)^{-2}=0.695u^2. \quad (19)$$

Here k is the maximum wave number for the Fermi gases of neutrons and protons. The LB calculation for the Fermi gas model gives

$$C=3.95t^{\frac{1}{2}}[(2t+1)e^{-1/t}+1-2t]$$
$$=(4.58u^3+3.29u)e^{-1.44/u^2}+3.29u-4.58u^3. \quad (20)$$

This equation is also plotted in Fig. 3, and evaluated in Table III.

In Table III we also present the LB results for square and Yukawa neutron-proton potentials. (See LB, Table I.) We have calculated C for a quasi-Yukawa potential by expressing the contribution to C for each of the Gaussians. We use a Yukawa potential for an intrinsic range b of 2.5×10^{-13}, and a depth parameter of 1.3:

$$V_Y=1.57(\hbar^2/M\times10^{-26})e^{-r/1.18}/(r/1.18). \quad (21)$$

Here the radial distance r is given in units of 10^{-13} cm. We fit V_Y within 10 percent over a range of r from 0.3 to 4×10^{-13} cm (a factor of almost 1000 in V_Y) with the sum of 4 Gaussian potentials:

$$V_Y'=(\hbar^2/M\times10^{-26})(0.12e^{-r^2/7.75}+0.55e^{-r^2/2.23}+2.6e^{-r^2/0.53}+8.4e^{-r^2/0.065}). \quad (22)$$

TABLE III. Summed oscillator strength (times A/NZ).

Nucleus	Neutron-proton potential	Nuclear radius parameter r_0 $r_0=1.2$	$r_0=1.5$
He^4, SHO	Gaussian	$1+1.12x$	$1+0.87x$
O^{16}, SHO	Gaussian	$1+0.99x$	$1+0.80x$
Ca^{40}, SHO	Gaussian	$1+0.94x$	$1+0.77x$
Fermi gas (LB)	Gaussian	$1+1.07x$	$1+0.96x$
Fermi gas (LB)	Square	$1+1.06x$	$1+0.80x$
Fermi gas (LB)	Yukawa	$1+0.76x$	$1+0.69x$
He^4, SHO	Quasi-Yukawa	$1+0.84x$	$1+0.72x$
O^{16}, SHO	Quasi-Yukawa	$1+0.73x$	$1+0.63x$
Ca^{40}, SHO	Quasi-Yukawa	$1+0.70x$	$1+0.61x$

In Table III x is the fraction of the neutron-proton force that has an exchange character. The coefficient of x gives the relative change in the summed oscillator strength, or in σ_{int}, due to complete exchange force. This coefficient C is plotted in Fig. 3, and given in Eqs. (16), (17), (18) for a calculation with simple harmonic oscillator (SHO) independent-particle model for He^4, O^{16}, and Ca^{40} respectively. The LB calculation (reference 2) for a Fermi gas model is given in Eq. (20) and Fig. 3 for a Gaussian neutron-proton potential, and in LB [Eqs. (20) and (21) and Table I] for the square and Yukawa neutron-proton potentials. The calculations for He, O, and Ca for a quasi-Yukawa potential are discussed following Eq. (22).

The 4 terms in V_Y' correspond to intrinsic ranges b for the 4 different Gaussians of 4.0, 2.1, 1.1, and 0.37 $\times10^{-13}$ cm respectively. These 4 Gaussians should be used with Fig. 3 with weights of 0.26, 0.35, 0.40, and 0.16 respectively. (Note that Fig. 3 is for a Gaussian potential of depth V_0 proportional to b^{-2} and that we are using Fig. 3 for different values of b.) We find the results for He, O, and Ca for a quasi-Yukawa potential given in the last three rows of Table III.

As a check on this method of calculating with a Yukawa potential we have used the curve marked LB in Fig. 3 for the LB Fermi gas model, together with V_Y' as a sum of 4 Gaussians to find the coefficient C for a Yukawa potential with the LB model. Our values of 0.78 (for $r_0=1.2$) and 0.71 (for $r_0=1.5$) are in good agreement with those calculated directly for V_Y by LB for the Fermi gas model: 0.76 (for $r_0=1.2$) and 0.69 (for $r_0=1.5$).

LB found that the coefficient C was not sensitive to the shape of the neutron-proton potential, or to the radius parameter r_0. We have now found that C is also not sensitive to the particular nuclear wave functions used: the Fermi gas model, or simple harmonic oscillator IPM for the closed-shell nuclei He, O, or C. The extreme range in the coefficient C for the 18 examples given in Table III is from 0.61 to 1.12. The LB rough average of 0.8 seems about as good an average as any. (It agrees quite well with the calculated values ranging from 0.70 to 0.84 for a Yukawa potential, with $r_0=1.2$, which we believe is the most appropriate set of parameters.) In any case, even a 20 percent change in C changes the integrated cross section $\sigma_{\text{int}}=0.015A(1+Cx)$ by only 7 percent. (Here we have taken the value $x=0.5$ for the approximate fraction of exchange force.)

We have here used the simple harmonic oscillator IPM for closed-shell nuclei filling the lowest, first, and second shells. It is very probable that heavier nuclei treated on this model would show quite good agreement with the results found here for Ca^{40}. (The curves for O and Ca in Fig. 3 agree quite closely.) Nuclei intermediate between closed shells might give a somewhat lower value of C, as the interference effects of the P_{ij} term in Eq. (12) would become relatively more important. Preliminary calculations on the B^{10} nucleus with simple harmonic oscillator IPM and Gaussian neutron-proton potential give a value of C about 25 percent lower than that for the closed-shell nuclei He and O. This calculation made in Cartesian coordinates, is not completely reliable, as arbitrary assumptions were made as to the filling of the neutron and proton shells in this coordinate system.

For large u, all the curves in Fig. 3 [Eqs. (16), (17), (18), and (20)] are proportional to u^{-3}. This result corresponds to the treatment without interference [LB, Eq. (14)] for the square-well neutron-proton potential. The u^{-3} dependence for fixed intrinsic range b corresponds to an r_0^{-3} dependence. That is, the average

value of $r_{ij}^2V(r_{ij})$ in Eq. (12) is proportional to the mean nucleon density. For small u, the IPM curves are proportional to u^2. For fixed b, small u corresponds to small r_0, or a small nucleus. The finite nuclear size then limits the average value of $r_{ij}^2V(r_{ij})$ to proportionality with r_0^2; i.e., proportionality to u^2. In the LB Fermi gas model, the coefficient is proportional to u for small u. Here LB used an infinite nucleus, the interference effect of the P_{ij} term greatly decreasing the value of the coefficient for small u, though the decrease due to the interference term is not as great as that considered here due to the finite nuclear size.

This discussion for large u and small u is not directly applicable to the actual case of u about 0.6. However the discussion indicates the similarity of the LB Fermi gas treatment and IPM treatment at least in the extreme cases of large u and small u.

Preliminary numerical results by Gell-Mann, Goldberger, and Thirring[3] (GGT) for the integrated *total* photonuclear cross section give an increase of about forty percent over the standard sum-rule result of $0.015A$ Mev-barns. Their numerical result agrees surprisingly well with the LB result (and that of this paper) of $0.8x$, using x about $\frac{1}{2}$. We might speculate briefly that these quite different calculations give similar results because the approximations used are more closely related than appears on the surface. The fundamental approximation of the GGT calculation is the assumption that the forward-scattering amplitude for extremely high-frequency electromagnetic waves is the same for A nucleons bound in a nucleus as for the A free nucleons. (Given this one assumption, the GGT calculation then proceeds using dispersion theory relations between the forward-scattering amplitude and the total photonuclear cross section. The numerical results are based on the difference of pion photoproduction cross sections for free and bound nucleons.) The GGT assumption of the high-frequency forward-scattering amplitude appears to be closely related to the assumption that the nucleus is essentially a nonrelativistic system. (For example, in atomic physics *if* we can calculate the forward-scattering amplitude using the atomic form factor, as is appropriate for a nonrelativistic system for frequencies far from those giving any appreciable absorption, we find that the atomic forward scattering is just that of Z free electrons.) The assumption that a nucleus is essentially a nonrelativistic system is, in turn, needed to justify the several approximations of the LB treatment (or that of this paper): (a) the use of a phenomenological treatment of the meson exchange currents, as in Siegert's theorem;[28] (b) the calculation of electric dipole processes only; and (c) the neglect of retardation in calculation of the matrix element. (Several theorists have suggested that the last two approximations tend to cancel.)

Thus it seems possible that the agreement of the GGT result with that of LB and this paper is caused by both calculations resting on the same basic assumption of neglect of relativistic effects in a nucleus. On the other hand, it is quite possible that any numerical agreement between the GGT and LB calculations is fortuitous, and may disappear completely when more accurate numerical calculations are made.

V. DISCUSSION

In I we concentrated on the calculation of the harmonic mean energy W_H for two nuclei. In this paper Eq. (6) gives $W_H=42A^{-\frac{1}{3}}$ Mev for a simple harmonic oscillator IPM with $r_0=1.2$, and pure ordinary forces. A Serber force gives about 40 percent increase in σ_{int}, and therefore in W_H, giving the value $W_H=60A^{-\frac{1}{3}}$ Mev.

This value of the harmonic mean energy, corrected for exchange effects, is somewhat low when compared with experiment, though it is not in serious disagreement with experimental results.

Since we have shown in Fig. 2 that our calculated bremsstrahlung-weighted cross section σ_b is in reasonable agreement with our preliminary interpretation of photonuclear experiments, the disagreement between the calculated and experimental harmonic mean energies implies a disagreement between the calculated and experimental values of σ_{int}, the experimental values being somewhat higher. Recent summaries,[12,13] give rather good agreement for medium and heavy nuclei between calculated and experimental σ_{int} (using $x=\frac{1}{2}$ for a Serber force). We believe that if the integrations were done up to an energy of 150 Mev (in accord with the GGT calculation) that the experimental cross sections would be somewhat higher than the calculated value for the whole range of nuclei. (See, for example, the Jones-Terwilliger value of σ_{int} for Ta.) Since the high-energy cross sections are still poorly known, we cannot do more than speculate on this question. Neutron-proton correlations, as for example in the quasi-deuteron model which may be a valid approximation for high-energy photons[30] would tend to decrease σ_b and to increase σ_{int}. Both effects would increase W_H.

We believe we have shown that a crude independent-particle model for the nuclear ground state gives results for the bremsstrahlung-weighted cross section σ_b, for the integrated cross section, and for the harmonic mean energy that are not inconsistent with present experimental data. More experimental data are needed, particularly in the energy region from 25 to about 100 Mev. Also an analysis of the experimental data to give the quantities σ_b and W_H as well as σ_{int} would be of use in comparing experiments with sum-rule calculations. The independent-particle model calculation should be refined, and deviations from the IPM (as in the quasi-deuteron model) should be studied.

[30] M. Q. Barton and J. H. Smith, Phys. Rev. **95**, 573 (1954); and Myers, Odian, Stein, and Wattenberg, Phys. Rev. **95**, 576 (1954).

ACKNOWLEDGMENT

We wish to thank D. C. Kent and S. Brote for their assistance in performing many calculations for this paper. We wish to thank E. G. Fuller, M. L. Goldberger, P. Morrison, and W. B. Payne for discussions of these problems.

APPENDIX

Harmonic Mean Energy

Here we derive certain well-known results in a different manner. First we wish to shown the relation between the Heisenberg uncertainty principle and the delta-function shape of the $\sigma(W)$ curve for simple harmonic oscillator wave functions. For simplicity we shall work with only one particle in a simple harmonic oscillator potential.

Using the notation and some equations from LB,[2] we have

$$\sum_n f_{0n}=1, \tag{A1}$$

$$\sum_n (E_n-E_0)f_{0n}=(2/M)(p^2)_{00}, \tag{A2}$$

$$\sum_n f_{0n}/(E_n-E_0)=(2M/\hbar^2)(z^2)_{00}. \tag{A3}$$

Here f_{0n} is the oscillator strength, z is the component of the displacement, and p of the momentum, along the polarization direction. Since $\bar{p}=\bar{z}=$ zero for the ground (0) state, we write

$$(\Delta p)^2=(p^2)_{00};\quad (\Delta z)^2=(z^2)_{00}. \tag{A4}$$

Using these equations, we find the mean energy $\bar{W}$ and the harmonic mean energy W_H:

$$\bar{W}=\sum_n (E_n-E_0)f_{0n}/\sum_n f_{0n}=(2/M)(\Delta p)^2, \tag{A5}$$

$$W_H=\sum_n f_{0n}/[\sum_n f_{0n}/(E_n-E_0)]=\hbar^2/2M(\Delta z)^2. \tag{A6}$$

For any shape of the photon absorption curve we must have $\bar{W}\geq W_H$. Using this inequality together with Eqs. (A5) and (A6), we find:

$$(2/M)(\Delta p)^2\geq\hbar^2/2M(\Delta z)^2,$$

or

$$(\Delta p)^2(\Delta z)^2\geq\hbar^2/4. \tag{A7}$$

This is a rather indirect method of deriving the Heisenberg uncertainty principle. Further, the equality between $\bar{W}$ and W_H holds only for a delta-function shape of the $\sigma(W)$ curve; while the equality in the Heisenberg uncertainty principle holds only for a simple harmonic oscillator potential. Thus we have related these two properties of simple harmonic oscillator wave functions.

For many particles in a simple harmonic oscillator IPM, we want to show that $W_H=\hbar\omega$. Using the notation of I,[1] we write the harmonic mean energy:

$$W_H=(\hbar^2/2M)A/(D+B), \tag{A8}$$

where the diagonal term is

$$D=(\sum_i z_i^2)_{00}=(\hbar/M\omega)\sum_n (n+\tfrac{1}{2})c_n, \tag{A9}$$

and the off-diagonal term B due to the Pauli principle correlations between protons is given by

$$B=-\sum_k\sum_l (z_{kl})^2. \tag{A10}$$

In these equations n is the quantum number for motion in the z direction; c_n is the number of protons that have quantum number n; and z_{kl} is the dipole matrix element between occupied states k and l. Using the value $(z_{kl})^2=(\hbar/2M\omega)$ (the larger quantum number) where $n_k=n_l\pm1$, we find that for all but the highest occupied level the contribution to B exactly cancels the contribution to D. For this highest level we have

$$D+B=(n+1)\hbar/2M\omega \text{ per nucleon.} \tag{A11}$$

We must multiply this result by the number of nucleons in the highest level with a given value of n, and sum. (For simplicity we have taken the case where the highest occupied level is completely full.)

$$\begin{aligned} D+B&=(2\hbar/M\omega)\sum_{n=0}^{N}(n+1)(N-n+1)\\ &=(\hbar/3M\omega)(N^3+6N^2+11N+6). \end{aligned} \tag{A12}$$

Here N is the total quantum number for the highest occupied level.

We wish to compare this summation with the mass number A in the numerator of Eq. (A8), expressed as

$$\begin{aligned} A&=2\sum_n (n+1)(n+2)\\ &=\tfrac{2}{3}(N^3+6N^2+11N+6). \end{aligned}$$

We find from Eqs. (A8), (A12), and (A13) that the harmonic mean energy is indeed $\hbar\omega$, as we knew it must be for a simple oscillator.

A completely analogous calculation has shown that the mean energy $\bar{W}$ also equals $\hbar\omega$.

Angular Distribution of Protons from the Reaction $Ti^{48}(d,p)Ti^{49}$†

WILLIAM W. PRATT*
Department of Physics, State University of Iowa, Iowa City, Iowa
(Received August 23, 1954)

The angular distribution has been measured for transitions to excited states in Ti^{49} at 1.40 and 1.74 Mev. The deuteron energy was 2.6 Mev. The angular distributions are characterized by a peak at about 75° angle of proton emergence with respect to the deuteron beam direction. These results are suggestive of a stripping reaction with significant Coulomb effects. A rough determination of absolute cross section values gives 0.05 mb, 0.57 mb, 0.35 mb, and 0.2 mb, respectively, for transitions to the ground state and excited states at 1.40 Mev, 1.74 Mev, and 2.45 Mev in Ti^{49}.

MEASUREMENTS of the angular distribution of protons resulting from 3-Mev deuteron bombardment of nickel[1] have indicated that, for this bombarding energy, the angular distribution of the protons is in agreement with the predictions of compound nucleus theory.[2] It was suggested[1] that the apparent absence of the stripping process in this case may be connected with a dependence of the ratio, σ(stripping)/σ(compound nucleus formation), on the relative values of the deuteron energy and the Coulomb barrier of the target nucleus. In an attempt to find other cases in which compound nucleus formation is predominant, measurements have been made using natural titanium as the target and a deuteron energy sufficiently low that the deuteron penetrability is of the same order of magnitude (a few percent for $l=0$ deuterons) as in the previous measurements with nickel.

Titanium was chosen as the target for this experiment since it has one predominat isotope (73.4 percent Ti^{48}) of known spin 0^+ (even-even isotope) leading to an isotope (Ti^{49}) with fairly well-spaced energy levels[3] and for which the ground state spin is known[4] to be $7/2^-$. The statistical theory of compound nucleus formation[2] predicts a rather distinctive angular distribution, symmetrical about 90°, for the case of a $0^+ \rightarrow 7/2^-$ transition.

A 0.5-mg/cm² target of TiO_2 was prepared on a silver backing from a suspension of TiO_2 in ethyl alcohol. The target was bombarded with deuterons of energy 2.6 Mev in the laboratory coordinate system. The emerging protons, after passing through absorbers of Ag and Al, were detected in Eastman NTA emulsions. The absorbers were employed to prevent any deuterons from reaching the emulsion and to reduce the proton range in the emulsion to a convenient length for range measurements with a calibrated microscope eyepiece scale. After corrections for proton energy loss in the absorbers were made,[5] the range-energy relation of Richards *et al.*[6] was used to deduce the proton energy. By applying this procedure to various regions of the emulsions, it was thus possible to obtain proton energy spectra corresponding to various angles of proton emergence, and to obtain the angular distributions of proton groups which are resolved from their neighbors.

Preliminary measurements indicated the ground state group of Ti^{49} to be of relatively weak intensity and to be appreciably overlapped by neighboring groups presumably due to the other isotopes. Consequently it was found to be impossible to obtain reliable angular distribution measurements for this group. The two excited states at 1.40 Mev and 1.74-Mev excitation[3] were, however, reasonably well resolved at all angles. The spectrum at 45° angle of proton emergence is shown in Fig. 1 for the energy region in the vicinity of the proton groups corresponding to these states. Groups 1 and 2 respectively correspond to the excited states in Ti^{49} at 1.40 and 1.74 Mev. Group 3, which is not well resolved from its neighbors at all angles, corresponds to the excited state in Ti^{49} at 2.45 Mev.[3]

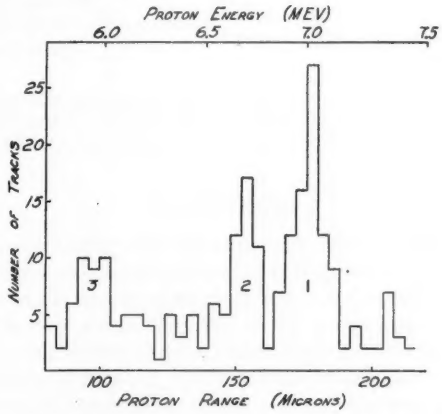

FIG. 1. Proton spectrum in the energy region corresponding to transitions to states in Ti^{49} at (1) 1.40 Mev, (2) 1.74 Mev, and (3) 2.45 Mev.

† This work was supported in part by the U. S. Atomic Energy Commission.
* Now at the Pennsylvania State University, State College, Pennsylvania.
[1] William W. Pratt, Phys. Rev. **94**, 1086 (1954); Phys. Rev. **95**, 1517 (1954).
[2] L. Wolfenstein, Phys. Rev. **82**, 690 (1951).
[3] G. F. Pieper, Phys. Rev. **87**, 215(A) (1952).
[4] C. D. Jeffries, Phys. Rev. **92**, 1096 (1953).
[5] Aron, Hoffman, and Williams, U. S. Atomic Energy Commission Report AECU-663, May 28, 1951 (unpublished).
[6] Richards, Johnson, Ajzenberg, and Laubenstein, Phys. Rev. **83**, 994 (1951).

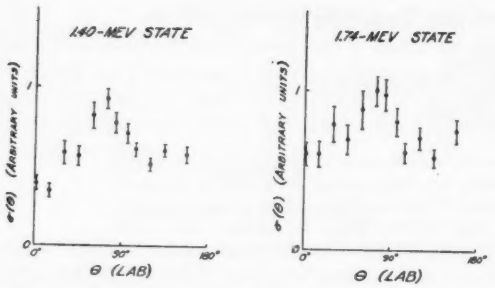

FIG. 2. Angular distribution of protons from the (d,p) reaction leading to excited states in Ti^{49} at 1.40 Mev and 1.74 Mev. The errors indicated are statistical standard deviations.

The angular distributions of Groups 1 and 2 are shown in Fig. 2. The statistical standard deviation in cross section values is of the order of 10 percent; and the angular resolution is of the order of 3°. Center-of-mass corrections are small compared with these values and have been neglected. It is apparent that the statistical theory of compound nucleus formation,[2] which is characterized by a symmetry of the angular distribution about 90°, is not applicable to these reactions. The stripping process, however, is known[7,8] to give rise to an angular distribution which is of the same general character as the data in Fig. 2. Although it is not possible to fit the data with the Butler theory,[7] the fact that the deuteron energy in this experiment is well below the Coulomb barrier of the target implies that Coulomb effects not accounted for in the Butler theory may be particularly important in this case. Computations have recently been carried out by Tobocman and Kalos,[8] which take into account Coulomb effects as well as proton absorption. These computations, for a particular choice of the proton scattering amplitudes β_l, result in an angular distribution which does indeed reproduce the general behavior of the experimental points.

From the known values of source thickness, integrated beam current, and solid angle observed, it is possible to determine the absolute values of the reaction cross sections. The total cross sections are found to be 5.7×10^{-28} cm² for the transition to the 1.40-Mev state of Ti^{49} and 3.5×10^{-28} cm² for the transition to the 1.74-Mev state. These values are believed to be accurate to within a factor of 2. The cross sections for the transitions to the ground state and to the 2.45-Mev state of Ti^{49} are estimated to be of the order of 0.5×10^{-28} cm² and 2×10^{-28} cm², respectively.

We are indebted to Dr. W. Tobocman and Dr. M. H. Kalos for making their calculations available to us prior to publication.

[7] S. T. Butler, Proc. Soc. (London) **A208**, 559 (1951).
[8] W. Tobocman and M. H. Kalos, following paper, Phys. Rev. **97**, 132 (1955).

PHYSICAL REVIEW VOLUME 97, NUMBER 1 JANUARY 1, 1955

Numerical Calculation of (d,p) Angular Distributions*

W. TOBOCMAN† AND M. H. KALOS
Laboratory of Nuclear Studies, Cornell University, Ithaca, New York
(Received September 20, 1954)

The (d,p) cross section has been calculated by taking into account the Coulomb interaction, the interaction of the liberated protons with the residual nucleus, and the scattering of the incident deuteron beam. These effects were found to be important in all the cases considered.

I. INTRODUCTION

WHEN a thin film of matter is bombarded with a monoenergetic beam of deuterons, one observes among the reaction products energy groups of protons. Each energy group can be identified with a level of the residual nucleus. By measuring the Q of such a reaction one can determine the energies of the associated levels of the residual nucleus. It has been shown in recent years that the shapes of the angular distributions of the proton groups can be used to fix the parities and learn something about the spins of the levels of the residual nucleus.[1] The intensities of the proton groups have been shown to be proportional to the reduced widths of these levels.[2] Thus the (d,p) reaction is a powerful tool for nuclear spectroscopy.

Previous theoretical treatments of the (d,p) reaction have been based on rather sweeping approximations. Nevertheless, these theories, in particular that due to S. T. Butler, have been able to describe the main aspects

* Assisted by the joint program of the U. S. Office of Naval Research and the U. S. Atomic Energy Commission.
† Now at the Princeton Institute for Advanced Study, Princeton, New Jersey.

[1] S. T. Butler, Proc. Roy. Soc. (London) **A208**, 559 (1951); A. B. Bhatia *et al.*, Phil. Mag. **43**, 485 (1952); R. Huby, Nature **166**, 552 (1950).
[2] R. Huby, Proc. Roy. Soc. (London) **A215**, 385 (1952); S. Yoshida, Progr. Theoret. Phys. Japan **10**, 1, 370 (1953); F. L. Friedman and W. Tobocman, Phys. Rev. **92**, 93 (1953); Fujimato, Kikuchi, and Yoshida, Progr. Theoret. Phys. Japan **11**, 3, 264 (1954).

of the (d,p) angular distributions, and the spins and parities determined in this way have agreed for the most part with the results of other methods. But the Butler theory has not been uniformly successful in matching angular distributions, and the reduced widths measured by means of the Butler theory have differed from those determined by other methods by large factors.

In an article by one of the authors[3] an approximate expression for the (d,p) cross section was derived which was suitable for numerical evaluation and which included effects neglected in previous treatments. The effects referred to are those caused by the Coulomb interaction, the specifically nuclear interaction between the liberated proton and the residual nucleus, and the scattering of the incident deuteron beam.

This expression for the (d,p) cross section has the following form:[4]

$$\sigma_L(\theta_P)=\gamma_L\frac{(2J+1)\hbar^3\epsilon^{\frac{1}{2}}(1+M_N/M_I)(1+M_D/M_I)^{-1}(1+M_P/M_F)^{-1}}{(2I+1)R|E_N|E_D^{\frac{1}{2}}E_P^{\frac{1}{2}}M_NM_D^{\frac{1}{2}}}\sum_{m=-L}^{L}|B^{Lm}|^2, \tag{1}$$

$$B^{Lm}=\sum_{l=0}^{\infty}P_l^{|m|}(\cos\theta_P)\sum_{\lambda}f_{l\lambda}{}^L\Gamma_{l\lambda}{}^{Lm}\exp\{i[\sigma_l(\eta_P)+\sigma_\lambda(\eta_D)+(\pi/2)(\lambda-l)]\}, \tag{2}$$

$$\Gamma_{l\lambda}{}^{Lm}=\frac{(2\lambda+1)(2l+1)}{(2L+1)}\left[\frac{(l-|m|)!}{(l+|m|)!}\right]^{\frac{1}{2}}(l\lambda00|l\lambda L0)(l\lambda m0|l\lambda Lm), \tag{3}$$

$$f_{l\lambda}{}^L=\frac{|K_N|}{h_L{}^{(1)}(i|K_N|R)}\int_{R(1+M_N/M_I)}^{\infty}drh_L{}^{(1)}(i|K_N|R)[F_\lambda(\eta_D,K_Dr)-\alpha_\lambda H_\lambda(\eta_D,K_Dr)]$$
$$\times\left[F_l\left(\eta_P,\frac{K_Pr}{1+M_N/M_I}\right)-\beta_l H_l\left(\eta_P,\frac{K_Pr}{1+M_N/M_I}\right)\right], \tag{4}$$

where θ_P = angle of the liberated proton with respect to the incident deuteron,
E_D = energy of the incident deuteron (center-of-mass),
E_P = energy of the liberated proton (center-of-mass),
ϵ = binding energy of the deuteron,
$E_N=E_D-E_P-\epsilon=-Q-\epsilon$,
R = radius of the target nucleus,
γ_L = reduced level width of the residual nucleus,
J = spin of the residual nucleus,
I = spin of the target nucleus,
M_P = proton mass,
M_N = neutron mass,
M_D = mass of the deuteron,
M_I = mass of the target nucleus,
M_F = mass of the residual nucleus,
L = orbital angular momentum of the captured neutron,
$(l\lambda m0|l\lambda Lm)$ = the Clebsch-Gordan coefficient,
$F_l(\eta,\rho)$ = regular radial Coulomb wave function,
$G_l(\eta,\rho)$ = irregular radial Coulomb wave function,
$H_l=F_l-iG_l$,
$\sigma_l(\eta)=\arg\Gamma(1+l+i\eta)$,
Z = atomic number of target nucleus,

$$\eta_D=\frac{Z}{137.04}\left[\frac{M_Dc^2}{2E_D}\left(1+\frac{M_D}{M_I}\right)^{-1}\right]^{\frac{1}{2}},$$

$$\eta_P=\frac{Z}{137.04}\left[\frac{M_Pc^2}{2E_P}\left(1+\frac{M_P}{M_F}\right)^{-1}\right]^{\frac{1}{2}},$$

$$K_D{}^2=2E_D\hbar^{-2}M_D(1+M_D/M_I)^{-1},$$
$$K_P{}^2=2E_P\hbar^{-2}M_P(1+M_P/M_F)^{-1},$$
$$|K_N|^2=2|E_N|M_N\hbar^{-2}(1+M_N/M_I)^{-1}.$$

The α_λ and β_l appearing in the expression for $f_{l\lambda}{}^L$ are the partial wave scattering amplitudes appropriate

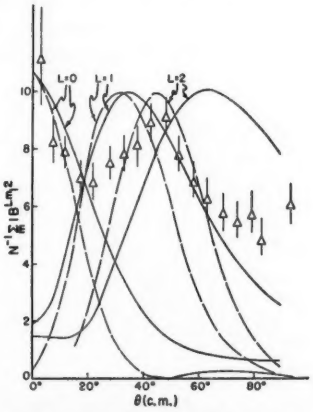

FIG. 1. The Coulomb effect on the (d,p) reaction. The angular distribution of protons from the $F^{19}(d,p)F^{20}$ reaction is calculated from the Butler theory (dashed lines) and from the Butler theory +Coulomb interaction (solid lines). $E_D=3.6$ Mev (lab), $Q=4.37$ Mev, $R=5.05\times10^{-13}$ cm.

[3] W. Tobocman, Phys. Rev. 94, 1655 (1954).

[4] In reference 3 the σ_L and σ_λ appear in Eqs. (26), (30), and (31) with the wrong sign.

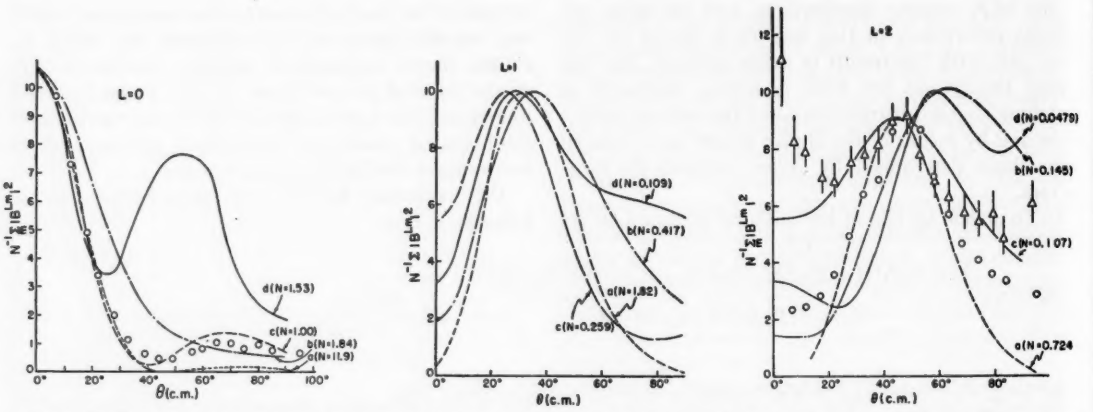

FIG. 2. The Coulomb and nuclear effects on the (d,p) reaction, for $L=0$, 1, 2. The angular distribution of protons from the $F^{19}(d,p)F^{20}$ reaction calculated from (*a*) Butler theory, (*b*) Butler+Coulomb, (*c*) Butler+Coulomb+absorption of protons with $l\leqslant 2$, (*d*) Butler +Coulomb+hard sphere scattering of protons. $E_D=3.6$ Mev (lab), $Q=4.37$ Mev, $R=5.05\times10^{-13}$ cm. Experimental points shown are due to Bromley *et al.* (see reference 5). The Q values corresponding to these points are $L=2$, triangles, $Q=4.37$ Mev; $L=2$, circles, $Q=3.72$ Mev; $L=0$, $Q=0.88$ Mev.

to the interaction of deuterons with the target nucleus and the interaction of protons with the residual nucleus respectively.

If one assumes that $0=Z=\alpha_\lambda=\beta_l$, then Eq. (2) becomes

$$B^{Lm}=\frac{-\delta_{m0}i^L R^2 K_P K_D(1+M_N/M_I)}{|K_N|(1+|K_N|^{-2}\kappa^2)}\left[\frac{d}{dr}j_L(\kappa r)\right.$$
$$\left.-j_L(\kappa r)\frac{d}{dr}\ln h_L^{(1)}(i|K_N|r)\right]_{r=R(1+M_N/M_I)}, \quad (5)$$

where $\boldsymbol{\kappa}=\mathbf{K}_D-(1+M_N/M_I)^{-1}\mathbf{K}_P$, $j_L(\rho)$=the spherical Bessel function, and $h_L^{(1)}(\rho)$=the spherical Hankel function of the first kind. This expression, introduced into Eq. (1), gives the Butler (d,p) cross section.

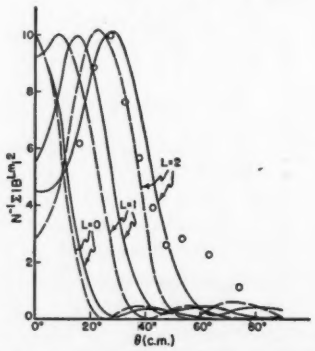

FIG. 3. The Coulomb effect on the (d,p) reaction. The angular distribution of protons from the $F^{19}(d,p)F^{20}$ reaction is calculated from the Butler theory (dashed lines) and from the Butler theory +Coulomb interaction (solid lines). $E_D=14.3$ Mev (lab), $Q=4.37$ Mev, $R=5.05\times10^{-13}$ cm. The experimental points are due to Black. (See reference 6.)

II. CALCULATION

We have used an I.B.M. card-programmed computer to evaluate the quantity $\sum_m|B^{Lm}|^2$ appearing in Eq. (1). This quantity is dimensionless and contains the angular dependence of the (d,p) cross section $\sigma_L(\theta_P)$. The computation was a direct numerical evaluation and involved no approximations. The results of our computations are displayed in Figs. 1–7 together with some experimental points.

A factor N is introduced to provide convenient normalization. The experimental points appearing on Fig. 2 were taken from the work of Bromley *et al.*[5] The Q-value 4.373 Mev is appropriate only to the points represented by the triangles which correspond to stripping due to the ground state of F^{20}. The two angular distributions represented by circles are due to two excited states of F^{20}. Since our expression for the (d,p) cross section is not very sensitive to variations in the value of Q, we thought it would be of interest to display the latter points. The points shown on Figs. 3 and 4 are due to Black,[6] and the points displayed on Fig. 5 are the results of work by Pratt.[7]

The computations involved various choices for the parameters Z, α_λ, and β_l. In the accompanying figures we identify the choice in the following manner.

(1) $Z=0$, $\alpha_\lambda=0$, $\beta_l=0$: "Butler theory."

(2) $Z=Z$ of target nucleus, $\alpha_\lambda=0$, $\beta_l=0$: "Butler +Coulomb."

(3) $Z=Z$ of target nucleus, $\alpha_\lambda=0$, $\beta_l=\frac{1}{2}$ for $l\leqslant l_1$, and $\beta_l=0$ for $l>l_1$: "Butler+Coulomb+absorption of protons with $l\leqslant l_1$."

(4) $Z=Z$ of target nucleus, $\alpha_\lambda=0$, $\beta_l=F_l(\eta_P,K_PR)/$

[5] Bromley, Bruner, and Fulbright, Phys. Rev. **89**, 396 (1952).
[6] C. F. Black, Ph.D. thesis, Massachusetts Institute of Technology 1953 (unpublished).
[7] W. W. Pratt, preceding paper [Phys. Rev. **97**, 131 (1954)].

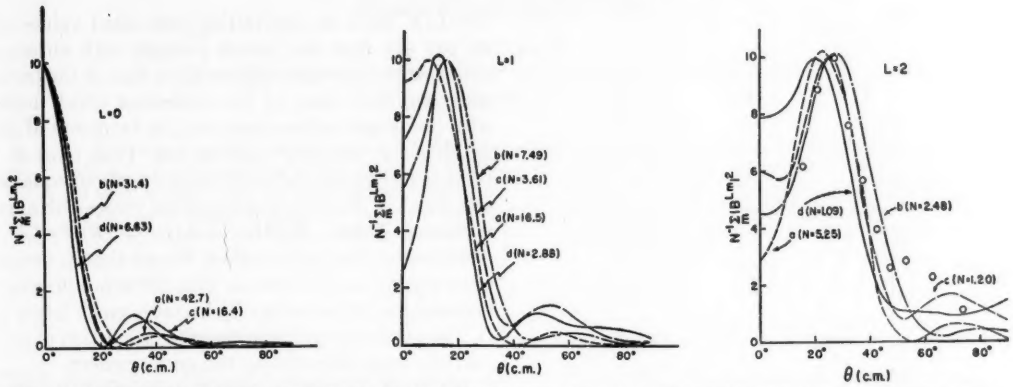

FIG. 4. The Coulomb and nuclear effects on the (d,p) reaction, for $L=0, 1, 2$. The angular distribution of protons from the $F^{19}(d,p)F^{20}$ reaction is calculated from (*a*) Butler theory, (*b*) Butler+Coulomb, (*c*) Butler+Coulomb+absorption of protons with $l\leqslant 4$, (*d*) Butler+Coulomb+hard sphere scattering of protons. $E_D=14.3$ Mev (lab), $Q=4.37$ Mev, $R=5.05\times10^{-13}$ cm. The experimental points are due to Black. (See reference 6.)

$H_l(\eta_P,K_PR)$: "Butler+Coulomb+hard sphere scattering for protons."

(5) $Z=Z$ of target nucleus, $\alpha_\lambda=\frac{1}{2}$ for $\lambda\leqslant\lambda_1$ and $\alpha_\lambda=0$ for $\lambda>\lambda_1$, $\beta_l=[F_l'(\eta_P,K_PR)+iKRF_l(\eta_P,K_PR)]/[H_l'(\eta_P,K_PR)+iKRH_l(\eta_P,K_PR)]$, $K=(K_P^2+1\times10^{-26}\ \text{cm}^{-2})^{\frac{1}{2}}$: "Butler+Coulomb+continuum theory for protons+absorption of deuterons with $\lambda\leqslant\lambda_1$," etc.

In Figs. 6 and 7 we have examples of how strongly the (d,p) cross section can be influenced by the nuclear effects represented by the scattering amplitudes α_λ and β_l. In Fig. 6, various combinations of models were employed as a basis for the choice of the scattering amplitudes. In Fig. 7 we investigate the effect of a resonance in one of the proton scattering amplitudes. To be specific, we assume no deuteron scattering and absorption of protons with l smaller than 3 except for one proton scattering amplitude which is given the resonance value

$$\beta_l=-2\bar{\gamma}\Gamma^{-1}K_PRH_l(\eta_P,K_PR)^{-2}=-10H_l(\eta_P,K_PR)^{-2},$$

Γ being the reaction width and $\bar{\gamma}$ being the reduced width of the proton resonance. The value $2\bar{\gamma}\Gamma^{-1}K_PR=10$ is chosen arbitrarily.

III. DISCUSSION

Inspection of the calculated angular distribution discloses that the effect of introducing the Coulomb interaction into the theory is to displace the angular distribution toward larger angles and to broaden the peaks and fill in the valleys. The value of the total cross section is reduced. In extreme cases, such as the one shown in Fig. 5, these Coulomb effects can be so

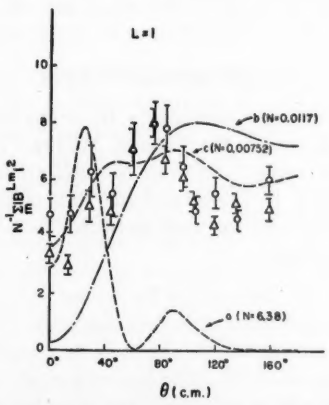

FIG. 5. The Coulomb and nuclear effects on the (d,p) reaction. The angular distribution of protons from the $Ti^{48}(d,p)Ti^{49}$ reaction is calculated from (*a*) Butler theory, (*b*) Butler+Coulomb, (*c*) Butler+Coulomb+absorption of protons with $l\leqslant1$. $E_D=2.60$ Mev (lab), $Q=4.46$ Mev, $R=6.49\times10^{-13}$ cm. The experimental points are due to Pratt. (See reference 7.) The triangles represent the reaction with $Q=4.46$ Mev and the circles represent the reaction with $Q=4.11$ Mev.

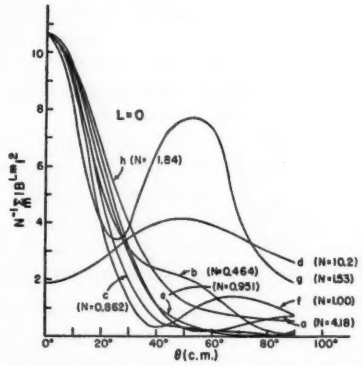

FIG. 6. The Coulomb effect, nuclear effect, and the effect due to the scattering of the incident deuteron beam on the (d,p) reaction. The angular distribution of protons from the $F^{19}(d,p)F^{20}$ reaction is calculated from Butler+Coulomb+(*a*) absorption of deuterons with $\lambda\leqslant2$, (*b*) continuum theory for protons, (*c*) absorption of deuterons with $\lambda\leqslant1$+absorption of protons with $l\leqslant2$, (*d*) absorption of deuterons with $\lambda\leqslant1$+hard sphere scattering for protons, (*e*) absorption of deuterons with $\lambda\leqslant1$+continuum theory for protons, (*f*) absorption of protons with $l\leqslant2$, (*g*) hard sphere scattering for protons, (*h*) nothing. $E_D=3.6$ Mev (lab), $Q=4.37$ Mev, $R=5.05\times10^{-13}$ cm.

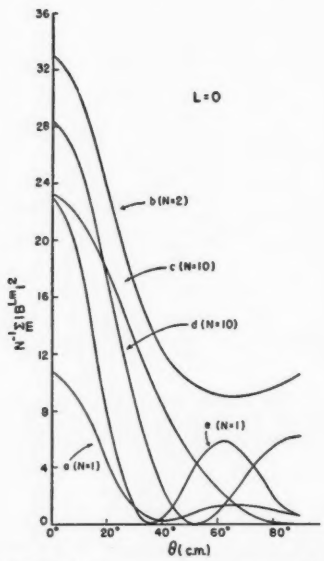

FIG. 7. The effects of resonances in the nuclear interaction on the (d,p) cross section. The angular distribution of protons from the $F^{19}(d,p)F^{20}$ reaction is calculated from Butler+Coulomb+absorption of protons with $l\leqslant 2+(a)$ no resonance, (b) resonance on the protons with $l=0$, (c) resonance on the protons with $l=1$, (d) resonance on the protons with $l=2$, (e) resonance on the protons with $l=3$. $E_D=3.6$ Mev (lab), $Q=4.37$ Mev, $R=5.05\times10^{-13}$ cm.

great as to distort completely the angular distribution. Even in a most favorable case where 14.3-Mev deuterons are incident on F^{19} (Fig. 3), we find that the Coulomb effects are not negligible although they are not great enough to make the choice of L uncertain.

One observes that the effect of introducing the nuclear interactions by giving α_λ and β_l nonzero values is in general opposite to the Coulomb effect—peaks are displaced toward smaller angles and become less broad. The nuclear effect on the total cross section, however, is in the same direction as the Coulomb effect, i.e., the total cross section is further reduced.

The nuclear effect on the (d,p) cross section is enhanced as the Coulomb effect becomes more important. This behavior can be explained as follows. When a neutron is captured with angular momentum $L\hbar$ from a deuteron of angular momentum $\lambda\hbar$, then the liberated proton has an angular momentum between $(\lambda+L)\hbar$ and $|\lambda-L|\hbar$. Since we are dealing with small values of L, we can say that the proton emerges with an angular momentum approximately equal to that of the incident deuteron. But most of the deuterons which interact with the target nucleus have angular momenta of about $R[2M_D(E_D-Ze^2/R)]^{\frac{1}{2}}=\lambda_0\hbar$ or less. Thus most of the protons emerge with angular momenta about equal to or less than $\lambda_0\hbar$. Now the proton partial waves with angular momenta below $R[2M_P(E_D+Q-Ze^2/R)]^{\frac{1}{2}}=l_0\hbar$ are distorted by the nuclear effect. We see that λ_0 decreases more rapidly with Z than l_0. This difference in behavior becomes less important as E_D becomes much larger than Q. Thus increasing Z increases the proportion of proton partial waves distorted by the nuclear effect.

We conclude that in order to determine the angular momentum of the captured particle from the deuteron-stripping angular distribution without making hypotheses about the scattering amplitudes for the incident deuterons and the emitted protons, the experiment must be performed with deuterons having energies well above the Coulomb barrier. However, even at such elevated energies the normalization of the cross section is still sufficiently sensitive to the Coulomb and nuclear effects to permit nothing better than a gross order of magnitude estimate of the reduced width when these effects are neglected.

Thus the presence of Coulomb and nuclear effects render the use of deuteron stripping to gain information about the spins, parities, and reduced widths of nuclear levels more cumbersome. On the other hand, deuteron stripping presents us with a new tool for the study of proton and neutron interactions with nuclei. For instance, it would be very interesting to study proton elastic scattering and the corresponding (d,p) reaction side by side, trying to fit the angular distributions from both experiments with the same set of scattering amplitudes.

IV. ACKNOWLEDGMENTS

The authors are indebted to H. Bethe for his help and encouragement. We thank W. W. Pratt for making his data available to us prior to publication. We also wish to thank R. Lesser and the staff of the Cornell Computing Center for their assistance in carrying out the computations.

Neutrinos from the Sun

A. M. CORMACK
Physics Department, University of Cape Town, Rondebosch, Cape, South Africa
(Received September 29, 1954)

The carbon cycle in the sun causes a large flux of neutrinos at the earth. The heat generated by these in the earth is calculated as a function of the neutrino magnetic moment. It is shown that this heat production is small compared to that resulting from the natural radioactivity of the core, that practically all of the carbon cycle energy liberated in the form of neutrinos in the sun is lost by the sun, and that the energy distribution of the neutrinos reaching the earth is practically the same as their energy distribution on creation in the sun.

1. INTRODUCTION

THE production of energy in the sun by means of the carbon cycle is the source of an enormous number of neutrinos, most of which escape from the sun producing a flux of between 10^{10} and 10^{11} neutrinos/cm^2 sec at the earth. In their passage through the earth, these might lose some of their energy by means of inelastic collisions with electrons and thus provide a source of heat over and above that provided by the natural radioactivity of the constituents of the earth and its possible contraction. It has been pointed out,[1] that heat generation in the earth by this means may be very small for two alternative reasons: (1) because both sun and earth are very transparent to neutrinos, or (2) because the sun is so opaque that most of the neutrino energy is dissipated in the sun, leaving little for the earth. The difference in the heat generated in the sun under these two conditions amounts to about 7 percent, an amount significant for astrophysics. The flux and energy distribution of the neutrinos reaching the earth is of interest for terrestrial experiments to detect the free neutrino, for example by inverse beta decay.[2]

2. INTERACTION OF NEUTRINOS WITH MATTER

The only ways by which neutrinos may lose energy to matter are by inverse beta decay and inelastic collisions. The cross section for inverse beta decay is known from detailed balancing arguments to be about 10^{-44} cm^2 and this is so small that the process may be ignored as far as neutrino absorption and heat generation in the sun and earth are concerned.

Inelastic collisions in which the neutrino could lose an appreciable amount of energy can only take place by means of the interaction of the magnetic moments of the neutrinos and electrons. If the former have zero rest-mass, the energy and angle relations between incident and scattered neutrinos and recoil electrons are the same as in the Compton effect and the cross section per unit solid angle per unit energy interval of the recoil electron has been found by Bethe[3] to be

$$\sigma(w)=\frac{\pi n^2}{mc^2}\left(\frac{e^2}{mc^2}\right)^2\frac{(E-W)}{EW(1+W)}, \quad (1)$$

where W and E are the energies of recoil electron and incident neutrino in units of mc^2 and n is the magnetic moment of the neutrino in Bohr magnetons. Nahmias,[4] interpreted his experimental results on the counting rates of well-shielded counters near a strong radium source on the basis of the above expression and was able to establish an upper limit for n of 1.8×10^{-4}. Since then, this limit has been progressively reduced and the latest result,[5] is $n<10^{-7}$.

If $\bar{W}$ is the mean energy loss of the neutrinos in a collision, the product $\sigma\bar{W}$ is readily found to be

$$\sigma\bar{W}=\pi n^2\left(\frac{e^2}{mc^2}\right)^2\left[\left(1+\frac{1}{E}\right)\log(1+W_m)-\left(\frac{W_m}{E}\right)\right]$$
$$=\pi n^2\left(\frac{e^2}{mc^2}\right)^2 f(E), \quad (2)$$

where $W_m=E/(1+1/2E)$ is the maximum energy of the recoil electrons.

3. SOLAR NEUTRINOS AND THEIR INTERACTION WITH THE EARTH

If one assumes that the carbon cycle is the source of the sun's energy and adopts a figure of 3.78×10^{33} ergs/sec for its energy output, the number of neutrinos produced in the sun is found to be 2.08×10^{38} per sec with an average energy of 0.93 Mev, if the data of Gamow and Critchfield[6] for the carbon cycle are used. Since there is no mechanism for the capture of neutrinos by the sun, all of them must leave the sun producing a flux of 7.4×10^{10} neutrinos/cm^2 sec at the earth.

[1] A. M. Cormack, Phys. Rev. **95**, 580 (1954).
[2] F. Reines and C. L. Cowan, Phys. Rev. **92**, 830 (1953).
[3] H. A. Bethe, Proc. Cambridge Phil. Soc. **31**, 108 (1935).
[4] M. E. Nahmias, Proc. Cambridge Phil. Soc. **31**, 90 (1935).
[5] C. L. Cowan and F. Reines (private communication). I should like to thank Drs. Cowan and Reines for making their results available to me before publication.
[6] G. Gamow and C. L. Critchfield, *Theory of Atomic Nucleus and Atomic Energy Sources* (Oxford University Press, London, 1949).

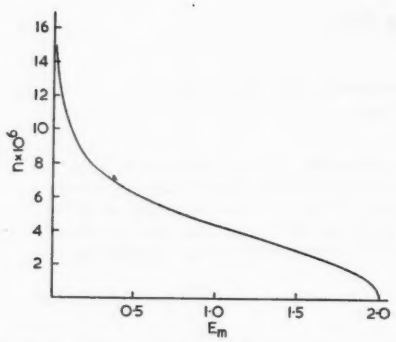

FIG. 1. The relation between E_m, the mean energy of neutrinos escaping from the sun, and the neutrino magnetic moment, n Bohr magnetons.

On their way out of the sun, they will lose energy by inelastic collisions and the mean energy of those arriving at the earth will be less than 0.93 Mev and may be estimated as follows. Suppose that all of the neutrinos are produced in the center of the sun with a mean energy E_0 and that E, $\rho(r)$, N_e are respectively the mean energy and density at a distance r from the center of the sun, and the number of electrons per gram of solar material. Then the mean energy loss of a neutrino transversing a thickness dr is

$$N_e\sigma(E)\bar{W}(E)\rho(r)dr, \tag{3}$$

and hence the mean energy, E_m, at the sun's radius, R, is the solution of

$$\int_{E_m}^{E}\frac{dE}{f(E)}=\pi n^2 N_e\left(\frac{e^2}{mc^2}\right)^2\int_0^R\rho(r)dr. \tag{4}$$

The value of E_m found from (4) will be correct only if the neutrino experiences a small number of collisions on its way out of the sun, but it will be at least of the right order of magnitude for a larger number of collisions since the crudeness of the treatment of the transfer problem will be somewhat offset by the assumption of a point source, rather than an extended source of energy production. Houtermans and Thirring[7] have treated the same problem somewhat differently. The advantage of the present treatment over theirs is this. They use σ itself, which is logarithmically divergent for the many free electrons in the sun, whereas $\sigma\bar{W}$ is finite for free electrons and is almost independent of the binding energy of the electron. It will be seen that, in view of the smallness of n established by Cowan and Reines, this advantage is one of principle only. If the neutrino flux at the earth is F and the number of electrons per gram of the earth is N_e, then the energy production in the earth will be

$$H=\pi n^2 N_e F\left(\frac{e^2}{mc^2}\right)^2 f(E_m)\ \text{ergs/g sec}. \tag{5}$$

[7] F. G. Houtermans and W. Thirring, Helv. Phys. Acta 27, 81 (1954).

The integral on the right-hand side of (4) has been evaluated on the assumption that the sun is a polytropic gas sphere of polytropic index 3, using the figures given for such a model by Eddington,[8] and the value found is 1.06×10^{12}. N_e and N_e have been taken as 4.06×10^{23} and 2.80×10^{23} on the assumption that the sun consists of 35 percent of hydrogen and 65 percent of heavier elements with a ratio of atomic number to mass number of 2, and that the earth is made of iron. Houtermans and Thirring,[7] have used more recent estimates of the density and chemical constitution of the sun, but the results do not depend critically on these. Equation (4) was solved for n as a function of E_m, numerical methods being used for $E_m>0.1$, and these results being combined with an analytical expression found by using the approximation $f(E)=W_m$, which is valid for $E_m<0.1$. The results are shown in Fig. 1 for $E_0=2\ mc^2$ which is approximately the mean energy of the neutrinos at the center of the sun. This relation between E_m and n was used to calculate H from (5), and H is shown as a function of n in Fig. 2. The shape of the curve in Fig. 2 is due to the fact that energy production in the earth may be small or zero either because both the sun and the earth are so transparent to neutrinos that there is no appreciable interaction with either, or because n is so large that the neutrinos lose most of their energy in the sun and are consequently unable to lose much more in the earth.

It is obvious from Fig. 1 that if $n<10^{-7}$, nearly all of the neutrino energy liberated in the sun (7 percent of the total) will escape, and also that the energy distribution of the neutrinos reaching the earth will be almost exactly the same as their energy distribution on creation in the sun.

4. HEAT PRODUCTION IN THE EARTH

It was hoped[1] that geophysical arguments could be used to place a limit on the heat generation in the earth by neutrinos and hence that limits could be placed on n by the use of the results shown in Fig. 2. Work on

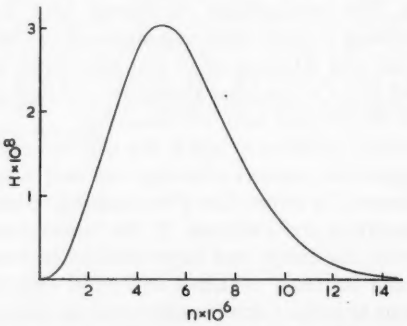

FIG. 2. The heat generation, H ergs/g/sec in the earth as a function of the neutrino magnetic moment, n Bohr magnetons.

[8] A. S. Eddington, *Internal Constitution of the Stars* (Cambridge University Press, London, 1930).

the heat balance of the earth's core, such as that of Bullard,[9,10] in connection with his theory of the earth's magnetism, indicate that geophysically significant rates of heat generation are about 1 to 3×10^{-8} erg/g sec, comparable to the heat generated by natural radioactivity in iron meteorites. Figure 2 shows that if $n<10^{-7}$, H is less than about 10^{-10} erg/g sec, and thus neutrino produced heat may be neglected in geophysical calculations. Also, no limits on the neutrino magnetic moment may be obtained on geophysical grounds.

[9] E. C. Bullard, Proc. Roy. Soc. (London) **A197**, 433 (1949).
[10] E. C. Bullard, Monthly Notices Roy. Astron. Soc. Geophys. Supp. **6**, 36 (1950).

5. CONCLUSIONS

The neutrinos produced in the sun undergo practically no inelastic collisions in either the sun or the earth, and reach to earth with almost the same energy that they had on creation in the sun.

I should like to thank Professor A. L. Hales for discussions on the heat balance of the earth's core.

PHYSICAL REVIEW VOLUME 97, NUMBER 1 JANUARY 1, 1955

Summing Studies of the Gamma Rays Following the Decays of Ba^{131}, Se^{75}, and Ru^{106}*

D. C. Lu, W. H. Kelly, and M. L. Wiedenbeck
Randall Laboratory of Physis, Univerity of Michigan, Ann Arbor, Michigan
(Received August 9, 1954)

Coincidences between the gamma rays following the decays in Ba^{131}, Se^{75}, and Ru^{106} have been examined with the summing technique. The experimental evidences lead to a new decay scheme for Ba^{131}. Some discrepancies with previous investigations are found in Se^{75}, which leads to a revision of the decay scheme.

I. Ba^{131}

THE γ rays emitted by Cs^{131} following K capture from Ba^{131} have been studied by several previous investigators.[1-3] Kurbatov *et al.*,[3] in the latest study, reported their energies to be 122, 214, 244, 370, and 496 kev. In the present investigation, the coincidences between these γ rays are studied, using the summing technique described previously.[4] It is found that the 122- and 496-kev γ rays are in cascade, whereas neither the 214-kev nor the 372-kev transition is in coincidence with any other γ rays except the K-capture x-rays. This is contrary to the findings of Kondaiah[1] and the previous belief that the 496-kev transition is the "cross-over" in parallel with the cascade comprising the 372- and 122-kev transitions.

The experimental result of the present study is presented in Fig. 1. The top curve represents the normal γ ray spectrum taken with the sample about 3 inches away from the NaI(Tl) crystal. It exhibits the existence of γ rays at 618, 496, 372, 214, and 122 kev. and a very strong peak at 30 kev due to Cs and Xe K x-rays. No positive sign of the 244-kev γ ray is noticed, though the 214-kev peak does appear to be somewhat broadened. Neither are there any positive indications of the weak γ rays at 108, 65, and 48 kev as previously reported.[3] The weak γ ray at 618 kev appears to be real, since its relative intensity changed very little when the sample is moved from 2 to 4 inches away from the phosphor. The peak at 85 kev is probably due to Ba^{133m} contamination. A weak peak at about 1.09 Mev is also noticed, (not shown) but no attempt was made to trace its half-life to see if it belongs to Ba^{131}.

When the sample was enclosed in a thin Lucite rod and introduced at the center of the phosphor, the summing spectrum, represented by the bottom curve, was obtained. Because of the sample thickness and the Auger effect, the K-capture x-rays are subjected to substantial absorption before they enter the phosphor. As a result, only part of the γ quanta entering the phosphor sum with a K-capture x-ray quantum. Indications of such summing are noticed at 122+30 kev, 214+30 kev, and 372+30 kev. The 496-kev transition sums with the 122-kev transition to form a strong sum peak at an energy somewhat higher than 618 kev because of further partial summing with K x-rays. Since the 122-kev transition is highly converted, some of the 496-kev quanta each sum with two K x-ray quanta. This leads to the odd shaped peak at 510 kev. A sum peak corresponding to the sum of two x-rays also appears at about 60 kev. No other sum peaks are noticed.

When the sample was contained in a thin copper capsule of 0.6-mm wall thickness to cut off the x-rays, and placed at the center of the phosphor, the summing spectrum represented by the middle curve was observed. It clearly indicates that neither the 372-kev nor the 214-kev γ ray is in coincidence with the 122-kev γ ray. If

* This study was supported by the Michigan Memorial Phoenix Project, University of Michigan.
[1] E. Kondaiah, Arkiv. Fysik **2**, 295 (1950).
[2] R. Canada and A. C. G. Mitchell, Phys. Rev. **83**, 76 (1951).
[3] Elliott, Cheng, Haskins, and Kurbatov, Phys. Rev. **88**, 263 (1952).
[4] D. C. Lu and M. L. Wiedenbeck, Phys. Rev. **94**, 501 (1954).

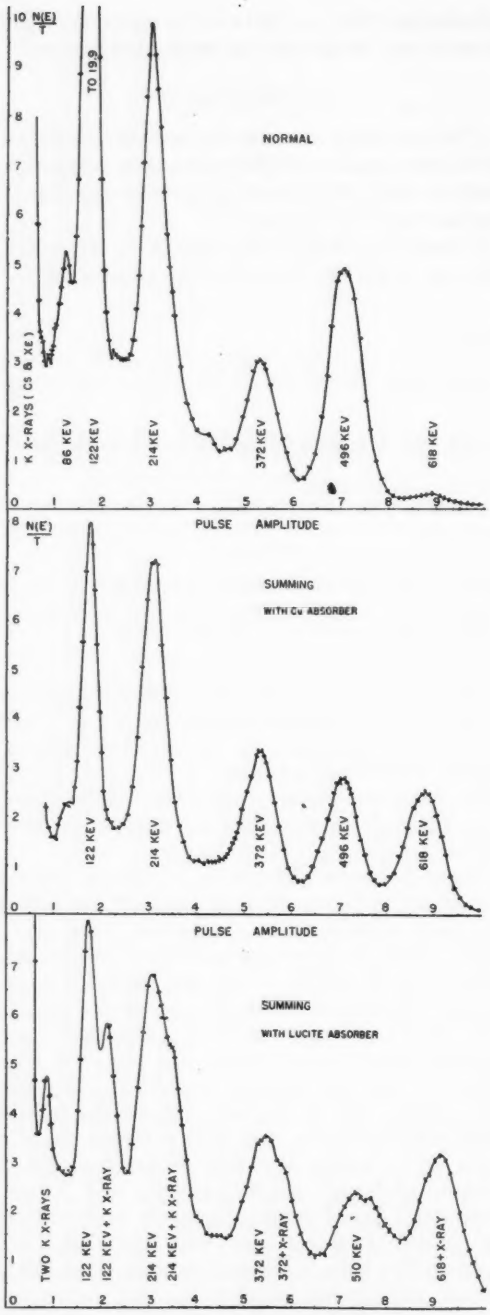

FIG. 1. γ-ray spectra of Cs^{131} following K capture in Ba^{131}. Energies in kev.

the 214- and 122-kev γ rays were in coincidence, a strong sum peak should appear at 336 kev. If the 372-kev γ ray were in coincidence with the 122-kev γ ray in the same manner as the 496-kev γ ray is, the summing effect would (a) reduce the intensity of the 496-kev peak by a factor α to form the sum peak at 618 kev, (b) reduce the intensity of the 372-kev peak, by the same factor α, to reinforce the peak at 496 kev. This would have resulted in a much higher peak at 496 than at 372 kev on the summing spectra. Similarly, using a thin gold capsule to cut off the 122-kev γ ray, one sees that the 372- and 214-kev γ rays do not sum with each other. The fact that both are in coincidence with K-capture x-rays (see Fig. 1, bottom curve) rules out the possibility that they may be in cascade through a meta-stable state. It is reasonable, therefore, to assume that they both go the the ground state, and are

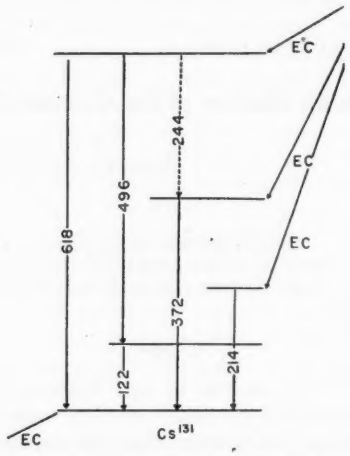

FIG. 2. Excited energy levels of Cs^{131}. Energies in kev.

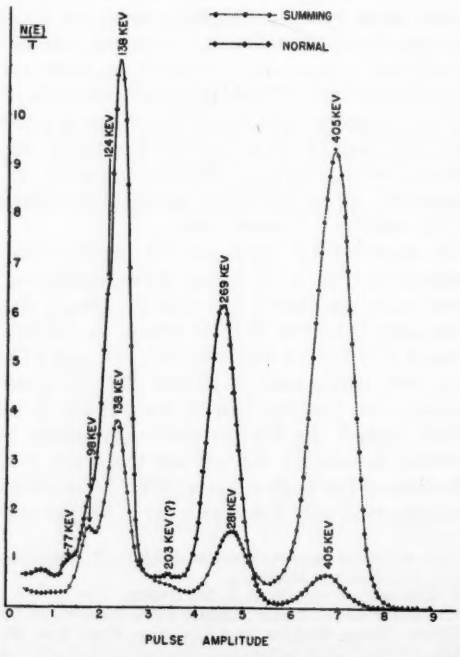

FIG. 3. γ-ray spectra of As^{75} following K capture in Se^{75}.

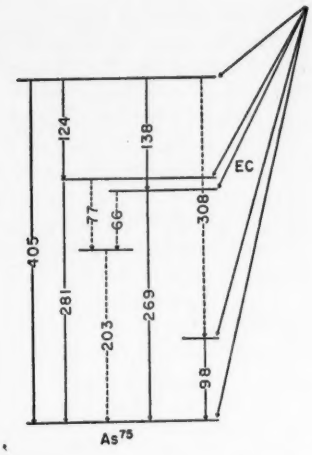

FIG. 4. Excited energy levels of As^{75}.

fed by separate electron capture processes. This leads to the decay scheme shown in Fig. 2.

The sum spectrum represented by the bottom curve in Fig. 1 also allows a rough estimate of the internal conversion coefficient e/γ of the 122-kev transition if one considers the following facts. The area under the sum peak at approximately 630 kev is proportional to the number of events of the type in which the detection of a 496-kev quantum is accompanied by the detection of a 122-kev quantum (with or without the accompanying detection of the K-capture x-ray quantum). The area under the sum peak at approximately 510 kev is proportional to the total of two types of events: (a) events in which the detection of a 496-kev quantum is accompanied by a 122-kev quantum which escaped detection; (b) events in which the detection of a 496-kev quantum is accompanied by an internal conversion with the K x-ray either being detected or not. If the efficiency of the phosphor for the detection of the 122-kev γ ray is ϵ, the relative numbers of the three types of events are evidently $\epsilon:1-\epsilon:e/\gamma$. The ratio of the area under the 510-kev sum peak to the area under the 630-kev sum peak is therefore proportional to $(1-\epsilon+e/\gamma)/\epsilon$. This must be multiplied by the numerical factor $(630/510)^{\frac{1}{2}}$ as a first order correction for the effect of the constant window width of the differential pulse amplitude analyzer. Thus

$$\frac{\text{Area}(510)}{\text{Area}(630)}=\left(\frac{630}{510}\right)^{\frac{1}{2}}\frac{1-\epsilon+(e/\gamma)}{\epsilon}.$$

While the exact value of ϵ is not known, it can be safely estimated to be 0.85 ± 0.08 from previous experimental evidence. The calculated value for e/γ is of the order of 0.6. Although this is a rather rough measurement, it is presented here since no other more accurate measurements have been reported.

II. Se^{75}

By using the summing technique, the γ rays of As^{75} following electron capture from Se^{75} have also been studied. The result is presented in Fig. 3. The normal spectrum shows peaks at 405, 269, and 138 kev, with indications of peaks at 124, 98, 77, and possibly 203 kev. Within experimental accuracy, these energy values are consistent with previous measurements by Ter-Pogossian *et al*,[5] Cork *et al*.,[6] and Jensen *et al*.[7] However, the intensities of the γ rays appear to be different from those measured by Jensen *et al*.,[7] who reported the relative intensities (in parenthesis) of the stronger γ rays as follows: 77 kev (14), 98 kev (6.5), 138 kev (24), 268 kev (71), and 405 kev (14). If one

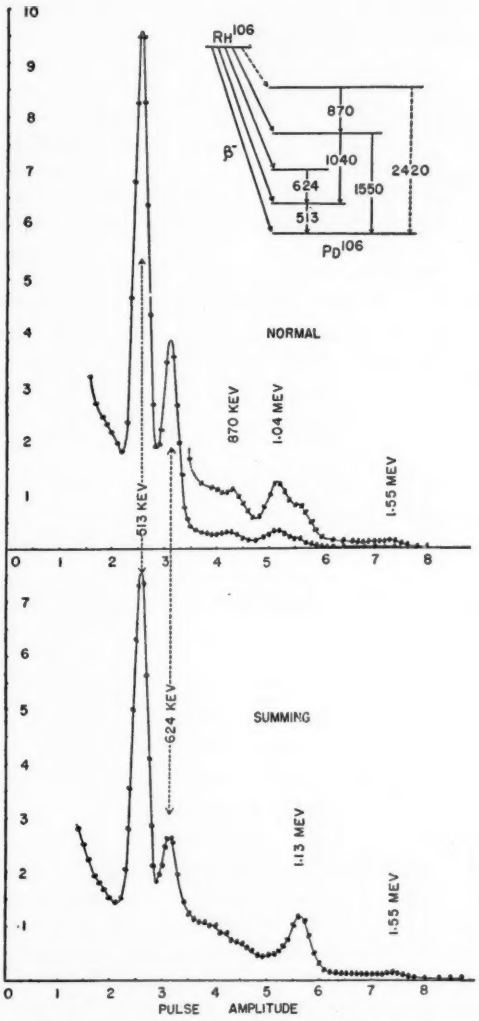

FIG. 5. γ-ray spectra of Pd^{106} following β decays of $Ru^{106}\rightarrow Rh^{106}\rightarrow Pd^{106}$.

[5] Ter-Pogossian, Robinson, and Cook, Phys. Rev. **75**, 995 (1949).
[6] Cork, Rutledge, Branyan, Stoddard, and LeBlanc, Phys. Rev. **79**, 889 (1950).
[7] Jensen, Laslett, Martin, Hughes, and Pratt, Phys. Rev. **90**, 557 (1953).

takes into consideration the energy dependent effect of the detection efficiency and the effect of the constant "window width" of the scintillation spectrometer, the present data indicates that the 138-kev γ ray is considerably stronger, and the 77-kev x-ray much weaker than measured by Jensen *et al.*[7] This is consistent with the recent work by Schardt *et al.*[8]

The dotted curve in Fig. 3 represents the summing spectrum obtained with the sample in the phosphor. The As K x-rays arising from K capture were cut off by the use of a thin Al absorber. Peaks are noticed at 405, 281, 138, and 98 kev. This infers the following: (1) The highest excited energy level involved is at 405 kev since no sum peak appears above this energy. (It is assumed here that no meta-stable states are present. DeBenedetti and McGowan[9] found no delayed coincidences in the 10^{-6}- to 10^{-3}-sec range.) Thus, any two γ rays whose energies add up to more than 405 kev cannot be in cascade. (2) The strong sum peak at 405 kev shows that the 138- and the 269-kev transitions are in cascade. (3) Since no indication of summing is noticed at 346 kev, the 77-kev γ ray appears not to be in cascade with the 269-kev γ ray as suggested by Jensen *et al.*,[7] whereas on the basis of the present investigation, there is no real objection from the standpoint of intensities in placing the 77-kev transition between excited levels at 203 and 281 kev as suggested by Cork *et al.*[6] (4) The 98-kev γ ray does not appear to sum with any γ ray of appreciable intensity. Therefore, it probably goes directly to the ground state and is fed by electron capture as proposed by Jensen *et al.*[7] (5) The 124-kev γ ray appears to sum with at least another γ ray. Among the observed sum peak energies, only 405 kev can be decomposed into combinations of observed γ ray energies involving 124 kev. It is therefore reasonable to assume that the 124-kev transition is from the 405 to the 281 excited level. The intensity of the 281 sum peak indicates that the 281-kev level is probably also fed by electron capture. These informations lead to the decay scheme shown in Fig. 4. It is a compromise between the decay schemes proposed by Jensen *et al.* and Cork *et al.*

III. Ru^{106}

The γ rays of Pd^{106}, following the successive β decays from Ru^{106} to Rh^{106} to Pd^{106}, have also been studied with the summing technique. The experimental result, represented by Fig. 5, is consistent with previous studies by D. E. Alburger,[10] and Klema and McGowan.[11]

[8] A. W. Schardt and J. P. Welker, Phys. Rev. **93**, 916 (1954).
[9] S. DeBenedetti and F. K. McGowan, Phys. Rev. **74**, 728 (1948).
[10] D. E. Alburger, Phys. Rev. **88**, 339 (1952).
[11] E. D. Klema and F. K. McGowan, Phys. Rev. **92**, 1469 (1953).

PHYSICAL REVIEW VOLUME 97, NUMBER 1 JANUARY 1, 1955

Gamma and X-Radiation in the Decay of Am^{241}†

H. JAFFE, T. O. PASSELL, C. I. BROWNE, AND I. PERLMAN
Radiation Laboratory and Department of Chemistry, University of California, Berkeley, California
(Received September 7, 1954)

The decay scheme of Am^{241} is discussed in terms of new information on the conversion electrons, gamma rays, and L series x-rays accompanying its alpha decay. The photons were measured with a scintillation spectrometer and a bent crystal spectrometer and the conversion electron spectrum was determined with a double focusing beta-ray spectrometer.

I. INTRODUCTION

THE decay properties of Am^{241} have received considerable attention because this isotope was one of the first transuranium alpha emitters which could be produced isotopically pure in amounts suitable for nuclear spectroscopic studies and the prominent gamma radiation clearly indicated a complex spectrum. Also, the specific activity was sufficiently high to permit examination of soft radiation and rare radiation. The close examination of the alpha spectrum has yielded five alpha groups which define uniquely four excited states of Np^{237}. It is of interest to coordinate these states with the electrons and electromagnetic radiation which result from their de-excitation, and from the properties to deduce something concerning the nuclear spectroscopic states of Np^{237}.

The isotope Am^{241}, first identified by Seaborg, James, and Morgan,[1] can be obtained in isotopically pure form from a mixture of plutonium isotopes which contains Pu^{241} as the only β^- emitter.[2] The alpha spectrum determined in this laboratory[3] and later modified[4] defines a series of energy levels which can form the

† This work was performed under the auspices of the U. S. Atomic Energy Commission.

[1] Seaborg, James, and Morgan, *The Transuranium Elements: Research Papers* (McGraw-Hill Book Company, Inc., New York, 1949), National Nuclear Energy Series, Plutonium Project Record, Vol. 14B, Div. IV, Paper No. 22.1, p. 1525.
[2] Ghiorso, James, Morgan, and Seaborg, Phys. Rev. **78**, 472 (1950).
[3] Asaro, Reynolds, and Perlman, Phys. Rev. **87**, 277 (1952).
[4] F. Asaro and I. Perlman, Phys. Rev. **93**, 1423 (1954).

basis for fitting the gamma-ray transitions (see Fig. 1). For the present, the gamma rays or conversion electrons observed by various authors will just be mentioned.

The early studies showed a prominent gamma ray of 62-kev and ~20-kev photons presumed to be L x-rays.[1] Several authors[5–7] observed conversion electron lines of a gamma ray of about this energy (reference 5, 59.4 kev; reference 6, 59.6 kev; reference 7, 59.0 kev), and the gamma ray itself has been measured with a scintillation spectrometer,[7] with proportional counters[7–9] and with a bent-crystal spectrometer[10] which lends itself to more precise measurement (reference 10, 59.78 kev; this paper, 59.62±0.06 kev). This gamma ray leads from the heavily populated state at 59.6 kev to the ground state.

A part of the early interpretation of the decay data was confused by the appearance of an alpha group in low intensity of 11 kev higher energy than that now thought to be the ground state transition and therefore all energy levels were considered to be 11 kev higher than the present interpretation. Wolfson[6] searched for M conversion lines of an 11-kev gamma ray without success and it was later shown[4] that the high-energy alpha group does not exist but was due to the principal alpha group, part of which bypassed one of the baffles in the spectrograph to a region of low magnetic field and registered as a high energy peak.

The 59.6-kev state (through which virtually all transitions pass) is de-excited to an appreciable extent by dropping through the 33.2 kev level (see Fig. 1). The first studies with the bent-crystal spectrometer[10] showed photons of 26.43 kev and 33.36 kev which conform with the alpha groups and add precisely to the energy of the crossover transition. Using a proportional counter, Beling, Newton, and Rose[8] observed the 26.4-kev photon but not that at 33.4 kev, and Newton and Rose[11] suggested that this photon, as well as a weak one at 38.0 kev, were K_α and K_β x-rays of lanthanum from fluorescence excitation by the 59.6-kev gamma ray. Lanthanum is an expected impurity in americium by virtue of its introduction as a carrier in the most usual procedure for isolating americium. This was indeed shown to be the case when these lines diminished upon further purification of the samples used in this laboratory. It is now known that the 33.2-kev transition is highly converted and the gamma ray is consequently not observed.

The next state above the 59.6-kev state lies at 103 kev and is fairly heavily populated. Of the several paths through which this state could de-excite only the transition to the 59.6-kev state has been observed and this through the conversion electron spectrum.[6] The 43.3-kev gamma transition has been observed through the conversion electron spectrum in the present work and also in that of Wolfson.[6] Conversion lines of a 99-kev photon have also been reported.[6,12] The reasons why this photon is assigned as shown in Fig. 1 and not to either a K x-ray or a gamma ray from the 103-kev state will appear in the later discussion. Other components of the decay scheme will also be discussed.

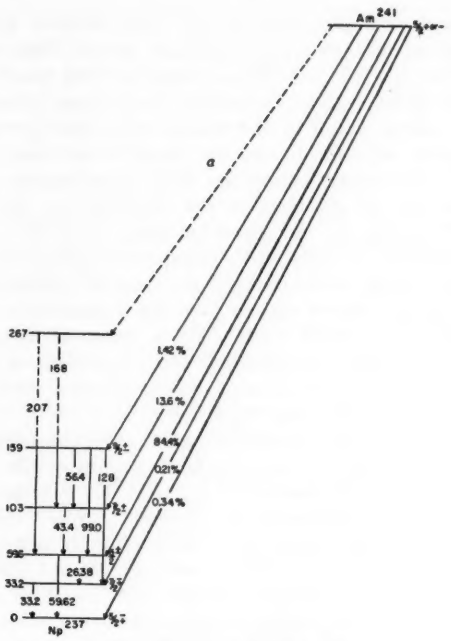

FIG. 1. Decay scheme of Am^{241}.

II. EXPERIMENTAL

The Am^{241} used in this investigation was obtained from plutonium that had undergone intense neutron irradiation and was separated by ion exchange techniques. Spectroscopic analysis indicated that the sample contained 0.5 percent lanthanum and negligible amounts of other impurities. Conversion electron and gamma-ray spectra were observed by using a double-focusing magnetic beta spectrometer, a bent-crystal photon spectrometer, and a scintillation spectrometer.

Beta-Ray Spectrometer

The general features of the double-focusing beta-ray spectrometer have been described by O'Kelly.[5] The detector used was a side window Geiger-Müller

[5] G. D. O'Kelley, Ph.D. thesis, University of California Radiation Laboratory Unclassified Document UCRL-1243, 1951 (unpublished).
[6] J. F. Wolfson (private communication).
[7] Freedman, Wagner, and Engelkemeir, Phys. Rev. 88, 1155 (1952).
[8] Beling, Newton, and Rose, Phys. Rev. 86, 797 (1952).
[9] West, Dawson, and Mandelberg, Phil. Mag. 43, 875 (1952).
[10] C. I. Browne, Ph.D. thesis, University of California Radiation Laboratory Unclassified Document UCRL-1764, 1952 (unpublished).
[11] J. O. Newton and B. Rose, Phys. Rev. 89, 1157 (1953).
[12] E. Church, Argonne National Laboratory Unclassified Report ANL-5141, November, 1953 (unpublished).

counter equipped with a very thin window which consisted of three vinyl copolymer plastic films supported on a grid of 0.001-in. tungsten wires spaced at 0.008-in. intervals on the end of a short copper cylinder. The energy cutoff of the window was determined in separate experiments and was found to be about 4.5 kev.[13] The energy calibration of the spectrometer was based on the positions of the 59.6-kev L_{III} line of Am^{241} (using the energy value reported below) and the 661-kev K line of Cs^{137}. The spectra reported in the present work were obtained by using a combination of a motor driven current-sweeping arrangement and a differential traffic counter set to stamp at frequent intervals. The transmission and resolution of the spectrometer at the time of this experiment were 0.3 percent and 1 percent, respectively.[13]

Two beta spectrometer samples were prepared by evaporation of the activity from a drop of distilled water on an aluminum leaf backing (177 micrograms per square centimeter in thickness). The activity covered an area about $\frac{3}{16}$ in. in diameter in each case. Thirty micrograms of Am^{241} were used in the sample from which the electron line data were obtained. The total conversion coefficient of the 59.6-kev gamma ray was obtained by using a smaller sample which contained only 1.3 micrograms to minimize coincidence corrections of the counting rates.

Bent-Crystal Spectrometer

The bent-crystal spectrometer has been previously described by Barton, Robinson, and Perlman[14] and somewhat modified by Browne.[10] The experimental approach was essentially the same used by the previous workers. Approximately 3 mg of americium was precipitated as the fluoride, dried, powdered, and mounted in a thin Pyrex capillary. The diameter of the capillary was about 0.012 in. and its width undoubtedly represented the limiting factor in the obtainable resolution. The sample was secured to a Lucite holder and this was mounted and aligned in the sample carriage.

An 0.008-in. thick topaz crystal elastically bent to a 10-in. radius was used to diffract the incident electromagnetic radiation. The 303 planes, whose spacing was determined as 1.356A in the unbent crystal,[10] were employed and the energies in kev were calculated using a conversion factor based upon the most recent values of the physical constants.[15]

The detector, mounted behind a collimator, consisted of a NaI (Tl activated) scintillation crystal with an RCA-5819 photomultiplier tube. A standard scaler and traffic counter were used to record the data.

As previously described,[14] measurements were made with the bent crystal in a fixed position while the sample on a mechanically driven carriage was swept slowly along the arc of the circle containing the bent crystal. The most commonly used rate of sweeping was 1/100° per minute with respect to the center of the focal circle. Photon lines were manifest by peaks in a plot of counting rate *versus* angular position which was read from a graduated scale mounted about the focal circle. The Bragg angle, and consequently the energy, was determined by observing the angular position of a photon line on both sides of the undiffracted beam or midpoint. The useful range of the bent-crystal spectrometer was 10 to 110 kev. Limits of error were calculated taking into account only the angular uncertainties. An accuracy of 0.01° in the Bragg angle was considered the limit of the spectrometer.

The observed line intensities were subject to correction for absorption and for reflectivity of the crystal. Corrections for absorption in the media between sample and detector (glass, air, topaz, etc.) were readily made and were based on the data of S. J. M. Allen tabulated by Compton and Allison.[16] The self-absorption correction was the most uncertain since some of the neptunium L x-rays fall in the immediate proximity of and between the three L edges of americium. The sample was treated as a cylindrical source using the relation given by Dixon[17] and the absorption coefficients were estimated in the following fashion. The coefficients above the L_I edge of americium and below the L_{III} edge were obtained using the "universal absorption curve" of Jönsson[18] and between the L_I and L_{III} edge by extrapolating the "absorption jump" values as defined by Compton and Allison.[19] Values for the L edges of americium were obtained by a Moseley extrapolation.

Lind, West, and DuMond[20] have found that the variation of reflectivity from a quartz crystal as a function of energy was inversely proportional to the square of the energy. Browne[10] observed that lines widely spaced in energy maintained the same intensity ratio when reflected from both quartz and topaz, indicating the same energy dependence for both crystals. This correction was made in calculating the relative intensities.

Scintillation Spectrometer

The scintillation spectrometer consisted of a NaI (Tl activated) crystal detector, 1.08 in. thick and 1.25 in. in diameter sealed to a Dumont 6292 photomultiplier tube. The output of this tube, after suitable amplification, was fed through a 50-channel pulse height

[13] T. O. Passell, Ph.D. thesis, University of California Radiation Laboratory Unclassified Document UCRL-2528, 1954 (unpublished).
[14] Barton, Robinson, and Perlman, Phys. Rev. **81**, 208 (1951).
[15] J. W. M. DuMond and E. R. Cohen, Revs. Modern Phys. **25**, 691 (1953).
[16] Arthur H. Compton and Samuel K. Allison, *X-rays in Theory and Experiment* (D. Van Nostrand Company, Inc., New York, 1935), p. 800.
[17] W. R. Dixon, Nucleonics **8**, No. 4, 68 (1951).
[18] E. Jönsson in Compton and Allison, see reference 16, p. 540.
[19] Arthur H. Compton and Samuel K. Allison, see reference 16, p. 529.
[20] Lind, West, and DuMond, Phys. Rev. **77**, 475 (1950).

analyzer. The sample for this study consisted of approximately 2.5 μg of the purified Am^{241}.

III. RESULTS

It will perhaps be simpler to discuss the gamma-ray transitions individually by all the methods applied rather than to group all that has been learned from each type of measurement. Before taking up the several transitions separately, mention will be made of the bent-crystal spectrometer studies as they apply to the earlier studies with impure americium.

Preliminary experiments with the bent-crystal spectrometer employing the Am^{241} sample used by Browne, showed the presence of the same gamma rays found in the earlier work. However, subsequent chemical treatment of the sample caused the intensity of the 33.4- and 38.0-kev gamma rays to decrease considerably relative to the 26.4- and 59.6-kev radiation, while the latter two lines maintained the same intensity ratio. As pointed out by Newton and Rose,[11] the anomalous lines correspond closely in energy to the dominant K x-rays of lanthanum, the usual chemical carrier for americium. With this in mind, portions of the old sample were spectroscopically analyzed and a lanthanum impurity was found amounting to about 20 percent of the americium. Thus it is reasonable to ascribe at least the bulk of these two lines to fluorescence excitation in the impurity. Likewise, several lower energy lines previously noted correspond closely to the extrapolated energies of the dominant americium L x-rays and are undoubtedly due to fluorescence excitation in the sample.

With the more highly purified americium, the bent-crystal spectrometer showed only a gamma ray at 26.38 kev, the 59.6-kev gamma ray, and its second order reflection at 29.81 kev, in addition to L x-rays. A careful search of the 30–50 kev region showed that any peaks present would have a maximum intensity of 2 percent of the 59.6-kev peak which is consistent with the lower limit set by Newton and Rose.[11] A portion of the spectrum observed with the bent-crystal spectrometer is shown in Fig. 2 and the data are incorporated in Table I.

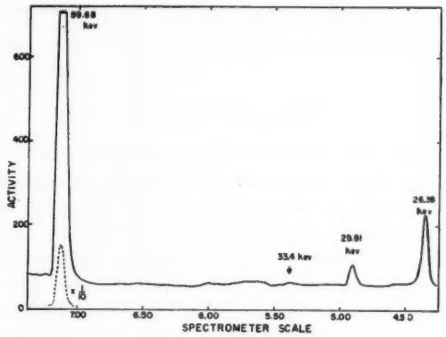

FIG. 2. Spectrum of the 25–70 kev region in the decay of Am^{241}.

59.62 Kev Transition

By far the most prominent gamma ray in Am^{241} decay is the one at 59.6 kev. Beling, Newton, and Rose[8] have shown that the intensity of this photon is 0.40 ±0.015 per alpha disintegration. The bent-crystal spectrometer gave its energy as 59.65±0.13 kev by first order reflection and 29.81±0.03 kev by second order. The value adopted is 59.62±0.06 kev from the second order reflection peak.

Electrons arising from the 59.6-kev transitions are

TABLE I. Conversion lines of Am^{241} decay.

	Conversion electrons				Gamma rays			
Line No. Fig. 3(a)	E_e^-(kev)	Shell	γ	Intensity (e^-/α)	$E\gamma$(kev)	I γ/α	Best E (kev)	Total intensity $(e^-+\gamma)/\alpha$
5	25.0	N	26.3	0.0068	26.38±0.04	0.04[a]	26.38±0.04	0.22[b]
1	10.6	L_I	33.1	0.067	...	...	33.24±0.1	~0.1
2	11.5	L_{II}	33.1	...	...	...		
7	27.3	M_I	33.1	0.018	...	...		
8	28.7	M_{III}	33.2	0.0012	...	...		
	31.7	N	33.2	0.004	...	...		
3	20.8	L_I	43.3	0.017	...	...	43.4±0.2	0.12[c]
4	21.8	L_{II}	43.4	0.035	...	...		
6	25.8	L_{III}	43.4	0.039	...	...		
				...	...	...	56±1	0.005
				...	...	...		
10	38.8	L_{III}	56.4	0.0015	...	...		
9	37.1	L_IL_{II}	59.6	0.236	59.65±0.13	0.40[d]	59.62±0.06	0.77
11	42.0	L_{III}	59.6	0.054	...	...		
12	54.4	M	59.8	0.064	...	...		
13	59.2	N	59.6	0.014	...	...		
Fig. 3(b)	77.9	L_IL_{II}	99.5	0.00062	...	...	99.5±1.0	0.0018
Fig. 3(b)	81.5	L_{III}	99.1	0.00037	101	0.00056		
Fig. 3(b)	95	M	100.7	0.00031	...	...		
	...	...	...	...	128	0.000056	128(?)	6×10^{-5}

[a] Based on the value (see reference 8) 0.4 per α for the absolute intensity of the 59.6-kev γ.
[b] Assuming that the ratio N conversion/total conversion is the same for the 26.4-kev γ as for the 59.6-kev γ.
[c] Assuming that the $L/(M+N)$ ratio is the same for the 43.4-kev γ as for the 44.1-kev γ in Cm^{243} decay.
[d] See reference 8.

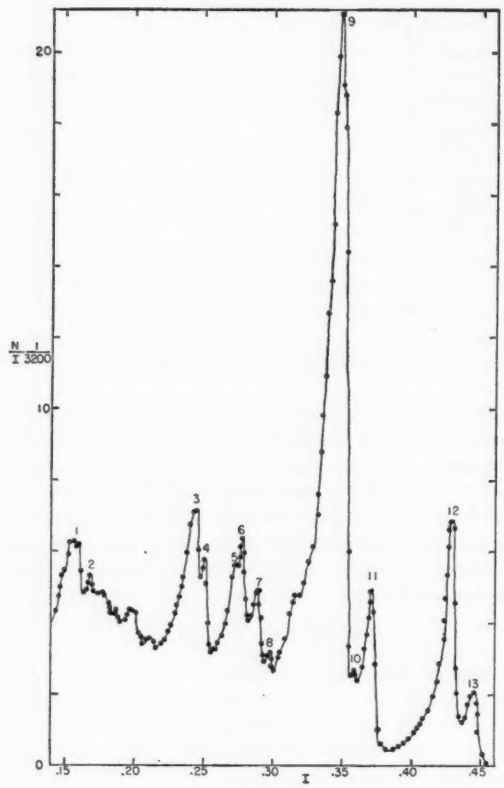

(a)

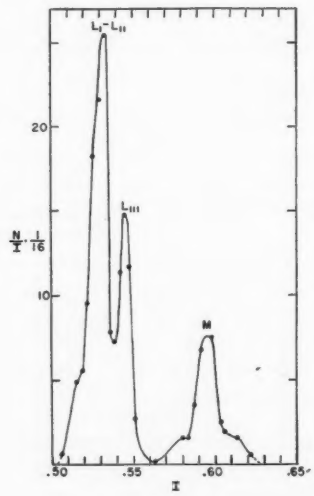

(b)

FIG. 3(a). Electron spectrum of Am^{241}. (b) Electron spectrum of Am^{241}.

designated by the numbers $9(L_I+L_{II})$, $11(L_{III})$, $12(M)$, and $13(N)$ in Fig. 3(a). All of these lines have been observed by Wolfson[6] and the agreement in relative intensities is fair. It is seen that the L_I+L_{II} line (9) exhibits a hip on the normally almost vertical forward edge. This may be taken to mean that the intensity of the L_{II} line is perhaps somewhat less than that of the L_I line. The L_{III} line (11) was clearly resolved. Since the $43.4M$ and $43.4N$ lines coincide energy-wise with the $59.6L_I+L_{II}$ lines and $59.6L_{III}$ lines, respectively, the calculated intensities of the former had to be subtracted from the apparent intensities of the latter. The intensities of $43.4M$ and $43.4N$ may be calculated by using the observed $L/M(4.0)$ and $L/N(22.8)$ ratios of $\gamma_{44.1}$ observed in Cm^{242} decay,[13] since these ratios do not vary appreciably among $E1$, $M1$, and $E2$ radiations in this energy range. The chief difficulty in procuring reliable intensity measurements lies in the uncertainties involved with the extrapolation of the low energy tail of a given line. In the present work, the $59.6L_{III}$ line was used as a model for drawing in the tails of unresolved lines. The corrected $(L_I+L_{II})/L_{III}$ ratio for $\gamma_{59.6}$ is 4.4 ± 1. This value is in fair agreement with the value of 6.4 ± 1.3 obtained by Wolfson[6] which includes the contribution of the M lines of the 43.4-kev transition.

From an experiment[13] using Cm^{242} the transmission of the spectrometer was found to be 0.3 percent. Using this value of the transmission along with an alpha-particle rate measurement of the Am^{241} sample, and assuming that 0.40 59.6-kev photons are emitted per alpha disintegration,[8] the total conversion coefficient of $\gamma_{59.6}$ was found to be 0.92 ± 0.10. A previously reported value for the total conversion coefficient of $\gamma_{59.6}$ was <1.5.[21] O'Kelly[5] reports the total L conversion coefficient to be about 0.7 which compares very favorably with our value of 0.72 ± 0.07. The 59.6 kev gamma ray may be assigned $E1$ character on the basis of its total L conversion coefficient. However, its $(L_I+L_{II})/L_{III}$ ratio (4.4) is more than twice that expected for an $E1$ transition from the calculations of Gellman, Griffith, and Stanley[22] and of Rose, Goertzel and Swift.[23] We shall return to this point in the discussion.

26.38-Kev Transition

In the earlier measurement with the bent-crystal spectrometer[10] this gamma ray was reported as 26.43 kev; from the present measurement, it is 26.38 ± 0.04 kev. The proportional counter measurement[8] showed a gamma ray of 26.3 kev present to the extent of 0.028 photon per alpha disintegration. Our corresponding abundance from the bent crystal spectrometer measurement is 0.04. Beling, Newton, and Rose[21] showed that this gamma ray is not in coincidence with that of 59.6 kev and since there is no alpha group in sufficient intensity populating states lower than the 59.6-kev

[21] Beling, Newton, and Rose, Phys. Rev. 87, 670 (1952).
[22] Gellman, Griffith, and Stanley, Phys. Rev. 85, 944 (1952).
[23] Extrapolations made from incomplete tables of conversion coefficients by Rose, Goertzel, and Swift (unpublished).

state and only one possible alpha group leading to a higher excited state,[3,4] it is likely that the 26.38-kev gamma ray arises from parallel de-excitation of the 59.6-kev state. The alpha spectrum[3,4] showed a weak alpha group of 26.4±0.5 kev greater energy than that populating the 59.6-kev state and this agreement gives adequate confirmation for placing the 26.38-kev transition as indicated in Fig. 1.

The L-shell conversion lines of this photon are largely obscured by Auger electrons and the M-shell lines by the L lines of the 43.4-kev photon. However, the N line is seen (line 5, Fig. 3a). If we make the crude assumption that the ratio N conversion/total conversion is the same for this gamma ray as for the 59.6-kev gamma ray, the total intensity of the 26.38 becomes 0.22 (Table I) and the total conversion coefficient is 5.5. The conversion coefficient cannot be larger than this because the intensities of the 59.62-kev transition (0.77) and the 26.38-kev transition (0.22) add to approximately 100 percent for the de-excitation of the 59.6-kev state. From this upper limit for the conversion coefficient the 26.38-kev transition must be $E1$ since $M1$ and higher multipole transitions have much higher conversion coefficients for the L shell alone. This assignment on the basis of similar reasoning has been made by Beling, Newton, and Rose.[21]

33.2-Kev Transition

This transition (Fig. 1) is the member presumed to cascade with the 26.38-kev transition to make up 59.6 kev. The gamma ray, as mentioned, has not been observed and Beling, Newton, and Rose[3] have set an upper limit of 0.05 percent of the alpha decay processes. If, according to the above reasoning, the population of the 33.2-kev transition is 22 percent (same as the 26.38-kev transition), then the conversion coefficient is >400. Also, since the 59.6- and 26.38-kev transitions are $E1$ (parity change), the 33.2-kev transition must involve no parity change and is therefore $E2$, $M1$ or a mixture.

Further information can be obtained from the conversion electron spectrum. From Table I and Fig. 3a it is noted that lines ascribable to L_{I}, L_{II}, M_{I}, M_{III}, and N conversion are found. The L conversion lines fall in the region of Auger electrons so absolute intensities and ratios are difficult to arrive at. A summation of all of these conversion lines gives about 0.1 transition per alpha particle as compared with 0.2 which should be the abundance of this transition. The data of Wolfson[6] (again disregarding the contribution by Auger electrons) gives a total abundance of about 0.13. These differences are probably not serious in view of the difficulties in measuring absolute abundances of soft electrons. The criterion for distinguishing between $M1$ and $E2$ character in this energy region is the $L_{\mathrm{I}}/L_{\mathrm{II}}$ conversion ratio. Since neither peak is observed clearly, it is not possible to draw any accurate conclusion, but from Wolfson's abundances it would appear that there is appreciable contribution from both types.

43.4-Kev Transition

The next energy level above 59.6 kev is at 103.0 kev. This state is populated by the second most abundant alpha group (13.6±1.4 percent) and is located at 104 kev on the basis of differences in alpha energies.[3,4] A more accurate energy can be obtained by adding to the 59.62-kev transition, the cascading transition of 43.4±0.2 kev giving 103.0±0.2 kev.

This state is de-excited almost entirely by the 43.4-kev transition as will appear in later discussion. The gamma ray has not been seen and an upper limit of about 1 percent per alpha particle can be set from the bent crystal spectrometer measurement which is about the same as the limit set with a proportional counter.[21]

The conversion electron spectrum showed clearly the L_{III} line while the L_{I}, L_{II}, M, and N lines fall at about the same positions as conversion lines of the 26.38 and 59.62-kev transitions. It is clear from the abundance of the L_{III} line alone that the conversion coefficient is too great for an $E1$ transition. If we assume that the L_{I} line has appreciable abundance, then the transition is an $M1$, $E2$ mixture; if most of this peak is due to other electrons, the transition takes on more $E2$ character. Higher multipoles are ruled out by the finding[21] that all alpha particles are in prompt coincidence (<1 μsec) with the 59.6-kev gamma ray.

If we add the intensities of the L electrons of this transition and correct this using the L/M ratio of the 44.1-kev $E2$ transition of Cm^{242}, the total abundance of the transition is about 12 percent as compared with 15 percent which one would expect from the alpha spectrum.

Transitions from the 159-Kev State

The lowest-energy alpha group yet detected populates a state 159 kev above the ground state to the extent of 1.42 percent.[3,4] There is some evidence for three competitive transitions from this level (Fig. 1) and of these the 99.5-kev transition is most definite.

A photon of approximately this energy (actually measured as 101±3 kev) was found with the scintillation spectrometer using a 1.1 g/cm² silver absorber in front of the sample to decrease the relative intensity of the 59.6-kev gamma ray (see Fig. 4). Gamma-gamma coincidence studies by Frank Stephens[24] showed this photon to be in coincidence with the 59.6-kev radiation so that it cannot be the crossover transition from the 103-kev state. Another possibility to be considered is that the photon peak consists of K x-rays from the internal conversion of a higher-energy gamma ray. Higher-energy gamma rays in very low intensity have been observed (see below), but unless

[24] Frank S. Stephens, Jr. (unpublished data, 1953).

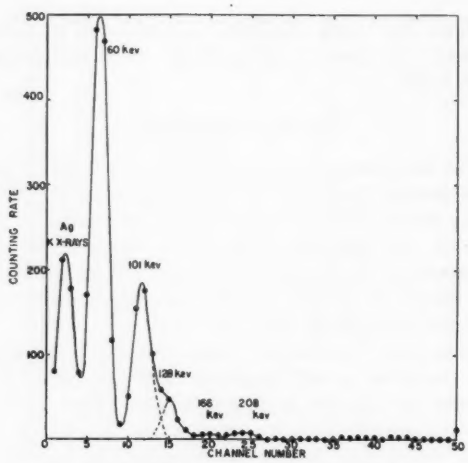

FIG. 4. Scintillation counter spectrum of Am^{241}.

they are highly converted this process could not account for the 101-kev photons. In a further effort to determine whether the 101-kev line was a gamma ray or the K x-ray multiplet, the width of the peak was compared with the electron capture K x-ray peak of the long-lived Am^{242}.[25] The width of the x-ray multiplet was more than 50 percent greater than that of the Am^{241} photon and thus it is reasonably certain that at least the bulk of the 101-kev radiation is of nuclear origin.

Evidence for a gamma ray of about this energy is also found in the conversion electron spectrum. As shown in Fig. 3b and Table I, lines were observed which can be assigned to the conversion electrons of a 99.5±1.0-kev gamma ray in the L_I+L_{II}, L_{III}, and M shells. Wolfson[6] also reported these three lines and in addition the N conversion line, and gave 99.0 kev as the energy. Similarly, Church[12] reported conversion lines of 98.9±0.3-kev gamma ray.

Church gave the gamma ray an $E2$ assignment on the basis of its L_{II}/L_{III} ratio and this is also deduced by Wolfson and in the present work. The L_{II}/L_{III} ratio of Wolfson is ~2, ours is ~1.7 and the theoretical ratio[22] lies right in this region. For $M1$ radiation the ratio would be about 10 and the L_I line would predominate over L_{II} and L_{III} by another factor of 10 contrary to observation. The conversion ratios for $E1$ radiation are in the proper range but the absolute conversion coefficient which we observe is much closer to the theoretical value for $E2$ radiation than for $E1$. (Theoretical values[23] for $E2$ and $E1$ are ~5 and ~0.1 respectively; our measurement, ~2.)

The principal evidence for a gamma ray of 56 kev is a line ascribed to L_{III} conversion (line 10, Fig. 3a). The reason for searching for such a transition is that from the other evidence there should be an $E2$ transition (or $E2$-$M1$ mixture) between the 159- and 103-kev states. The total intensity of the transition as shown in Table I is based on the premise that the transition is indeed $E2$.

A very weak gamma ray of about 128 kev could be resolved from the 101-kev peak found with the scintillation spectrometer (Fig. 4). This could be the transition between the 159-kev and 33-kev states. Wolfson reported a very soft electron line which could be interpreted as the K line of a 127-kev gamma ray, but beyond this there is no further evidence for this transition.

Higher Energy Levels

There were indications of two very weak gamma rays at 168 and 207 kev (Fig. 4) and, if they are real, they must of course come from some higher state or states than those for which alpha groups have been detected. It is interesting to note that transitions of these energies are prominent in the β^- decay of U^{237}.[26] These are entered in Fig. 1 according to part of the decay scheme deduced[26] for U^{237}. Using the conversion coefficient and K/L ratios of Wagner and co-workers[26] for the 207-kev transition, along with more recent theoretical data,[23] this transition appears to be $M1$ with some $E2$ admixture.

L X-Rays

Fifteen neptunium L x-rays and two americium L x-rays were observed with the bent crystal spectrometer. Table II presents the energies and the corrected relative intensities of these lines. Also included are the x-ray energies obtained from a Moseley extrapolation based upon the L series lines of thorium and uranium as tabulated by Siegbahn.[27] The agreement is good

TABLE II. L x-rays observed in the decay of Am^{241}.

Line	Transition	Observed energy (kev)	Siegbahn's extrapolated energy (kev)	Corrected relative intensity
Np $L_{\alpha 2}$	L_3–M_4	13.79±0.04	13.76	7
Np $L_{\alpha 1}$	L_3–M_5	13.98±0.04	13.94	64
Np L_η	L_2–M_1	15.90±0.06	15.85	2
Np $L_{\beta 6}$	L_3–N_1	16.15±0.06	16.11	1
Np $L_{\beta 2}$	L_3–N_5	16.89±0.02	16.88	13
Np $L_{\beta 4}$	L_1–M_2	17.10±0.02	17.06	16
Np $L_{\beta 6}$	L_3–$O_{4,5}$	17.58±0.06	17.51	3
Np $L_{\beta 1}$	L_2–M_4	17.78±0.01	17.74	100
Np $L_{\beta 3}$	L_1–M_3	18.02±0.02	17.98	13
Np $L_{\gamma 5}$	L_2–N_1	20.15±0.08	20.09	2
Np $L_{\gamma 1}$	L_2–N_4	20.82±0.02	20.77	34
Np $L_{\gamma 2}$	L_1–N_2	21.12±0.04	21.09	8
Np $L_{\gamma 3}$	L_1–N_3	21.31±0.04	21.34	7
Np $L_{\gamma 6}$	L_2–O_4	21.51±0.04	21.49	10
Np $L_{\gamma 4-\gamma 4'}$	L_1–$O_{2,3}$	22.19±0.04	22.19	3
Am $L_{\alpha 1}$	L_3–M_5	14.66±0.03	14.61	10
Am $L_{\beta 1}$	L_2–M_4	18.76±0.04	18.80	6

[25] H. Jaffe, Ph.D. thesis, University of California Radiation Laboratory Unclassified Document UCRL-2537, 1954 (unpublished).

[26] Wagner, Freedman, Engelkemeir, and Huizenga, Phys. Rev. 89, 502 (1953).

[27] M. Siegbahn, *Spektroskopie der Röntgenstrahlen* (Julius Springer, Berlin, 1931).

although the experimental results are in general slightly higher than extrapolated values.

The americium x-rays (Am $L\alpha_1$ and Am $L\beta_1$) are due to fluorescence excitation of the sample by the 26.4 and 59.6 kev gamma rays. The $L\beta_1$ and $L\alpha_1$ are the most prominent lines from the L_{II} and L_{III} shells respectively. Radiation from the L_I shell of americium is not observed, principally because of the low fluorescence yield.[28]

One of the uses for which such x-ray data are potentially valuable is to determine the events which follow the actual internal conversion process. However, in this case, with four separate gamma transitions contributing appreciably to the subsequent x-ray spectrum, the situation is too complex for analysis with the data at hand. In a simpler situation, accurate data on conversion electrons from the three L subshells would define the initial L vacancies and the x-rays observed could then be used to determine Auger coefficients (nonradiative filling) and Coster-Krönig coefficients (shift of an L_I vacancy to an L_{III} vacancy with the ejection of an M or higher lying electron).

We can, however, compare with other measurements relative intensities of the L x-rays arising from a particular L subshell because such ratios should be independent of the manner in which the vacancy was created. Such a comparison is shown in Table III for the present Am^{241} data, the data of Browne[10] for the Pa^{233} decay process, and those in Compton and Allison for the fluorescence excitation of uranium. Because of resolution difficulties in the $L_{\beta 2}$–$L_{\beta 4}$ and $L_{\gamma 2}$–$L_{\gamma 3}$–$L_{\gamma 6}$ multiplets, the intensities of these lines are somewhat doubtful.

On the basis of the corrected relative intensities of Table II, the relative quantum yields (photon intensities) of the three L subshells may be calculated. This is done by summing the intensities of all observed lines that arise from a particular L level and assuming that the abundance of other lines from this level of insufficient intensity to be detected can be ignored. The quantum yields of the three L subshells fall in the ratios: $L_I:L_{II}:L_{III}=1/3.2/1.9$.

Kinsey[28] has discussed the fluorescence yields of the three L shells using a combination of experimental data[29] and theoretical calculations, and arrived at values of 0.16, 0.59, and 0.41 for an L_I, L_{II}, and L_{III} vacancy, respectively, for uranium. Kinsey also estimates that 60 percent of the L_I vacancies would undergo a Coster-Krönig transition in which the L_I vacancy shift to the L_{III} level with the ejection of an M shell electron. Experimental studies at this laboratory have generally indicated a lower incidence for such a transition. If we employ Kinsey's fluorescence yields, but for the moment ignore the Coster-Krönig effect, the L vacancy ratios calculated from the above quantum yields are $L_I:L_{II}:L_{III}=1.0/0.90/0.76$. A crude estimate of $L_I:L_{III}$ conversion ratio in Am^{241} based on the conversion electron data is 3. This would indicate a Coster-Krönig effect of about 40 percent. However, more precise electron data in the very low-energy region is needed in order to calculate a reliable value for the magnitude of this type of transition.

TABLE III. Relative intensities of the L x-rays arising from a given L vacancy.

Vacant shell	Line	Transition	Relative intensity of x-radiation from this shell vacancy			Percentage abundance in Am^{241}
			Am^{241}	Pa^{233}	C and A	
L_1	$L_{\beta 4}$	L_1–M_2	123	135	98	35
	$L_{\beta 3}$	L_1–M_3	100	100	100	28
	$L_{\beta 10}$	L_1–M_4	...	7	0	...
	$L_{\beta 9}$	L_1–M_5	...	10	0	...
	$L_{\gamma 2}$	L_1–N_2	58	55	36	17
	$L_{\gamma 3}$	L_1–N_3	49	66	33	14
	$L_{\gamma 4}$	L_1–O_3	21	24	0	6
L_2	L_η	L_2–M_1	2	2	2	1.5
	$L_{\beta 1}$	L_2–M_4	100	100	100	67
	$L_{\gamma 5}$	L_2–N_1	2	1.5	0	1.3
	$L_{\gamma 1}$	L_2–N_4	34	36	24	23
	$L_{\gamma 6}$	L_2–O_4	10	15	4.4	7
L_3	L_l	L_3–M_1	...	...	3.4	...
	$L_{\alpha 2}$	L_3–M_4	12	13	11	8.5
	$L_{\alpha 1}$	L_3–M_5	100	100	100	72
	$L_{\beta 6}$	L_3–N_1	2	2	1.6	1.5
	$L_{\beta 2}$	L_3–N_5	20	35	28	14
	$L_{\beta 7}$	L_3–O_1	...	...	0.4	...
	$L_{\beta 5}$	L_3–$O_{4,5}$	5	...	6.4	4

IV. DISCUSSION

This discussion will be concerned principally with a summary of the major radiations of Am^{241} and of what can be said about the quantum state designations of the Np^{237} energy levels.

From the alpha spectrum and the analysis of the gamma-ray transitions, it appears that more than 99 percent of the transitions go through the 59.6-kev state. This state is de-excited directly to the ground state to the extent of about 0.77 and through the 26.4-kev and 33.2-kev cascade in 0.23 of the events.

As already discussed, the 59.6-kev transition is almost surely $E1$. However, two separate investigations have shown the $(L_I+L_{II})/L_{III}$ conversion ratio to be at least twice the theoretical value. It has also been pointed out that this transition is abnormal in its long lifetime (6×10^{-8} sec) which is $\sim4\times10^5$ times the value calculated from the Weisskopf formula. Rasmussen[30] has discussed reasons for this peculiarity in terms of the unified (collective and individual-particle) model of the nucleus. He pointed out that the odd proton in two states (in this case the ground state and the 59.6-kev state) may have quite different wave functions even though the spins may be the same or similar. Thus, although the nuclear spin change in the $E1$ transition is 1 or 0, the change in l or j may be greater and introduces a large slowing down of the transition.

[28] B. B. Kinsey, Can. J. Research A26, 404 (1948).

[29] See reference 16, pp. 640–644.

[30] J. O. Rasmussen, Jr., Arkiv Fysik 7, 185 (1953).

Although normally an $E1$ transition might be expected to be pure, in this case the abnormal lifetime suggests that there could be $M2$ admixture. It is perhaps not worthwhile to speculate how reasonable it is to expect competition between these transitions in view of the large uncertainties and unknown factors which influence gamma-ray lifetimes. If there is $M2$ admixture, this would be in the direction of bringing the conversion coefficients and conversion ratios into line.

The ground-state spin of Np^{237} has been measured[31] as 5/2, and according to the shell model the odd protons in this region should have odd parity. There is, however, no convincing experimental evidence that all ground states of the odd-proton nuclei in this region do have the same parity and there should be some reservation in accepting this premise. Rasmussen[30] has considered the possibility that the 5/2 ground state of Am^{241} and the 5/2 59.6-kev state of Np^{237} (see mention below that this state has spin 5/2) have the same parity and consequently the ground state of Np^{237} would have opposite parity. He used this supposition to arrive at a qualitative selection rule for the relative degree of population of the Np^{237} states in the alpha decay of Am^{241} and cited some supporting evidence in harmony with the unified (collective and single-particle) model.

Frazer and Milton[32] have found angular anisotropy between alpha particles and the 59.6-kev gamma ray which they have interpreted as consistent only with the spin assignment of 5/2 or 7/2 for the intermediate state. If, as we assume, the spin of the 59.6-kev state is 5/2, there are two interpretations giving opposite results on the parity for this state. One explanation is that the 5/2 spin states of Am^{241} ground state and the 59.6-kev state of Np^{237} have opposite parity and the alpha particle is emitted as a p-wave. Alternatively, Rasmussen has suggested that the parities are the same and that the anisotropy is explained by an s-wave and d-wave mixture.

Since this matter is not resolved we can give only the alternate assignments as shown in Fig. 1.

If the ground state of Np^{237} is taken to have odd parity, then the 59.6-kev state must have even parity since the two states are connected by an $E1$ transition. Since the 26.4-kev transition is $E1$ and the 33.2 transition $E2$, the 33.2-kev state must have the same parity as the ground state.

The 59.6-kev state has been interpreted[30,4] as the fundamental state (with spin 5/2) of a rotational band according to the Bohr-Mottelson[33] model. Such members of a rotational band of an odd nucleon case have spins I_0, I_0+1, I_0+2 . . ., where I_0 is the spin of the fundamental state, and all have the same parity. The agreement of the measured energy level spacings of the next two highest states is in exact agreement with the theory for the spin sequence 5/2, 7/2, 9/2 and the alpha spectrum populating these states looks remarkably like the well characterized rotational spectra of even-even nuclei in this region (see, for example, Asaro and Perlman[4,34]). For this reason the 59.6, 103, and 159-kev states are assigned the sequence $5/2\pm$, $7/2\pm$, $9/2\pm$. The character of the 43.4- and 99.5-kev transitions as partially identified above is also in agreement with these assignments.

It is not possible to state whether the 128-kev transition is correctly placed and in agreement with the quantum states assigned, because almost nothing is known of its internal conversion characteristics. Similarly little can be said of the 207- and 168-kev transitions. If the supposition, previously mentioned, that the 207-kev transition is an $M1$–$E2$ mixture is true, then the 267-kev state has the same parity as the 59.6-kev state.

V. ACKNOWLEDGMENT

The authors wish to thank Professor B. B. Cunningham for making available the americium used in this study. Discussions with Dr. F. Asaro, Mr. F. Stephens, and Dr. J. O. Rasmussen have been most helpful.

[31] F. S. Tomkins, Phys. Rev. **73**, 1214 (1948).
[32] J. S. Fraser and J. C. D. Milton, Phys. Rev. **94**, 795(A) (1954).
[33] A. Bohr and B. R. Mottelson, Kgl. Danske Videnskab. Selskab, Mat.-fys. Medd. **27**, No. 16 (1953); A. Bohr, *Rotational States of Atomic Nuclei* (Ejnar Munksgaards, Copenhagen, 1954).
[34] F. Asaro and I. Perlman, Phys. Rev. **94**, 381 (1954).

Mean Free Path for Shower Production by High-Energy Pi Mesons*

FRITZ E. FROEHLICH† AND KURT SITTE‡
Department of Physics, Syracuse University, Syracuse, New York
(Received June 7, 1954; revised manuscript received September 17, 1954)

In order to investigate a possible difference in the mean free paths for shower production by protons and by π mesons of very high energy, an experiment was carried out at Echo Lake, Colorado (altitude 3260 m) in which the rate of production of penetrating showers by the atmospheric N component was studied as a function of the absorber thickness up to a total of 650-g/cm² Pb, or about four proton mean free paths. A difference in the cross sections would then result in the "filtering out" of the component with the shorter mean free path, and manifest itself in an attenuation curve which is the superposition of two exponentials rather than a single exponential curve. By splitting the top absorber into three sections and using three top trays instead of the usual one, with the rigid condition that only a single counter in each tray be discharged, losses due to the complete absorption of all secondaries of an interaction occurring in the top absorber were minimized and could be estimated from the results of the runs with smaller absorber thicknesses in which the lead absorber was distributed in various ways between and above the trays. Three further counter trays, placed in a lead pile, were used to select five types of showers of different multiplicity. The average energy of the primaries of these events were estimated to be about 5.3 Bev ("low-energy group"), 8.3 Bev ("medium-energy group"), and 16–20 Bev ("high-energy group"). Even after correcting for spurious events, the rates of the two latter groups—for which a substantial π-meson component can be expected—do not fit a straight line on a semilogarithmic plot, thus indicating that the mean free paths of the two components are not identical. Under the assumption of equal detection probability for the interactions of both types of primaries, the mean free path for shower production by π mesons of both energy groups is found to exceed 320 g/cm². It must be stressed that these results should not be interpreted as a proof for an interaction cross section smaller than the geometrical nuclear cross section, but rather as an indication that in collisions of very energetic π mesons, the number of π-meson secondaries emitted differs from that resulting from proton collisions, perhaps because of a larger probability for the production of other secondary particles.

I. INTRODUCTION

ALTHOUGH considerable effort has gone into the study of the interaction cross section of the energetic π mesons ejected in cosmic-ray nuclear interactions, no generally accepted picture has as yet evolved. It is probably generally conceded that, if the experimental techniques applied are very carefully designed so that collisions with small energy transfer (especially nuclear scattering) are not disregarded, the results of the measurements tend to approach the "geometrical" nuclear cross section. This is very clearly demonstrated in the summaries given, for instance, by Rochester and Rosser[1] and by Camerini *et al.*[2] However, it is of interest to note for the following considerations that in most experiments in which only energetic interactions were recorded—that is, when meson reproduction by mesons was demanded—a mean free path well in excess of the geometrical value was obtained. Thus, the cloud chamber investigations of Fretter[3] and of Brown and McKay[4] yielded mean free paths in lead of 750 g/cm² and 316 g/cm², respectively, and Piccioni's[5] earlier counter experiments gave for iron a value of 1200 g/cm². Perhaps the most noticeable exception is the recent cloud-chamber study of Duller and Walker[6] in which secondary mean free paths approaching the geometrical value with increasing particle energy were reported.

It should, however, be noted that in most of these experiments the particles were identified only as "shower secondaries"—and therefore were probably for the most part, but not exclusively, π mesons,—and that the energy of the particles was usually known only very roughly, but in most cases did not exceed an average value around 1 Bev. For energies around and below a few Bev, however, measurements of the interaction mean free path of nucleons have led to conflicting results, and the claim has frequently been made that in this energy region the cross section decreases sensitively with decreasing primary energy (e.g., Walker,[7] Sitte,[8] Boehmer and Bridge[9]). Although this conclusion has more recently been disputed (Froehlich *et al.*,[10] Sitte[11]), a geometrical interaction cross section can be considered as completely assured only for nucleons of several Bev energy. Thus it appeared of interest to study the cross section for collisions of π mesons of similarly high energies. This problem is also of importance for the propagation of the nucleonic cascade in the atmosphere: at energies around 10 Bev, decay and nuclear interactions become of comparable probability, in the lower parts of the atmosphere, if the mean free path has the

* Supported by the Geophysics Research Division, Air Force Cambridge Research Center, Cambridge 39, Massachusetts. Part of this work is included in the Ph.D. thesis submitted by Fritz E. Froehlich at Syracuse University, Syracuse, New York.
† Now at Bell Telephone Laboratories, Inc., Whippany, New Jersey.
‡ At present at the Department of Physics, Israel Institute of Technology, Haifa, Israel.
[1] G. D. Rochester and W. G. V. Rosser, Repts. Progr. Phys. **14**, 227 (1951).
[2] Camerini, Lock, and Perkins in *Progress in Cosmic-Ray Physics*, edited by J. G. Wilson (North-Holland Publishing Company, Amsterdam, 1952), Chap. 1.
[3] W. B. Fretter, Phys. Rev. **76**, 511 (1949).
[4] W. W. Brown and A. S. McKay, Phys. Rev. **77**, 342 (1950).
[5] O. Piccioni, Phys. Rev. **77**, 1 (1950) and Phys. Rev. **77**, 6 (1950).
[6] N. M. Duller and W. D. Walker, Phys. Rev. **93**, 215 (1954).
[7] W. D. Walker, Phys. Rev. **77**, 686 (1950).
[8] K. Sitte, Phys. Rev. **78**, 714 (1950).
[9] H. W. Boehmer and H. S. Bridge, Phys. Rev. **85**, 863 (1952).
[10] Froehlich, Harth, and Sitte, Phys. Rev. **87**, 504 (1952).
[11] K. Sitte, Acta Phys. Austriaca **6**, 167 (1952).

geometrical value. These energetic π mesons may then play an important part in the development of the nuclear cascade.

Since for protons of similarly high energies practically every interaction results in meson production, i.e., in the production of a penetrating shower, it appeared plausible to approach the problem of π-meson interactions in the same way, by studying showers produced by these particles. π mesons whose energies are around or above 10 Bev have even at mountain altitude a reasonable chance to escape decay until they collide with a nucleus. Thus, the beam of energetic N particles incident from the air on a shower-detecting arrangement will contain a few percent of π mesons together with the more abundant nucleons, the exact ratio depending on energy and altitude and being determined by the ratio of the mean free paths for collision and for decay. It is then possible to demonstrate a difference between the properties of the two main components of the atmospheric N component, if such a difference exists, in the following way: Assume, for instance, that π mesons have an appreciably smaller cross section than nucleons. Then one can "filter out" these particles by observing shower production under a very thick absorber, since the attenuation of the two components will be greatly different. To quote an example: if, for instance, the incident beam is composed of 5 percent π mesons and 95 percent protons, and if the mean free path in lead of the former is 660 g/cm² or four times that of the protons, then the beam of N-particles emerging from an absorber of 660 g/cm² thickness will consist of an about equal number of protons and of π mesons, and a determination of the mean free path of this mixture will yield a value which is easily distinguished from that found for the unfiltered atmospheric N component. A simple calculation shows that this method will produce statistically significant results in a reasonable length of time if the ratio of the mean free paths of the two types of N particles is at least 1.5. The method is, therefore, adequate for at least a preliminary study of the shower production by π mesons of very high energies, for which no other source than the atmospheric N component is available.

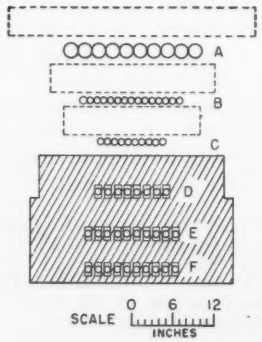

FIG. 1. Schematic diagram of the experimental arrangement.

II. THE EXPERIMENTAL METHOD

1. Description of the Arrangement

In a counter experiment designed to measure collision mean free paths, the customary procedure is to place a set of trays arranged to detect penetrating showers (in the following referred to as the "P set") under absorbers of various thicknesses, making sure that all events are rejected in which an interaction occurred already in the top absorber, regardless of possible subsequent collisions in the P set. Thus, for instance, if the interactions of charged N particles are being studied, the P set will be supplemented by a top tray which must be struck by exactly one particle, and all cases must be rejected in which more than one top counter is discharged. However, this method will obviously fail if, as in the present experiment, very thick absorbers must be used. Even if the P set is arranged to select showers of high multiplicity and penetration, one cannot exclude the possibility that some interactions had taken place in the top absorber, but had failed to trigger more than one counter of the top tray, either due to the absorption of the shower particles or due to their spread and the geometrical inefficiency of the counter tray.

This failure can be eliminated, or at least greatly diminished, by splitting the top absorber in three sections and placing individual "top trays" under every one of the absorber layers, demanding that in each of these three trays one and only one counter be discharged. In this way, none of the trays has to be covered by more than about 220 g/cm² although a total of three times that amount is used in this experiment, and absorbers of even more than 220 g/cm² have been considered safe in other experiments.

The experimental arrangement is shown schematically in Fig. 1. Of the three top trays A, B, and C, tray A consisted of ten counters of sensitive area 2 in.×24 in., tray B of fifteen counters 1 in.×20 in., and tray C of ten counters 1 in.×16 in. Below this "top telescope," the P set begins with a production layer of 4-in. Pb+$\frac{1}{4}$-in. Fe, and contains three trays of counters: tray D with eight counters of 1 in.×16 in., trays E and F each with ten counters of 1 in.×20 in. The individual counters of these trays were separated by $\frac{1}{2}$-in. lead strips. The absorber between D and E was 4-in. Pb+$\frac{1}{4}$-in. Fe, and that between E and F 3-in. Pb+$\frac{1}{4}$-in. Fe. Heavy side shielding (8-in. Pb) protected the trays of the P set in all directions against soft particles traveling under a large angle.

The counter pulses, equalized by diode clippers, were fed into conventional integrating circuits and cathode followers, all located in the trays. The output pulses then were fed into a set of discriminators, and their shaped outputs were mixed to define the various events chosen for the records. While the selection in all cases was based on the passage of a single, unaccompanied particle through the three top trays A, B, and C, five

different types of showers were continuously recorded. For the purpose of a simple description of the events, the following notation will be used throughout: A subscript n to the letter marking the tray (A_n) means that *exactly* n of its counters were struck; and a superscript m (B^m) denotes events in which m *or more* B counters were discharged. Furthermore, wherever possible the abbreviations "T" and "P" will be used for the top telescope (consisting of the three trays A, B, and C) and for the P set (of trays D, E, and F), respectively. Thus, the five types of shower events recorded can be written as:

$$T_1P^{221}=(A_1B_1C_1D^2E^2F^1);\quad T_1P^{222}=(A_1B_1C_1D^2E^2F^2),$$

$$T_1P^{321}=(A_1B_1C_1D^3E^2F^1);\quad T_1P^{332}=(A_1B_1C_1D^3E^3F^2),$$

$$T_1P^{333}=(A_1B_1C_1D^3E^3F^3).$$

The first group of events, consisting of a telescope particle, two or more particles at trays D and E, and at least one shower particle reaching tray F, comprises showers of comparatively low energy. The second and third, expected to be of about comparable frequency, form a medium-energy group, and the last two which require high multiplicities in several trays of the P set, will be mostly due to very energetic primaries. It is, therefore, mainly in the two latter groups that one may expect an effect if the π-meson component can be enriched by passing the N radiation through a thick absorber. A rough estimate of the primary energies of the three groups will be given in the Appendix.

2. Correction for Spurious Events

Since the rates of the large showers under very thick absorbers become exceedingly small, not only constant and careful checks on the stability of the arrangement is required, but also careful evaluation of all spurious effects. These can be divided into two groups: spurious events which give rise to counts without being due to interactions of N particles and therefore increase the rate of "showers" registered, and losses due to inefficiencies still remaining in spite of the precautions taken in the design of the arrangement. In this section, the effects of the first kind leading to spurious counts will be discussed.

Three types of events are the main contributors: (a) counts due to double or triple knock-on showers;[12] (b) counts due to random coincidences of two or more incident penetrating particles, all but one missing the top trays; and (c) nuclear interactions initiated by μ mesons. Their importance for the various groups of showers will be discussed separately.

(a) Knock-on showers affect the recorded rates in two ways. On the one hand, knock-on showers occurring in the P set above the three trays may be mistaken for penetrating events, thus increasing the number of showers registered. On the other hand, knock-on electrons originated in one of the three lead absorbers by the N particle traversing the top telescope and accompanying it to the level of one of the top trays, may reduce the apparent rate of traversals without interaction and hence the recorded shower rate. This effect is not negligible already for an arrangement using a single top tray (although it seems to have escaped the notice of most experimenters in this field), but it becomes particularly important in an experiment such as the present one where the passage of an unaccompanied particle is demanded at three trays.

To make the appropriate corrections, single and double knock-on rates for the individual trays (e.g., $T_1D^2E^1F^1$, $T_1D^3E^1F^1$, and also $A^2B_1C_1P^{221}$ and so on) were continuously recorded and checked. From the results the probabilities for knock-on accompaniment of a certain multiplicity were computed for all the trays. These figures, together with the "telescope rate" T_1P^{111} which was likewise continuously recorded, were then used to obtain the spurious contributions. The corrections for knock-on events in the top absorbers were calculated in the same way. Since three top trays were used, it is essential to consider also the possibility of knock-on events occurring at more than one tray.

It may be mentioned that spurious events in the P set have an appreciable effect only on the smallest showers (T_1P^{221}) at all absorber thicknesses, and on the events T_1P^{321} under the thickest absorber. In all other cases the corrections are quite negligible as a result of the experimental condition demanding multiplicity at three shielded trays.

(b) The most important contribution in this group comes from coincidences of a "telescope" meson traversing all top trays, with another meson that misses them. All possible combinations have been carefully analyzed, in Fig. 2 these spurious events contributing most to the shower types T_1P^{221} and T_1P^{222} are sketched. They include coincidences of the kind $(T_1P^{221})+(T_0P^{111})$ for the second shower group.

Most of the rates involved were likewise recorded during the experiment; others could be computed from the measured rates (like for instance the events T_0P^{111} since only T^0P^{111} was registered). The resolving times of the integrating circuits and of the coincidence system were measured both with a double-pulse generator and by observation of random coincidences at high counting rates. The rates of chance coincidences of the type shown in Fig. 2 could therefore be calculated. The contributions were small but not negligible for the shower groups T_1P^{221} and T_1P^{222}, especially in the shielded runs. All the other shower groups were practically unaffected since they all involve either knock-on events together with random coincidences, or triple coincidences.

[12] Under this heading are comprised all events recorded in the apparatus described as nonpenetrating secondary events produced by a single penetrating particle.

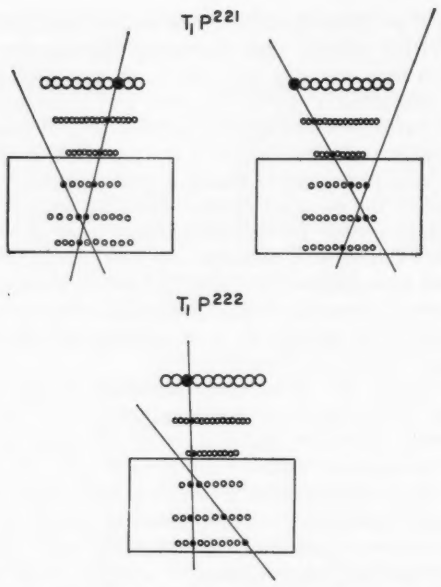

FIG. 2. Chance coincidences contributing spurious counts to the shower groups T_1P^{221} and T_1P^{222}.

(c) Corrections for nuclear interactions initiated by μ mesons can be calculated if one assumes that structure and composition of these showers, and hence the probability of their detection in the apparatus, do not differ significantly from those originated by N particles. Writing I_N and I_μ for the intensities of the N component and of the μ mesons, $p(\lambda_N)$ and $p(\lambda_\mu)$ for the probabilities that a shower is initiated in the production layer between trays C and D (λ_N and λ_μ are the interaction mean free paths of the two components), and $P(n)$ for the detection probability for a shower of n particles, one has for the numbers N_N, N_μ of showers due to the two kinds of primaries:

$$N_N = I_N p(\lambda_N) P(n),$$
$$N_\mu = I_\mu p(\lambda_\mu) P(n); \quad (1)$$

therefore, since $p(\lambda_N) = (1-e^{-\xi/\lambda_N})$, $p(\lambda_\mu) = (1-e^{-\xi/\lambda_\mu})$, with ξ = thickness of the production layer,

$$(N_\mu/N_N) = (I_\mu/I_N)(1-e^{-\xi/\lambda_\mu})/(1-e^{-\xi/\lambda_N}). \quad (2)$$

The cross section for nuclear interactions of μ mesons has now been measured by various authors (e.g., George,[13] Amaldi *et al.*,[14] Barrett *et al.*[15]) and the values obtained agree reasonably well, considering the smallness of the effect and the arbitrariness of the definition of a shower. For events of size and penetration comparable to that of the present experiment, a cross section of $5\text{–}6\times10^{-30}$ cm^2 per nucleon, or about 1/10 000 of that of a high-energy nucleon, is probably correct. The contributions of μ-meson initiated showers have therefore been computed with this value, corresponding to $\lambda_\mu = 1.6\times10^6$ g/cm^2 in lead, and for $(I_\mu/I_N) = 20$ in the unshielded run. In evaluating the intensity ratio under the various absorber thicknesses used, the attenuation of the N component was taken from the observed shower frequencies, and that of the μ mesons from their well-known range spectrum. The thickness ξ of the producing layer was 4-in. Pb+$\frac{1}{4}$-in. Fe.

The resulting contributions of μ-meson-initiated showers are quite negligible for small absorber thicknesses, but become increasingly important under thick absorbers. Under 650 g/cm^2 Pb, for instance, these spurious contributions amount to 4.4 percent of all recorded interactions in the low-energy group, and to 5.6 percent of the recorded medium-energy showers and 6.5 percent of the most energetic group.

A summary of the fractional contributions of the various corrections is given in Table I.

III. RESULTS

1. Effect of Thick Absorbers

Like the commonly neglected knock-on correction, a possible absorption of all the secondaries of an event occurring in the top lead absorber, and thus preceding the interaction in the producing layer, must be very carefully watched. As it has been said, the splitting of the 650-g/cm^2 absorber minimized this effect, but it should not be *a priori* assumed that it eliminates it since nuclear interactions with small energy transfer preceding large showers are rare, but by no means

TABLE I. Fractional contributions (in percent) of the three main corrections to the observed shower rates: knock-on showers, chance coincidences, and μ-meson-initiated nuclear interactions.

Absorber thickness (g/cm^2 Pb)	Type of correction	Shower group T_1P^{221}	T_1P^{222}	T_1P^{231}	T_1P^{232}	T_1P^{233}
0	knock-on	−3.4	− 0.1	−0.8	...	...
	coincid.	−0.1	− 0.5	...	...	...
	μ mesons	...	...	...	...	...
198[a]	knock-on	+2.4	+10.3	+9.8	+10.4	+10.4
	coincid.	−1.7	− 0.9	...	...	...
	μ mesons	−0.8	− 1.0	−1.0	− 1.1	− 1.1
440	knock-on	−4.4	+10.2	+8.6	+10.4	+10.4
	coincid.	−4.2	− 3.6	...	...	...
	μ mesons	−2.7	− 3.7	−3.7	− 4.0	− 4.0
650[a]	knock-on	−9.2	+10.1	+8.3	+10.4	+10.4
	coincid.	−6.5	− 8.1	...	...	...
	μ mesons	−4.3	− 5.5	−5.5	− 6.4	− 6.4

[a] The values listed refer to the run with equal absorber distribution.

[13] E. P. George, *Progress in Cosmic Ray Physics*, edited by J. G. Wilson (North-Holland Publishing Company, Amsterdam, 1952), p. 395.
[14] Amaldi, Castagnoli, Gigli, and Sciuti, Nuovo cimento 9, 453 (1952).
[15] Barrett, Bollinger, Cocconi, Eisenberg, and Greisen, Revs. Modern Phys. 24, 133 (1952).

impossible (e.g., Froehlich *et al.*[10]). It was therefore decided to obtain quantitative evidence on the influence of the absorption effect by repeating the measurements at equal total absorber thickness in various distributions over the three shelves.

Normally, the obvious absorber arrangement would be equal shielding of the three top trays A, B, and C, so that the maximum absorber thickness over any shelf would be about 220 g/cm². To study the losses occurring in this thickness, the run with the smallest amount of absorber (198 g/cm²) was carried out in three arrangements: equal distribution (66 g/cm² on each shelf), $\frac{2}{3}$ on top and no absorber above C, and the entire amount above A with both B and C unshielded. Similarly, in order to continue the absorption curve beyond the 200-g/cm² region the maximum absorber was likewise redistributed during part of the run, with 340-g/cm² shielding of A and approximately 90 g/cm² and 220 g/cm² above trays B and C, respectively.

If the absorption effect were negligible, the rates should remain unaffected by the redistribution. In fact, however, they changed quite noticeably. Thus, in the run with the 198-g/cm² absorber the shower rates, after correction for knock-ons, were the same as long as no shelf carried more than $\frac{2}{3}$ of the total, but they increased by 10–15 percent when all the absorber was placed on top of tray A. Similarly, the redistribution of the 650-g/cm² absorber led to an increase of the shower rates of several percent.

To evaluate the corrections for the shower rates, write $f(x)$ for the fraction of interactions in an absorber of thickness x whose secondaries are entirely stopped in x before reaching the tray immediately beneath the absorber, or else are emitted under so large an angle that they miss it. Thus $f(0)=0$, and it can be assumed that also for sufficiently small values of x the value of $f(x)$ remains negligible. The first control run with the redistributed 198-g/cm² absorber shows, for instance, that this is true at least up to $x=130$ g/cm². Generally, however, the number of nucleons emerging from the three layers x_1, x_2, x_3 either without having interacted, or after an interaction with sufficiently small energy transfer, will be (writing for the total absorber thickness $x=x_1+x_2+x_3$):

$$\begin{aligned} N &= N_0\{e^{-x/\lambda}+f(x_1)(1-e^{-x_1/\lambda})e^{-(x_2+x_3)/\lambda} \\ &\quad +f(x_2)(1-e^{-x_2/\lambda})e^{-(x_1+x_3)/\lambda} \\ &\quad +f(x_3)(1-e^{-x_3/\lambda})e^{-(x_1+x_2)/\lambda}\} \\ &= N_0e^{-x/\lambda}\{1+\sum_{i=1}^{3} f(x_1)(e^{x_i/\lambda}-1)\}. \end{aligned} \tag{3}$$

TABLE II. Shower rates in counts/hour, corrected for spurious events and for the effect of the thick absorbers, for the various groups of showers recorded. (The errors include the statistical standard uncertainties, and the effects of the uncertainties in the corrections.)

Events \ Absorber thickness (g/cm² Pb)	0	198	440	650
T_1P_{321}	8.43±0.15	2.99 ±0.07	0.768±0.026	0.301 ±0.016
T_1P_{322}	5.06±0.12	1.47 ±0.048	0.391±0.019	0.160 ±0.008
T_1P_{331}	5.12±0.12	1.56 ±0.048	0.385±0.011	0.142 ±0.011
T_1P_{332}	2.42±0.08	0.624±0.029	0.151±0.011	0.063 ±0.0047
T_1P_{333}	1.69±0.08	0.373±0.022	0.107±0.009	0.0408±0.0037

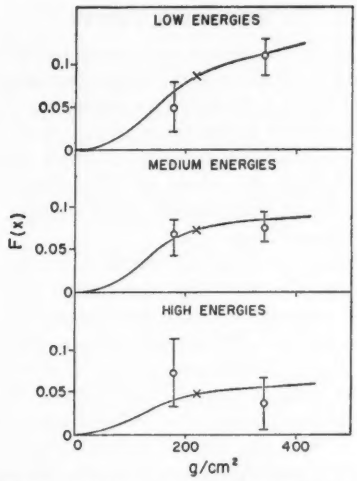

FIG. 3. Fractions $f(x)$ of showers originating in the top absorber, and not detected by the top trays, as a function of the absorber thickness x. [Crosses indicate the extrapolated values $f(220)$.]

In particular, the observed increase of the 198-g/cm² run when the entire absorber was placed on top of the arrangement yields values of $f(198)$ between 0.033 and 0.066 for the various shower groups. Similarly, the values of $f(x)$ corresponding to the thicknesses used in the 650-g/cm² run can then be obtained. Starting with an extrapolated value for the equal-absorber distribution one can compute the value of $f(x)$ for $x=340$ g/cm², and check the accuracy of the first choice of $f(220)$ from the plot of $f(x)$ made with this value. If necessary, an improved correction $f(220)$ is determined, and the procedure is repeated until a satisfactory smooth curve $f(x)$ is obtained. A mean free path $\lambda=164$ g/cm² was assumed throughout; in view of the evidence presented below favoring a long mean free path for the production of large showers this may seem incorrect, but since the criterion for the rejection by the top trays is very much less stringent than that for shower selection, it is likely that even the smallest, elastic interactions must be included so that the use of the geometrical cross section appears justified.

The results of this calculation are summarized in Fig. 3 which shows the fractions $f(x)$ of undetected showers as a function of the absorber thickness x. The corrections to be applied to the recorded rates are now easily computed with the help of Eq. (3).

2. Attenuating Curves

A summary of the shower rates, corrected for spurious events and for the effect of the thick absorbers, is given in Table II,[16] and is shown in a semilogarithmic plot in Fig. 4. The curves demonstrate clearly that the rates are not attenuated according to a simple exponential law, and that on the whole the deviations from the expected straight lines become more striking with increasing shower energy.

It should be noted that this nonlinearity may appear enhanced by the fact that the initial slope of the curves also increases with the average primary energy, and for the events T_1P^{333}, for which an average initiating energy of about 20 Bev was estimated, corresponds to a mean free path of only (135±12)-g/cm² Pb: significantly below the "geometrical" value of 164 g/cm². This, at the first moment, dismaying result may, however, not be unreasonable. If, for example, the commonly neglected correction for the effect of thick absorbers is omitted, an initial slope consistent with the geometric mean free path of 164 g/cm² is found. However, since the above correction increases with increasing absorber thickness, by omitting the correction the deviation from linearity of the curves becomes larger yet. Furthermore, in reviewing the data obtained in earlier work (e.g., Walker,[7] Boehmer and Bridge,[9] and Gottlieb[17]) one finds with a high consistency mean free paths shorter than those corresponding to the geometrical nuclear cross section, although in many cases including that value within the limits of the experimental errors; but there seems to be no experiment in which a longer mean free path was observed. This accumulated evidence should perhaps not be considered as purely accidental, and it may well be that at very high primary energies the true interaction cross section exceeds that usually designated as "geometrical." In any case, even if the curves were drawn with an initial slope of 164 g/cm², they would still be far from linear; the over-all attenuations between 0 and 650 g/cm² for the five groups of showers corresponds to mean free paths still significantly in excess of that value.

It must therefore be assumed that the attenuation curves are the result of the superposition of at least two curves. It is not possible to explain the observed curvatures in terms of a known background radiation superimposed on the N radiation. Mu mesons would be the only known particles capable of giving such a background. However, the effect of spurious contribution of mu mesons has been carefully evaluated. In all cases of importance—with the exception of mu-meson-initiated nuclear events—their effect was shown to be largest for the lowest-multiplicity shower events. The magnitude of the correction for mu-meson-initiated nuclear showers is small, and even assuming a reasonable error in the estimate of its effect could in no way explain the magnitude of the observed curvature in the high-multiplicity events. Furthermore, the attenuation and the relative abundance of a background radiation capable of explaining the observed effect does not fit anything that can be expected from the mu meson component.

It must, therefore, be concluded that the observed attenuation curves are the result of the superposition of curves belonging to different components of the N radiation, and that at least one of them has a mean free path for shower production which is considerably longer than that of the proton component.

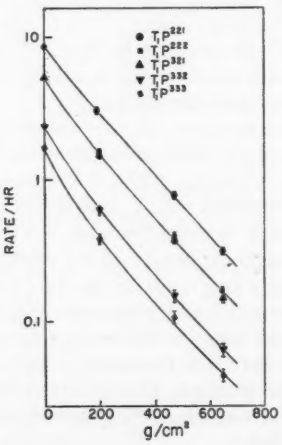

FIG. 4. Observed shower rates, corrected for spurious events and for the effect of the thick absorbers, as a function of the absorber thickness.

3. Barometer Effect

Since the value of the mean free path affects the branching ratio between nuclear interaction and decay —a larger value obviously favoring the latter—a consequence of a longer mean free path of one of the constituents of the N component that might be detectable, is a changed barometer effect of the "filtered" radiation emerging from a thick absorber. The N component, thus enriched in the less interacting particles, should show a reduced barometer coefficient, and a simple calculation shows that the magnitude of the effect is just big enough to make its detection possible, under favorable circumstances, in an experiment of the kind reported here. It was, therefore, decided to analyze the data of the run with the heaviest lead shielding with respect to pressure variation, and to determine the barometer coefficient of the high-energy group. Pressure records were obtained with each rate reading,[18] and the barometer coefficient was calculated according to

[16] The errors quoted include the statistical standard uncertainties, and the effects of the uncertainties in the corrections.

[17] M. B. Gottlieb, Phys. Rev. 82, 349 (1951).

[18] We are indebted to Dr. H. S. Bridge and Mr. E. Todd for supplying us with copies of their continuous pressure records taken with a Bendix Aviation Corporation Micro-Barograph accurate to 0.01 inch of Hg.

standard procedure.[19] Unfortunately, earlier indications of a reduced barometer effect were not borne out by the final analysis which gave for the high-energy group a coefficient of $-(10.8\pm3.0)$ percent, consistent both with the N component value of -11.7 percent and with the expected smaller value for the "enriched" mixture (8–9 percent).

IV. DISCUSSION AND CONCLUSIONS

1. Mean Free Path for Shower Production

For a quantitative analysis of the data presented above, the following basic assumptions will now be made:

(1) After correction for spurious effects, all the recorded showers are due either to proton or to π meson primaries of high energy. Other possible components of the N radiation can be neglected.

(2) In the high-energy region concerned, showers produced by those two kinds of primaries do not differ appreciably in their structure and composition. The detection probability P for the two contributing types of showers is, therefore, the same.

With these two assumptions, the rate R_t of showers observed under an absorber t can be written as follows:

$$R_t=N_0P\{\alpha(1-e^{-\xi/\Lambda})\cdot e^{-t/\Lambda} +(1-\alpha)\cdot(1-e^{-\xi/\lambda})\cdot e^{-t/\lambda}\}, \quad (4)$$

where N_0 stands for the total number of N particles incident from the air, α for the fraction of π mesons among them, ξ for the thickness of the production layer, Λ and λ for the mean free path for shower production by π mesons and by protons, respectively. Writing A_t for the attenuation ratio $A_t=R_t/R_0$ (R_0= rate at $t=0$), one has

$$A_t=\frac{\alpha(1-e^{-\xi/\Lambda})e^{-t/\Lambda}+(1-\alpha)(1-e^{-\xi/\lambda})e^{-t/\lambda}}{\alpha(1-e^{-\xi/\Lambda})+(1-\alpha)\cdot(1-e^{-\xi/\lambda})}. \quad (5)$$

A general method for evaluating such an equation for Λ and a test for consistency with the assumption that the attenuation of the observed rate with increasing absorber thickness consists of the superposition of the exponential attenuation of two components with different mean free paths, is to subtract the contribution of one of the components and demand that a semi-logarithmic plot of the remainder *vs* the absorber thickness is a straight line. Letting

$$\beta=\frac{\alpha(1-e^{-\xi/\Lambda})}{\alpha(1-e^{-\xi/\Lambda})+(1-\alpha)(1-e^{-\xi/\lambda})},$$

then

$$A_t=\beta e^{-t/\Lambda}+(1-\beta)e^{-t/\lambda}, \quad (6)$$

where β represents the fraction of the rate R_0 which is π meson initiated. First from the fact that under the smallest absorber thickness $A_{t1}=198$ g/cm^2 the N-component beam still consists predominantly of protons, it is a good approximation to set $A_{t1}=A_1=\exp(-t_1/\lambda)$ or generally $\exp(-t/\lambda)=(A_1)^{t/t_1}$. Now if the experimental data are consistent with the superposition of two exponential functions, one should be able to adjust the parameter β so that, employing the experimental data for the A's a plot of the function $G(\beta,t)=\ln\{A_t-(1-\beta)(A_1)^{t/t_1}\}$ *vs* t is a straight line. The negative reciprocal of the slope of this graph is, of course, Λ.

In order to be able to put upper and lower limits on the value of Λ thus obtained, the following procedure was adopted: For each β_i chosen, two points of the function $G(\beta_i,t)$ were plotted at each absorber thickness employing the values $A\pm$ one standard statistical error, as given in Table II. Now, remembering that at the point $t=0$ no statistical error appears in $G(\beta,0)$, the above procedure then immediately indicates whether for a particular β_i chosen, the points $G(\beta_i,t)$ may be connected by a straight line, and the upper and lower limit of its slope should such a straight line exist. Regions of interest were investigated taking β in steps of 0.001.

Combined averages of T_1P^{222} and T_1P^{321} were used to determine Λ for the medium-energy group and T_1P^{332} and T_1P^{333} for the high-energy group. It was found that straight lines exist for the graph of $G(\beta,t)$ *versus* t only for values of β between 3 and 11 percent for the high-energy group. Similarly in the medium-energy case only values of β between 2 and 7 percent would lead to straight lines. In the latter case, where the contribution from π mesons is expected to be already small, the comparatively large experimental errors permitted the determination of only a lower limit for Λ; the upper limit yielding the trivial solutions $\Lambda=\infty$. The solutions for Λ thus obtained are:

High-energy group:

$$\Lambda_{\min}=320 \text{ g/cm}^2,$$
$$\Lambda_{Av}=425 \text{ g/cm}^2,$$
$$\Lambda_{\max}=900 \text{ g/cm}^2;$$

Medium-energy group:

$$\Lambda_{\min}=328 \text{ g/cm}^2,$$
$$\Lambda_{Av}=425 \text{ g/cm}^2.$$

Λ_{Av} was obtained using the mean value of the A's for which a straight line could only be obtained for $\beta=9$ percent and 5 percent for the high- and medium-energy groups respectively. The lower limit of Λ was found for $\beta=11$ percent and 7 percent respectively, while the upper value of Λ comes from $\beta=4$ percent in the case of the high-energy group.

For the low energy events T_1P^{221}, it is seen from the graphs of Fig. 4 that no appreciable π meson component appears to be present in the incident beam.

[19] E.g., L. Janossy and G. D. Rochester, Proc. Roy. Soc. (London) A181, 186 (1944); L. Janossy, *Cosmic Rays* (Clarendon Press, Oxford, 1948).

Accordingly, the data have not been analyzed for π meson mean free path.

2. Summary

The fact that even the minimum mean free paths compatible with the data obtained in this experiment are still considerably larger than those corresponding to a geometrical cross section, requires some attention. It is certainly in disagreement with the conclusions of Duller and Walker[6] who find mean free paths for secondary interactions ranging from (1700_{-500}^{+1200}) for 1-Bev particles, to the near-geometrical value of (180_{-45}^{+85}) at $\gtrsim$4-Bev initiating energy. If the present results are taken at their face value, it would thus appear that with further increasing energy, the cross section for shower production begins to decrease again.

Before accepting such a conclusion, one must carefully examine its basis. As it has been emphasized before, the experiment reported here is designed to study the production of showers of high multiplicity and high penetration, and hence from its results the cross section for this process is obtained, but not that for interaction with a nucleus nor even for "shower production." The identification of the two cross sections: "interaction" and "production of large showers," may appear plausible because of its validity for proton collisions, but it is certainly not necessarily correct. One can easily conceive of at least two ways in which the characteristic features of the collisions of the two kinds of particles may differ: first, although the maximum energy transfer in a collision between a π meson of about 10 Bev and a nucleon is practically the same as that in a collision between two particles of nucleonic mass, the average number of secondaries produced and the multiplicity distribution may differ, with a bias in favor of smaller showers for π meson primaries. Secondly, energetic π mesons may dissipate an appreciable fraction of their energy—significantly more than protons—in the production of particles other than secondary π mesons. This second possibility has support in the results of Schein[20] who observed the production of hyperons of the V_1^0 type by π mesons of only 230 Mev. It may well be that this process becomes quite frequent for π mesons of 10 Bev and higher energies, and that, therefore, in these collisions less dense showers are originated. In both cases, the second basic assumption for the evaluation as presented in IV.1—that of equal detection probability for proton showers and for π-meson showers—would not hold, or better it would apply only to an arbitrary selection of the π-meson interactions.

In conclusion, it can therefore be said that the results of this experiment should be interpreted as a proof for fundamental differences between the characteristics of the interactions of the various components of the N radiation at very high energies. As the mean free path for the production of large penetrating showers, which is geometrical for protons, is larger than 328 g/cm² and 320 g/cm², respectively, for π mesons of average energy around 8 Bev and 15–20 Bev. But the present experiment does not yield evidence for the nature of these differences; a study especially designed for this purpose would have to supplement it.

TABLE III. Contributions (in counts/hour) of various primary energy intervals to the groups of showers recorded.

E_p(Bev) \ Events	T_1P^{221}	T_1P^{222}	T_1P^{231}	T_1P^{232}	T_1P^{233}
1	0.60	0.14	0.12	...	...
1– 2	2.27	0.82	0.80	0.05	...
2– 4	2.93	1.32	1.21	0.14	0.01
4– 6	1.83	1.22	1.20	0.35	0.10
6–10	1.26	1.00	0.85	0.47	0.23
10–20	0.89	0.88	0.78	0.71	0.66
>20	0.45	0.44	0.86	0.84	0.82
Total (R_{cal})	10.23	5.82	5.82	2.56	1.82
R_{exp}	8.43±0.15	5.06±0.12	5.12±0.12	2.42±0.08	1.69±0.08

[20] M. Schein, *Proceedings of the Third Annual Rochester Conference on High Energy Physics* (Interscience Publishing Company, New York, 1953).

V. ACKNOWLEDGMENTS

The experiment reported here was carried out at the facilities of the Inter-University High Altitude Laboratories at Echo Lake, Colorado, and the authors wish to express their gratitude to Professors Byron E. Cohn and Mario Iona, Jr., of the University of Denver, for their continuous cooperation. Thanks are also due Professor P. G. Bergmann of Syracuse University for a number of discussions and to Mr. J. G. Askowith who kept the arrangement in operation for several weeks, and assisted in running it for a longer time.

VI. APPENDIX: AVERAGE ENERGIES OF THE SHOWERS

The two main obstacles in an attempt to estimate the average primary energy from the shower rate are uncertainties (a) in the flux of the N component, and (b) in the determination of the detection probability.

As to the first, both theoretical arguments (e.g., Messel and Ritson,[21] Clemental and Ferrari[22]) and direct observation[10] have now established that at mountain altitude, the spectrum of the N component resembles, in the energy region of about 10 Bev, very closely that of the primary cosmic radiation, and its intensity can be obtained in a good approximation from the primary flux under the assumption of exponential attenuation with a mean free path of 117 g/cm². Accordingly, the calculations were based on the energy spectrum of Singer,[23] normalized to an integral directional intensity of 0.85×10^{-4} particles/cm² sec sterad.

As to the second, the main difficulty lies in the fact that data on the characteristics of showers in lead, like

[21] H. Messel and D. M. Ritson, Proc. Phys. Soc. (London) A63, 1359 (1950).
[22] E. Clemental and F. Ferrari, Nuovo cimento 9, 572 (1952).
[23] S. F. Singer, Phys. Rev. 80, 47 (1950).

multiplicity distribution, range of secondaries etc., are available only up to primary energies of 10 Bev,[10] so that extrapolations had to be used. The method of calculation was that previously applied:[8,10] given the (differential) energy spectrum $s(E)$ and the multiplicity distribution $M(E)$, one computes first for each multiplicity the average numbers m, m', m'' of shower particles present at the levels of the trays D, E, and F, taking into account cascade multiplication as well as absorption and geometrical losses. From these figures, the probability $P(n,n',n'')$ is then obtained that this shower will discharge n or more, n' or more, and n'' or more counters of the three shower-detecting trays, and consequently the contribution of the energy interval (E,dE) to the events of the type $T_1P^{n,n',n''}$ is

$$dR_{n,n',n''}=s(E)\sum_{M}M(E)P(n,n',n'')dE.$$

Integration over E yields the "calculated rates" which may serve as a check on the reliability of the method, and similarly, the average primary energies are now directly computed. Table III summarizes the contributions R_{cal} in counts/hour for the various shower groups. In the last row, the observes rates R_{exp} of the unshielded run are added for comparison, and it is seen that the agreement is surprisingly good: in no case are the deviations larger than 20 percent.

The average energies computed from this distribution are:

Events T_1P^{221}: $\langle E_p\rangle$ = 5.3 Bev,
T_1P^{222}: $\langle E_p\rangle$ = 7.9 Bev,
T_1P^{321}: $\langle E_p\rangle$ = 8.7 Bev,
T_1P^{332}: $\langle E_p\rangle$ = 16.4 Bev,
T_1P^{333}: $\langle E_p\rangle$ = 20.4 Bev.

If the agreement between all the observed and calculated rates is not to be considered as wholly fortuitous, these energy values should likewise be accurate within about 20 percent.

PHYSICAL REVIEW VOLUME 97, NUMBER 1 JANUARY 1, 1955

Penetrating Showers in Light and Heavy Elements*

JOSEPH G. ASKOWITH AND KURT SITTE†
Department of Physics, Syracuse University, Syracuse, New York
(Received June 7, 1954; revised manuscript received September 17, 1954)

A large cloud chamber fitted with one thick "producer plate" of light materials and with eight ¼-in. lead plates was operated at Echo Lake, Colorado (altitude 3260 m) to record penetrating showers originating in three light elements (Li, C, Al) and in lead. The average primary energies, estimated with the "F-plot" method of Duller and Walker, were between 20 and 25 Bev. From a comparison of the shower rates in the producer plates and in the top lead plate, upper and lower limits for the transparencies of the light elements are obtained, the latter if correction is made for the differences in the primary energies. More reliable values, however, are derived from a direct comparison of the rates in the three light elements. This yields a value of $\lambda=(2.55\pm0.25)\times10^{-13}$ cm for the mean free path in nuclear matter, and accordingly transparencies of (15±7) percent, (12±4) percent, and (6±3) percent, respectively for Li, C, and Al. It is shown that second-generation effects are not negligible even in light nuclei, and that they can account for the observed differences in the average multiplicities of showers initiated in the four elements studied. At a primary energy of 25 Bev, the average multiplicity of a nucleon-nucleon collision is about 3.4. The contribution of the π mesons to the intranuclear cascade is very small. This agrees well with the observed mean free path for shower production in the lead plates by secondary particles, which varies from (380±35) g/cm² for secondaries from light elements to (475±70) g/cm² for secondaries from lead. Since nuclear scattering in the lead plates was observed for secondaries from the light elements and from lead with mean free paths of (370±35) g/cm² and (300±36) g/cm² respectively, the total interaction mean free path in lead, comprising both scattering and secondary showers, is very nearly the same for secondaries emerging from light and heavy elements—about (190±25) g/cm²—and is also close to the geometrical value.

I. INTRODUCTION

MEASUREMENTS of the cross section for shower production as a function of the atomic weight of the target nucleus are of interest for a variety of reasons, but in particular because they provide the most direct means of studying the problem of the "mean free path of nucleons in nuclear matter," and that of the significance of second-generation effects in collisions of a nucleon with a nucleus (the intranuclear cascade). From the latter effect, evidence can also be derived on the interaction mean free path of π mesons in nuclear matter.

Since Cocconi's early paper on this subject,[1] it has become customary in high-energy interactions to use the concept of nuclear transparency as a quantitative expression of the deviation of the collision cross section from the geometrical nuclear cross section. Of the numerous papers on this subject, the experiments of Rolloson[2] and Froman *et al.*[3] with water may be men-

* Supported by the Geophysics Research Division, Air Force Cambridge Research Center, Cambridge 39, Massachusetts.
† At present at the Department of Physics, Israel Institute of Technology, Haifa, Israel.

[1] G. Cocconi, Phys. Rev. **75**, 1075 (1949).
[2] G. W. Rolloson, Phys. Rev. **87**, 71 (1952).
[3] Froman, Kenney, and Regener, Phys. Rev. **91**, 707 (1953).

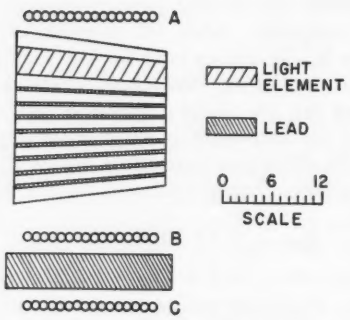

FIG. 1. Schematic diagram of the experimental arrangement.

tioned, and the attempt of Froman[4] to systematize the earlier results. The most widely studied light element is carbon, and here the results of most authors like Walker *et al.*,[5] Cool and Piccioni,[6] Boehmer and Bridge,[7] and others generally agree on a mean free path of about 80 g/cm², or a transparency of about 20 percent, even at rather high primary energy. However, Brown,[8] recording only very energetic events, found a collision cross section equal to the geometrical value.

Unfortunately, it appears that the experimental techniques applied in most of these studies are subject to serious criticism. Basically, two different methods are commonly used: in "counter-type" experiments the material under investigation is placed as an absorber on top of a set which records penetrating showers initiated by an unaccompanied primary, and the attenuation of the shower rate is measured as a function of the absorber thickness. In "chamber-type" experiments the shower production rate in light elements is directly compared with that in a heavy standard element, usually lead. The reliability of the first method, therefore, depends on the accuracy of the assumption that for all thicknesses used, every interaction that may have taken place in the top absorber is efficiently detected, and the corresponding event eliminated. This assumption is based on the premise that it is extremely unlikely for a nuclear interaction with high energy and large energy transfer to be preceded by one with a small transfer: an argument that has lost some strength in view of more recent results.[9] Indeed, it could be shown[10] that for instance the results of Boehmer and Bridge,[7] which indicate a variation with the primary energy of the collision mean free path in lead between the "geometrical" value of about 160 g/cm² and 300 g/cm², are quite compatible with the assumption of a geometrical cross section for all energies if only correction is made for the effect of small, undetected interactions in the top absorber. A similar effect should exist, and be even more pronounced, for interactions in light elements where "glancing" collisions are comparatively more frequent than in heavy elements, and this effect would falsify the conclusions on nuclear transparency derived from this type of experiment.

The cloud chamber method, on the other hand, suffers from the fact that the selection of triggering events is usually based on a certain multiplicity of shower secondaries striking the detection tray or trays. Since for a given primary energy the average multiplicity of the showers produced in heavy elements is larger than that of light-element showers,[11] this method is therefore biased in favor of detection of heavy-element showers for which it covers a larger part of the primary spectrum, and a direct comparison of the two shower rates again yields too high values for the transparency.

It was therefore decided to re-investigate the transparency problem with methods designed to avoid these pitfalls.

II. ARRANGEMENT AND PROCEDURE

The experimental arrangement, shown schematically in Fig. 1, consisted of a large cloud chamber in which the showers were produced, and a counter control selecting high-energy events. The aluminum-walled cloud chamber, of dimensions 18 in.×18 in. in its central plane and 18 in. deep, was fitted with a light-material "producer plate" near the chamber top and with eight ¼-in. lead plates below it. Three elements were used as shower producers: lithium, carbon, and aluminum. The lithium plate was encased in a thin-walled steel box and had an average thickness of 4.9 g/cm², the carbon producer was a 10.3-g/cm² sheet of pure graphite, and the aluminum plate had a thickness of 10.5 g/cm². The chamber expanded to both sides through expansion valves of a pneumatic-relay type like that used in an earlier chamber,[9] and was usually filled with an argon-oxygen mixture containing about 80 percent of the inert gas, and with vapor of an isopropyl alcohol-water mixture. Rear illumination was used, and stereoscopic pictures were taken with a two-lens camera under angles of about 12° from the axis.

The three counter trays *A*, *B*, and *C* shown in Fig. 1 selected the triggering events. Showers were recorded when a single particle incident at *A* struck in coincidence with at least three particles at *B* and two or more at *C*. Tray *C* was separated from *B* by a layer of 4-in. Pb. In this way, only high-energy local interactions (and the unavoidable background of air showers) triggered the chamber. The experiment was carried out at Echo Lake, Colorado, altitude 3260 m.

While thus the experimental arrangement was of the

[4] D. Froman, Phys. Rev. **88**, 172(A) (1952).
[5] Walker, Walker, and Greisen, Phys. Rev. **80**, 546 (1950).
[6] R. L. Cool and O. Piccioni, Brookhaven National Laboratory Report No. 119, 1952 (unpublished); O. Piccioni and R. L. Cool, Phys. Rev. **87**, 216(A) (1952).
[7] H. W. Boehmer and H. S. Bridge, Phys. Rev. **85**, 863 (1950).
[8] R. R. Brown, Phys. Rev. **87**, 999 (1952).
[9] Froehlich, Harth, and Sitte, Phys. Rev. **81**, 504 (1952).
[10] K. Sitte, Acta Phys. Austriaca **6**, 167 (1952).
[11] See, for example, Lovati, Mura, Salvini, and Tagliaferri, Nuovo cimento **7**, 943 (1950).

conventional type, the method of evaluation differed from that previously used. A comparison of the shower rates in the light elements with the rate of showers starting in the first lead plate—the only one for which the geometry is still sufficiently close to that of events from the light-element producers—served only to derive maximum and minimum values for the interaction mean free paths. A value that can be considered much more reliable was obtained from a comparison of the rates of events in the three light elements, using as standards in each case the total number of interactions initiated, during the respective operating times, in the eight lead plates. In this way, the error due to the energy bias mentioned above is minimized, and the statistical accuracy improved. Besides, the average primary energies could be estimated, and thus the appropriate small corrections could be made.

For essential parts of the discussion, the angular distribution of the shower particles and the multiplicity distribution of the showers are likewise needed. Again it was assumed that showers initiated in the producer plates, and those starting from the first lead plate, are detected with equal probability, so that a comparison of these distributions can be made without further corrections.

III. EXPERIMENTAL RESULTS

1. Angular and Multiplicity Distribution. Average Primary Energies

In the lithium run, a total of 97 showers originating in the producer plate were obtained, together with 428 showers starting in the lead plates, 60 of which came from the first plate. The corresponding figures for the carbon run were 94, 227, and 34, and for the aluminum run 86, 255, and 34. In this survey, events with less than three shower particles ejected in the primary collision were omitted even if, owing to secondary interactions in the material between producer plate and counters, they were able to trigger the arrangement.

A qualitative argument may be introduced here in order to stress the importance of recording the distributions in multiplicity and angular spread. In discussing transparency of the nuclei and mean free path of the secondaries, it is essential to assess correctly the influence of second-generation effects. Now evidently both the multiplicity distribution and the angular distribution of the showers originating in different elements will remain identical as long as these effects are negligible, while both will be affected if the shower is the result of an intranuclear cascade rather than of a nucleon-nucleon collision.

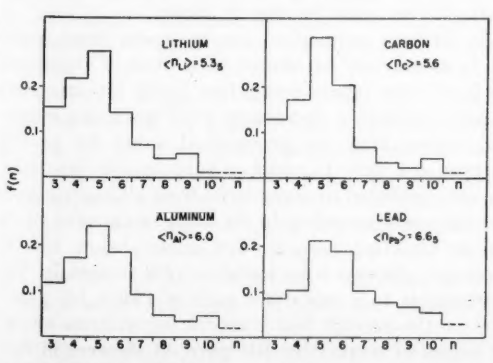

FIG. 2. Multiplicity distributions and average multiplicities $\langle n \rangle$.

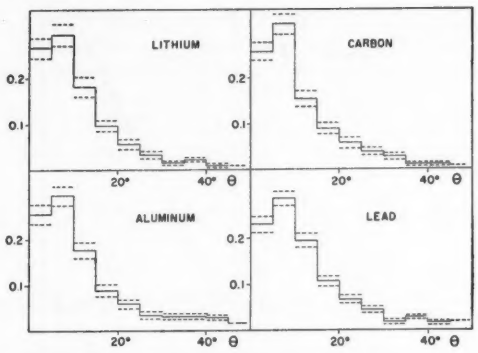

FIG. 3. Angular distributions $\Delta N/\Delta\theta$ of shower particles as a function of the laboratory zenith angle θ.

The multiplicity distributions and angular distributions observed in this experiment are reproduced in Fig. 2 and Fig. 3. An inspection of these histograms shows significant differences between the light-element showers and those originating in lead (the lead date are taken from all three runs). This is further borne out by the trend in the average particle numbers obtained from the multiplicity distributions of Fig. 2, which range from 5.35 for lithium to 6.65 for lead. An even better proof for the reality of the difference can be given if the "F plots" of Duller and Walker[12] are constructed. These authors have shown that for a nucleon-nucleon collision, under the assumption of isotropic distribution of the secondaries in the center-of-mass system, the fraction $F(\theta)$ of shower particles emitted, in the laboratory system, under an angle less than θ satisfies the relation,

$$\tan^2\theta = (1/\gamma_c^2)[F(\theta)/1-F(\theta)], \qquad (1)$$

where γ_c is the energy of the primary in the center-of-mass system, expressed in multiples of its rest mass. Plotting the observable quantity $F/(1-F)$ against $\tan^2\theta$ one expects, therefore, to obtain a straight line, the slope of which defines the average primary energy. This was verified by Duller and Walker on their own data and on those taken from Bristol stars, and it was again found true with the data obtained in this experiment as shown in Fig. 4 where the quantities $F(\theta)/[1-F(\theta)]$ corresponding to the distributions of Fig. 3 are reproduced in a logarithmical plot. Straight lines that fit the experimental points can be found for all three

[12] N. M. Duller and W. D. Walker, Phys. Rev. 93, 215 (1954).

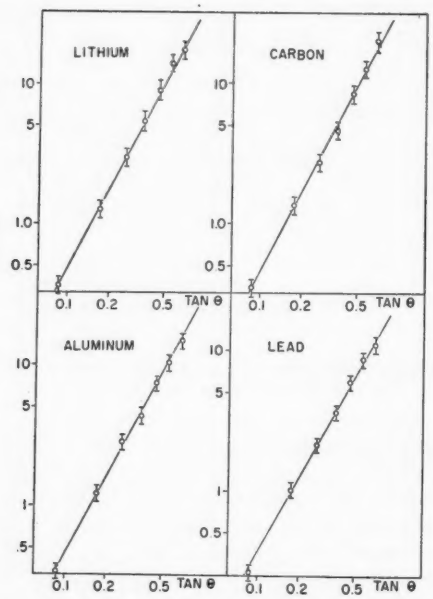

FIG. 4. "F plots": $\log(F/1-F)$ *vs* $\log(\tan\theta)$, for all four elements.

elements; however, the average primary energies derived from these graphs for the showers from the various elements differ noticeably. The average kinetic energies obtained from Eq. (1) are 25.3 Bev, 25.0 Bev, 23.6 Bev, and 21.3 Bev, respectively for Li, C, Al, and Pb, with probable errors lying between 0.5 and 0.8 Bev. Thus, no significant difference appears to exist between the primary energies of showers originating in Li and C, while the Al showers and even more so the Pb showers, are on the average initiated by somewhat less energetic primaries.

These kinetic energies will later on be used to make the appropriate corrections for the differences in the primary flux of the showers starting in the four elements.

2. Secondary Interactions

Nuclear interactions of the shower secondaries in the lower lead plates were divided into two groups: a process was defined as a "secondary shower" if at least two relativistic particles emerged from the plate, or at least one additional meson—relativistic or not—was created in the interaction. A process was called "nuclear scattering" if the incident shower particle, in traversing the plate, was deflected by 10°, or if one or more non-relativistic heavy "star particles" were ejected from the plate but no mesons were created.

The survey of the lithium run showed 36 scatterings and 29 secondary showers in 1637 traversals. In the carbon run, 1649 observed traversals yielded 31 scatterings and 33 showers, while the corresponding figures for the aluminum run were 1609, 30, and 32. Since no significant difference is found between the data for the three light elements, they will be lumped together and compared, as the secondary interactions of shower particles from light elements, with the total of the interactions found in all three runs for the secondaries of showers initiated in the first lead plate. For these events, 2398 traversals gave 58 scatterings and 37 showers. In all cases, only events were included in the survey for which a charged relativistic secondary particle could be definitely established as the interacting particle.

If the average inclination of the tracks is taken into account, the 97 scattering events in 4895 traversals for the light-element showers correspond to a mean free path for nuclear scattering $\lambda_{sc}=(370\pm35)$ g/cm², and similarly, the 95 secondary showers give a mean free path $\lambda_{sh}=(380\pm35)$ g/cm². From the lead data, one computes $\lambda_{sc}=(300\pm36)$ g/cm², and $\lambda_{sh}=(475\pm70)$ g/cm². It is of interest to note that, although the distribution between scattering and shower production in lead may differ for secondaries from light elements and those from lead, the total interaction mean free path comprising both kinds of events is the same, well within the experimental errors: the figures quoted above give $\lambda_{int}=(190\pm15)$ g/cm² for secondaries from light elements, and $\lambda_{int}=(185\pm20)$ g/cm² for secondaries from lead, both close to the geometrical mean free path of 164 g/cm².

During the same run, a total of 54 interactions definitely induced by neutral particles was observed for light-element showers (19+21+14), against 29 interactions for lead-shower secondaries. Assuming that the interaction mean free path of neutrons is the same as that for charged particles, one computes with these figures a ratio of shower neutrons to charged secondaries of (0.28 ± 0.05) for the light elements, and (0.31 ± 0.07) for lead. If the number of protons emitted in a shower is equal to that of the neutrons, the light-element showers—taking an average multiplicity of 5.6—would thus consist on the average of 4 mesons and 1.6 protons, while for lead showers a meson multiplicity of about 4.5 is obtained. However, the assumption of an equal mean free path may not be correct; if the interaction cross section of the neutrons were geometrical, the π-meson multiplicities would be slightly higher.

As far as a comparison can be made, these results are in satisfactory agreement with those of Duller and Walker[12] who report mean free paths for secondary shower production decreasing with increasing energy, and approaching the geometrical value for particle energies $\gtrsim 4$ Bev. In order to substantiate this point, showers produced by secondaries from all four elements were grouped according to the angle of emission of the shower-initiating particle. For angles below 10°, 91 secondary showers were found in 4238 traversals. This corresponds to a mean free path of (340 ± 36) g/cm². The on-the-average less energetic secondaries ejected at angles of more than 10° gave 40 showers in 3055 traversals, and hence a mean free path of (560 ± 90)

g/cm². A more direct attempt to determine the dependence on the secondary energy of the mean free path was not deemed worth while with the material on hand.

IV. DISCUSSION

1. Primary Collision Mean Free Path

Two ways are now open to determine the mean free path for shower production by the primaries. Although its results have only a limited value, it is instructive to apply first the usual method of comparing, for each run, the rates of showers produced in the light element and in the first lead plate. Writing n_{el} and n_{Pb} for the numbers of events recorded, x_{el} and x_{Pb} for the respective producer thicknesses, and λ_{el}, λ_{Pb} for the mean free paths, one has obviously

$$n_{el}/n_{Pb}=[1-\exp(-x_{el}/\lambda_{el})]/\exp(-x_{el}/\lambda_{el}) \times[1-\exp(-x_{Pb}/\lambda_{Pb})] =[\exp(x_{el}/\lambda_{el})-1]/[1-\exp(-x_{Pb}/\lambda_{Pb})], \quad (2)$$

if no correction is made for the difference in the average primary energy. This error may now be eliminated. Under the assumption of a power law for the energy spectrum, a more correct expression for the ratio n_{el}/n_{Pb} is

$$n_{el}/n_{Pb}=(E_{Pb}/E_{el})^{\gamma}[\exp(x_{el}/\lambda_{el})-1]/ [1-\exp(-x_{Pb}/\lambda_{Pb})], \quad (3)$$

where E_{el}, E_{Pb} are the average kinetic energies of the showers. For the evaluation of (3), the spectrum of Barrett *et al.*[13] has been used which gives an exponent $\gamma=1.18$ in the energy region concerned. Although it is derived for the primary cosmic radiation, there are good reasons to believe that practically the same spectrum also applies to the proton component at mountain altitude.[9,14]

The results of the calculations, with λ_{Pb} taken to be 164 g/cm², are summarized in Table I. In spite of the low accuracy resulting from the comparatively small number of lead showers, it is seen that the uncorrected mean free paths are in good agreement with most of the older data, while those computed according to (3) yield values of transparencies lower than those usually accepted.

However, it should be borne in mind that, from the foregoing reasons, Eq. (2) is bound to lead to an overestimate of the transparency, or in other words, to its possible maximum value which would be correct only if the primary energies for light-element showers and for lead showers were the same. On the other hand, Eq. (3) gives a minimum transparency valid only if lead showers can still be properly described as pure nucleon-nucleon collisions without the interference of second-generation effects. Otherwise, the estimates of the primary energy obtained from the F plots is too low, and the energy bias is overcompensated. Now it is already clearly demonstrated by the graphs of Figs. 2 and 3, and will be further documented below, that particularly in lead showers, second-generation effects play a significant part, and consequently the results of Eq. (3) will underestimate the transparency.

TABLE I. Mean free paths for shower production λ_{el} and transparencies t_{el} obtained from comparison with lead.

Element	Uncorrected [Eq. (2)] λ_{el} (g/cm²)	Uncorrected [Eq. (2)] t_{el} (%)	Corrected [Eq. (3)] λ_{el} (g/cm²)	Corrected [Eq. (3)] t_{el} (%)
Li	$69\pm^{11}_{8}$	$23\pm^{11}_{10}$	$57\pm^{8}_{7}$	$7\pm^{11}_{13}$
C	$90\pm^{13}_{10}$	$29\pm^{9}_{9}$	$75\pm^{11}_{9}$	$15\pm^{11}_{14}$
Al	$99\pm^{14}_{12}$	$16\pm^{10}_{11}$	$93\pm^{12}_{10}$	$11\pm^{10}_{11}$

The second method, consisting of a comparison of the rates in the three light elements, is therefore more promising since in this case the energy estimates are more reliable, and any remaining slight error is of negligible effect on the corrections made. However, a direct comparison of shower rates obtained at different periods extending over many months would be a dubious procedure and could easily introduce systematic errors. Hence it was decided to use, instead of the absolute rates, the ratios R_{Li}, R_C, and R_{Al} of the numbers of events starting in the light-element producer plates to the numbers of showers originating in all lead plates. By taking the lead showers as a standard of comparison only, no additional energy bias is introduced and the differences in the detection probabilities for showers starting in different plates likewise do not affect the validity of the procedure.

Then, writing $S(E_{el})$ for the respective primary intensities, one has evidently

$$R_{Li}:R_C:R_{Al}=S(E_{Li})[\exp(x_{Li}/\lambda_{Li})-1]:S(E_C) \cdot[\exp(x_C/\lambda_C)-1]:S(E_{Al})[\exp(x_{Al}/\lambda_{Al})-1]. \quad (4)$$

To evaluate (4), one may proceed directly to a determination of the mean free path in nuclear matter λ. With this parameter, the transparency t of a nucleus of radius r_n has the well-known approximate form

$$t(\lambda/r_n)=(\lambda^2/2r_n^2)\{1-(1-2r_n/\lambda)\exp(-2r_n/\lambda)\}. \quad (5)$$

For light nuclei, the more accurate numerical computations of R. W. Safford, reported by Rossi,[15] should be used.

Since by definition for any element, $\lambda_{el}=\lambda_{el}^0(1-t)$ where λ_{el}^0 is the geometrical mean free path, it follows that, for instance, for the two elements Li and Al the

[13] Barrett, Bollinger, Cocconi, Eisenberg, and Greisen, Revs. Modern Phys. 24, 133 (1952).

[14] Sitte, Froehlich, and Nadelhaft, Phys. Rev. 97, 166, (1955).

[15] B. Rossi, *High-Energy Particles* (Prentice-Hall Publications, Inc., New York, 1952), p. 360 ff.

relation holds:

$$R_{Li}/R_{Al}=S(E_{Li})\{\exp[x_{Li}/\lambda_{Li}{}^0(1-t_{Li})]-1\}/ S(E_{Al})\{\exp[x_{Al}/\lambda_{Al}{}^0(1-t_{Al})]-1\}, \quad (6)$$

or again using a power law for the energy spectrum,

$$(R_{Li}/R_{Al})(E_{Li}/E_{Al})^\gamma=\{\exp[x_{Li}/\lambda_{Li}{}^0(1-t_{Li})]-1\} \times\exp[x_{Al}/\lambda_{Al}{}^0(1-t_{Al})]-1\}=\Phi(\lambda). \quad (7)$$

An analogous expression can be written down for $(R_C/R_{Al})(E_C/E_{Al})$. Since the left-hand side of (7) is known from the experimental data, a graphical solution for the only unknown λ can now be obtained. The solutions computed from the two relations overlap in the region 2.30×10^{-13} cm $\leq\lambda\leq 2.80\times10^{-13}$ cm; hence the value of $(2.55\pm0.25)\times10^{-13}$ cm will be used below. The collision mean free paths and transparencies of the light elements calculated with this value are summarized in Table II. They are considerably lower than those previously reported: a discrepancy which was to be expected in view of the overestimates of the transparency inherent in the earlier experiments.

2. Estimate of Second-Generation Effects

The importance of second-generation effects of the primary can now be estimated by calculating, with the mean free path in nuclear matter given above, the probability that the incident particle undergoes more than one collision inside the target nucleus. In order to do this, consider the probability P_1 that the primary will collide just once while traversing the nucleus. With the same simple model that leads to Eq. (5) one has evidently, writing b for the impact parameter and r_1 for the interaction radius,

$$r_n{}^2\pi P_1=2\pi/\lambda\int_0^{r_1+r_n}\int_0^{2(r_n{}^2-b^2)^{\frac{1}{2}}}\exp(-x/\lambda) \times\exp\{-[2(r_n{}^2-b^2)^{\frac{1}{2}}-x]/\lambda\}bdbdx, \quad (8)$$

which gives, for $r_1\ll r_n$,

$$P_1=(\lambda^2/r_n{}^2)[1-(1+2r_n/\lambda+2r_n{}^2/\lambda^2) \times\exp(-2r_n/\lambda)]. \quad (9)$$

For smaller nuclear radii r_n, numerical integration has to be carried out. Similarly, the probability $P_{\geq1}$ that the primary interacts *at least* once, is for $r_1\ll r_n$

$$P_{\geq1}=1-(\lambda^2/2r_n{}^2)\{1-(1+2r_n/\lambda)\exp(-2r_n/\lambda)\} \quad (10)$$

[corresponding to the transparency formula (5)]. For the more general cases, the transparency data given by Rossi[15] can be used to obtain $P_{\geq1}$.

The simplest criterion for the importance of the second-generation effects is, then, the value of the expression $(P_{\geq1}-P_1)/P_{\geq1}$ which measures the fraction of events among all interactions in which the primary collides more than once. Second-generation effects can be neglected if $(P_{\geq1}-P_1)/P_{\geq1}\ll1$, which for $r_1\ll r_n$ means

$$(P_{\geq1}-P_1)/P_{\geq1} =\frac{1-\frac{3\lambda^2}{2r_n}\left\{1-\left(1+\frac{\lambda}{r_n}+\frac{4\lambda^2}{3r_n{}^2}\right)\exp\left(-\frac{2r_n}{\lambda}\right)\right\}}{1-\frac{\lambda^2}{2r_n{}^2}\left\{1-\left(1+\frac{2r_n}{\lambda}\right)\exp\left(-\frac{2r_n}{\lambda}\right)\right\}}\ll1. \quad (11)$$

The quantity $(P_{\geq1}-P_1)/P_{\geq1}$ is plotted as a function of r_n/λ in Fig. 5, the approximate expressions (9) and (10) being used so that all elements can be represented on the same graph. Since only the ratio of the probabilities is needed, the results are not significantly modified if the more correct values for the P's are introduced. The relative probabilities for repeated interactions in the four nuclei Li, C, Al, and Pb are likewise indicated, based on the value for $\lambda=(2.55\pm0.25)\times10^{-13}$ cm as derived in sect. IV.1. It is seen that already for light elements the probability for a second collision is by no means very small, while for elements as heavy as lead it approaches certainty.

This result gains importance in connection with the increasing evidence from various recent experiments[12,14,16] that even high-energy collisions are not completely inelastic, but that the primary retains a sizeable fraction—perhaps 20–25 percent of its initial energy. Its second interaction inside the target nucleus should, therefore, contribute a fair share to the total meson production. Assuming that the incident 25-Bev particle continues, after the collision, with a kinetic energy of 5 Bev, a check on the average multiplicities in the four nuclei Li, C, Al, and Pb has been made on the basis of the Fermi theory.[17] In order to get numerical agreement, its results had to be renormalized so that the primary nucleon-nucleon collision produces about 3.4 charged secondaries. The total meson production by a 25-Bev primary in these four elements is, then, about 3.9, 4.1, 4.5, and 4.8 charged shower particles respectively, and it is seen that, by taking into account also the increase in the number of shower protons, the

TABLE II. Mean free path for shower production λ_{el} and transparency t_{el} obtained from comparison of the shower rates of the light elements.

Element	λ_{el} (g/cm²)	t_{el} (%)
Li	62±5	15±7
C	72±3.5	12±4
Al	88±3.5	6±3

[16] Kaplon, Klose, Ritson, and Walker, Phys. Rev. **91**, 1537 (1953).

[17] E. Fermi, Progr. Theoret. Phys. **5**, 570 (1950); Phys. Rev. **81**, 863 (1951).

differences in the average numbers of shower particles observed in this experiment can well be explained by second-generation collisions of the primary only.

Consider now the intranuclear interactions of the shower secondaries: the number of these collisions increases strongly between lithium ($r_n = 2.65\times10^{-13}$ cm) and aluminum ($r_n = 4.14\times10^{-13}$ cm), and since the average energy of the secondaries is of the order of 2 Bev, their contribution to the production of shower particles should likewise be appreciable in the bigger nuclei, Al and Pb, if the mean free path for shower production in nuclear matter were the same for π mesons as for protons. The fact that the observed differences can be accounted for on the basis of primary interactions only, must therefore be interpreted as demonstrating that intranuclear shower production by π mesons of around 2 Bev can occur only with a mean free path considerably above that found for protons, 2.55×10^{-13} cm. This is in agreement with the data on λ_{sh} derived from the interactions in the lead plates (Sec. III.2): the value of $\lambda_{sh} = 380$ g/cm^2 corresponds to a mean free path in nuclear matter of about 18.5×10^{-13} cm,[15] and with this value even the heavier nuclei become highly transparent to the shower secondaries.

3. Conclusions

In summarizing the results, the following conclusions can be drawn:

(1) The suspected systematic errors in previous experiments which led to an overestimate of the transparency, appear to be real and significant. By using a method less sensitive to these errors, transparencies somewhat lower than those generally quoted are found: (15±7) percent for Li, (12±4) percent for C, and (6±3) percent for Al. They correspond to a mean free path in nuclear matter of $(2.55\pm0.25)\times10^{-13}$ cm.

(2) Second-generation collisions of the primaries are of importance even for light nuclei, and contribute to the meson production in the intranuclear cascade. The average numbers of shower particles found in this experiment lead to a multiplicity of about 3.4 for a nucleon-nucleon collision at 25-Bev primary energy, and the differences between the various elements can be explained by the contributions from the subsequent interactions of the primary in the target nucleus.

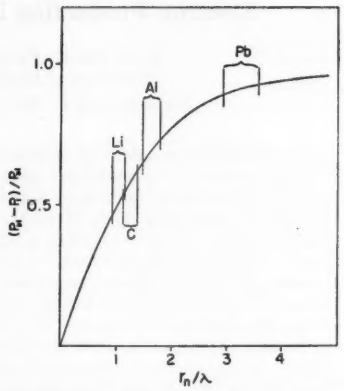

FIG. 5. $(P_{\geq1}-P_1)/P_{\geq1}$, the fraction of events in which the primary undergoes more than one collision, as a function of r_n/λ.

(3) It follows from the preceding that the contribution of the shower secondaries to the intranuclear cascade in light or medium-heavy nuclei is insignificant. Consequently, their mean free path in nuclear matter must be longer than that of the primary. This is in agreement with the observations on secondary shower production in the lead plates below the producers. The mean free paths for shower production derived from them correspond to a mean free path in nuclear matter of about 7 times the value for the primaries.

(4) Since in light elements the scattering mean free path of the secondaries is of the same order as that for shower production, these nuclei are also highly transparent with respect to scattering. It can therefore be expected that the "*F*-plot" method of energy determination will yield reliable results at least for not too heavy nuclei.

V. ACKNOWLEDGMENTS

The experimental work was carried out at the facilities of the Inter-University High Altitude Laboratories at Echo Lake, Colorado, and the authors are obliged to Professors Byron E. Cohn and Mario Iona, Jr., of the University of Denver for their cooperation.

Electron Production in High-Energy Nuclear Interactions*

KURT SITTE,† FRITZ E. FROEHLICH,‡ AND IRVING NADELHAFT
Department of Physics, Syracuse University, Syracuse, New York

(Received June 7, 1954; revised manuscript received September 17, 1954)

An experiment was carried out at Echo Lake (altitude 3260 m) and Mt. Evans (altitude 4300 m), Colorado, in order to measure the dependence on the primary energy of the fractional energy transfer to the electronic component, in nuclear interactions of about 10–100 Bev. Showers produced in a carbon block were grouped according to their multiplicity of penetrating particles as registered by a hodoscope, and the corresponding electron density was determined by a liquid scintillator placed under an appropriate lead shield. Since the shower multiplicity can be related to the primary energy, and the scintillator pulses can be calibrated by recording air showers, the number of electrons produced could thus be measured as a function of the primary energy. If, according to the Bristol data, in collisions around 50-Bev primary energy, the production of K particles consumes a fraction of the primary energy equal to that given to the π mesons, and if π^0 decay is the only major contributor to the electronic cascade, one must expect a decrease of the fractional energy transfer to the electron component by about $\frac{1}{2}$ between a maximum at 20–30 Bev and a more constant lower level at 50–100 Bev. This is not borne out by the experimental results which demonstrate a constant, or slightly increasing, fractional transfer at energies above 20 Bev. The results lead, therefore, to the conclusion that either, contrary to the Bristol observations, π-meson production predominates even at high energies, or else that a process or processes other than π^0 decay must be responsible for a considerable part of the electron component produced in collisions with primary energies above a few 10^{10} ev.

I. INTRODUCTION

EVER since the absence of an appreciable electronic component in the primary cosmic radiation has been established, the explanation of the composition of the large mixed air showers has been a challenging problem. Qualitatively the picture was well understood as soon as the discovery of the neutral π meson provided a mechanism of efficient energy transfer from the nuclear cascade to the electron component. Quantitatively, however, the attempts to explain a composition of about 98 percent electrons against 1 percent nucleons and 1 percent μ mesons at the customary observation levels was less successful. Calculations carried out by Amaldi and his collaborators,[1] for instance, on the basis of the Fermi theory of meson production,[2] lead to results very similar to those of Molière and Budini[3] who used the Heisenberg theory.[4] In both cases, as in similar attempts we have made with simplified models and various assumptions on meson production, it is just barely possible to adjust the available parameters to fit the experimental data either on the abundance of penetrating particles or on the ratio of μ mesons to nucleons, but the agreement is not satisfactory for both abundance and abundance ratio. Moreover, in all these calculations two basic assumptions have been made and are essential for their at least partial success, the validity of which must now be seriously doubted: first, that the nuclear collisions at air shower energies are completely inelastic, and second, that in these collisions most of the primary energy is dissipated in the production of π mesons with no other seriously competing process.

The first assumption seems to be refuted by the results by Kaplon *et al.*[5] who recently found that the absorption mean free path, even at energies around 10^{12} ev, is still about the same as the well-known $\sim$120 g/cm^2 repeatedly established for energies of a few Bev.[6] This same conclusion was also reached from part of the data obtained in this experiment (see Sec. III). The second assumption is in flat contradiction to the recent observations on K particles. Here the original results of the Bristol group[7] have now been confirmed by more recent work,[8,9] and demonstrate that already at energies of around 50 Bev about one-half of the energy transferred to the meson component goes to those of the heavier variety.

Since no efficient mechanism of energy transfer from K mesons to electrons is known—the few recorded examples[10] make it appear a rather rare phenomenon—these new facts raise serious difficulties for the theory of mixed air showers. Unless other, hitherto unobserved mechanisms exist which divert an appreciable amount of energy to the electron component, their composition can hardly be understood.

* Supported in part by the U. S. Atomic Energy Commission.
† At present at the Department of Physics, Israel Institute of Technology, Haifa, Irsael.
‡ Now at Bell Telephone Laboratories, Inc., Whippany, New Jersey.
[1] Amaldi, Mezzetti, and Stoppini, Nuovo cimento **10**, 803 (1953).
[2] E. Fermi, Progr. Theoret. Phys. **5**, 570 (1950); Phys. Rev. **81**, 683 (1951).
[3] G. Molière and Budini in *Kosmische Strahlung* edited by W. Heisenberg (Springer, Berlin, 1953).
[4] W. Heisenberg, Z. Physik **126**, 569 (1949).
[5] Kaplon, Klose, Ritson, and Walker, Phys. Rev. **91**, 1573 (1953).
[6] E.g., J. Tinlot, Phys. Rev. **73**, 1476 (1948); **74**, 1197 (1948).
[7] C. F. Powell, International Conference on High-Energy Physics, Copenhagen, 1952 (unpublished).
[8] R. R. Daniels and D. H. Perkins, Report on the International Congress On Cosmic Radiation, Bagnères de Bigorre, 1953 (unpublished), p. 159.
[9] J. Mulvey, Report on the International Congress on Cosmic Radiation, Bagnères de Bigorre, 1953 (unpublished), p. 198.
[10] Bridge, Courant, De Staebler, and Rossi, Phys. Rev. **91**, 1024 (1953).

The direct evidence on electron production in high-energy showers, mostly expressed in terms of the ratio of π^0 mesons to shower particles, is scanty and rather conflicting. Thus, for instance, the Rochester group[11] finds at energies around 10^{12} ev a value of 0.5 for the ratio of neutral mesons to shower particles, while Peters *et al.*[12] at a still higher energy derive a ratio of (1.0 ± 0.1): both in disagreement with the Bristol data[13] of 0.25, quoted as consistent with the well-known value of about 0.5 for the ratio of neutral to charged π mesons at energies of a few Bev,[14,15] and with the reduction of number and energy of the π-meson component at very high energies. A further investigation seemed, therefore, worth while.

If π^0 mesons are the only particles responsible for the bulk of the electrons in mixed showers, then a conspicuous change in the fraction of the primary energy transferred to the electron component should occur in the primary energy interval between about 10 and 100 Bev. At the lower limit, practically no K particles are produced and one-third of the energy dissipated in the collision should appear in the electronic cascade produced; at the higher limit, π^0 mesons can carry away only one-sixth of the transferred energy, and consequently the fraction of the primary energy found in the electron component should be only about one-half of what it is for a 10-Bev shower. An experiment was, therefore, designed in order to measure this fraction of the primary energy which is given to the electronic component, and to investigate its variation with the primary energy in the region of about 10 to 100 Bev. It should be emphasized already at this point that for the purpose of this experiment, a very precise determination of the absolute values of this transfer, or of the primary energy, is not necessary: it will suffice to establish the existence of absence of a variation of the transfer ratio with energy, by a factor of the order one-half and in an interval covering approximately the limits mentioned above.

II. EXPERIMENTAL ARRANGEMENT

A technique must be applied which permits the determination of the energy carried by the electron component of a hard shower and an estimate of its primary energy. As to the first, three simple facts concerning electron cascades are of help: first, that the number of electrons at the cascade maximum is very nearly proportional to the energy of the initiating electron or photon; second, that the position of the cascade maximum varies only logarithmically with the primary energy; and finally, that the variation of the particle number in the neighborhood of the cascade maximum is very slow. If, therefore, an arrangement is chosen which registers the number of electrons at a position corresponding to, say, the cascade maximum of the electron shower originated by a π^0 meson of the average secondary energy of a 30-Bev shower, this same arrangement can serve as an efficient recorder of the particle numbers, and hence of the energy, of the electron component for all primary energies between 10 and 100 Bev.

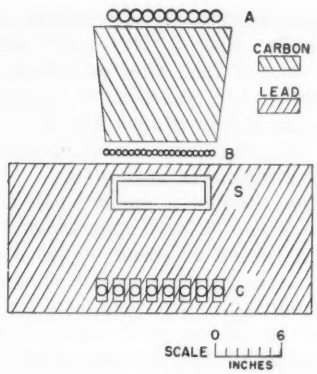

FIG. 1. Schematic view of the experimental arrangement.

These considerations can also be used to establish the approximate number of soft particles expected at this absorber depth. It will be of the order of, though somewhat smaller than, the number of electrons at the maximum of a cascade originated by a single photon which carries the entire energy transferred to all the photons emitted, as the decay products of the π^0 mesons, in the forward direction. At 10-Bev primary energy, the lowest energy of interest for this experiment, the total photon energy thus emitted is of the order of 1.5 Bev, and the corresponding number of electrons at the cascade maximum is therefore about 12,[16] so that a proper minimum setting of the electron-recording device will be to the equivalent of around 10 relativistic particles, including the hard shower secondaries.

Accordingly, the arrangement shown schematically in Fig. 1 was chosen. It consists of three trays of Geiger counters A, B, and C, and a liquid scintillator S as electron detector. The top tray A of ten counters of 1-in.$\times$16-in. active area is set to detect single incident particles while the circuits of B and C are arranged so that in order to produce a signal, three and two counters respectively must be struck. Tray B contains sixteen counters of $\frac{1}{2}$ in.$\times$16-in. and the output of each counter is also fed into a hodoscope; tray C holds eight 1-in. $\times$16-in. counters, separated from each other by $\frac{1}{2}$-in. lead.

[11] M. F. Kaplon and D. M. Ritson, Phys. Rev. **90**, 716 (1953).
[12] Lal, Pal, Peters, and Swami, Proc. Indian Acad. Sci. **36**, 75 (1952).
[13] E.g., D. H. Parkins, Proceedings of the Third Annual Rochester Conference On High Energy Nuclear Physics (Interscience Publishers, Inc., New York, 1953), pp. 43–46.
[14] G. Salvini and Y. Kim, Phys. Rev. **85**, 921 (1952).
[15] Froehlich, Harth, and Sitte, Phys. Rev. **87**, 504 (1952).
[16] In these and all the following computations on electron showers, the tables of cascade functions by L. Janossy and H. Messel [Proc. Roy. Irish Acad. **A15**, 217 (1951)], have been used if the initiating energy was above 1 Bev, and the results of R. R. Wilson obtained with the Monte Carlo method [Phys. Rev. **84**, 100 (1951)] for lower energies.

The arrangement thus registers showers produced in the top absorber layer Σ, (42 g/cm^2 carbon) which arrive at B with at least three secondaries, penetrate the absorbers Σ_2 (1-in. Pb$\pm\frac{1}{4}$-in. Fe) and Σ_3 (6-in. Pb) and still contain at least two particles at C. Heavy side shielding by 8-in. Pb reduces to a minimum the spurious masterpulses arising from air showers.

The electron detector S was a Lucite box of $\frac{1}{8}$-in. wall thickness and of inner dimensions 2 in.$\times$8 in. $\times$16 in. filled with a 3 percent terphenyl solution in phenylcyclohexane to which 40 mg of diphenylhexatriene had been added. Thus, electrons emerging from Σ_2 with the critical energy in lead will just about penetrate the scintillator, but particles of much lower energy will not produce pulses of the same standard size. The scintillator box was enclosed in a larger reflecting case in which four 5819-photomultiplier tubes were mounted in pairs, facing the long sides of the box. Their signals were fed through preamplifiers into an addition circuit, the output of which was than considered a sufficiently accurate measure of the number of shower particles, independent of the exact location of the traversals. This pulse than passed through a linear amplifier and was displayed, with a suitable delay, on the screen of an oscilloscope the sweep of which was triggered by the counter masterpulse. The pulse height on the screen was set so that its variation by a factor well over ten could still be read easily without overloading the amplifier or the scope. An approximate setting was obtained by reducing to one-tenth of its former value the amplification of the linear amplifier, after adjusting the pulse height setting on the scope so that the pulses of single μ mesons traversing the scintillator vertically were just readable. The method used for the more accurate calibration will be described in the next section. The sixteen hodoscope bulbs recording the discharge in tray B were mounted, together with the usual mechanical register and a clock, around the screen, and were photographed together with the scintillator pulse. In this way, both the multiplicity of the nuclear interaction and the amount of energy given to the electron component were recorded for each individual event.

III. ESTIMATES OF PRIMARY ENERGY AND ELECTRON DENSITY

Two independent methods were used to determine, at least approximately, the energy of the shower primary. First, if one is willing to rely on the available data on the average multiplicities of a nuclear interaction in a light element as a function of the primary energy, one can classify the recorded events as to the number of B-counters struck, compute for each group the most probable number of particles striking the tray area,[17] and thus after slight corrections for the average number of electrons emerging from the carbon absorber and for the "grey" particles which may reach the counters, directly ascribe an average primary energy to each group. For the latter correction, the data of Camerini *et al.*[18] were used. Although they refer to smaller primary energies, they show clearly that both the number of grey tracks and their angular distribution vary only slowly with the primary energy, and that their average energy is very nearly constant. The extrapolation of these data to the higher energies recorded in this experiment will, therefore, cause no appreciable error. For the estimate of the average multiplicities as a function of the primary energy, experimental data are lacking in the energy region of interest but the theoretical results of Messel *et al.*[19] can be used. Although they are based on the plural theory[20] of meson production, they fit the experimental data very well in the region where a comparison is possible, and it can be expected that they remain at least a good approximation over the entire interval under study.

As an independent check, for each energy—and hence for each average multiplicity—the probability can be evaluated that exactly a given number of counters is struck. If, then, the energy spectrum of the incident shower primaries were known, the absolute frequencies of these events could be calculated. However, while the nucleon spectrum at mountain altitude is sufficiently well known up to about 10 Bev,[15,21,22] nothing is known about its continuation to 100 Bev. But since in the neighborhood of 10 Bev, not only the absolute intensity of the charged N component agrees rather well with the value obtained from the primary flux at the top of the atmosphere (see Winckler *et al.*,[23] Singer[24]) under the assumption of exponential attenuation with a mean free path of 118 g/cm^2, but also the shape of the spectrum is practically identical with that of the primary cosmic radiation,[15] one will suspect that the same might be true also for higher energies. This assumption also agrees with the theoretical predictions (See Messel and Ritson,[25] Clemental and Ferrari[26]), and it was furthermore subjected to an experimental check in the following way: Even if the absolute energies related to each discharge multiplicity at tray B or electron density in S are unknown, it can safely be assumed that on the average the more complex events belong to the higher energies. If, therefore, the attenuation with altitude of these multiplicity or pulse height groups is measured, the result will yield a clue to the energy spectrum. An equal attenuation for

[17] See E. Schrödinger, Proc. Phys. Soc. (London) **A64**, 1040 (1951).

[18] Camerini, Davies, Fowler, Franzinetti, Lock, Muirhead, Perkins, and Yekutieli, Phil. Mag. **42**, 1241 (1951).

[19] Messel, Potts, and McCusker, Phil. Mag. **43**, 889 (1952).

[20] W. Heitler and L. Janossy, Proc. Phys. Soc. (London) **A62**, 374 (1949).

[21] Glaser, Hamermesh, and Safonov, Phys. Rev. **80**, 625 (1950).

[22] W. L. Whittemore and R. P. Shutt, Phys. Rev. **86**, 940 (1952).

[23] Winckler, Stix, Dwight, and Sabin, Phys. Rev. **79**, 656 (1950).

[24] S. F. Singer, Phys. Rev. **80**, 47 (1950).

[25] H. Messel and D. M. Ritson, Proc. Phys. Soc. (London) **A63**, 1359 (1950).

[26] E. Clemental and F. Ferrari, Nuovo cimento **9**, 572 (1952).

all groups, corresponding to a mean free path of 117 g/cm², would indicate that the spectrum remains essentially unchanged over the entire energy interval studied, while a variation of the spectrum of the N component on its descent through the atmosphere would be demonstrated by different attenuation mean free paths for the various groups.

Measurements were therefore carried out both at Echo Lake (altitude 3260 m) and at Mt. Evans (altitude 4300 m). The recorded events were divided into groups of given numbers of counters struck, and of equal pulse heights from the scintillator, and the rates of these individual groups of events were obtained. The results are summarized in Fig. 2 for the multiplicity group, and in Fig. 3 for the pulse height groups. The full lines correspond in each case to the attenuation expected for a mean free path of 117 g/cm²; it is seen that all the data can be well represented by this absorption law, so that the use of the energy spectrum of the primary cosmic radiation for the charged N component at mountain altitude and for the energy region studied is justified. At the same time, the results confirm and extend to energies below 100 Bev, the observations of the Rochester group[11] according to which at energies around 10^{12} ev the absorption law of the N component is essentially the same as that for low-energy nucleonic events. It seems, therefore, that the degree of inelasticity of a nuclear interaction reaches its maximum value already at a few Bev primary energy, and remains more or less constant for all energies.

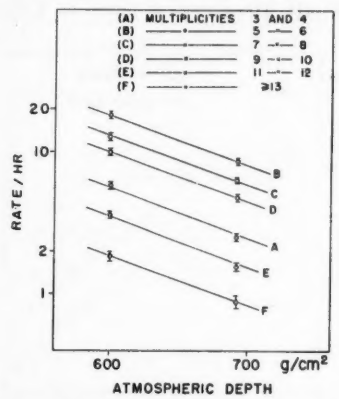

FIG. 2. Rates of showers grouped according to their multiplicities at tray B, recorded at Echo Lake and at Mt. Evans. The solid line represents attenuation with a mean free path of 117 g/cm².

With the energy spectrum of the incident particles known, the expected frequency distribution of the multiplicities recorded in tray B can now be calculated. The computation of the detection probabilities of the showers in the set is somewhat tedious, but it can be done with a reasonable accuracy as it has been shown,

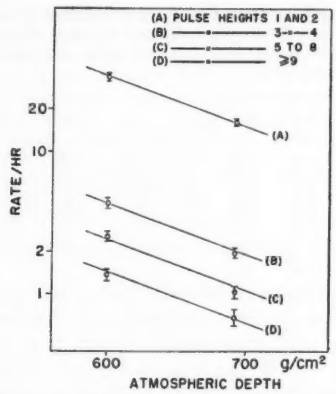

FIG. 3. Rates of showers grouped according to the oscilloscope pulse height (measured in arbitrary units), recorded at Echo Lake and at Mt. Evans. The solid line represents attenuation with a mean free path of 117 g/cm².

for instance, by Gregory and Tinlot[27] and in some earlier papers of the Syracuse group.[15,28]

The results on the estimate of the primary energies are summarized in Fig. 4 and Table I. The smooth curve in Fig. 4 represents the calculated shower rate, the dashed step curve the calculated multiplicity distribution in tray B, and the full step curve the observed distribution. It should be noted that the smooth curve and the step curves have different abscissas and hence cannot be expected to coincide (unless the top scale showing multiplicities were drawn in nonlinear steps). The two step curves agree as well as it can be expected; the apparent slight trend to overestimate the smaller and to underestimate the higher multiplicities may be a consequence of the assumption of a constant interaction mean free path in carbon (80 g/cm²) for all energies. It may well be

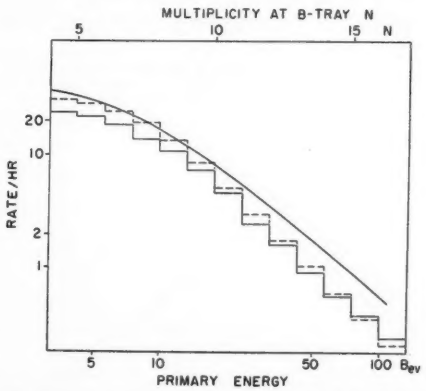

FIG. 4. Smooth curve: Shower rate calculated from theoretical multiplicity data; full step curve: calculated multiplicity distribution in tray B; dashed step curve: observed multiplicity distribution in tray B.

[27] B. Gregory and J. Tinlot, Phys. Rev. **75**, 519 (1949).
[28] K. Sitte, Acta Phys. Austriaca **6**, 167 (1952).

TABLE I. Observed rates per hour of showers of various multiplicities at tray B, average primary energies $\langle E_p\rangle_M$ and $\langle E_p\rangle_R$ computed from multiplicity and rate data, and adopted average primary energies $\langle E_p\rangle$.

Multiplicity	7	8–9	10–11	12	13	14	15
Rate/hour	25	10	4	1.8	0.9	0.55	0.4
$\langle E_p\rangle_M$(Bev)	6	12	26	46	65	85	100
$\langle E_p\rangle_R$(Bev)	8	16	30	50	70	95	120
$\langle E_p\rangle$ (Bev)	7	15	30	50	70	90	120

that with increasing primary energy the transparency of the carbon nucleus decreases, and a value closer to the geometrical cross section should have been used.

Table I shows the observed rates of the various multiplicity groups at tray B, the corresponding average primary energies $\langle E_p\rangle_M$ estimated directly from the theoretical data,[19] and the average energies $\langle E_p\rangle_R$ taken from the rate computations reproduced in Fig. 4. The agreement between the two energy estimates is satisfactory, and in view of this consistency, "true average energies" $\langle E_p\rangle$ were assigned to each multiplicity group. They are listed in the last row of Table I.

The calibration of the number of particles traversing the scintillator was based on the fact that the density spectrum of air showers at Echo Lake is very well known, in particular through the thorough work of Cocconi and Tongiorgi.[20] By placing the unshielded scintillator in the center of a triangular arrangement of large Geiger counters and triggering the oscilloscope sweep by triple coincidences of these counters, the frequency distribution of pulses originated by air showers was obtained, and from the co-ordination of the pulse rates with the air shower density distribution an absolute calibration could be achieved. The side length of the triangle was about 2½ m, and the counter size 2 in.×24 in., so that in the density interval concerned, the necessary corrections for a variation with density of the triggering probability was very small. Besides, it may be noticed that the electron energy at which the scintillator begins to record efficiently, and that necessary to penetrate the usual counter walls are very nearly the same so that the data of Cocconi and Tongiorgi can be used without further adjustment. The results of the calibration run are reproduced in Fig. 5 which shows the observed rates per hour of pulses of various heights (in arbitrary units), and in the top scale the corresponding air shower densities in particles/m². From it the number of particles traversing the scintillator is immediately obtained. Incidentally, the calibration run showed that the preliminary setting described above had been rather satisfactory: the assumed 10-particle pulses were found to correspond to that of 9.1 incident air-shower electrons.

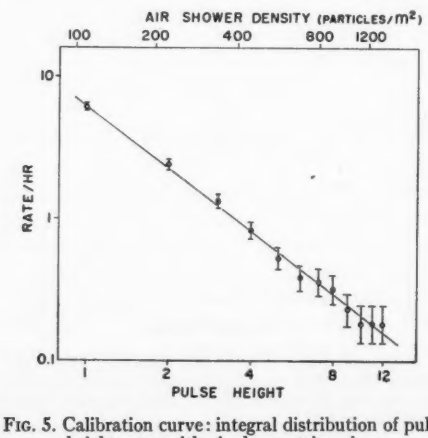

FIG. 5. Calibration curve: integral distribution of pulse height rates with air shower triggering.

[20] G. Cocconi and V. C. Tongiorgi, Phys. Rev. 75, 1058 (1949).

IV. RESULTS AND DISCUSSION

A summary of the data obtained in the two runs at Echo Lake and Mt. Evans is given in Table II. Here the numbers and the rates of events with a given pulse height on the oscilloscope screen, measured in the same arbitrary units as before, are listed. The pulse height distribution curves are also reproduced in Fig. 6. These are the uncorrected data; in order to reduce them to true electron densities, it is necessary for each single event to subtract from the particle number deduced according to the calibration curve of Fig. 5, the numbers of penetrating particles in the initial shower and in the secondary events that may have taken place in the lead absorber on top of the scintillator. To estimate the latter effect, a mean free path for secondary shower production of 260 g/cm² was assumed, and the multiplicity data obtained in an earlier experiment[15] were used. Similarly, an average correction for secondary events produced by shower neutrons was applied.

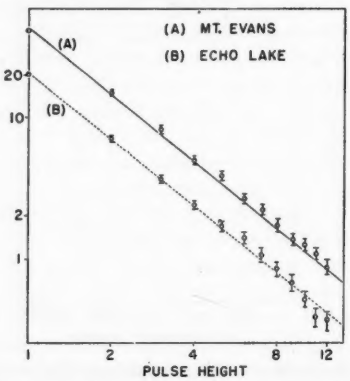

FIG. 6. Integral distribution of pulse height rate with hard-shower triggering; runs at Echo Lake and Mt. Evans.

In this way, for each multiplicity of the initial shower—and thus, according to the arguments of Sec.

III and the data of Fig. 4, for known average primary energies—the distribution of electron densities could be obtained. The results are reproduced in Fig. 7. Pulse heights are again measured in the same arbitrary units as above; height 12 in. represents in fact an integral value since it comprises all events where the trace of the pulse exceeded a certain height. In principle, it would be possible to try to fit these histograms with curves computed under the assumption that charge fluctuations of a unique secondary particle, the π meson, are responsible for the distribution; but in view of the crudeness of many of the estimates used, and in particular also of the lack of information on the total multiplicity distribution in a shower of given primary energy, any conclusions from the results of such a comparison cannot be considered as sufficiently reliable.

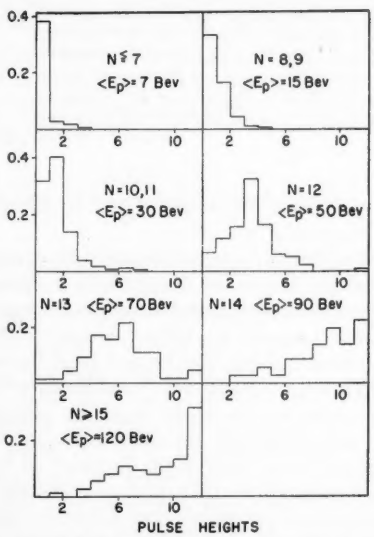

FIG. 7. Differential distributions of the numbers of electrons recorded in the hard showers of various primary energies.

But in averaging over the distribution curves of Figs. 7, an average value for the number of electrons as a function of the primary energy can be computed which, though probably an underestimate of the true absolute numbers, nevertheless will exhibit correctly any trends of this function. The result is shown in Fig. 8 where the average numbers N_{el} thus obtained, divided by the average shower energy $\langle E_p \rangle$, are plotted against $\langle E_p \rangle$. As it has been pointed out in Sec. I, this quantity $N_{el}/\langle E_p \rangle$ which also represents the fractional transfer of the primary energy to the electronic component, should decrease after passing through a maximum near 20–30 Bev if K particles are produced in as high an abundance as suggested by the Bristol data, and if no other process but π^0 decay contributes significantly to the electron production. No such

TABLE II. Numbers and rates of the oscilloscope pulse heights (in arbitrary units) in the hard showers recorded at Echo Lake and at Mt. Evans.

Pulse height	Echo Lake run No. of events	Time (hr)	Rate/hr	Mt. Evans run No. of events	Time (hr)	Rate/hr
1	1029	52.33	19.7 ±0.6	1746	42.25	41.3 ±1.0
2	564	79.48	7.09 ±0.29	639	42.25	15.1 ±0.6
3	209	52.33	3.65 ±0.27	349	42.25	8.25 ±0.44
4	191	79.48	2.40 ±0.17	211	42.25	4.99 ±0.35
5	98	52.33	1.71 ±0.19	165	42.25	3.90 ±0.22
6	112	79.48	1.41 ±0.12	134	50.70	2.64 ±0.24
7	62	52.33	1.08 ±0.15	112	50.70	2.21 ±0.22
8	68	79.48	0.855 ±0.10	87	50.70	1.72 ±0.19
9	39	52.33	0.68 ±0.12	69	50.70	1.36 ±0.17
10	41	79.48	0.52 ±0.08	64	50.70	1.26 ±0.15
11	22	52.33	0.38 ±0.09	55	50.70	1.09 ±0.14
12	29	79.49	0.365 ±0.06	44	50.70	0.87 ±0.12

decrease is found; in fact, the curve appears to level off at a value possibly somewhat higher than that observed at 20 Bev. However, in view of the experimental uncertainties this latter observation cannot be given much weight.

However, the absence of the conspicuous maximum of the curve as demanded by the current ideas must be considered as firmly established, and as it has been stated above, it could not be masked by the possible inaccuracies of the various energy estimates. One is, therefore, forced to the conclusion that either the Bristol observations of a large energy transfer to the K component are incorrect, and that even at high energies π mesons carry away practically all of the energy dissipated in the collision; or alternatively that π^0 decay is not the only, or the only major, source of the electronic cascades found in high-energy collisions.

At this stage, any suggestion concerning the nature of possible other contributing processes would be purely speculative and should therefore be omitted. The only safe conclusion is that this process, or these processes, must develop within a time of less than 10^{-9} sec, and that it must reach a significant level at primary energies of about 50–100 Bev. It may also be said that this does not necessarily require new unstable particles; rather, the results here reported might give further

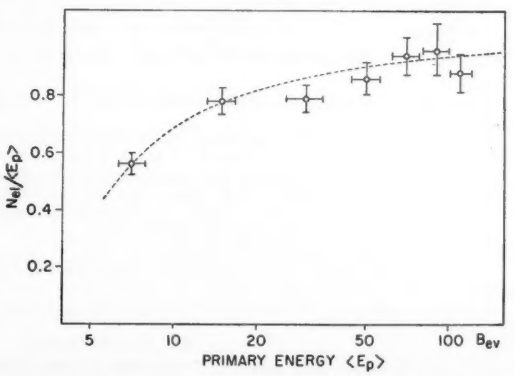

FIG. 8. Relative number of electrons $N_{el}\langle E_p \rangle$ as a function of the primary energy $\langle E_p \rangle$ of the showers.

impetus to a more extensive study of the decay modes of the various heavy particles already known.

V. ACKNOWLEDGMENTS

The facilities of the Inter-University High Altitude Laboratories at Echo Lake and Mt. Evans, Colorado, were available for the experiment, and the authors wish to express their thanks to Profs. Byron E. Cohn and Mario Iona, Jr., of the University of Denver for their continuous support. Thanks are also due to Prof. I. L. Kofsky of Smith College, and to J. G. Askowith, K. Clum, J. E. Rizzo, and D. L. Stierwalt of Syracuse University, for their assistance in preparation and running of the experiment.

PHYSICAL REVIEW VOLUME 97, NUMBER 1 JANUARY 1, 1955

A Cloud-Chamber Study of Cosmic-Ray Air Showers at Sea Level*

KENNETH E. RELF†
Radiation Laboratory, University of California, Berkeley, California
(Received February 1, 1954; revised manuscript received August 4, 1954)

A diffusion-type cloud chamber eight feet long, four feet wide, and five inches deep has been used to study the lateral structure of cosmic-ray air showers in a region near the core. Three showers were recorded in which the core lay within sixty to ninety centimeters from some point on the periphery of the chamber. The results show that the lateral distribution of the shower particles in all but one photograph follow exceedingly well the Molière distribution. The deviations from the Molière distribution are almost all within the expected Gaussian fluctuations. In those pictures exhibiting little or no gradient, the deviations from the average density were normal.

I. INTRODUCTION

MANY mechanisms have been considered as possible explanations for the origin of the electron-photon component of air showers. Among these are (1) the impinging of high-energy primary electrons upon the air molecules of the upper atmosphere,[1] (2) the deceleration of primary protons as they pass near an air nucleus and undergo a bremsstrahlung process analogous to that of electrons,[2] and (3) the emission of high-energy neutral mesons in a high-energy nuclear collision.[3,4] That air showers originate from high-energy nuclear collisions is the most reasonable hypothesis at the present time because such processes are known to occur[5] and because recent experiments on the composition of air showers show that they contain not only electrons and photons but also penetrating particles and an N component.[6,7] This hypothesis also overcomes the difficulty of explaining how primary electrons can acquire energies of the order of 10^{15} to 10^{16} electrons volts in interstellar space.[8]

Several attempts have been made to measure directly the lateral distribution of the particles in extensive air showers. Noteworthy among these are the experiments of Williams[9] analyzed by Blatt,[10] Singer,[11] the Cornell group[12] (Cocconi *et al.*), Fretter and Ise,[13] Barrett,[14] El-Mofty,[15] Hazen,[16,17] Heineman,[18] and Kasnitz.[19] A study of these experiments would seem to indicate that multiple cores probably do exist, but that they are separated either by very large distances so that only one core is observed, or that they are separated by very small distances which makes their detection difficult.

Theoretical predictions of the angular and lateral spread of the air-shower particles have been made by several workers.[20–31] The Molière distribution function[32]

* This work was supported in its entirety by the U. S. Atomic Energy Commission.
† Now at Atomic Power Division, Bettis Field, Pittsburgh, Pennsylvania.
[1] J. G. Wilson, editor, *Progress in Cosmic Ray Physics* (Interscience Publishers, Inc., New York, 1952); also (North-Holland Publishing Company, Amsterdam, 1952), 324–327; M. F. Kaplon and D. M. Ritson, Phys. Rev. **88**, 386 (1952).
[2] J. L. Powell, Phys. Rev. **75**, 32 (1949).
[3] Lewis, Oppenheimer, and Wouthuysen, Phys. Rev. **73**, 127 (1948).
[4] E. Fermi, Phys. Rev. **81**, 683 (1951); E. Fermi, Progr. Theoret. Phys. (Japan) **5**, 570 (1950).
[5] Lord, Fainberg, and Schein, Phys. Rev. **80**, 970 (1950).
[6] J. G. Wilson, editor, *Progress in Cosmic Ray Physics* (Interscience Publishers, Inc., New York, 1952); also (North-Holland Publishing Company, Amsterdam, 1952), 326.
[7] G. Cocconi, Phys. Rev. **79**, 1006 (1950).
[8] E. Fermi, Phys. Rev. **75**, 1169 (1949).
[9] R. W. Williams, Phys. Rev. **74**, 1689 (1948).
[10] J. M. Blatt, Phys. Rev. **75**, 1584 (1949).
[11] S. F. Singer, Phys. Rev. **81**, 579 (1951).
[12] Cocconi, Cocconi Tongiorgi, and Greisen, Phys. Rev. **76**, 1020 (1949).
[13] W. B. Fretter and J. Ise, Jr., Phys. Rev. **78**, 92(A) (1950).
[14] P. H. Barrett, Phys. Rev. **84**, 339 (1951).
[15] Osman El-Mofty, Phys. Rev. **92**, 461 (1953).
[16] W. E. Hazen, Phys. Rev. **85**, 455 (1952).
[17] Hazen, Williams, and Randall, Phys. Rev. **93**, 578 (1954).
[18] R. E. Heineman and W. E. Hazen, Phys. Rev. **90**, 496 (1953).
[19] Harold L. Kasnitz and Kurt Sitte, Phys. Rev. **94**, 977 (1954).
[20] L. Eyges and S. Fernbach, Phys. Rev. **82**, 23 (1951); S. Fernbach, Phys. Rev. **82**, 288 (1951).
[21] H. Euler and H. Wergeland, Astrophys. Nor. **3**, 1651 (1940); Naturwiss. **28**, 41 (1940).
[22] H. A. Bethe, Phys. Rev. **59**, 684(A) (1941); L. W. Nordheim, Phys. Rev. **59**, 929(A) (1941); Jane Roberg, Phys. Rev. **62**, 304(A) (1942).
[23] L. Landau, J. Phys. U.S.S.R. **3**, 237 (1940).

is, however, the only total (i.e., integrated over all energies) distribution function available to experimenters for evaluating their results.

Blatt[10] has made as detailed a study of the Molière function as the available literature permits. The obvious errors in the Molière calculation center around a few well-defined points: (1) the computations neglect ionization loss, being based on Approximation A defined by Rossi and Greisen,[33] (2) the over-all structure function is almost certainly wrong because of the use of Arley's approximation to find the total number of low-energy electrons, and because of using Approximation A, which gives an incorrect partial structure function for low-energy electrons, (3) an incorrect partial structure function for electrons near the critical energy was used, since it was only an extrapolation of the high-energy partial structure function. The combined effect of using the incorrect partial structure function for low energies and of underestimating the number of low-energy electrons is to make the Molière function less peaked than the true one. Blatt states that the magnitude of this effect is not known at this time. The form of the Molière function currently in use is the one offered by Bethe.[34] It is

$$\rho[N(t),r']=\frac{0.454}{r'}N(t)(1+4r')\exp[-4(r')^{\frac{3}{2}}].$$

The terminology is as follows: $\rho[N(t),r']$ = the particle density at a depth t below the top of the atmosphere; $N(t)$ = the total number of electrons at depth t; r' = the distance from the shower axis measured in units of the characteristic scattering length, r_1, defined by $r_1=(X_0/\epsilon)E_s=74$ meters at sea level, where X_0 = a radiation length (330 meters at sea level), ϵ = the critical energy for air (83 Mev), and $E_s=21$ Mev.

In this paper are presented the results of some work performed with a diffusion-type cloud chamber of unusually large size, operated for 730 consecutive hours. The purpose in building the large chamber was to attempt to obtain photographs of the cores of air showers where the structure is not well known. A brief description of the arrangement of the apparatus is given and the experimental results are discussed. A complete description of the cloud chamber has been submitted to another publication.

II. DESCRIPTION OF THE APPARATUS

The cloud chamber selected for this experiment was a downward diffusion-type chamber using methyl alcohol as the condensant vapor and air as the noncondensable gas. A diffusion-type chamber was an obvious solution to the demand for a large area, since the mechanical difficulties involved in the design of an expansion chamber of similar size would be prohibitive. The actual area of the chamber was 32 square feet, of which 21 square feet were photographed (avoiding use of the region near the walls). The sensitive depth was about three inches out of a total chamber depth of five inches. Nonstereoscopic photographs were obtained through the chamber top with the aid of six mirrors. The clearing field was usually about 30 volts (the top being negative), though for occasional short intervals it was turned off or increased to about 100 volts. The chamber was operated out-of-doors with only a canvas tent over it.

The Geiger tubes were 30 inches long with an outside diameter of $1\frac{1}{2}$ inches. Four such tubes were used in a fourfold-coincidence circuit with the tubes arranged in a manner similar to that used by Cocconi.[12] Three tubes parallel to each other and to the horizontal plane were placed at the vertices of an equilateral triangle eight inches on a side, and were enclosed in a lead housing with two-inch side walls and a one-inch roof. These three tubes were placed beneath the chamber with the geometric centers of the cloud chamber and of the lead house lying on a common vertical line. One additional counter tube was situated one meter from the lead house to prevent the recording of coincidences caused by showers produced in the lead shield surrounding the counter tubes. This arrangement of counters does not meet the requirement proposed by Cocconi[35] for recording extensive showers, but it was believed that the photographs themselves would provide the distinction between narrow showers, other irrelevant events, and large air showers. The results confirmed this expectation.

A sample cloud chamber picture is shown in Fig. 1.

III. THE EXPERIMENTAL RESULTS

1. Criteria for Shower-Track Identification

The three criteria established for identifying the shower tracks were direction, length, and age, the age being estimated by the density and sharpness of the track.

Most of the shower tracks in a photograph appeared to be nearly parallel. This is to be expected if a shower has a single core (or one dominant core) around which the shower particles are radially symmetric.

The projected length of a track helped to decide whether or not it was to be attributed to a shower

[34] S. Z. Belenky, J. Phys. U.S.S.R. 8, 9 (1944).
[25] Jane Roberg and L. W. Nordheim, Phys. Rev. 75, 444 (1949).
[26] Y. Fujimoto and S. Hayakawa, Progr. Theoret. Phys. (Japan) 4, 579 (1949).
[27] J. Nishimura and K. Kamata, Progr. Theoret. Phys. (Japan) 5, 899 (1950).
[28] L. Janossy, *Cosmic Rays* (Oxford University Press, London, 1950), second edition, pp. 324–327.
[29] A. Borsellino, Nuovo cimento 7, 700(A) (1950); A. Borsellino, Nuovo cimento 7 (No. 3 bis) 1950.
[30] H. S. Green and H. Messel, Phys. Rev. 88, 331 (1952).
[31] G. Molière, Phys. Rev. 93, 636 (1954).
[32] G. Molière, *Cosmic Radiation*, edited by W. Heisenberg (Dover Publications, New York, 1946), 26–40.
[33] B. Rossi and K. Greisen, Revs. Modern Phys. 13, 240 (1941).
[34] H. Bethe, Phys. Rev. 72, 172 (1947).
[35] G. Cocconi, Revs. Modern Phys. 21, 26 (1949).

FIG. 1. Sample cloud-chamber picture. Total number of shower tracks, 2906; average number of tracks per 300-cm² sections, 46.3. (The standard deviation from 46.3 is 14.1.)

particle. Most showers arrive at angles not greater than 30° from the vertical.[9] The projected length of a track arriving at 30° from the vertical and viewed directly from above, computed on the basis of a sensitive chamber depth of three inches, was 1.75 inches. This meant that all shower tracks could be expected to be no longer than half the distance between the heating wires which, together with the alcohol trays, formed a natural grid structure in the photograph.

The age of the track was suggested by its blackness and its sharpness. A track satisfying the criteria of direction and length was often eliminated because it was considered too faint or too dark or too diffuse. In the final analysis, the age of the track was usually the deciding factor. The direction and length of a track served as a rapid means of sorting out those tracks believed to be true shower tracks, while careful study of the age served as the final discriminating test.

Each of these criteria had its limitations because of the influence of other phenomena. The directions of the individual tracks, for example, were influenced by scattering and by distortion from viewing the tracks as a point projection. Because of the very high energies of the electrons, the individual scattering of the particles was not large enough to alter appreciably the dominant direction of the tracks. The distortion introduced by viewing the tracks as a point projection was far more significant in altering the apparent direction of a track. Completely parallel vertical tracks appeared as dots directly under the lens and elsewhere as lines directed toward the point under the lens. Similar tracks parallel to a line from the lens to one corner of the chamber all appear to be directed toward that corner. The angle the shower axis made with the vertical could be determined by finding that point on the photograph (or off the edge of the photograph) where the extensions of the tracks intersected, and using that point and the geometry of the chamber and lens to calculate their direction. The direction of the tracks was useful in determining whether or not they belonged to the shower, because they followed this definite pattern if they were parallel to one another.

The lengths of the tracks in any one photograph were not always the same, because the direction of arrival of the shower may have been along the line of sight of the lens. In this case some of the tracks were observed end-on and appeared as round dots or as very, very short tracks. The tracks were then not only of varying lengths but also of varying apparent age. The criterion of direction was useful for those cases in which the criteria of length and age were doubtful. The procedure in each picture was to ascertain the approximate azimuthal direction of arrival, and then to evaluate each track with the different effects constantly in mind. Each picture was counted at least twice with the aid of a viewer, and finally, in the making of the Ozalid tracings (see Sec. III.2), each track received a final discriminating evaluation before being traced as a true shower track.

The effect of the normal random cosmic-ray background was determined by making a series of random exposures and counting the straight background tracks. There was an average of three sharp straight tracks per section, but they were not usually parallel. These three sharp tracks could be mistaken for counter controlled shower tracks if they happened to be parallel to the shower tracks. It is safe to say, however, that on the average less than two background tracks were counted per section as belonging to a shower. Since the numbers per section ranged from 6 to 104, it can be seen that background introduced a negligible error.

There was an average of seventeen tracks per section in a random photograph, but there was no difficulty in sorting out the straight tracks. The remainder were crooked, indicating that they were low energy electrons, or they were broad and slightly curved, indicating that they had been formed more than 0.4 second before the flashing of the lights.

A last consideration was the probability of a random shower's occurring between the time the desired shower particles traversed the chamber and the time the photograph was taken. An estimate of this probability was made in the following manner. The delay-time was measured to be 0.4 second. The average counting rate was two counts per hour. Assuming that a random shower would have to arrive at least 0.1 second before the picture was taken, the following result for the probability that a random shower would arrive during the delay-time was formulated:

$$\frac{\text{(Time interval in which a shower must arrive to be photographed)}}{\text{(Total time interval between counts)}} = \frac{0.4-0.1}{30\ \text{min}\times 60\ \text{sec}} = \frac{1}{6000}.$$

This probability was considered sufficiently small to be neglected.

The criteria of direction, length, and age, therefore, were believed to be necessary and sufficient to judge whether or not a given track was produced by a shower particle, when the other relevant factors just discussed were considered. When there was a great uncertainty as to the number of shower tracks in a section, the range was recorded, i.e., the minimum and the maximum counts. Uncertainties occurred when it became necessary to "read" a track through curtains[36] in the chamber, or when a track seemed to be on the borderline of belonging. After a few minutes of observation, eye fatigue set in and the ability to make fine discriminations became lessened. Frequent rests were necessary. Each picture studied contained about 1000 shower tracks or more, and each track had to be individually evaluated.

2. Method of Data Reduction

The process of obtaining the final data from the original negatives involved three steps. The first step was to make enlarged positive transparencies $8\frac{1}{2}\times 8\frac{1}{2}$ inches on Kodalith Film from the original $1\frac{1}{4}$- $\times 1\frac{1}{4}$-inch negatives. Second, Ozalid tracings of the shower tracks in each picture were made by placing the transparency together with a sheet of Ozalid tracing paper over a specially-made light box and drawing in each individual track. During this procedure, the original film was at hand in a viewer so that each track could be studied before drawing it in as a true shower track. When the tracing had been completed, it was run through the Ozalid machine to produce a print.

The third operation was the actual locating of the shower axis. When the gradient was steep and the track-count per section[37] was large (e.g., 25 or greater) over a sufficiently large area of the picture, the procedure was as follows: Two sections were selected whose counts could be called reasonably identical (perhaps 5 to 10 percent difference). The geometric center of each of these two sections was located. These two midpoints were connected, the joining line bisected, and a perpendicular to it drawn in the direction of the shower axis. Visual inspection of the picture allowed one to select the quadrant in which the axis lay. Two other sections at the far end of the chamber were selected in which the track count was quite certain. (Most pictures had areas in which the contrast was very good, the background low, and the shower tracks clearly visible.) The midpoints of these sections were located, the connecting line drawn, this line bisected, and the perpendicular drawn out to intersect the first perpendicular that was drawn. The intersection determined the position of the shower axis. The procedure is illustrated in Fig. 2. This was not always the final choice of the position, because the final choice had to be a point which satisfied best the over-all density distribution. Other combinations of two best sections were selected, and a number of perpendiculars were drawn to see if there was an area in which most of them intersected. A suitable compromise point was then chosen. When the position of the shower axis had been tentatively selected, the accuracy of the choice was judged by drawing arcs of different radii with the tentative axis position as center through the chamber area and noting if these arcs passed through or near points of similar density. Large errors in the choice of position were readily detected.

When the shower axis had been located in this manner, the distances of the geometric centers of each of the sections from the core position were measured and recorded. Convenient intervals of distance were assumed (e.g., 0.5–0.59 meter) and a chart prepared in which the number of tracks in a section was entered in the appropriate column designating the distance of the geometric center of this section from the axis position. Upon completion of the chart, the number of tracks in each distance interval was averaged and this value taken as the average number to be expected at a distance from the core corresponding to the midpoint of that interval. A graph was made with the number of tracks per section as the ordinate and the distance from the shower axis as the abscissa. A smooth curve was

[36] A curtain refers to an area of fog looking like a waterfall, which at times appeared in the chamber.

[37] The sections referred to throughout the paper are the areas formed by the apparent intersections of the heating wires running lengthwise of the chamber and the alcohol trays running crosswise. Each area is about 300 square centimeters.

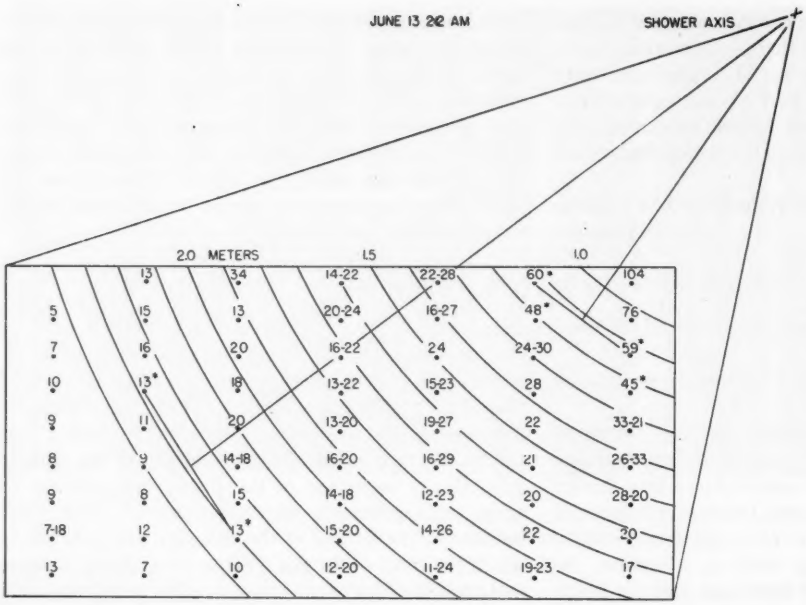

FIG. 2. Illustration of the procedure for locating the shower axis when a gradient across the chamber could be determined.

drawn through the points in such a way as to represent best the data.

A second method of locating the shower axis involved the use of the Molière distribution function as approximated by Bethe. This method was used when the gradient was not considered sufficiently large to use the first method. An order-of-magnitude value for the gradient between 0.5 and 1.5 meters from the core for the three showers in which the core was located was fifteen tracks per half-meter. Sections of the picture were chosen in which the track counts were considered to be quite certain. (As mentioned earlier, almost every picture has a few of these sections in which the shower tracks were very well defined.) These sections were chosen from widely separated areas of the picture rather than from one local area. The values of these densities were used to enter a "Molière chart," previously prepared, and from this chart distances were read off corresponding to the densities obtained from the photograph. For a given density, different distances were read off corresponding to varying values of N (Sec. I) in the Molière equation. A table was prepared in which the distances corresponding to the chosen densities were set forth for fixed values of N. Circles were described about the center of the selected sections, their radii being the distances from the core read from the Molière chart for the particular density assigned to the section. The intersections of the circles defined an area in which the axis of the shower must have hit. A choice could be made for a best fit. When the position had been determined, the data were plotted in the manner described in the preceding paragraph.

The location of the shower axis was carried out in this case by fitting the Molière function to the experimental data. Other experiments of this type had not yielded data of adequate detail to allow this to be done as accurately as has been done here. In the pictures to be discussed later, the shower axis was always between 0.6 meter and 1 meter from some point on the periphery of the cloud chamber. This gave a very detailed picture of the shower structure up to 60 centimeters from the core. The methods of locating the shower axis may be summarized by stating that they depend only on the assumption that the electron-photon showers are radially symmetric about their axes.

The secondary purpose of the experiment was to study the statistical distribution of the electrons near the core. For these small distances no special analysis was made. The charts made earlier for purposes of locating the core showed that nearly all the section track counts for a given radius lay within the average number plus or minus the standard deviation, i.e., $\sqrt{n}$.

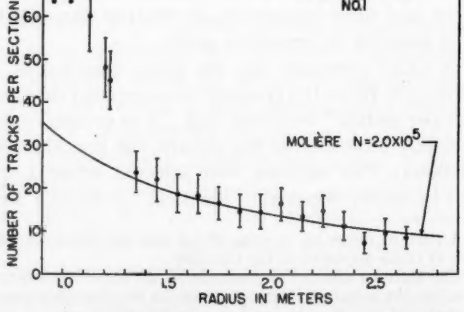

FIG. 3. The density distribution for shower No. 1, Table I.

TABLE I. Summary of numerical results obtained from the experiment.*

Shower number	No. of shower tracks in chamber	Average No. per section	Standard deviation	Estimated No. of shower particles	Estimated energy of initiating ray (ev)	Distance of axis from chamber center (meters)	Gradient observable	Height of origin (radiation lengths)	Angle with respect to vertical
1	1708			2.0×10^5	2.15×10^{14}	1.85	yes	14	8
2	1042			1.91×10^5	2.0×10^{14}	1.65	yes	14	13
3	643			1.0×10^5	9.7×10^{13}	1.5	yes	13	18
4	1641	28.8	10.1	*10^6*	*3×10^{15}*	*4*	no	15	24
5	651	11.2	5.6	*3×10^5*	*10^{15}*	*3.6*	no	14.5	7
6	625	9.6	4.8	*3×10^5*	*10^{15}*	*4*	no	14.5	26
7	418	6.8	3.8	*3×10^5*	*10^{15}*	*4.6*	no	14.5	7
8	2906	46.3	14.1	*$>10^6$*	*3×10^{15}*	*4*	no	15	11
9	1078	17.2	6.1	*3×10^5*	*10^{15}*	*3*	no	14.5	9
10	693	11.2	5.5	*3×10^5*	*10^{15}*	*3.6*	no	14.5	9
11	345	5.6	3.5	*10^5*	*9.7×10^{13}*	*2.6*	no	13	12
12	632	10.0	3.7	*3×10^5*	*10^{15}*	*4*	no	14.5	21

* The numbers in italics are order-of-magnitude estimates only.

The exception to this deviation is discussed in connection with the picture in which it is found.

The data obtained in this experiment have been analyzed, then, in one of two ways. For those pictures exhibiting a definite gradient, the shower axis was located and the radial density distribution determined and plotted. For those pictures exhibiting a nearly flat distribution, the actual distribution was compared with the Poisson distribution.

3. Discussion of the Photographs Obtained

The numerical data obtained from the photographs are presented in Table I and the density distributions for the three showers exhibiting gradients are illustrated in Figs. 3, 4, and 5. Figure 6 is illustrative of the density distributions in the photographs which did not show a gradient.

The density distribution shown in Fig. 3 departs from the Molière distribution between 0.9 meter and 1.3 meters from the core. This deviation from the Molière distribution function may be explained in several ways, the most likely being: (1) the Molière function itself may be in error,[31] (2) multiple cores may exist, or (3) the tracks observed may not be those of electrons but those of other particles associated with the shower. Each of these possibilities can be examined in detail as far as existing knowledge, both experimental and theoretical, permits. Consider the Molière function. The Molière function, as pointed out in Sec. I, is known to be in error in the form of the structure function itself, and in the estimation of low-energy electrons. Furthermore the Molière function is calculated only for the maximum of the shower. The combined effect of underestimating the number of low-energy electrons and using the incorrect partial structure function for low energies tends to make the Molière function less peaked than the true one. No estimate of the magnitude of this effect is available at the time of writing. The added possibility that the shower may not be fully developed (i.e., has not yet reached its maximum) would seem to be sufficient explanation for the observed sudden increase of density at distances close to the core.

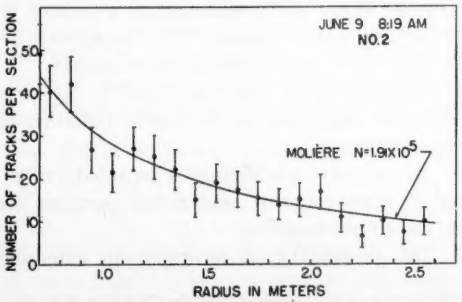

FIG. 4. The density distribution for shower No. 2, Table I.

The existence of multiple cores is a possibility, but the photograph does not suggest this. The chamber area enclosed by an arc of 1.3 meters radius measured from the shower axis is about 0.16 square meter. Careful scrutiny of this area on the photograph reveals no obvious clusters of tracks.

It is possible that the sharp increase in density as one approaches the core is caused by the presence of tracks other than those of shower electrons. Experimental data on the composition of shower cores indicate that the ratio of penetrating particles to electrons is usually about two or three percent near the core, but this ratio is observed to be much greater in some instances.[12,38,39]

The conclusion is that this shower is best described by attributing it to the development of a single core. The disagreement with the Molière function near the core is explained by assuming that the shower has not yet reached its maximum and (or) that it is a shower in which the ratio of penetrating particles to electrons is larger than usual.

For those pictures not exhibiting a gradient, the

[38] C. B. A. McCusker and D. D. Millar, Proc. Phys. Soc. (London) **A64**, 915 (1951).

[39] Watase, Oda, Higashi, and Kubozoe, J. Phys. Soc. Japan **6**, 403 (1951).

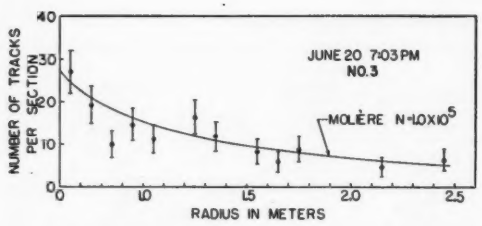

FIG. 5. The density distribution for shower No. 3, Table I.

average densities and the standard deviations were computed and tabulated in Table I. In addition, the integral density distribution was plotted on probability paper. Those plots indicated that the distributions were practically Poissonian. Figure 6 is an example of the density distribution as it appears when plotted on probability paper.

For these showers, an estimate of the distances from the center of the chamber at which the shower axes struck was made in the following way. Figure 7 can be used as a specific example to illustrate the method. The average value of 28.8 tracks per section was used to enter the Molière chart. The particular value of N selected was chosen by assuming the effective length of the chamber to be two meters. Sliding this length along the horizontal line corresponding to 28.8 tracks per section, one finds a Molière curve that fits inside the limits of 28.8 ± 10 (the standard deviation) over a length of two meters. The core was assumed to have struck at the midpoint of this interval, i.e., three meters away. The results obtained are listed in Table I. The estimated energies of the initiators that are listed were obtained from cascade shower theory on the basis of a single core.[40] The angles listed are the angles that the shower axes make with the vertical. These were estimated in the manner described in Sec. III.1.

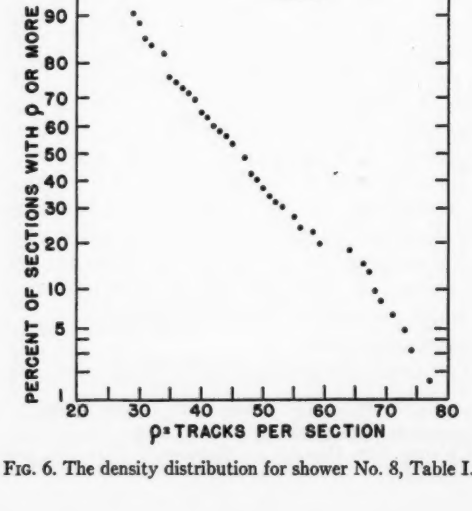

FIG. 6. The density distribution for shower No. 8, Table I.

IV. CONCLUSIONS

That only three showers exhibited an appreciable gradient was an expected result. Singer,[11] working at sea level, obtained the following differential number spectrum for air showers:

$$f(N)dN=2.5\times10^{4}N^{-2.4}dN \text{ hr}^{-1} \text{ min}^{-2}.$$

The total number of particles N in the individual showers exhibiting a gradient varied from 1.0×10^{5} to 1.9×10^{5}. The average distance of the shower axis from the center of the chamber was computed to be 1.7

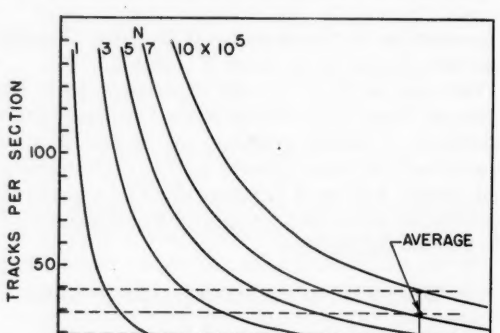

FIG. 7. Illustration of the procedure for locating the shower axis when little or no gradient is present.

meters. The number of showers whose size lay between 1.0×10^{5} and 1.9×10^{5} particles and whose axis struck within a radius of 1.7 meters from the chamber center during a time interval of 540 hours was calculated to be approximately five. Agreement within a factor two was considered to be good in view of the approximations.[9,13]

That air showers might originate at these low altitudes was also not unreasonable in the light of the hypothesis advanced by Cocconi,[7] *viz.*, that an extensive air shower is not a special event, but rather a "unique process in which the cosmic radiation present in the lower atmosphere is created." This hypothesis is supported by several experimental observations:

1. All the types of particles found in extensive air showers are also found in the cosmic radiation in the lower atmosphere.

2. An extensive air shower is recorded every time three or more coherent penetrating particles coming from the air are recorded.

3. The probability of recording an extensive air

[40] Bruno Rossi, *High-Energy Particles* (Prentice-Hall, Inc., New York, 1952), first edition, 259.

shower accompanying the N component increases with increasing energy of the N component.[41]

Clay[42] and his collaborators have also considered the question of whether or not the continuous cosmic radiation and the extensive air showers are produced by the same processes. They pointed out that if two conditions prevailed—namely, that (1) the primary proton producing the mesons had a high energy, and (2) the initial collision occurred in the lower atmosphere—then the mesons and their secondaries would be observed as a shower. Experimental evidence confirming the theory that the large air showers were produced at low levels was provided by experiments on the barometric coefficient.[43] The variation of intensity of the soft and penetrating components with air pressure was found to be the same as the decrease in the number of protons in the atmosphere,[44] being 14 percent and 15 percent per centimeter Hg respectively.

If the air showers are initiated by neutral mesons produced by the high-energy primaries, their height of origin depends on the cross sections for collisions between the primaries and the air nuclei. According to Rossi,[45] the best-established experimental result yielding this information is the curve giving the rate of occurrence of high-energy nuclear interactions as a function of depth in the atmosphere as obtained by Tinlot.[46] These nuclear interactions can be produced by protons, neutrons, and pi mesons, defined as the N component or "N rays." (The high-energy alpha particles and heavier nuclei in the upper atmosphere are not included in this terminology.) From the data obtained by Tinlot, the N rays are absorbed exponentially with a collision mean free path of about 120 g/cm² in air.[44] At an elevation of 3260 meters the intensity of the N-component capable of producing nuclear interactions is about one percent of the total number of ionizing particles in the shower.[47] At altitudes of 6000 meters and higher, therefore, there should be an abundance of high-energy particles capable of initiating electron-photon showers.

Greisen[41] pointed out that if a large fraction of the energy in a nuclear interaction is given to mesons, and the charged mesons interact further with air nuclei to produce more mesons while the neutral mesons decay into two photons to initiate air showers, a consistent picture can be formulated. The result of such a sequence is that most of the energy, after five to ten collision mean free paths, would be transferred to the electronic component leaving ten to twenty percent about equally divided between nucleons and mu mesons. Five mean free paths represent 600 g/cm² or 4500 meters, slightly lower than the computed height of the maximum for those showers observed in this experiment. Tinlot records ten high-energy nuclear events per hour at 600 g/cm² and twenty high-energy events at 500 g/cm². Further evidence of the occurrence of high-energy nuclear events at low altitudes is found in data from photographic emulsions. Gerosa and Setti[48] observed an emulsion star at 4550 meters with a singly charged primary and two well-defined forward cones of particles with angles 0.004 and 0.1 radian respectively. The energy of the event was estimated as 10^{13} electron volts.

A quantitative picture of the nature of the high-energy event causing the shower has been formulated by Hazen and his collaborators.[49] They have applied the Fermi theory of high-energy nucleon-nucleon collisions to the problem of determining the energy distribution, the energy dependence of the angular distribution, and the number of emitted pi mesons as a function of primary energy and impact parameter. The total number of emitted neutral mesons for several values of primary nucleon energy and two values of impact parameter is presented in Table II. Two cases are considered; one in which only pi mesons are produced and one in which nucleon-antinucleon pairs are produced. The latter is considered important when W/Mc^2 is equal to or greater than 100, i.e., when the primary nucleon energy in the laboratory system exceeds 5×10^{12} electron volts. Some calculations were made for this experiment utilizing the work of Hazen. The procedure was as follows:

TABLE II. A reproduction of part of Table I from the paper by Hazen, Heineman, and Lennox with the number of neutral mesons emitted for various primary energies and impact parameters.

Primary nucleon energy W' (ev)	Impact parameter (nucleons and mesons) $\rho=0.959$	0.990	Impact parameter (mesons only) $\rho=0.959$	0.990
	Total number of neutral mesons emitted			
1.2×10^{12}	1.3	0.72	3.3	1.7
1.9×10^{13}	2.6	1.4	6.5	3.5
1.2×10^{14}	4.2	2.3	10.3	5.5
4.7×10^{14}	5.9	3.2	14.6	7.8
1.9×10^{15}	8.3	4.5	21	11.0
1.2×10^{16}	13	7.2	33	17.3
1.9×10^{17}	26	14.3	65	35

1. The energy of the initiating ray was estimated by calculating the total number of particles in the shower from the Molière function, and using cascade shower theory[40] to compute the energy required to produce that number of particles at the maximum of the shower.

2. The initiating ray was assumed to be a photon produced by the decay of a neutral meson. Most photons are emitted at a minimum angle defined by[49]

$$\sin\theta_{\min}/2=Mc^2/U,$$

[41] Greisen, Walker, and Walker, Phys. Rev. **80**, 535 (1950).
[42] J. Clay, Phys. Rev. **81**, 645 (1951).
[43] J. Clay, Physica **16**, 278 (1949).
[44] D. J. X. Montgomery, *Cosmic Ray Physics* (Princeton University Press, Princeton, 1941), first edition, 324.
[45] Bruno Rossi, *High-Energy Particles* (Prentice-Hall, Inc., New York, 1952), first edition, 486.
[46] J. H. Tinlot, Phys. Rev. **73**, 1476 (1948); **74**, 1197 (1948).
[47] G. Cocconi and V. Cocconi Tongiorgi, Phys. Rev. **79**, 730 (1950).
[48] A. Gerosa and R. L. Setti, Nuovo cimento **8**, 601 (1951).
[49] Bruno Rossi, *High-Energy Particles* (Prentice-Hall, Inc., New York, 1942), first edition, 199.

where $\frac{1}{2}U=E_1=E_2$, the energies of the emitted photons; $\theta_{\min}$ = the minimum angle between the decay photons in the laboratory system, and Mc^2 = the rest energy of the neutral meson. The energy of the neutral meson is then taken to be twice the value of the photon energy computed in step one above. On this basis the estimated energies of the mesons in this experiment lie between 2×10^{14} and 2×10^{15} electron volts. The primary nucleon energies to be associated with these neutral-meson energies are not uniquely determined, because the neutral mesons are emitted with a distribution of energies. Any reasonable primary energy yields a number of neutral mesons as shown in Table II, but the percentage of that number whose energy exceeds a given energy decreases with increasing meson energy. By requiring that at least two neutral mesons be produced, one can compute a minimum energy for the primary nucleon. The reason for requiring at least two is that it is known from the angular distribution of the emitted mesons that one-half of them will be emitted in the backward direction and one-half in the forward direction.[50] The minimum value for W_1' is computed to be about 1.2×10^{16} ev. From Table II, it is seen that a total of 13 neutral mesons are emitted, and from the work of Hazen about 25 percent of these (or 3) have energies greater than 2×10^{14} ev. Half of these are to be found in the forward cone and half in the backward cone. The angular width of these cones is about 14° in the center-of-mass system estimated from Table II of the Hazen paper. This corresponds to about 5×10^{-5} radian in the laboratory system. If the two neutral mesons were emitted at the extreme angle of 5×10^{-5} radian, the separation of the two main shower axes 6 km below the point of origin would be about 30 cm. Each neutral meson, however, decays into two photons with individual energies of 10^{14} ev. The minimum angle between these photons is given by the equation above and is computed to be about 10^{-6} radian. The separation between cores due to the two photons of a single neutral meson produced at a height of about 6 km is then calculated to be 0.6 cm. The two cores produced either by the individual neutral mesons or by the decay photons would not have been observed in this experiment because of overlapping.

The results of this experiment, then, may be summarized as follows:

1. Multiple cores were not observed. Each shower, within statistical errors, consists of a single core. This observation is not inconsistent with the Fermi theory of nucleon-nucleon collisions, which predicts multiple cores, because they would be so closely spaced as to be unresolved in this experiment. However, this does not imply that air showers are necessarily originated by the decay of neutral mesons. The data obtained from this experiment do not allow one to make any definite statements about the detailed mechanism of air-shower origin or to discriminate between different modes of origin.

2. The Molière distribution function describes the lateral structure of these showers up to distances of sixty centimeters from the shower axis within Gaussian fluctuations.

3. The statistical distribution of the shower particles three to four meters from the shower axis is Poissonian.

Our first result, the absence of multiple cores, is typical of the results of other workers who have sought to identify multiple cores on the basis of density observations alone. Those who have reason to believe in the existence of multiple cores base their belief on data obtained from energy distributions[9,16] with the exception of one.[18] The second result can be considered to extend the results of Williams[9] and of Cocconi, Tongiorgi, and Greisen[12] from two or three meters down to distances of one meter and less. The third result is not a surprising one; it is to be expected as was pointed out by Blatt.[10]

ACKNOWLEDGMENTS

I would like to express my deepest appreciation to Professor Wilson M. Powell for suggesting this project and for his sustained effort and interest in bringing it to a successful conclusion. To Mr. Richard Lander I would like to express my gratitude for his excellent assistance in the building and operation of the chamber, the analysis of the film, and the making of the drawings. For the excellent work done in the early stages of developing the chamber, I am deeply indebted to Mr. Baxter Armstrong. I wish to acknowledge the kindness of Professors R. W. Brode and W. B. Fretter in allowing me to operate the chamber on the Cosmic-Ray Deck and to utilize other of their facilities. My thanks are also extended to all members of the cloud-chamber group who helped during the construction and operation of the chamber.

[50] Hazen, Heineman, and Lennox, Phys. Rev. 86, 198 (1952).

Λ^0 Production in Nuclei*

ROBERT JASTROW†
Brookhaven National Laboratory, Upton, New York
(Received September 27, 1954)

Nuclear cross sections for Λ^0 production are interpreted in terms of production by pion-nucleon and nucleon-nucleon interactions.

CURRENT information concerning the Λ^0 particle[1] is drawn largely from studies of its production in the heavier nuclei. If the existing evidence for the similarity of the Λ^0-N and N-N interactions ($N \equiv$ nucleon) is accepted,[2] it becomes possible to deduce from the data on nuclear production some characteristics of Λ^0 production in elementary π-N or N-N collisions. The present note reports on a calculation designed for this purpose, in which the Λ^0, produced at a point in the nuclear interior, and moving in the conventional nuclear potential well of some 25 Mev, is followed by Monte Carlo methods through a succession of nucleon collisions until it emerges from the nucleus or its kinetic energy falls below 25 Mev; in the latter event it is regarded as captured.

The results provide estimates of the fraction of Λ^0's captured in nuclei of various sizes (Fig. 1; Table I), the initial energy distribution of Λ^0 particles at production (Fig. 4), and the relation between nuclear cross sections for Λ^0 production and the cross sections for production in π-N or N-N collisions (Tables I, II).

The calculation refers specifically to Λ^0 production in the 1.5-Bev π^- beam available at the Brookhaven cosmotron. However, the nature of the primary particle enters principally in the value assumed for its total cross section in nuclear matter; in the Bev region this is roughly the same for pions and nucleons and insensitive to energy changes, hence the results should apply to nucleon primaries also, at energies of a few Bev.[3]

It is assumed that the nuclear interactions of the incident pion may be represented by the π^--p cross section. The magnitude of $\sigma(\pi^-,p)$ at 1.5 Bev is 33 mb,[4] composed of 70 percent inelastic and 30 percent elastic scattering, the latter confined within 30° in the laboratory system.[5,6]

The nucleus is described by the plane projection of a spherical distribution of nuclear matter. The circular area of the projection is divided into 35 zones in Pb and 20 zones in C, in each of which a fraction of the incident pion beam interacts, determined by the cross-sectional area of the zone and the attenuation of the beam in passing through the nuclear region above.

The subsequent history of an interaction is followed by Monte Carlo techniques. The pion may scatter elastically or inelastically, with respective weights 0.3 and 0.7, and elastically scattered pions are pursued until they suffer an inelastic scattering or leave the nucleus. The elastic angular distribution is represented by the assignment of weights 0.3, 0.4, and 0.3 to the angles −15°, 0°, and 15°, respectively.

It is assumed that a Λ^0 of given initial kinetic energy is produced in each inelastic pion scattering. The pion is regarded as energetically incapable of Λ^0 production after an inelastic scattering and is not considered further. The newly created Λ^0 is followed through collisions with nucleons up to the point of escape or capture. A crude description of Λ^0-N scattering was presumed adequate for the present purpose: the Λ^0 is assigned the measured n-p cross section, taken as isotropic, for its interaction; the internal motion of the nucleons is represented by a division of the

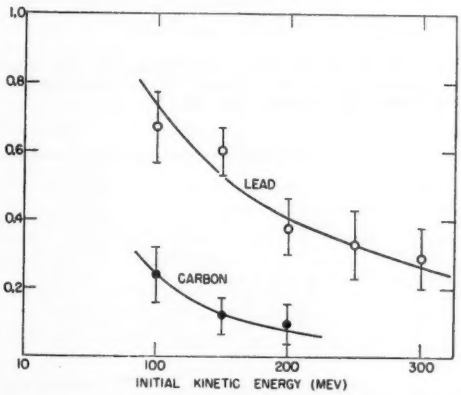

FIG. 1. Fraction of Λ^0's captured in the nucleus, *vs* T, the initial kinetic energy of the Λ^0.

* Research performed at Brookhaven National Laboratory, under the auspices of the U. S. Atomic Energy Commission.

† Permanent address: Nucleonics Division, Naval Research Laboratory, Washington, D. C.

[1] $\Lambda^0 \rightarrow p + \pi^- + 37$ Mev, with a lifetime of 3×10^{-10} second.

[2] Light nuclear fragments emitted from cosmic-ray stars have been observed to disintegrate spontaneously under circumstances indicating the decay of a Λ^0 bound in the fragment, and in a few favorable cases it has been possible to deduce the binding of the Λ^0, assuming the Q of its decay to be 37 Mev. [Ciok, Danysz, and Gierula, Nuovo cimento **11**, 436 (1954); C. F. Powell, Nature **173**, 469 (1954).] The results are of the order of 0–5 Mev of binding, and suggest that the interaction of the Λ^0 with nuclear matter is comparable to, but somewhat weaker than, that of the nucleon.

[3] Primaries of greater energy can produce additional particles—pions and knock-on nucleons—having sufficient energy for Λ^0 production.

[4] Cool, Madansky, and Piccioni, Phys. Rev. **93**, 249 (1954).

[5] Crussard, Walker, and Koshiba, Phys. Rev. **94**, 736 (1954); **95**, 852 (1954).

[6] R. P. Shutt (private communication). (1.4 Bev.)

Fermi circle (a projection of the Fermi sphere) into 5 zones; and the scattered Λ^0 is permitted to emerge in one of 4 states, corresponding to scattering angles of 0°, ±90°, and 180° in the center-of-mass system of the Λ^0 and recoiling nucleon. Collisions which leave the nucleon within the Fermi circle are voided; however, the exclusion principle is not applied to the Λ^0.

Initial kinetic energies of 100, 150, 200, 250, and 300 Mev were assumed for production in Pb, and 100, 150, and 200 Mev for C, the trend of the results indicating that nuclear capture and secondary interactions were unimportant above these energies. A total of 175 pion interactions were followed in C, and 435 in Pb.

The resulting yields of Λ^0's must be multiplied by the probability, assumed $\ll 1$, for Λ^0 production in a single π-N collision.

FRACTION CAPTURED; ENERGY AND ANGLE DISTRIBUTIONS

Figure 1 indicates the fraction of Λ^0's captured in C and Pb, as a function of T, the initial kinetic energy of the Λ^0. The variation with T is rapid, and some knowledge of the actual distribution of initial energies is needed for an estimate of the mean capture probability.

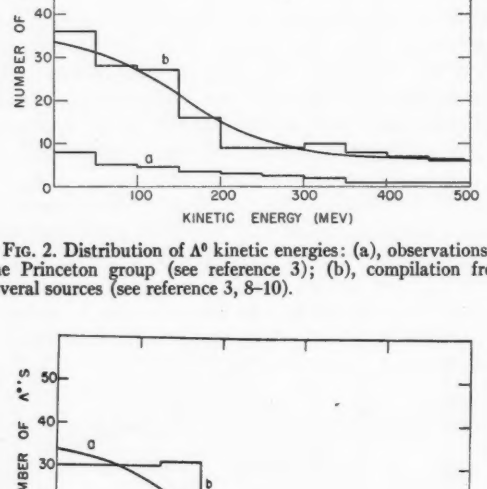

FIG. 2. Distribution of Λ^0 kinetic energies: (a), observations of the Princeton group (see reference 3); (b), compilation from several sources (see reference 3, 8–10).

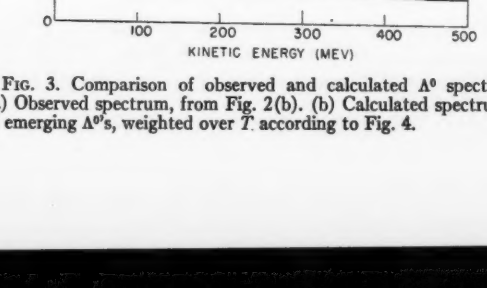

FIG. 3. Comparison of observed and calculated Λ^0 spectra. (a) Observed spectrum, from Fig. 2(b). (b) Calculated spectrum of emerging Λ^0's, weighted over T according to Fig. 4.

Information concerning the initial energy distribution may be obtained from a comparison of the observed spectrum with the calculated spectrum of Λ^0's emerging from Pb, which also depends strongly on T. Although the spectra associated with individual values of T are far from the observed spectrum, a composite distribution in fair agreement with experiment may be obtained by adding suitably weighted contributions from all values. The assignment of relative weights constitutes the desired T-distribution.

The Λ^0 spectrum seen in cosmic ray events by the Princeton group[7] is shown in Fig. 2(a), and a compilation of data from this and other sources in Fig. 2(b).[8–10]

Figure 3 presents the calculated composite distribution of emerging Λ^0's, (3b), compared with observation, (3a); the spectrum of initial Λ^0 energies required to obtain (3b) is given by Fig. 4.[11] Table I lists the fraction captured, averaged over the T distribution of Fig. 4.

The distribution of angles between the line of flight of the Λ^0 and the direction of the primary is generally observed to be strongly forward. Figure 5(a), for example, gives the angular distribution of 10 Λ^0's reported by Fretter *et al.*,[9] with a mean angle of 35°. In the Monte Carlo calculations, initial angles of ±30° were assigned to the Λ^0 at production; the resultant angular distribution of emerging Λ's, weighted over T according to Fig. 4, is shown in Fig. 5b.

TABLE I. Cross sections for Λ^0 production by 1.5-Bev π^- mesons ($\alpha=0.03$).

	(a) Captured (mb)	(b) Emerging[a] (mb)	(c) Mean fraction captured[a]
C	0.6	5.8	0.10
Cu	8.5	13.5	0.39
Ag	15.7	17.3	0.48
Pb	27.2	23.8	0.54

[a] Averaged over initial Λ^0 energy according to Fig. 4.

CROSS SECTIONS

The nuclear cross sections for Λ^0 production are proportional to the probability, α, for Λ^0 production in a single interaction of the primary with a nucleon. They are given in Table I for $\alpha=0.03$, referring to incident 1.5-Bev π^- mesons, for which cross sections are observed of approximately 1 mb for Λ^0 production[12] and 33 mb for total interaction.[4] The listed Ag and Cu cross sections were obtained by interpolation, assuming a power law for the variation with atomic number: $\sigma=kA^m$, with k and m derived from the values for Pb

[7] Ballam, Harris, Hodson, Rau, Reynolds, Treiman, and Vidale, Phys. Rev. **91**, 1019 (1954).
[8] Leighton, Wanlass, and Anderson, Phys. Rev. **89**, 148 (1953).
[9] Fretter, May, and Nakada, Phys. Rev. **89**, 168 (1953).
[10] Bridge, Peyrou, Rossi, and Stafford, Phys. Rev. **91**, 362 (1953).
[11] The range above 300 Mev is taken directly from Fig. 3a.
[12] Fowler, Shutt, Thorndike, and Whittemore, Phys. Rev. **93** 861 (1953).

and C. We find for total production [columns (a) plus (b)], $\sigma=1.02A^{0.74}$, and for emerging Λ^0's, $\sigma=1.68^{0.80}$.[13]

The corresponding interpretation of Λ^0 yields by nucleon primaries in terms of (direct) N-N production is complicated by the existence of an alternative (indirect) process, *viz.*, creation of a fast pion by N-N collision and subsequent Λ^0 production by a π-N interaction in the same nucleus. The Z dependence of the yields may differentiate between these alternatives, as noted by Reynolds,[14] because indirect production requires a greater thickness of nuclear matter than direct, and will contribute little in light nuclei. This expectation is verified by Table II, in which the cross sections for direct and indirect production are compared for several nuclei. These were obtained by assuming all particles to travel forward, reducing the computation to a succession of simple integrations. Nuclear Λ^0 capture was represented by a Λ^0 absorption or capture cross section of 20 mb,[15] and the additional refinement of a nonuniform profile of nuclear density was introduced,[16] the direct/indirect ratio in carbon being appreciably affected by the increased transparency of the diffuse boundary. The collision cross sections employed were appropriate to π-N and N-N events at Cosmotron energies.

TABLE II. Production of Λ^0 particles by nucleons: (a) by direct N-N interaction; (b) by pion intermediaries. Listed are the ratios of nuclear cross sections for Λ^0 production to elementary cross sections for Λ^0 production by an N-N interaction [column (a)], or a π-N interaction [column (b)].

	Direct (a)	Indirect (b)
C	5.6	0.12
Cu	12.9	0.64
Pb	27.0	1.34

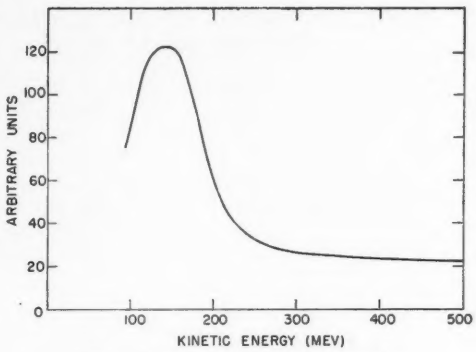

FIG. 4. Distribution of initial Λ^0 energies.

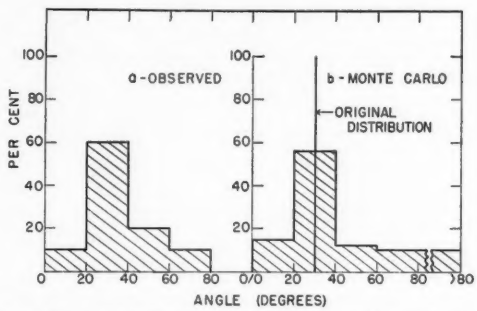

FIG. 5. Λ^0 angular distribution. (a) Fretter *et al.* (see reference 9). (b) Calculated distribution of Λ^0's emerging from Pb.

As in the Monte Carlo calculations, the nuclear yields are proportional to the cross section (σ_0) for Λ^0 production in an elementary π-N or N-N interaction.[17] Table II gives the ratios of nuclear to elementary cross sections; these ratios represent the effective numbers of nucleons contributing to Λ^0 production.

Power law approximations to Table II yield: $\sigma/\sigma_0=2.00Z^{0.47}$ (direct); $\sigma/\sigma_0=0.011Z^{0.92}$ (indirect).

A cross section of ~1 mb has been reported[18] for the Λ^0 yield from Pb placed in the forward neutron beam of the cosmotron, of maximum energy 2.2 Bev. Table II(b) indicates that this value may be attributed entirely to indirect production if a cross section of 0.5 Mb, consistent with observations of Fowler *et al.*,[12] is assumed for π-N production of Λ^0's. On the other hand, if Walker's Λ^0's originated directly in N-N interaction, II(a) indicates a corresponding cross section of 0.02 mb for N-N Λ^0 production averaged over the 1–2 Bev region.

[13] The frequency of emission of an unstable nuclear fragment (one containing a Λ^0) may be estimated from these cross sections and observations on disintegrations produced by 2 Bev protons: For the majority of unstable fragments observed, $Z\geq 3$. We note a cross section of ~10 mb for production of Be^7 by 2-Bev protons on Ag [Baker, Friedlander, and Hudis, Phys. Rev. **95**, 612 (1954)], and estimate 50 mb for the production of all fragments with $Z\geq 3$. The angular distribution of the Be^7 nuclei is strongly forward, suggesting direct ejection as the production mechanism, rather than evaporation. If the fragments are directly ejected, Λ^0's contained therein must have been created in the interaction causing the ejection. The probability (P) for unstable fragment emission is then the product of the chance for Λ^0 production among the neutrons of the fragment by the chance for its ejection from the nucleus. For Ag($\sigma_{geom}=1370$ mb) we have (Table I), $P=4\times(15.7/1370)\times(50/1370)=1:400$. The observed frequencies of emission are lower: 1:1000 for cosmic-ray primaries and 1:1500 for 3-Bev proton primaries (J. Fry, private communication).

The cross section for tritium emission from Ag at 3 Bev is perhaps 200 mb [300 mb in Pb; W. F. Libby (private communication)], indicating a frequency of 1:70 for excited triton production by the previous arguments, whereas few excited tritons are actually seen. It is possible that the Λ^0-N bond is too weak for formation and ejection of an unstable triton.

[14] G. T. Reynolds, Proceedings of the Fourth Annual Rochester High-Energy Conference (University of Rochester Press, Rochester, 1954).

[15] An absorption cross section of 20 mb represents the Λ^0 capture process to the extent of yielding a fraction absorbed (i.e., captured) of ~0.5 in Pb, in agreement with the Monte Carlo result of Table I(c).

[16] R. Jastrow and J. Roberts, Phys. Rev. **85**, 757 (1952).

[17] The cross sections for indirect production are also proportional to the probability for creation of a fast pion by N-N collision, which we estimate as 0.03 for pions of momentum greater than 1.5 Bev/c, from the work of Fowler, Shutt, Thorndike, and Whittemore on n-p interactions at ~1.8 Bev [Phys. Rev. **95**, 1026 (1954)].

[18] R. W. Walker, dissertation, Yale University, 1954 (to be published).

Cross Sections for Producing High-Energy Neutrons from Carbon Targets Bombarded by Protons, Deuterons, and He^3 Particles

LARRY SCHECTER, WALTER E. CRANDALL, GEORGE P. MILLBURN, AND JOHN ISE, JR.
Radiation Laboratory, Department of Physics, University of California, Berkeley, California

(Received September 27, 1954)

The differential cross sections, $d\sigma/d\Omega$, for producing neutrons with energy in excess of 20 Mev from carbon targets bombarded by 340-Mev protons, 190-Mev deuterons, and 490-Mev He^3 particles were measured. The absolute cross sections were determined by counting identical carbon targets and neutron detector foils in equivalent geometry and utilizing the known ratios of excitation functions for the neutron and bombarding particles.

INTRODUCTION

HIGH-ENERGY neutron beams have been produced at Berkeley in a variety of ways: 90-Mev neutrons result from stripping 190-Mev deuterons;[1,2] 270-Mev neutrons result from exchange collisions of 340-Mev protons inside light nuclei;[3] 160-Mev neutrons result from stripping 490-Mev He^3 ions.[4] This report concerns the measurement of the differential cross sections for each of these processes.

EXPERIMENTAL METHOD

Angular Distribution

Each of the ions mentioned above was accelerated to full energy in the 184-inch cyclotron (Fig. 1) and struck a laminated $\frac{3}{8}$-inch carbon target of truncated wedge shape (Fig. 2) placed on a probe, producing high-energy neutrons over a range of angles. In order to measure the angular distribution of these neutrons, pure graphite detector foils, $1\frac{11}{16}$ inches in diameter and $\frac{1}{8}$ inch thick, were placed every few degrees around the cyclotron over a horizontal range of 25° and a vertical range of 12°. No monitor was needed, as all detector foils received exactly the same exposure time, about one-half hour. The detector foils were placed directly on the tank wall, so that the effects of wall scattering were minimized. As the neutron activation threshold in carbon is about 20 Mev,[5] neutrons degraded below this energy by inelastic collisions with the dees, walls, and shielding are not detected.

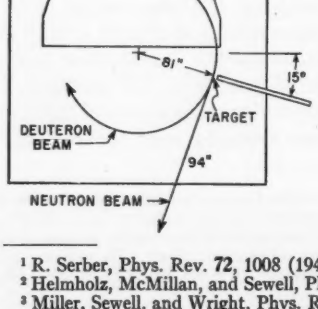

FIG. 1. Experimental arrangement. The carbon detector foils were placed on the outer surface of the vacuum chamber wall.

Following bombardment, the activity in each of the foils was measured under an end-window Geiger counter in a lead shield. After the usual corrections for counter dead time and background, each of the observed activities was corrected to a standard distance beneath the counter by means of an empirically determined factor. The only activity observed in the detector foils was the 20.5-minute C^{11} formed by the $(n,2n)$ reaction on C^{12}.[6]

The number of countable events per unit time C_f produced by the $(n,2n)$ reaction in each foil at time t_c after the beginning of a bombardment of duration t_b is

$$C_f(t_c)=\epsilon^{-\lambda t_c}(\epsilon^{\lambda t_b}-1)\int_{20}^{\infty} N_f n(E)\sigma(E)_{n,2n}\eta dE, \quad (1)$$

where N_f is the number of carbon atoms per cm^2 in the foil, $n(E)$ is the differential neutron spectrum incident on the foil per unit time, $\sigma(E)_{n,2n}$ is the $(n,2n)$ excitation function in carbon, η is the over-call efficiency for counting a decaying C^{11} atom in the standard geometry and λ is the decay constant for the 20.5-minute C^{11} activity. We can define an average $(n,2n)$ cross section in carbon,

$$\int_{20}^{\infty} n(E)\sigma_n(E)dE=\bar{\sigma}_{n,2n}N_n, \quad (2)$$

where N_n is the total number of neutrons incident on the foil per unit time.

Then

$$C_f(t_c)=\epsilon^{-\lambda t_c}(\epsilon^{\lambda t_b}-1)N_f\eta\bar{\sigma}_{n,2n}N_n. \quad (3)$$

All counting rates can be corrected to some standard time t_0,

$$C_f(t_0)=C_f(t_c)\epsilon^{\lambda(t_c-t_0)}, \quad (4)$$

so that

$$C_f(t_0)=\epsilon^{-\lambda t_0}(\epsilon^{\lambda t_b}-1)N_f\eta\bar{\sigma}_{n,2n}N_n. \quad (5)$$

[1] R. Serber, Phys. Rev. **72**, 1008 (1947).
[2] Helmholz, McMillan, and Sewell, Phys. Rev. **72**, 1003 (1947).
[3] Miller, Sewell, and Wright, Phys. Rev. **81**, 374 (1951).
[4] Ise, Pyle, Hicks, and Main, Rev. Sci. Instr. **25**, 437 (1954).
[5] Brolley, Fowler, and Schlacks, Phys. Rev. **88**, 618 (1952).
[6] *Nuclear Data*, National Bureau of Standards Circular No. 499 (U. S. Government Printing Office, Washington, D. C., 1950).

N_n will be given by

$$N_n = N_t N_d \frac{d\sigma}{d\Omega}(\theta)\Delta\Omega, \tag{6}$$

where N_t is the number of carbon atoms per cm² in the target, N_d is the number of monoergic deuterons (or protons, or He^3 ions) incident on the target per unit time, $d\sigma/d\Omega(\theta)$ is the differential cross section in carbon for the production of neutrons by deuterons (or protons, or He^3 ions), and $\Delta\Omega = A/r^2$ is the solid angle subtended by the detector foil. The differential cross section at the angle of the jth foil then becomes

$$\frac{d\sigma}{d\Omega}(\theta_j) = \frac{C_j(t_0)}{\bar{\sigma}_{n,2n} N_f N_t N_d \eta \Delta\Omega_j e^{-\lambda t_0}(e^{\lambda t_b} - 1)}, \tag{7}$$

and the ratio of cross sections for two foils is

$$\frac{d\sigma}{d\Omega}(\theta_j) \Big/ \frac{d\sigma}{d\Omega}(\theta_k) = \frac{r_j^2 C_j(t_0)}{r_k^2 C_k(t_0)}. \tag{8}$$

The angular distributions are then just the adjusted counting rates in each foil, compared to the rate in the foil at 0°, and weighted by the square of the distance between detector foil and target. The counting statistics obtained for each foil were of the order of 1 percent. The distances, of the order of 100 inches, were measured to less than ½ percent. All counting rates were corrected for neutron attenuation in the cyclotron tank walls. Each distribution was determined several times with good reproducibility.

Differential Cross Section

The absolute differential cross section for the production of high-energy neutrons by the various ions was measured at 0° by exposing the target and a single detector foil in a short bombardment, of the order of 20 seconds' duration. After exposure, the detector foil was counted in exactly the same geometry as that used in the determination of the angular distribution. The target was separated, after exposure, into its components, three ⅛-inch truncated wedge sections. Each segment was placed in a dummy graphite form cut from the same stock, so that the assembly had the same right circular cylindrical shape as the detector foil. This was done so that, to the Geiger counter, the target foil should appear equivalent to the detector foil with respect to back-scattering, absorption, and physical geometry. The target-segment counting rates with and without the dummy form differed only by a few percent.

Although the detector foil was exposed uniformly over its volume, each target segment activity was confined to the ½-inch inside edge of the wedge, owing to the manner of its exposure. It was necessary to determine the effect of this nonuniform activity distribution, so that the counting rate could be compared directly to that of the detector foil. For this purpose, a ⅛ inch diameter disk of ⅛ inch thick graphite was activated, and the C^{11} activity was determined as a function of the radial displacement of the disk (approximating a point source) from a point below the center of the Geiger tube.[7]

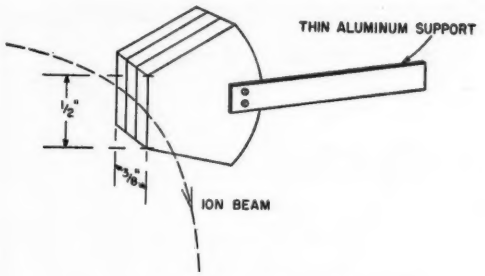

FIG. 2. Details of the carbon target assembly.

At a sufficient distance below the Geiger tube there should be no change in the "effective" solid angle. At the standard distance, to which all counting rates were empirically corrected with an uncertainty of about 1 percent, it was found that this solid angle changed only slowly out to about ½ inch, and was down by 15 percent when the lateral displacement of the point source was 1 inch. Since the target activity was confined within a radius of ¼ inch or so, the effective relative solid angle was unity. For the detector foil, the effective solid angle was determined by integrating the product of the radius and the solid angle for the point source over the radius. This integral was normalized to the foil area, and the effective relative solid angle turned out to be about 0.95.

In the target foils, slight amounts of impurities caused decay activities longer than the desired 20.5-minute period. These longer activities amounted to only a few percent, when the bombardment was kept short, and were subtracted. The total activity in the target was taken to be the sum of the activities in the segments.

The 20.5-minute counting rate C_t produced by monoergic ions (say, deuterons) in the target and adjusted to some time t_0 is

$$C_t(t_0) = e^{-\lambda t_0}(e^{\lambda t_b} - 1) N_d N_t \sigma(190)_{d,dn} \eta, \tag{9}$$

where $\sigma(190)_{d,dn}$ is the cross section for the production of C^{11} by deuterons of 190 Mev. [For the other ions, Eq. (9) would contain N_p and $\sigma(340)_{p,pn}$ or N_{He^3} and $\sigma(490)_{He^3,He^3n}$.] Substituting for N_d from Eq. (9) into Eq. (7), we have

$$\frac{d\sigma}{d\Omega}(0°) = \frac{1}{N_f \Omega_f} \frac{\sigma(190)_{d,dn}}{\bar{\sigma}(90)_{n,2n}} \frac{C_0°(t_0)}{C_t(t_0)}. \tag{10}$$

[7] Aamodt, Peterson, and Phillips, Phys. Rev. 88, 739 (1952).

FIG. 3. Angular distribution of neutrons from deuteron stripping in carbon. The triangles and circles represent vertical and horizontal distributions, respectively.

RESULTS AND DISCUSSION

Deuterons

The angular distribution of neutrons from 190-Mev deuterons on carbon was determined first, in order to check the experimental method, since this distribution had previously been predicted[1] and verified.[2] The results are shown in Fig. 3. The points at 20° and 25° could not be corrected for attenuation of neutrons in the internal deflector system of the cyclotron, and are very probably too low. Foils placed at 90° in the target region showed less than 1 percent background activity. As the general agreement with the previous work was satisfactory, the absolute differential cross section at 0° was determined by the method described above. The ratio $\sigma(190)_{d,dn}/\bar{\sigma}(90)_{n,2n}$ (Table I) was determined by an auxiliary experiment to an accuracy of roughly 10 percent,[8] using as a neutron detector a recoil proton scintillation counter telescope for just the neutron spectrum involved, and was found to be consistent with the results of McMillan and York.[9]

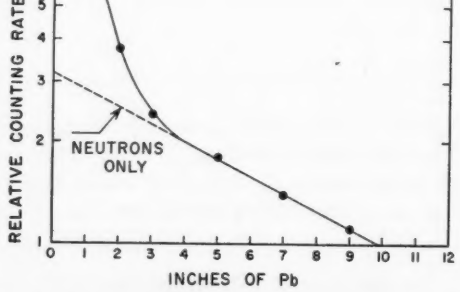

FIG. 4. Determination of the neutron-proton ratio at the detector foil position. Linear extrapolation of the neutron attenuation curve in Pb shows that the neutrons comprised 32 percent of the total activity observed.

TABLE I. Ratios of cross sections for the production of C^{11} by various ions to cross sections for the production of C^{11} by neutrons of the related energies.

$\sigma(190)_{d,dn}/\bar{\sigma}(90)_{n,2n}$ [a]	2.72
$\sigma(340)_{p,pn}/\bar{\sigma}(270)_{n,2n}$ [b]	1.95
$\sigma(490)_{He^3,He^3n}/\bar{\sigma}(160)_{n,2n}$ [a]	4.30

[a] See reference 8.
[b] See reference 7.

The target-foil counting rates were corrected for activity due to secondary reactions in the thick target, which amounted to about 2 percent. The final result, given in Table II, is substantially in agreement with earlier work of Knox.[10] The total cross section for deuteron stripping has been determined,[11,12] and is, of course, larger than that found by integrating the present distribution, which extends only to about 15°.

Protons

The angular distribution of neutrons from 340-Mev protons was checked and found to be in general agreement with the work of Miller, Sewell, and Wright.[3] The determination of the absolute differential cross section at 0° was complicated by the presence of primary protons at the detector foil position. The proton-neutron ratio at this position was determined by plotting the logarithm of the counting rate as a function of thickness of lead, in several foils placed along the 0° line, as in Fig. 4. The counting rate from neutrons alone is then the intercept of the linearly extrapolated neutron attenuation curve. The ratio of cross sections for the production of C^{11} in the target and in the detector, $\sigma(340)_{p,pn}/\bar{\sigma}(270)_{n,2n}$, is known to roughly 10 percent (Table I).[7,13] The final result is given in Table II.

He^3 Ions

The angular distribution of neutrons from 490-Mev He^3 ions, determined by the method described above,

TABLE II. Differential cross sections at 0° for the production of high-energy neutrons by various ions.

Ion	$\frac{d\sigma}{d\Omega}(0°)$ barns/steradian
340-Mev proton	0.22±0.05
190-Mev deuteron	3.2 ±0.5
490-Mev He^3 ion	2.0 ±0.4

[8] W. Birnbaum *et al.*, Phys. Rev. **95**, 649 (1954).
[9] E. M. McMillan and H. York, Phys. Rev. **73**, 262 (1948).
[10] W. J. Knox (unpublished).
[11] L. Schecter *et al.*, Phys. Rev. **90**, 633 (1953).
[12] G. P. Millburn *et al.*, Phys. Rev. **95**, 1268 (1954).
[13] Warshaw, Swanson, and Rosenfeld, Phys. Rev. **95**, 649 (1954).

is shown in Fig. 5. The half width at half maximum is about 5.5°. This narrow beam suggests that the neutrons are produced primarily by stripping, since an estimate of the width to be expected from the ratio of binding energy to kinetic energy is $\theta \sim (\epsilon/E_{\mathrm{He}^3})^{\frac{1}{2}} = 7°$. The angular distribution to be expected from theoretical considerations, using an approximate wave function for the He^3 nucleus, has been calculated by Heckrotte.[14]

The production of high-energy neutrons from the interaction of high-energy He^3 nuclei with heavier target nuclei results from the stripping off of one or both of the protons of He^3. One would not, however, expect the two protons to be stripped off simultaneously, so that we need consider the effect of only one proton's being stripped off. The cross section and the angular and energy distributions can be calculated in a manner similar to that for the production of neutrons or protons from the stripping of high-energy deuterons.[1]

It must be recognized, though, that in calculating the angular and energy distributions it is necessary to take into account the interaction between the neutron and the remaining proton after the stripping event. The interaction can lead to the formation of a deuteron;[4,15] or if the neutron and proton remain unbound, the interaction can be expected to influence their subsequent motion. Because of the virtual level of low relative energy in the singlet $p-n$ state, the effect of interaction is to reduce substantially the half width of the momentum distribution of the neutron (or proton) from

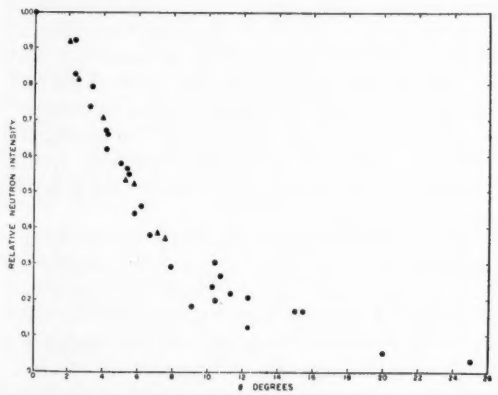

FIG. 5. Angular distribution of neutrons from He^3 stripping in carbon. The triangles and circles represent vertical and horizontal distributions, respectively.

[14] W. Heckrotte (private communication).
[15] W. Heckrotte, thesis, University of California Radiation Laboratory Report UCRL-1868, April 14, 1952 (unpublished).

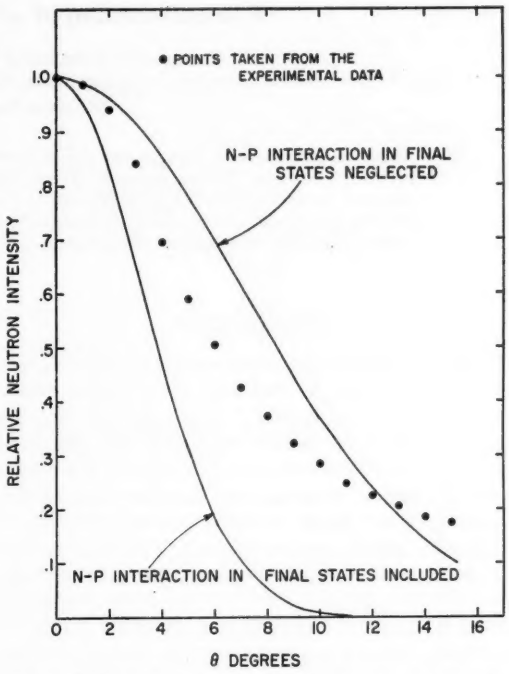
● POINTS TAKEN FROM THE EXPERIMENTAL DATA
N-P INTERACTION IN FINAL STATES NEGLECTED
N-P INTERACTION IN FINAL STATES INCLUDED
RELATIVE NEUTRON INTENSITY
θ DEGREES

FIG. 6. Theoretical angular distribution of neutrons from He^3 stripping.

what would be obtained with neglect of this interaction between the outgoing neutron and proton. The calculated angular distribution of the neutrons, a simple Gaussian form being assumed for the He^3 wave function, is shown in Fig. 6. The angular distribution that results when the interaction between the outgoing neutron and proton is neglected is also shown for the sake of comparison.

The ratio of cross sections for the production of C^{11} in the target and the detector, $\sigma(490)_{\mathrm{He}^3,\,\mathrm{He}^3n}/\bar{\sigma}(160)_{n,\,2n}$, was measured with the telescope to about 10 percent (Table I).[8] The final result is given in Table II.

ACKNOWLEDGMENTS

This work was done under the general supervision and with the helpful interest of Dr. C. M. Van Atta. We are indebted to J. T. Vale and the cyclotron staff for their assistance and cooperation. Thanks are due to Wallace Birnbaum, Marian Whitehead, Robert V. Pyle, Donald A. Hicks, and Robert M. Main for their helpful assistance. The authors especially wish to thank Warren Heckrotte for his valuable discussions.

Photoproduction of π^0 Mesons from Protons*

Y. GOLDSCHMIDT-CLERMONT,† L. S. OSBORNE, AND M. SCOTT‡
Physics Department and Laboratory for Nuclear Sience, Massachusets Institute of Technology, Cambridge, Masschusetts
(Received September 3, 1954)

The yield of π^0 mesons from gamma rays on protons has been measured as a function of center-of-mass angle for gamma-ray energies from 170 Mev to 340 Mev. The results are shown to be consistent with a model of production predominantly through a $J=\frac{3}{2}$, isotopic spin, $\frac{3}{2}$, state, which is resonant at about 300 Mev gamma-ray energy. There is evidence for S-state production and possibly electric quadrupole, P-wave production through the resonant state.

I. INTRODUCTION

THE production of neutral mesons by photons was first observed by Panofsky *et al.*[1] Later experments were done by others[2–5] which showed that the excitation curve for gamma rays less than 300 Mev agreed with a cross section $\sigma \sim p^3$, where p is the meson center-of-mass momentum, and that the angular distribution in the center of mass behaved roughly as $d\sigma/d\Omega \sim 2+3\sin^2\theta$.

In addition, the California Institute of Technology group[6] found that the cross section went through a maximum at about 300 Mev and decreased markedly for greater energies in a manner reminiscent of resonant interactions. The purpose of this experiment was to measure this process in more detail.

An explanation of the process was examined by a "strong coupling" theory based on a resonant state of the nucleon.[7,8] Theoretical descriptions of the process have been given in terms of partial waves through intermediate states.[9,10] Watson[11] and Aizu[12] have derived the formal relationship between the photoproduction and scattering of mesons. Ross[13] has developed a semiphenomenological description by calculating the photoproduction of mesons in perturbation theory and adding the experimentally known scattering. Chew and Salzman[14] have calculated meson photoproduction directly using a cutoff theory which has given agreement with scattering experiments.

II. EXPERIMENTAL PROCEDURE

The experimental data was acquired in two runs. The gamma-ray beam from the Massachusetts Institute of Technology electron synchrotron was passed through a high-pressure hydrogen tank and emulsions were placed around the beam to pick up the recoil protons from the π^0-meson production process. The layout is shown in Fig. 1. The gamma-ray beam passed through a defining collimator and two protecting collimators into the tank through a $\frac{1}{4}$-in. aluminum window and out a $\frac{1}{2}$-in. aluminum window. Two four-inch lead walls screened the emulsions from particles coming directly from the windows. The end plates of the tank could be removed to give access into the tank: there was an additional port with provision for electrical leads for thermocouples. A fiber board "dark room" was set up at one end of the tank for loading and unloading the emulsions. These were mounted on an aluminum circle which was slipped into place at the center of the tank. There was a thin wall integrating ionization chamber[15] upstream from the tank and a thick-walled chamber downstream, both for monitoring purposes. Around the outside of the tank was a container for a dry-ice and alcohol mixture.

If nuclear emulsions are exposed for several minutes to hydrogen at room temperatures the hydrogen will reduce the AgBr such that the plate, when developed, will be impossibly blackened. The temperature coefficient of this reaction is such that, at a temperature of $-60°$C, a week's exposure to hydrogen at 40 atmospheres gives no perceptible blackening. For this reason the gas tank was cooled by a mixture of dry ice and methyl alcohol. This treatment did not appear to diminish the sensitivity of the plates for our purposes.

Figure 2 shows the angle in the laboratory system and range in nuclear emulsion for the π^0 recoil proton for various gamma-ray energies and meson center-of-mass angle, θ. It is evident that the proton angle and range is markedly asymmetric with respect to meson angle. A systematic error of 1° in proton angle would change the predicted gamma-ray energy by 10 Mev for cos-

* This work was supported in part by the joint program of the Office of Naval Research and the U. S. Atomic Energy Commission.
† Now at CERN, Geneva, Switzerland.
‡ Now at the University of Illinois, Urbana, Illinois.
[1] Panofsky, Steinberger, and Stetler, Phys. Rev. **86**, 180 (1952).
[2] A. Silverman and M. Stearns, Phys. Rev. **88**, 1225 (1952).
[3] G. Cocconi and A. Silverman, Phys. Rev. **88**, 1230 (1952).
[4] Goldschmidt-Clearmont, Osborne, and Scott, Phys. Rev. **89**, 329 (1953).
[5] C. G. Andre, University of California Radiation Laboratory Report UCRL-2425 (unpublished).
[6] Walker, Oakley, and Jollestrup, Phys. Rev. **89**, 1301 (1953).
[7] K. A. Brueckner and K. M. Case, Phys. Rev. **83**, 1141 (1951).
[8] Y. Fujimoto and H. Miyazawa, Prog. Theoret. Phys. **5**, 1052 (1950).
[9] K. A. Brueckener and K. M. Watson, Phys. Rev. **92**, 1025 (1953).
[10] B. T. Feld, Phys. Rev. **89**, 330 (1953).
[11] K. M. Watson, Phys. Rev. **95**, 228 (1954).
[12] K. Aizu, Japanese Conference on High Energy Physics, 1953 (unpublished).
[13] M. Ross, Phys. Rev. **94**, 454 (1954).
[14] Chew, Proceedings of the Fourth Annual Rochester Conference on High Energy Nuclear Physics (University of Rochester Press, Rochester, 1954).
[15] H. Ratz, thesis, Massachusetts Institute of Technology, 1951 (unpublished).

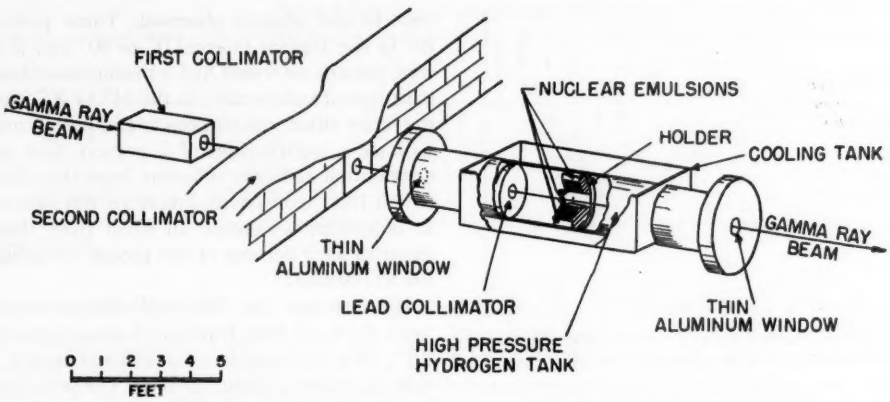

FIG. 1. Schematic of the exposure arrangement, showing the passage of the gamma-ray beam through the hydrogen tank and the placement of the plates.

$\theta=0.7$ and 2 Mev for $\cos\theta=-0.07$. An error in proton energy of 10 percent would change the center-of-mass angle 3° for $\cos\theta=-0.7$ and 1° for $\cos\theta=0.7$. Since the excitation curve was expected to be varying rapidly with energy we wished to avoid errors that would distort the angular distribution or excitation curve. This was one reason that all proton energies were measured by their range rather than by grain counting. In order to stop the protons the detecting emulsion consisted of 6 pellicles (4 in the first run) stacked onto a glass backed emulsion. The protons were tracked through from pellicle to pellicle. The stack of emulsions were glued together with Krylon. The stack was mounted with clips onto a Bakelite support which was mounted in turn to the aluminum ring that fitted into the tank. When in place, the angle between the plane including the beam and the surface of the emulsion was 22°. The protons came into the stack at a relatively grazing angle which insured that over 90 percent of the protons would stop in the stack.

The tank and collimators were aligned with respect to the beam. The plates were inserted into the tank and the tank evacuated. The tank was cooled by the dry ice and methyl alcohol mixture and then flushed with hydrogen several times. The hydrogen was passed over activated charcoal at liquid air temperatures for purification in the second run. During the run the temperature of the gas was measured at various points in the tank; the mean temperature was −65°. The synchrotron was run at an electron energy of 320 Mev for run 1 and 355 Mev for run 2 as calibrated by magnetic field measurements. This agreed within 5 Mev of the energy calculated by noting the cut-off in energy of the proton recoils from the π^0 production.

After the run the emulsion stacks were removed and a set of x-ray marks passed through them as reference points. The pellicles were separated by dipping the stack for a few minutes in acetone. The pellicles were developed by the hot-cold method with the hot bath (~20°C) at less than usual temperature to underdevelop the emulsions so that they would effectively cut off tracks of particles with energy greater than $\frac{1}{5}$ rest mass energy. The pellicles were shrunk to original size after washing by addition of alcohol to a water bath and deposited on fixed 25 micron plates.

The secondary beam monitors were calibrated by using a shower-integrating ionization chamber placed through a stack of lead.[15] This calibrating scheme has yielded cross sections which have been consistently higher by a factor of about 1.5 compared to other laboratories. By using a portable ion chamber, an intercalibration was performed with the Cornell Synchrotron and the Illinois Betatron laboratories which indeed showed this same factor. In this paper we will quote cross sections based on the calibrations of these laboratories since they find mutual agreement. This will have

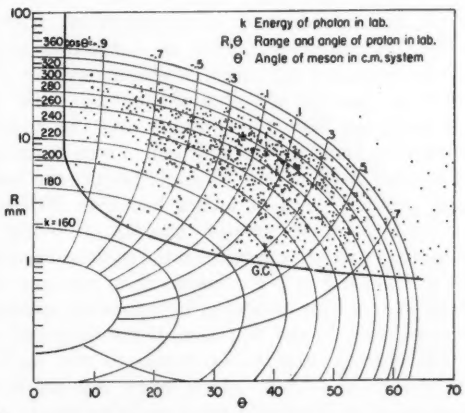

FIG. 2. Plot of events for run No. 1. Each dot represents a recoil proton plotted with respect to its angle in the laboratory system and its range in nuclear emulsion. The superimposed lines give the energy of the photon responsible and the cosine of the meson center-of-mass angle. The line labelled G.C. gives the lower limit to observe recoils because of insufficient range in the gas to get to the plates. The points occurring outside of the π^0 plot are mainly photoprotons from impurities in the gas.

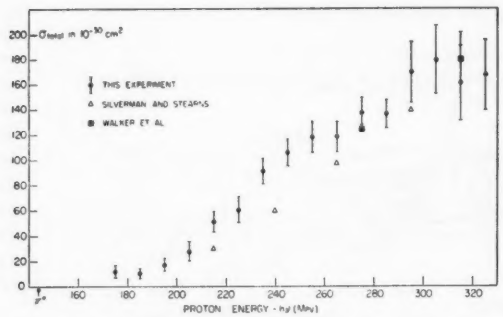

FIG. 3. The total cross section for $\gamma+p\rightarrow\pi^0+p$. The other points refer to the work in references 2 and 6.

the merit of allowing intercomparison with their cross sections. The discrepancy remains unexplained.

The gas was spectroscopically analyzed for impurities. For run 1 there were 0.5 percent and run 2, 0.3 percent impurities by volume, mainly O_2 and N_2.

III. THE DATA

The top pellicle of a stack was scanned for all proton tracks whose dip into the emulsion would correspond to a particle coming from the beam. The number of tracks not meeting this condition was about 10 percent of the total. Each track was traced through the stack to its ending. In some cases the track left the stack or suffered a nuclear collision; in such a case, grain counting gave its residual range. Each track was entered into a plot similar to Fig. 2, which shows the total results of the first run.

The kinematics of the π^0 reaction demanded that all protons be emitted at angles less than 64°. The protons found at angles greater than this were attributed to lower energy interactions with the nuclei of the impurities. The measurement of photoprotons from a 300-Mev bremsstrahlung beam on compound nuclei has been measured by other experimenters.[16–18] The number of protons we obtained agreed with the yields predicted from these results and the amount of impurities found in the hydrogen. From the measured angular distributions, we could predict the background protons found at angles less than 90° from those found at angles greater than 90°. It would be possible to get recoil protons from the nuclear Compton effect or from n-p or p-p collisions from neutrons and protons in the beam produced by materials upstream or downstream. In the first case, if one supposed the reaction cross section to be equal to the nucleon Thompson cross section, which seems reasonable experimentally,[19,20] this would give a contribution of 1 percent to the protons observed. These protons would fall in the angular interval 0° to 90° and if this effect were present we would find a proton contribution, after background subtraction, in the 64° to 90° interval. For the latter effect, calculations from known cross sections indicate a contribution of 2 percent, and an angular distribution radically different from that found in the 90° to 180° hemisphere. Following the subtraction due to impurities we obtain an effect from these sources equal to 3 ± 3 percent of the proton contribution from the π^0 reaction.

We estimate that the angle measurement of each track deviated from true with a mean square spread of 2.5°. This corresponds to an average energy resolution over all angles of about 10 Mev. The scanning involved less than 5 percent loss of tracks over-all. The possibility of missing the high-energy protons because of thin tracks was checked by scanning lower pellicles in the stack where the now lower-energy protons gave a clear track in pellicles with less general background. This correction amounted to about 30 percent at the highest energy. The total number of tracks recorded was about 1700. The reaction kinematics computed to get the diagram of Fig. 2 was done by assuming the mass of the π^0 meson to be 136 Mev. A more recent determination of the π^+, π^0 mass difference by Chinowsky and Steinberger[21] does not affect our results significantly. The line labeled G.C. in Fig. 2 shows the limitations in energy and angle of this detecting scheme. The line drawn across the bottom of the figure corresponds to the limit of protons energetic enough to traverse the gas to the emulsions. In addition, the lead protectors masked protons making an angle less than 8° with the beam.

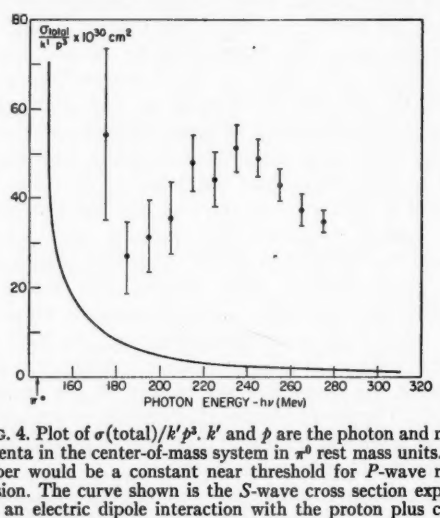

FIG. 4. Plot of $\sigma(\text{total})/k'p^3$. k' and p are the photon and meson momenta in the center-of-mass system in π^0 rest mass units. This number would be a constant near threshold for P-wave meson emission. The curve shown is the S-wave cross section expected from an electric dipole interaction with the proton plus charge exchange production.

[16] H. Levinthal and A. Silverman, Phys. Rev. **82**, 822 (1951).
[17] R. Littauer and J. Keck, Phys. Rev. **86**, 105 (1952).
[18] B. T. Feld *et al.*, Phys. Rev. **94**, 1000 (1954).
[19] A. Silverman (private communication). The nuclear Compton effect was measured to be less than 5 times Thompson cross section.
[20] Pugh, Frisch, and Gomez, Phys. Rev. **95**, 590 (1954).
[21] W. Chinowsky and J. Steinberger, Phys. Rev. **93**, 586 (1954).

TABLE I. Summary of experimental data.

Photon energy	A_0^0	A_1^0	A_2^0	A_2^+ Cal. Tech.[a]	A_2^+ Cornell[b]	$A_0^0+(5/3)A_2^0$
220	6.7±0.5	−2.5±1.3	− 5.9±2.2	−5.1	− 3.2±2.0	− 2.9±3.6
250	12.5±1.2	−2.0±2.3	− 7.8±4.3	−7.5	− 7.5±1.8	− 0.5±6.5
270	13 ±1.2	−2.0±1.5	− 8 ±3.5	−8.4	−11.4±2.0	− 1.9±5.5
290	18.3±1.3	−1.5±1.5	−17.4±3.1	−8.4		−11 ±4.5
320	17.3±1.4	+0.9±2.0	−10.7±4.0	−6.5		− 0.8±6.8

[a] See references 22 and 23.
[b] See reference 24.

IV. RESULTS

The total number of tracks in each energy interval was counted and the total cross section computed. A correction has to be applied since the full angular range is not quite observed. This is done by extrapolating the measured angular distribution assuming no higher power of $\cos\theta$ than $\cos^2\theta$. The lowest energy point (175 Mev) is computed by using the extrapolated front to back ratio which we measure at higher energies. The results are plotted in Fig. 3 with the results of other experiments,[2,6] where their differential cross sections have been reduced to total cross sections, by using our measured angular distribution. The behavior of the curve with energy is shown in Fig. 4 by plotting $\sigma/k'p^3$ against photon laboratory energy. p is the meson momentum and k' the photon energy in the center-of-mass system both being measured in π^0-meson mass units. One would expect a constant for this number near threshold; however, our points are well above threshold.

The tracks were divided into five energy intervals for an analysis of angular distribution. A least-squares fit to the formula

$$d\sigma/d\Omega = A_0^0 + A_1^0 \cos\theta + A_2^0 \cos^2\theta$$

was made. The results are shown in Table I.[22–24] From these coefficients a front-to-back ratio was computed and is plotted in Fig. 5.

V. DISCUSSION

If we allow all possible electromagnetic interaction leading to emitted mesons in angular momentum states $l \leq 1$, the angular distribution, which gives three parameters $(A_0^0 A_1^0 A_2^0)$, would not allow computation of the eight parameters (4 complex transition matrix elements) to describe the process. Watson's formalism shows that the phase angle of these matrix elements is given by the scattering phase shift so, with these given, we have 8 real numbers to be found which give the electromagnetic transition element through either a $\frac{3}{2}$ or $\frac{1}{2}$ isotopic spin state. In addition we can relate the π^+ to π^0 cross sections, giving then 6 numbers to calculate 8 unknowns. This is possible with π^+ and π^0 mesons from protons since the so called "recoil" terms appear in the isotopic spin, $\frac{1}{2}$, matrix with the same sign and relative magnitude. If we can use the threshold energy dependence to separate S and P states, we would have 8 numbers. Our experimental errors forbid such a project and we will confine our arguments to an analysis which assumes the largest contribution to come from a $P_{\frac{3}{2}}$ state.

On the above assumption, it is shown below that the total cross section is almost wholly a measure of the magnetic-dipole, $J=\frac{3}{2}$ interaction. The behavior with energy is not in general disagreement with models assuming a resonant interaction in this state. On Fig. 4 we have plotted a curve showing the contribution to the total cross section if we assumed an S-wave contribution through an electric dipole interaction with the proton plus charge exchange scattering of the π^+ meson in the S state; this contribution is below what we can observe.

The front to back ratio being less than one is an indication of the admixture of a different parity state

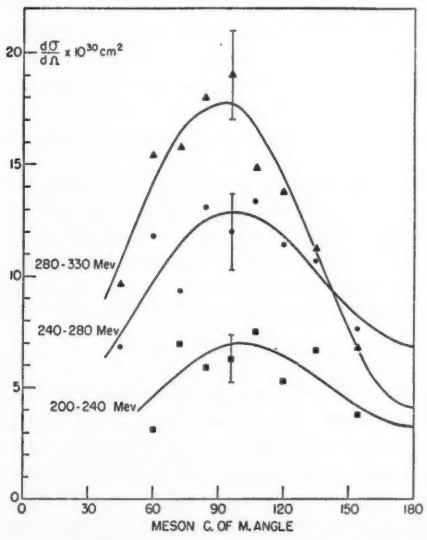

FIG. 5. Angular distribution of π^0 mesons in the center-of-mass system for three different energy intervals. A typical error (standard deviation) is shown on one point of each curve. The solid lines are the best fit to the expansion $d\sigma = A_0 + A_1\cos\theta + A_2\cos^2\theta$.

[22] Walker, Teasdale, Peterson, Vette, and Oakley (private communication).
[23] Tollestrup, Keck, and Worlock (private communication).
[24] Jenkins, Luckey, Palfrey, and Wilson, Phys. Rev. **95**, 179 (1954).

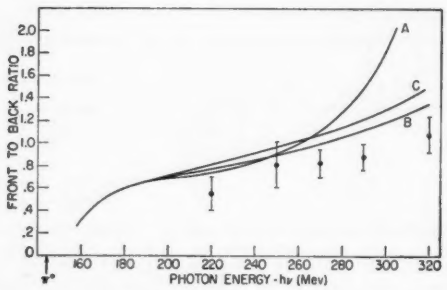

FIG. 6. Measured ratio of mesons produced in the forward hemisphere to back hemisphere in the center-of-mass system. The solid curves are taken from Watson's paper. They give the front to back ratio assuming predominant production in the $J=\frac{3}{2}$, $I=\frac{3}{2}$ state with S-wave production through an electric-dipole interaction with the proton and charge exchange production. The three curves are calculated then by assuming (A) Fermi-Metropolis (see reference 25), (B) Glicksman (see reference 26), (C) Martin scattering phase shifts (see reference 27).

and it seems logical to assume this an S state. Figure 6 shows that this asymmetry is consistent with Watson's formalism which explains the S state by the sum of charge exchange scattering and direct π^0 S-wave production through the proton dipole moment. It can be seen that our experiment favors those scattering phase shifts[25-27] where α_{33} goes thorugh 90° and the other P phase shifts are small. We may estimate the amount of S state by using this formalism and assuming that the interference between S and P terms is dominated by the $P_{\frac{3}{2}}$ scattering phase shift, α_{33}, (using Watson's notation):

$$d\sigma(\text{interference}) \sim 2\,\text{Im}(A^*C)\cos\theta \sim 2|A||C|\cos\alpha_{33}\cos\theta,$$

where $|A|$ and $|C|$ are proportional to the absolute values of the S and P matrix elements for electromagnetic production. Using the α_{33} of reference 26, we obtain

$$\sigma_{\text{total}}(S\text{ wave}) = (4\pm3)\times10^{-30}\text{ cm}^2$$

as an average between photon energies from 200 Mev to 300 Mev. This is about 3 percent of the total π^0 cross section. It is about 4 percent of the total π^+ S-wave cross section. The latter is obtained by assuming the main π^0 P-wave contribution to be through an isotopic spin $\frac{3}{2}$ state and therefore

$$\sigma^+(S\text{ wave}) \simeq \sigma^+ - \tfrac{1}{2}\sigma^0.$$

The amount of S-wave expected from an electric dipole interaction with the proton would be about $(\mu/M)^2$ times the π^+ S wave, where μ and M are the meson and nucleon mass respectively. This factor is 2 percent. In addition we expect charge exchange scattering proportional to $|\alpha_1-\alpha_3|^2$ which is of the same order of magnitude. α_1 and α_3 are the S-wave scattering phase shifts for isotopic spins $\frac{1}{2}$ and $\frac{3}{2}$ respectively.

Column 5 of Table I gives the number $A_0+(5/3)A_2$ which would be 0 for the magnetic dipole, $P_{\frac{1}{2}}$, term,

$$d\sigma \sim 5-3\cos^2\theta = 2+3\sin^2\theta.$$

It cannot be said that this experiment clearly proves a deviation from this behavior. However, there could be several explanations for departure from this angular distribution. We assume meson states of $l\leq1$ which is reasonable since the effect appears at low energies. One could have a magnetic dipole interaction leading to a $P_{\frac{1}{2}}$ state or an electric quardupole leading to a $P_{\frac{3}{2}}$ state. Experimentally these would be qualitatively distinguished, in the first case, by a rapid change in angular distribution as the scattering phase shifts in the $P_{\frac{1}{2}}$ and $P_{\frac{3}{2}}$ states changed with respect to one another and thereby changed the interference term. In the second case, if the interaction occurred through the main $\frac{3}{2}$, $\frac{3}{2}$ state the interference term would be independent of the phase shift, and the change in angular distribution would occur through the, presumably, slower changes in the electromagnetic transition elements. The slim evidence given here allows no choice between the two. It is of interest to calculate the contribution of electric quadrupole transitions to explain our results. Using Watson's notation,

$$\begin{aligned} d\sigma &\sim \tfrac{1}{2}|C|^2(5-3\cos^2\theta)+\tfrac{1}{2}\,\text{Im}(E^*C)(3\cos^2\theta-1) \\ &\qquad +\tfrac{1}{8}|E|^2(1+\cos^2\theta) \\ &= \tfrac{1}{2}|C|^2(5-3\cos^2\theta)\pm\tfrac{1}{2}|E||C|(3\cos^2\theta-1) \\ &\qquad +\tfrac{1}{8}|E|^2(1+\cos^2\theta), \end{aligned}$$

we obtain as an average from 200 to 340 Mev,

$$|E|/|C| = 0.25\pm0.18.$$

The contribution to the total cross section from the quadrupole term is then 0.5±0.5 percent of the main term, or roughly $(0.5\pm0.5)\times10^{-30}$ cm². Preliminary calculations by Chew and Salzman[14] on π^0 photoproduction indicate, on theoretical grounds, an expected quadrupole term of this order of magnitude and sign.

The presence of an additional P-wave term is also expected from the angular distribution of π^+ mesons as measured by the California Institute of Technology groups.[22,23] At high energies (400 Mev) they find that the coefficient of the $\cos^2\theta$ term, A_2^+, becomes positive which would be possible only with another radiative transition, P-wave term. Feld has shown that their results can be described by the addition of the electric quadrupole interaction.

Since there is doubt about the detailed character of the P-wave angular distribution, we cannot analyze the π^+ cross section into a P- and S-wave contribution uniquely. However, if all P-wave contributions were through an isotopic spin $\frac{3}{2}$ state the ratio of the $\cos^2\theta$ term in π^0 and π^+ angular distributions would be 2 to 1.

[25] E. Fermi and N. Metropolis (unpublished).
[26] M. Glicksman, Proceedings of the Fourth Annual Rochester Conference on High Energy Nuclear Physics (University of Rochester, Rochester, 1954).
[27] R. L. Martin, Phys. Rev. 94, 765 (1954).

This coefficient, A_2^+, in the photoproduction of π^+ mesons, as determined at Cornell[24] and the California Institute of Technology,[22,23] is tabulated in Table I. At high energies the ratio of 2 to 1 appears correct. At lower energies the agreement is less satisfactory.

VI. CONCLUSIONS

The behavior of the π^0 photoproduction cross section between gamma-ray energies of 170 Mev and 320 Mev is well fitted by a model with over 90 percent of the production going through a magnetic dipole $J=\frac{3}{2}$, isotopic spin $\frac{3}{2}$, state resonant at about 300 Mev. There is a small amount (3 percent) of S-state production consistent with direct production of π^0 mesons by interaction with the dipole moment of the proton and through charge exchange of charged mesons. The interference of S and P waves is such as to favor the α_{33} scattering phase shift going through 90°. There is a suggestion of another mode of P-wave production, perhaps by electric quadrupole radiation through a $J=\frac{3}{2}$ state or magnetic dipole through a $J=\frac{1}{2}$ state.

The authors wish to thank particularly Mrs. T. Kallmes, Mrs. D. Calhoun, Mrs. K. Lurie, and Mr. J. Russell for their tireless and invaluable aid in the scanning and measuring they did on the nuclear emulsions.

PHYSICAL REVIEW VOLUME 97, NUMBER 1 JANUARY 1, 1955

Analysis of a High-Energy Cosmic-Ray Shower. I. Soft Component and Trident Process*

M. KOSHIBA AND M. F. KAPLON
University of Rochester, Rochester, New York

(Received August 5, 1954)

An analysis is presented of the soft component arising from a high energy nuclear shower ($\sim 3\times10^{13}$ ev) observed in stripped emulsion. The chief results obtained are: (1) The production ratio of neutral π mesons to charged shower particles is 0.50 ± 0.11; (2) the lifetime of the neutral π meson is found to be $(1_{-0.5}^{+1})\times10^{-14}$ sec; (3) the mean free path for direct electron pair production by high-energy electrons is found to be 4.4 and 1.1 radiation units for electrons in the energy intervals 1 to 10 Bev and 10 to 100 Bev, respectively.

INTRODUCTION

THE event considered in this paper was found in a stack of twenty-four 4 in.×6 in.×400μ G-5 stripped emulsions, packed in direct contact with each other and flown for 8 hours at 102 000 ft at 55° geomagnetic latitude. The emulsions were mounted on glass before development and processed by the usual temperature methods. After development each plate was cut into four 3 in.×2 in. sections for microscopic observation. The emulsion stack was then consecutively mounted and aligned on Lucite frames using heavy nuclei as markers.[1]

The event is of the type $3+36_p$,[2] and was so situated that the shower particles traversed 3.1 cm before leaving the outside edge of the stack; the average path length per emulsion was 2 mm. Of the 36 shower particles emanating directly from the star, 25 formed a narrow cone of half opening angle $=1.08\times10^{-2}$ radian. Due to the high degree of alignment attained, each individual track could be followed through successive emulsions without any ambiguity (target diagrams were made in each emulsion). After traversing 3.97 mm one of the shower particles underwent a nuclear interaction producing a $0+12_p$ star (I_1) in which two of the secondary particles were in the narrow cone of the original event; one of these was almost exactly in the direction of the particle producing the star I_1 and it made another nuclear interaction of the type $13+16_p$(I_2) after traversing an additional 24 mm.

The angular distribution of the primary star is plotted in Fig. 1. On the assumption that the primary was a proton, the kinematical energy is found to be $3.7\times10^4Mc^2$ using the median angle method[3] and $(3.4_{-2.5}^{+3.5})\times10^4Mc^2$ using the statistical method of Castagnoli *et al.*[4]

ENERGY MEASUREMENTS OF VERY HIGH-ENERGY PARTICLES

Due to the very high energy in the soft component produced in this event, the conventional method of measuring the multiple Coulomb scattering fails. However, the high degree of collimation makes possible the measurement of the relative scattering between particles.[5] In this method we measure the relative separation of two tracks and derive the mean second difference ($\bar{D}'_{\rm rel}$) for a fixed cell length t. In this type of

* This research was supported in part by the U. S. Air Force through the Office of Scientific Research of the Air Research and Development Command.

[1] J. Crussard *et al.*, Phys. Rev. **93**, 253 (1954).

[2] This is the notation introduced by the Bristol group; $B+S_p$ means a star with B gray+black prongs ($I/I_0\geq1.5$) and S shower particles ($I/I_0<1.5$) produced by a singly charged particle (p). The subscript n denotes a neutral primary.

[3] M. F. Kaplon and D. M. Ritson, Phys. Rev. **88**, 386 (1952).

[4] C. Castagnoli *et al.*, Nuovo cimento **10**, 1539 (1953).

[5] Lord, Fainberg, and Schein, Phys. Rev. **80**, 970 (1950).

FIG. 1. Integral angular distributions of the charged particle. and electron pairs arising from the primary nuclear interactions The solid circles represent shower particles and the crosses represent electron pairs $E_p \sim (3.4_{-2.5}^{+2.6}) \times 10^4 Mc^2$.

measurement stage motion noise is entirely eliminated and the error introduced by distortion is also eliminated except for any local distortions in regions whose dimensions are of the order of the relative separation between the tracks being scattered; these local distortions are caused by small-size contaminants or crystallization and can usually be eliminated by inspection. The only sources of error left to contribute to the noise are those due to hair line setting and the random distribution of the grains along the tracks. Since we can reset the direction of the hair line in each measurement to coincide with the direction of the two tracks (which are almost parallel), this source can be reduced considerably and is evidently independent of cell size. The overall noise $\bar{N}$ resulting from the above two sources was found to be 0.1μ for the hair line setting on an individual minimum ionizing track; thus the noise for the relative scattering measurement is $\sqrt{2} \times 0.1\mu$ and the true relative scattering is $\bar{D}_{\text{rel}} = (\bar{D'}_{\text{rel}}{}^2 - 2\bar{N}^2)^{\frac{1}{2}}$. $\bar{D}_{\text{rel}}$ may also be obtained by use of the third differences or by noise elimination between cell sizes of different length. The relative scattering in degrees/100μ between the tracks 1 and 2 is given if both particles have unit charge, by

$$\bar{\alpha}_{1,2} = 0.573 \bar{D}_{1,2}/(t/100)^{\frac{1}{2}} = K[1/(p\beta c)_1{}^2 + 1/(p\beta c)_2{}^2]^{\frac{1}{2}},$$

where t is the cell length, K is a constant slightly dependent on t,[6] p is the momentum, and βc the velocity. The lower and higher momentum of the two particles satisfy

$$(p\beta c)_{1,2} \leqslant (p\beta c)_{\text{low}} \leqslant \sqrt{2}(p\beta c)_{1,2} \leqslant (p\beta c)_{\text{high}},$$
$$(p\beta c)_{\text{low}} + (p\beta c)_{\text{high}} \geqslant 2\sqrt{2}(p\beta c)_{1,2},$$

where we define $(p\beta c)_{1,2} = K/\bar{\alpha}_{1,2}$. If relative scattering measurements are done between tracks 1, 2 and 3, then

$$\bar{D'}_{i,j}{}^2 = \bar{D}_i{}^2 + \bar{D}_j{}^2 + 2\bar{N}^2;$$
$$\bar{D}_i{}^2 = (\bar{D'}_{i,j}{}^2 + \bar{D'}_{i,k}{}^2 - \bar{D'}_{j,k}{}^2 - 2\bar{N}^2)/2,$$

[6] L. Voyvodic and E. Pickup, Phys. Rev. 85, 91 (1952).

and the individual momenta p_i are in principle obtainable (in practice, of course, sufficient statistics must be available to make the fluctuations smaller than the noise[7]). For the value of $\bar{N} = 0.1\mu$ and 2000μ cells one can measure values of $p\beta c$ up to $\sim$40 Bev. (it is worth noting here that for this type of measurement successive cells need not be in the same emulsion). For the measurements done in this paper 500μ cells were used over the central 1500μ of the tracks in each emulsion in order to reduce to a minimum any extreme distortions at the air or glass surfaces of the emulsion.

THE SOFT COMPONENT

The detailed survey of the shower in each emulsion showed that in addition to the original 25 shower particles in the narrow core, 29 electron pairs and 12 apparent tridents[8] were produced within 30.8 mm from

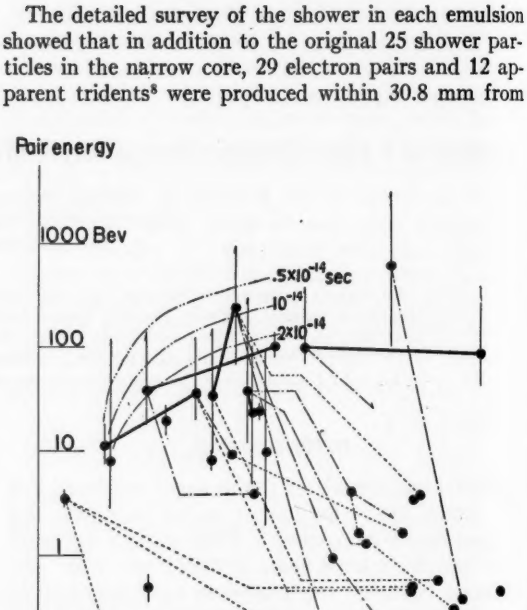

FIG. 2. Genetic relation of the electron pairs observed in the forward cone of the primary nuclear interaction.

[7] The relative fractional error in this measurement will be

$$\delta(\bar{D}_i) \approx (c^2/4q)^{\frac{1}{2}}(\Delta_{ij,i}{}^2 + \Delta_{jk,i}{}^2 + \Delta_{kj,i}{}^2 + 2\bar{n}_i{}^2)^{\frac{1}{2}},$$

where q is the number of independent measurements, $\Delta_{ij,i} = \bar{D}_{i,j}/\bar{D}_i$, $\bar{n}_i = \bar{N}/\bar{D}_i$ and $c \sim 1$. A further point to be noted here is that scattering measurements on electron tracks cannot extend over very long path lengths due to the high probability for bremsstrahlung. This approach is indeed better suited for measurements on the hard component.

[8] In emulsion the term trident is qualitatively applied to an event in which an electron track at minimum ionization suddenly changes into a track at 3×minimum ionization, this track subsequently resolving itself into three minimum ionizing electron tracks. Events of this nature were first observed by C. F. Powell, Nuovo cimento Suppl. 6, 370 (1949) and Bradt, Kaplon, and Peters, Helv. Phys. Acta 23, 24 (1950). M. Block and D. T. King

the shower origin in the cone defined by the narrow core. The energies of these events and the distance of their origin from the original star are plotted on a semi-logarithmic scale in Fig. 2. Solid broad lines connecting two high-energy pairs indicate they are spatially correlated, being less than 10μ apart in the plane normal to the shower axis. A dotted line connecting a high-energy pair with one of lower energy means that these are within 10μ of each other in the plane normal to the shower axis and a dashed line connecting two pairs means that the origin of the created pair is spatially unresolvable ($\leqslant 0.2\mu$) from the parent electron track; these are the apparent tridents. From this figure we can easily separate the high-energy electron pairs directly produced by the γ rays from π^0 decay from those of secondary origin.

LIFETIME OF THE π^0 MESON

In order to estimate the lifetime of the π^0 meson we consider the distribution $P(x)$ of converted electron pairs from π^0 decay for observations extended to an infinite length. This is given by[9]

$$P(x)dx=[2/(\lambda_c-\lambda_\tau)][\exp(-x/\lambda_c)-\exp(-x/\lambda_\tau)]dx,$$

where $P(x)$ is the average number of primary electron pairs arising from the 2γ decay of a π^0 meson of energy $\gamma\mu c^2$, the γ rays being converted in dx at a distance x from the shower origin; λ_c is the γ ray conversion length = (97) (radiation length) and $\lambda_\tau=\gamma\beta c\tau$, τ being the proper lifetime of the π^0 meson. The mean conversion distance and its rms deviation are given by $\langle x\rangle=\lambda_c+\lambda_\tau$ and

$$[\langle(x-\langle x\rangle)^2\rangle]^{\frac{1}{2}}=(\lambda_c^2+\lambda_\tau^2)^{\frac{1}{2}}\approx\lambda_c;\quad \lambda_c\gg\lambda_\tau.$$

Since our observation length is $\sim\lambda_c$, λ_τ is determined by the slope of the near edge of the pair distribution as shown schematically in Fig. 3. This method has the advantage of requiring neither a knowledge of the cascade development nor an accurate knowledge of λ_c (or its energy dependence, if such exists). It suffers, however, from poor statistics, a defect which can be remedied in time. Application of this method results in a value for $\tau=(1_{-0.5}^{+1})\times10^{-14}$ sec. (The energy-distance relations for $\tau=0.5\times10^{-14}$, 10^{-14}, and 2×10^{-14} sec are plotted in Fig. 2.)

NEUTRAL TO CHARGE RATIO

The neutral to charge ratio R is defined as $R=N_{\pi^0}/N_s$, where N_{π^0} is the number of π^0 mesons produced in the shower and N_s is the total number of charged shower particles ($N_s=N_s'+N_{\pi^\pm}$, where N_s' thus represents

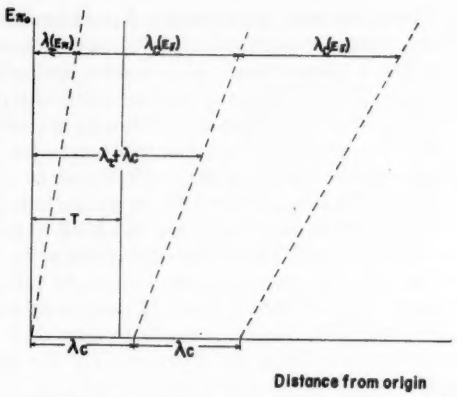

FIG. 3. Schematic representation of method of determining π^0 lifetime. (In this diagram an allowance has been made for a possible energy variation of the conversion length λ_c, of γ rays.)

those charged shower particles which are not charged π mesons). N_s is a directly measurable number but N_{π^0} must be deduced from observations on the soft component in the shower, assumed to originate from the 2γ decay of π^0 mesons. In this section we deduce the ratio R for this shower by two different methods (which however do not give statistically independent estimates).

The two methods differ only in the way of estimating N_{π^0}, the original number of neutral π mesons. From Appendix A the average number of primary pairs within a distance X from the point of emission of a single π^0 meson of energy $E_{\pi^0}=\gamma\mu c^2$ is given by

$$P(\tau,\gamma)=2\{1-[1/(1-\lambda_\tau(\gamma)/\lambda_c)]\times[\exp(-X/\lambda_c)-(\lambda_\tau(\gamma)/\lambda_c)\exp(-X/\lambda_\tau(\gamma))]\}.$$

To deduce the number of initial π^0 mesons from the above relation the number of primary pairs must be known. Inspection of Fig. 2 strongly suggests that those pairs of $E>10$ Bev are of a primary nature (arising directly from π^0 decay γ rays) while those with $E<10$ Bev are chiefly secondary. To apply the above equation those pairs with $E>10$ Bev which are not classified as bremsstrahlung or trident pairs were grouped into two classes: (1) $10\leqslant E\leqslant100$ Bev and (2) $E>100$ Bev. The first class has ten pairs with $\langle E\rangle=42$ Bev and the second three pairs with $\langle E\rangle=320$ Bev. Using the above equation for these two energy classes, the initial number of π^0 mesons in the narrow cone containing 26 charged shower particles (one extra charged shower particle arises in this cone from the interaction I_1) is deduced and we find $R=0.53\pm0.17$ for $\tau=10^{-14}$ sec and $R=0.48\pm0.16$ for $\tau=0.5\times10^{-14}$ sec. In this estimate no correction has been made for bremsstrahlung accompanying meson production.[10] If it is assumed that the majority of charged shower particles are π mesons this correction is quite small and reduces the above values for R by approximately 0.02.

[Phys. Rev. **95**, 171 (1954)] review the observations on tridents and make a quantitative estimate of the background of pseudo-tridents. These results from the conversion of the highly collimated bremsstrahlung accompanying fast electrons and are qualitatively indistinguishable from the true tridents which represent electron pair production by an electron.

[9] This equation is obtained by differentiating Eq. (2A) of Appendix A.

[10] L. Schiff, Phys. Rev. **76**, 89 (1949).

An alternative way of estimating N_{π^0} which is free of this possible ambiguity is to use those 5 groups of pairs in Fig. 2 (those connected by a solid line) which are strongly spatially correlated and for which each pair of the group can be considered as a directly converted pair from the same π^0 decay. For this estimation the resulting expression for P_2 of Appendix A must be used. With $\langle E_{\pi^0}\rangle = 150$ Bev and $\lambda_e = 3.75$ cm we find using P_2 that $R = 0.71 \pm 0.28$ for $\tau = 10^{-14}$ sec and $R = 0.66 \pm 0.26$ for $\tau = 0.5 \times 10^{-14}$ sec. The values of R obtained by the above two methods are rather sensitive to the value of λ_e (in both instances we use $\lambda_e = 3.75$ cm in emulsion); if λ_e is reduced by a factor of two the values of R obtained are also reduced by approximately the same factor.

A check on the determinations of R given above can be made by making use of only those observations within distances small compared to the conversion length.[11] This method is essentially identical to the first except that it restricts itself to consideration only of those pairs lying within the first 13 mm; this restriction further precludes the possibility of including secondary γ ray pairs. We have applied this method for the distances 5, 7, 9, 11, and 13 mm from the shower origin with the inclusion of all γ-ray pairs of $E > 1$ Bev which do not appear to be of a secondary nature and obtain for the corresponding values of R: 0.48, 0.47, 0.46, 0.46, and 0.53. In applying this method a correction has been made for bremsstrahlung accompanying meson production (assuming mainly $\pi^{\pm}$ mesons) and a finite π^0 lifetime of 5×10^{-15} sec has been taken into account by decreasing the available γ ray path length assuming $\langle E_{\pi^0}\rangle \approx 50$ Bev. The average value of R determined this way is 0.48 ± 0.20.

From the above observations we deduce the best value of R as 0.50 ± 0.11 (for $\tau = 5 \times 10^{-15}$ sec) in excellent agreement with previous results for very high energy interactions reported from this laboratory,[3,11] but rather different from the result of $R = 0.25$ reported by the Bristol group.[12]

TRIDENT PROCESS

By an apparent trident we mean an event where an electron pair originates in the emulsion so close to another electron that its origin is spatially unresolvable ($\leqslant 0.2\mu$) from the accompanying electron. As has been pointed out previously,[8] the true trident process, electron pair production by an electron, is qualitatively indistinguishable from the pseudo-trident process which is the conversion of highly collimated accompanying bremsstrahlung. An attempt to account for this background on a statistical basis has been made by Block and King;[8] an extension of their work will be presented in Appendix B.

We attempt here at first to eliminate this background (referred to as B.S. pairs) by the imposition of certain criteria which must be satisfied by an apparent trident for it to be classified as direct pair production by an electron. The criteria are:

$$\theta_i > [\bar{\alpha}_i^2(t) + \bar{\alpha}_N^2]^{\frac{1}{2}} \quad \text{for all } i = 1, 2, 3, \tag{1}$$

$$\theta_1 > [\bar{\alpha}_1^2(t) + \bar{\alpha}_N^2]^{\frac{1}{2}} \quad \text{for } E_1 > E_2, E_3. \tag{2}$$

In the above, θ_i is the deflection angle of the ith electron, $\bar{\alpha}_i(t)$ the deflection due to its multiple Coulomb scattering in the distance t used for measurement of deflection, $\bar{\alpha}_N$ the contribution as noise of the scattering of the the reference track used to measure the deflection, and E_i the energy of the ith electron; here $i = 1$, 2, and 3 refer to the three electrons forming the trident. The first criterion is to be applied when no energy distinction can be made between the three electrons and ensures that at least the incident electron has been deflected at the point of origin of the trident; the second criterion applies to the case in which the highest energy electron of the trident has been deflected but does not necessarily insure that the trident primary was deflected. In Table I all apparent tridents are listed. Column 1 identifies the event listing the three members of the trident T_x^i ($i = 1$, 2, 3), column 2 gives the primary energy in Bev and the origin of the incident electron (o refers to the energy estimate by opening angle and s by scattering), column 3 the distance of the parent electron from its source, column 4 the projected deflection angle in milliradians, column 5 the energy in Bev of each member of the trident, and column 6 the identification as a true trident using criteria (1) or (2) or a ? indicating no verdict.

In Table II the tridents are divided into two groups according to the primary electron energy (column 1), the second and third columns give the average and the total track length of all the electrons in each energy region (in radiation units), the fourth the number of observed B.S. pairs, the fifth the number of observed apparent tridents, the sixth the total number of B.S. pairs corrected by the method of Appendix B, the seventh the number of true tridents, the eighth and ninth the mean free path in radiation units for B.S. pairs and tridents, and the tenth an upper limit for the trident mean free path using criteria (1) and (2). (In Table II we have not included one of the observed pairs in the soft development as a B.S. pair since there is a strong indication from its direction that it results from the secondary interaction I_1.)

In applying the criteria (1) and (2) given previously

[11] Kaplon, Walker, and Koshiba, Phys. Rev. **93**, 1424 (1954).

[12] R. R. Daniel *et al.*, Phil. Mag. **43**, 753 (1952); J. H. Mulvey, Proc. Roy. Soc. (London) **221**, 367 (1954). Both find $R = 0.25$ in marked contrast with our result. It should be pointed out that both these experiments were done on glass backed emulsions. In particular, the latter experiment, which derives its result from the analysis of a very large star, suffers particularly from this disadvantage in that all electron pairs could not be positively identified due to the interposition of the glass backing. In addition, in this analysis, the use of cascade theory, especially at the beginning of the development is subject to error since the slope of the rise in the development is quite sensitive to a small admixture of high-energy photons.

TABLE I. Observational data on the parent electrons forming tridents and the electron members of the tridents.

Trident	Primary origin and energy (Bev)		Distance (mm) of primary from its origin	Projected angles of deflection (milliradians)	Energies of trident members (Bev)	Identification
T_1^1				10 ± 8.5	0.082	
T_1^2	P_6^2	$18(o)_{-8}^{+42}$	2.4	-1.02 ± 1.8	0.83	(2)
T_1^3		$>17(s)$		1.67 ± 0.22	>9.0	
T_2^1				-0.38 ± 0.96	1.2 ± 0.4	
T_2^2	P_{10}^1	$18(o)_{-13.2}^{+\infty}$	7.15	-1.08 ± 0.5	$2.6_{-2.06}^{+3.6}$	(a)
T_2^3		$5(s)_{-1.7}^{+5.7}$		-0.2 ± 0.36	$4.6_{-1.0}^{+2.0}$	
T_3^1				...	$1.7_{-0.4}^{+0.9}$	
T_3^2	P_{11}^2	$19(o)_{-13}^{+\infty}$	6.85	...	>3.7	(?)
T_3^3		$3.0(s)_{-1.2}^{+6.1}$		...	$3.35_{-0.8}^{+1.8}$	
T_4^1				...	>2.3	
T_4^2	P_{11}^1	$19(o)_{-13}^{+\infty}$	7.8	...	$0.6_{-0.15}^{+0.3}$	(?)
T_4^3		$2.8_{-1.0}^{+4.8}$		...	$0.67_{-0.22}^{+0.34}$	
T_5^1				0.34 ± 0.3	>17	
T_5^2	P_{19}^1	$>50(o)$	4.7	0.14 ± 3.6	0.27	(2)
T_5^3		$\sim30(s)$		14.3	<0.1	
T_6^1				1.7 ± 1.5	...	(2)
T_6^2	P_{16}^2	$\sim100(o)$	11.3	-5.0 ± 1.5	...	
T_6^3		$>13.5(s)$		-24.3 ± 1.5	...	
T_7^1				...	$1.75_{-0.4}^{+0.9}$	
T_7^2	T_3^3	$3.35_{-0.8}^{+1.8}$	0.41	...	$1.05_{-0.27}^{+0.55}$	(?)
T_7^3				...	$0.55_{-0.14}^{+0.28}$	
T_8^1				24.6 ± 0.75	...	
T_8^2	T_9^2	>3.7	6.93	37.4 ± 0.75	...	(1)
T_8^3				57.2 ± 0.75	...	
T_9^1				-3.7 ± 0.75	...	
T_9^2	P_{12}^2	$<92(o)$	14.1	0.65 ± 0.75	...	(?)
T_9^3		$>68(s)$		11.3 ± 0.75	...	
T_{10}^1				16.1 ± 2.0	0.35	
T_{10}^2	P_7^2	$\sim200(o)$	6.39	6.9 ± 1.7	0.59	(?)
T_{10}^3		$>35(s)$		0.08 ± 0.15	...	
T_{11}^1				0.013 ± 0.2	...	
T_{11}^2	P_7^1	26–35(s)	6.88	53.7 ± 50	0.0091	(?)
T_{11}^3				-27.5 ± 3.7	0.042	
T_{12}^1				...	0.022	
T_{12}^2	$T_{10}^3(P_7^2)$	$\sim200(o)$	$12.49(P_7^2)$	...	0.035	(?)
T_{12}^3		$>35(s)$	$6.1(T_{10}^3)$	...	...	

[a] See text.

we have given criterion (1) a weight factor of unity since it certainly ensures that the incident electron was deflected at the point of origin of the trident; a weight factor of $\frac{1}{2}$ is given criterion (2) due to its weaker nature (this is due to the impossibility of determining in the trident the continuation of the incident electron). In addition event T_2 is given a weight of $\frac{1}{2}$ because of the low probability of finding a B.S. pair as an apparent trident for the energy and distance from the parent of this event. We then find $N_T \geq 1.5$ for both energy ranges resulting in $\lambda_T \leq 10.45$ radiation units for $1 \leq E \leq 10$ Bev and $\lambda_T \leq 4.72$ radiation units for $10 < E \leq 100$ Bev.

To improve the direct estimation of an upper limit for λ_T we have calculated in Appendix B the contribution of the converted accompanying bremsradiation to the apparent trident cases. Applying the results of

TABLE II. Classification of electrons into energy groups and the numbers of tridents and converted bremsstrahlung γ rays (B.S. pairs) associated with these electrons.

Energy range of electrons in Bev	Average electron track length (rad. lengths)	Total track length (rad. lengths)	No. of observed B.S. pairs	No. of apparent tridents	Corrected No. of B.S. pairs	Corrected No. of tridents	$\lambda_{B.S.}$ (rad. lengths)	λ_T (rad. lengths)	Upper limit for λ_T by direct identification
10–100	0.6	7.08	4	8	5.6	6.4	1.26	1.1	4.72
1–10	0.56	15.69	8	4	8.5	3.5	1.85	4.5	10.45

Appendix B we find that 1.6 of the apparent tridents in the high energy range and 0.5 in the low energy range could be due to B.S. pairs. The resulting mean free paths turn out to be $\lambda_T=4.5$ and 1.1 radiation units for $1\leqslant E\leqslant 10$ Bev and $10<E\leqslant 100$ Bev respectively and the mean free path for B.S. pairs in radiation units is $\lambda_{B.S.}=1.85$ and 1.26 respectively for the above two energy ranges.

A check on the above figures is furnished as follows. A high energy electron in one radiation unit will emit on the average ≈ 3.2 photons with energy $>(1/10)$ the primary electron energy, so that $\lambda_{brems}\approx 1/3.2$. Since $\lambda_{B.S.}$ should approximately equal $\lambda_{brems}+\lambda_{conv}$, we find $\lambda_{B.S.}\approx 0.3+9/7=1.6$ in good agreement with the values for $\lambda_{B.S.}$ obtained above.

CONCLUSIONS

The analysis of the soft component arising from a very high-energy nuclear interaction has given the following results.

(a) The production ratio of neutral π mesons to charged shower particles for this event is determined as $R=0.50\pm 0.11$ in agreement with previous results from this laboratory[3,11] and others,[13] but in disagreement with a lower value reported by the Bristol group.[12] The determination of this ratio is of importance for its implications with respect to heavy-meson production at high energies. Since

$$R=N_{\pi^0}/(N_{\pi^\pm}+N_s')=(N_{\pi^0}/N_{\pi^\pm})/(1+N_s'/N_{\pi^\pm}),$$
$$N_s'/N_{\pi^\pm}=(N_{\pi^0}/N_{\pi^\pm})/R-1,$$

a knowledge of R and the ratio $N_{\pi^0}/N_{\pi^\pm}$ will set an upper limit to the relative production efficiency of heavy mesons as compared to $\pi^\pm$ mesons (it is an upper limit since N_s' may contain some protons as well as heavy mesons). We assume that charge independence holds at these high energies so that $N_{\pi^0}/N_{\pi^\pm}=0.5$; we then find that $N_s'/N_{\pi^\pm}<0.28$ implying that particles other than π mesons are quite inefficiently produced at these high energies. (In this connection it is worth noting that Sitte, Froehlich, and Nadelhaft,[14] in a study of electron production in high-energy nuclear interactions, ~10 to 100 Bev, have found that the fractional energy transfer to the electron component is constant or slightly increasing for energies above 20 Bev. This is inconsistent with the result expected if the Bristol value of $R=0.25$ is correct, since then heavy meson production should compete with π meson production and if charge independence is assumed to hold, the fractional energy transfer to the electron component should decrease by about $\frac{1}{2}$ in the absence of any other source of the soft component. It seems to us that their results favor the observations reported in this paper.)

The conclusions stated in this paragraph rest upon the validity of charge independence at high energies and the assumption that directly produced π^0 mesons are the sole source of high-energy γ rays in nuclear interactions. If other sources of γ rays or π^0 mesons should exist, these conclusions are invalid; however in this case the γ rays must be either directly produced or be the decay products of very short-lived particles other than π^0 mesons having a lifetime $<10^{-14}$ sec and the π^0 mesons if secondary in nature must be decay products of unstable particles of even shorter lifetime.

(b) The lifetime of the π^0 meson is estimated to be $(1_{-0.5}{}^{+1})\times 10^{-14}$ sec in good agreement with previous values reported in the literature.[15]

(c) The mean free path for an electron to produce an electron pair (trident process) was found to be 4.5 and 1.1 radiation lengths for electron energies in the range 1 to 10 and 10 to 100 Bev, respectively.[16] Though the statistics are low it is believed that these values are not in error by more than a factor of two. This result, which for the high energy range (>10 Bev) is in rather marked disagreement with theory,[17] implies that for these energies the trident process becomes of comparable importance with bremsstrahlung and pair conversion in the soft cascade development. If further work should substantiate the validity of the results reported in this paper, the high-energy soft cascade (as well as the theory of the trident process) should certainly be reassessed.

We should like to express our appreciation to Miss B. Hull for her assistance in scanning and to the Office of Naval Research for its aid in obtaining the balloon exposure.

APPENDIX A

We consider a π^0 meson of energy $E_{\pi^0}=\gamma\mu c^2$ and proper lifetime τ. Let γ_0 be the γ-ray conversion length and $\lambda_\tau=\gamma\beta c\tau$ the decay length for the π^0 meson decay into two γ rays. The probability that the π^0 meson decays in dy at a distance y from its point of origin, the first of the two γ rays converts at t_1 in dt_1 and the

[13] Lal, Pal, and Rama (private communication); they find $R=0.4\pm 0.08$ for the energy region 50 to 250 Bev/nucleon. P. Freier and J. Naugle, Duke Conference on Cosmic Radiation (unpublished), find $R=0.46\pm 0.09$ from the analysis of a very high-energy interaction produced by a heavy nucleus.

[14] Sitte, Froehlich, and Nadelhaft, Phys. Rev. (to be published). We are indebted to the authors for a prepublication copy.

[15] Kaplon, Peters, and Ritson, Phys. Rev. **85**, 932 (1952); R. R. Daniel *et al.*, Phil. Mag. **43**, 753 (1952); J. J. Lord *et al.*, Phys. Rev. **87**, 538 (1952), B. M. Amand, Proc. Roy. Soc. (London) **220**, 183 (1953): the last paper reviews the results, to that date, on the lifetime of the π^0 meson and has a complete bibliography.

[16] P. Freier and J. Naugle, Duke Conference on Cosmic Radiation and private communication; for electron energies $E>2$ Bev, and extending up to 50 Bev, they find the trident mean free path $\lambda_T\leqslant 11$ cm of emulsion or 3.7 radiation units in excellent agreement with the results reported here.

[17] Block, King, and Wada, Phys. Rev. **96**, 1628 (1954), have recently evaluated and compared the theoretical predictions for the true trident process. From their results we obtain $\lambda_T\approx 14$ and 8 radiation units for electron energies of 10 and 100 Bev respectively. These values correspond to the cross sections with inclusion of screening. The corresponding values for the unscreened cross sections are approximately 12 and 5.5 radiation units for electron energies of 10 and 100 Bev. We are indebted to Drs. Block, King, and Wada for a prepublication copy of their paper.

second at t_2 in dt_2 (measured from the origin) is given by:

$$P(y,t_1,t_2)dydt_1dt_2=\exp(-y/\lambda_\tau)(dy/\lambda_\tau)\times\exp[-(t_1-y)/\lambda_e](dt_1/\lambda_e)\times\exp[-(t_2-y)/\lambda_e](dt_2/\lambda_e). \quad (1A)$$

The probability of observing both converted γ rays from the single π^0 meson within a distance X from the origin is given by:

$$P_2=\int_0^X dy\int_y^X dt_1\int_y^X dt_2 P(y,t_1,t_2).$$

The probability that only one γ ray is converted within the distance X from the origin is given by

$$P_1=2\int_0^X dy\int_y^X dt_1\int_X^\infty dt_2 P(y,t_1,t_2).$$

The above integrations are easily performed and one then finds that the probable number of pairs observed at a distance X from the origin arising from a single π^0 meson is:

$$2P_2+P_1=2\{1-[1/(\lambda_e-\lambda_\tau)]\times[\lambda_e\exp(-X/\lambda_e)-\lambda_\tau\exp(-X/\lambda_\tau)]\}. \quad (2A)$$

APPENDIX B

In this appendix we calculate the background contribution from the conversion of the bremsstrahlung accompanying high energy electrons to the trident process (pseudo-tridents).[18] To calculate the probability of finding a converted bremsstrahlung pair within a certain distance of the parent electron, we need to consider the angles of emission of the γ rays as well as the scattering of the parent electron. The former effect is important for those γ rays which have not travelled far before conversion into electron pairs, whereas the latter is important for those γ rays which have travelled a considerable distance before conversion into electron pairs.

Consider a fast electron moving in the x direction incident on an absorber in the xy plane. The distribution in y of the displacement due to multiple Coulomb scattering of the electron projected onto the xy plane after traversing a distance t has been derived by Rossi and Greisen[19] and is given by

$$H(t,y)=(1/\pi)^{\frac{1}{2}}(3w^2/4t^3)^{\frac{1}{2}}\exp(-3w^2y^2/4t^3), \quad (B1)$$

where the notation above is that of Rossi and Greisen.

If the reference axis is inclined to the x direction by a small angle θ_0, the distribution is given by

$$H(t,y,\theta_0)=(1/\pi)^{\frac{1}{2}}(3w^2/4t^3)^{\frac{1}{2}}\exp[-3w^2(y-\theta_0 t)^2/4t^3]. \quad (B1')$$

We assume a Gaussian distribution for the angle of emission of the γ rays by the electrons with the root-mean-square angle α:

$$P(\theta_0)d\theta_0=(1/2\pi\alpha^2)^{\frac{1}{2}}\exp(-\theta_0^2/2\alpha^2). \quad (B2)$$

The probability distribution of the separation between the γ ray and its parent electron at a distance t from the point of emission of the γ ray will be given by

$$Q(t,y)=\int_{-\infty}^{\infty}P(\theta_0)H(t,y,\theta_0)d\theta_0=(1/\pi t^2)^{\frac{1}{2}}(1/(4t/3w^2+2\alpha^2)^{\frac{1}{2}})\times\exp[-(y/t)^2(1/(4t/3w^2+2\alpha^2)]. \quad (B3)$$

A fast electron traversing an absorber will emit a spectrum of bremsstrahlung γ rays; we denote the mean free path for emitting photons of energy exceeding some critical value by λ' and we may consider that for each portion of the electron track there are dz/λ' photons emitted. (z as well as all other quantities having the dimensions of a length are measured in radiation units.) The total number of pairs converted in dt at a distance t from the origin of the parent electron will then be

$$p(t)dt=\int_0^t(dz/\lambda')\exp[-(7/9)(t-z)](7/9)dt=(dt/\lambda')[1-\exp(-7t/9)]. \quad (B4)$$

The probability of these converted pairs lying within a distance y at t from the parent electron will be

$$M(y,t)=(1/p(t)dt)\int_0^t(dz/\lambda')\times\exp[-(7/9)(t-z)](7/9)dt\int_{-y}^{y}Q(t-z,y)dy, \quad (B5)$$

and the probability of finding an electron pair within a distance y of all those pairs which were converted at distances extending from the electron origin up to T will be

$$N(y,T)=\int_0^T M(y,t)p(t)dt\Big/\int_0^T p(t)dt. \quad (B6)$$

We note that in these expressions for $M(y,t)$ and $N(y,T)$ the mean free path λ' does not appear; this is a consequence of the assumption that the distribution in θ_0 is not dependent on the energy of the emitted γ ray.

[18] The analysis given here is an extension of that done by Block and King (see reference 8) in that an attempt has been made to take into account the characteristic angle of emission and the origin of the bremsstrahlung γ rays whose conversion contributes to the background of tridents. We are indebted to them for a prepublication copy of their manuscript.

[19] B. Rossi and K. Greisen, Revs. Modern Phys. 13, 240 (1941).

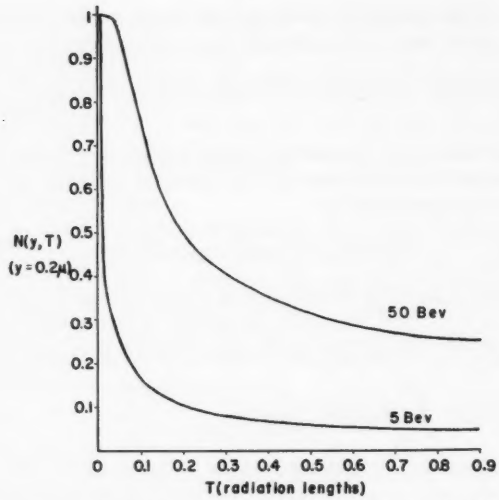

FIG. 4. Fraction of converted bremsstrahlung (B.S. pairs) lying within 0.2μ projected distance of the parent electron as a function of distance of the electron in absorber.

The above integrations are performed to obtain

$$M(y,t)=(7/9)\{1/[1-\exp(-7t/9)]\}\times\int_0^t d\epsilon\,\exp(-7\epsilon/9)E(y,\epsilon), \quad \text{(B5')}$$

$$N(y,T)=\frac{7}{9}\frac{1}{T-(9/7)[1-\exp(-7T/9)]}\times\int_0^T d\epsilon(T-\epsilon)\exp(-7\epsilon/9)E(y,\epsilon), \quad \text{(B6')}$$

where $E(y,\epsilon)$ is defined as

$$E(y,\epsilon)=(4/\pi)^{\frac{1}{2}}\int_0^{y/f(\epsilon)}\exp(-\phi^2)d\phi, \quad \text{(B7)}$$

$$f(\epsilon)=\epsilon(4\epsilon/3w^2+2\alpha^2)^{\frac{1}{2}}$$
$$=\epsilon(\tfrac{2}{3}\langle\theta^2_{\text{scatt}}\rangle+2\langle\theta^2_{\text{open}}\rangle)^{\frac{1}{2}}.$$

For emulsion we use the value of the scattering constant $K=26$ corresponding to 7.75 Mev radians/(radiation length)$^{\frac{1}{2}}$ and we have

$$(\langle\theta^2_{\text{scatt}}\rangle)^{\frac{1}{2}}=(7.75/p\beta)(t)^{\frac{1}{2}}\approx(7.75/E_0)(t)^{\frac{1}{2}}. \quad \text{(B8)}$$

For $(\langle\theta^2_{\text{open}}\rangle)^{\frac{1}{2}}$ we use the results of Stearns,[20] for $k/E_0=0.5$ and obtain

$$(\langle\theta^2_{\text{open}}\rangle)^{\frac{1}{2}}=0.67(mc^2/E_0)\log(E_0/mc^2). \quad \text{(B9)}$$

The average opening angle given by expression (B9) refers to the angle of emission of γ rays with respect to the incident electron; the angle between the γ ray and the secondary electron, which is the one of interest here, will be given approximately by increasing (B9) by a factor of $\sqrt{2}$. This factor is cancelled by another factor of $\sqrt{2}$ which is required to convert the spatial angle to a projected angle. It is also possible that the scattering constant should be increased since the physical case in question here corresponds to larger cell lengths and no cutoff in scattering.[6]

The numerical integration for (B6') was carried out for $y=0.2\mu$ and for $E_0=50$ and 5 Bev. The results are given in Fig. 4.

[20] M. Stearns, Phys. Rev. **76**, 836 (1949).

Direct Detection of Soft Radiation above 50 Kilometers in the Auroral Zone*

L. H. MEREDITH,† M. B. GOTTLIEB, AND J. A. VAN ALLEN
Department of Physics, State University of Iowa, Iowa City, Iowa
(Received August 17, 1954)

In two high-altitude rocket flights of thin-walled Geiger tubes at geomagnetic latitudes 64° and 74°N, a considerable intensity of soft radiation has been encountered above 50 kilometers altitude. No such radiation has been found in flights of identical equipment at 88.5° and at 55.6°. The radiation is tentatively interpreted as the high-energy tail of the auroral spectrum. It may consist of electrons.

I. INTRODUCTION

DURING the summers of 1952 and 1953 single Geiger tubes were flown to altitudes of up to 100 km in a series of rocket flights spanning the geomagnetic latitude range from 55.6° to the pole. These flights employed the "rockoon" system developed at the State University of Iowa; *viz.*, a small rocket is carried by balloon to an altitude of about 60 000 feet and then fired from its balloon suspension in a near vertical direction. During both the balloon and rocket phases of the flight the counting rate of the Geiger tube is telemetered to a shipboard receiving station. During the rocket phase of the flight this counting rate serves to determine the charged particle flux above the atmosphere. The rockoon system is described elsewhere.[1]

II. FLIGHT RESULTS

Up to the time of this report there have been five successful rockoon flights of single Geiger tube apparatus. Two of these flights were made at a geomagnetic latitude of 88.5° in 1952 and another at 55.6° in 1953. The results obtained in the 1952 flights have been reported previously.[2] The results of the new flight at 55.6° are shown in Fig. 1. In common with the results of numerous previous rocket flights of apparatus of this sort at other latitudes, it can be seen that the counting rate first increased as the apparatus moved upward through the atmosphere. It then passed over the Regener-Pfotzer maximum, was constant above about 50 km, and then passed over the maximum again on the descent. The existence of a high altitude plateau in the counting rate curve has been a characteristic feature of all previous results. The magnitude of the plateau counting rate has been used to determine the omnidirectional intensity of charged cosmic ray particles above the atmosphere over a wide range of latitudes.[2]

A marked qualitative difference of results has been obtained, however, in the other two 1953 flights which, as part of a systematic latitude survey by this laboratory, happened to have been made in the auroral zone. Pertinent data on these two flights are tabulated in Table I. Included in Table I are the measured effective lengths of the individual Victoreen 1B85 Geiger tubes. The tubes had an effective diameter of 1.91 cm and an omnidirectional efficiency for minimum ionizing, singly charged particles of 0.98 $(=\epsilon)$. The quantity in the table is the product of this efficiency by the geometrical factor of the cylindrical tube for radiation arriving isotropically from one hemisphere only. Thus, the hemispherical average directional particle intensity in $(\text{cm}^2 \text{ sec sterad})^{-1}$ is found by dividing the observed counting rate by ϵG_{iso}. This gross method is applicable with reasonable accuracy in fields of flux which are not markedly anisotropic but is, of course, inapplicable to directional beams.

The observed counting rates in Flights 13 and 20 are shown as a function of flight time in Figs. 2 and 3. In these figures, as in Fig. 1, the time scale for the rocket phase of the flight has been expanded by a factor of sixty over that for the balloon phase. From Figs. 2 and 3, it is seen that the counting rates pass over the usual maximum at some 20 km altitude, then decrease as though approaching the usual high altitude plateau. But instead of leveling off, they then increase sharply with increasing altitude, eventually decrease again, and below 50 km on the down-leg of the trajectory reproduce the usual cosmic ray results.

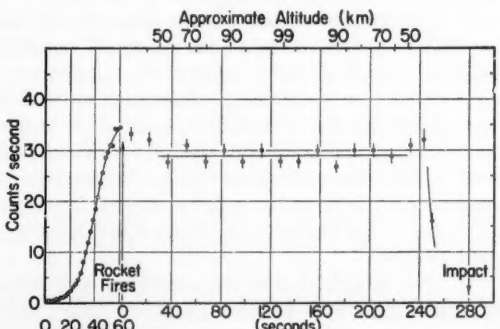

FIG. 1. Counting rate of a single Geiger tube as a function of time during flight. S.U.I. Flight 23 at geomagnetic latitude 55.6°N. On 3 September 1953, 1510 G.C.T.

* Assisted by joint program of the Office of Naval Research, the U. S. Atomic Energy Commission, and the Navy Bureau of Aeronautics; and by the Research Corporation.
† Present address: James Forrestal Research Center, Princeton University, New Jersey.
[1] J. A. Van Allen and M. B. Gottlieb in *Rocket Exploration of the Upper Atmosphere* (Pergamon Press, London, and Interscience Publishers, New York, 1954).
[2] J. A. Van Allen, Nuovo cimento **10**, 630 (1953).

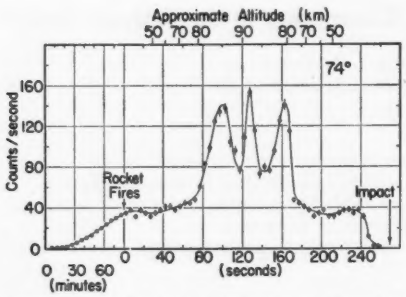

FIG. 2. Counting rate of a single Geiger tube as a function of time during flight. S.U.I. Flight 13 at geomagnetic latitude 74°N.

The increase above 50 km is seen to be a major effect, far exceeding any possibility for statistical fluctuation.

In the figures no corrections have been made for loss of counts due to finite resolving time of the instrumentation. On the basis of laboratory tests such loss would not have exceeded 2 percent in any case.

It should be noted that the precise firing time of the rocket in Flight 20 was uncertain by about ten seconds and may be shown too early in the figure.

III. CONSIDERATIONS PERTAINING TO VALIDITY

Since no such observations have been previously reported, it is of utmost importance to critically consider their validity. Pending further flights, we present the following considerations as the foundation for reporting the present observations at this time.

(a) Strong, clean radio telemetering signals were received throughout both flights; all received scaler pulses (scale-of-16) were of proper amplitude and of characteristic appearance and time-spacing. Hence we believe that it was not possible for any radio interference in the telemetering link to have contributed spurious "counts".

(b) There was no evidence of microphonism, even during the burning period of the rocket propellant. And indeed, the entire anomaly in the results occurred during the free, "vacuum" flight of the vehicle.

(c) The smooth transition of the counting rate from the balloon phases to the rocket phases of the flights provides overall evidence against the occurrence of any significant mechanical dislocation of circuit elements during the accelerative period of the rocket's flight (about a three second period, with maximum axial acceleration of about 60 g). Thereafter the apparatus is subjected to negligible inertial forces until its return to the dense atmosphere on the down-leg of the trajectory.

(d) The performance of the apparatus with respect to temperature is as follows. The 1B85 Geiger tubes, themselves, are the most temperature sensitive element of the apparatus. Their performance does not change appreciably over at least the temperature range $-10°C$ to $+35°C$. At considerably lower temperatures the Geiger tubes fail to quench and pass into continuous, erratic discharge; at considerably higher temperatures they cease counting. The temperature tendencies in a rockoon flight are the following: (i) During the balloon ascent, of approximately an hour's duration, the apparatus tends to cool due to its passage through the cold stratosphere. (ii) During the rocket flight phase the skin of the rocket, and hence the apparatus interior to it, is heated by aerodynamic friction. In addition there is some heating by conduction from the hot motor and combustion chamber. Provision for using the sun's radiation to counteract tendency (i) was made in the manner found effective in balloon flight, *viz.*, the exterior of the rocket was painted black to increase the absorption of sunlight; then a blanket of dead air around it, during the balloon phase of the flight, was provided by a large transparent plastic bag which was held away from the metallic body of the rocket by loosely tied Styrofoam rings. In addition, the rocket complete with instrumentation was kept under a heated tent on the launching deck of the ship during inflation of the balloon and other preparations. In an earlier rockoon flight in which the rocket failed to fire these provisions were found to be sufficient to keep the temperature of the instrumentation in the range of proper operability for over 10 hours.

In numerous previous rocket flights of similar time duration, tendency (ii) has been found to result in negligible heating of apparatus which is not in good conductive contact with the rocket skin or which is reasonably massive. The Geiger tubes were mounted so as to satisfy these conditions.

Since the counting rates during the potentially cooling balloon phases of Flights 13 and 20 were thoroughly normal and since the tendency thereafter is for heating and consequent suppression, if anything, of the counting rates and not for spurious augmentation, we believe it quite unlikely that any excessive temperature variations occurred.

TABLE I. General data.

Rockoon flight number	S.U.I.-13	S.U.I.-20
Geographic location of launching	62° 30.5′ N 64° 13.5′ W	53° 08′ N 54° 45′ W
Geomagnetic latitude of launching (Centered dipole)	74°	64°
Date	28 July 1953	30 August 1953
Time of firing of rocket (G.C.T)	1100	2224
Approximate firing altitude	17.4 km	21.3 km
Effective length of Geiger tube	6.3 cm	6.5 cm
ϵG_{180}	67 cm² sterad	69 cm² sterad

(e) The Geiger tube supply was a 900-volt dry battery. The B+ supplies for the circuits were of less than 150 volts. To prevent high voltage corona the interior of the nose shell was kept at sea level pressure by a pressure tight seal utilizing an annular "O" ring. In laboratory tests at a gauge pressure of 20 psi there was negligible leakage over a period of several hours. In addition, all corona-susceptible circuit elements were coated with either silicone grease or an acrylic spray. Tests of the significant protions of the equipment in a laboratory vacuum chamber yielded no evidence of corona over the full range of pressures down to 0.01 mm of Hg. Any failure of the pressure seal in flight would have to be coupled with a leak rate and corona mechanism of diabolical ingenuity and precision of dependence on time during the flight to have accounted for the anomalous results of Figs. 2 and 3, and for their prompt cessation at 50 kilometers altitude on the descent of the rocket—at an atmospheric pressur- considerably below the usual corona level for highe voltage apparatus of this sort.

(f) Finally and most importantly there are the following gross evidences for reliable operation of the equipment:

(i) In both flights, the observed particle intensities at the Regener-Pfotzer maximum are closely the same on both upward and downward phases of the flight and are, moreover, closely equal to each other and to the values observed in other non-anomalous flights of nearly identical equipment at both more northerly and more southerly geomagnetic locations.

(ii) The intensities on the incipient plateaus of both up- and down-legs of both flights are all equal to each other within their limited statistical accuracies and are, in addition, consistent with interpolation between accurate values at lower and higher latitudes.

A numerical summary of matters (i) and (ii) is given in Table II. Intensities were obtained by dividing the appropriate observed counting rates by the corresponding values of ϵG_{iso}, a quantity which was somewhat different for different counters.

(g) The time dependence of counting rate in the terminal portions of the curves of Flights 13 and 20 is also found to be consistent with ballistic calculations on rate of fall of the rocket through the atmosphere.

TABLE II. Comparison of hemispheric average directional particle intensities from several flights.

Rockoon flight number	Geomagnetic latitude	Intensity at Regener-Pfotzer maximum (cm² sec sterad)⁻¹	Intensity on high altitude plateau (cm² sec sterad)⁻¹
S.U.I. 4, 5	88.5°	0.57±0.02	0.48±0.01
13	74°	0.57±0.03	<0.50±0.05[a]
20	64°	0.57±0.02	<0.50±0.05[a]
23	55.6°	0.53±0.02	0.44±0.01

[a] The "plateau" values for Flights 13 and 20 are the averages of up- and down-leg values of intensity during the periods of their incipient plateaus. They are properly to be regarded as upper limits, since a clear flat plateau did not occur in these cases.

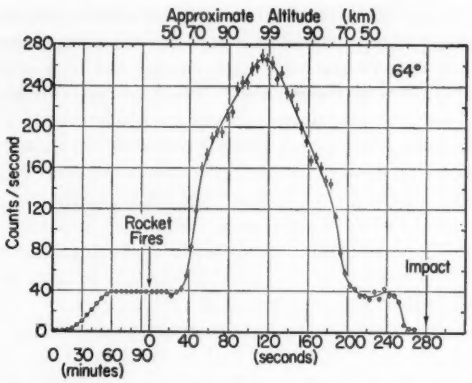

FIG. 3. Counting rate of a single Geiger tube as a function of time during flight. S.U.I. Flight 20 at geomagnetic latitude 64°N.

IV. DISCUSSION OF RESULTS

As detailed in the previous section, our confidence in the validity of the present results rests on the evident reliability of the data obtained during the early and latter portions of each flight and on our inability to propose any reasonable grounds for doubting the proper operation of the equipment during the intermediate portions.

If this point of view be accepted, then it becomes fruitful to discuss the possible significance of the results in a preliminary way.

We have tentatively discarded, subject to further investigation, such conceivable possibilities as radioactive atomic bomb dust—somehow suspended at high altitudes in these latitudes—and as accidental outbursts of relatively hard x-rays[3] from the sun. Rather, it appears more reasonable to identify the directly observed radiation with aurorae. Our reasons for this inclination are as follows:

(a) Auroral displays, as observed from the ground, typically do not extend below 100 km. Yet cases have been reliably reported of visual aurorae to much lower altitudes.[4] In any event, the particle intensities observed by us are only of the order of 10 to 20 particles/(cm² sec), if in the form of a directional beam; or of the order of 2 to 3.5 particles/(cm² sec sterad) if arriving isotropically over a hemisphere.[5] Since such intensities are many orders of magnitude smaller than those

[3] The atmospheric depth at 50 km is 1.05 g/cm²; at 100 km about 0.006 g/cm². The minimum wall thickness of the nose shell plus one counter wall is 0.4 g/cm².

[4] See following general references: L. Harang, *The Aurorae* (John Wiley and Sons, Inc., New York, 1951); S. Chapman, J. Geophys. Research 55, 361 (1950); V. C. A. Ferraro, Advances in Physics 2, 265 (1953).

[5] Consistent with the auroral point of view, we have tentatively assumed that the observed radiation is of particle character and not of electromagnetic character. This assumption is being subjected to direct test in further experiments.

estimated to be required to produce visible aurorae, it is reasonable to conjecture that the radiation observed by us is only the very high energy tail of a steeply falling auroral energy spectrum. The rare occurrence of visual aurorae down to ~60-km altitude does show that such energies for auroral particles are indeed intrinsically possible in the mechanism for their origin.

(b) Visually observed aurorae are typically confined to two narrow bands of geomagnetic latitude—one band in the northern hemisphere and another similar band (less well studied) in the southern hemisphere.[4,6] The maximum frequency of occurrence of visual aurorae occurs at about 70° geomagnetic latitude in both hemispheres. In Fig. 4, the solid line is a smoothed adaptation of the auroral frequency *vs* latitude plot of Vestine.[6] On the same plot are shown the geomagnetic latitudes of our five rockoon flights of single Geiger tube apparatus, all of the same wall thickness. The circles are at the latitudes of 55.6° and 88.5° respectively and represent one flight at the former and two flights at the latter latitude all of which showed "normal" cosmic-ray plateaus—i.e., "negative" results from the present point of view. The crosses are at the latitudes of 64° and 74°, of Flights 20 and 13, both of which yielded anomalously high counting rates above 50 km as described above—i.e., "positive" results. (The ordinates at which the points are plotted have no significance.) Thus, there is meager, though suggestive, evidence that the soft radiation is confined to the auroral zone as the term is ordinarily understood. It is clear that many more flights are needed to establish the latitude dependence of the incidence of the soft radiation with satisfactory certainty.

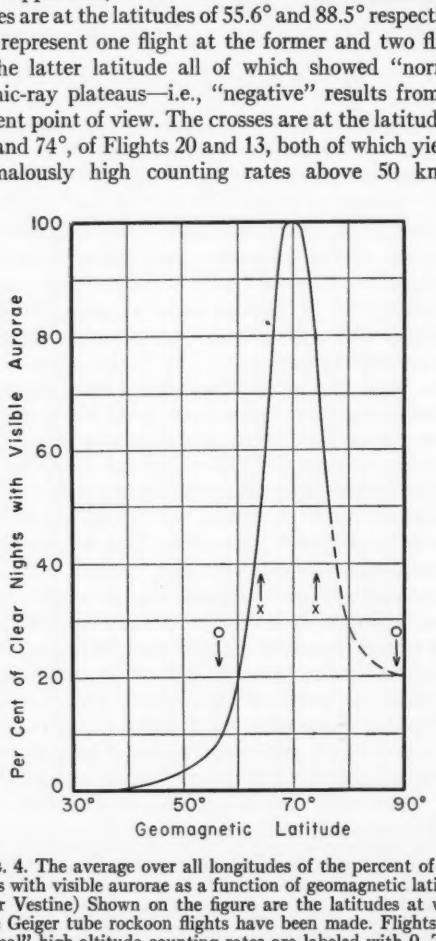

FIG. 4. The average over all longitudes of the percent of clear nights with visible aurorae as a function of geomagnetic latitude. (After Vestine) Shown on the figure are the latitudes at which single Geiger tube rockoon flights have been made. Flights with "normal" high-altitude counting rates are labeled with 0. Those with "anomalously" high counting rates at high altitudes are labeled by *x*. The ordinates of 0 and *x* have no significance.

[6] E. H. Vestine, Terrestrial Magnetism and Atm. Elec. **49**, 77 (1944).

Numerous previous rocket flights of single Geiger tubes at lower latitudes have yielded normal cosmic ray plateaus (i.e., "negative" results). But none of these equipments had quite thin enough walls for inclusion in the present series.

(c) The variation of counting rate with altitude in Flight 20 (Fig. 3) might be plausibly interpreted simply as the atmospheric absorption of the high-energy tail of an auroral energy spectrum which is falling off steeply with increasing energy. But no such interpretation could be adequate for the data of Flight 13 (Fig. 2). Here there are three distinct peaks of counting rate with decided dips between. Several possible explanations of these features have been considered: (i) Rapid time variation of the intensity of the soft radiation, with marked changes within a few seconds at a given point. (ii) A sharply directional beam of radiation coupled with rapid end-over-end tumbling of the rocket in such a way as to present a markedly different effective Geiger tube area to the beam at successive times. (The axis of the Geiger tube was parallel to the long axis of the rocket.) (iii) Spatial inhomogeneity of the beam.

It appears that the rapidity of time variation required by explanation (i) is not out of the question but is rather too great to be consonant with typical auroral observation.

Possibility (ii) has a certain numerical plausibility; but since the rf radiation pattern of the radio telemetering system in the rocket consists of a number of axially symmetrical lobes of different intensity with nulls between, any such end-over-end tumbling of the rocket would be revealed in a corresponding fluctuation in the rf signal strength at the receiving station. No such fluctuation was observed. Moreover, the magnetic rigidity of particles of the observed atmospheric penetration is so low that it is unlikely to have a sharply directional beam over any large distance in the earth's magnetic field.

Possibility (iii) appears to us as the most attractive—especially since visual aurorae often present a complex spatial distribution of optical intensity. The horizontal velocity of the rocket was not measured but is expected to be ~200 m/sec (estimate based on angle of launching). During flight, the rocket's speed is never less than the magnitude of its horizontal velocity, even at the peak of flight. Hence, the reasonable scale of spatial inhomogeneity of the order of 4 km would suffice to

account for the high-altitude structure of Fig. 2. Such a scale of spatial inhomogeneity is common in aurorae.[4,7]

V. PROPOSED WORKING HYPOTHESES

In view of the flight observations presented and the discussion of Sec. IV, the following working hypotheses are proposed:

(a) The soft radiation observed in Flights 13 and 20 consists of particles in the high-energy tail of the energy spectrum of auroral corpuscles.

(b) The rapid increase of the intensity above 50 km is primarily due to the diminution of atmospheric absorption. The atmospheric depth at 50 km is 1.05 g/cm². Thus a particle originating outside the atmosphere must penetrate a minimum of 1.05 g/cm² of atmosphere and an additional 0.4 g/cm² of aluminum in order to be registered in our apparatus. At the peak of the trajectories, the atmospheric depth is negligible in comparison with the apparatus wall. Table III lists the kinetic energies and magnetic rigidities of electrons and protons whose ranges are 0.4 and 1.45 g/cm², respectively. Hence, if the radiation consists of protons, for example, energies up to 35 Mev must be present. And of course, because of oblique, spiraling paths in the atmosphere, there are certainly higher energies present.

(c) The detailed, high-altitude features of Fig. 2 (in particular) are due primarily to spatial inhomogeneities.

(d) The observed particles are the high-energy survivors of a beam ("streamer") of particles of far lower average energy and of far greater total intensity. The original beam, as it approaches the earth, moves approximately along a magnetic line of force (almost vertically at our point of observation) since the "guiding centers" of the individual component particles do so. The beam is visualized as being compounded of more or less helically moving particles, the helices being of all pitches and the particles having a wide range of magnetic rigidities.

If it is indeed correct that the scale of the spatial inhomogeneity is of the order of 4 km as previously discussed, then on the foregoing picture it is evident that the radii of curvature of component particles' orbits in the earth's magnetic field must not exceed a small fraction of this distance or inhomogeneities of this scale would be destroyed. An interesting consequence follows from this argument (after Vegard[7]) as applied to the present situation. It was seen in Table III that a proton must have a magnetic rigidity of at least 1.7×10^8 volts in order to merely penetrate the apparatus. Such a proton moving normally to the earth's magnetic field has a radius of curvature of ~8 kilometers. On the other hand an electron of the necessary minimum range has a radius of curvature of 70 meters. Hence, on this basis we propose the further working hypothesis that our observed soft radiation consists predominantly of electrons.

TABLE III. Kinetic energy E and magnetic rigidity R[a] for specified ionization range.

Ionization range g/cm²	electrons E Mev	electrons R volts[a]	protons E Mev	protons R volts[a]
0.4	0.96	1.4×10^6	16	1.7×10^8
1.45	3.2	3.2×10^6	35	2.6×10^8

[a] Units of magnetic rigidity are given in volts.

(e) The observed particles do not arrive in Stoermer-type trajectories from a source very distant from the earth (e.g., the sun). In order that a particle reach the top of the atmosphere at 64° in a Stoermer-type trajectory from infinity, its magnetic rigidity must exceed 5.4×10^8 volts. A proton of this rigidity has an air range of 17 g/cm² and would therefore (in spite of some curvature of its trajectory) penetrate down into the atmosphere much more deeply than observed (that is, down to an altitude of ~30 km). An electron of this rigidity would penetrate well into the cosmic-ray transition maximum at ~20 km.

VI. COMMENTS

The above hypotheses are obviously of a tentative nature. A large variety of additional experiments is required for their critical establishment or destruction. Among such experiments may be mentioned: (a) systematic study of latitude dependence. (b) direct identification of nature of radiation by (for example) determination of range and specific ionization. (c) use of thinner walled detectors and flights of such detectors to higher altitudes. (d) study of temporal fluctuations and detailed correlation with in situ auroral observations of other types (visual, radar, etc.) and with related solar and geomagnetic observations.

Finally we are able to remark that since the above account was prepared, the Iowa group has obtained fresh confirmation of the 1953 results reported herein in a recent series of firings at geomagnetic latitudes (70±2)°N (July 1954). Details will be reported in a subsequent paper.

VII. ACKNOWLEDGMENTS

The authors are particularly indebted to the following individuals for assistance: Lieutenant Malcolm S. Jones, United States Navy, formerly of the Office of Naval Research, Dr. R. A. Ellis, Jr., and Mr. J. G. Sentinella.

The flights were made possible by the cooperation of the General Mills Aeronautical Laboratories and of the officers and men of the U.S.S. Staten Island (AGB-5) and of the U.S.C.G.C. Eastwind (AGB-279).

[7] L. Vegard, Phil. Mag. 42, 47 (1921).

Cosmic-Ray Studies of Penetrating Showers and Bremsstrahlung at 11 200 Feet by Using Plastic Scintillation Counters*

C. N. Chou and Marcel Schein
Department of Physics, University of Chicago, Chicago, Illinois
(Received September 17, 1954)

An apparatus was designed to study penetrating showers produced by high-energy cosmic rays. For this purpose, four anthracene-in-polystyrene plastic scintillators of 1 and 2 cm thickness were used with lead plates of thicknesses 2.00 cm, 2.25 cm, and 2.25 cm, respectively, interposed between them. In addition to these scintillation counters, four trays of G-M counters and an arrangement of anticoincidence counters were used. Data on penetrating showers produced in a graphite block and a polystyrene scintillator were obtained. It was found that in the energy range from 2 to 20 Bev, the resulting integral energy spectra of the π^0 mesons can be represented by a power law with an exponent equal to -1.7 ± 0.2 in polystyrene, with no filter for the primaries. Similar results were obtained in graphite and in polystyrene with primaries filtered through 10 cm of lead. The multiplicity of the charged mesons in the penetrating showers produced in graphite can be described by a power law with an exponent -4.2 ± 0.5, in general agreement with cloud chamber results. It was found that the energy distribution of bremsstrahlung γ rays and the flux of the μ mesons producing this bremsstrahlung in a lead block of 10 cm thickness is in agreement with theory.

I. INTRODUCTION

A LARGE number of different experimental results have been reported concerning the production of penetrating showers by cosmic-rays. The early work has been summarized by T. G. Walsh and O. Piccioni.[1] The experimental techniques used more recently mainly consisted of the use of photographic emulsions,[2–5] cloud chambers,[6–18] or G-M counters.[19–23] The use of photographic emulsions is particularly suitable for the detailed study of individual events involving charged particles or in some favorable cases, also photons. In the case of using G-M counter arrangements, frequently one finds it difficult to interpret the data unambiguously. This is chiefly due to the fact that the penetrating secondaries are frequently emitted under very narrow angles. In the case of multiplate cloud chamber studies of cascade showers produced by photons originating from the decay of π^0 mesons produced in penetrating showers, it is practically impossible to count the number of secondaries as the shower develops under the lead plates when the energy is considerably higher than a few Bev. In this last respect, a large scintillation counter is more suitable since it is capable of giving a light output proportional to the total number of minimum particles passing through it. Hence it can be used reliably to register the number of electrons in the development of a cascade shower through lead.

Plastic scintillators placed between lead plates are particularly suitable for this purpose. Plastic scintillators can be made in large sizes. Their performance has been found to be reliable and adequate for quantitative measurements.[24] Scintillation counters made of anthracene-in-polystyrene plastic plates have previously been used here for the measurement of cascade showers initiated by high-energy photons and electrons at sea-level.[25] An apparatus utilizing plastic scintillators was constructed for the measurement of penetrating showers produced by cosmic-ray primaries and the cascades in penetrating showers initiated by photons or electrons in the energy range of from 1 Bev to about 50 Bev. The measurements were carried out at Climax (altitude 11 200 ft) from August to October in 1953. Data were obtained on the energy spectrum of π^0 mesons and the multiplicity spectrum of charged particles in penetrating showers in a graphite block. Additional measurements on the spectrum of π^0 mesons were carried out in polystyrene, which contained equal numbers of carbon and hydrogen molecules. A somewhat modified apparatus was also used to obtain data on bremsstrahlung produced by cosmic-ray μ mesons in a lead block above the apparatus.

* Supported by the joint program of the Office of Naval Research and the U. S. Atomic Energy Commission.
[1] T. G. Walsh and O. Piccioni, Phys. Rev. **80**, 619 (1950).
[2] Lord, Fainberg, and Schein, Phys. Rev. **80**, 970 (1950).
[3] E. Pickup and L. Voyvodic, Phys. Rev. **84**, 1190 (1951).
[4] J. G. Wilson, *Progress in Cosmic-Ray Physics* (Interscience Publishers, New York, 1952), Camerini, Lock, and Perkins, pp. 1–58.
[5] M. Kaplon and D. Ritson, Phys. Rev. **85**, 932 (1952).
[6] J. R. Green, Phys. Rev. **80**, 832 (1950).
[7] G. Salvini, Nuovo cimento **8**, 798 (1951).
[8] B. P. Gregory and J. H. Tinlot, Phys. Rev. **81**, 667 (1951); **81**, 675 (1951).
[9] M. B. Gottlieb, Phys. Rev. **82**, 349 (1951).
[10] A. J. Hartzler, Phys. Rev. **82**, 359 (1951).
[11] W. B. Fretter, Phys. Rev. **83**, 1053 (1951).
[12] G. Salvini and Y. B. Kim, Phys. Rev. **88**, 40 (1951).
[13] H. W. Boehmer and H. S. Bridge, Phys. Rev. **85**, 863 (1952).
[14] C. B. A. McCusker and D. D. Millar, Proc. Phys. Soc. (London) **A65**, 758 (1952).
[15] Chang, Del Castillo, and Grodzins, Phys. Rev. **89**, 408 (1953).
[16] A. B. Weaver, Phys. Rev. **90**, 86 (1953).
[17] N. M. Duller and W. D. Walker, Phys. Rev. **93**, 215 (1954).
[18] von M. Deutschmann, Z. Naturforsch. **9a**, 477 (1954).
[19] M. L. Vidale and M. Schein, Nuovo cimento **8**, 774 (1951).
[20] R. R. Brown, Phys. Rev. **87**, 999 (1952).
[21] McCusker, Porter, and Wilson, Phys. Rev. **91**, 384 (1953).
[22] K. Greisen and W. D. Walker, Phys. Rev. **90**, 915 (1953).
[23] K. Sitte, Phys. Rev. **88**, 172 (1952).
[24] C. N. Chou, Phys. Rev. **87**, 376 (1952); Phys. Rev. **87**, 903 (1952).
[25] C. N. Chou, Phys. Rev. **90**, 473 (1953).

II. EXPERIMENTAL ARRANGEMENT

The geometry of the experimental arrangement drawn to scale is shown in Fig. 1. S_1, S_2, S_3, and S_4 are four anthracene-in-polystyrene plastic scintillators. S_3 has the cross-sectional area of 18×9 cm² and is 1.8 in thickness, S_2 and S_4 are correspondingly $18\times18\times0.9$, and S_1 $18\times18\times1.8$. As shown in the figure, each scintillator was coupled through a Lucite light-pipe to a magnetically shielded RCA 5819 photomultiplier tube. Between the scintillators, S_3, S_2, S_4, and S_1 lead plates of thicknesses 2.00, 2.25, and 2.25 cm respectively are interposed. A, C, and D are parallel trays of metal G-M counters, and B is a cross tray to A. Each G-M counter is one inch in diameter. The counters E are in anticoincidence and their purpose is to protect the scintillators from registering particles from the sides. Hence practically all events registered were due to particles from above except for very energetic neutrons. During part of the experiment, above the counter tray A the lead block PB was placed. Between the bottom scintillator S_1 and the G-M counter tray C a lead block of 6 cm thickness is placed on top of which an aluminum plate of 2-cm thickness is located in order to cut off the effect of the low energy backward shower particles produced in the 6-cm lead block. For the same purpose another aluminium plate of 1-cm thickness was placed under the G-M counter tray B. Between the counter trays C and D 12 cm of lead was interposed. G is a graphite block in which penetrating showers were generated and which was in the position indicated in Fig. 1 during part of the experiment. All the scintillators and the G-M trays C and D are shielded with lead block and trays of lead shot as shown in the figure. The overall shielding corresponded to at least 8 cm of lead. Within the solid angle defined by the G-M counter trays A and B and scintillator S_3, a cosmic-ray particle of sufficient energy coming vertically downward could produce nuclear events in the scintillators or the lead plates interposed between them, and also in the graphite block G or the lead block PB when they were in position. At the same time, cascade showers initiated by the

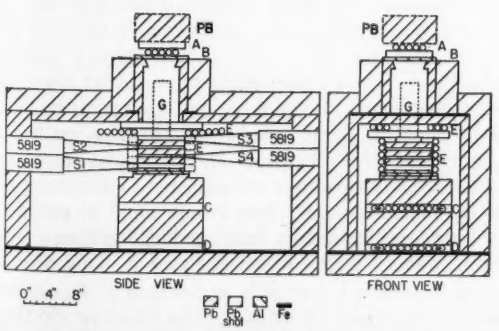

FIG. 1. Experimental arrangement. G denotes graphite block. PB denotes lead block. A, B, C, and D denote G-M counter trays. E denotes anticoincidence side G-M counters. S_1, S_2, S_3, and S_4 denote plastic scintillators with Lucite light pipes.

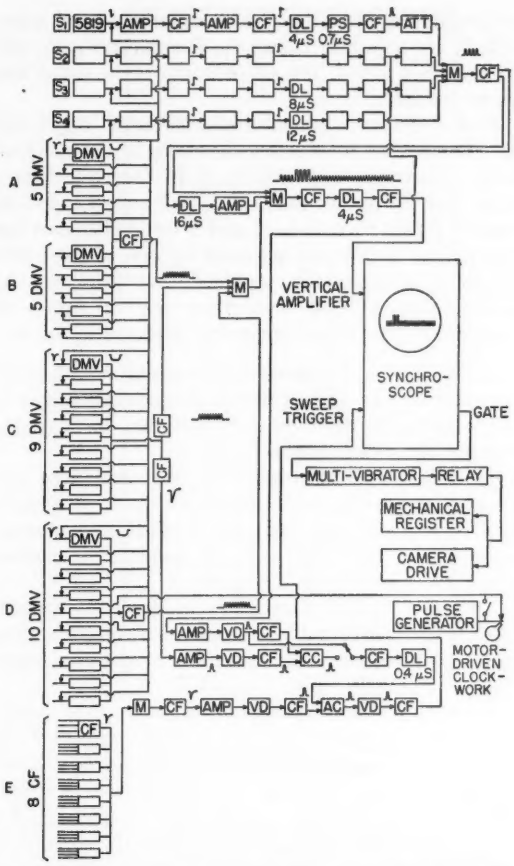

FIG. 2. Block diagram of the recording circuits. The abbreviations have the following meanings: S_1, S_2, S_3, and S_4, scintillator inputs; *AMP*, amplifier; *CF*, cathode follower; *DL*, delay line unit; *PS*, pulse shaping unit; *ATT*, attenuator; *M*, mixing unit; *DMV*, delaying multi-vibrator; *VD*, voltage discriminator; *CC*, coincident circuit; *AC*, anti-coincident circuit. The approximate wave-forms at various points are also given. The numbers below *PS* and *DL* give the width of the pulse and the time of delay, respectively, in μsec.

electromagnetic components of an event could develop through the whole counter arrangement. These developments were recorded by the scintillators and the G-M counters. However, large air showers were excluded by the anticoincidence counters E. Figure 2 shows a block diagram of the recording circuits. The pulse shape is indicated at various points. The pulses from the four photo-multiplier tubes which viewed the four plastic scintillators S_1, S_2, S_3, and S_4 were delayed by 4 μsec, 0 μsec, 8 μsec, and 12 μsec, respectively. They were then shaped to a square pulse of a width of 0.7 μsec each. This was done by using shorted delay-lines. The four pulses P_1 were adjusted to the same size and then mixed. These same pulses P_1 were amplified about 10 times in amplitude and delayed 16 μsec. These will be called P_2. The differentiated outputs of the delaying

multivibrators from the G-M counter pulses of trays AB, C, and D will be called P_3. The pulses P_1, P_2, and P_3 were then mixed. The whole length of the sweep was about 160 μsec.

Part of the output pulse of scintillator S_2 (Fig. 1 and Fig. 2) was used for starting the sweep of the synchroscope (Tektronix Type 513D). A 10^{-5} sec coincidence of part of the output pulse of S_2 and any of the G-M counter pulses from trays A and B could also start the sweep. The sweep was actuated by one of these two triggering arrangements provided that there was no anticoincidence pulse present in any of the G-M counters E. The actual triggering used was as follows:

(1) $S_2{}^m$: A pulse was required in scintillator S_2 corresponding to 3 or 4 times the maximum pulse height in the Landau distribution corresponding to a singly charged minimum ionization particle.

(2) AB-$S_2{}^s$: G-M coincidence between any one counter from trays A or B and a pulse in S_2. Any pulse in S_2 corresponding to about one fourth of the maximum pulse height of a singly charged minimum ionization particle was used for this purpose.

(3) AB-$S_2{}^m$: Coincidence of any one G-M counter pulse from trays A or B and a pulse in S_2 corresponding to 3 or 4 times the maximum pulse height of a singly charged minimum ionization particle.

When the sweep was triggered the two sets of scintillator pulse outputs P_1 and P_2, and the outputs P_3 of all the G-M counters in trays AB, C, and D, delayed by various time intervals by the respective multivibrators, were fed into a synchroscope. A photographic record was made and a gate pulse from the scope then actuated the mechanical register and the camera drive to advance the film forward by one frame and to wait for the next event. A pulse generator produced pulses similar to the four pulses due to S_1, S_2, S_3, and S_4. This same pulse generator produced pulses similar to pulses from G-M trays AB, C, and D. The pulses from the pulse generator could be fed into the input of the vacuum tube circuit. A motor-driven clock work actuated these calibration signals once every hour.

The apparatus was installed at Climax and kept running continuously from August to October 1953. The analysis of several thousand events which were registered is included in this paper.

III. EXPERIMENTAL PROCEDURE

Throughout the experiment, runs were made with triggering AB-$S_2{}^s$ (with or without the lead block PB). Out of these runs those events were selected in which only one single G-M counter in the trays C and D was triggered. It will be explained later that these must be due to singly charged minimum ionization particles. As explained above, both nuclear events and electromagnetic cascade showers could develop through the whole counter arrangement. A procedure of analysis was devised to separate and analyze these events. The pulse sizes observed in scintillators S_3, S_2, S_4, and S_1 were first converted to equivalent number of singly charged minimum ionization particles from the results obtained above based on AB-$S_2{}^s$ events. In our analysis only events in which none of the G-M counters E on the side was fired were included. It was also assumed that the observed events were all "usual" events amenable to the statistics of averages. The following types of events were selected by this apparatus:

(1) Singly Charged Penetrating Particles

The lead block PB was in position. In these events one and only one G-M counter in trays A, B, and C was actuated and not accompanied by a pulse in E, and the scintillators S_3, S_2, S_4, and S_1 showed pulses for single minimum-ionization particles. These events were assumed to be due to high-energy μ mesons. A small fraction, however, could be due to high-energy protons or π mesons, and corrections could be made from the known rate of nuclear interactions as described in a later subsection. The effect has been found to be too small (2–3 percent of nuclear component) to be of any significance. The probability of an electron traversing the whole thickness of matter without producing secondaries to be detected was entirely negligible. The actually observed pulse size distribution in all the scintillators empirically observed supported this interpretation. These singly charged minimum ionization particles were mainly used for calibration purposes.

(2) Bremsstrahlung Produced in the Lead Block PB by μ Mesons

One and only one G-M counter in trays A, B, and D was fired. One or more than one G-M counter in tray C was fired. The photon produced in the process of bremsstrahlung in PB developed into cascade showers passing through the scintillators S_3, S_2, S_4, and S_1. Their energy was determined from cascade theory.[25,26] Graphs for photons of different energies were plotted showing the number of electrons expected from shower theory passing through the four scintillators after traversing the lead plates interposed between them. In the analysis of this subsection and subsections (3) and (4) we analyzed only events which gave a pulse in scintillator S_2 of a height equal to or greater than that corresponding to 16 minimum ionization particles. This requirement of large number of particles made the average statistics very good. Then a best fit among the four scintillator readings was adjusted to determine the energy of the photon. These events could be produced by knock-on electrons in lead block PB accompanying the primary μ meson which initiated it. This effect is found to be small, especially in the case of high-energy secondaries, which varies as E'^{-2} for knock-on electrons and as E'^{-1} for bremsstrahlung, where E' denotes the energy of the secondary.

[25] K. Ott, Z. Naturforsch. **9a**, 488 (1954).

(3) Penetrating Showers Produced in Graphite Block *G*

The lead block *PB* was in position. The triggering arrangement $AB-S_2^m$ was used. A proton having traversed the lead block *PB* could produce a penetrating shower in the graphite block *G*. The few charged π mesons and the primary proton were registered in the top scintillator S_3. The total energy of the π^0 mesons was measured by that of photon-initiated cascade showers as described in subsection (2) above.[25,26] These events could also be interpreted as due to a small nuclear star in the top scintillator S_3 and not in the graphite block *G*. However, this type of events were eliminated by applying the criterion described in the following subsection. In the present analysis we measured the maximum number of charged π mesons produced in the graphite block *G* up to 10 only. because of the background effect of nuclear stars.

(4) Penetrating Showers Produced in Scintillator S_3

We identified these events from triggering arrangements S_2^m, $AB-S_2^s$, and $AB-S_2^m$. In separating nuclear interactions from electromagnetic cascade showers results of photographic emulsion investigations were used as a partial guide.[4] Additional information was obtained from the registration of G-M counters in trays *C* and *D*.

Thus, the nuclear events occurred in scintillator S_3 and the subsequent development of the photons from the decay of the π^0 mesons were identified and the energy of photons determined. Using similar criterions, we rejected events which could have been confused with events discussed in earlier subsections.

IV. DISCUSSION OF RESULTS

First the range of validity of the energy measurements of the cascade showers will be briefly discussed here. The apparatus could yield reliable results for the measurement of cascade showers initiated by photons or electrons of total energies in the range of 1 Bev to 30 Bev. However, in the energy range less than 2 Bev, the sensitivity of identifying a cascade shower event dropped off. This is because of the fact that in the analysis procedure adopted, allowance was made for the fluctuation in the shower theory. This range of allowance fell below the minimum pulse required in the present analysis when the cascade theory was less than 2 Bev.

(a) Penetrating Showers from Graphite and Polystyrene

The procedure of analysis has been explained in subsections III (3) and (4) above. For the study of the nuclear interactions produced in the graphite block *G*, the triggering arrangement used was that of $AB-S_2^m$ with the lead block *PB* in position. The effect of the bremsstrahlung had been corrected for using the results obtained in subsection (b) which will be described below. From the distribution of scintillation pulses in S_3, the multiplicity spectrum is shown in Fig. 3, showing the integral shower frequency *vs* the number of shower particles n_s. The slope of the straight line in the log-log plot drawn through the most reliable range has the value of -4.2 ± 0.5. This agrees satisfactorily with the value of -3.8 ± 0.6 obtained from cloud chamber experiment for carbon for n_s equal to or greater than 7, at a comparable altitude of 2960 m.[18] The range of validity in this experiment is $4<n_s<9$.

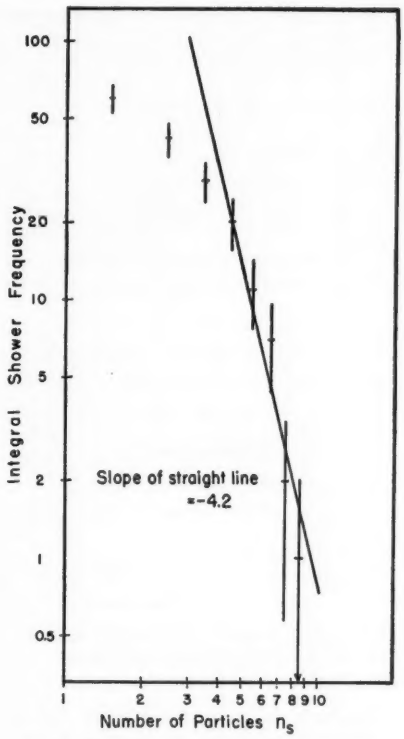

FIG. 3. Multiplicity spectrum of penetrating showers produced in graphite.

Figure 4 shows the integral frequency *vs* energy of π^0 mesons produced from cosmic-ray nuclear interactions in the graphite block *G*. These data were obtained with the triggering arrangement $AB-S_2^m$ with the lead block *PB* in position. It can be represented by a relationship of the form $E^{-\gamma}$, with γ equal to -1.2 ± 0.2.

In the investigation of penetrating showers produced in the polystyrene plate, the triggering arrangement $AB-S_2^m$ was used, with and without the lead block *PB* in position. The results are shown in Fig. 5. The integral frequency *vs* energy of π^0 mesons produced from cosmic ray nuclear interactions can again be represented by an expression of the form $E^{-\gamma}$. The exponent γ has the value -1.7 ± 0.2 for the events observed without the lead filter *PB*, and has the value -1.4 ± 0.2 for the

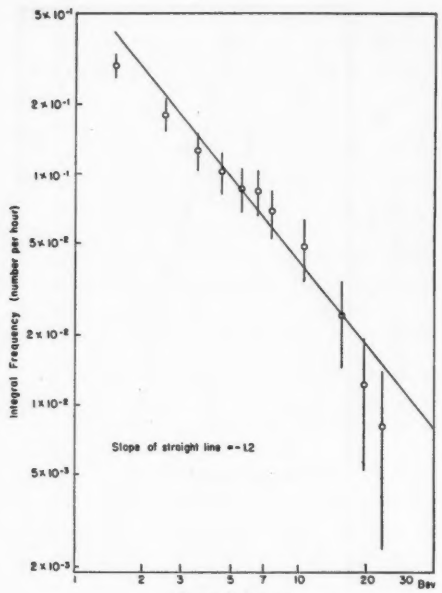

FIG. 4. Integral frequency of π^0 mesons in penetrating showers produced in graphite.

events observed with the lead filter *PB* placed in position. This latter value can be compared with the value of -1.2 ± 0.2 for a similar expression for the integral frequency *vs* energy of π^0 mesons produced in the graphite block *G* as discussed previously, since both sets of data were obtained under comparable condition of being both with the lead block *PB* in position. The curves seem to indicate that the exponent γ is slightly smaller (in absolute value) in the measurements obtained with the lead block *PB* in position than in those obtained without the lead block. The reason is probably that with the lead block in position the nuclear events observed consisted of both events produced by cosmic-ray primaries in the air and by secondaries produced in the lead block *PB*, which were of somewhat lower energies than the primaries. It is a known fact that the exponent γ decreases for π^0 mesons of lower energies, which are mostly produced by cosmic rays of lower energies. In the present experiment, the exponent γ in the expression $E^{-\gamma}$ for the integral frequency *vs* energy of π^0 mesons relationship for polystyrene has been found to be -1.7 ± 0.2, as mentioned above. The same exponent has been reported to be -1.5 ± 0.2, for carbon obtained in cloud chamber experiment at approximately the same altitude.[18] Entirely different experimental techniques were used. At least in the high energy range, the method used in the present experiment should give more reliable information because of the intrinsic limitation of cloud chamber technique with respect to recording large number of particles.

It was attempted to make an estimate of the frequency of nuclear interactions by high energy cosmic-ray particles with the target materials, for events in which photons (presumably originated from the decay of the π^0 mesons) of a total energy of at least 3 Bev were observed. When the lead block *PB* was in position, the contribution of *PB* to these observed events is estimated to be equal to 0.03 per hour, or 0.013 cm^{-2} $sterad^{-1}$ $hour^{-1}$ L^{-1}, where L is the geometric collision length of the nuclei. A summary of the results is given in Table I. It is seen that they are not inconsistent with the values of the intensity of protons of comparable energy at the same altitude,[27] account must be taken of the fact that we detected and observed only those nuclear interactions in which at least one π^0 meson was produced which in turn decayed into photons which developed in the lead plate between the scintillators S_3 and S_2 into a cascade shower of at least about 16 electrons in order to trigger the recording system.

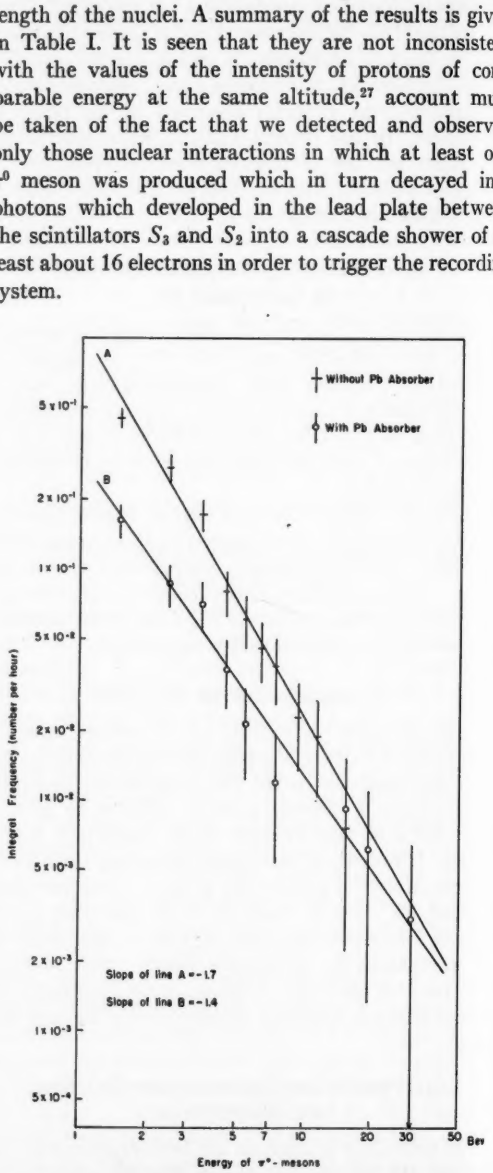

FIG. 5. Integral frequency of π^0 mesons in penetrating showers produced in polystyrene.

[27] B. Rossi, Revs. Modern Phys. **20**, 537 (1948).

(b) Bremsstrahlung Produced in the Lead Block *PB* by Cosmic-Ray μ Mesons

In analyzing the data from the set of experiment using the triggering arrangement $AB-S_2{}^m$ with the lead block *PB* in position, events were found which could be identified as due to bremsstrahlung produced in the lead block by the μ mesons. The procedure adopted for the analysis was described in subsection III (2) above. The results are shown in Fig. 6. These results will be compared with the theoretically expected values. Since it is generally assumed that μ mesons have spin $\frac{1}{2}$, the interaction cross section for complete screening[28] of bremsstrahlung production for μ mesons of spin $\frac{1}{2}$ is assumed. Also it is assumed that the primary differential energy spectrum of the high-energy μ mesons is given by an expression of the form[29]

$$N(E)dE \propto (E+E_0)^{-3}dE,$$

where E_0 is a constant denoting the ionization loss of the μ mesons from the point of production up to the altitude considered. Integrating numerically, we obtain the cross section for the production of photons of energies between E' and $E'+dE'$ averaged over the whole μ-meson spectrum given by the expression

$$\bar{\sigma}(E')dE' = \text{const}\,(E')^{-2.85}.$$

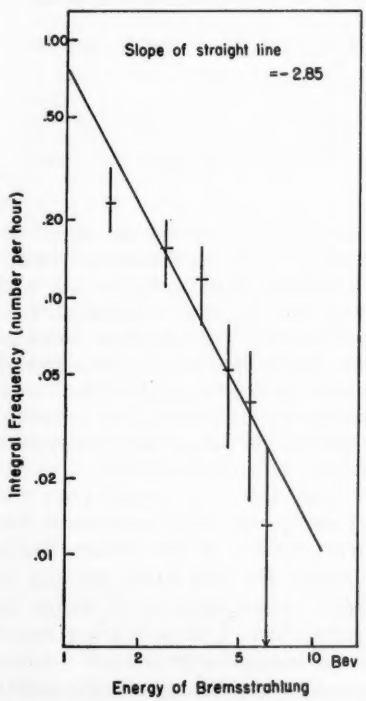

FIG. 6. Energy spectrum of bremsstrahlung produced by μ mesons in lead.

[28] R. F. Christy and S. Kusaka, Phys. Rev. 59, 414 (1941).
[29] Barrett, Bollinger, Cocconi, Eisenberg, and Greisen, Revs. Modern Phys. 24, 133 (1952).

TABLE I. Frequency of nuclear interactions by high-energy cosmic rays in the target material in which photons were originated (presumably from the decay of π^0 mesons) with a total energy of at least 3 Bev.

Target material	With or without lead block *PB*	Rate per hour	Rate (in cm^{-2} sterad^{-1} hour^{-1} L^{-1})[a]
Graphite block *G*	with	0.15	0.027
Plastic scintillator S_3	without	0.17	0.23
Plastic scintillator S_3	with	0.037	0.051

[a] *L* denotes the geometrical collision length of the nuclei of the target material.

This expression should give the energy distribution of the bremsstrahlung produced by the assumed spectrum of μ mesons. The straight line drawn in Fig. 6 is of a slope equal to -2.85. It is seen that the agreement is satisfactory within the statistical errors. We integrate the preceding cross section for photons of energies greater than 2 Bev and obtain the total cross section given by

$$\sigma_{\text{theoret}} = 3.2\times10^{-28}\ \text{cm}^2.$$

This calculated total cross section is made use of, and the observed intensity of bremsstrahlung with energies higher than 2 Bev is compared with the observed flux intensity of μ mesons underground.[30] It is found that the flux intensity corresponds to that of μ mesons of energies higher than about 10 Bev. This latter value is of expected order of magnitude and serves as a check of the general correctness of the theory and the assumptions adopted in the calculations.

V. CONCLUDING REMARKS

Part of the present results obtained with large plastic scintillation counter measurements concerning the production of penetrating showers in light materials by high energy cosmic rays are in agreement with some earlier results of others using different methods of measurement. The integral frequency *vs* energy of the π^0 mesons produced in polystyrene relationship can be represented by a power law with an exponent equal to -1.7 ± 0.2 when no heavy filter was used. The validity of this relationship probably extends over an energy range of the π^0 mesons from 2 to 20 Bev. At the high energy end, our conclusions seem still reliable in contrast to other methods. The results obtained with the lead block *PB* in position and also the results obtained with the graphite block *G* as target material check the internal consistency of the method of analysis of the data obtained with the present apparatus. The relationship of the integral frequency *vs* the multiplicity of the charged mesons in the penetrating showers produced in the graphite block *G* can be described by a power law with an exponent equal to -4.2 ± 0.5 in the range of 4–9 particles. In the analysis of the pene-

[30] J. G. Wilson, *Progress in Cosmic Ray Physics* (Interscience Publishers, New York, 1952), E. P. George, pp. 395–450.

trating showers produced in the light materials, the effect of heavy meson production is considered small. This is justified from the cloud chamber investigations carried out at approximately the same altitude and in approximately the same energy range.[18]

The results concerning the bremsstrahlung produced by high energy cosmic-ray μ mesons confirm the essential correctness of the assumptions based upon which the calculations were made.

We wish to thank Mr. R. Hansen of the High Altitude Observatory at Climax, Colorado, for his very valuable cooperation.

PHYSICAL REVIEW VOLUME 97, NUMBER 1 JANUARY 1, 1955

New Formulation of the General Theory of Relativity

G. SZEKERES
University of Adelaide, Adelaide, South Australia
(Received February 23, 1954)

The principle of equivalence is partly abandoned as a basis for general relativity, and cosmic time is introduced as a new field variable. Field equations are obtained which take account of the self-energy of the gravitational field. The central symmetrical solution of the new field equations shows a significant deviation from the well-known Schwarzschild solution. It is free from singularities and gives a slightly smaller value for the perihelion motion of planetary orbits. Other consequences of the new formalism are:

(a) A rigorous definition can be given to the concept of ether.
(b) The energy-stress tensor of gravitational fields can be defined in a satisfactory manner.
(c) The gravitational field energy of a particle is distributed continuously over the space and its integral is equal to the gravitational mass of the particle.
(d) There are proper gravitational waves, generated by oscillating matter and propagating with the velocity of light.
(e) There is a noticable ether drift which tends to increase the gravitational mass of a body of given inertial mass.
(f) The ratio of gravitational and inertial mass of radiating energy is twice the corresponding ratio for neutral static matter.
(g) Hubble's recession-constant is equal to the reciprocal of the age of the universe.

An outstanding problem is to determine the coupling constant between the gravitational field and the cosmic time field. The value $\beta=1$ is strongly suggested by cosmological considerations. An experimental determination is possible if the rate of advance of the perihelion of the Mercury orbit is known more accurately.

1. INTRODUCTION

THE general theory of relativity rests upon the so-called *principle of equivalence* which states that: (a) It is possible to choose at every point of the space-time continuum a frame of reference which is Galilean at that particular point, i.e., in which special relativity holds in the immediate neighborhood of the point. (b) All frames of reference are equivalent in the sense that there is no general physical property which would distinguish one particular frame (or even a whole class of frames) from among the others.[1]

The two statements have an entirely different standing. Whereas postulate (a) is firmly established and supported by a considerable mass of experimental evidence, postulate (b) rests upon an essentially negative statement which obviously cannot be verified directly. In fact its validity has often been challenged in view of certain conceptual difficulties which arise from it both on the cosmical and local scales.

On the cosmical scale, postulate (b) is clearly in conflict with one of the most important cosmological principles known as *Weyl's postulate*, which necessarily leads to the notion of absolute cosmic time.[2] Although no formulation of Weyl's postulate has ever been given which would reveal that cosmic time has any noticeable physical effects, the conceptual conflict between the two principles can hardly be denied.

On the local scale, it is a well-known weakness of general relativity that it is incapable of defining the energy-stress tensor of the gravitational field in a satisfactory manner. The only known quantity which can be regarded as a substitute for the energy tensor is a pseudo-tensor which, if the principle of equivalence is accepted, can be transformed away in a suitable frame of reference. Closely connected with this is the following observation which was actually the starting point of the present investigations.

[1] A third postulate, often quoted in connection with the principle of equivalence, requires that physical laws should have a form which does not depend on the particular frame which one happens to use. This is not really a physical but an epistemological postulate; it expresses the belief that physical laws can be put in a particular mathematical form, the desirability of which can hardly be disputed.

[2] See H. Bondi, *Cosmology* (Cambridge University Press, Cambridge, 1952), p. 70.

In Einstein's law of gravitation,[3]

$$-R_{mn}+\tfrac{1}{2}Rg_{mn}=T_{mn}, \qquad (1)$$

the quantity T_{mn} on the right is the total energy-stress tensor which receives contributions from any source of energy that is present. Thus if electromagnetic field alone is present—no neutral matter—then one has to put the Maxwell-Poynting tensor for T_{mn}, multiplied, of course, by the constant of gravitation. This expresses the fact that electromagnetic energy, like any other other form of energy, creates gravitation. On the other hand, if gravitational field alone is present, i.e., in "empty space," nothing is put for T_{mn}, although it can hardly be denied that gravitational fields contain energy. If we accept the principle that every sort of energy creates gravitation, then T_{mn} should never be zero, not even in empty space, but should be equal to the energy-stress tensor of the gravitational field if other fields are absent.

On the intermediary (planetary) scale there is a further difficulty connected with the principle of equivalence, the problem of inertia. It is well known that apart from local variations of the gravitational field, a frame of reference which does not rotate with respect to distant stars and nebulas is very nearly a Galilean frame. This remarkable fact, first emphasized by E. Mach, remains a most unlikely coincidence when viewed in the light of the principle of equivalence. The usual explanation, based on Mach's principle which makes the distant stars and galaxies themselves responsible for inertia, does not resolve the difficulties completely. What is obviously needed is some sort of physical reality which, propagating in space and time, would determine the frames of inertia at every point.

To resolve these difficulties which seem to be inherent in the principle of equivalence, various modifications of the formalism of general relativity have been proposed. Without striving for completeness, I shall only mention some of the suggestions that have been made more recently. One is an attempt by Hoyle[4] to incorporate Weyl's postulate in the framework of general relativity. Hoyle describes the motion of Weyl's cosmological substratum by a time-like vector field C_m which is supposed to be curl-free (in order to satisfy Weyl's postulate), so that its covariant derivative,

$$C_{mn}=C_{m;n}=C_{m,n}-\left\{\begin{matrix} r \\ mn \end{matrix}\right\}C_r,$$

is a symmetric tensor. Here $C_{m,n}$ denotes the partial derivative $\partial C_m/\partial x_n$. He then proposes a modification of Eq. (1) by adding the term C_{mn} to the right-hand side. The purpose of the term is to replace Einstein's cosmological term and is supposed to be of the same order of smallness as the latter, hence negligible in planetary dimensions. This in any case precludes any measurable effects and extricates the theory from the range of direct experimental verification.

Another modification of general relativity has been proposed by Rosen[5] and more recently by Kohler.[6] These authors introduce a second metric tensor corresponding to a flat space-time which would provide a sort of Galilean background to the gravitational metric. This enables them of course to define the gravitational energy-stress tensor in a quite satisfactory manner. Nevertheless, from the point of view of relativity the procedure must be regarded as a retrograde step, since it renders the introducing of the proper (gravitational) metric tensor rather pointless, or at least somewhat artificial.

The basic idea of the present investigations is similar to Hoyle's: We introduce a scalar field variable τ, called *cosmic time*, and postulate an interaction between the metrical and τ fields. The interaction, however, is supposed to be quite macroscopic, and certainly not of cosmical smallness like in Hoyle's theory. The field equations are obtained from Hamilton's principle, using a Lagrangian which involves both the curvature scalar and a scalar derived from the τ field. The field equations are then solved for the central symmetrical case, under the assumption that the field-generating body is at absolute rest, i.e., at rest relatively to the inertial system determined by the gradient of τ. We shall call this inertial system the *ether*. According to this definition, *ether is a state of motion determined uniquely by the gradient of τ at every point of the space-time continuum.*

The central symmetrical solution has several interesting features. First, it has no Schwarzschild-type singularity but is continuous everywhere including the origin. Consequently, its geodesics are not identical with those in Schwarzschild's solution. Assuming that planetary orbits are geodesics in the metrical field, one obtains a perennial precession of the perihelion which is $[1-(\beta/6(2+\beta))]$ times the Einstein value, where β is a certain positive constant. On cosmological grounds there is some reason to believe that the value of the constant β is 1. This would give for Mercury 40.5″ per century instead of 43″, a value which is certainly not ruled out by present experimental determinations. For the deflection of light in the sun's gravitational field one obtains the same value as in ordinary relativity, except for terms of second order smallness.

Another feature of the solution is that it is possible to define with the help of T_{mn} and the τ field an energy-momentum vector density ρ^n in such a manner that the integral of ρ^0 over the whole space has a finite value and in fact is equal to the gravitational mass of the central symmetrical body. Thus the energy density of neutral matter is continuously distributed over the space, instead of being concentrated in singularities.

[3] Roman indices go from 0 to 3. The metric ground form in a locally Galilean frame is $ds^2=dx_0^2-dx_1^2-dx_2^2-dx_3^2$.

[4] F. Hoyle, Monthly Notices Roy. Astron. Soc. **108**, 372 (1948) and **109**, 365 (1949).

[5] N. Rosen, Phys. Rev. **57**, 147 (1940).

[6] M. Kohler, Z. Physik **131**, 571 (1952) and **134**, 286 (1953).

The explicit expression for ρ^n is

$$\rho^n=\frac{1}{8\pi\kappa}(C_kC^k)^{-1}(2C^sC_s{}^n-C^nC_s{}^s), \tag{2}$$

where κ is the gravitational constant. In the case of an ideal fluid with rest density μ and isotropic pressure p, resting in the ether,[7] this gives

$$\rho=\rho^0=\mu+3p, \quad \rho^1=\rho^2=\rho^3=0. \tag{3}$$

If the fluid is moving with uniform velocity v relatively to the ether[8] in the direction of the positive x_1 axis and the pressure is negligible, then in a frame moving with the fluid we get

$$\rho^0=(1-v^2)^{-\frac{1}{2}}\mu, \quad \rho^1=v(1-v^2)^{-\frac{1}{2}}\mu, \quad \rho^2=\rho^3=0. \tag{4}$$

Thus the gravitational mass density is $(1-v^2)^{-\frac{1}{2}}\mu$, as opposed to the inertial mass density which is μ. This is a typical ether-drift effect which, if it exists, cannot be reconciled with the principle of equivalence.

If α is the angular distance from the south pole of the ecliptic of the sun's direction of absolute motion, v_s its absolute velocity, and v_e the orbital velocity of the earth relatively to the sun, then the square of the absolute velocity of the earth is between the values $v_s^2+v_e^2 \pm 2v_ev_s\sin\alpha$, and the maximum seasonal variation of the factor $(1-v^2)^{-\frac{1}{2}}$ is

$$|(1-v_s^2-v_e^2-2v_ev_s\sin\alpha)^{-\frac{1}{2}} - (1-v_s^2-v_e^2+2v_ev_s\sin\alpha)^{-\frac{1}{2}}| \sim 2v_ev_s|\sin\alpha|.$$

A seasonal variation of the same magnitude can therefore be predicted for the gravitational acceleration at any point of the earth's surface. To estimate the magnitude of the effect, we have to know the direction and magnitude of the absolute velocity of the solar system. This was determined by Miller from ether-drift experiments of the Michelson-Morley type,[9] the positive outcome of which is yet unexplained. According to Miller $\alpha=7°$, $v_s=0.7\times10^{-3}$, and since $v_e=10^{-4}$, the relative magnitude of the above effect is expected to be 1.7×10^{-8}. This is perhaps just within the limits of observability with present-day experimental techniques.

In a frame which rests in the ether, the components of the vector density (4) become

$$\rho^0=\frac{1+v^2}{1-v^2}\mu, \quad \rho^1=\frac{2v}{1-v^2}\mu, \quad \rho^2=\rho^3=0. \tag{5}$$

Hence the gravitational mass of a high-velocity particle with rest mass m is not $(1-v^2)^{-\frac{1}{2}}m$ but $(1+v^2)(1-v^2)^{-\frac{3}{2}}m$. In the limiting case of photons $v=1$, and therefore the gravitational mass is double the inertial mass, i.e., *the apparent gravitational constant of radiating energy is twice the gravitational constant of static matter.* The same result can be obtained from formula (2) directly, if one puts for $T_n{}^m$ the energy-stress tensor of isotropic radiation. The result is quite unexpected and it throws a new light on the fact that Einstein's light deflection value is twice the Newtonian value.

In Sec. 7 it will be shown that the scalar quantity $\Psi=\Box\tau$ propagates in waves generated by nonstatic matter. Thus inertial frames are affected by every change in the matter distribution of distant parts of the universe, the disturbance being propagated with the velocity of light. So our new formulation of general relativity removes the most important conceptural difficulties which arise from the principle of equivalence, without upsetting the logical structure of the theory.

The new formalism may also help in clearing up some difficulties which have arisen in connection with recent experimental findings of Finlay-Freundlich. In the early days of relativity Einstein predicted that the Fraunhofer lines in light coming from heavy stars must show a shift towards the red, in the proportion $q=(g_{00})^{\frac{1}{2}}$. Recent measurements of the sun by Finlay-Freundlich[10] seem to indicate that at the central portions of the disk, the observed red shift is considerably smaller than the predicted value, but increases rapidly towards the limb, eventually exceeding the Einstein value. It has been suggested[11] that part of the observed effect is nongravitational and is due to photon-photon collisions. There is, however, a small residual red shift which may be due to gravitational effects and which is about one-fifth of the Einstein value, a result which is also confirmed by observations on Sirius B.

At the end of Sec. 6 it will be shown that if one makes the perfectly plausible assumption that in Bohr's frequency relation,

$$E_2-E_1=h\nu,$$

ν is to be measured not in metric but in cosmic time units, then the higher metric frequency of light emitted by an atom on the sun just compensates the red shift to be expected and the observed gravitational red shift should be zero. It appears therefore that the actual (experimental) red shift of a photon is not 1/5 but 6/5 times the theoretical value. It is interesting to note in this connection that Freundlich's deflection value for photons in the sun's gravitational field also exceeds the predicted value, by about the same amount. It is not unlikely that the two discrepancies have a common origin.

There are various cosmological models compatible with the new field equations. One of them, corresponding to $\beta=1$, is a particularly simple one. It has a linear expansion law and has the constant energy density 3/2 when measured in absolute cosmical units.

[7] The velocity of light is taken to be 1.

[8] It is assumed in the calculations that there is no significant ether drag by the moving body.

[9] D. C. Miller, Revs. Modern Phys. 5, 203 (1933). Miller found for optical phenomena an ether drag coefficient 0.0514.

[10] E. Finlay-Freundlich, Nachr. Akad. Wiss. Göttingen Math.-physik. Kl., 1954a, No. 7 (1954).

[11] E. Finlay-Freundlich, Proc. Phys. Soc. (London) **A67**, 192 (1954) and M. Born, Proc. Phys. Soc. (London) **A67**, 193 (1954).

2. THE FIELD EQUATIONS

The fundamental assumption underlying these investigations is that cosmic time τ is not a mere coordinate but a scalar field variable which has the property that its gradient,

$$C_m=\tau_{,m}=\partial\tau/\partial x_m, \tag{6}$$

is a time-like vector, $g^{mn}C_mC_n>0$. Since we want to derive the field equations from Hamilton's principle, the fundamental problem is to find a suitable expression for the world Lagrangian density in which the action of the τ field has been incorporated. In postulating a Lagrangian we cannot very well reply on empirical considerations since nothing definite is known about the interaction of the g_{mn} and τ fields. In fact physicists have never found it necessary (or even desirable) to postulate the existence of a τ field at all. Hence we must reply on certain principles which are partly aesthetic (e.g., formal simplicity from the mathematical point of view) and partly motivated by the results we expect to find.

Let R_{mrsn} be the covariant Riemannian curvature tensor and

$$R=g^{mn}g^{rs}R_{mrsn} \tag{7}$$

the curvature scalar. The corresponding density is written

$$\mathfrak{R}=\Delta^{\frac{1}{2}}R, \quad \Delta=-\det g_{mn}. \tag{8}$$

Now put

$$C_{mn}=C_{m;n}=C_{m,n}-C_r\left\{\begin{matrix} r \\ mn \end{matrix}\right\}, \tag{9}$$

$$C_{mrsn}=C_{mr}C_{sn}, \tag{10}$$

$$C=g^{mn}g^{rs}C_{mrsn}, \quad \mathfrak{C}=\Delta^{\frac{1}{2}}C. \tag{11}$$

Clearly C_{mn} is a symmetrical tensor,

$$C_{mn}=\tau_{,m,n}-\left\{\begin{matrix} r \\ mn \end{matrix}\right\}\tau_{,r}=C_{nm}. \tag{12}$$

With these notations, the following expression suggests itself as a suitable Lagrangian density:

$$\mathfrak{L}=\mathfrak{R}+\tfrac{1}{2}\beta\mathfrak{C}, \tag{13}$$

where β is a suitable constant. The numerical value of the coupling constant β depends on the normalization of τ and is left undetermined for the time being.

From the mathematical-aesthetic point of view it is quite natural to combine the scalars R and C. Expressions (7) and (11) have a very similar form, and a glance at (10) shows that C_{mnrs} forms a kind of symmetrical counterpart to the tensor R_{mnrs}. In fact C_{mnrs} has the symmetries

$$C_{mnrs}=C_{nmrs}=C_{mnsr}=C_{rsmn},$$

whereas R_{mnrs} has the well-known symmetries

$$R_{mnrs}=-R_{nmrs}=-R_{mnsr}=R_{rsmn},$$

$$R_{mnrs}+R_{mrsn}+R_{msnr}=0.$$

Note also that C_{mnrs} does not involve higher than second-order derivatives of τ. Of course, a final justification of postulate (13) must be postponed until we have explored some of its physical consequences.

Hamilton's principle requires that

$$\delta\int(\mathfrak{R}+\tfrac{1}{2}\beta\mathfrak{C})d^4x=0 \tag{14}$$

for any variation of g_{mn} and τ which vanishes at the boundary of the domain of integration. Variation of g_{mn} gives

$$\delta\mathfrak{R}=(\mathfrak{R}_{mn}-\tfrac{1}{2}\mathfrak{R}g_{mn})\delta g^{mn},$$

where

$$R_{mn}=g^{rs}R_{rmns}.$$

δC is obtained from (10), (11), and (12). We have

$$C_{mr}=C_{m,r}-\tfrac{1}{2}g^{ns}(g_{sm,r}+g_{sr,m}-g_{rm,s})C_n,$$

and a routine calculation gives, using partial integration and the relation $\delta g_{mn}=-g_{mr}g_{ns}\delta g^{rs}$,

$$\delta\mathfrak{C}=\{-C_m\mathfrak{C}_n{}^r{}_{;r}-C_n\mathfrak{C}_m{}^r{}_{;r}+C_{mn}\mathfrak{C}_r{}^r+C^r\mathfrak{C}_{mn;r}-\tfrac{1}{2}g_{mn}\mathfrak{C}\}\delta g^{mn}.$$

Hence the gravitational field equations are

$$R_{mn}-\tfrac{1}{2}Rg_{mn}+\beta T_{mn}=0, \tag{15}$$

where

$$T_{mn}=-\tfrac{1}{2}C_mC_n{}^r{}_{;r}-\tfrac{1}{2}C_nC_m{}^r{}_{;r}+\tfrac{1}{2}C_{mn}C_r{}^r+\tfrac{1}{2}C^rC_{mn;r}-\tfrac{1}{4}g_{mn}C. \tag{16}$$

T_{mn} is the gravitational field energy-stress tensor, it satisfies the conservation law

$$T_n{}^m{}_{;m}=0. \tag{17}$$

This follows immediately from (9). (17) is a "weak" conservation law, i.e., not an identity but valid only in consequence of the field equations.

Leaving g_{mn} unchanged and varying τ one obtains the supplementary field equation,

$$C^{mn}{}_{;n;m}=0. \tag{18}$$

Since the term $\frac{1}{2}\beta C$ in (13) is macroscopic, of the same order of magnitude as R, it cannot replace the cosmological term, like in Hoyle's theory. Therefore, when dealing with the cosmological situation we shall have to add another term of cosmical smallness to the Lagrangian. Instead of the usual $-\gamma\Delta^{\frac{1}{2}}$, where γ is a small constant of dimension (length)$^{-2}$, we shall add the term $-\gamma\tau^{-2}\Delta^{\frac{1}{2}}$ to the right-hand side of (13), where γ is an absolute constant provided that the unit of cosmic time is adjusted to the unit of metric length. It is assumed here that τ is measured from an absolute origin so that at the present epoch it has a very large value (in ordinary units). The final form of the Lagrangian is therefore

$$\mathfrak{L}=\mathfrak{R}+\tfrac{1}{2}\beta\mathfrak{C}-\gamma\tau^{-2}\Delta^{\frac{1}{2}}. \tag{19}$$

Hamilton's principle gives the cosmological field equations

$$R_{mn}-\tfrac{1}{2}Rg_{mn}+\beta T_{mn}+\tfrac{1}{2}\gamma\tau^{-2}g_{mn}=0, \tag{20}$$

where T_{mn} is defined by (16), and

$$\beta C^{mn}{}_{;n;m}+2\gamma\tau^{-3}=0. \tag{21}$$

In the next section it will be shown that there exist simple cosmological solutions of these equations and a particularly simple model is obtained if $\beta=1$ and γ has the value $\frac{3}{2}$.

3. COSMOLOGICAL MODELS

In order to obtain some information regarding the constants β and γ we begin with the discussion of some simple cosmological models which are compatible with the field equations. Our standpoint is that a cosmological model is "empty," i.e., *it derives all its energy from its gravitational field*. Later on we shall verify the correctness of this view in the case of a central symmetrical neutral body.

In all what follows, Greek suffixes shall run from 1 to 3 only. For reasons of uniformity it is desirable that in a cosmological model the line element shall have the form[12]

$$g_{00}=1,\quad g_{0\mu}=0,\quad g_{\mu\nu}=-\left(\delta_{\mu\nu}+\frac{K}{1-r^2K}x_\mu x_\nu\right)F,$$

where F is a function of $t=x_4$ alone, $r^2=x_1^2+x_2^2+x_3^2$, and K is a constant. In addition we require that also τ shall be a function of t alone. In a strictly uniform universe we may even expect to find $K=0$ and $d\tau/dt=\alpha=$const. I am going to show now that the field equations have in fact solutions of this simple form. By adjusting the unit of cosmic time to the unit of metric time (i.e., by using a suitable normalizing factor for τ) we can make $\alpha=1$, and hence

$$\tau=t. \tag{22}$$

For the metric tensor we put

$$g_{00}=1,\quad g_{0\mu}=0,\quad g_{\mu\nu}=-\delta_{\mu\nu}F(t). \tag{23}$$

The only nonvanishing Christoffel symbols are

$$\left\{\begin{matrix}0\\ \mu\nu\end{matrix}\right\}=\tfrac{1}{2}F'\delta_{\mu\nu},\quad \left\{\begin{matrix}\mu\\ 0\nu\end{matrix}\right\}=\tfrac{1}{2}(F'/F)\delta_{\mu\nu} \tag{24}$$

and they give

$$R_{00}=\tfrac{3}{2}(F''/F)-\tfrac{3}{4}(F'/F)^2,\quad R_{0\mu}=0,$$
$$R_{\mu\nu}=[\tfrac{1}{2}(F''/F)+\tfrac{1}{4}(F'/F)^2]g_{\mu\nu},$$
$$R=3F''/F,$$

hence

$$R_{00}-\tfrac{1}{2}g_{00}R=-\tfrac{3}{4}(F'/F)^2, \tag{25}$$
$$R_{0\mu}-\tfrac{1}{2}g_{0\mu}R=0, \tag{25'}$$
$$R_{\mu\nu}-\tfrac{1}{2}g_{\mu\nu}R=[-(F''/F)+\tfrac{1}{4}(F'/F)^2]g_{\mu\nu}. \tag{25''}$$

[12] Reference 2, p. 102.

Similarly, we obtain from (9), (11), (22), (23), and (24):

$$C_0=1,\quad C_\mu=0,\quad C_{00}=C_{0\mu}=0,\quad C_{\mu\nu}=-\tfrac{1}{2}F'\delta_{\mu\nu},$$
$$C_r{}^r=\tfrac{3}{2}(F'/F),\quad C=\tfrac{3}{4}(F'/F)^2,$$
$$C_0{}^r{}_{;r}=-\tfrac{3}{4}(F'/F)^2,\quad C_\mu{}^r{}_{;r}=0,\quad C_{00;0}=C_{0\mu;0}=0,$$
$$C_{\mu\nu;0}=\tfrac{1}{2}[(F''/F)-(F'/F)^2]g_{\mu\nu};$$

hence by (16),

$$T_{00}=\tfrac{9}{16}(F'/F)^2,\quad T_{0\mu}=0, \tag{26}$$
$$T_{\mu\nu}=\tfrac{1}{4}[(F''/F)-\tfrac{1}{4}(F'/F)^2]g_{\mu\nu}. \tag{26'}$$

These, together with (20) and (25)–(25''), give

$$(\tfrac{9}{16}\beta-\tfrac{3}{4})(F'/F)^2+\tfrac{1}{2}\gamma t^{-2}=0, \tag{27}$$

$$(\tfrac{1}{4}\beta-1)(F''/F)+(\tfrac{1}{4}-\tfrac{1}{16}\beta)(F'/F)^2+\tfrac{1}{2}\gamma t^{-2}=0. \tag{28}$$

Finally, (21) gives

$$-\tfrac{3}{2}\beta\frac{F'}{F}\frac{F''}{F}+\tfrac{3}{8}\beta\left(\frac{F'}{F}\right)^3+2\gamma t^{-3}=0. \tag{29}$$

Equation (27) shows that F must have the form[13]

$$F=t^\alpha, \tag{30}$$

and the equations give the relations

$$(\tfrac{9}{16}\beta-\tfrac{3}{4})\alpha^2+\tfrac{1}{2}\gamma=0,$$
$$(\tfrac{1}{4}\beta-1)(\alpha^2-\alpha)+(\tfrac{1}{4}-\tfrac{1}{16}\beta)\alpha^2+\tfrac{1}{2}\gamma=0,$$
$$-\tfrac{3}{2}\beta\alpha(\alpha^2-\alpha)+\tfrac{3}{8}\beta\alpha^3+2\gamma=0.$$

Eliminating γ from the first two equations, we get, assuming that $\alpha\neq0$,

$$\beta=8/(3\alpha+2); \tag{31}$$

hence, by the first equation,

$$\gamma=\tfrac{3}{2}\alpha^2(3\alpha-4)/(3\alpha+2). \tag{32}$$

The third equation is also satisfied by these values, and we get a one-parameter family of solutions.

Discarding $\alpha=0$ which gives $\gamma=0$ and leads to a flat space, the most promising solution is the one corresponding to $\alpha=2$ which leads to a linearly expanding model. It gives

$$\beta=1,\quad \gamma=\tfrac{3}{2}, \tag{33}$$

and the line element becomes

$$ds^2=dt^2-t^2\sum dx_\mu{}^2.$$

Properties of the more general model,

$$g_{00}=1,\quad g_{0\mu}=0,\quad g_{\mu\nu}=-t^\alpha\delta_{\mu\nu},\quad \alpha>0 \tag{34}$$

will be investigated in the last section. For later reference we note the following formulas which follow easily

[13] Apart from a constant factor, which however can be made 1 by a trivial transformation of the space coordinates.

from (24), (26), (26′), (30), (31), (32), and (34):

$$\left\{\begin{matrix}0\\ \mu\nu\end{matrix}\right\}=\tfrac{1}{2}\alpha t^{\alpha-1}\delta_{\mu\nu},\quad \left\{\begin{matrix}\mu\\ 0\nu\end{matrix}\right\}=\tfrac{1}{2}\alpha t^{-1}\delta_{\mu\nu}, \tag{35}$$

$$T_0{}^0=\tfrac{9}{16}\alpha^2t^{-2},\quad T^\mu{}_\nu=\tfrac{1}{16}\alpha(3\alpha-4)t^{-2}\delta_{\mu\nu}, \tag{36}$$

$$T=T^\tau{}_\tau=\tfrac{3}{8}\alpha(3\alpha-2)t^{-2}.$$

4. THE GRAVITATIONAL FIELD OF A CENTRAL SYMMETRICAL BODY

We proceed now to integrate the field equations under the assumption that the cosmological term can be neglected and that the metric tensor has the form

$$g_{00}=g,\quad g_{0\mu}=0,\quad g_{\mu\nu}=-[\delta_{\mu\nu}+(f-1)\xi_\mu\xi_\nu], \tag{37}$$

where for abbreviation we have put

$$\xi_\mu=x_\mu/r,$$

and f and g are functions of $r=(x_1{}^2+x_2{}^2+x_3{}^2)^{\frac{1}{2}}$ alone. We also assume that τ depends only on t, or in other words that the body is at rest relatively to the ether. From (37) we obtain

$$g^{00}=g^{-1},\quad g^{0\mu}=0,\quad g^{\mu\nu}=-\delta_{\mu\nu}+(1-f^{-1})\xi_\mu\xi_\nu, \tag{38}$$

$$\Delta=fg,$$

and the nonvanishing Christoffel symbols are

$$\left\{\begin{matrix}\mu\\ 00\end{matrix}\right\}=-\frac{1}{2}\frac{g'}{f}\xi_\mu,\quad \left\{\begin{matrix}0\\ \mu0\end{matrix}\right\}=-\frac{1}{2}\frac{g'}{g}\xi_\mu,$$

$$\left\{\begin{matrix}\mu\\ \nu\rho\end{matrix}\right\}=-\frac{1}{2}\frac{f'}{f}\xi_\mu\xi_\nu\xi_\rho+\frac{1}{r}(1-f^{-1})\xi_\mu(\delta_{\nu\rho}-\xi_\nu\xi_\rho), \tag{39}$$

$$\left\{\begin{matrix}\rho\\ \mu\rho\end{matrix}\right\}=-\frac{1}{2}\frac{f'}{f}\xi_\mu.$$

They give the following expressions:[14]

$$R_{00}-\tfrac{1}{2}g_{00}R=\frac{1}{r^2}g\left\{1-f^{-1}+r\frac{f'}{f^2}\right\}, \tag{40}$$

$$R_{0\mu}-\tfrac{1}{2}g_{0\mu}R=0, \tag{40′}$$

$$R_{\mu\nu}-\tfrac{1}{2}g_{\mu\nu}R=\left[-\frac{1}{r}\frac{g'}{g}+\frac{1}{r^2}(f-1)\right]\xi_\mu\xi_\nu$$
$$+f^{-1}\left[-\frac{1}{2}\frac{g''}{g}+\frac{1}{4}\left(\frac{g'}{g}\right)^2+\frac{1}{4}\frac{f'g'}{fg}-\frac{1}{2r}\left(\frac{g'}{g}-\frac{f'}{f}\right)\right](\delta_{\mu\nu}-\xi_\mu\xi_\nu). \tag{40″}$$

[14] See P. G. Bergmann, *Introduction to the Theory of Relativity* (Prentice-Hall, Inc., New York, 1942), p. 201.

Since τ only depends on t, we obtain by (6), (9), (11), (38), (39)

$$C_0=\tau',\quad C_\mu=0,\quad C^0=g^{-1}\tau',\quad C^\mu=0,\quad C_{00}=\tau'',$$

$$C_0{}^0=g^{-1}\tau'',\quad C_{\mu\nu}=C_\nu{}^\mu=0,\quad C_{0\mu}=-\frac{1}{2}\frac{g'}{g}\tau'\xi_\mu,$$

$$C_0{}^\mu=-\frac{1}{2}\frac{g'}{fg}\tau'\xi_\mu,\quad C_\mu{}^0=-\frac{1}{2}\frac{g'}{g^2}\tau'\xi_\mu,$$

$$C_\tau{}^\tau=g^{-1}\tau'',\quad C=g^{-2}(\tau'')^2-\tfrac{1}{2}(g')^2f^{-1}g^{-3}(\tau')^2,$$

$$C_0{}^\tau{}_{;\tau}=\frac{1}{f}\left[\frac{1}{2}\frac{g''}{g}-\frac{1}{4}\left(\frac{g'}{g}\right)^2-\frac{1}{4}\frac{f'g'}{fg}+\frac{1}{r}\frac{g'}{g}\right]\tau'+\frac{1}{g}\tau'',$$

$$C_\mu{}^\tau{}_{;\tau}=-\frac{g'}{g^2}\tau''\xi_\mu,$$

$$C_{00;0}=\tau'''+\frac{1}{2}\frac{(g')^2}{fg}\tau',\quad C_{0\mu;0}=-\frac{g'}{g}\tau''\xi_\mu,$$

$$C_{\mu\nu;0}=\frac{1}{2}\left(\frac{g'}{g}\right)^2\tau'\xi_\mu\xi_\nu,$$

$$C^{\mu\tau}{}_{;\tau;\mu}=\frac{1}{fg}\left(\frac{g''}{g}-2\left(\frac{g'}{g}\right)^2-\frac{1}{2}\frac{f'g'}{fg}+\frac{2}{r}\frac{g'}{g}\right)\tau'',$$

$$C^{0\tau}{}_{;\tau;0}=\frac{1}{fg}\left(\frac{1}{2}\frac{g''}{g}+\frac{1}{4}\left(\frac{g'}{g}\right)^2-\frac{1}{4}\frac{f'g'}{fg}+\frac{1}{r}\frac{g'}{g}\right)\tau''+\frac{1}{g^2}\tau'''.$$

With these values one obtains

$$T_{00}=\frac{1}{f}\left[-\frac{1}{2}\frac{g''}{g}+\frac{5}{8}\left(\frac{g'}{g}\right)^2+\frac{1}{4}\frac{f'g'}{fg}-\frac{1}{r}\frac{g'}{g}\right](\tau')^2$$
$$+\tfrac{1}{4}g^{-1}(\tau'')^2-\tfrac{1}{2}g^{-1}\tau'\tau'', \tag{41}$$

$$T_{0\mu}=-\tfrac{1}{4}(g'/g^2)\tau'\tau''\xi_\mu, \tag{41′}$$

$$T_{\mu\nu}=-\frac{1}{g}\left[\frac{1}{8}\left(\frac{g'}{g}\tau'\right)^2-\frac{1}{4}\frac{f}{g}(\tau'')^2\right]\xi_\mu\xi_\nu$$
$$-\frac{1}{fg}\left[\frac{1}{8}\left(\frac{g'}{g}\tau'\right)^2-\frac{1}{4}\frac{f}{g}(\tau'')^2\right](\delta_{\mu\nu}-\xi_\mu\xi_\nu), \tag{41″}$$

$$C^{\tau\sigma}{}_{;\sigma;\tau}=\frac{1}{fg}\left[\frac{3}{2}\frac{g''}{g}-\frac{7}{4}\left(\frac{g'}{g}\right)^2-\frac{3}{4}\frac{f'g'}{fg}+\frac{3}{r}\frac{g'}{g}\right]\tau''+\frac{1}{g^2}\tau'''. \tag{42}$$

Hence, using the field equations (15) and (18), we

obtain from (40)–(40″), (41)–(41″), and (42)

$$\frac{1}{r^2}g\left(1-f^{-1}+r\frac{f'}{f^2}\right)+\beta f^{-1}\left[\frac{1}{2}\frac{g''}{g}-\frac{5}{8}\left(\frac{g'}{g}\right)^2-\frac{1}{4}\frac{f'g'}{fg}+\frac{1}{r}\frac{g'}{g}\right](\tau')^2+\tfrac{1}{4}\beta g^{-1}(\tau'')^2-\tfrac{1}{2}\beta g^{-1}\tau'\tau''=0, \quad (43)$$

$$(g'/g^2)\tau'\tau''=0, \quad (44)$$

$$-\frac{1}{r}\frac{g'}{g}+\frac{1}{r^2}(f-1)+\beta g^{-1}\left[\frac{1}{8}\left(\frac{g'}{g}\tau'\right)^2-\frac{1}{4}\frac{f}{g}(\tau'')^2\right]=0, \quad (45)$$

$$f^{-1}\left[\frac{1}{2}\frac{g''}{g}-\frac{1}{4}\left(\frac{g'}{g}\right)^2-\frac{1}{4}\frac{f'g'}{fg}+\frac{1}{2r}\left(\frac{g'}{g}-\frac{f'}{f}\right)\right]+\tfrac{1}{8}\beta(g')^2f^{-1}g^{-3}(\tau')^2-\tfrac{1}{4}\beta g^{-2}(\tau'')^2=0, \quad (46)$$

$$\left[\frac{3}{2}\frac{g''}{g}-\frac{7}{4}\left(\frac{g'}{g}\right)^2-\frac{3}{4}\frac{f'g'}{fg}+\frac{3}{r}\frac{g'}{g}\right]\tau''+\frac{f}{g}\tau'''=0. \quad (47)$$

These equations can be satisfied with $g'=0$, but then (43), (45), and (46) give $f=1$, $\tau''=0$, i.e., a flat space. Discarding this possibility we assume $g'\neq 0$; hence, by (44), $\tau''=0$ and $\tau'=\text{const}$. Using a suitable scale factor for τ, we may put $\tau'=1$, and the field equations (43), (45), and (46) become

$$\frac{1}{r^2}\left(f-1+r\frac{f'}{f}\right)+\beta g^{-1}\left[\frac{1}{2}\frac{g''}{g}-\frac{5}{8}\left(\frac{g'}{g}\right)^2-\frac{1}{4}\frac{f'g'}{fg}+\frac{1}{r}\frac{g'}{g}\right]=0, \quad (48)$$

$$f=1+r\frac{g'}{g}-\tfrac{1}{8}\beta r^2\frac{(g')^2}{g^3}, \quad (49)$$

$$\frac{f'}{f}=\left[r\frac{g''}{g}-\tfrac{1}{2}r\left(\frac{g'}{g}\right)^2+\frac{g'}{g}+\tfrac{1}{4}r\beta\frac{(g')^2}{g^3}\right]\left(1+\tfrac{1}{2}r\frac{g'}{g}\right)^{-1}. \quad (50)$$

These are three equations to be satisfied by the functions f and g. Substituting f and f'/f from (49) and (50) into (48), we obtain

$$\left(1+\frac{1}{2}\frac{\beta}{g}\right)\left[\frac{g''}{g}+\frac{2}{r}\frac{g'}{g}-\left(\frac{g'}{g}\right)^2\right]+\left(\frac{g'}{g}\right)^2\left(1+\tfrac{1}{4}\frac{\beta}{g}\right)\left(1-\tfrac{1}{4}\beta r\frac{g'}{g^2}\right)=0. \quad (51)$$

The same relation is obtained if f'/f is expressed from (49) and substituted into (50). This shows that Eqs. (48)–(50) are compatible.

Equation (51) can be satisfied by a power series which is regular at $r=\infty$. If the unit of time is chosen so that $g(\infty)=1$, then the power series begins with the terms

$$g=1-\frac{2m}{r}+\frac{\beta}{2+\beta}\frac{m^2}{r^2}+O\left(\frac{m^3}{r^3}\right),$$
$$g^{-1}=1+\frac{2m}{r}+\frac{8+3\beta}{2+\beta}\frac{m^2}{r^2}+O\left(\frac{m^3}{r^3}\right), \quad (52)$$

where m is a constant. From (49) we get

$$f=1+\frac{2m}{r}+\frac{16+2\beta-\beta^2}{4+2\beta}\frac{m^2}{r^2}+O\left(\frac{m^3}{r^3}\right),$$
$$f^{-1}=1-\frac{2m}{r}=\frac{6\beta+\beta^2}{4+2\beta}\frac{m^2}{r^2}+O\left(\frac{m^3}{r^3}\right). \quad (53)$$

We shall see presently that m is the gravitational radius of the attracting body.

Equation (51) can be brought to a more manageable form by making the substitution $u=1/r$ and regarding u as a function of g. We obtain

$$\frac{dg}{dr}=-\frac{u^2}{u'},\quad \frac{d^2g}{dr^2}=\frac{2u^3}{u'}-u^4\frac{u''}{(u')^3}, \quad (54)$$

where $u'=du/dg$ and $u''=d^2u/dg^2$. This transforms (51) into the linear equation

$$g(g+\tfrac{1}{2}\beta)u''+\tfrac{1}{4}\beta u'-\tfrac{1}{4}(\beta/g^2)(g+\tfrac{1}{4}\beta)u=0. \quad (55)$$

The initial conditions are, by (52),

$$u(1)=0,\quad u'(1)=-1/2m. \quad (56)$$

The general solution of (55) is

$$u=c_1\exp\left(1+\frac{1}{2}\frac{\beta}{g}\right)^{\frac{1}{2}}\left[\left(1+\frac{1}{2}\frac{\beta}{g}\right)^{\frac{1}{2}}+1\right]^{-1}+c_2\exp\left[-\left(1+\frac{1}{2}\frac{\beta}{g}\right)^{\frac{1}{2}}\right]\left[\left(1+\frac{1}{2}\frac{\beta}{g}\right)^{\frac{1}{2}}-1\right]^{-1}.$$

Noting the boundary conditions (56) we obtain

$$u=\frac{1}{2m}\left\{[1+(1+\tfrac{1}{2}\beta)^{-1}]\left[\left(1+\frac{1}{2}\frac{\beta}{g}\right)^{\frac{1}{2}}+1\right]^{-1}\times\exp\left[\left(1+\frac{1}{2}\frac{\beta}{g}\right)^{\frac{1}{2}}-(1+\tfrac{1}{2}\beta)^{\frac{1}{2}}\right]-[1-(1+\tfrac{1}{2}\beta)^{-1}]\left[\left(1+\frac{1}{2}\frac{\beta}{g}\right)^{\frac{1}{2}}-1\right]^{-1}\times\exp[(1+\tfrac{1}{2}\beta)^{\frac{1}{2}}-(1+\tfrac{1}{2}\beta g^{-1})^{\frac{1}{2}}]\right\}. \quad (57)$$

Hence $u(g)$ increases monotonically from 0 to $+\infty$ when g decreases from 1 to 0. In particular $g(r)>0$ for $r>0$ and *there is no Schwarzschild-type singularity of the metric tensor* at some finite distance from the origin.

We proceed now to work out some of the geometrical and physical consequences of the solution.

5. PLANETARY ORBITS

The equations of geodesics are, by (39),

$$\frac{d^2x_\mu}{ds^2}+\left(\frac{1}{2}\frac{f'}{f}+\frac{1}{rf}-\frac{1}{r}\right)\xi_\mu\left(\frac{dr}{ds}\right)^2$$
$$+\frac{1}{r}\left(1-\frac{1}{f}\right)\xi_\mu\sum_\nu\left(\frac{dx_\nu}{ds}\right)^2+\frac{1}{2}\frac{g'}{f}\xi_\mu\left(\frac{dt}{ds}\right)^2=0, \quad (58)$$

$$\frac{d^2t}{ds^2}+\frac{g'}{g}\frac{dt}{ds}\frac{dr}{ds}=0. \quad (59)$$

If we note that

$$\frac{dx_\mu}{ds}=\frac{dx_\mu}{dt}\frac{dt}{ds},$$

$$\frac{d^2x_\mu}{ds^2}=\frac{d^2x_\mu}{dt^2}\left(\frac{dt}{ds}\right)^2+\frac{dx_\mu}{dt}\frac{d^2t}{ds^2}=\left(\frac{d^2x_\mu}{dt^2}-\frac{g'}{g}\frac{dx_\mu}{dt}\frac{dr}{dt}\right)\left(\frac{dt}{ds}\right)^2$$

by (59), we obtain from (58), after cancelling by $(dt/ds)^2$ and writing $v^2=\sum_\nu(dx_\nu/dt)^2$,

$$\frac{d^2x_\mu}{dt^2}+\left(\frac{1}{2}\frac{f'}{f}+\frac{1}{rf}-\frac{1}{r}\right)\xi_\mu\left(\frac{dr}{dt}\right)^2+\frac{1}{r}\left(1-\frac{1}{f}\right)\xi_\mu v^2$$
$$+\frac{1}{2}\frac{g'}{f}\xi_\mu-\frac{g'}{g}\frac{dx_\mu}{dt}\frac{dr}{dt}=0. \quad (58')$$

If we assume that m/r is small, this gives by (52) and (53):

$$\frac{d^2x_\mu}{dt^2}+\frac{m}{r^2}\xi_\mu=\left\{3\frac{m}{r^2}\left(\frac{dr}{dt}\right)^2\left[1+O\left(\frac{m}{r}\right)\right]\right.$$
$$-\frac{2m}{r^2}v^2\left[1+O\left(\frac{m}{r}\right)\right]+\left(2+\frac{\beta}{2+\beta}\right)\frac{m^2}{r^3}$$
$$\left.\times\left[1+O\left(\frac{m}{r}\right)\right]\right\}\xi_\mu+\frac{2m}{r^2}\left[1+O\left(\frac{m}{r}\right)\right]\frac{dr}{dt}\frac{dx_\mu}{dt}. \quad (60)$$

The equation shows that m is the gravitational radius of the attracting body, i.e.,

$$m=\kappa M, \quad (61)$$

where M is the mass in ordinary units. The terms on the right-hand side of (60) represent radial and tangential disturbing accelerations. They are identical with those in general relativity with the exception of the term $[\beta m^2/(2+\beta)r^3]\xi_\mu$ which represents a radial outwards disturbing accelerations whose magnitude is

$$F=\beta m^2/(2+\beta)r^3. \quad (62)$$

The effect of the disturbance can most conveniently be computed by Herschel's method. Let e be the eccentricity, a the length of the the major semiaxis. ω the longitude of the major axis of the instantaneous orbit, and θ the true anomaly. Then we have

$$r=a(1-e^2)(1+e\cos\theta)^{-1}$$

and

$$d\theta/dt=h/r^2,$$

where $h^2=ma(1-e^2)$. By (62), the radial disturbing acceleration is

$$F=\frac{m^3}{r^2h^2}\frac{\beta}{2+\beta}(1+e\cos\theta),$$

which gives[15]

$$\frac{d\omega}{dt}=-\frac{F}{e}\frac{h}{m}\cos\theta=-\frac{m^2}{r^2he}\frac{\beta}{2+\beta}\cos\theta(1+e\cos\theta),$$

hence

$$\frac{d\omega}{d\theta}=\frac{d\omega}{dt}\frac{r^2}{h}=-\frac{m^2}{h^2e}\frac{\beta}{2+\beta}\cos\theta(1+e\cos\theta).$$

For a complete revolution

$$\Delta\omega=-\frac{\beta}{2+\beta}\frac{m^2}{h^2}\pi,$$

and the rate of advance of the perihelion due to the disturbance is

$$\frac{1}{2\pi}\Delta\omega=-\frac{\beta}{4+2\beta}\frac{m^2}{h^2}.$$

This represents a perennial motion of the perihelion in a sense opposite to the motion of the planet. Therefore it must be subtracted from the Einstein value $3m^2/h^2$, and the total rate of advance is

$$\frac{1}{2\pi}\Delta\omega=\left(3-\frac{\beta}{4+2\beta}\right)\frac{m^2}{h^2}. \quad (63)$$

Thus, *by measuring the rate of advance of the perihelion of planets or asteroids it is possible to determine the value of the coupling constant β experimentally.*

For geodesic null lines, v is very nearly 1 and (60) becomes

$$\frac{d^2x_\mu}{dt^2}+\frac{3m}{r^2}\left\{1-\left(\frac{dr}{dt}\right)^2\left[1+O\left(\frac{m}{r}\right)\right]\right\}\xi_\mu$$
$$-\frac{2m}{r^2}\frac{dr}{dt}\frac{dx_\mu}{dt}\left[1+O\left(\frac{m}{r}\right)\right]=0. \quad (60')$$

[15] See W. H. Besant, *Dynamics* (G. Bell and Sons, London, 1902), p. 207.

Here the term which depends on β has disappeared and the equation gives the same result for the deflection of light in the sun's gravitational field as the general theory of relativity.

6. GRAVITATIONAL ENERGY

(41), (41″), (52), and (53) give the following expression for the components of the gravitational field energy-stress tensor:

$$T_{00}=\frac{6+\beta}{4+2\beta}\frac{m^2}{r^4}+O\left(\frac{m^3}{r^5}\right), \tag{64}$$

$$T_{0\mu}=0, \tag{64'}$$

$$T_{\mu\nu}=\frac{m^2}{r^4}(\xi_\mu\xi_\nu-\tfrac{1}{2}\delta_{\mu\nu})+O\left(\frac{m^3}{r^5}\right). \tag{64''}$$

Apart from numerical factors they have the same form as Maxwell's energy-stress, tensor in Coulomb fields which lends a strong support to the correctness of postulate (13).

Consider now the vector density

$$\rho^n=(\beta/8\pi\kappa)(C_kC^k)^{-1}(2C^r\mathfrak{T}_r{}^n-C^n\mathfrak{T}), \tag{65}$$

where $T=T_r{}^r$. Using the frame of Sec. 4 in which $C_0=1$, $C_\mu=0$, we get

$$\rho=\rho^0=(\beta/8\pi\kappa)(2\mathfrak{T}_0{}^0-\mathfrak{T}), \quad \rho^\mu=0. \tag{66}$$

We shall show now that

$$4\pi\int_0^\infty \rho r^2dr=M=\frac{1}{\kappa}m. \tag{67}$$

By (37), (41), (41″), (49), and (50),

$$T=\frac{1}{fg}\left(-\frac{1}{2}\frac{g''}{g}+\frac{3}{4}\left(\frac{g'}{g}\right)^2+\frac{1}{4}\frac{f'g'}{fg}-\frac{1}{r}\frac{g'}{g}\right),$$

$$2\mathfrak{T}_0{}^0-\mathfrak{T}=(fg)^{-\frac{1}{2}}\left(-\frac{1}{2}\frac{g''}{g}+\frac{1}{2}\left(\frac{g'}{g}\right)^2+\frac{1}{4}\frac{f'g'}{fg}-\frac{1}{r}\frac{g'}{g}\right)$$

$$=\left[g+rg'-\tfrac{1}{8}\beta r^2\left(\frac{g'}{g}\right)^2\right]^{-\frac{1}{2}}(1+\tfrac{1}{2}rg')^{-1}$$

$$\times\left(-\frac{1}{2}\frac{g''}{g}+\frac{1}{4}\left(\frac{g'}{g}\right)^2-\frac{1}{r}\frac{g'}{g}\right.$$

$$\left.+\tfrac{1}{8}r\left(\frac{g'}{g}\right)^3+\tfrac{1}{16}r\beta\frac{(g')^3}{g^4}\right);$$

hence, introducing the variable $u=1/r$,

$$\int_0^\infty(2\mathfrak{T}_0{}^0-\mathfrak{T})r^2dr$$

$$=-\int_0^1 u'\left[g-\frac{u}{u'}-\tfrac{1}{8}\beta\left(\frac{u}{u'g}\right)^2\right]^{-\frac{1}{2}}\left(1-\frac{1}{2}\frac{u}{u'g}\right)^{-1}$$

$$\times\left[\frac{1}{2}\frac{u''}{(u')^3g}+\frac{1}{4}\frac{1}{(u'g)^2}-\frac{1}{8}\frac{u}{(u'g)^3}-\frac{1}{16}\frac{\beta}{g}\frac{u}{(u'g)^3}\right]dg$$

$$=\int_0^1[g^3(u')^2-g^2uu'-\tfrac{1}{8}\beta u^2]^{-\frac{1}{2}}\left(u'-\frac{1}{2}\frac{u}{g}\right)^{-1}$$

$$\times\left(\frac{1}{2}u''+\frac{1}{4}\frac{u'}{g}-\frac{1}{8}\frac{u}{g^2}-\frac{1}{16}\beta\frac{u}{g^3}\right)dg. \tag{68}$$

Now we obtain for

$$U=g^3(u')^2-g^2uu'-\tfrac{1}{8}\beta u^2,$$

by differentiating with respect to g and substituting for u'' from (55),

$$dU/dg=2g^3u'u''-g^2uu''+2g^2(u')^2-(2g+\tfrac{1}{4}\beta)uu'$$

$$=\frac{4g+\beta}{2g+\beta}\left[g^2(u')^2-uu'-\frac{1}{8}\frac{\beta}{g}u^2\right]$$

$$=\frac{4g+\beta}{g(2g+\beta)}U.$$

Hence, observing the boundary conditions (56),

$$U=g^3(u')^2-g^2uu'-\tfrac{1}{8}\beta u^2=(4m^2)^{-1}(1+\tfrac{1}{2}\beta)^{-1}g(g+\tfrac{1}{2}\beta). \tag{69}$$

Similarly, we get from (55):

$$\frac{1}{2}u''+\frac{1}{4}\frac{u'}{g}-\frac{1}{8}\frac{u}{g^2}-\frac{1}{16}\beta\frac{u}{g^3}=\frac{1}{4}\frac{u'}{g+\frac{1}{2}\beta}-\frac{1}{8}\frac{u}{g(g+\frac{1}{2}\beta)}. \tag{70}$$

Substituting (69) and (70) into (68) we get

$$\int_0^\infty(2\mathfrak{T}_0{}^0-\mathfrak{T})r^2dr=\tfrac{1}{2}m(1+\tfrac{1}{2}\beta)^{\frac{1}{2}}\int_0^1 g^{-\frac{1}{2}}(g+\tfrac{1}{2}\beta)^{-\frac{1}{2}}dg$$

$$=2m/\beta,$$

which together with (66) gives the desired result. It can be shown similarly that any other linear combination of $\mathfrak{T}_0{}^0$ and $\mathfrak{T}$ in (66) would give an infinite value for the integral (67).

Equation (67) shows that if we *define* ρ^n to be the gravitational energy-momentum density vector then the integral of ρ^0 over the whole space is equal to the gravitational mass of the body. This is an expression of the fact that *the total mass of neutral matter comes from the energy of its gravitational field.*

To compare our result with the Newtonian theory of gravitation, consider the energy-stress tensor of a perfect fluid with rest density μ and isotropic pressure p. We have, in absolute gravitational units,

$$\beta T_{mn}=8\pi\kappa[\mu u_m u_n+p(u_m u_n-g_{mn})]$$

where u_m is the world direction of the fluid.[16] It follows that in a Galilean frame with respect to which the fluid is at rest,

$$\frac{\beta}{8\pi\kappa}\mathfrak{T}_0{}^0=\mu,\quad \frac{\beta}{8\pi\kappa}\mathfrak{T}_\sigma{}^\rho=-p\delta_\sigma{}^\rho,\quad \frac{\beta}{8\pi\kappa}\mathfrak{T}=\mu-3p.$$

Hence assuming that the fluid is at absolute rest,

$$\rho=\frac{\beta}{8\pi\kappa}(2\mathfrak{T}_0{}^0-\mathfrak{T})=\mu+3p, \tag{71}$$

which verifies formula (3) of the introduction. It shows that not μ but $\mu+3p$ is the gravitational field producing density from the point of view of Newtonian attraction. In the case of isotropic radiation of density μ one has $p=\frac{1}{3}\mu$ which gives $\rho=2\mu$, i.e., twice the inertial mass density.

If the fluid is moving with velocity v relatively to the ether, say in the positive x_1 direction, then

$$C^0=(1-v^2)^{-\frac{1}{2}},\quad C^1=-v(1-v^2)^{-\frac{1}{2}},\quad C^2=C^3=0,$$

which by (65) gives

$$\rho^0=(1-v^2)^{-\frac{1}{2}}(\mu+3p),\quad \rho'=v(1-v^2)^{-\frac{1}{2}}(\mu-p),\quad \rho^2=\rho^3=0. \tag{71'}$$

From this, formula (4) follows immediately. The formula shows the curious fact that from the point of view of gravitational attraction particles behave roughly as if they were moving with velocity $2v$ instead of v relatively to the ether. This explains the appearance of the term $3p$ in formula (71). To the (inertial) rest mass density one has to add a gravitational mass correction due to the kinetic energy of the particles of the fluid relatively to the ether.

Finally, consider the quantity

$$q=(C_rC^r)^{-\frac{1}{2}}. \tag{72}$$

In the central symmetrical field it has the value

$$q=g^{\frac{1}{2}}=1-(m/r)+O(m^2/r^2),$$

when r is large, and it can be regarded as an expression for the gravitational potential. Thus in the present theory it is possible to define the Newtonian potential in an invariant way. For small r, we have from (57):

$$q\sim(\tfrac{1}{2}\beta)^{\frac{1}{2}}[\log(m/r)]^{-1},$$

which shows roughly the behavior of the gravitational potential near the origin.

[16] H. Weyl, *Space-Time-Matter* (Dover Publications, New York, 1922), p. 205.

The geometrical significance of q is that it gives the ratio of the units of local "metric" or "proper" time and "cosmic" time. If therefore we make the assumption, as suggested at the end of the introduction, that in Bohr's frequency relation

$$E_1-E_2=h\nu,$$

ν is expressed not in metric but in cosmic time units, then measured in metric time units the relation takes the form

$$E_1-E_2=hq\nu. \tag{73}$$

From this it follows immediately that the observed Einstein shift is zero, provided that photons behave like particles with rest mass zero and velocity 1.

7. GRAVITATIONAL WAVES

Let us assume that the field is weak and the frame very nearly Galilean and resting in ether, i.e.,

$$g_{mn}=\bar{g}_{mn}+\gamma_{mn},\quad \tau=t+\varphi, \tag{74}$$

where $\bar{g}_{mn}$ is the metric tensor corresponding to the line element $dt^2-(dx_1{}^2+dx_2{}^2+dx_3{}^2)$, and the quantities γ_{mn}, φ are sufficiently small so that products can be neglected. Using the notations

$$\gamma=\gamma_r{}^r,\quad \gamma_m=\gamma^r{}_{m,r},$$

we get

$$R_{mn}=\tfrac{1}{2}\Box\gamma_{mn}-\tfrac{1}{2}(\gamma_{m,n}+\gamma_{n,m})+\tfrac{1}{2}\gamma_{,m,n}, \tag{75}$$

and

$$R=\Box\gamma-\gamma^m{}_{,m}, \tag{74'}$$

where

$$\Box=g^{mn}\partial^2/\partial x_m\partial x_n=\partial^2/\partial t^2-(\partial^2/\partial x_1{}^2+\partial^2/\partial x_2{}^2+\partial^2/\partial x_3{}^2).$$

We also have, from (74),

$$C_m=\bar{C}_m+\varphi_{,m},$$

where $\bar{C}_0=1$, $\bar{C}_\mu=0$ for $\mu\neq0$,

$$C_{mn}=C_{m,n}-C_r\left\{\begin{matrix}r\\mn\end{matrix}\right\}$$

$$=\varphi_{,m,n}-\tfrac{1}{2}(\gamma_{0m,n}+\gamma_{0n,m}-\gamma_{mn,0}),$$

$$C^{mn}{}_{;n;m}=\Box\Box\varphi-\Box\gamma_0+\tfrac{1}{2}\gamma^m{}_{,m,0}.$$

Hence, writing

$$\Psi=C_m{}^m=\Box\varphi-\gamma_0+\tfrac{1}{2}\gamma_{,0} \tag{76}$$

for the covariant d'Alembertian of φ and using (75'), field equation (18) takes the form

$$\Box\Psi=\tfrac{1}{2}R_{,0}. \tag{77}$$

A remarkable feature of this wave equation is that, unlike the gravitational wave equations of general relativity, it holds in an arbitrary frame of the form (74) and there is no need to impose further auxiliary conditions upon the coordinates.[17] It should be noted

[17] For a criticism of such auxiliary conditions see F. A. Kaempffer, Can. J. Phys. 31, 501 (1953).

in this connection that (77) is the outcome of the secondary field equation (18) which has no counterpart in ordinary relativity. The approximate equations corresponding to the primary field equations (15) can be obtained from (75) and

$$T_{mn}=\tfrac{1}{2}\varphi_{,m,n,0}-\tfrac{1}{2}(\delta_{m0}\Box\varphi_{,n}+\delta_{n0}\Box\varphi_{,m})$$
$$+\tfrac{1}{4}\delta_{m0}(\Box\gamma_{0n}+\gamma_{0,n}-\gamma_{n,0})$$
$$+\tfrac{1}{4}(\Box\gamma_{0m}+\gamma_{0,m}-\gamma_{m,0})$$
$$-\tfrac{1}{4}(\gamma_{0m,n,0}+\gamma_{0n,m,0}-\gamma_{mm,0,0}). \quad (78)$$

They determine the change of the local gravitational field under the influence of the incoming Ψ waves.

Equation (77) shows that the Ψ waves propagate with the velocity of light and are generated by oscillating matter. In fact, if tension-free matter with rest density μ is present, then $R=8\pi\kappa\mu$, and (77) becomes

$$\Box\Psi=4\pi\kappa\partial\mu/\partial t. \quad (79)$$

In an arbitrary nearly Galilean frame which is not resting in ether, it takes the form

$$\Box\Psi=4\pi\kappa C^m\partial\mu/\partial x_m. \quad (79')$$

The wave equation (77) has an interesting corollary. We have seen in Sec. 6 that the gravitational mass density ρ^0 is not strictly proportional to the inertial mass density, as postulated by the principle of equivalence, but the ratio of the two densities depends on the state of motion of matter. Since inertial mass is conserved, we cannot expect the same to be true for the gravitational mass. The rate of creation of gravitational mass density is given by the expression $\rho^n{}_{,n}$. Using a frame which rests in ether we obtain

$$\rho^n=\frac{1}{8\pi\kappa}\beta(C_kC^k)^{-1}(2C^r\mathfrak{T}_r{}^n-C^n\mathfrak{T})=-\frac{1}{4\pi\kappa}R_0{}^n;$$

hence, by (75) and (75′),

$$\rho^n{}_{,n}=-\frac{1}{4\pi\kappa}R_0{}^n{}_{,n}=-\frac{1}{8\pi\kappa}(\Box\gamma_{,0}-\gamma^n{}_{,n,0})$$
$$=-\frac{1}{8\pi\kappa}R_{,0}. \quad (80)$$

Combining (77) and (80), we find

$$\Box\Psi=-4\pi\kappa\rho^n{}_{,n}. \quad (81)$$

The equation shows that the creation rate of gravitational mass can be regarded as the "charge" which is responsible for the generation of Ψ waves.

If matter of density μ is present, then Eq. (80) takes the form

$$\rho^n{}_{,n}=-\partial\mu/\partial t. \quad (82)$$

One can give the following interpretation of this peculiar relation.

When a particle moves in the ether, then gravitational mass is continuously annihilated in the front half and created in the back half of the field of the particle.[18] In other words, the ether drift transforms particles into a dipole with respect to the creation charge so that the ether drift vector forms the axis of polarization. In order to account for Eq. (82), the strength of the dipole ought to be equal to mv, where m is the gravitational rest mass of the particle and v its absolute velocity.

8. PROPERTIES OF THE COSMOLOGICAL MODEL

We shall investigate now some properties of the cosmological model found in Sec. 3. Its line element is

$$dt^2-t^\alpha(dx_1{}^2+dx_2{}^2+dx_3{}^2), \quad (83)$$

for some positive constant α. The equations of a geodesics passing through the origin in any direction are, by formula (35) of Sec. 3,

$$\frac{d^2r}{ds^2}+\frac{\alpha}{t}\frac{dr}{ds}\frac{dt}{ds}=0, \quad (84)$$

$$\frac{d^2t}{ds^2}+\tfrac{1}{2}\alpha t^{\alpha-1}\left(\frac{dr}{ds}\right)^2=0. \quad (84')$$

An integral of this is

$$\left(\frac{dt}{ds}\right)^2-t^\alpha\left(\frac{dr}{ds}\right)^2=1, \quad (85)$$

which, with (84′), gives

$$t\frac{d^2t}{ds^2}+\tfrac{1}{2}\alpha\left(\frac{dt}{ds}\right)^2=\tfrac{1}{2}\alpha.$$

This gives, on integration,

$$dt/ds=[1+(b/t)^\alpha]^{\frac{1}{2}},$$

where b is a constant. Hence, by (85),

$$dr/ds=b^{\frac{1}{2}\alpha}t^{-\alpha},$$
$$dr/dt=(b/t)^{\frac{1}{2}\alpha}(b^\alpha+t^\alpha)^{-\frac{1}{2}}.$$

Since the velocity of light is $c=t^{-\frac{1}{2}\alpha}$, the velocity of the particle with respect to the frame (83) is, at the time t,

$$v=[1+(t/b)^\alpha]^{-\frac{1}{2}}. \quad (86)$$

The particle slows down and at $t=\infty$ comes to a rest. If at time t_0 the velocity was v_0, then by (86)

$$b^\alpha=t_0{}^\alpha v_0{}^2(1-v_0{}^2)^{-1},$$

hence

$$v=v_0[v_0{}^2+(1-v_0{}^2)(t/t_0)^\alpha]^{-\frac{1}{2}}. \quad (87)$$

[18] Preliminary calculations made on the field of central bodies in absolute motion confirm the existence of such an effect. There seems to be a continuous inwards flux of gravitational mass in the front half and an equivalent outwards flux in the trailing half of the particle.

This shows that if the particle was at rest in the frame (83) then it will always remain so. Therefore (83) can be regarded as a suitable frame to describe cosmic phenomena. But the (metric) distance between two points with fixed coordinates increases with time, hence the model (83) represents an expanding universe.

For a particle with rest mass m, we obtain from (87)

$$m(1-v^2)^{-\frac{1}{2}}=m(1-v_0^2)^{-\frac{1}{2}}[1-v_0^2+v_0^2(t_0/t)^\alpha]^{\frac{1}{2}};$$

or, if E is the energy of the particle,

$$E=E_0[1-v_0^2+v_0^2(t/t_0)^\alpha]^{\frac{1}{2}}. \tag{88}$$

In the limiting case of photons, $v_0=1$; hence[19]

$$\nu=\nu_0(t_0/t)^{\frac{1}{2}\alpha}. \tag{89}$$

This expresses Hubble's law and shows that the value of the recession constant is $\frac{1}{2}\alpha/t$. If $\alpha=2$, the recession constant is simply $1/t$.

The model (83) represents a universe with uniform matter distribution. The density of gravitational energy at some epoch t and in gravitational units is

$$8\pi\kappa\rho=\beta(2\mathfrak{T}_0^0-\mathfrak{T})=\frac{6\alpha}{3\alpha+2}t^{\frac{1}{2}\alpha-2}, \tag{90}$$

by formulas (31) and (36). If the gravitational radius is measured not in metric length but in units of the cosmologically more satisfactory space coordinates x_ν, then we have to multiply the quantity (90) by $t^{-\frac{1}{2}\alpha}$:

$$8\pi\kappa t^{-\frac{1}{2}\alpha}\rho=\frac{6\alpha}{3\alpha+2}t^{\alpha-2}. \tag{90'}$$

This gives the density in "cosmic units." If, in particular, $\alpha=2$, then the gravitational mass measured in cosmic units is a pure number and the density has the constant value $\frac{3}{2}$. The simplicity of this result lends a strong support in favor of the value $\alpha=2$.

To compare (90) with experimental values, it is more convenient to use the conventional coordinates $y_\mu=t^{\frac{1}{2}\alpha}x_\mu$ at the fixed epoch t. The density in these coordinates and in ordinary units is

$$\rho=\frac{1}{4\pi k}\frac{3\alpha}{3\alpha+2}t^{-2}, \tag{91}$$

or

$$\rho=\frac{3}{16\pi\kappa}t^{-2} \tag{91'}$$

if $\alpha=2$. This is half of the value found by Hoyle. In Hoyle's corresponding formula,

$$\rho=\frac{3}{8\pi\kappa}T^{-2},$$

T is a constant and so is the density in ordinary units. Because of the expansion of the universe, this can only be true if matter is created continuously, which is indeed a basic conclusion of Hoyle's theory. From the present theory it appears that "continuous creation" is largely a matter of interpretation and depends on the units in which energy is measured at various epochs. In fact, if measured in absolute cosmic units, as explained above, then the total energy of a fixed region of the universe remains constant, apart from statistical fluctuations. This of course does not imply that the number of protons and electrons in a fixed region must remain constant. This would only be true if the gravitational radius of a proton, measured in cosmic units, would remain a constant, which is very doubtful, to say the least. The size of elementary particles, however, is a question which by its very nature lies outside the scope of a purely gravitational theory.

[19] The method used here for calculating the red shift is based on the particle picture of photons. It has the advantage that its applicability is not restricted to any particular type of frame.

Collision Matrices for the Compound Nucleus*

R. G. THOMAS
University of California, Los Alamos, Scientific Laboratory Los Alamos, New Mexico
(Received August 23, 1954)

The collision matrix found by Newton to satisfy at all excitation energies the requirement that it describe an excited nucleus whose decay is independent of the mode of formation is shown to imply the vanishing of the absorption cross sections at high energies where the levels overlap and therefore does not describe a compound nucleus in the usual sense. The essential characteristic of this matrix is the high degree of the correlations of the signs of the square roots $\gamma_{\lambda c}$ of the reduced level widths for the various levels λ and channels c. On the other hand, a collision matrix, which is similar to one first considered by Bethe and involves $\gamma_{\lambda c}$ whose signs are uncorrelated, implies energy average decays that are independent of the formation mode and absorption cross sections that are of the order of magnitude of the nuclear area at high energies. These matrices are derived and discussed by using the R-matrix theory of Wigner, Eisenbud, and Teichmann. It is shown that the Bethe form of the collision matrix, which is valid only if all of the partial level widths are much less than the spacings, may be modified by means of the Teichmann-Wigner channel elimination procedure so that it is also valid in situations where some of the partial widths exceed the spacings. The form of the compound-nucleus collision matrix thus obtained is similar to one deduced by Weisskopf by considerations involving the compound-nucleus hypothesis and the reciprocity theorem. The pole strength functions s_c, which are the averages of the ratios of reduced widths $\gamma_{\lambda c}^2$ to level spacings, and their Stieltjes energy transforms are decisive in the determination of the behavior of these collision matrices and their associated cross sections. The s functions and their transforms are presented and discussed in the cases of the strong-coupling and complex square well potential representations of the particle-nuclei interactions. The latter representation with an additional surface absorption is also considered. The present theory indicates that the imaginary part of the complex square well potential should increase with the absorption width, and it suggests a "giant resonance" interpretation of the average cross-section behaviors. The effect of the compound-nucleus on non-compound-nucleus processes such as stripping and pickup is also mentioned.

I. INTRODUCTION[1]

THE concept of the compound nucleus has been useful for the understanding of many nuclear reaction phenomena ever since it was first proposed by Bohr.[2] Subsequent to this proposal, derivations were given of the form of the collision matrix U describing the compound nucleus under various conditions. In particular, Wigner and Eisenbud[3] derived by means of their R-matrix theory a generalized one-level collision matrix which revealed that if the average total level width $\langle\Gamma_\lambda\rangle_{Av}$[4] is small enough compared with the mean level spacing D, then at all excitation energies in the vicinity of the levels the nuclear system described by U will decay in accordance with the well known one-level Breit-Wigner resonance formula as a compound nucleus independently of its mode of formation.

Recently there has appeared an interesting deduction by Newton[5] of a form of U which satisfies the requirement of independent decay at *all* excitation energies and for any value of the ratio $\langle\Gamma_\lambda\rangle_{Av}/D$. The essentials of his deduction involved consideration of only the unitary and symmetry properties of U. It was shown that this U implied that the square-roots of the reduced level widths of the associated R matrix are of the highly correlated form $\gamma_{\lambda c}=a_\lambda b_c$, the factor a_λ referring to the levels λ and the factor b_c to the channels c. However, according to the present considerations, the absorption cross sections implied by Newton's U tend to vanish at sufficiently high nuclear excitations where there are many decay channels and the levels overlap, contrary to experience and to the compound-nucleus concept.

One aim of the investigation reported here was therefore to obtain by means of the R-matrix theory a form of the collision matrix which would satisfy the compound-nucleus requirement of independent decay at least *on the average*, rather than at *all* excitation energies, and for any value of $\langle\Gamma_\lambda\rangle_{Av}/D$, thus extending the Wigner-Eisenbud result. This was accomplished by assuming that the signs of the $\gamma_{\lambda c}$ appearing in Wigner's[6] many-level expansion for U are uncorrelated, quite contrary to the conditions involved in Newton's U. The collision matrix and its associated average cross sections thereby obtained are similar to those deduced by Bethe[7] many years ago. In Bethe's derivation it was assumed that the signs of the matrix elements for the formation and decay of the various intermediate levels are uncorrelated. When the levels overlap, both results lead to average absorption cross sections of the order of the nuclear area, in conformity with the compound-nucleus concept, but they are restricted to situations where *all* of the average partial level widths $\langle\Gamma_{\lambda c}\rangle_{Av}$ for the channels c are less than D.

The recent extensive fast neutron total cross-section measurements by Barschall, Nereson and others,[8] and

* Work performed under the auspices of the U. S. Atomic Energy Commission.

[1] A preliminary account of some aspects of this paper was given at the September 1953 meeting of the American Physical Society [R. G. Thomas, Phys. Rev. 92, 1094(A) (1953)].

[2] N. Bohr, Nature 137, 344 (1936); Science 86, 161 (1937).

[3] E. P. Wigner and L. Eisenbud, Phys. Rev. 72, 29 (1947).

[4] The symbol $\langle\ \rangle_{Av}$ is often used to denote averages with respect to the levels λ, the number of contributing λ being roughly $\langle\Gamma_\lambda\rangle_{Av}/D$ when this ratio exceeds unity, where D is the mean level spacing.

[5] T. D. Newton, Can. J. Phys. 30, 53 (1952).

[6] E. P. Wigner, Phys. Rev. 70, 606 (1946).

[7] H. A. Bethe, Revs. Modern Phys. 9, 69 (1937), Sec. 56D.

[8] H. H. Barschall, Phys. Rev. 86, 431 (1952); Miller, Adair, Bockelman, and Darden, Phys. Rev. 88, 83 (1952); Norris Nereson and Sperry Darden, Phys. Rev. 89, 775 (1953); 94, 1678 (1954).

their interpretation by Feshbach, Porter, and Weisskopf[9] have revealed that a complex square well potential provides a satisfactory representation of the neutron-nucleus interaction. One implication of this model is that at certain excitation energies the mean partial width $\langle\Gamma_{\lambda n}\rangle_{Av}$ for the incident neutron channel n considerably exceeds D, thus violating the criterion for applicability of the Bethe collision matrix. The second aim was therefore to find a U which would also be valid in such circumstances. This was effected by means of the channel elimination procedure and reduced R-matrix theory developed by Teichmann and Wigner.[10] In the final form the compound-nucleus collision matrix leads to expressions for the nuclear reaction cross sections which are of the form predicted by Weisskopf[11] from considerations of the compound-nucleus assumption and the reciprocity theorem; these expressions are restricted to circumstances where the mean of the $\langle\Gamma_{\lambda c}\rangle_{Av}$ for the participating channels c is less than D. One object of the present work may thus be stated as the determination of the conditions for the existence of the compound nucleus which has been assumed in the previous work.

There are observed to be certain nuclear reaction phenomena which are not interpretable as proceeding through the intermediary of a compound nucleus. Noteworthy are the high-energy direct and exchange collisions, the stripping and pickup reactions which are prominent at intermediate energies as well. The signs of the $\gamma_{\lambda c}$ associated with these processes no doubt have significant correlations, although this matter has not yet been quantitatively investigated. It is hoped that the material presented herein will provide not only a better understanding of the compound-nucleus processes but also permit the inclusion of their contribution to and effect on the non-compound-nucleus processes in the theoretical interpretation of the latter.

II. NOTATION

Although the present treatment utilizes the various R-matrix relations given by Teichmann and Wigner,[10] it is desirable to introduce the modifications of their notations that are indicated in Table I. The use of a reduced width having the dimensions of energy, rather than energy-times-distance, is natural and leads to dimensionless quantities in standard notation for the quantities characterizing the external wave functions at the nuclear surface. The present notation will also facilitate comparisons with the results of Feshbach and Weisskopf.[12,13] The R matrix will be dimensionless, and its diagonal component referring to the entrance channel will be related to the reciprocal of the important quantity f which appears in their work.

[9] Feshbach, Porter, and Weisskopf, Phys. Rev. **96**, 448 (1954).
[10] T. Teichmann and E. P. Wigner, Phys. Rev. **87**, 123 (1952), referred to as TW.
[11] J. M. Blatt and V. F. Weisskopf, *Theoretical Nuclear Physics* (John Wiley and Sons, Inc., New York, 1952), Chap. VIII.
[12] H. Feshbach and V. F. Weisskopf, Phys. Rev. **76**, 1550 (1949).
[13] Feshbach, Peaslee, and Weisskopf, Phys. Rev. **71**, 1451 (1947).

TABLE I. Relations between the present notation and that of TW.

Present notation	Teichmann and Wigner
$\gamma_{\lambda c}$	$\gamma_{\lambda c}a_c^{-\frac{1}{2}}$
R_{st}	$a_s^{-\frac{1}{2}}R_{st}a_t^{-\frac{1}{2}}$
$\mathfrak{V}_c$	$\alpha_c a_c^{-\frac{1}{2}}$
$\mathfrak{D}_c=\rho_c\mathfrak{V}_c'$ $=\mathfrak{D}_c+B_c\mathfrak{V}_c$	$\alpha_c a_c^{-\frac{1}{2}}+\beta_c a_c^{\frac{1}{2}}$
$\mathfrak{D}_c a_c^{-\frac{1}{2}}-\mathfrak{V}_c a_c^{-\frac{1}{2}}$	β_c
B_c	$-a_c^{\frac{1}{2}}b_c=1-a_c b_c$
$F_c,\ G_c$	$k_c^{\frac{1}{2}}F_c,\ k_c^{\frac{1}{2}}G_c$
$'\equiv d/d\rho_c$	$'\equiv d/dr_c$

The regular and irregular external radial functions for channels c are designated $F_c(\rho)$ and $G_c(\rho)$, respectively, as is customary when discussing charged particle reactions.[14] These quantities and their derivatives with respect to $\rho_c=k_c r_c$ appear in the theoretical development evaluated at the channel radii where $r_c=a_c$. However, these four quantities are related through the Wronskian,

$$F_c'G_c-G_c'F_c=1,$$

so that it is actually necessary to introduce only three independent quantities. For these we use the real and imaginary parts of a complex quantity L which is the radius a times the logarithmic derivative at $r=a$ of an outgoing wave $O=G+iF$ (omitting the subscript c):

$$L=\rho O'/O=S+iP,$$
$$S=\rho(FF'+GG')/(F^2+G^2),$$
$$P=\rho/(F^2+G^2),$$

and

$$\phi=\tan^{-1}(F/G),$$

which is the negative of the *hard-sphere potential scattering phase shift*. The real part S of L appears as a factor in the level shift expressions and is therefore referred to as the *shift factor* while the imaginary part P appears as a factor in the level width expressions and is referred to as the *penetration factor*. If the energy of relative motion in a channel is negative, the analytical continuation of the outgoing wave O is the real, exponentially-decaying Whittaker function $W_{-\eta,l+\frac{1}{2}}(2\rho)$, where $\eta=Z_1Z_2e^2/\hbar v$ and hl is the channel orbital angular momentum, so that[15]

$$S=\rho W'/W,\quad P=0.$$

The development actually involves the barred quantities

$$\bar{L}=L-B=\bar{S}+i\bar{P},$$
$$\bar{S}=S-B,\quad \bar{P}=P,$$

where the B are the real, constant boundary conditions satisfied by the proper solutions X_λ of energy E_λ at the radii a_c of the channels c. The bar will always be

[14] Bloch, Hull, Broyles, Bouricius, Freeman, and Breit, Revs. Modern Phys. **23**, 147 (1951).
[15] R. G. Thomas, Phys. Rev. **88**, 1109 (1952).

omitted. The various quantities L_c, S_c, P_c, B_c, etc. appear as the components of the diagonal matrices L, S, P, B, etc., these matrices being referred to respectively as the logarithmic derivative, shift, penetration, boundary-condition matrices.

III. THE GENERAL EXPRESSIONS FOR THE COLLISION MATRIX

The general expressions for the collision matrix in terms of the R matrix and its parameters $\gamma_{\lambda c}$, E_λ as derived by Wigner, Eisenbud, Teichmann, and Newton[3,5,10] are summarized here in the present notation. The collision matrix is conveniently written

$$U=\Omega V\Omega, \tag{1}$$

the factors being the unitary, diagonal, potential-scattering matrix,[16]

$$\Omega=\exp(-i\phi), \tag{1a}$$

and the unitary, symmetric matrix

$$V=1+2iP^{\frac{1}{2}}(1-RL)^{-1}RP^{\frac{1}{2}}, \tag{1b}$$

which will also be referred to as a collision matrix. L and P are the diagonal, logarithmic derivative and barrier penetration matrices, the components of which are given in II. It is often useful to separate the real, symmetrical R matrix into two terms

$$R=R^0+R', \tag{2}$$

with

$$R'=\sum_\lambda(\gamma_\lambda\times\gamma_\lambda)/(E_\lambda-E),$$

and the R^0 matrix as the sum of the contributions from the remaining levels not included in the λ sum, or if R' is a uniform R matrix, similar to Wigner's uniform R function,[17] as the difference $(R-R')$. With this separation,

$$(1-RL)^{-1}R=(1-R^0L)^{-1}R^0 +(1-R^0L)^{-1}(1-R'L')^{-1}R'(1-LR^0)^{-1}, \tag{3}$$

where

$$L'=L(1-R^0L)^{-1}.$$

By means of the procedure indicated in Wigner's paper on resonance reactions[6] or in Appendix A of this paper, it may be deduced that

$$(1-R'L')^{-1}R'=\sum_{\lambda\mu}A_{\lambda\mu}(\gamma_\lambda\times\gamma_\mu), \tag{4}$$

where the components of the symmetrical level matrix A are obtained from the level matrix relation,

$$A=(\bar{E}-E-\xi)^{-1}, \tag{5}$$

and the subscripts λ, μ refer to the levels λ of R'. Here the components of the complex, symmetrical level matrix,

$$\xi=-\Delta+\tfrac{1}{2}i\Gamma, \tag{6}$$

are given by the channel scalar products,

$$\xi_{\lambda\mu}=(\gamma_\lambda,L'\gamma_\mu); \tag{6a}$$

the real part Δ of ξ is referred to as the shift matrix and twice the imaginary part $\frac{1}{2}\Gamma$ to the width matrix, their respective components being given by the scalar products

$$\tfrac{1}{2}\Gamma_{\lambda\mu}=(\alpha_\lambda{}^*,P\alpha_\mu), \quad \Delta_{\lambda\mu}=(\alpha_\lambda{}^*,(L^*R^0L-S)\alpha_\mu), \tag{6b}$$

where

$$\alpha_\lambda=(1-R^0L)^{-1}\gamma_\lambda.$$

The components of the real, diagonal matrix $\bar{E}$ are the proper values E_λ, and the real, diagonal matrix E is the energy E times the unit matrix. By substituting (4) into (3) one obtains

$$(1-RL)^{-1}R=(1-R^0L)^{-1}R^0+\sum_{\lambda\mu}A_{\lambda\mu}(\alpha_\lambda\times\alpha_\mu). \tag{7}$$

If only one level is considered in the λ sum, the substitution of (7) into (1) leads to the Wigner-Eisenbud generalized one-level collision matrix.[3]

If the matrix R^0 is diagonal, (1) may be rewritten

$$U=\Omega'V'\Omega', \tag{8}$$

where

$$\begin{aligned}
&\Omega'=\exp(-i\phi'),\\
&\phi'=\phi-\tan^{-1}[R^0P/(1-R^0S)],\\
&V'=1+2iP'^{\frac{1}{2}}(1-R'L')^{-1}R'P'^{\frac{1}{2}},\\
&L'=S'+iP',\\
&S'=[S(1-R^0S)-R^0P^2]/|1-R^0L|^2,\\
&P'=P/|1-R^0L|^2.
\end{aligned}$$

$-\phi'$ is a potential scattering phase which includes the contribution to the hard-sphere phase from R^0, and P' is a penetration factor similarly modified. The components of the width and shift matrices given by (6b) simplify to

$$\begin{aligned}
&\tfrac{1}{2}\Gamma_{\lambda\mu}=\tfrac{1}{2}\textstyle\sum_c\Gamma_{\lambda\mu c},\\
&\Gamma_{\lambda\mu c}=2P_c'\gamma_{\lambda c}\gamma_{\mu c};
\end{aligned} \tag{8a}$$

$$\begin{aligned}
&\Delta_{\lambda\mu}=\textstyle\sum_c\Delta_{\lambda\mu c},\\
&\Delta_{\lambda\mu c}=-S_c'\gamma_{\lambda c}\gamma_{\mu c}.
\end{aligned} \tag{8b}$$

The primes will henceforth be omitted.

If the symmetric matrix $(\bar{E}-\xi)$ has no double characteristic values, it may be put in the diagonal form $H=F-\frac{1}{2}i\Gamma$ by means of a complex, orthogonal matrix T,[6]

$$H=T(\bar{E}-\xi)T^{-1},$$

so that

$$A=\tilde{T}(H-E)^{-1}T,$$

and

$$(1-RL)^{-1}R=\sum_\nu(\delta_\nu\times\delta_\nu)/(F_\nu-E-\tfrac{1}{2}i\Gamma_\nu), \tag{9}$$

where

$$\delta_\nu=\sum_\lambda T_{\nu\lambda}\alpha_\lambda.$$

The $\delta_{\nu c}$ and H_ν are in general complex and energy dependent in contrast with the parameters $\gamma_{\lambda c}$ and E_λ of

[16] The Coulomb phase for charged particle channels has not been included.

[17] E. P. Wigner, Proc. Cambridge Phil. Soc. **47**, 790 (1951).

the R matrix which are real and constant. From the nature of the T matrix it may be deduced that[18]

$$\Gamma_\nu \leqslant 2\sum_c P_c|\delta_{\nu c}|^2. \tag{9a}$$

A procedure for the determination of the $\delta_{\nu c}$ and H_ν has been indicated by TW. The H_ν are the roots of the determinantal equation

$$|1-R(H_\nu)L|=0, \tag{10a}$$

and the $\delta_{\nu c}$ are the solutions of the associated homogeneous equations,

$$[1-R(H_\nu)L]\delta_\nu=0, \tag{10b}$$

with the normalization

$$(\delta_\nu, (\dot{L}+L\dot{R}L)\delta_\nu)=1, \tag{10c}$$

the dot denoting differentiation with respect to energy. This procedure leads to essentially the same results as obtained by Kapur and Peierls[19] using complex, energy-dependent boundary conditions $B_c=L_c$ (unbarred) rather than the real, energy-independent B_c of the R-matrix theory.

IV. NEWTON'S COLLISION MATRIX

Newton's collision matrix[5] satisfies for any value of $\langle\Gamma_\lambda\rangle_{Av}/D$ the requirement that the probabilities for the various modes of decay be independent of the formation mode *at all excitation energies*. A much simpler derivation of this matrix may be obtained by proceeding directly from the R-matrix expressions (4) and (1b). From these expressions it is evident that if the ratios (V_{st}/V_{ut}), s, $u\neq t$, are to be independent of t, the $\gamma_{\lambda c}$ must be factorizable as

$$\gamma_{\lambda c}=a_\lambda b_c, \tag{11}$$

so that the collision matrix becomes

$$V=1+2i(G\times G)(a,Aa), \tag{12}$$

where the vector

$$G=P^{\frac{1}{2}}b,$$

and the scalar product with respect to levels,

$$(a,Aa)=\sum_{\lambda\mu} a_\lambda A_{\lambda\mu}a_\mu,$$

being a function of energy but not of the formation mode. With this form the components of the ξ matrix simplify to

$$\xi_{\lambda\mu}=\zeta a_\lambda a_\mu,$$

where the channel scalar product

$$\zeta=-\Delta+\tfrac{1}{2}i\Gamma=(b,Lb),$$
$$\Delta=-\sum_c S_c b_c^2, \quad \Gamma=\sum_c \Gamma_c, \quad \Gamma_c=2G_c^2.$$

It may be deduced that

$$(a,Aa)=(t-\zeta)^{-1},$$

where

$$t^{-1}=\sum_\lambda a_\lambda^2/(E_\lambda-E).$$

Newton's collision matrix is therefore

$$V=1+2i(G\times G)/(t+\Delta-\tfrac{1}{2}i\Gamma), \tag{13}$$

which closely resembles the collision matrix for the one-level R matrix. As noted by Teichmann,[20] this resemblance is to be expected because with the $\gamma_{\lambda c}$ given by (11) the R matrix reduces to the expression $(b\times b)/t$ which is of rank one as is the one-level R matrix, $(\gamma_\lambda\times\gamma_\lambda)/(E_\lambda-E)$.

According to (13) the various reaction cross sections resulting from incident waves of angular momentum $\hbar l$ are

$$\sigma_{st}^{(l)}=(\pi/k_s^2)(2l+1)(4\Gamma_s\Gamma_t/\Gamma^2)\sin^2\tau, \tag{14}$$

where

$$\tau=\tan^{-1}[\tfrac{1}{2}\Gamma/(t+\Delta)].$$

It was also shown by Teichmann[20] that these cross sections may readily be averaged if $a_\lambda^2=a_\mu^2=\cdots 1$ and if the levels are uniformly spaced by an amount D, in which case

$$t=-(D/\pi)\tan(\pi E/D).$$

With this expression for the quantity t the averages are found to be

$$\langle\sigma_{st}^{(l)}\rangle_{Av}=(\pi/k_s^2)(2l+1)(4\Gamma_s\Gamma_t/\Gamma^2)$$
$$\times\frac{(\pi\Gamma/2D)[1+(\pi\Gamma/2D)]}{(\pi\Delta/D)^2+[1+(\pi\Gamma/2D)]^2}. \tag{15}$$

By choosing the $B_c=S_c$ at a particular energy of interest, the level shift Δ will vanish at that energy and will be negligible in the vicinity of it. Therefore, in the region of overlapping levels where $\pi\Gamma/2D\gg 1$, (15) simplifies to

$$\langle\sigma_{st}^{(l)}\rangle_{Av}=(\pi/k_s^2)(2l+1)(4\Gamma_s\Gamma_t/\Gamma^2),$$

and the total absorption of the lth partial wave is

$$\langle\sigma_s^{(l)}\rangle_{Av}=\sum_t\langle\sigma_{st}^{(l)}\rangle_{Av}=(\pi/k_s^2)(2l+1)(4\Gamma_s/\Gamma).$$

If $\rho=ka\gg 1$, many partial waves contribute so that the usual approximate procedure[20] for summing these may be applied to obtain

$$\langle\sigma_s\rangle_{Av}\approx\sum_{l=0}^{\rho}\langle\sigma_s^{(l)}\rangle_{Av}\approx\pi a^2(1+\rho^{-1})^2\langle 4\Gamma_s/\Gamma\rangle_{Av}. \tag{16}$$

It is apparent that if there are many channels for absorption so that $\Gamma\gg 4\Gamma_s$, $\langle\sigma_s\rangle_{Av}$ becomes much less than the magnitude πa^2 suggested by the compound-nucleus concept, and it does not seem likely that this is a consequence of the special assumptions made in connection

[18] G. Breit, Phys. Rev. **69**, 472 (1946). In this paper Breit has also succeeded in deriving an expansion similar to (9) for a certain nuclear model having an arbitrary number of channels.

[19] P. L. Kapur and R. Peierls, Proc. Roy. Soc. (London) **A166**, 277 (1937).

[20] T. Teichmann, Phys. Rev. **77**, 506 (1950).

with (15). This tendency for the absorptions to vanish is evidently due to destructive interference of the various contributing levels caused by the extreme correlations of the signs of the $\gamma_{\lambda c}$, the arrangement of these signs being the same at each level to within a common factor ± 1. Such destructive interference is also evident in the results obtained by Kalckar, Oppenheimer, and Serber[21] as well as Bohr, Peierls, and Placzek.[22]

In view of this defect, we shall seek another form for the compound-nucleus collision matrix. However, Newton's result does show that the requirements of independent decay and of absorption cross sections of the order πa^2 cannot be satisfied at all excitations, and therefore that the appropriate form can be expected to satisfy these only on the average.

V. "BETHE'S COLLISION MATRIX"

Bethe has derived an expression for the averages of the reaction cross sections which is valid even if the levels overlap provided that all of the average partial level widths $\langle\Gamma_{\lambda c}\rangle_{Av}$ are smaller than the mean spacing D. His derivation is based on the assumption that the signs of the matrix elements for the formation and decay of the various intermediate nuclear states are uncorrelated, and the result thereby obtained shows that the excited nucleus will decay on the average with probabilities which are independent of the formation mode and that the average total absorption cross sections will be of the order of magnitude of the nuclear area, in conformity with the compound-nucleus hypothesis. Although the concept of a collision matrix had not been introduced at the time of his work, the form of this matrix can of course be inferred from his equations. The purpose of this section is to rederive Bethe's result using the more rigorous R-matrix theory and to show that in this theory the signs of the $\gamma_{\lambda c}$ for the states of the compound nucleus must be considered as uncorrelated.[23]

The set of equations (10) for the determination of the parameters of the collision matrix can be solved approximately in the case of uncorrelated signs and overlapping levels by the standard perturbation-theory procedures such as those reviewed by Morse and Feshbach.[24] However, for simplicity we shall use a less rigorous procedure which leads to essentially the same result.

With the recognition that in the case of interest the nondiagonal components of the ξ matrix given by (6) will be smaller in absolute magnitude than the diagonal components, one can attempt an expansion of the matrix expression for A given by (5) in a power series about the diagonal part $\epsilon=\bar{E}-E-\xi+\xi'$ whose components are $\epsilon_\lambda=E_\lambda+\Delta_\lambda-E-\frac{1}{2}i\Gamma_\lambda$, where ξ' is the nondiagonal part of ξ. The result is that

$$A=\epsilon^{-1}+\epsilon^{-1}\xi'\epsilon^{-1}+\cdots, \tag{17}$$

and therefore

$$(1-RL)^{-1}R=\sum_\lambda(\gamma_\lambda\times\gamma_\lambda)/\epsilon_\lambda + \sum_{\lambda\mu}\epsilon_\lambda^{-1}(\gamma_\lambda\times\gamma_\mu)\xi_{\lambda\mu}'\epsilon_\mu^{-1}+\cdots \tag{18}$$

the components of which are

$$[(1-RL)^{-1}R]_{st}=\sum_\lambda(\gamma_{\lambda s}\gamma_{\lambda t}/\epsilon_\lambda) + i\sum_c P_c\sum_\lambda(\gamma_{\lambda s}\gamma_{\lambda c}/\epsilon_\lambda)\times\sum_{\mu(\neq\lambda)}(\gamma_{\mu c}\gamma_{\mu t}/\epsilon_\mu)+\cdots. \tag{18a}$$

For simplicity we have set $B_c=L_c$(unbarred) so that the level shift matrix may temporarily be disregarded, and the expressions given by (8a) for the resulting components of ξ' have been used to arrive at (18a) from (18). We proceed now to determine the conditions for the validity of the approximation (19), below, for the collision matrix which is obtained by neglecting all but the first term of (18) or (18a). For this determination the sum over the channels c of (18a) is considered in two parts: (1) the contributions from the channels s and t; (2) the contributions from the remaining channels. If the $\mu=\lambda$ terms are added to the μ sum of (18a), which it is permissible to do if the total level widths are much larger than the spacings, the contribution from the channel t is observed to be $iP_t\sum_\mu\gamma_{\mu t}^2/\epsilon_\mu$ times the contribution from the first sum of (18a). By replacing this μ sum by an integration, it may readily be estimated as $\pi\langle\gamma_{\mu t}^2\rangle_{Av}/D$. The contribution from the channel s may be determined in a similar manner. The magnitude of the contribution from the s and t channels together is thus $\frac{1}{2}\pi\langle\Gamma_{\lambda s}\rangle_{Av}D^{-1}+\frac{1}{2}\pi\langle\Gamma_{\lambda t}\rangle_{Av}D^{-1}$ times that from the first sum of (18) or (18a). In the consideration of the contribution (2) from the remaining channels, it is evident that no two of the same $\gamma_{\lambda c}$ appear multiplied together. Since the signs of these are presumed to be uncorrelated, the most-probable value of this contribution is zero; its root-mean-square magnitude may be estimated as follows: The rms magnitude of the contribution to the components of ξ' from the remaining channels may be estimated as equal to $\frac{1}{2}\langle\Gamma_\lambda\rangle_{Av}$, the average magnitude of the diagonal components of ξ, divided by the square root of the number of open channels $c\neq s,t$, this number being approximately equal to $\langle\Gamma_\lambda/\Gamma_{\lambda c}\rangle_{Av}$, the average being with respect to both λ and c. The magnitude of the contribution from the μ sum of ϵ_μ, the individual terms having random signs, may be estimated as $(2\pi/\langle\Gamma_\lambda\rangle_{Av}D)^{\frac{1}{2}}$. The rms magnitude of the contribution to the second sum of (18a) from these channels is thus estimated as the channel average of $(\pi\langle\Gamma_{\lambda c}\rangle_{Av}/2D)^{\frac{1}{2}}$ times the first sum. A necessary condition for the validity of

[21] Kalckar, Oppenheimer, and Serber, Phys. Rev. 52, 273 (1937).
[22] Bohr, Peierls, and Placzek, Nature 144, 200 (1939).
[23] These signs should be random for those λ in an energy interval of width comparable to $\langle\Gamma_\lambda\rangle_{Av}$ centered at the energy E of interest. According to the TW sum rule, $\Sigma_\lambda\gamma_{\lambda s}\gamma_{\lambda t}=0$ if $s\neq t$ so that they cannot be completely uncorrelated with respect to arbitrarily large energy intervals.
[24] P. M. Morse and H. Feshbach, *Methods of Theoretical Physics* (McGraw-Hill Book Company, New York, 1953), Vol. II, Chap. 9.

the approximation

$$V=1+2iP^{\frac{1}{2}}\sum_{\lambda}\frac{(\gamma_\lambda\times\gamma_\lambda)}{E_\lambda-E-\frac{1}{2}i\Gamma_\lambda}P^{\frac{1}{2}} \tag{19}$$

is therefore that all of the ratios $\pi\langle\Gamma_{\lambda c}\rangle_{Av}/2D$ must be much less than unity, as imposed by the contribution (1). The third and higher terms of the expansion (18a) are proportional to the square and higher powers of these ratios. If the level shifts Δ_λ are included in the denominators of (19), it is apparent that the ratios $\pi\langle\Delta_{\lambda c}\rangle_{Av}/D$ must also be less than unity. Equation (19) is recognized as the many-level approximation to the collision matrix which is valid in general when the total level widths are much less than their spacings.[6] It is also noted that this result corresponds to the equality condition of the relation (9a).

The reaction cross sections obtained from (19) are

$$\sigma_{st}^{(l)}=\frac{4\pi}{k_s^2}(2l+1)\sum_{\lambda\mu}\frac{P_sP_t\gamma_{\lambda s}\gamma_{\mu s}\gamma_{\lambda t}\gamma_{\mu t}}{(E_\lambda-E-\frac{1}{2}i\Gamma_\lambda)(E_\mu-E+\frac{1}{2}i\Gamma_\mu)}. \tag{20}$$

Following the procedure indicated by Bethe, the averages of these with respect to an energy interval δ, which is large compared with the total widths, are found to be

$$\langle\sigma_{st}^{(l)}\rangle_{Av}=\frac{4\pi}{k_s^2}(2l+1)\frac{\pi}{\delta}\sum_{\lambda\mu(\text{in}\delta)}\frac{P_sP_t(\Gamma_\lambda+\Gamma_\mu)\gamma_{\lambda s}\gamma_{\mu s}\gamma_{\lambda t}\gamma_{\mu t}}{(E_\lambda-E_\mu)^2+\frac{1}{4}(\Gamma_\lambda+\Gamma_\mu)^2}, \tag{21}$$

the sums being now restricted to levels within the interval δ. For each level in the λ sum there will be about $\langle\Gamma_\lambda\rangle_{Av}/D$ levels contributing from the μ sum and thus about $\delta\langle\Gamma_\lambda\rangle_{Av}/D^2$ pairs altogether. In view of the random nature of the $\gamma_{\lambda c}$ signs, the contribution from the terms with $\lambda\neq\mu$ will be proportional to the square-root of this number of pairs in contrast with the number δ/D of contributions from the positive-definite terms with $\lambda=\mu$. The cross-product terms may therefore be neglected so that

$$\langle\sigma_{st}^{(l)}\rangle_{Av}=(\pi/k_s^2)(2l+1)(T_sT_t/\textstyle\sum_c T_c), \tag{22}$$

where the

$$T_c=2\pi\langle\Gamma_{\lambda c}\rangle_{Av}/D$$

are quantities similar to Weisskopf's transmission factors.[11] Evidently the decay of the compound nucleus is on the average independent of the formation mode. By summing over decay channels t, the total absorption cross section for the lth partial wave is obtained,[25]

$$\langle\sigma_s^{(l)}\rangle_{Av}=(\pi/k_s^2)(2l+1)T_s. \tag{23}$$

When the bombarding energy is greater than the barrier height, the penetration factors $P_l\approx ka$, and the strong-coupling theory (see Sec. IX) suggests that the ratios $\langle\gamma_{\lambda c}^2\rangle_{Av}/D\approx(\pi Ka)^{-1}$ where $K\approx1\times10^{13}$ cm^{-1} is a wave number characteristic of nucleon motion within the nucleus. Under these conditions the transmission factor is $T=(4k/K)$, which is of the order of magnitude unity at moderate and high energies, and the summing procedure leading to (16) indicates that the total absorption is of the order of magnitude of the nuclear area. However, it is noted that when T_c is of the order unity, the ratio $\pi\langle\Gamma_{\lambda c}\rangle_{Av}/2D$ is also of this order, and the expansion (19) is not valid. It is also noted that transmission factors calculated from (22) can exceed unity for high energies (that is, if $4k$ exceeds K) in violation of the requirement that the collision matrix be unitary. The next two sections are devoted to the development of an alternative procedure which avoids these difficulties by dealing with an expansion similar to (18a) except for the nonappearance of the objectionable contributions from the s and t channels in the ξ' matrix. This avoidance is accomplished by means of the channel elimination procedure and the reduced R-matrix theory of TW. The result thereby obtained is similar to (22) though valid under the less restrictive condition, imposed by the channel contribution (2) above, that the mean with respect to channels c of the $\langle\Gamma_{\lambda c}\rangle_{Av}$ be less than D; the transmission factors that are obtained cannot exceed unity and are of the form proposed by Weisskopf.

VI. THE REDUCED R AND U MATRICES

In the present notation the basic R-matrix relation, Eq. (6′) of TW, is

$$\mathfrak{U}=R(\mathfrak{D}-B\mathfrak{U})=R\bar{\mathfrak{D}}. \tag{24}$$

According to this expression the value $\mathfrak{U}$ of the radial part of the wave function on any particular channel surface is linearly related by the components of the R matrix to the derivative quantities $\mathfrak{D}$ and the boundary conditions B of all channels. Following TW the channels are separated into groups e (eliminated) and r (retained), whereupon the matrix relation (24) reduces to two submatrix relations,

$$\mathfrak{U}_e=R_{ee}\bar{\mathfrak{D}}_e+R_{er}\bar{\mathfrak{D}}_r,\quad \mathfrak{U}_r=R_{rr}\bar{\mathfrak{D}}_r+R_{re}\bar{\mathfrak{D}}_e. \tag{25}$$

It is to be noted that the subscripts e and r refer respectively to the groups of e and r channels, rather than to particular channels. If the group of e channels comprises only reaction and negative-energy channels, which have no incident waves, then its logarithmic derivatives at the nuclear surface are known to be those of an outgoing wave O or a negative-energy function W, so that

$$\bar{L}_e=\bar{\mathfrak{D}}_e\mathfrak{U}_e^{-1}=\mathfrak{D}_e\mathfrak{U}_e^{-1}-B_e=L_e-B_e. \tag{26}$$

As usual the bar will be omitted. By substituting (26) into (25) and solving, one obtains

$$\mathfrak{U}_e=\mathfrak{R}_{er}\mathfrak{D}_r,\quad \mathfrak{U}_r=\mathfrak{R}_{rr}\mathfrak{D}_r, \tag{27}$$

where

$$\mathfrak{R}_{rr}=R_{rr}+R_{re}L_e(1-R_{ee}L_e)^{-1}R_{er},$$
$$\mathfrak{R}_{er}=(1-R_{ee}L_e)^{-1}R_{er}.$$

[25] This sum includes compound elastic scattering (see Sec. VIII).

$\mathfrak{R}_{rr}$ is the symmetrical reduced R matrix; it is not necessarily real as is the ordinary R matrix.

By means of the procedures indicated in the various papers on the R-matrix theory, it is possible to obtain directly from (27) the general expressions for the collision matrices; they are

$$V_{rr}=1+2iP_r^{\frac{1}{2}}(1-\mathfrak{R}_{rr}L_r)^{-1}\mathfrak{R}_{rr}P_r^{\frac{1}{2}}, \tag{28a}$$

$$V_{er}=2iP_e^{\frac{1}{2}}\mathfrak{R}_{er}(1-L_r\mathfrak{R}_{rr})^{-1}P_r^{\frac{1}{2}}. \tag{28b}$$

V_{rr} is referred to as the reduced collision matrix; it is not necessarily unitary as is the ordinary collision matrix. As in the deduction of (4), the inverse of the channel matrix appearing in (27) in the definitions of $\mathfrak{R}_{rr}$ and $\mathfrak{R}_{er}$ can be expressed in terms of the inverse of a level matrix A:

$$\mathfrak{R}_{rr}=R^0{}_{rr}+R^0{}_{re}L'_{ee}R^0{}_{er}+\sum_{\lambda\mu}(\omega_{\lambda r}\times\omega_{\mu r})A_{\lambda\mu}, \tag{29}$$

where

$$\omega_{\lambda r}=\gamma_{\lambda r}+R^0{}_{re}L'_{ee}\gamma_{\lambda e};$$

and

$$\mathfrak{R}_{er}=\sum_{\lambda\mu}(\alpha_{\lambda e}\times\gamma_{\mu r})A_{\lambda\mu},$$

where

$$\alpha_{\lambda e}=(1-R^0{}_{ee}L_e)^{-1}\gamma_{\lambda e}, \quad L'_{ee}=L_e(1-R^0{}_{ee}L_e)^{-1}.$$

As in (5) and (6) the components of the symmetrical level matrix A are obtained from the matrix relation

$$A=(\bar{E}-E-\xi)^{-1}, \tag{30a}$$

in which the components of the complex, symmetrica level matrix $\xi=-\Delta+\frac{1}{2}i\Gamma$ are given by the scalar products with respect to *eliminated* channels only,

$$\xi_{\lambda\mu}=(\gamma_{\lambda e},L'_{ee}\gamma_{\mu e}), \tag{30b}$$

in contrast with the corresponding expression (6a) in which the scalar product was with respect to *all* channels; as before the components of the real, diagonal matrix $\bar{E}$ are the proper values E_λ and the real, diagonal matrix E is the energy E times the unit matrix. Expressions similar to (6b) are obtained for the components of the total width and shift matrices Γ and Δ of the eliminated channels. The derivation of (29), which is lengthy though straightforward, is indicated in Appendix A. Henceforth we shall consider that $R^0=0$, so that Eqs. (29) simplify to

$$\mathfrak{R}_{rr}=\sum_{\lambda\mu}(\gamma_{\lambda r}\times\gamma_{\mu r})A_{\lambda\mu}, \tag{29a}$$

$$\mathfrak{R}_{er}=\sum_{\lambda\mu}(\gamma_{\lambda e}\times\gamma_{\mu r})A_{\lambda\mu}. \tag{29b}$$

The expressions for $\mathfrak{R}_{er}$ and V_{er} have been given here for completeness and will not be needed in the further developments.

If there is only one r channel, the entrance channel, and if $R^0=0$, (29a) reduces to the quadratic form

$$\mathfrak{R}_r=\sum_{\lambda\mu}\gamma_{\lambda r}A_{\lambda\mu}\gamma_{\mu r}. \tag{31}$$

$\mathfrak{R}_r$ is referred to as the reduced R function and is related to the quantity f_r, which appears in the work of Feshbach, Peaslee, and Weisskopf:[13]

$$\mathfrak{R}_r=(f_r-B_r)^{-1}. \tag{31a}$$

VII. "WEISSKOPF'S COLLISION MATRIX"

If the signs of the $\gamma_{\lambda c}$ are uncorrelated, the arguments used to justify the approximation (19) to (4) and (1) may also be used to justify the approximation

$$\mathfrak{R}_{rr}=\sum_\lambda(\gamma_{\lambda r}\times\gamma_{\lambda r})/(E_\lambda+\Delta_\lambda-E-\tfrac{1}{2}i\Gamma_\lambda) \tag{32}$$

to (29a), the widths Γ_λ and shifts Δ_λ of this expression being the diagonal components of the total width and shift matrices for the eliminated channels. However, (32) is valid under the less restrictive condition that the means with respect to λ and c of the partial level widths and shifts for the eliminated channels be less than the spacings, because the contributions to the second sum from the channels s, t have been eliminated in the expansion corresponding to (18a) for the components of $\mathfrak{R}_{rr}$.

When the Γ_λ are much larger than the spacings D, it is permissible to replace the individual widths and shifts in (32) by suitable averages with respect to an energy interval of size comparable to the $\langle\Gamma_\lambda\rangle_{Av}$:

$$\Gamma_\lambda\approx\langle\Gamma_\lambda\rangle_{Av}\equiv\Gamma(E), \quad \Delta_\lambda\approx\langle\Delta_\lambda\rangle_{Av}\equiv\Delta(E). \tag{33}$$

Both Γ and Δ are expected to be mildly energy-dependent because of the presence of the energy dependent factors P and S in the individual contributing terms and of possible systematic long-range variations of the reduced widths of the eliminated channels. This approximation is reasonable because it is not expected that the individual level widths and shifts will deviate significantly from one another, and the results obtained are usually not sensitive to the actual values of Γ and Δ. We will also apply (33) in those circumstances where the Γ_λ are narrow or comparable to D by allowing the Γ and Δ to vary in an appropriate manner from level to level.

Approximations (32) and (33) together lead to the interesting result that the various components of the reduced R matrix can be obtained approximately by simply evaluating the components of the ordinary R matrix at the complex energy $\mathcal{E}=E-\Delta+\frac{1}{2}i\Gamma$:

$$\mathfrak{R}_{rr}(E)\approx R_{rr}(\mathcal{E}). \tag{34}$$

This result is particularly useful because the latter components are analytical functions of the complex energy $\mathcal{E}$.[26] Thus the diagonal components of the R matrix are meromorphic functions, the imaginary parts of which are non-negative on the upper-half plane and nonpositive on the lower; their poles E_λ are confined to the real axis and have negative residues $-\gamma_{\lambda c}{}^2$. In this connection frequent reference will be made to the *pole strength function*[16,26] s_c for channel c which is defined as the sum of the $\gamma_{\lambda c}{}^2$ per unit energy interval of the E_λ,

[26] E. P. Wigner, Ann. Math. **53**, 36 (1951); **55**, 7 (1952).

averaged with respect to an interval of appropriate length.

The following procedure will now be used for the determination of the various components of the collision matrix. For the determination of a particular diagonal component, one eliminates explicit reference to all but the channel referred to by that component, while for the determination of a particular nondiagonal component, one eliminates explicit reference to all but the two channels referred to by that component. First we consider the diagonal components.

Diagonal Components

If there is only one r channel, the reduced collision matrix given by (28) together with (1) becomes the reduced collision function for the r channel; it is conveniently written (the r subscripts being omitted)

$$U=\exp(-2i\phi)(1-\Re L^*)/(1-\Re L). \tag{35}$$

It may be noted that if the reduced R function is approximated by one level of the diagonal component of the R matrix of (34), Eq. (35) reduces to the familiar one-level approximation to the collision function as given by Feshbach, Peaslee, and Weisskopf.[18]

By the introduction of Wigner's statistical R function R',[17,26]

$$R'=\sum_{\lambda'}\gamma_{\lambda'}{}^2/(E_{\lambda'}-E), \tag{36}$$

it is possible to develop a useful representation for the approximation (34) which is expected to be rather accurate when the absorption width is small (as well as large) compared with the mean level spacing D. The R' function has the property that in an energy interval I containing the energy E of interest and of a length such that $D\ll I\ll s(ds/dE)$, where $s(E)$ is the strength of R in the vicinity of E, its poles $E_{\lambda'}$ and residues $-\gamma_{\lambda'}{}^2$ are equal to those of R whereas outside of I they maintain the same statistical distributions as within and thus will in general differ from those of R which may evidence long-range fluctuations. The strength s of R' is thus everywhere equal to the strength $s(E)$ of R at the energy E. R' has therefore the useful property of approaching $i\pi s(E)$ when evaluated at a complex energy whose imaginary part is large compared with D, as is evident by replacing the sum over levels in (36) by an integration for the evaluation. The R' function is then added to and subtracted from the right side of (34) and the sums in the combination $(R-R')$ approximated by integrations, whereupon one obtains

$$\Re(E)=R'(\mathcal{E})+\bar{R}(\mathcal{E})-i\pi s(E), \tag{37}$$

in which

$$\bar{R}(\mathcal{E})=\bar{R}^{\mathrm{Re}}+i\bar{R}^{\mathrm{Im}}=\int s(E_\lambda)dE_\lambda/(E_\lambda-\mathcal{E}) \tag{37a}$$

is the Stieltjes transform[27] of $s(E)$, the inverse of which is

$$s(E-\Delta)=\lim_{\Gamma\to 0_+}(1/\pi)\bar{R}^{\mathrm{Im}}(\mathcal{E}). \tag{37b}$$

The representation (37) has the expected behavior in the two extremes: $\Gamma\gg D$, $\Re=\bar{R}$; $\Gamma\ll D$, $\Re=\bar{R}^{\mathrm{Re}}+R'$. The former result may be obtained simply by replacing the sum over the levels of R by an integration; according to (35) the corresponding collision function is

$$\bar{U}=\exp(-2i\phi)(1-\bar{R}L^*)/(1-\bar{R}L), \tag{38a}$$

the bar having been placed over U to indicate that $\Re$ has been replaced by $\bar{R}$. This function manifests no resonances and is essentially constant in the interval I. In the latter extreme, the term $\bar{R}^{\mathrm{Re}}$ represents the net contribution to R from the levels outside of I; in the limit $\Gamma=0$, it is the principal part of the integral of (37a). The collision function (35) for this case is conveniently rewritten

$$U=\exp(-2i\phi')(1-R'L'^*)/(1-R'L'), \tag{38b}$$

where

$$L'=L/(1-\bar{R}^{\mathrm{Re}}L),$$

and

$$\phi'=\phi-\tan^{-1}[\bar{R}^{\mathrm{Re}}P/(1-\bar{R}^{\mathrm{Re}}S)]$$

is the negative of the actual potential scattering phase shift. For example, in the collisions of slow neutrons with nuclei, the potential scattering term appearing in elastic scattering is found to be modified by a factor $(1-\bar{R}^{\mathrm{Re}})$ by which the radius is multiplied; according to (37b) the average of the reduced widths $\gamma_\lambda{}^2$ of the resonances is $D\bar{R}^{\mathrm{Im}}/\pi$.

Nondiagonal Components

For the evaluation of the st nondiagonal component of U, one can eliminate explicit reference to all but the s and t channels by introducing the reduced R matrix with components $\Re_{ss}$, $\Re_{tt}$, $\Re_{st}$ into the expression (28a) for the reduced collision matrix. By inverting the two-channel matrix $(1-\Re_{rr}L_r)$, one finds the nondiagonal component of the V_{rr} matrix to be

$$V_{st}=2iP_s{}^{\frac{1}{2}}\Re_{st}P_t{}^{\frac{1}{2}}\mathfrak{D}^{-1}, \tag{39}$$

the determinant being

$$\mathfrak{D}=(1-L_s\Re_{ss})(1-L_t\Re_{tt})-L_s\Re_{st}{}^2L_t.$$

The approximations (34) may be used for the various $\Re$ components, the Γ_λ and Δ_λ now including contributions from the partial widths and shifts of all but the s and t channels. When $\langle\Gamma_\lambda\rangle_{Av}\gg D$, it can be shown by means of Radamacher's theorem[20] that $|\Re_{st}|^2$ averaged with respect to all possible choices of the random signs of the $\gamma_{\lambda c}$ is equal to $2\pi s_s s_t D/\langle\Gamma_\lambda\rangle_{Av}$, which is negligible compared with the product $\Re_{ss}\Re_{tt}=\bar{R}_s\bar{R}_t\approx\pi^2 s_s s_t$. Equation (39) may therefore be replaced

$$V_{st}=2iP_s{}^{\frac{1}{2}}\sum_\lambda\frac{\theta_{\lambda s}\theta_{\lambda t}}{E_\lambda+\Delta_\lambda-E-\frac{1}{2}i\Gamma_\lambda}P_t{}^{\frac{1}{2}}, \tag{40}$$

[27] D. M. Widder, *The Laplace Transform* (Princeton University Press, Princeton, 1941).

where

$$\theta_{\lambda s}=(1-L_s\bar{R}_s)^{-1}\gamma_{\lambda s}.$$

Since $L_c\bar{R}_c\approx\frac{1}{2}i\pi\langle\Gamma_{\lambda c}\rangle_{Av}D^{-1}-\pi\langle\Delta_{\lambda c}\rangle_{Av}D^{-1}$, it is apparent that as expected (40) differs from (19) when the absolute magnitudes of these quantities approach or exceed unity. There is the additional difference that the widths and shifts in the denominators of (19) include contributions from all channels. However, when $\langle\Gamma_\lambda\rangle_{Av}\gg D$, this difference is negligible and for convenience the widths and shifts of (40) may be regarded as the respective totals, as in (19). The collision matrix thereby obtained has the advantage of being a valid approximation when $\langle\Gamma_\lambda\rangle_{Av}\ll D$ as well as when $\langle\Gamma_\lambda\rangle_{Av}\gg D$. One would also presume it to be reasonably accurate when $\langle\Gamma_\lambda\rangle_{Av}\sim D$, although in this case one can refer directly to (39). However, it is noted that this form of the collision matrix may violate the relation (9a), although to order of the channel mean of the ratios $\langle\Gamma_{\lambda c}\rangle_{Av}/D$, which necessarily must be small. This slight defect is readily amended by considering the partial widths and shifts which contribute to the respective totals to be

$$\Gamma_{\lambda c}=2P_c|\theta_{\lambda c}|^2,\quad \Delta_{\lambda c}=-S_c|\theta_{\lambda c}|^2, \tag{41}$$

rather than $2P_c\gamma_{\lambda c}^2$ and $-S_c\gamma_{\lambda c}^2$. The equality alternative of (9a) is then satisfied. As shown in the next section, the expressions for the average reaction cross sections which may be deduced from (40) are of the same form as those derived by Weisskopf.[11] We will therefore refer to (40) with the modifications indicated above as Weisskopf's collision matrix, although it was not explicitly considered by him in this manner. Finally it should be noted that although the nondiagonal components of V have been expressed in the expansion form (9), the diagonal components have not. No particular significance is attributed to this departure other than that it does appear to make V unitary.

VIII. AVERAGE CROSS SECTIONS

Scattering and Absorption

Convenient expressions for the energy averages of the cross sections for scattering and absorption of an incident beam of particles have been given by Feshbach, Porter, and Weisskopf.[9] For the lth partial wave and in units of $(\pi/k^2)(2l+1)$ they are:

total,	$\langle\sigma_0\rangle_{Av}=2-\langle U\rangle_{Av}-\langle U^*\rangle_{Av}$;
total elastic,	$\langle\sigma_e\rangle_{Av}=\langle\|1-U\|^2\rangle_{Av}$;
potential elastic,	$\langle\sigma_{pe}\rangle_{Av}=\|1-\langle U\rangle_{Av}\|^2$;
compound elastic,	$\langle\sigma_{ce}\rangle_{Av}=\langle\|U\|^2\rangle_{Av}-\|\langle U\rangle_{Av}\|^2$;
absorption,	$\langle\sigma_a\rangle_{Av}=1-\langle\|U\|^2\rangle_{Av}$;
compound-nucleus formation,	$\langle\sigma_C\rangle_{Av}=1-\|\langle U\rangle_{Av}\|^2$. (42)

U is the diagonal component of the collision matrix which refers to the incident beam. The cross section for compound-nucleus formation is by definition the sum of the absorption and compound elastic scattering cross sections, and it may be verified that the total elastic scattering is the sum of the potential elastic and compound elastic cross sections.

In view of the fact that all of the poles of the collision function are situated in the lower half of the complex energy plane, with the exception of those on the real axis associated with bound states,[28] the path of integration involved in the averaging of U may be displaced, without crossing poles, far enough upwards so that R' becomes essentially equal to $i\pi s(E)$, and therefore $\mathfrak{R}=\bar{R}$ according to (37). If the average is with respect to an energy interval I such that $D\ll I\ll s(ds/dE)^{-1}$, it may be presumed that the contributions from the connecting sides of the contour effectively cancel and that $\bar{R}$ is nearly constant on the displaced path, in which case

$$\langle U\rangle_{Av}=\bar{U}, \tag{43}$$

the quantity $\bar{U}$ being given by (38a). The interval I must also be small enough so that the external functions S, P, and ϕ may be considered as constants. It is then evident that $\langle\sigma_0\rangle_{Av}$, $\langle\sigma_{pe}\rangle_{Av}$, and $\langle\sigma_C\rangle_{Av}$ are obtained by simply substituting $\bar{U}$ for $\langle U\rangle_{Av}$ in (42). This result has already been noted by Feshbach *et al.*[9]

No such simple results of a general nature can be obtained for the quantity $\langle|U|^2\rangle_{Av}$, which also appears in (42), because its poles are situated in both halves of the $\mathcal{E}$ plane. However, by assuming that the $\gamma_{\lambda'}^2$ of R' are all equal and the levels $E_{\lambda'}$ uniformly spaced by an amount D so that

$$R'=\pi s\tan(\pi\mathcal{E}/D), \tag{44a}$$

then it is not difficult to include the residues of the poles of $|U|^2$ in the contour used to derive (43). The result is that

$$(1-|\langle U\rangle_{Av}|^2)^{-1}=(1-\langle|U|^2\rangle_{Av})^{-1}+(1-w^{-1})^{-1}, \tag{44b}$$

where

$$w=\exp(-2\pi\Gamma/D),$$

Γ being the total width for absorption, and therefore the remaining cross sections are

$$\begin{aligned}\langle\sigma_a\rangle_{Av}&=T[(1-w)/(1-w+wT)],\\ \langle\sigma_{ce}\rangle_{Av}&=T[wT/(1-w+wT)],\end{aligned} \tag{45}$$

where

$$T=\langle\sigma_C\rangle_{Av}=1-|\bar{U}|^2 \tag{45a}$$

is the transmission factor in the form proposed by Weisskopf.[11] This result has already been obtained in a somewhat different manner by Snowden and Whitehead.[29]

According to (45) the relative probabilities of compound elastic scattering and absorption are wT and

[28] W. Schützer and J. Tiomno, Phys. Rev. **83**, 249 (1951); Marcos Moshinsky, Anais acad. brasil. ciênc. **25**, 343 (1953).

[29] S. C. Snowden and W. D. Whitehead, Phys. Rev. **94**, 1267 (1954).

$(1-w)$, respectively. The following interpretation of these probabilities has been suggested by Porter:[30] According to Weisskopf[11,31] a period $2\pi\hbar/D$ may be attributed to the compound nucleus. Since the decay rate for absorption is $\Gamma/\hbar$, the probability for absorption in this period is $(1-w)$ while that of no absorption is w. At the end of each period the system is presumed to be in a configuration for decay into the entrance channel from which it was formed, and the probability for penetration through this channel is the transmission factor T, a quantity which by definition cannot exceed unity. Therefore, the chance of the occurrence of compound elastic scattering in one period is wT. The periodic motion of the compound nucleus is repeated until there is decay either one way or the other.

Both the detailed calculation by means of (44a) and the interpretation involving the attribution of a period to the compound nucleus depend upon the assumption of a uniform level spacing. This assumption may be questioned because the alternative view that the behavior of the compound nucleus is "chaotic" would imply that as in the familiar one-level resonance formula the relative probabilities for these decays are T for the entrance channel and the corresponding transmission factor $2\pi\Gamma/D$ for absorption. In this case, the probability for compound elastic scattering is relatively larger than wT, especially when $w\ll 1$ or equivalently $2\pi\Gamma/D\gg 1$. This alternative view may correspond to something like a random distribution for the level spacings. Unfortunately there is scant experimental information regarding this distribution, and the true behavior may lie anywhere between these extremes.

Reactions

The average reaction cross sections may be obtained from (40) in the same manner as (22) was obtained from (19), the only difference in the result being that the transmission factors are now $2\pi/D$ times the level averages of the $\Gamma_{\lambda c}$ of (41):

$$T_c=4\bar{R}^{\mathrm{Im}}P_c/|1-\bar{R}_cL_c|^2. \tag{46}$$

It may be verified that this T is the same as that of (45a). In other words, the channel transmission factors are just $k^2/\pi(2l+1)$ times the corresponding cross sections for compound-nucleus formation. This is the well known conclusion arrived at by Weisskopf[11] by considering the quantity defined as $\langle\sigma_C\rangle_{Nw}$ in (42) as the cross section for the actual formation of a compound nucleus and by applying the reciprocity theorem to the hypothesis of independent decay. In the present deliberations we have attempted to show in what circumstances these considerations are valid.

As a conclusion to this subsection, an application is mentioned of the collision matrices (19) or (40) in which the signs of the $\gamma_{\lambda c}$ are uncorrelated. If the reader will refer to the general expressions (4.6) or (4.7) given by Blatt and Biedenharn[32] for the differential cross sections of nuclear reaction products, he will notice that there occur sums of products in which $l_1=l_2$, $l_1'=l_2'$, $J_1=J_2$ and products in which one or more of these equalities are not satisfied. If these cross sections are averaged over an energy interval which is large compared with $\langle\Gamma_\lambda\rangle_{Nw}$, then the arguments used to derive (22) from (20) can be applied to show that the latter products are negligible compared with the former. As noted by Blatt and Biedenharn, the resulting expression with just the former products is the basis of the treatment by Hauser and Feshbach[33] of neutron inelastic scattering.

IX. THE POLE STRENGTH FUNCTION

According to the results of the last two sections, the pole strength function $s(E)$ and its Stieltjes transform (37a) are decisive in the determination of the behaviors of the various average reaction and scattering cross sections. The expressions for $s(E)$ and its transform are discussed in this section for various interaction representations of current interest.

1. The Strong-Coupling Theory

In this theory, the strength function may be approximately represented by the monotonically decreasing function[17]

$$\begin{aligned} s(E)&=(\pi Ka)^{-1}, && E>-B;\\ &=0, && E<-B, \end{aligned} \tag{47}$$

where

$$K=[2M(E+T+B)/\hbar^2]^{\frac{1}{2}}$$

is the wave number characteristic of the motion of a nucleon of mass M in a nucleus excited by the capture of a nucleon of energy E; T is the corresponding kinetic energy for an unexcited nucleus; and B is the binding energy of the nucleon to the nucleus. The Stieltjes transform of (47) is

$$\begin{aligned} \bar{R}(E-\Delta+\tfrac{1}{2}i\Gamma)&=(\hbar^2/2Ma^2T)^{\frac{1}{2}}(x-iy)\left\{\frac{1}{2\pi}\log\frac{(1+x)^2+y^2}{(1-x)^2+y^2}\right.\\ &\left.+i\left[1-\frac{1}{\pi}\tan^{-1}\frac{y}{1+x}-\frac{1}{\pi}\tan^{-1}\frac{y}{1-x}\right]\right\}, \end{aligned} \tag{48}$$

where

$$\begin{aligned} x&=[\tfrac{1}{2}T/H^2+\tfrac{1}{4}\Gamma^2]^{\frac{1}{2}}[(H^2+\tfrac{1}{4}\Gamma^2)^{\frac{1}{2}}+H]^{\frac{1}{2}},\\ y&=[\tfrac{1}{2}T/H^2+\tfrac{1}{4}\Gamma^2]^{\frac{1}{2}}[(H^2+\tfrac{1}{4}\Gamma^2)^{\frac{1}{2}}-H]^{\frac{1}{2}},\\ H&=E-\Delta+T+B, \end{aligned}$$

the inverse tangents being evaluated in the first quadrant. According to the estimates of Appendix B, the

[30] C. E. Porter (private communication).
[31] Victor F. Weisskopf, Helv. Phys. Acta 23, 187 (1950).
[32] J. M. Blatt and L. C. Biedenharn, Revs. Modern Phys. 24, 258 (1952), in particular reference 13.
[33] W. Hauser and H. Feshbach, Phys. Rev. 87, 366 (1952).

absorption width Γ is generally much less than the characteristic kinetic energy T, which is expected to be about 20 Mev, so that the above expression may accurately be approximated by

$$\bar{R}(E-\Delta+\tfrac{1}{2}i\Gamma)=s(E-\Delta)\log[(H^{\frac{1}{2}}+T^{\frac{1}{2}})/(H^{\frac{1}{2}}-T^{\frac{1}{2}})]+i\pi s(E-\Delta), \quad (48a)$$

which is independent of Γ. In typical cases, the real and imaginary parts of this transform are of about the same magnitude. It should be emphasized that in this theory the potential scattering is not given by the hard-sphere formula but by that which is obtained from the phase shift $-\phi'$ of (38b).[17]

In the Feshbach-Weisskopf continuum theory,[12] it is assumed that $\bar{R}=i/Ka$, which corresponds to constant K and constant strength s extending in energy from $-\infty$ to ∞, and to a wave function of the form $\exp(-iKr)$ at the nuclear surface.[1] A more realistic function would be of the form $\exp(K'-iK)r$ with a damping coefficient K' of about the same magnitude as K.[9] This modified wave function corresponds to an $\bar{R}$ of the form (48a).

2. The Complex Square Well Representation

As monotonic strength functions such as (47) do not appear to be in accord with the recent experimental results on total neutron cross sections,[8] it is tempting to consider nonmonotonic functions such as

$$s(E)=(1/2\pi)\textstyle\sum_p \zeta_p^2 W_p/[(E_p-E)^2+\frac{1}{4}W_p^2], \quad (49a)$$

with transforms

$$\bar{R}(\mathcal{E})=\textstyle\sum_p \zeta_p^2/(E_p-\mathcal{E}-\frac{1}{2}iW_p) \quad (49b)$$

which are similar to ordinary R functions with levels p and reduced widths ζ_p^2. The calculations of Bohr and Mottelson[34] provide some justification for the general form of (49a) on the basis of a shell model with level positions E_p and core couplings proportional to W_p. This analysis also indicates that

$$\zeta_p^2 \approx \hbar^2/Ma^2, \quad (49c)$$

which is the characteristic single-particle reduced width. This magnitude is to be expected since in the limit of no coupling, (49b) should reduce to a single-particle R function and $s(E)$ to a sum of delta functions each of total strength $\hbar^2/Ma^2$ at the positions E_p of the single-particle levels. Moreover, if the coupling is large compared with the single-particle level spacing $\pi\hbar^2K/Ma$, it may be shown by approximating the sum in (49a) by an integration that the strong-coupling value (47) for the strength is approached. It is also evident that if the W_p are sufficiently small, the corresponding expansion parameters $\pi\langle\Gamma_{\lambda c}\rangle_{Av}/2D=\pi s_c P_c$ of Sec. V can exceed unity, especially in the vicinity of the single-particle levels p.

[34] Aage Bohr and Ben R. Mottelson, Kgl. Danske Videnskab. Selskab, Mat.-fys. Medd. **27**, 16 (1953).

It has been shown by Wigner[35] that the reciprocal logarithmic derivative of any real continuous potential of finite range may be expanded as an R function. The R function for the complex square well potential should therefore be a special case of the expansion (49b). In fact by setting the ζ_p^2 and W_p equal to constants with respective values $\hbar^2/Ma^2$ and W, and by choosing the level positions to be $E_p=(\hbar^2/2Ma^2)(p-\frac{1}{2})^2\pi^2-V_0$ with p ranging from 1 to ∞ and V_0 an arbitrary energy, the expansion is obtained for $R=Z^{-1}\tan Z$, where

$$Z^2=(2Ma^2/\hbar^2)[(E-\Delta+V_0)+\tfrac{1}{2}i(\Gamma+W)],$$

which is just the expression for the reciprocal logarithmic derivative of a complex square well wave function of zero relative orbital angular momentum. It may also be shown that the corresponding expansions for complex square well wave functions of arbitrary angular momentum $\hbar l$ may be obtained with the same ζ_p^2 and W if one sets the boundary condition $B=-l$; the level positions, however, occur at the values $E=E_p$ which are associated with the zeros of the Bessel function $F_{l-1}(\rho_{pl})$ where $\rho=(2Ma^2/\hbar^2)^{\frac{1}{2}}(E-\Delta+V_0)^{\frac{1}{2}}$. The relation between $\mathfrak{R}$ and the logarithmic derivative f for this boundary condition is given by (31a).

The expansion (49b) for $\bar{R}$ suggests a "giant resonance" interpretation for the average cross-section data. If the width $\Gamma+W_p$ is small compared with the single-particle level spacing, one may over a limited energy range approximate the $\bar{R}$ of (49b) when substituted in the $\bar{U}$ of (38a) by one shell level p plus a real, constant $\bar{R}^0$ contribution from the remaining levels. Resonance formulas are thereby obtained for scattering and absorption in which the entrance channel width is given by the single-particle width $2P\zeta_p^2/|1-\bar{R}^0L|^2$ and the absorption width by $\Gamma+W_p$; the level spacing is that characteristic of a single-particle potential. By averaging over these giant resonances, the averages of the strong-coupling theory are obtained. In applications the interpretation is complicated by the fact that there will be one such resonance for each partial wave that is effective.

The complex square well representation for particle-nuclei interactions at intermediate energies has been considered by many physicists.[36] For a recent account of the interpretation of the neutron interaction cross sections in terms of it, the reader is referred to the paper by Feshbach, Porter, and Weisskopf.[9] The main results of the present investigation in this connection are the demonstration of the relation to the R-matrix or resonance theory and the theoretical indication of the dependence of the imaginary part of the potential on the absorption width. Francis and Watson[37] have investigated formally the matter of equivalent two-body

[35] E. P. Wigner, Am. Math. Monthly **59**, 669 (1952).

[36] Ostrofsky, Breit, and Johnson, Phys. Rev. **49**, 22 (1936); H. A. Bethe, Phys. Rev. **57**, 1125 (1940); Robert E. Le Levier and David S. Saxon, Phys. Rev. **87**, 40 (1952); D. M. Chase and F. Rohrlich, Phys. Rev. **94**, 81 (1954).

[37] N. C. Francis and K. M. Watson, Phys. Rev. **92**, 291 (1953).

potentials by considering the multiple scattering of an incident beam of particles traversing the target nucleus.

As an alternative to the introduction of the continuous, nonmonotonic $s(E)$ of (49a), one may suppose that the behavior of the average total neutron cross sections is due to the presence in the R function expansion of strong shell levels in addition to the usual weak levels which are needed to explain the narrow resonances. Such a state of affairs is depicted in Fig. (1a) where the strength s is represented by the height of the vertical lines for the individual levels; the representation of the strength function (49a) is shown in Fig. (1b). The former situation is actually somewhat unrealistic because of the strictly formal nature of the R-matrix levels. A mixing of the weak and strong levels is to be expected, the consequence of which is the dissolution of the strong levels and a modulation of the strengths of the weak levels, as indicated by Fig. (1b). Experimentally it is not easy to distinguish between these two alternatives because when the imaginary part of the potential is relatively small, the average total cross sections depend primarily on the real part of $\bar{R}$, which is essentially the same in the two cases. Direct determinations of s would therefore be desirable. This can be done by studying the behavior of the $\langle\gamma_{\lambda c}^2\rangle_{Av}$ for individual resonances[38] and by measuring the deviations from the simple exponential dependence of the transmissions involved in the measurements of total cross sections, these deviations resulting from the fluctuations, caused by the presence of many unresolved resonances, of the actual cross section about its average.[39]

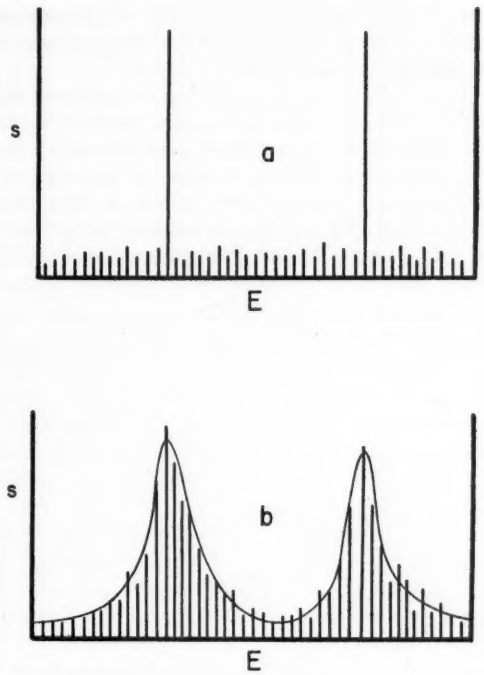

FIG. 1. The strengths $s=\gamma_\lambda^2/D$ of the levels of two nuclear models are represented by the heights of vertical lines at the level positions. a: There are strong, widely spaced levels in addition to weak levels of the strong-coupling type with narrow spacing; b: As a result of mixing of the strong and weak levels of a, the strong levels are weakened and their weak neighbors are strengthened.

3. Surface Absorption Model

A nucleon-nucleus interaction of current interest is one with a finite surface absorption in addition to the volume interaction; this absorption can be represented by a pure imaginary delta function potential of strength $i\alpha\hbar^2/2Ma$ appended to the complex well volume interaction. By integrating the wave equation across this surface, one finds that the logarithmic derivative is changed by a finite amount $-i\alpha/a$. The $\bar{R}$ function just outside of this surface is, therefore,

$$\bar{R}_+=(\bar{R}_-^{-1}-i\alpha)^{-1}, \tag{50a}$$

where $\bar{R}_-$ is the $\bar{R}$ function for the internal potential. According to the inversion formula (37b), the strength function corresponding to (50a) is just $1/\pi$ times the imaginary part of $\bar{R}_+$,

$$s(E-\Delta)=\pi^{-1}(\bar{R}_-{}^{\mathrm{Im}}+\alpha|\bar{R}_-|^2)/(1+\alpha^2|\bar{R}_-|^2). \tag{50b}$$

In the consideration of such a model, Bohr and Mottelson[34] have given an alternative derivation of (50b) for the case where $\bar{R}_-$ is real.

[38] Carter, Harvey, Hughes, and Pilcher, Phys. Rev. **96**, 113 (1954).

[39] R. G. Thomas, to be published.

X. CONCLUDING REMARKS

Although this investigation has primarily been concerned with magnitudes and energy dependences, it may be appropriate to include a remark concerning the angular distributions of the products of the decay of the compound nucleus. It has been a common misconception that the theory of the compound nucleus predicts that these distributions be isotropic. It should be stated that there are no indications from the present treatment that this is necessarily so. This matter has already been thoroughly investigated by Wolfenstein[40] as well as Hauser and Feshbach[33] who show that the theory of the compound nucleus requires only that these distributions be symmetric with respect to a plane perpendicular to the beam direction when averaged over a sufficient number of resonance levels. This symmetry is indeed a consequence of the lack of correlations of the signs of the $\gamma_{\lambda c}$. These authors also show that a sufficient condition for isotropy is that the energy levels of the compound and residual nuclei be sufficiently dense and have a dependence on their respective spins J which is proportional to $2J+1$ for the range of J values that can participate. According to reference 45, significant de-

[40] L. Wolfenstein, Phys. Rev. **82**, 690 (1951).

partures from such a dependence may occur at moderate energies. More general conditions of a necessary nature for isotropy are not known at present.

A concluding remark concerning the non-compound-nucleus processes may also be appropriate. It has been shown that if the signs of the $\gamma_{\lambda c}$ for the nuclear levels are uncorrelated, for any manner of excitation these levels will superpose in such a way as to form a compound nucleus; it has been a common belief that for the region of the configuration space where the nuclear interactions are very strong, these signs will indeed be uncorrelated. However, there is a nuclear surface region where the interactions are not particularly strong and non-compound nucleus processes, such as stripping and pickup, can occur. The R-matrix theory, being general, can account for these processes if the channel radii are extended to the limit of the nuclear interactions, but if this is done, the signs of the $\gamma_{\lambda c}$ would become correlated and some of the deductions in IX concerning the strength functions would lose their validity. A tractable approach to the theory of nuclear reactions may therefore be one where the channel radii are small enough to permit the application of the compound-nucleus theory to the internal, strong-interaction region, the effects of the nuclear interactions in the external region being accounted for by the running-wave Green's-function method.[41] The collision matrix would be expressed as

$$U=U_C+\Delta U, \tag{51}$$

where U_C represents the compound-nucleus contribution and ΔU the additional contribution from the external interactions. As a first approximation the wave functions of the compound nucleus system could be used in the matrix elements for the evaluation of the components of ΔU, rather than plane waves as in the Born approximation.[42] The equivalent two-body representations, such as the complex square well, would be particularly useful for this purpose. According to (51), the resulting collision cross section will contain contributions proportional to $|U_C|^2$ for the compound-nucleus processes, to $|\Delta U|^2$ for the non-compound-nucleus processes, and to the interference terms $U_C\Delta U^*+U_C^*\Delta U$.[43] It is evident that the interference contributions will vanish if averaged over an energy interval containing a sufficient number of levels of the compound nucleus.

[41] The R-matrix theory is based on the *standing-wave* Green's-function method. In fact, the components of the R matrix are the values of the Green's function at the entrances to the various pairs of channels.

[42] See, e.g., E. Gerjuoy, Phys. Rev. **91**, 645 (1953).

[43] The effect of the compound nucleus on the stripping contribution has been considered by N. C. Francis and K. M. Watson, Phys. Rev. **93**, 313 (1954); J. Horowitz and A. M. L. Messiah, J. phys. et radium **14**, 695 (1953); and W. Tobocman, Phys. Rev. **94**, 1655 (1954).

APPENDIX A. DERIVATION OF EQ. (29)

It is necessary to invert the submatrix $(1-R_{ee}L_e)$ in (27). With the separation (2) for the R-matrix, one finds

$$(1-R_{ee}L_e)^{-1}=(1-R^0_{ee}L_e)^{-1}(1-R'_{ee}L'_{ee})^{-1}, \tag{A1}$$

with L'_{ee} given in connection with (29). The inversion procedure[5,6] is to assume an expansion

$$(1-R'_{ee}L'_{ee})^{-1}=1+\textstyle\sum_{\mu\nu}(\gamma_{\mu e}\times\beta_{\nu e})A_{\mu\nu}, \tag{A2}$$

with

$$\beta_{\nu e}=L'_{ee}\gamma_{\lambda e}$$

and level coefficients $A_{\mu\nu}$ which are presumably functions of the energy. By multiplying both sides of (A2) by $(1-R'_{ee}L'_{ee})$ one obtains

$$-\sum_{\lambda}\frac{(\gamma_{\lambda e}\times\beta_{\lambda e})}{E_\lambda-E}+\sum_{\mu\nu}(\gamma_{\mu e}\times\beta_{\nu e})A_{\mu\nu}$$
$$-\sum_{\lambda\mu\nu}\frac{(\gamma_{\lambda e}\times\beta_{\nu e})}{E_\lambda-E}A_{\mu\nu}\xi_{\lambda\mu}=0, \tag{A3}$$

after making use of the identities

$$M(x\times y)N=(Mx\times\tilde{N}y),$$
$$(x\times y)(z\times w)=\zeta(x\times w) \tag{A4}$$

in which x, y, z, w are arbitrary vectors, M and N are arbitrary matrices, the transpose of the latter being $\tilde{N}$, and $\zeta=(y,z)$ is a scalar product over channels; the $\xi_{\lambda\mu}$ are given by (30b). Equation (A3) may be rearranged to read

$$\sum_{\lambda\nu}(\gamma_{\lambda e}\times\beta_{\nu e})\left[-\frac{\delta_{\lambda\nu}}{E_\lambda-E}+A_{\lambda\nu}-\sum_{\mu}\frac{\xi_{\lambda\mu}A_{\mu\nu}}{E_\lambda-E}\right]=0 \tag{A5a}$$

which is satisfied if for all λ, ν

$$(E_\lambda-E)A_{\lambda\nu}-\textstyle\sum_\mu\xi_{\lambda\mu}A_{\mu\nu}=\delta_{\lambda\nu}. \tag{A5b}$$

The matrix equivalent of this set of equations is (30a). The expansions (A2) and (A1) are then substituted into the expressions (27) for $\mathcal{R}_{rr}$ and $\mathcal{R}_{er}$. By repeated applications of (A4) and (A5b) these complicated expressions finally reduce to those of (29).

APPENDIX B. ESTIMATES OF THE TOTAL REACTION WIDTH

The following procedure for estimating the total nuclear decay width is essentially the same as that previously used by Weisskopf.[44] A compound nucleus of excitation energy E_C, total spin J, emits particles of spin i with relative orbital angular momentum hl, in groups of energy ϵ, leaving the residual nucleus with

[44] V. F. Weisskopf, Phys. Rev. **52**, 295 (1937).

total spin I and excitation energy $(E_C-B-\epsilon)$, where B is the binding energy of the emitted particle to the ground state of the residual nucleus; $\mathbf{s}=\mathbf{i}+\mathbf{I}$ is the channel spin. By assuming that the levels in the residual nucleus are sufficiently dense so that the sum over levels can be replaced by an integration, the total width for the decay of a compound-nucleus level of spin J becomes

$$\Gamma^J=\sum_{Il_s}\frac{1}{2\pi}D_C{}^J(E_C)\int_0^{E_C-B}\frac{T_{l\epsilon}d\epsilon}{D_R{}^I(E_C-B-\epsilon)}, \quad \text{(B1)}$$

where $D_C{}^J$ and $D_R{}^I$ are the mean level spacings of the compound and residual nuclei with spins J and I, respectively, and $T_{l\epsilon}$ is the transmission factor for channel $l\epsilon$. It is necessary to make the reasonable assumption that the level densities as a function of spin are proportional to the spin statistical factor,[45] at least over the range of participating spin values:

$$D_C{}^J=D_C/(2J+1), \quad D_R{}^I=D_R/(2I+1), \quad \text{(B2)}$$

D_C and D_R being independent of the spins J and I, respectively. By noting that

$$\sum_{I_s}(2I+1)=(2J+1)(2l+1)(2i+1)$$

and

$$\sigma_C(\epsilon)=(\pi\hbar^2/2M\epsilon)\sum_l(2l+1)T_{l\epsilon}$$

is the cross section for the inverse process of compound nucleus formation when the residual nuclei of excitation $(E_C-B-\epsilon)$ are bombarded by particles of energy ϵ, where M is the reduced mass, one obtains

$$\Gamma=\frac{(2i+1)MD_C(E_C)}{\pi^2\hbar^2}\int_0^{E_C-B}\frac{\epsilon\sigma_C(\epsilon)d\epsilon}{D_R(E_c-B-\epsilon)}, \quad \text{(B3)}$$

which is independent of J and identical to the original expression given by Weisskopf. In order to arrive at an order of magnitude estimate of Γ, it is assumed that $D_C(E)=D_R(E)=c\times\exp(-E/T)$ both functions having the same factor c and temperature T, at least in the region of excitation energies where the main contributions to the integral in (B3) arise; furthermore it is assumed that the energies of the emitted neutrons are all equal to $2T$, their average, that $\sigma_C(\epsilon)=\pi a^2$, being independent of the state of excitation of the residual nucleus, and that $E_c\gg B$, so that one obtains[46]

$$\Gamma\approx 2(2i+1)MT^2a^2\pi^{-1}\hbar^{-2}\exp(-B/T). \quad \text{(B4)}$$

As a typical example, we put $a=8\times10^{-13}$ cm, $T=3$ Mev, for neutron decay, obtaining $\Gamma\approx2.5$ Mev.

The usual statistical-theory assumption that $\sigma_C(\epsilon)$ is independent of the state of excitation of the residual nucleus being bombarded in the inverse process is subject to question because it implies an eventual violation of the Wigner sum rule,[10] $\sum_c\gamma_{\lambda c}{}^2\lesssim 3\hbar^2/2Ma^2$. By considering this rule, an upper-limit estimate for Γ can be made which should not be exceeded by the estimate (B4). If in the alternative expression for the width, $\sum_c 2P_c\gamma_{\lambda c}{}^2$, the barrier factors are replaced by a mean value $(4Ma^2T/\hbar^2)^{\frac{1}{2}}$ corresponding to $l=0$ neutrons of energy $2T$, and the remaining sum replaced by the above sum rule, one concludes that

$$\Gamma\lesssim(36\hbar^2T/Ma^2)^{\frac{1}{2}}. \quad \text{(B5)}$$

For the example cited above, $\Gamma\lesssim 8.5$ Mev. It should probably be required that (B3) be considerably less than the right side of (B5) because the negative-energy channels, which do not contribute to the width $(P=0)$, are to be included in the sum rule. As the temperature T is expected to be a monotonically increasing function of the excitation energy, an energy will ultimately be reached where (B3) exceeds (B5). In the example, this energy would correspond to $T=4.4$ Mev.

In the usual statistical-theory applications, the temperature enters in an expression which refers to the product of the reduced width and the level spacing rather than to the level spacing itself. This is because $\sigma_C(\epsilon)$ is generally assumed to be independent of the state of excitation of the residual nucleus. Although the actual nuclear temperature is expected to increase monotonically with the excitation, the above considerations show that it may preferable to use a more nearly constant temperature to represent this product. There is indeed experimental evidence that the temperature referring to this product actually decreases with increasing excitation indicating that the $\sigma_C(\epsilon)$, or equivalently the $\langle\gamma_{\lambda c}{}^2\rangle_{Av}$, for the bombardment of excited nuclei decrease considerably with the excitation of these nuclei.[47]

[45] Claude Bloch, Phys. Rev. **93**, 1094 (1954). There is also expected to be an additional factor $\exp[-(J+\frac{1}{2})^2/2\sigma^2]$ in the dependence of the level densities on the spins J (and I). According to estimates made of the dispersion coefficient σ using the individual-particle model, Bloch finds significant deviations from the $2J+1$ dependence due to this factor for values of J as low as three and nuclear excitations less than 12 Mev.

[46] By substituting in this formula the estimate $T^2\approx 20E/A$, the energy unit being Mev, and $a=1.4\times10^{-13}A^{\frac{1}{3}}$ cm, D. C. Peaslee obtains $\Gamma\approx(4/3)E_CA^{-\frac{1}{3}}\exp(-B/T)$. Because of a misprint, a different formula was given in a publication by him [Phys. Rev. **86**, 269 (1952)]. As a result the $\bar{\Gamma}$ of his Table I are somewhat overestimated. However, the factors f were also overestimated so that the qualitative conclusions of his paper remain essentially unchanged. [D. C. Peaslee (private communication).]

[47] B. L. Cohen, Phys. Rev. **92**, 1245 (1953).

Letters to the Editor

PUBLICATION of brief reports of important discoveries in physics may be secured by addressing them to this department. The closing date for this department is five weeks prior to the date of issue. No proof will be sent to the authors. The Board of Editors does not hold itself responsible for the opinions expressed by the correspondents. Communications should not exceed 600 words in length and should be submitted in duplicate.

Paramagnetic Resonance in Low Fields

GEORGES J. BÉNÉ AND R. C. EXTERMANN
Institute of Physics, University of Geneva, Geneva, Switzerland
(Received November 16, 1954)

A PAPER, recently published in this journal,[1] gives a theory and some preliminary results about paramagnetic resonance in low fields. The theory may be derived from the Bloch formulation of the nuclear resonance with a correction similar to that applied by Van Vleck and Weisskopf to the Lorentz theory of line broadening for an harmonic oscillator.

A test of this theory is given by the relative variation of the gyromagnetic ratio g from its free-spin value, as a function of $\omega\tau$, obtained from the equation giving χ'' when χ'' is maximized as a function of $\omega_0\tau$ for constant $\omega\tau$, where ω_0=Larmor frequency, τ=relaxation time, and ω=angular frequency of the rf field.

The purpose of this letter is to point out that, a few years ago,[2] we predicted, by analogy with dielectrics,[3] such a law of variation for the frequency of maximum absorption. We assumed only that, for resonant relaxating systems, the approach to equilibrium is given, in the static case, not by an exponential law (which would lead to Debye equations when an rf field is applied), but by damped oscillations:

$$\alpha(t)=\gamma e^{-t/\tau}\cos(\omega_0 t+\psi), \tag{1}$$

where τ is the relaxation time, ω_0 the resonance frequency, and γ and ψ two constants to be determined. This type of relation leads to the expression

$$\chi=\gamma\int_0^\infty e^{-t/\tau}\cos(\omega_0 t+\psi)e^{i\omega t}dt, \tag{2}$$

for the complex susceptibility

$$\chi=\chi'-i\chi'' \tag{3}$$

in an applied alternating field, giving

$$\chi''=\tfrac{1}{2}\chi_0\left(\frac{\omega\tau}{1+\tau^2(\omega_0+\omega)^2}+\frac{\omega\tau}{1+\tau^2(\omega_0-\omega)^2}\right). \tag{4}$$

This is exactly the formula derived by Garstens[1] [Eq. (18)]. When we maximize χ'' as a function of $\omega_0\tau$ for constant $\omega\tau$, we can obtain the quoted variation of $\Delta\gamma/\gamma$ as a function of $\omega\tau$. If we maximize χ'' as a function of ω, for constant ω_0, χ'' has a maximum when $\omega=\omega_M$, with

$$\omega_M=(1+\omega_0^2\tau^2)^{\frac{1}{2}}/\tau. \tag{5}$$

This formula is given in reference 2.

It would be interesting to test the relation (5) by plotting $\chi''(\omega)$ for a number of field intensities. A modulation of the frequency will be required in this case.

[1] M. A. Garstens, Phys. Rev. 93, 1228 (1954).
[2] G. J. Béné and R. C. Extermann, Arch. sci. (Genève) 4, 436 (1951).
[3] H. Fröhlich, *Theory of Dielectrics* (Clarendon Press, Oxford, 1949).

Electron Resonance in Gas Discharges

D. J. E. INGRAM AND J. G. TAPLEY
University of Southampton, Southampton, England
(Received November 6, 1954)

WE have recently observed electron resonance absorption in gas discharges at low pressures, and the initial results show that this should be a very sensitive method of studying the variation of free ion concentration, as well as giving other useful information. The absorption lines were obtained by normal paramagnetic resonance techniques,[1] using a cavity resonator that had been constructed so that the discharge took place in the region of maximum microwave magnetic field strength. The effective volume of the discharge was about 4 cc, and, with this arrangement, absorption lines of quite large magnitude could be produced.

Preliminary experiments using air in the discharge tube gave a resonance of about 200-gauss half-width, and a spectroscopic splitting factor of 2.0±0.05. The intensity of the absorption varied markedly with pressure. The absorption line first appears as the pressure reaches a value low enough for the discharge to strike, and then increases rapidly in intensity as the pressure is further reduced, passing through a maximum as the discharge reaches its brightest conditions, and then decreases slowly to a small value, as the pressure falls into the hard vacuum region. The width of the absorption line also decreases, after the maximum in intensity has been passed, having a value of about 90 gauss, at a pressure of 10^{-2} mm Hg.

There are three effects which may be responsible for the absorption: (*i*) spin resonance from the positive ions and free electrons, (*ii*) spin resonance from the dissociated, but un-ionized atoms, as observed by Beringer and Rawson for hydrogen and oxygen,[2,3] and (*iii*) cyclotron resonance from the electron motion. Rough estimates of the signal magnitude indicate that (*i*) and (*ii*) by themselves would not produce the large intensity observed, and that most of the absorption may be due to cyclotron resonance. The width of the reso-

nance line was found to decrease when the electrodes were cooled to 200°K, however, and the width also varied with the particular gas filling the discharge tube. This would indicate that there is some effect due to the positive ions, or dissociated atoms, the high effective temperature of the discharge averaging out their fine and hyperfine splittings.[2,3] Initial measurements on various gases are summarized in Table I.

TABLE I. Variation of width with gas in discharge tube.

Gas	Half-widths at maximum intensity (gauss) 290°K	200°K
Argon	115	60
Oxygen	135	85
Carbon dioxide	150	110

A systematic survey of other gases, and of the variation in intensity and width of the absorption, with both the pressure, and the temperature, of the discharge, is being made, and will be reported shortly.

[1] B. Bleaney and K. W. H. Stevens, Repts. Progr. Phys. **56**, 108 (1953).
[2] R. Beringer and E. B. Rawson, Phys. Rev. **87**, 228 (1952).
[3] E. B. Rawson and R. Beringer, Phys. Rev. **88**, 677 (1952).

Paramagnetic Resonance Absorption in Graphite Compounds*

B. SMALLER, G. R. HENNIG, AND E. L. YASAITIS
Chemistry Division, Argonne National Laboratory, Lemont, Illinois
(Received November 12, 1954)

A VERY narrow resonance line had been found, as previously reported,[1] in the bisulfate compounds of graphite. Several other compounds of graphite have also been found to show a similar resonance. The compounds to be described here contain alkali or alkaline earth metals, which act weakly as donor impurities, i.e., furnish some electrons to the graphite conduction band.

The metal-graphite compounds were prepared by reacting a solution of the metal in liquid ammonia with purified flakes of Madagascar natural graphite. The compounds were prepared and washed with liquid ammonia at −78°C and sealed with ammonia into quartz tubes. The compounds contained ammonia in addition to the metal, but consistent analyses have not yet been obtained. The presence of the ammonia was shown to have no effect on the resonance by preparing a potassium-graphite compound (No. 144, Table I) directly in the metal vapor.

The resonance detection equipment was of the regenerative oscillator-detector scheme using the dual-field modulation and has been described previously.[2] Measurements were made initially at 350 Mc/sec and then at 4.25 and 15.4 Mc/sec to reduce magnetic field inhomogeneities. The results at the latter frequency are shown in Table I for the various metals. The effect of metal concentration has not yet been determined quantitatively because of the difficulty of assaying. When the concentration was obviously high, no resonance appeared. The two lithium compounds (No. 137 and No. 149) showed signal intensities in the ratio 2:1 indicative of comparable concentration ratios.

TABLE I. Resonance line width in compounds of graphite and metals.

Metal constituent	Sample No.	ΔH, 300°K (milligauss)	ΔH, 77°K (milligauss)
Li (conc.)	137	100	70
Li (dil.)	149	86	60
Na	164	115	77
K	144[a]	350[b]	
K	141	275	275
Ca	156	130	75
Ba	140		<300[c]

[a] Compound prepared *in vacuo*, does not contain ammonia.
[b] Measured at 4.25 Mc/sec.
[c] Measured at 355 Mc/sec.

It may be significant that the metal-graphite compounds show relaxation times of the order anticipated by theory for metallic resonances.[3] The lack of such agreement with experimental results in finely dispersed and bulk alkali metals has been attributed to skin depth effects, and thus one might postulate that the layer type (lamellar) structure of the graphite compounds minimizes such effects. The linear dependence of line width on temperature predicted by theory has been found to require modification by, perhaps, a spin-orbit interaction term. The results in Table I appear to bear out this effect.

* Based on work performed under the auspices of the U. S. Atomic Energy Commission.
[1] Hennig, Smaller, and Yasaitis, Phys. Rev. **95**, 1088 (1954).
[2] B. Smaller and E. L. Yasaitis, Rev. Sci. Instr. **24**, 991 (1953).
[3] A. Overhauser, Phys. Rev. **89**, 689 (1953).

InSb Photovoltaic Cell*

G. R. MITCHELL, A. E. GOLDBERG, AND S. W. KURNICK
Chicago Midway Laboratories, Chicago, Illinois
(Received November 5, 1954)

A CRYSTAL of InSb containing a photosensitive junction has been prepared by the crystal-pulling technique. During crystal growth the melt was doped to produce a *p-n* transition. A specimen 1 cm×0.1 cm ×0.025 cm was cut from the crystal so as to include the the transition region. This specimen exhibited a dark resistance of about 20 000 ohms at 77°K and no noticeable rectification. The photoresponse at 77°K has been determined using the specimen as a photovoltaic cell. The spectral response extended to about 5.7μ; this limit agrees very well with the transmission data of

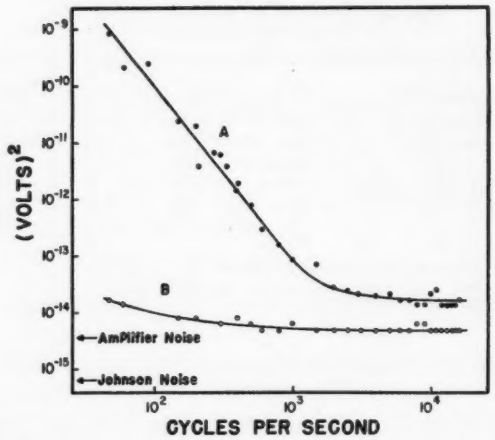

FIG. 1. Noise spectra (13-cps band width) for InSb photocell cooled to 77°K. *A* is for 300°K background. *B* is for 77°K background.

Avery *et al.*[1] for pure InSb. The time constant of the response was less than 2 microseconds, the minimum value that could be measured with our present apparatus.

Figure 1 shows noise spectra for the cell at 77°K. Curve *A* was observed when the cell was exposed to room-temperature radiation. Curve *B* was observed when the cell was covered with a light shield at 77°K. Shielding decreased the noise at all frequencies. The noise given by curve *B* is virtually amplifier noise and the slight rise at low frequencies is attributed to a small radiation leak. The Johnson noise for the cell was below amplifier noise. For the cell exposed to 300°K radiation the noise showed a white spectrum above 2 kc/sec while below 2 kc/sec it followed an approximate f^{-d} law with $d \cong 3$. This result is a curious one since the cell was operated without bias.

It is interesting to compare the detectivity of the cell exposed to a 300°K background with the limiting detectivity set by photon noise.[2] To compute the latter, it is assumed that the cell has unity quantum efficiency for $\lambda < 5.5\mu$ and cuts off abruptly. Considering only the noise created by random arrival of photons, the theoretical detectivity of a 1 mm² cell is calculated to be 1.1×10^{-8} sec/photon. The measured detectivity is 0.09×10^{-8} sec/photon. The conditions of measurement were: cell area 1 mm², responsivity 10.5 volts/(watt/cm²) at 2μ, noise 0.11 microvolt for $f > 2$ kilocycles and a band width of 13 cps.

A more detailed account of this work will be published in the future.

The authors are indebted to Mr. H. Berman for valuable discussion and criticism.

* This research was supported in whole by the U. S. Air Force.

[1] Avery, Goodwin, Lawson, and Moss, Proc. Phys. Soc. (London) **B67**, 761 (1954).

[2] R. Clark Jones, *Advances in Electronics* (Academic Press, Inc., New York, 1953), Vol. V, pp. 19–23.

Energies of the *K* Transitions of π^- Mesonic X-Rays*

M. STEARNS, M. B. STEARNS, S. DEBENEDETTI, AND L. LEIPUNER

Carnegie Institute of Technology, Pittsburgh, Pennsylvania

(Received October 22, 1954)

IN a previous letter[1] we reported on the energy shifts, presumably arising from specifically nuclear interactions, of the $2p \rightarrow 1s$ π-mesonic x-rays in lithium and beryllium. For these elements the energy was measured with the critical absorption technique. Here we wish to report further on measurements of *K*-transition energy shifts in carbon, nitrogen, oxygen, and fluorine. Since the critical absorption method could not be extended to these elements, the energy was determined by a measurement of pulse height.

The experimental setup has been previously described.[2] For the present measurements the scale of the pulse height selector was calibrated by means of other mesonic x-ray lines whose energies could be calculated sufficiently accurately (see Table I). The experimental procedure was to bracket each *K* line under investigation with two or more calibration lines. The line to be measured and its calibrating lines were run alternately at least three times. Usually the reproducibility was excellent, peaks drifting only a fraction of a channel, so that the data could be added to give better statistics. μ-meson transitions were used as the calibrating lines for oxygen and fluorine since for $Z \gtrsim 17$ there may be measurable nuclear shifts in the π $3d \rightarrow 2p$ transition energies

TABLE I. Computed energies of $2p \rightarrow 1s$ transitions and their calibrating lines.

Element for π $2p \rightarrow 1s$	Element for calibration	Type meson	Type of transition	Uncorr. trans. energy[a] (kev)	Vac. polar. corr.[b] (kev)	Finite size corr.[c] (kev)	Corrected energy (kev)
	P	π	$4f \rightarrow 3d$	40.4	+0.10		40.5
	F	π	$3d \rightarrow 2p$	41.4	+0.13		41.5
Be				*43.8*	*+0.20*	*−0.12*	*43.9*
	Cl	π	$4f \rightarrow 3d$	51.9	+0.15		52.1
	Al	π	$3d \rightarrow 2p$	86.7	+0.37		87.1
C		π		*99.2*	*+0.57*	*−0.76*	*99.0*
	Si	π	$3d \rightarrow 2p$	100.6	+0.43		101.0
	P	π	$3d \rightarrow 2p$	115.6	+0.53		116.1
N				*135.4*	*+0.84*	*−1.57*	*134.6*
	S	π	$3d \rightarrow 2p$	131.6	+0.63		132.2
	Cl	π	$3d \rightarrow 2p$	148.7	+0.74		149.4
	O	μ	$2p \rightarrow 1s$	134.4	+0.77	−1.28	133.9
O				*177.3*	*+1.20*	*−2.92*	*175.5*
	F	μ	$2p \rightarrow 1s$	170.3	+1.04	−2.31	169.0
	K	π	$3d \rightarrow 2p$	186.0	+0.97		186.9
	F	μ	$2p \rightarrow 1s$	170.3	+1.04	−2.31	169.0
F				*225.0*	*+1.60*	*−5.27*	*221.3*
	Na	μ	$2p \rightarrow 1s$	254.8	+1.73	−5.84	250.7

[a] The π^- energies were calculated with the Klein-Gordon equation by using the reduced π^--meson mass (assuming $m_{\pi^-} = 272.5 m_e$) and a point-charge Coulomb potential. The μ^- energies were calculated similarly, but with the Dirac equation and the assumption $m_{\mu^-} = 207.0 m_e$.

[b] Vacuum polarization correction; H. C. Corben and A. Mickelwait, Phys. Rev. (to be published).

[c] Finite size correction; made by using hydrogenic wave functions in a first order perturbation calculation neglecting the specifically nuclear interaction between meson and nucleus.

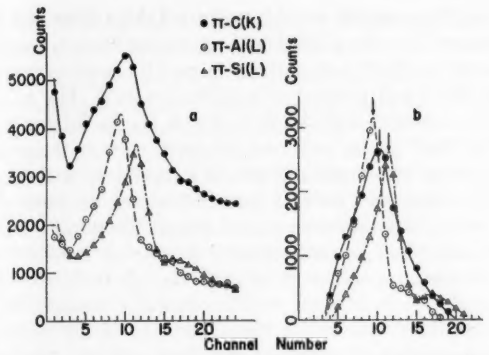

FIG. 1. Typical set of data for carbon and its calibration lines. Part (a) shows the data as obtained directly on the pulse height selector. Part (b) shows the peaks obtained after subtracting the background. In this particular run the shift obtained for carbon was (-5.6 ± 3) percent.

themselves. For $Z\lesssim16$ no discernible shifts were found when checks were made of the $3d\rightarrow2p$ π lines against $2p\rightarrow1s$ μ lines (of comparable energy).

Typical runs are shown in Figs. 1(a) and 2(a). After subtraction of background [Figs. 1(b) and 2(b)] the peak positions were determined and the energy of the investigated line was obtained by interpolation. Several runs of the kind described were made for each element and the resultant energies were then averaged to obtain the final measured energy.

The theoretical energies of the π $2p\rightarrow1s$ transitions were computed without taking into account nuclear

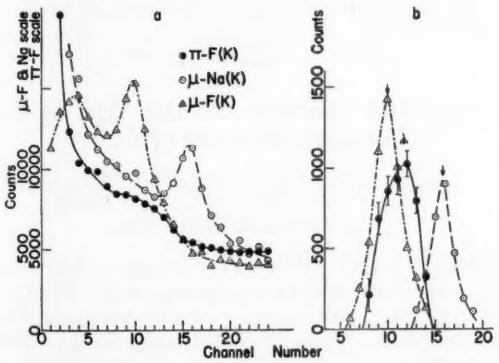

FIG. 2. Typical set of data for fluorine and its calibration lines. Part (a) shows the data as obtained directly on the pulse height selector. Part (b) shows the peaks obtained after subtracting the background. In this particular run the shift obtained for fluorine was (-14.5 ± 4) percent. The fluorine K yield is quite small, about 10 percent that of carbon (see reference 2).

interactions (Table I). The result of the comparison between the experimental and calculated energy is shown in Fig. 3 in the form of percentage shifts. The errors indicated express the reproducibility of the data when one takes into consideration statistics, background subtraction, and the consistency of repeated runs. However, they do not include possible systematic errors such as Compton degradation and the presence of unresolved lines in the observed peaks.

The effect of Compton degradation in the target material was investigated experimentally with radioactive sources and was found to produce no detectable shift in peak position, although some broadening of the line was observed on the low-energy side. Unresolved lines can arise from μ mesons stopping in the target, from π mesons stopping in surrounding materials, and from higher π-meson K transitions. There is good experimental evidence that the contribution from stopped μ mesons is negligible. A weak π carbon line arising from mesons stopping in counters could be observed, but its effect on the determination of the peak position could be adequately estimated. Perhaps the most troublesome of the unresolved lines would be the $3p\rightarrow1s$ π-meson transition which is 18 percent higher than the $2p\rightarrow1s$ line under investigation. The effect of any such additional K transition would be to make the observed peak energies appear too high and therefore give smaller measured shifts than would exist for pure $2p\rightarrow1s$ lines. A measure of such an effect might be obtained by comparing with the critical absorption technique. In the case of beryllium, where the energy could be measured by both methods, the agreement is within the accuracy of the experiments. For carbon only a lower limit on the energy shift could be obtained with the critical absorption technique, and this is in agreement with the measured peak position energy. This would indicate that for these elements there is not very much of the higher K lines in the observed peaks; however, their relative abundance is likely to increase with higher Z. Such an additional component might reveal itself as a broadening of the peaks, and indeed we observe that the π K lines are wider than the

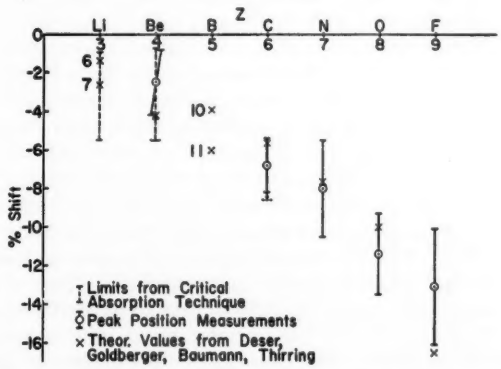

FIG. 3. Percent shift of the measured K transition peak energies relative to the calculated $2p\rightarrow1s$ lines. Measurements from both peak position and critical absorber work are shown. The errors indicated are estimates of standard deviations and do not include possible systematic errors. Agreement with the theoretical points may be fortuitous for the several reasons given in the text.

calibrating lines of the same energy. Though the additional width could be due to nuclear capture from the $1s$ level, it is possible that it originates at least in part from this unresolved line. In the case of μ mesons a corresponding broadening is not observed, but the different behavior of the two mesons could be explained in terms of the large nuclear capture probability of pions in the $2p$ state, which thus depresses the $2p \rightarrow 1s$ line relative to the $3p \rightarrow 1s$.

There have been some recent theoretical investigations[3,4] on the nuclear shifts of the $1s$ π-mesonic level. In Fig. 3 we have plotted the results obtained from the paper of Deser, Goldberger, Bauman, and Thirring. The agreement with experiment is quite good. However, this may be fortuitous both because of some possible $3p \rightarrow 1s$ admixture in our peaks, and because of the extrapolation and oversimplification involved in the theoretical estimate. In addition our preliminary results on boron, though not yet sufficiently consistent to be reported, seem to contradict the trend indicated in Fig. 3.

* Supported in part by the U. S. Atomic Energy Commission.

[1] Stearns, Stearns, DeBenedetti, and Leipuner, Phys. Rev. **96**, 804 (1954).
[2] Stearns, DeBenedetti, Stearns, and Leipuner, Phys. Rev. **93**, 1123 (1954).
[3] G. C. Wick (unpublished).
[4] Deser, Goldberger, Baumann, and Thirring, Phys. Rev. **96**, 774 (1954).

Average Number of Neutrons Emitted During the Spontaneous Fission of Cf^{252}*

W. W. T. Crane, G. H. Higgins, and S. G. Thompson
University of California, Radiation Laboratory, Livermore, California

(Received November 4, 1954)

THE average number of neutrons per spontaneous fission of Cf^{252} has been found to be 3.10 ± 0.15 by the manganous sulphate moderator-absorber system.

Since the discovery of spontaneous fission by Petrzhak and Flerov[1] in 1940, measurements of the number of neutrons per fission, ν, have been made upon various nuclides. Littler[2,3] and Barclay, Galbraith, and Whitehouse[4] found the best value of $\nu(U^{238}) = 2.4 \pm 0.2$, and the latter authors report $\nu(Th^{232}) = 2.6 \pm 0.3$. Recently, Barclay and Whitehouse[5] measured $\nu(Cm^{242}) = 3.0 \pm 0.3$.

Since the ratio of alpha decay to spontaneous fission is only about 42 in the decay of Cf^{252},[6] there is no measurable contribution from (α,n) reactions on low Z elements to the total number of neutrons observed from a sample. For this reason, Cf^{252} makes an ideal standard for the calibration of other neutron counting devices.

A sample of Cf^{252} of about 5×10^{-3} micrograms was mounted on a one-inch platinum disk and the number of fissions per minute was determined by direct counting. The sample was placed in a Lucite tube and immersed in a tank filled with saturated $MnSO_4$ solution until the Mn^{56} radioactivity formed by neutron capture in Mn^{55} had reached an equilibrium level. The sample was removed and the intensity of the radiations from the Mn^{56} in the tank was measured with an immersion counter which utilized an NaI crystal as a detector. The tank and counter were calibrated by measuring the activity produced from a standardized mock fission source,[7] and by comparing the activity produced by the fission spectrum from Cm^{244} in this tank with that produced in a tank which was large enough to be essentially infinite for the absorption of the neutrons from standard polonium-beryllium sources. Neutrons from the polonium-beryllium sources are presumed to be more energetic than those from any spontaneous fission source.

Over-all errors in the average value obtained from several measurements are thought to be less than 5 percent. Work is continuing on several other heavy element nuclides.

We wish to express our gratitude to J. Harper and L. Mann for their work on the electronic equipment.

* This work was performed under the auspices of the U. S. Atomic Energy Commission.

[1] K. A. Petrzhak and G. N. Flerov, Acad. Sci. (U.S.S.R.) **28**, 500 (1940).
[2] D. J. Littler, Proc. Phys. Soc. (London) **A64**, 638 (1951).
[3] D. J. Littler, Proc. Phys. Soc. (London) **A65**, 203 (1952).
[4] Barclay, Galbraith, and Whitehouse, Proc. Phys. Soc. (London) **A65**, 73 (1952).
[5] F. R. Barclay and W. J. Whitehouse, Proc. Phys. Soc. (London) **A66**, 447 (1953).
[6] Ghiorso, Thompson, Choppin, and Harvey, Phys. Rev. **94**, 1081 (1954).
[7] D. S. Martin, Atomic Energy Commission Report AECD-3077 (unpublished).

Hyperfine Splitting and the Sign of the Magnetic Moment of Cs^{134m}

L. S. Goodman and S. Wexler
Argonne National Laboratory, Lemont, Illinois

(Received November 12, 1954)

PREVIOUSLY published low-frequency data[1,2] from magnetic resonance experiments with 3.1-hr Cs^{134m} atomic beams, when correctly substituted in the Breit-Rabi equation, yield a hyperfine splitting $\Delta\nu = 3684.3 \pm 0.5$ Mc/sec if a positive nuclear magnetic moment is assumed, and $\Delta\nu = 3695 \pm 0.5$ Mc/sec if this magnetic moment is taken to be negative.

The direct hyperfine transition in Cs^{134m} has been observed at 3684.5 ± 0.5 Mc/sec in an atomic beam experiment at this laboratory. The previous data and the present measurement are consistent only with the assumption of a positive nuclear magnetic moment.

Details will be published in a paper to be submitted in the near future.

[1] V. W. Cohen and D. A. Gilbert, Phys. Rev. **95**, 569 (1954).
[2] L. S. Goodman and S. Wexler, Phys. Rev. **95**, 570 (1954).

Nuclear Hyperfine Structure Interaction in 3.1-hr Cs^{134m}*

D. A. GILBERT AND VICTOR W. COHEN
Brookhaven National Laboratory, Upton, New York
(Received November 19, 1954)

WE have performed a magnetic resonance atomic beam experiment[1,2] on 3.1-hr Cs^{134m} to observe the transitions $\Delta F=\pm 1$. In a magnetic field in the neighborhood of 1 gauss the spectrum was split into many components. The central π component $(17/2, +1/2 \rightleftarrows 15/2, -1/2)$ and $(17/2, -1/2 \rightleftarrows 15/2, +1/2)$ is field-independent and extremely narrow compared to the others. The frequency of the center of this line is equal to $\Delta W/h$, where ΔW is the hyperfine structure interaction energy. We observe this line at several values of the magnetic field. It had a width of approximately 100 kc/sec and a center at 3684.594 Mc/sec. The principal limitation on the accuracy was noise modulation on the 2K42 Klystron used as a source. The results of four runs at differing magnetic fields gave a total spread in peak frequency of about 15 kc/sec. In view of this we feel that ± 20 kc/sec is a conservative estimate of error. This result, combined with that computed from reference 1,[3] serves to confirm the assumption of a positive sign for the nuclear magnetic moment.

The high precision in the determination of ΔW will be of interest for possible study of hyperfine structure anomaly in the 2.3-yr and the 3.1-hr states of Cs^{134}. Work toward this objective is in progress.

* Work performed under the auspices of the U. S. Atomic Energy Commission.
[1] V. W. Cohen and D. A. Gilbert, Phys. Rev. **95**, 569 (1954).
[2] L. Goodman and S. Wexler, Phys. Rev. **95**, 570 (1954).
[3] In computing data of reference 1 an error was made in the sign of g_I. A recomputation gives 3684.2 ± 0.6 Mc/sec.

Deuteron Stripping and the Problem of Nuclear Radii

L. N. COOPER* AND W. TOBOCMAN
Institute for Advanced Study, Princeton, New Jersey
(Received November 16, 1954)

RECENT experiments on high-energy electron scattering[1] and on the transition energies of mu mesonic atoms[2] have been interpreted[3,4] as indicating that the charged matter inside the nucleus is confined approximately within a sphere of radius $R \simeq 1.2 \times A^{\frac{1}{3}} \times 10^{-13}$ cm or smaller. On the other hand, experiments like those on 90-Mev neutron scattering[5,6] or inelastic collision cross sections[7,8] (which are sensitive to the distribution of nuclear matter as distinguished from charged matter) seem to indicate that the nuclear matter is not confined to such a small volume. Such results have suggested the possibility that protons occupy a smaller volume than neutrons in the nucleus, and an attempt to justify such a hypothesis has recently been published.[9]

The purpose of this note is to point out that the measurement of cross sections for deuteron stripping (or pick-up) reactions can provide a direct experimental measurement of the difference in the probability for finding a proton or a neutron at the surface of a nucleus. These cross sections are in fact just proportional to the probability for finding the stripped-off (picked-up) particle at the surface of the residual (target) nucleus.[10] Thus, for example, if one measured the cross sections for (d,p) and (d,n) reactions leading to similar residual nuclei, one could calculate the reduced width (which is proportional to the probability for finding the particle at the nuclear surface) for the last proton or the last neutron of each residual nucleus. If the protons are indeed confined to a smaller volume than the neutrons, one should find the proton reduced widths characteristically smaller than the neutron reduced widths.

Such an effect apparently has been noted in one case by Fujimoto, Kikuchi, and Yoshida.[11] They calculated the reduced widths for three corresponding levels in the mirror nuclei Mg^{25} and Al^{25} from measurements made on the $Mg^{24}(d,p)Mg^{25}$ and $Mg^{24}(d,n)Al^{25}$ reactions. The reduced widths for Mg^{25} were found to be about 10 times greater than the reduced widths for Al^{25}. This discrepancy appears to be too great to be accounted for by the fact that these workers neglected the Coulomb interaction and the interaction of the liberated particle with residual nucleus in their calculations.

Rough estimates of the dependence of the reduced widths on the distributions of protons and neutrons show that the ratio of reduced widths, γ_p/γ_n, is quite sensitive to differences in the distributions. If one chooses a uniform neutron density to a radius of $R=1.4A^{\frac{1}{3}}\times 10^{-13}$ cm, and a proton density with a rms value $\langle r^2\rangle^{\frac{1}{2}}=1.0A^{\frac{1}{3}}\times 10^{-13}$ cm (equivalent to a uniform density to $R=1.2A^{\frac{1}{3}}\times 10^{-13}$ cm), then choosing various shapes for the proton density results in values of γ_p/γ_n of the order of $\frac{1}{6}$, independent of A (assuming the shape to be independent of A). Thus if such a difference in distributions were the explanation of the experimental results cited above, it should easily be detected by a comparison of corresponding (d,p) and (d,n) cross sections.

The mirror nuclei are particularly well suited for the measurements suggested above because it is to be expected that the other factors affecting the reduced widths would be the same. For example, one might compare reduced widths calculated from measurements of the cross sections for the $Ca^{40}(d,p)Ca^{41}$ and $Ca^{40}(d,n)Sc^{41}$ reactions. These two reactions are (excluding Coulomb effects) symmetrical with respect to the roles played by protons and neutrons. Since at the relevant energies the Coulomb interaction can be taken into account[10] in calculating the reduced widths, a discrepancy in the reduced widths from two such reactions [especially at the higher energies where the Coulomb

effects diminish] would indicate that the neutron and proton distributions were not identical. This in the case of mirror nuclei would be quite surprising.

Heavier nuclei are also of great interest because it is for them that the experiments which have suggested distribution differences are most reliable. It is not possible, however, to get complete symmetry between protons and neutrons once one leaves the region of the mirror nuclei. Instead one can choose cases in which neutron and proton shells are completed in the respective residual nuclei. These are advantageous because factors other than distribution differences which might influence the reduced widths are minimized, while at the same time the possibility of separating the ground state level from other levels so that a measurement can be made is enhanced. An example would be $Tl^{205}(d,n)Pb^{206}$ and $Pb^{207}(d,p)Pb^{208}$.

Note added in proof.—Our attention has been called to related experimental and theoretical work on pickup processes by W. N. Hess and B. J. Moyer, Phys. Rev. **96**, 859 (A) (1954); and W. N. Hess, thesis, University of California Radiation Laboratory Report UCRL-2670, 1954 (unpublished).

* National Science Foundation Post-Doctoral Fellow.

[1] Hofstadter, Fechter, and McIntyre, Phys. Rev. **92**, 978 (1953); Hofstadter, Hahn, Knudsen, and McIntyre, Phys. Rev. **95**, 512 (1954); Pidd, Hammer, and Raka, Phys. Rev. **92**, 436 (1953).
[2] V. L. Fitch and J. Rainwater, Phys. Rev. **92**, 789 (1953).
[3] L. I. Schiff, Phys. Rev. **92**, 988 (1953); Yennie, Ravenhall, and Wilson, Phys. Rev. **95**, 500 (1954).
[4] L. N. Cooper and E. M. Henley, Phys. Rev. **92**, 801 (1953).
[5] Cook, Macmillan, Peterson, and Sewell, Phys. Rev. **75**, 7 (1949).
[6] Fernbach, Serber, and Taylor, Phys. Rev. **75**, 1352 (1949).
[7] Millburn, Birnbaum, Crandall, and Schecter, Phys. Rev. **95**, 1268 (1954); (see also for other references).
[8] W. Heckrotte, Phys. Rev. **95**, 1279 (1954).
[9] M. H. Johnson and E. Teller, Phys. Rev. **93**, 357 (1954).
[10] W. Tobocman, Phys. Rev. **94**, 1655 (1954).
[11] Fujimoto, Kikuchi, and Yoshida, Progr. Theoret. Phys. (Japan) **11**, 264 (1954).

Angular Correlation Effects in Unstable Particle Decay*

S. B. Treiman, Geo. T. Reynolds, and A. L. Hodson
Palmer Physical Laboratory, Princeton University, Princeton, New Jersey
(Received November 2, 1954)

ONE line of approach in the attempt to reconcile the long lifetimes and copious production of the new unstable particles is to suppose that the particles have high spin angular momentum.[1] This view is beset with grave difficulties, but the assumption of large spin does lead to testable consequences. In particular one might expect to find strong angular correlation effects in both the production and decay processes of the high spin particles.

There is some preliminary evidence, from Brookhaven[2] as well as from cosmic-ray experiments,[3] that Λ^0 particles are produced in states of high orbital angular momentum. This is by no means conclusive proof of high spin, but it is suggestive. The purpose of the present note is to discuss an experimental method which can provide a lower-limit estimate of the spins of unstable particles which undergo two-body decay. This consists in searching for angular correlation effects in the decay processes. Quite aside from the question of whether the assumption of large spin will ultimately prove adequate to account for their metastability, it is of course a matter of considerable interest to determine the spins of the new unstable particles. Preliminary evidence reported in the following letter[4] indicates that there may be at least one species of V^0 particle which has spin greater than one-half.

Consider a particle which undergoes two-body decay. The normal to the decay plane, $\mathbf{n}$, must be perpendicular to the line of flight of the unstable particle. Let $\mathbf{N}$ be some reference vector which is normal to the line of flight and which is defined independently of the decay normal $\mathbf{n}$. For example, in the case of single V^0-particle events, one may define $\mathbf{N}$ as the normal to the plane containing the line of flight of the primary particle which produces the nuclear interaction and the line of flight of the emerging V^0 particle. In events where two unstable particles come from a common nuclear interaction, an alternate choice for $\mathbf{N}$ would be the normal to the plane containing the two unstable particles. (It is events of this kind which are discussed in the following letter.)

In either case, if the unstable particle decays isotropically in its rest frame, the angle η between $\mathbf{n}$ and $\mathbf{N}$ should take on all possible values with uniform probability. Now spin zero and spin one-half particles must in fact decay isotropically, for reasons of parity and angular momentum conservation. Thus, any statistically significant departure from a uniform distribution in η for a series of decay events would immediately imply spin greater than one-half. The converse, however, is not necessarily true: a uniform distribution in η does not rule out spin greater than one-half, since the spins may be randomly oriented with respect to the reference vector $\mathbf{N}$.

The most general form of the angular distribution in the case of a particle of spin S which undergoes two-body decay can easily be obtained by the methods of Wolfenstein.[5] In the rest system of the unstable particle, the final state wave function ψ has definite parity and is an eigenfunction of angular momentum corresponding to eigenvalue S. The outgoing intensity $|\psi|^2$ must therefore transform under rotations as a sum of spherical harmonics of even parity. After one sums over final spin states, the spherical harmonic of maximum degree which can appear in the expression for the outgoing intensity is either $2S$ or $2S-1$ (according as S is integer or half-odd integer).[5]

The angular distribution in the rest frame of the unstable particle is therefore

$$I(\theta,\varphi)=\sum_{L=0}^{L_{\max}}\sum_{M=-L}^{L}C_L{}^M Y_L{}^M(\theta,\varphi),$$

$$L_{\max}=\begin{cases}2S \text{ (integral } S)\\ 2S-1 \text{ (half-odd integral } S),\end{cases}$$

where L can take on only even values. Suppose that the unstable particle travels along the z axis in the laboratory system; and suppose the y axis is chosen along the direction of the reference vector **N**. Then the azimuthal angle φ is just equal to the angle η between **N** and the normal to the decay plane, **n**. The most general form of the probability distribution in η is therefore given by

$$p(\eta)=\int I(\theta,\eta)\sin\theta d\theta$$

$$=\sum_{M=0,2,\ldots}^{L_{\max}}(A_M\cos M\eta+B_M\sin M\eta).$$

A lower limit on S can thus be obtained by determining the largest value of M required to fit the decay data for a series of events. (This is only a lower limit because some of the coefficients in the above expression may vanish; for randomly oriented spins, for example, only A_0 will be nonzero.)

* This work was supported by the U. S. Office of Naval Research and the Atomic Energy Commission.

[1] An excellent summary of theoretical views on the unstable particles, by M. Gell-Mann and A. Pais, will appear in the Proceedings of the International Physics Conference, Glasgow, July 1954.

[2] Fowler, Shutt, Thorndike, and Whittemore, Phys. Rev. **93**, 861 (1954).

[3] G. T. Reynolds and S. B. Treiman, Phys. Rev. **94**, 207 (1954).

[4] Ballam, Hodson, Martin, Rau, Reynolds, and Treiman, following Letter [Phys. Rev. **97**, 245 (1954)].

[5] L. Wolfenstein, Phys. Rev. **75**, 1664 (1949).

Orientation of Planes in Double V^0 Decay Events*

J. Ballam, A. L. Hodson, W. Martin, R. Ronald Rau, Geo. T. Reynolds, and S. B. Treiman
Palmer Physical Laboratory, Princeton University, Princeton, New Jersey

(Received November 2, 1954)

In a set of 30 000 photographs taken of a Wilson cloud chamber operated in a magnetic field,[1] seven events have been found in which a pair of V^0 particles appear to come from a common origin.[2] These have been analyzed for possible angular correlations between the decay planes, as discussed in the preceding letter.[3]

The illuminated region of the chamber has average dimensions 16 in.×16 in. ×5 in. A stereo camera with lens separation of 17° takes two photographs of each event. The spatial geometry of each event is reconstructed by projecting the two views onto a screen through an optical system identical with that used to photograph the chamber. The space coordinates of a particular point on a track are determined by moving the projector parallel to the optic axis of the lenses, until the point appears stationary on the screen when the two views are projected in rapid succession. The screen-projector distance measures the z coordinate of the point (a correction is made for chamber expansion); and the location on the screen determines the x and y coordinates. This procedure is repeated for many points along each relevant track, so that a spatial reconstruction of the entire event is obtained. An alternate procedure, which determines directly the orientation of the decay planes, consists in tilting the screen until the images of both decay tracks of a particular V^0 event appear stationary when the two stereo views are projected in rapid succession. This procedure is less accurate than the one described above, but in every case the two methods agreed to within a few degrees.

In each event a search was made for all possible origins of the two V^0 particles. We assume that the V^0 particles undergo two-body decay, so that the origin for a given V^0 must lie in its decay plane and the line connecting the origin with the decay point must pass

Table I. Summary of geometrical data for ten V^0-particle pairs. δ is angle of noncoplanarity with assumed origin. θ_1 is angle between lines of flight of $V_a{}^0$ and $V_b{}^0$. θ_2 is angle between decay planes of $V_a{}^0$ and $V_b{}^0$. η is angle between decay plane and plane containing lines of flight of $V_a{}^0$ and $V_b{}^0$. The last column gives the identification.

Event	V^0	δ	θ_1	θ_2	η	Ident.
26–5946	a	1.4°	36.6°	76.6°	14.8± 4°	···
	b	2.1			88.5± 5	···
56–240	a	2.7	31.8	78.5	16.0±11	···
	b	3.7			62.6±10	···
69–210	a	0.6	43.8	45.2	29.0± 3	···
	b	2.1			63.7± 3	θ^0
73–29	a	0.5	20.6	62.2	25.3± 5	Λ^0
	b	0.8			85.8± 5	θ^0
95–622	a	1.3	41.4	72.5	39.8± 3	θ^0
	b	0.4			78.3± 4	θ^0
126B–30034	a	0.7	3.1	44.8	4.4± 3	···
	b	0.2			40.0± 3	···
146B–40761	a	0.1	14.5	88.0	17.0± 3	···
	b	0.4			72.4± 4	···
Brookhaven	a				27 ±10	Λ^0
	b				70 ± 5	θ^0
Brookhaven	a				18 ± 7	Λ^0
	b				60 ± 6	θ^0
Thompson *et al.*	a				10.6	θ^0
	b				26.5	Λ^0

between the two decay tracks. Evidently, we can only locate origins which give rise to more than one charged particle passing into the illuminated region of the chamber. In each of the seven V^0 pair events, however, there was one, and only one, such origin for each decay plane and this origin was in fact common to both planes. This suggests that in each event the two V^0 particles indeed came from a common origin, which we had correctly located.

The results of the analysis are summarized in Table I. The angle of "noncoplanarity," δ, is the angle between the line of flight of the V^0 particle and the decay plane. Within the experimental errors, the assumed origin in each case lies in the decay plane. It is the angle η between the decay plane and the plane containing the lines of flight of the two V^0 particles that is of particular interest. By convention, $\eta_a < \eta_b$. Normals are chosen so that $\eta \leq 90°$. The errors in η arise mainly from the uncertainties in the precise location of the origin. Table I also includes two V^0-pair events obtained by the Brookhaven group[4] and one event obtained by Thompson *et al.*[5]

In Fig. 1 each event is represented by a point in the $\eta_a - \eta_b$ plane. Since $\eta_a < \eta_b$, the points are constrained to lie to the right of the 45° line. As discussed in the preceding letter, if both of the V^0 particles involved in each event have spin less than one, the points should be uniformly distributed over the plane to the right of the 45° line. Although only 10 events are represented in the figure and the statistics are correspondingly poor, there appears to be a significant clustering of points in the region of small η_a, large η_b. We can think of no bias in our experimental procedure which would tend to distort the true distribution.

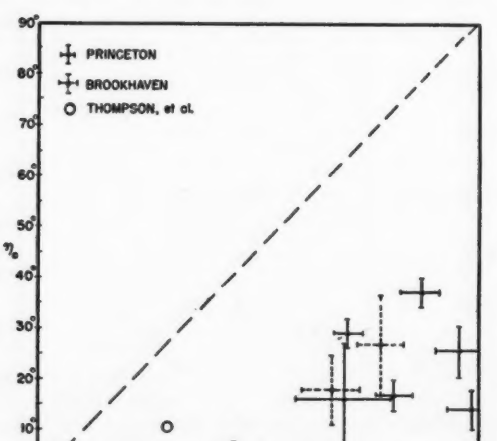

FIG. 1. Distribution of events in the $\eta_a - \eta_b$ plane for ten V^0-particle pairs; η is the angle between the decay plane of an individual V^0 particle and the plane containing the lines of flight of the two V^0 particles of the pair. The subscripts a and b distinguish the two V^0 particles and have been chosen in such a way that $\eta_a < \eta_b$.

Insofar as this apparently nonuniform distribution is accepted as statistically significant, we can conclude that at least one type of V^0 particle involved in our sample has spin greater than one-half.

Unfortunately, identification of the V^0 particles could be made in only a few cases—and then only on the basis of angles and ionizations, assuming that we are dealing only with a mixture of $\Lambda^0 \rightarrow p + \pi^- + 37$ Mev and $\theta^0 \rightarrow \pi^+ + \pi^- + 214$ Mev. Thus, the statement that a certain particle is a θ^0 means that on the basis of angles and ionizations the event is consistent with θ^0 and inconsistent with Λ^0. Event 95–622, which appears to involve a pair of θ^0-particles, has been described elsewhere.[6]

There is of course no way to determine in our events whether the two V^0 particles are produced in a single elementary act or in two separate interactions. The very existence of correlation effects, however, would seem to favor the first possibility.

* This work was supported by the U. S. Office of Naval Research and the Atomic Energy Commission.

[1] Hodson, Ballam, Arnold, Harris, Rau, Reynolds, and Treiman, Phys. Rev. **96**, 1089 (1954).

[2] The same set of photographs gave about 250 single V^0 events, 60 V^+ events, and several additional V^0 pairs; the latter were not accepted for the present analysis, however, because it was not possible to determine reliably whether the two V^0 particles came from a common origin.

[3] Treiman, Reynolds, and Hodson, preceding Letter [Phys. Rev. **97**, 244 (1954)].

[4] Fowler, Shutt, Thorndike, and Whittemore, Phys. Rev. **93**, 961 (1954).

[5] Thompson, Burwell, Huggett, and Karzmark, Phys. Rev. **95**, 1576 (1954).

[6] D. R. Harris and A. L. Hodson, Phys. **95**, 661 (1954).

Spectrometry of Recoils from Neutrino Emission in Argon-37

ARTHUR H. SNELL AND FRANCES PLEASONTON
Oak Ridge National Laboratory, Oak Ridge, Tennessee
(Received October 22, 1954)

AS has been recognized for some time, argon-37 offers unusual advantages for neutrino recoil experimentation in that it is monatomic and gaseous and captures orbital electrons without gamma emission, so that neutrino emission should be the predominant mechanism which could give recoil. The recoils have been observed by Rodeback and Allen[1] through the use of coincidence time-of-flight methods and very recently by Kofoed-Hansen[2] in a parallel-plate, crossed-field spectrometer. The energy of the radioactive transition is known to be 816 kev,[3] from which one would predict a recoil energy of 9.66 ev for the Cl^{37} atoms; the latter are known to be multiply-charged because of the emission of Auger electrons.[4]

We have found that it is possible to examine these low-energy recoils in detail and under high resolution

by means of magnetic and electric deflection spectrometry. The apparatus consists of a conical field-free source volume containing the argon at total pressures (including impurities) of 1 to 3×10^{-5} mm of mercury. A slightly diverging beam of the recoils emerges from the narrow end of this volume and is subjected to momentum or energy analysis by deflection through 96.5 degrees in the magnetic case or 90 degrees in the electric case. Both instruments focus in two directions, the former by using oblique incidence and exit from the magnetic field, and the latter by using sectors of spherical plates. The source volume is insulated from the deflection chamber in both instruments, so that a small pre-deflection acceleration can be applied if desired. Post-deflection acceleration of 5 kilovolts is applied to enable detection of the ions by means of an electron multiplier. Strong differential pumping is necessary to forestall an overwhelming background from radioactive gas that otherwise would move to the region of the detector.

In magnetic deflection the peaks attributable to ions of e/m values 2/37, 3/37, and 4/37 have been observed. They are completely resolved, and the charge 2 and charge 4 peaks are about half as intense as the charge 3 peak. Charge 1 and charge 5 peaks have not yet been observed in magnetic deflection. The positions of the peaks indicate a recoil energy of 10 ± 1 ev.

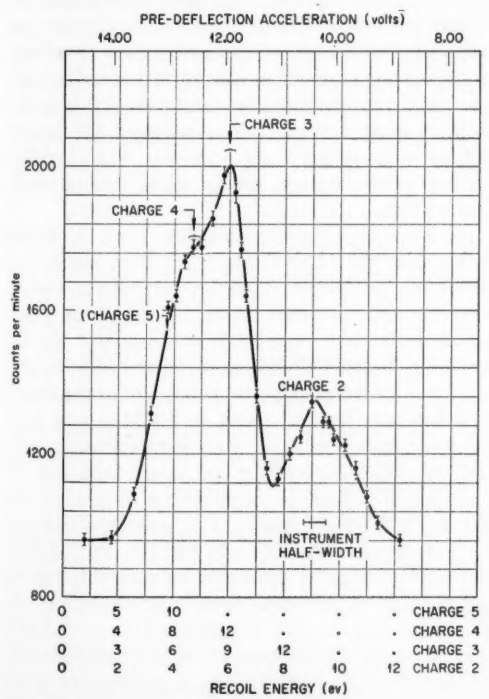

FIG. 1. Electric deflection of multiply-charged chlorine-37 recoil ions. Pre-deflection acceleration (top scale) chosen to favor observation of the charge 2 peak. Potential on deflecting plates + and −4.444 volts with respect to ground. The recoil energy scales (bottom) vary with the ionic charge. The transmission half-width of the instrument is small compared with the natural width of the charge 2 peak. Background has not been subtracted from the ordinate scale. Because of the multiple abscissa scale, the data are presented as counts per minute rather than counts per minute per unit energy interval.

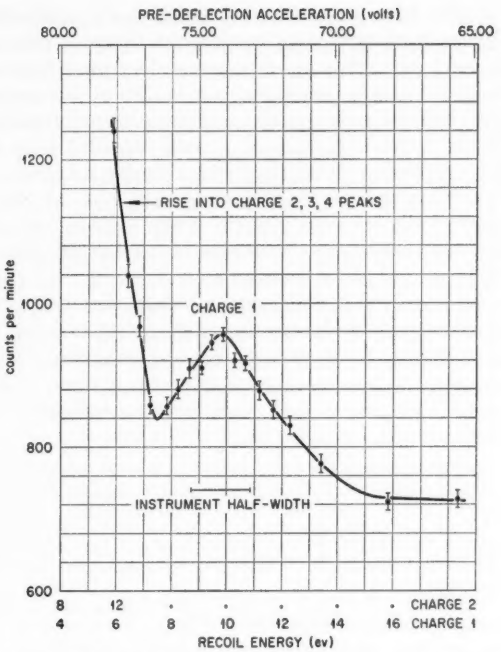

FIG. 2. Electric deflection of singly-charged chlorine-37 recoil ions. Potential on deflecting plates + and −25.00 volts with respect to ground. The limits of error indicated in both figures refer to the 50 percent probability interval.

Some of the results of the electric deflection are presented in the accompanying figures. In obtaining these data the potentials of the deflecting plates were maintained constant, symmetrically positive and negative with respect to ground, and the pre-deflection acceleration was varied in passing over the spectrum. The data of Fig. 1 were obtained with a view toward studying the structure of the charge 2 peak. The complex of charge 3, 4, and 5 peaks is in principle not resolvable with this instrument because of the large natural width of the lines. It will be noticed that the charge 2 peak has a half-value width of about 2.4 ev on the recoil energy scale; this is close to the width to be expected from thermal motion plus recoil from emission of one 2400-ev Auger electron, as indicated by a computation performed for us on a random walk basis by Prof. J. M. Jauch.

The recoil energy indicated in Fig. 1 by the positions of the charge 2 and 3 peaks is close to 9.0 ev. Considerably better opportunity for accurate measurement of this energy is offered by the singly-charged ions because the charge 1 peak remains resolved from the others up to predeflection accelerations of 70 or 80 volts, and under these conditions small perturbing effects such as stray magnetic fields, contact potentials, and surface

charging have lesser effect. (Indeed, one is compelled toward these conditions because the charge 1 peak is so weak that it has to be compressed by pre-deflection acceleration into the transmission width of the instrument before it can be made to stand above background.) Figure 2 shows the charge 1 peak observed with 75 volts applied to the source volume. The peak appears at 9.8 ± 0.2 ev on the recoil energy scale, but the recoil energy scale is itself uncertain within ±0.5 ev because of a small uncertainty in the present value of the calibration constant of the spectrometer.

In summary, the observations show that the recoil ions are of mass 37, have an energy spread that can be accounted for by thermal motion and recoil from Auger electron emission, and possess an energy of recoil within about 7 percent of that predicted from emission of a single neutrino with an energy of 816 kev.

[1] G. W. Rodeback and J. S. Allen, Phys. Rev. **86**, 446 (1952).
[2] We are indebted to Prof. Kofoed-Hansen for communicating his results to us during the course of our investigation.
[3] Richards, Smith, and Browne, Phys. Rev. **80**, 524 (1952); Schoenfeld, Duborg, Preston, and Goodman, Phys. Rev. **85**, 873 (1952); Emmerich, Singer, and Kurbatov, Phys. Rev. **94**, 113 (1954).
[4] S. Wexler, Phys. Rev. **93**, 182 (1954); M. S. Perlman and J. A. Miskel, Phys. Rev. **91**, 899 (1953).

Isomerism in Al^{26}*

R. W. Kavanagh, W. R. Mills, and R. Sherr†
Kellogg Radiation Laboratory, California Institute of Technology, Pasadena, California
(Received November 16, 1954)

It has been suggested that the 6.7-second state of Al^{26}, which exhibits a superallowed transition to Mg^{26}, might not be the ground state.[1] Perhaps the most direct evidence for this contention comes from comparison of the mass of Al^{26} (mass of Al^{26} − mass of $Mg^{26}=4.00\pm0.03$ Mev) as determined from nuclear reaction Q-values[2] and the β-decay energy $E_\beta+2m_0c^2=4.2\pm0.1$ Mev.[3] Also suggestive are the facts that the neutron yield of the reaction $Al^{27}(\gamma,n)Al^{26}$ is three times the positron yield,[3,4] and that the ratio of γ-ray yield to positron yield observed in $Mg^{25}(p,\gamma)$ varies with bombarding energy.[5] In the present work we have confirmed the latter observation and, by a new measurement of the β-decay energy and of γ-ray spectra, established the location of the 6.7-second state.

The yield of positrons and γ-rays from a 10-kev target[6] of Mg^{25} as a function of proton energy is shown in Fig. 1. To obtain these data an end-window β counter and a thick-walled γ counter were placed near the target and the beam was interrupted at a rate of 60 cps; the γ counter counted continuously but the β counter recorded only when the beam was off the target. If the γ counter had a linear efficiency-*vs*-energy response, its counting rate would be proportional to the capture cross section regardless of the mode of decay of the compound level. Since a thick-walled γ counter approximates this condition fairly well,[7] the γ yield of Fig. 1 can be taken to represent to a good approximation the capture cross section, while the positron yield is proportional to the number of captures which terminate in the 6.7-second state. The wide variation of the ratio of the two curves suggest that a varying fraction of the captures must terminate in a state of Al^{26} having a half-life much longer than 7 seconds. For example, at 958-kev proton energy, nearly all of the captures go to this state.

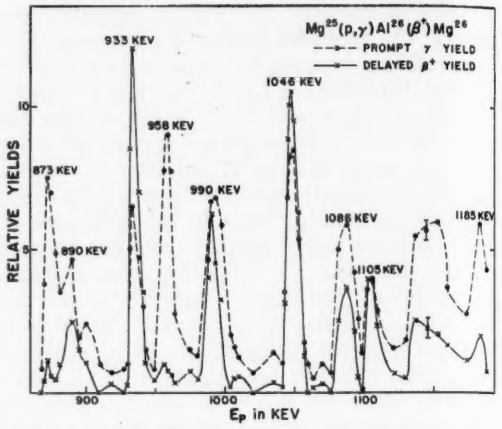

FIG. 1. Yield of prompt γ rays in a thick-walled counter compared to the yield of delayed positrons in an end-window counter, as a function of the energy of protons bombarding a 10-kev Mg^{25} target.

An 8-mg/cm² $Mg^{25}O$ target on 1-mil Al backing, placed with the MgO facing the proton beam from a 3-Mev electrostatic accelerator, was bombarded in a magnetic lens spectrometer to determine the positron spectrum. The beam was again interrupted at the 60-cps rate with positron detection permitted only while the beam was off the target. The Kurie plot of the resulting spectrum was straight down to 1.5 Mev and had an end-point energy of 3.20 ± 0.05 Mev, including a 0.02-Mev correction for backing and target thickness. With a half-life of 6.68 ± 0.11 seconds,[8] the ft-value is 3120 ± 290 seconds, in agreement with other measurements for $0\rightarrow0$ transitions: 3275 ± 75 for O^{14}, and 3220 ± 200 for Cl^{34}.[10,11] From the difference between this end-point and Q-values from other work,[2] the excitation of the 6.7-second state in Al^{26} is calculated to be 0.22 ± 0.06 Mev; a recent determination[12] of the threshold of the reaction $Mg^{26}(p,n)Al^{26}$, giving a preliminary Q-value of 4.886 ± 0.010 Mev, leads to the value 0.12 ± 0.06 Mev. This confirms that the positron-emitting state is not the ground state.

Gamma-ray spectra at a number of resonances have been examined with a crystal spectrometer, using 4 in.×4 in. and 1½ in.×1½ in. NaI crystals, with the following results. At the 958-kev resonance, where the positron yield is low, γ rays are observed having energies

0.416±0.004, 0.511 (weak), 1.67±0.02, 2.08±0.02, and 5.23±0.05 Mev, with no others of comparable intensity. The 0.416- and 1.67-Mev γ rays are in coincidence (within the resolving time of 4 μsec), while the 0.416- and 2.08-Mev γ rays are not. The 0.416- and 1.67-Mev γ ray intensities are about equal and twice that of the 2.08-Mev γ ray. These γ-ray energies fit well into the level scheme of Browne,[13] and the short half-life of the 0.416-Mev transition verifies his conclusion that the 0.418-Mev level is not the 6.7-second positron-emitting state. The 0.416-Mev γ ray was also observed in varying intensity ratio to the annihilation radiation, at 697-, 730-, 990-, 1046-, and 1086-kev bombarding energy.

At 730-kev proton energy, where the positron yield is relatively high, the 0.416-Mev and 0.511-Mev γ rays have about the same intensity. There also appear several new γ rays: three in prompt coincidence with energies 0.833± 0.006, 1.022±0.006, and 5.00±0.05 Mev, and two, not checked for coincidence, with energies 1.44±0.03 and 2.46±0.03 Mev. The last two may account for the fact that the 0.833-Mev γ ray is about 50 percent more intense than the 1.022-Mev γ ray. (For example, a level in Al^{26} at 3.51 Mev would be consistent with these and the considerations below.) The 0.833- and 1.022-Mev γ rays were also found with similar intensity ratios at proton energies of 730, 933, 990, 1046, and 1086 kev.

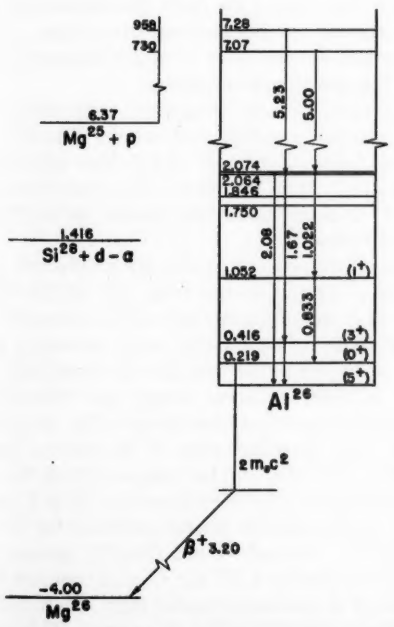

FIG. 2. Energy levels of Al^{26}. The spins indicated form a set consistent with the experimental data and the shell model. Levels below 2.1 Mev other than those at 0.219 and 2.074 Mev are those given in reference 13.

The 1185-kev resonance reveals only a 0.588±0.005-Mev γ ray, other γ rays having less than about one percent of its intensity: the resonance is therefore attributed to $Mg^{25}(p,p')$ terminating in the known first excited state[14] of Mg^{25}. The peak at 873 kev in Fig. 1 is attributed chiefly to F^{19} contamination.

The γ- and β-ray data suggest that the 1.67- and 2.08-Mev γ rays branch from the 2.064-Mev level previously reported[13] from the reaction $Si^{28}(d,\alpha)Al^{26}$, and that the 0.833- and 1.022-Mev γ rays originate from the reported 1.052-Mev level and a new level at 2.074 ±0.013 Mev, respectively. Regarding the latter as the second $T=1$ state with spin 2^+, which would not be expected to show up in the reaction $Si^{28}(d,\alpha)Al^{26}$, would not be inconsistent with the observed γ-ray data, and is suggested as the expected analogue of the 1.83-Mev level in Mg^{26}. The 0.833-Mev γ-ray assignment places the isomeric level at 0.219±0.013 Mev, in close agreement with the expected location of the analogue of the Mg^{26} ground state.

Assuming the shell model and jj-coupling for the odd $d^{5/2}$ neutron and proton requires that the states with $J=0$, 2, and 4 have isotopic spin $T=1$, and the states with $J=1$, 3, and 5 have $T=0$. An assignment of spins to the levels of Al^{26} (taking even parity) consistent with the observations is shown in Fig. 2. $J=5$ is taken for the ground state because of the absence of 1.83-Mev delayed γ-radiation in a thick $Mg^{25}O$ sample irradiated for three hours in a $\frac{3}{4}$-μa beam of 1.5-Mev protons.[15] If the ground state had $J=3$, an allowed 1.2-Mev positron transition to the first excited state of Mg^{26}, followed by a 1.83-Mev γ ray, would be expected, with a half-life of several minutes to several hours. A calculated half-life of about 5×10^4 years results for this transition if $J=5$ and log ft is taken to be 13.

We are grateful to C. A. Barnes, R. F. Christy, T. Lauritsen, and S. A. Moszkowski for helpful discussions.

* Assisted by the joint program of the U. S. Office of Naval Research and the U. S. Atomic Energy Commission.

† Present address: Physics Department, Princeton University, Princeton, New Jersey.

[1] S. A. Moszkowski and D. C. Peaslee, Phys. Rev. **93**, 455 (1954).

[2] Using the Q-values from the following reactions: $Mg^{25}(d,p)Mg^{26}$: Van Patter, Sperduto, Endt, Buechner, and Enge, Phys. Rev. **85**, 142 (1952); $Mg^{24}(d,p)Mg^{25}$: D. M. Van Patter *et al.*, Phys. Rev. **85**, 142 (1952); $Al^{27}(p,\alpha)Mg^{24}$: Donahue, Jones, McEllistrem, and Richards, Phys. Rev. **89**, 824 (1953); $Si^{29}(d,\alpha)Al^{27}$: D. M. Van Patter *et al.*, Phys. Rev. **85**, 142 (1952); $Si^{29}(n,\gamma)Si^{29}$: B. B. Kinsey and G. A. Bartholomew, Can. J. Research **31**, 537 (1953); $Si^{28}(d,\alpha)Al^{26}$: C. P. Browne, Phys. Rev. **95**, 860 (1954).

[3] Haslam, Roberts, and Robb, Can. J. Phys. **32**, 361 (1954).

[4] Montalbetti, Katz, and Goldemberg, Phys. Rev. **91**, 659 (1953).

[5] Kluyver, van der Leun, and Endt, Phys. Rev. **94**, 1795 (1954).

[6] Russell, Taylor, and Cooper, Rev. Sci. Instr. **23**, 764 (1952), describe target preparation method. Isotopic material supplied by Oak Ridge.

[7] See, e. g., Fowler, Lauritsen, and Lauritsen, Revs. Modern Phys. **20**, 236 (1948).

[8] Hunt, Jones, Churchill, and Hancock, Proc. Phys. Soc. (London) **67**, 443 (1954).

[9] J. B. Gerhart, Phys. Rev. **95**, 288 (1954).

[10] D. Green and J. R. Richardson, Phys. Rev. **96**, 858 (1954).

[11] P. Stähelin, Helv. Phys. Acta, **26**, 691 (1953).
[12] Kington, Bair, and Willard (private communication).
[13] C. P. Browne, Phys. Rev. **95**, 860 (1954).
[14] Endt, Enge, Haffner, and Buechner, Phys. Rev. **87**, 27 (1952).
[15] Simanton, Rightmire, Long, and Kohman, Phys. Rev. **96**, 1711 (1954), have successfully isolated long-lived aluminum ($T_{\frac{1}{2}}$ estimated to be about 10^6 years) from a deuteron bombardment of natural magnesium.

Slowing Down of Polarized Protons*

E. Heiberg, U. Kruse, J. Marshall, L. Marshall, and F. Solmitz
Institute for Nuclear Studies, The University of Chicago, Chicago, Illinois
(Received October 20, 1954)

SEVERAL mechanisms for depolarization of protons as they are slowed down in matter have been discussed by Wolfenstein,[1] who concludes that these are ineffective. Furthermore the additional depolarizing processes which we have been able to think of do not promise to be larger. Nevertheless an experimental knowledge of depolarization effects is necessary in the interpretation of many experiments. To this end we have degraded the energy of a polarized proton beam in several different substances.

A 425-Mev 54 percent polarized proton beam was used, produced by scattering the 435-Mev average energy circulating protons elastically at 14° from a Be target in the cyclotron. The polarization of the external proton beam so produced was determined by measuring the asymmetry of elastic scattering from Be at the same angle. In addition, the asymmetries of elastic scattering at 20° and at 30° were measured in a geometry subsequently used to measure asymmetries for the beam degraded in energy.

Next the beam was degraded to E' in paraffin, in C, in Cu, and in Pb. The asymmetry of elastic scattering of the degraded beam by beryllium was again measured at 20° and at 30°. The geometry was such that no protons scattered by more than 2.2° in the slowing down material could reach the Be. In passing through the 2-inch thick Be scatterer, the mean energy of the beam was still further reduced from E' to E. The emergent energy E was determined by range measurement in Cu.

TABLE I. Proton polarization *versus* energy attenuation.

Average energy of degraded beam Mev	Attenuating material	Percent asymmetry of elastic scattering (thickness of Cu filter given in parentheses) 20°		30°	
425[a]	None	63.2±9.3 48.7±3.7	(5.25 in.) (5 in.)	6.7±9.5	(5.25 in.)
240	15.25 in. CH_2 10 in. C 2.311 in. Cu 2.378 in. Pb	50.0±1.6 50.0±1.8 46.5±2.2 46.8±2.6	(2.25 in.)	13.0± 4.3 11.2± 5.2 −4.8± 5.4 −7.0± 8.5	(2.25 in.)
	10 in. C	57.0±2.8	(2.75 in.)	21.9±13.0	(2.75 in.)
186	12 in. CH_2 + 10 in. C	64 ±8	(1 in.)	33 ± 5	(1 in.)
~115	12 in. CH_2 + 14 in. C	35.8±3.6	($\frac{1}{2}$ in.)	23.3±10.3	($\frac{1}{2}$ in.)

[a] Initial polarization of 425-Mev beam =53.6±1.3 percent.

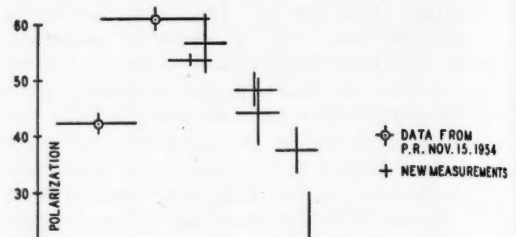

FIG. 1. Polarization of 425-Mev protons effected by elastic scattering on Be plotted as a function of laboratory angle of scattering.

The counter telescopes which measured the scattered protons were provided with copper filters such that quasi-nucleon-scattered protons could not produce a coincidence count. For the filter, that thickness of copper was chosen for which the range curve had dropped to about two thirds of the distance down from the "knee." In Table I are given the effective energy E, the thicknesses of the various attenuators, and the corresponding asymmetries of elastic scattering measured at the two laboratory angles.

In addition we have measured, with considerably better statistical accuracy and angular definition than previously,[2] the polarization of 425-Mev protons scattered elastically from Be and find the dependence shown in Fig. 1. It is similar to that known for Be,[2] C,[3] and He^3 at 310 Mev.

The asymmetries are practically unaffected by degradation of proton energy from 430 to 150 Mev regardless of Z and of nuclear spin of the attenuator. The slight increase in asymmetry with decreasing proton energy we ascribe to the fact that the elastic diffraction pattern is wider at lower energy and therefore the polarization curves (corresponding to Fig. 1) are wider.

In principle the polarization of the protons degraded from 425 to 240 Mev can be computed from the asymmetry measured at 240 Mev shown in Table I, together with the polarization by elastic scattering for Be at 20° and 240 Mev. Instead we use (50±10) percent measured[2] at 310 Mev and 20° for C, and compute for the polarization of protons degraded from 425 to 240 Mev, $P=\frac{1}{2}(50\pm2)/(50\pm10)=50\pm10$ percent. This number we compare with the polarization of 53.6±1.3 percent measured for the 425-Mev beam. One sees that within the error no depolarization has occurred.

Similarly, using the corresponding asymmetry in Table I together with the elastic polarization measured for carbon at 20° and 140 Mev, 78±10 percent,[4] we compute for the polarization of the beam degraded to 186 Mev, $P=\frac{1}{2}(64\pm8)/(78\pm10)=41\pm7$ percent, which is not meaningfully different from the polarization of the 425-Mev beam.

We do not compute polarizations at 30° because at this angle probably equal numbers of elastically and inelastically scattered protons reach the counters.

For the proton beam degraded to ~115 Mev, only protons of energy more than 100 Mev were measured. Range measurement showed that 60 percent of these protons had energy between 100 and 120 Mev, the remainder having somewhat higher energies. We interpret the low measured asymmetry as due to a decreased ability of elastic scattering to polarize below 150 Mev.

This result is anticipated by the elastic scattering asymmetry of 6±2 percent measured[5] near 70 Mev for Be at 20°, and by a decreased polarization observed at Harwell[6] below 140 Mev.

The present results show that for this energy range no small-angle interactions effect depolarization within the accuracy of these measurements.

* Research supported by a joint program of the U. S. Office of Naval Research and the U. S. Atomic Energy Commission.

[1] L. Wolfenstein, Phys. Rev. **75**, 1664 (1949).
[2] de Carvalho, Marshall, and Marshall, Phys. Rev. **96**, 1081 (1954).
[3] Chamberlain, Segrè, Tripp, Wiegand, and Ypsilantis, Phys. Rev. **96**, 807 (1954).
[4] J. M. Dixon and D. C. Salter, Nature **173**, 946 (1954).
[5] Karl Strauch, Bull. Am. Phys. Soc. **29**, No. 7, 19 (1954).
[6] N. F. Ramsey (private communication via U. Kruse).

Proceedings of the American Physical Society

Minutes of the 1954 Fall Meeting of the New England Section at Hanover, New Hampshire, on October 23, 1954

THE New England Section of the American Physical Society held its annual Fall Meeting on Saturday, October 23, 1954, in Wilder Laboratory of Dartmouth College, Hanover, New Hampshire. The morning session was opened with a welcoming address by Dean Donald H. Morrison of the Faculty of Dartmouth College. There followed four invited papers:

"Some Optical Analogues in Microwave Experiments," GORDON F. HULL, *Dartmouth.*

"Optically Induced Polarization of Atoms and Nuclei," ROBERT H. DICKE, *Princeton.*

"Recent Results in Magnetic Analysis of Nuclear Reactions," WILLIAM W. BUECHNER, *M.I.T.*

"Servomechanisms," PHILIPPE E. LECORBEILLER, *Harvard.*

At the business meeting, following lunch, the following officers were elected to serve until the Fall Meeting of 1955:

William W. Watson, Yale University, Chairman
Harold Krauss, University of Connecticut, Vice Chairman
William M. Preston, Harvard University, Secretary-Treasurer
Gerald Holton, Harvard University, Council
Karl Woodcock, Bates College, Council

Following the business meeting, nine contributed papers were presented. The abstracts follow.

W. M. PRESTON
Secretary-Treasurer, New England Section
Harvard University
Cambridge, Massachusetts

1. Physics and Oceanography. F. T. DIETZ, *University of Rhode Island.*—The relatively new science of oceanography has many facets of interest to the physicist. Some contributions of physicists to oceanography are mentioned and certain current problems of interest are presented.

2. Energy Levels from Some (α,n) Type Reactions.* W. T. DOYLE AND A. R. QUINTON, *Yale University.*—Targets of B^{10}, B^{11}, F^{19}, and P^{31} have been bombarded with an 8-Mev cyclotron beam and the energies of the resulting neutron groups measured by means of a proportional counter telescope fitted with a proton radiator and aluminum absorbers. The boron targets give results agreeing with the known level structure for N^{13} and N^{14}. Levels at 0.4, 1.1, 2.2 Mev of excitation are observed in Na^{22} with a ground state Q value of -2.0 Mev. The negative Q value levels have been checked by the threshold method using a BF_3 filled counter. This latter technique yields the result $Q=-5.7$ Mev for the reaction $P^{31}(\alpha,n)Cl^{34}$ and hence the mass value 33.9854 amu for Cl^{34}.

* Supported by the Office of Naval Research.

3. Total Cross Sections for High Energy Neutrons. VAUGHN CULLER AND R. W. WANIEK, *Harvard University.*—The total cross sections for high energy neutrons have been determined for 12 elements (H, D, C, O, Al, Si, Cl, Ti, Fe, Cu, Hg, and Pb) at several energies between 61 and 107 Mev. A discussion of the experimental techniques and a consideration of energy and angular resolution of the scintillation counter telescope employed will be given.

4. Preliminary Results with the Correlation of Meteorological Parameters with Cosmic Ray Neutron Intensities.* J. A. LOCKWOOD AND H. E. YINGST, *University of New Hampshire.*—A study of the effect of variations in such meteorological parameters as barometric pressure, specific humidity, cloud cover, and temperature upon the neutron component of cosmic rays (at ground surfaces) is now being made. Neutron intensity monitors have been established at sea level and at 6290 ft (Mt. Washington). The high energy neutron component is monitored by BF_3 proportional counters embedded in a lead-paraffin pile. Neutrons of energies <0.4 ev are detected by BF_3 tubes in a paraffin telescope which is covered alternately by Sn or Cd shields. The barometric coefficient for lead-paraffin pile is (-9.8 ± 0.3) percent cm Hg^{-1}. A 27-day variation for the high energy component has been found in agreement with results of Fonger and Simpson.[1] The results of the effect of barometric pressure, humidity, cloud cover, and temperature upon the low energy neutrons will be presented.

* Supported by the Geophysical Research Division, Air Force Cambirdge Research Center.
[1] W. H. Fonger, Phys. Rev. 91, 351 (1954).

5. Diode Characteristics of Metal Point Contacts on Vacuum Heated Germanium.* RICHARD B. ALLEN AND H. E. FARNSWORTH, *Brown University.*—A germanium crystal was heated in vacuo in contact only with quartz and graphite. Magnetic controls allowed the catwhisker contact to be made without removing the sample from the vacuum system. Details of the experimental vacuum tube construction are discussed. Heating the sample to above 800°C followed by quick cooling (radiation quenched) to room temperatures nearly destroyed the rectification. Admission of dry air did not restore the rectification. Annealing at lower temperatures partially restored the rectification. The rectification ratio was cycled several times by thermal treatment while maintaining high vacuum conditions. These results differ from those of Esaki who reported a loss of rectification by vacuum heating germanium, but no recovery by vacuum annealing. The low level resistance of semiconductor point contacts is an exponential function of the reciprocal of the absolute temperature. From this function an activation potential may be calculated. Radiation quenching lowered the activation potential while annealing restored it to its previous value. The Schottky diode theory predicts that the activation potential of a metal-semiconductor point contact is dependent on the work function of the metal. Meyerhof reported no

dependence on the metallic work function for measurements made in air.

* This work is sponsored by the International Business Machines Corporation.

6. Imperfections in Germanium Single Crystals. A. SMAKULA, J. KALNAJS, AND V. SILS, *M. I. T.*—It is well-known that germanium shows anomalies in some of its physical properties, such as Hall effect, magnetoresistance, conductivity, and infrared absorption.[1] For an explanation of these anomalies, impurities (or imperfections) of the order of 10^{20} per cm^3 are assumed, which is in contradiction with spectrochemical analysis. In our study of crystal imperfections we determined the lattice constant precisely on four single crystals of highest purity (n-type). Simultaneously, we determined the density accurately by hydrostatic weighing. These densities compared with those computed from the lattice constants show a positive difference of 0.002 to 0.005 g/cm^3. It is assumed that germanium contains interstitial impurities of oxygen or germanium of the order of $10^{19}/cm^3$.

[1] K. Lark-Horovitz, *The New Electronics in the Present State of Physics*, F. S. Brackett, Editor (American Association for the Advancement of Science, Washington, D. C., 1954), pp. 57 to 127.

7. Faraday Effect in a Polycrystalline Ferrite.* DAVID PARK, *Williams College*.—In a polycrystalline mass in which the crystallites are oriented completely at random, the permeability tensor μ is diagonal and no magneto-optical rotation will occur. But if there is a slight degree of alignment, so that the average magnetization $\bar{M}$ is not zero, then μ is no longer diagonal. The off-diagonal components, which are responsible for the Faraday effect,[1] can be shown to be proportional to $\bar{M}$ if $\bar{M}$ is small. In calculating the spectrum of μ it is assumed that the resonant frequencies of the individual crystallites are statistically distributed,[2] and then one can show that the interaction between crystallites does not greatly affect the form of the spectra. If the spectra of the diagonal parts of μ are known, those of the off-diagonal parts can be calculated. Sample curves will be shown and compared with available data.

* This work was supported by the Sprague Electric Company.
[1] C. L. Hogan, Bell System Tech. J. 31, 1 (1952); Revs. Modern Phys. 25, 253 (1953).
[2] D. Park, Phys. Rev. 95, 652 (1954); Phys. Rev. (to be published).

8. A Vectorial Approach to the Principal Equation of Rigid-Body Kinematics. DAN E. CHRISTIE, *Bowdoin College*.—In textbooks on intermediate mechanics the kinematical principle that any instantaneous motion of a rigid body is screw motion is usually deduced quite directly and logically from a special case. This special case asserts that any motion of a rigid body with one point fixed is instantaneously rotation. The justification of this special proposition is not always so direct. Often, for instance, Euler's theorem on finite displacements is proved using spherical geometry, and then an argument about a limiting case is discussed.

It is here suggested that a derivation based on methods more germane to the subject might be preferable. A simple development using vectors is given. In this derivation repeated use is made of the following anticommutative relation: $\mathbf{V}_P \cdot \mathbf{R} = -\mathbf{V}_R \cdot \mathbf{P}$ (for position vectors $\mathbf{P}$ and $\mathbf{R}$ relative to the fixed point as origin, $\mathbf{V}_P$ denoting the velocity vector for the point whose position vector is $\mathbf{P}$, etc.). It is demonstrated that the only velocity pattern consistent with this relation is one of the type given by the formula $\mathbf{V}_R = \boldsymbol{\Omega} \times \mathbf{R}$, and hence that the motion is instantaneously a rotation.

9. Hertz's Abandonment of the Concept of Force in the Logical Clarification of Classical Mechanics. ROBERT S. COHEN, *Wesleyan University*.—In the sixty years since Heinrich Hertz died, philosophical explication of physical theories has been an expanding concern of logicians, philosophers, and physicists. In part, this has taken the form of analysis of terms and concepts, e.g., the debate over proposed requirements of operational definition. In part, this concern for clarity has led to axiomatic and other varieties of logical reconstruction of theories. That relativistic and quantum mechanical notions are not the only sources for such research is perhaps most convincingly shown by the great *Principles of Mechanics* in which Hertz set forth a basic scheme from which the general laws of classical mechanics might be deduced. The heart of his proposal consists in his acute critique of standard usage of the general laws (which, e.g., derives a universally applicable principle such as that of least action on the basis of the assumption of fixed conservative interparticle forces) together with his constructive use of the notions of time, position, and inertia to build a mechanics without forces. What results is a lucid and compact theory with a minimum of physical assumptions and a sparseness of anthropomorphic language; force and energy are purely auxiliary or short-hand concepts. Finally Hertz deliberately formulates certain criteria for those who reconstruct theoretical structures.

MINUTES OF THE 1954 AUTUMN MEETING OF THE NEW YORK STATE SECTION AT BROOKHAVEN NATIONAL LABORATORY, NOVEMBER 12–13, 1954

THE thirty-second meeting of the New York State Section was held at Brookhaven National Laboratory, Upton, Long Island, on November 12 and 13, 1954.

One paper, and the preceding address of welcome by R. A. Patterson, constituted the Friday morning session. Friday afternoon was devoted to three papers on neutron physics, followed by tours of the Brookhaven Reactor Building and the "Hot" Chemistry Laboratory. Friday sessions closed with cocktails and dinner and a lecture by D. H. Menzel on "The Physics of Flying Saucers."

Two papers on Saturday morning preceded a tour of the Cosmotron, which brought the meetings to a close. It is not possible to name all of the many staff members at Brookhaven whose efforts made this meeting a profitable and enjoyable one, but among them, deserving of special mention, are George B. Collins, Chairman of the Cosmotron Department, who took on the responsibility of arranging the program, and Mariette Kuper, Execu-

tive Aide to the Director, whose efficient handling of the many details kept things running smoothly.

Titles of the papers presented at the meeting are as follows:

Physics at Brookhaven National Laboratory. G. N. GLASOE.

Neutron Physics at Brookhaven. D. J. HUGHES.

Neutron Diffraction Experiments. G. H. VINEYARD.

Nuclear Energy as a Source of Power. C. WILLIAMS.

New Unstable Particles. R. K. ADAIR.

Experimental Program Centered around the Cosmotron. L. W. SMITH.

L. W. PHILLIPS, *Secretary*
New York State Section
American Physical Society
The University of Buffalo
Buffalo 14, New York

CONTENTS—*Continued*

Letters to the Editor:

Paramagnetic Resonance in Low Fields . . . . . Georges J. Béné and R. C. Extermann 238

Electron Resonance in Gas Discharges . . . . . D. J. E. Ingram and J. G. Tapley 238

Paramagnetic Resonance Absorption in Graphite Compounds . . . . . B. Smaller, G. R. Hennig, and E. L. Yasaitis 239

InSb Photovoltaic Cell . . . . . G. R. Mitchell, A. E. Goldberg, and S. W. Kurnick 239

Energies of the K Transitions of π^- Mesonic X-Rays . . . . . M. Stearns, M. B. Stearns, S. DeBenedetti, and L. Leipuner 240

Average Number of Neutrons Emitted During the Spontaneous Fission of Cf^{252} . . . . . W. W. T. Crane, G. H. Higgins, and S. G. Thompson 242

Hyperfine Splitting and the Sign of the Magnetic Moment of Cs^{134m} . . . . . L. S. Goodman and S. Wexler 242

Nuclear Hyperfine Structure Interaction in 3.1-hr Cs^{134m} . D. A. Gilbert and Victor W. Cohen 243

Deuteron Stripping and the Problem of Nuclear Radii . . . L. N. Cooper and W. Tobocman 243

Angular Correlation Effects in Unstable Particle Decay . . . . . S. B. Treiman, Geo. T. Reynolds, and A. L. Hodson 244

Orientation of Planes in Double V^0 Decay Events . . . . . J. Ballam, A. L. Hodson, W. Martin, R. Ronald Rau, Geo. T. Reynolds, and S. B. Treiman 245

Spectrometry of Recoils from Neutrino Emission in Argon-37 . . . . . Arthur H. Snell and Frances Pleasonton 246

Isotopism in Al^{26} . . . . . R. W. Kavanagh, W. R. Mills, and R. Sherr 248

Slowing Down of Polarized Protons . . . . . E. Heiberg, U. Kruse, J. Marshall, L. Marshall, and F. Solmitz 250

Proceedings of the American Physical Society:

Minutes of the 1954 Fall Meeting of the New England Section at Hanover, New Hampshire, on October 23, 1954 252

Minutes of the 1954 Autumn Meeting of the New York State Section at Brookhaven National Laboratory, November 12–13, 1954 253

CONTENTS

THE PHYSICAL REVIEW SECOND SERIES, VOLUME 97, NO. 1 JANUARY 1, 1955

Pressure-Volume Isotherms of He^4 below 4.2°K . . . . . William E. Keller 1
Second Virial Coefficients of Helium from the Exp-Six Potential . . . . . John E. Kilpatrick, William E. Keller, and Edward F. Hammel 9
Experiments on the Behavior of an Ionized Gas in a Magnetic Field . . . . . Winston H. Bostick and Morton A. Levine 13
Thickness of the Helium Film as a Function of Height . . . . . Lothar Meyer 22
Flow of Helium II through Narrow Slits . . . . . R. T. Swim and H. E. Rorschach, Jr. 25
Double Scattering of Electrons with Magnetic Interaction . . . . . H. Mendlowitz and K. M. Case 33
Infrared Lattice Absorption in Ionic and Homopolar Crystals . . . . . Melvin Lax and Elias Burstein 39
Soft X-Ray Absorption of Evaporated Thin Films of Tellurium . . . . . Robert W. Woodruff and M. Parker Givens 52
Domain Rotation in Nickel Ferrite . . . . . Fielding Brown and Charles L. Gravel 55
Magnetic Rotation Phenomena in a Polycrystalline Ferrite . . . . . David Park 60
Effect of Strong Electrostatic Fields on the Resistance of Tungsten Wires in High Vacua . . . . . W. J. Dunhotels and A. H. Weber 66
Empirical Relation between Superconductivity and the Number of Valence Electrons per Atom . . . . . B. T. Matthias 74
Paramagnetic Resonance Absorption in Praseodymium Trichloride . . . . . John H. Anderson and Clyde A. Hutchison, Jr. 76
Macroscopic Aspects of Neutron Interaction in Magnetics . . . . . Louis Gold 79
Energy Distributions of Field Dependent Secondary Electrons . . . . Frank A. Brand and Harold Jacobs 81
Microwave Spectra of Tritium Iodide and Tritium Bromide . . . B. Rosenblum and A. H. Nethercot, Jr. 84
Age of Meteorites by the $A^{40}-K^{40}$ Method . . . . . G. J. Wasserburg and R. J. Hayden 86
Long-Lived Isomer of Np^{236} . . . . . M. H. Studier, J. E. Gindler, and C. M. Stevens 88
Coulomb Excitation of Neodymium . B. E. Simmons, D. M. Van Patter, K. F. Famularo, and R. V. Stuart 89
Radioactivity of In^{117} and Sb^{117} . . . . . Carl L. McGinnis 93
Decay Scheme of the Mirror Nucleus P^{33} and Related Results . . . . . H. Roderick, O. Lönsjö, and W. E. Meyerhof 97
Half-Life of Yttrium-90 . . . . . Herbert L. Volchok and J. Laurence Kulp 102
Energy Levels of Hf^{179} . . . . . P. Marmier and F. Boehm 103
Angular Distribution of Gamma Rays from Proton Capture in B^{11} . . . . . H. E. Gove and E. G. Paul 104
Electron-Neutrino Angular Correlation in the Beta Decay of $Neon^{19}$ . . . . . D. R. Maxson, J. S. Allen, and W. K. Jentschke 109
Studies on the Isomeric Pair, Nb^{93m} and Nb^{93} . . . . . Hirdaya B. Mathur, Earl K. Hyde, Charles A. Levine, and Per K. Kofstad 117
Decay of V^{49} . . . . . W. S. Lyon 121
Independent-Particle Model and the Nuclear Photoeffect. II . . . . . J. S. Levinger 122
Angular Distribution of Protons from the Reaction $Ti^{48}(d,p)Ti^{49}$ . . . . . William W. Pratt 131
Numerical Calculation of (d,p) Angular Distributions . . . . . W. Tobocman and M. H. Kalos 132
Neutrinos from the Sun . . . . . A. M. Cormack 137
Summing Studies of the Gamma Rays Following the Decays of Be^{7}, Se^{75}, and Eu^{152} . . . . . D. C. Lu, W. H. Kelly, and M. L. Wiedenbeck 139
Gamma and X-Radiation in the Decay of Am^{241} . . . H. Jaffe, T. O. Passell, C. I. Browne, and I. Perlman 142
Mean Free Path for Shower Production by High-Energy Pi Mesons . . . Fritz E. Froehlich and Kurt Sitte 151
Penetrating Showers in Light and Heavy Elements . . . . . Joseph G. Ashworth and Kurt Sitte 159
Electron Production in High-Energy Nuclear Interactions . . . . . Kurt Sitte, Fritz E. Froehlich, and Irving Nadelhaft 166
Cloud-Chamber Study of Cosmic-Ray Air Showers at Sea Level . . . . . Kenneth E. Reif 172
A^3 Production in Nuclei . . . . . Robert Jastrow 181
Cross Sections for Producing High-Energy Neutrons from Carbon Targets Bombarded by Protons, Deuterons, and He^3 Particles . Larry Schecter, Walter E. Crandall, George P. Millburn, and John Ise, Jr. 184
Photoproduction of π^0 Mesons from Protons . . . Y. Goldschmidt-Clermont, L. S. Osborne, and M. Scott 188
Analysis of a High-Energy Cosmic-Ray Shower. I. Soft Component and Trident Process . . . . . M. Koshiba and M. F. Kaplon 193
Direct Detection of Soft Radiation above 50 Kilometers in the Auroral Zone . . . . . L. H. Meredith, M. B. Gottlieb, and J. A. Van Allen 201
Cosmic-Ray Studies of Penetrating Showers and Bremsstrahlung at 11 200 Feet by Using Plastic Scintillation Counters . . . . . C. N. Chou and Marcel Schein 206
New Formulation of the General Theory of Relativity . . . . . G. Szekeres 212
Collision Matrices for the Compound Nucleus . . . . . R. G. Thomas 224

(*continued on cover three*)

LANCASTER PRESS, INC., LANCASTER, PA.